THE PETROLOGICAL EVOLUTION OF THE LATE PALEOZOIC A-TYPE GRANITES OF THE COBEQUID HIGHLANDS, CANADA

by

Angeliki Papoutsa

Submitted in partial fulfilment of the requirements
for the degree of Doctor of Philosophy

at

Dalhousie University
Halifax, Nova Scotia
May 2015

TABLE OF CONTENTS

LIST OF TABLES

LIST OF FIGURES

ABSTRACT

A-type granites comprise a distinct group of granitoid rocks the origin of which is well-debated. Their major alkaline characteristics are well-defined, however, little is known about the origins of the trace element and mineralogical variations they present. This thesis aims to determine the geological processes responsible for geochemical and mineralogical variations observed in the late Paleozoic A-type granites of the Cobequid Highlands. The eastern Cobequid Highlands contain complex plutons (Wentworth and Pleasant Hills) with calcic amphibole-bearing granites (calcic granites), whereas in the west, the North River and Cape Chignecto plutons contain only biotite-bearing granites. Sodic amphibole-bearing granites (sodic-granites) are found only in the Wentworth pluton.

The Wentworth calcic and sodic granites show systematic differences in whole-rock chemistry, ε_{Nd}, magmatic temperatures, volatile contents and viscosity of the melt and, therefore, indicate derivation from different sources. Similar systematic differences have been identified between the biotite and calcic granites on a regional scale and, therefore, the mineralogically different granite types are not comagmatic. The biotite and calcic granites were both derived by similar degrees of partial melting of the crust, with the calcic granite being formed under elevated temperatures. Chemical and isotopic variations between the biotite and calcic granites correspond with the contrasting character of the two Neoproterozoic crustal blocks in the area. The sodic granites are the extreme fractionates of a coeval mafic melt that was underplated during extension.

In post-magmatic stages the granites were affected by several events of hydrothermal alteration. Hydrothermal fluids repeatedly mobilized the REE from the granites, resulting in the formation of distinct hydrothermal assemblages that can be correlated with specific types of hydrothermal alteration and the evolution of the shear zone. Regionally, precipitation of REE increases with time as the fluids became progressively more oxidizing and Fe-rich. The highest REE concentrations are found close to the Cobequid Fault and are possibly associated with a ca 320 Ma IOCG mineralizing event.

The early crustal evolution of Avalonia is further reviewed and new paleoreconstruction models are proposed over the last billion years. This may have implications on the current concepts of “proto-Avalonia” and engage new future research.

LIST OF ABBREVIATIONS USED

a.p.f.u.	atoms per formula unit
ACNK	Al_2O_3/ ($CaO+Na_2O+K_2O$)
Aln	Allanite
Amp	Amphibole
An	Anorthite
And	Andradite
ANK	Al_2O_3/ (Na_2O+K_2O)
Arf	Arfvedsonite
ASI	Aluminum Saturation Index
b.d.	below detection limit
Bar	Barite
BSE	Back-Scattered Electron
Bt	Biotite
CAB	Calc-Alkaline Basalt
Cal	Calcite
CAM	Cambrian
CARB	Carboniferous
CCP	Cape Chignecto pluton
Cer	Cerianite
Cher	Chernovite
Chl	Chlorite
CHUR	Chondrite Uniform Reservoir
Crs	Coarse-grained

DCHZ	Deep Crustal Hot Zone
DEV	Devonian
DMM	Depleted mantle
DR	Debert River pluton
EDI	Ediacaran
EDS	Energy Dispersive Spectrometry
EM	Enriched Mantle
EMB	Eight Mile Brook pluton
Ep	Epidote
Eqgrnr	Equigranular
Fe-actin	Ferro-actinolite
Fe-eck	Ferro-eckermannite
Fe-ed	Ferro-edenite
Fe-richt	Ferro-richterite
Fe-winch	Ferro-winchite
FGL	Frog Lake pluton
FLG	Fountain Lake Group
Fn	Fine-grained
FOZO	Focal Zone mantle reservoir
Fsp	Feldspar
GB	Gain Brook pluton
Gbr	Gabbro
Gr	Granite
Grnlr	Granular
Grnph	Granophyric

GSB	Gunshot Brook pluton
GSC	Geological Survey of Canada
Hbl	Hornblende
HFSE	High Field Strength Elements
HG	Horton Group
HIMU	High-μ mantle
Hing	Hingganite
HP-LT	High pressure-Low temperature
HREE	Heavy Rare-Earth Elements
Hy-bas	Hydroxylbastnäsite
IAT	Island Arc Tholeiite
ICP	Ion Coupled Plasma
ICS	International Commission of Stratigraphy
Ilm	Ilmenite
INAA	Instrumental Neutron Activation Analysis
IOCG	Iron oxide-Copper-Gold
LOI	Loss On Ignition
LREE	Light Rare Earth Elements
Mag	Magnetite
MALI	Modified Alkali-Lime Index
MCS	McCallum Settlement pluton
ME	Mount Ephraim pluton
Med	Medium-grained
MORB	Mid-Ocean Ridge Basalt
NRP	North River pluton

OFB	Ocean Floor Basalt
OIA	Ocean Island Alkali basalt
OIT	Ocean Island Tholeiite
ORD	Ordovician
Par	Parisite
PHP	Pleasant Hills pluton
Plg	Plagioclase
PM	Polson Mountain pluton
PREMA	Prevalent Mantle
Py	Pyrite
Pyr	Pyrochroite
QFM	Quartz-Fayalite-Magnetite buffer
Qz	Quartz
RBF	Rockland Brook Fault
Rbk	Riebeckite
REE	Rare Earth Elements
SAMBA	South America-BAltica
SEM	Scanning Electron Microscope
SHRIMP	Super High Resolution Ion Microprobe
SIL	Silurian
SMB	Six Mile Brook pluton
Syn	Synchysite
Thr	Thorite
Ti-min	TiO_2 mineral
Tit	Titanite

UTM	Universal Transverse Mercator coordinate
WDS	Wavelength Dispersive Spectrometry
WP	Wentworth pluton
Zrn	Zircon

ACKNOWLEDGEMENTS

It would be impossible for me to complete this thesis without the support and contribution of several people. First of all, I would like to thank my supervisor Georgia Pe-Piper for allowing me to work on this fascinating project. I will never forget her support and constant dedication to my academic development and well-being. I would also like to thank David Piper for his invaluable help during fieldwork, his advice during manuscript preparations, and critical reviews that challenged me to do my best all these years. Sincere thanks to Yana Fedortchouk and Nick Culshaw for all their guidance and feedback as members of my supervisory committee. I am grateful to Dr Rebecca Jamieson and Dr Richard Cox for participating in my examining committee and also Dr Nelson Eby for agreeing to be my external examiner. Their insightful comments greatly improved this thesis.

I am grateful for all the support I received from the faculty members from the Department of Earth Sciences in Dalhousie University, and the Department of Geology in Saint Mary's University. I would also like to thank Dan Macdonald for his assistance during the electron microprobe analyses at Dalhousie University, and Xiang Yang for his support while I used the Scanning Electron Microscope at Saint Mary's University. I will always appreciate the guidance I received from Randolph Corney while I used several pieces of equipment in the Department of Geology, and during sample preparation. Also I would like to thank Howard Donohoe and Yuanyuan Zhang for all the interesting and informative conversations we had all these years.

I must thank the Editors and reviewers for their contributions on the publications included in this work. Thank you Laurie Reisberg (ed), Sylvio Vlach, and Brendan Murphy for editing and reviewing my work in Chemical Geology. I greatly appreciate the contributions of Lee Groat (ed), Kathryn Goodenough, and the anonymous reviewer from Canadian Mineralogist. I am grateful to Christian Koeberl (ed), Greg Shellnutt, and Bernard Bonin from Geological Society of America Bulletin for their helpful comments that will definitely improve my submitted work.

My research was funded mainly by a NSERC Discovery Grant to my supervisor Georgia Pe-Piper, but I was also financially supported by the Faculty of Graduate Studies at Dalhousie University.

Finally I would like to thank my family and my friends in Canada and Greece. I feel blessed to be surrounded by people who love and supported me throughout my studies, and helped me to achieve my goals.

CHAPTER 1 INTRODUCTION

The granitoid rocks have been extensively studied in igneous petrology since they provide evidence of continental crustal growth and are closely related to geodynamics. Chappell and White (1974) proposed the first "genetic alphabet" classification scheme, in which all granites can be classified into four major types related to specific conditions of crustal formation. These proposed granitic types, which were different in terms of composition and magmatic sources (Table 1.1), included the S-type (sedimentary protolith- peraluminous composition), I-type (igneous protolith- metaluminous composition), M-type (mantle conditions – calc-alkaline chemistry), and a fourth alkaline type. No letter was attributed to the latter at the time, but it included alkaline granites enriched in incompatible elements. It was suggested that a probable source was a crustal residue from a previous event of partial melting and that these granites "are always formed late in the history of a fold belt". Thus, the alphabet classification scheme was originally based predominantly on geochemical criteria. Soon after the pioneering work of Chappell and White (1974), Loiselle and Wones (1979) related the fourth granitic type to rift zones and generation within stable continental blocks. They proposed the letter "A" for this granitoid group and the term "A-type" was, therefore, established predominantly due to their anorogenic affinity.

The mainly tectonic affiliation of the term "A-type" was a deviation from the original concept of "genetic alphabet" classification scheme which was based predominantly on geochemical characteristics and magmatic sources (Table 1.1). Furthermore the I-, S-, and M-types were all associated only with crustal formation. Although M-type is often confused as "mantle-derived", its original definition

Table 1. 1 Mineralogical and geochemical criteria for the alphabet classification scheme for granites.

Granite type	Characteristic minerals	Geochemical features	Magma sources
S	cordierite, garnet, muscovite, biotite	Peraluminous	Meta-sedimentary sequences
I	hornblende	Metaluminous	Igneous crustal rocks
M	hornblende	Calc-alkaline, volcanic arc signature	Subducted oceanic crust
A*	arfvedsonite, aegirine, hornblende biotite	Alkaline, within-plate affinities	fractionation of mafic melts, partial melting of granodiorite/ tonalite, granulitic residue from previous melting event

Notes: * A-type term was not introduced with the original classification scheme.

referred to "crustal sources associated with mantle conditions", such as melting of subducted oceanic crust. As stated in the submitted abstract of Chappell and White (1974) "The chemical composition of granites precludes the possibility of direct mantle derivation". One of the proposed origins of A-type granites was the fractionation of alkali basalts (Loiselle and Wones, 1979) and, therefore, this granitoid group was not of a strictly crustal origin, a further deviation from the original concept of the alphabet classification scheme. Despite their original definition, A-type granites now include not only anorogenic but post-orogenic rocks as well (Maniar and Piccoli, 1989; Creaser et al., 1991), a fact that led researchers to propose a geochemical classification of these rocks instead of a tectonic one (e.g. Whalen et al., 1987, Fig 1.1).

Frost and Frost (2010) proposed the term "ferroan" instead of "A-type", since in the literature the majority of the described A-type granites, from different tectonic settings, are ferroan rocks. Several petrogenetic models have been proposed in the past

decades for these granitoids, and as a result, the term itself and the origin of A-type granites became the subject of one of the biggest debates in igneous petrology.

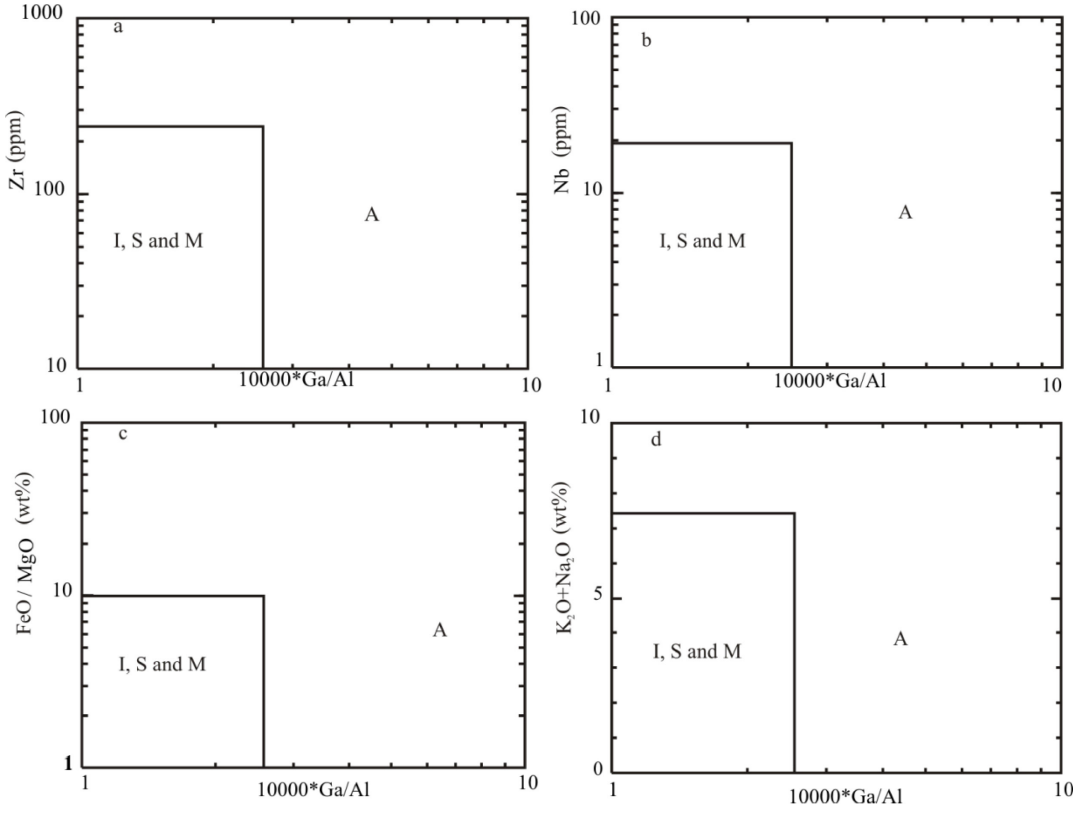

Chapter 1. 1 Geochemical classification of the S-, I-, M-, and A-type granites according to Whalen et al. (1987).

1.1 THEORETICAL BACKGROUND OF A-TYPE GRANITES

The term "A-type granite" initially referred to granites that were generated along continental rift zones with mildly alkaline geochemistry and crystallized under low water fugacities (Loiselle and Wones, 1979). The fact that this type of granite is richer in Fe, K, rare metals and REE compared to other type of granites (Fig. 1.1) implies a distinctive petrogenesis. The first petrogenetic model suggested that A-type granites derive from fractionation of mantle-derived alkali basalt with or a without crustal contribution. When a crustal source was involved, it was hypothesized to be anhydrous granulitic lower crust

(Collins et al., 1982). The A-type granite group was further proposed to be a highly fractionated subgroup of I-type granites (Whalen et al., 1987).

Creaser et al. (1991), however, demonstrated that partial melting of granulitic crust cannot produce A-type magmas, because such a melt would be depleted in Si, Fe and K and enriched in Ca and Al compared to the protolith; such geochemical features are not found in A-type granites. Partial melting of tonalitic to granodioritic crust, instead, can produce A-type magmas (Creaser et al., 1991; Frost and Frost, 2010). Experimental results suggest that the dehydration melting of calc-alkaline granitoids in the shallow crust gives rise to A-type granitic melts (Patiño-Douce, 1997). The high temperatures required for such melting imply the involvement of hot mafic magma close to the Earth's surface, which can also have a chemical contribution (Patiño-Douce, 1997). Metaluminous A-type granites can also form by differentiation of a tholeitic basalt magma, whereas peralkaline granites may form by differentiation of transitional and alkali basalt (Frost and Frost, 2010).

A-type granites, although they have specific chemical characteristics, may present important mineral variations. The major mineralogical diversity observed in A-type granites worldwide is that of primary ferromagnesian minerals hosted in these rocks. These granitoid rocks may contain biotite, amphibole and/or clinopyroxene of varying compositions, that led researchers in the last few years to identify contrasting A-type associations and magmatic conditions in alkaline provinces (Gualda and Vlach, 2007; Shellnutt and Iizuka, 2011).

A-type granites are related to mineralization of REEs and rare metals such as Nb, Y, Ta, Th and U (Schmitt et al., 2002). However, the conditions under which these

mineral deposits formed are still poorly understood. The development of a magmatic model that could explain the enrichment of A-type granitic magmas in these metals could give an economic potential to the study of these rocks.

1.2 STATEMENT OF THE PROBLEM

A large number of different geological processes and origins have been attributed to the formation of the A-type granites, and the mineralogical diversity in these rocks appears to be potentially of great importance for understanding their petrogenesis. The main purpose of this thesis is to investigate mineralogical and geochemical variations observed in A-type granites and correlate them with specific magmatic processes and sources, thus providing further insight to their complicated petrogenesis, which has been the subject of debate for years. Furthermore, this work aims to correlate the petrogenesis of these rocks with the evolution of the crust, and its structure as the result of its previous tectonic history.

The Cobequid Highlands in Nova Scotia provide a unique opportunity for such a study. A large number of coeval A-type granite plutons were emplaced along the active faults of a developing shear zone in the late Paleozoic. These granitic plutons were emplaced under the same regional tectonic regime, which is well understood, and although they have similar overall geochemistry, they present important differences in mineralogy and trace element geochemistry. The Wentworth pluton is richer in Zr, Nb and Y than the other plutons, whereas the North River pluton appears to be the most depleted in these elements. The A-type granites of the area also present a distinct bimodality in Mg, a trend that is observed principally in the Pleasant Hills and

Wentworth plutons, and is best defined in the latter (Fig. 1.2). This bimodality is not the result of post-magmatic alteration and represents a primary feature of these rocks.

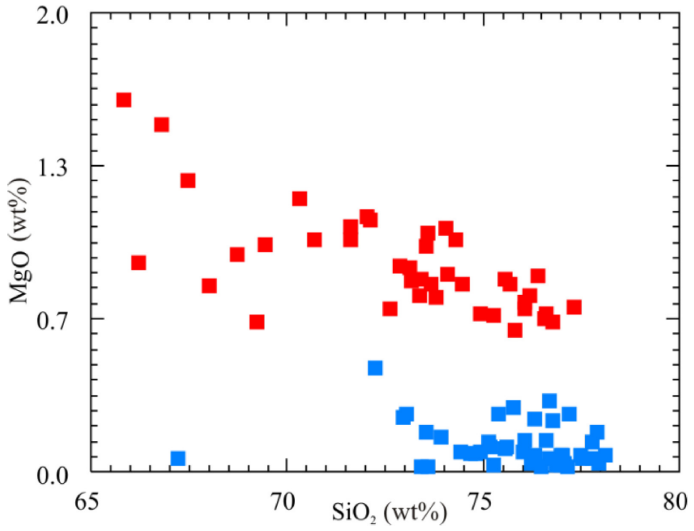

Figure 1. 2 Harker-type diagram showing the bimodal distribution of Mg in the granites of the Wentworth pluton (Papoutsa, 2012).

In terms of mineralogical composition, the Pleasant Hills and the Wentworth plutons are the only intrusions in which the granites contain amphibole as ferromagnesian phase (Pe-Piper et al., 1998a; Pe-Piper, 2007), whereas the majority of the A-type granites of the other Late Paleozoic plutons contain principally biotite (Pe-Piper, 1991; Pe-Piper, 1995b). Furthermore, the granites of the Wentworth Pluton are the only ones regionally that contain sodic amphibole as a primary magmatic phase (Pe-Piper, 2007). In the same intrusion a complete sequence of REE-Nb-Y minerals from magmatic to hydrothermal stages has been identified (Papoutsa and Pe-Piper, 2013). However, no similar work has been done on the other plutons of the shear zone.

Certain questions arise when it comes to a correlation between mineralogy and geochemistry. Geochemically all the late Paleozoic plutons of the Cobequid Shear Zone show, in general, the same alkalinity ranging from peralkaline to peraluminous (Pe-Piper

and Piper, 2003), however it is only the Wentworth Pluton that contains alkali minerals such as sodic amphibole (Pe-Piper, 2007). The cause for the apparent bimodality of Mg and the reason why this is the only element that presents such a trend is not understood. The REE-Y-Nb enrichment of A-type granites is considered one of the primary diagnostic features of these rocks and has been commonly used in the classification of these rocks (Eby, 1992; Whalen et al., 1987). However, there is no clear correlation between whole-rock geochemistry and the mineralogy of REE-host phases that could shed light into the exact nature and conditions of this enrichment.

The mineralogical diversity of the A-type granites in the Cobequid Highlands may, thus, reflect a rather complex magmatic system, providing the opportunity to investigate the impact of source heterogeneity and contrasting magmatic conditions on the mineralogy of the A-type granites, with limited control of tectonic variations. Such a study would provide further insight into the origin of some primary mineralogical features of A-type granites, and lead to a better understanding of their petrogenesis.

1.3 GEOLOGICAL SETTING

1.3.1 COBEQUID HIGHLANDS

The Cobequid Highlands are located in the Avalon terrane of the Canadian Appalachians, just north of the Cobequid Fault, which separates this terrane from the Meguma terrane (Fig. 1.3). The late Paleozoic plutons and their extrusive equivalents in the Cobequid Highlands are underlain by Neoproterozoic rocks, minor Silurian to Lower Devonian sedimentary rocks(Pe-Piper and Piper, 2003). Within the Cobequid Highlands the Cobequid Shear Zone consists of a series of late Paleozoic faults that were active

during latest Devonian to earliest Carboniferous (Pe-Piper and Piper, 2003). The main faults within theCobequid Shear Zone (Kirkhill, Rockland Brook and Portapique faults) are sub-parallel to each other and to the Cobequid fault, while second order shear zones form splays (Pe-Piper and Piper, 2003). This fault system continues northwestward to the Hollow Fault in the Antigonish Highlands and the fault zone along the northwestern coast of Cape Breton Island (Fig. 1.3). The faults of the Cobequid Shear Zone merge to the southwest with the Cobequid-Chedabucto fault zone, which was initiated in the late Carboniferous and marks the northern limit of the Minas basin (Mawer and White, 1987; Pe-Piper and Piper, 2003). The late Paleozoic plutons were emplaced along the faults of the actively deforming Cobequid Shear Zone and consist mainly of granitic and gabbroic bodies (Fig. 1.3).

In the late Devonian, the Rheic Ocean was subducted beneath Nova Scotia producing the voluminous South Mountain Batholith and satellite plutons (Clarke et al., 1997). Towards the end of the Devonian, incipient closure of the Rheic Ocean at promontories led to orogen-parallel dextral strike slip faulting (Hibbard and Waldron, 2009), resulting in distributed extension in the Magdalen Basin (Fig. 1.3) as a step-over zone. Crustal thinning continued through at least the early Carboniferous, accompanied by underplating of a thick gabbroic layer beneath the Gulf of St Lawrence (Marillier and Verhoef, 1989; Marillier and Reid, 1990). It is suggested that this magma reached the surface through the basin-margin faults to give flood basalts >1 km thick in the Fisset Brook Formation of western Cape Breton Island and the Fountain Lake Group of the Cobequid Highlands (Pe-Piper and Piper, 1998a).

All late Paleozoic granites in the Cobequid Highlands have A-type affinities, whereas the gabbros are ferro-gabbros. Synchronous with the plutons are the bimodal volcanic rocks of the Fountain Lake Group that show similar chemical affinities with their intrusive equivalents (Dessureau et al., 2000; Pe-Piper and Piper, 2003).

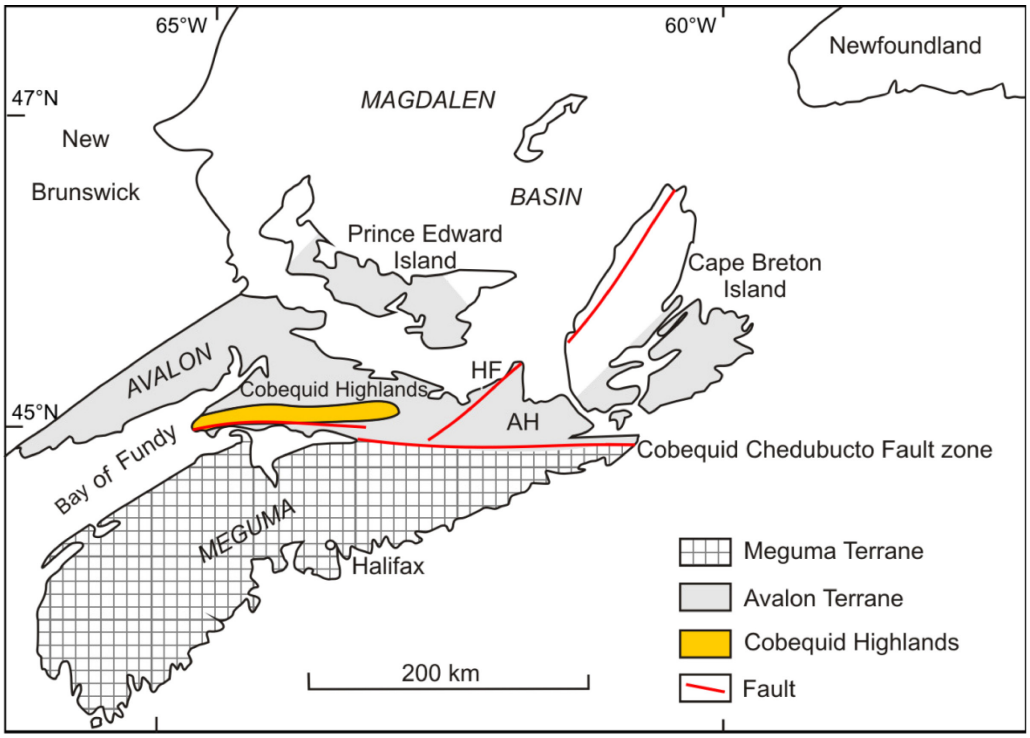

Figure 1.3 Simplified geological map of the Canadian Maritimes showing the location of the Cobequid Highlands, the Avalon and Meguma terranes and the Magdalen basin (modified from Pe-Piper and Piper, 2003). HF= Hollow Fault, AH= Antigonish Highlands.

1.3.2 AVALONIAN COUNTRY ROCK

The Avalonian crust, exposed as the basement rocks in the Cobequid Highlands, may represent the lower-crustal rocks that had potentially been involved in the petrogenesis of the late Paleozoic A-type granites. The Avalon terrane of the northern Appalachians in mainland Nova Scotia is characterized by Neoproterozoic (653-570 Ma) arc-related sequences, uncomformably overlain by thin lower Paleozoic supracrustal

rocks (Murphy and Nance, 2002). This terrane comprises a series of collisional blocks including I-type plutons, coeval volcanic rocks, minor oceanic crust and clastic sedimentary successions (Pe-Piper and Murphy, 1989; Murphy, 2002).

In the Cobequid Highlands, the Neoproterozoic basement has been divided into two major blocks, separated by the Rockland Brook fault (Pe-Piper and Piper, 2003). To the north lies the Jeffers Block, whereas the Bass River Block is located just south of the Rockland Brook fault (Fig. 1.4). The Rockland Brook fault appears to be a reactivated Neoproterozoic fault (Pe-Piper and Piper, 2003) and is considered to represent a structural front, the straight segments of which define a steep, parallel-walled ductile shear zone (Miller, 1991).

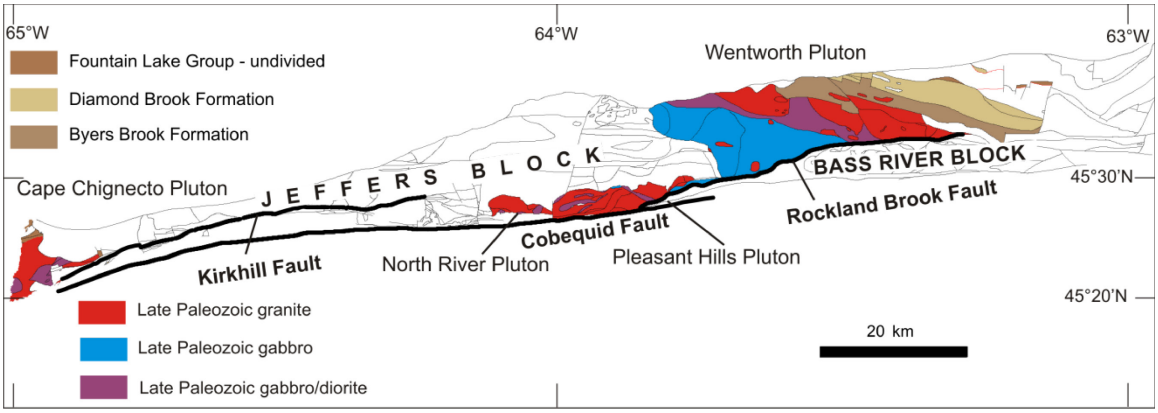

Figure 1. 4 Simplified geological map of the Cobequid Highlands showing the location of the studied plutons, major faults and the Neoproterozoic crustal blocks (modified from Pe-Piper and Piper, 2003).

The two Neoproterozoic blocks show differences in stratigraphy and radiogenic (Pb and Nd) isotope signature (Pe-Piper and Piper, 1998b; MacHattie and White, 2012). The Jeffers Block comprises a basement of Cryogenian greenschist to amphibolite facies gneisses, covered by late Neoproterozoic volcanic and volcaniclastic rocks, interbedded with sedimentary rocks, and with small high-level (Ediacaran-Ordovician) plutons. The

Bass River Block consists of a Tonian basement of greenschist- lower greenschist, platformal metasedimentary rocks and ocean floor metabasalts, and late Neoproterozoic (Ediacaran) plutonic rocks (Pe-Piper et al., 1996; MacHattie and White, 2012).

Lithostratigraphic correlations of volcanic and sedimentary rocks between the Cobequid and the Antigonish Highlands suggest that these two areas share the same basement and similar volcanic and depositional history (Murphy et al., 1991). It is therefore argued that the Cobequid and Antigonish Highlands were parts of the same volcanic arc during the Neoproterozoic. Furthermore, the Cobequid Highlands were juxtaposed against the Antigonish Highlands until early Carboniferous, before the 30 km dextral displacement on the Cobequid fault and the development of the Stellarton Basin (Murphy et al., 1991).

The Antigonish Highlands are representative of typical west Avalonian crust and provide a record of four major igneous events. The oldest episode is the 615 Ma igneous event which records early rifting, and resulted in the emplacement of mafic, intermediate and felsic rocks (Murphy et al., 2008). The second igneous event occurred in early Cambrian in a post-arc, transtensional setting, represented by bimodal volcanic and plutonic rocks (Murphy et al., 2008). Middle Ordovician magmatism in the Antigonish Highlands is expressed by bimodal alkaline magmatism that includes A-type granites and A-type rhyolites. The youngest magmatic episode occurred in middle Devonian after the collision of Avalonia with Laurentia and resulted in the extrusion of the McArras Brook basalts (Murphy et al., 2008).

The only recognized A-type granitic plutons in the Antigonish Highlands are, therefore, of Ordovician age. These granites are interpreted to have been derived from

crystal fractionation of a parent mafic magma and assimilation with crustal materials, during extension in an ensialic island arc regime (Escarraga et al., 2011).

1.3.3 PREVIOUS WORK ON THE LATE PALEOZOIC PLUTONS OF THE COBEQUID HIGHLANDS

The Cobequid Highlands comprise a large number of plutonic bodies with varying complexity. Specific late Paleozoic granitic plutons were selected for detailed study throughout the region, on the basis of variable petrology, distribution of igneous phases and relative age. The late Paleozoic plutons selected for this study are the Wentworth and Pleasant Hills plutons (complex intrusions with significant amounts of gabbro) in the eastern part, the North River pluton in the central part (small intrusion with minor gabbro), and the Cape Chignecto pluton in the western part of the Cobequid Highlands (granite intrusion with moderate amounts of gabbro).

The Wentworth pluton is located just north of the Rockland Brook fault and consists of a zone of granite of different generations in its northeastern part, that has a gradational contact with a large gabbroic body in the southwestern part (Fig. 1.4) (Pe-Piper and Piper, 2003). At its northern edge, the Wentworth pluton intrudes Silurian country rock and is onlapped by Carboniferous sedimentary rocks (Koukouvelas et al.,2002). The main granite of the Wentworth pluton is an alkali-feldspar granite that is found is outcrops of hundreds of meters within the pluton. Fine-grained granite and porphyritic rhyolite occur as E-W striking sheets tens to hundreds of metres wide in the eastern part of the pluton (Pe-Piper, 1998). The pluton has an ESE-striking contact with coeval volcanic rocks of the Byers Brook Formation (Fig. 1.4). The transition from granite to Byers Brook rhyolite is represented by sheets of homogeneous very fine-

grained granite and porphyritic rhyolite exposed at the western part of the Wentworth pluton. These are locally flow banded and interlayered with minor volcaniclastic sedimentary rocks and basalt flows (Pe-Piper, 1998). The main granite of the Wentworth pluton is in places intruded by gabbro bodies with chilled margins. The gabbro is younger (357±4 Ma, Table 1.2) than most mafic intrusions in the Cobequid Highlands and post-dates the emplacement of most Wentworth Pluton granites (362±2 Ma, Table 1.2). In the transition zone between the gabbro and the granite, the two lithologies show irregular, lobate contacts in which the gabbro is chilled against the granite (Pe-Piper, 1998). Late granites have lobate contacts with chilled margins against the gabbro, or occur as pods in the latter (Koukouvelas et al., 2002). A few contacts show mixing between the two magmas and the hybridized rocks appear inhomogeneous and have the composition of a granodiorite (Pe-Piper, 1998). Syn-magmatic deformation is observed through pre-crystallization fabrics where oriented feldspars were found in granodiorites close to the contact with the gabbro. Aplite veins are found throughout the pluton and crosscut all main lithologies (Pe-Piper, 1998).

The Pleasant Hills pluton (361 ± 2 Ma, Table 1.2) is located just southwest of the Wentworth pluton (Fig. 1.4).The southeastern margin of the Pleasant Hills pluton is in contact with the Rockland Brook fault whereas its southwestern part is just north of the Cobequid fault (Fig. 1.4). It is a composite intrusion consisting of gabbro, granodiorite and granites some of which are high-level porphyries (Pe-Piper et al., 1989). The pluton intrudes sedimentary rocks of the synchronous Horton Group, Silurian sedimentary rocks and Neoproterozoic volcaniclastic rocks (Pe-Piper et al., 1998). Geochronological data (Table 1.2) suggest that the pluton was emplaced within a period of a few million years.

The granite and the gabbro in the Pleasant Hills pluton, however, appear to be of several generations, based on cross-cutting relationships (Pe-Piper and Piper, 1998a). The Pleasant Hills pluton is divided by a shear zone into a western and eastern part. The mafic rocks are dominant in the eastern part of the pluton and along the southern margin of the intrusion. The main body of the pluton is a coarse grained alkali-feldspar granite that shows locally rapakivi texture, elongate sub-parallel to the length of the pluton (Pe-Piper and Piper, 1998a). Finer-grained granite occurs mainly at the northern and northeastern parts of the pluton along with small bodies of gabbro that predate the granite. The main granite is cut by porphyritic rhyolite bodies at the northern part of the pluton (Pe-Piper and Piper, 1998a). Lobate contacts between granite and gabbro suggest contemporaneous emplacement. In the eastern part of the pluton, dominant gabbro is cut by the main coarse-grained alkali feldspar granite. Younger mafic dykes are common and are in places deformed with the granites, whereas aplite veins cut all other lithologies and are oriented in conjugate sets striking NE and NW (Pe-Piper and Piper, 1998a). The pluton was emplaced during dextral shear and along its southern margin planar mylonitic shear zones are deformed by ductile folds that have been interpreted as deep-level deformation (Koukouvelas et al., 2002). Younger movement of the Rockland Brook fault resulted in brittle deformation that overprints the ductile structures (Miller, 1991). Koukouvelas et al. (1996) interpreted that flat-lying planes that cut all the lithologies in the pluton as transtensional features. C-S structures and asymmetrical folds suggest a southward direction of movement. Syn-magmatic deformation was also observed at a microscopic scale where pre-full orientation of plagioclase in gabbros and granites is parallel to the

foliation of small granite dykes and overprinted by solid-state deformation of plagioclase and quartz (Koukouvelas et al., 1996).

The North River pluton (356 ± 17 Ma, Rb-Sr errorchron, Pe-Piper et al., 1989) is a small teardrop-shaped intrusion in the central part of the Cobequid Shear Zone, between the Rockland Brook and Kirkhill faults (Fig. 1.4). The long axis of the pluton is subparallel to the trace of the Cobequid fault and no more than 2 km away from it. The southern part of the North River pluton is pervasively fractured (Pe-Piper, 1991). The dominant igneous phase in the North River pluton is a coarse grained alkali feldspar granophyric granite that becomes finer grained equigranular or porphyritic, towards the margins of the intrusion (Pe-Piper, 1991). Gabbroic rocks in the North River pluton appear to predate the main granite, since the former is cut by the latter and the granite shows chilled margins against the gabbro. Coeval granite and gabbro, however, are observed in this pluton, in areas where the granite occurs as pods within the gabbro with evidence of hybridization (Pe-Piper, 1991). Late microgranite sheets and gabbro dykes cut other lithologies in the pluton and also the country rock. In the northern part of the pluton, south-dipping small granite dykes are isoclinally folded under ductile-solid-state conditions, indicating northward thrusting (Koukouvelas et al., 2002). Sigmoidal foliation planes that are at an angle to the rock foliation are interpreted as solid-state foliation while flame structures at the rim of mafic xenoliths suggest magmatic flow during NW thrust movements. Tension gashes in the granite that were created during that movement are filled with secondary epidote and quartz and are ductilely folded (Koukouvelas et al., 1996). Brittle deformation in the North River pluton is expressed by flat-lying E-W shear zones that are chatacterized by cataclastic zones in which the displacement of aplite

dykes suggests a displacement up to hundreds of metres top-to-south (Koukouvelas et al., 1996).

The Cape Chignecto pluton is located in the western part of the Cobequid Highlands (Fig. 1.4). It lies north of the Cobequid fault and west of the Kirkhill fault (Pe-Piper, 1995). The main phases of the pluton are a variably deformed, medium-grained alkali-feldspar pink granite and gabbro (Pe-Piper, 1995b). The gabbro may occur as small bodies or sheet-like intrusions in the granites and has a thickness of hundreds of metres along the southern margin of the pluton. Most contacts with granites are tectonized, however igneous contacts are present as well where the gabbro is chilled against the granite (Waldron et al., 1989). The presence of intermediate hybrid rocks indicates coeval emplacement of mafic and felsic magmas. The granites of the Cape Chignecto pluton show a variety of textures including equigranular, inequigranular, graphic, and granophyric. Locally, granites were found to contain miarolitic cavities, suggesting a rather shallow emplacement (Pe-Piper, 1995b). Late mafic sheets in granite have developed strong foliation parallel to their margins and contain elongated pods and lenses of fractured foliated granite (Waldron et al., 1989). Foliated mafic sheets to the north of the pluton appear to form an anastomosing network of subhorizontal orientation, while strongly foliated granites to the south show C-S structures indicative of N-vergent overthrusting on the subhorizontal to SE-dipping shear planes (Koukouvelas et al., 1996). Brittle fractures in the Cape Chignecto pluton are associated with hematite staining and green secondary biotite (Waldron et al., 1989). To the north of the pluton, foliations and lineations are weakly developed but mm-scale shear zones show intense mylonitic foliation. The orientation of these shear zones is variable but most of them dip E or SE.

The alkaline affinity of the late Paleozoic granites in the Cobequid Highlands has been interpreted as the result of magma genesis from partial melting of the lower crust during crustal extension (Pe-Piper et al., 1988; 1991; 1998). Pe-Piper et al. (1991) concluded that variations in trace elements such as Nb and Zn are related to variable conditions of partial melting. Variations in large ion lithophile elements (LILE) such as Th and Rb were taken to have been influenced by segregation during magma expulsion from a crystal mush during shear (Koukouvelas et al., 2002). In the Wentworth pluton, Pe-Piper (2007) examined the mineralogical variations of amphiboles and concluded that sodic amphiboles are dominant in the early granites of the Wentworth pluton, whereas calcic amphibole is present in most late granites. Therefore it was interpreted that anatexis of pre-existing granites by the intrusion of voluminous gabbro influenced the type of amphibole crystallized in the Wentworth pluton. In the same intrusion Papoutsa and Pe-Piper (2013) identified a paragenetic sequence of REE-Nb-Y-rich minerals from magmatic to hydrothermal stages, suggesting a post-magmatic mobilization of these elements. In the Pleasant Hills pluton Pe-Piper et al. (1998) concluded that the granites show an enrichment in high field strength elements (HFSE) and a decrease in Sr, Ba and Ca that was associated with probable fractionation of hornblende and calcic plagioclase. The main granite of the North River pluton, on the other hand, shows a distinct geochemical character in being less alkali than the rest of the plutons and has smaller concentrations of Nb, Y, Zr. However the high alkalies and SiO2 are still indicative of a subalkalic A-type granite (Pe-Piper, 1991).

Table 1. 2 Published geochronological controls for late Paleozoic magmatic and related post-magmatic events in the Cobequid Highlands.

Geological Unit	Mineral	Method	Age	Reference
Main magmatic phase				
Early granites of the Wentworth pluton	zircon	U-Pb	362±2	Doig et al. (1996)
	arfvedsonite	Ar-Ar	368±4	Pe-Piper et al. (2004)
Late granites (probable-syn gabbro granites)	arfvedsonite	Ar-Ar	356±3	Pe-Piper et al. (2004)
Wentworth gabbro	hornblende	Ar-Ar	357±4	Pe-Piper et al. (2004)
	biotite	Ar-Ar	353±2	Pe-Piper et al. (2004)
Byers Brook Formation (Upper)	zircon	U-Pb	358±1	Dunning et al. (2002)
Diamond Brook Formation (Upper)		palynology	348±3	Utting et al. (1989), Menning et al. (2006)
Diamond Brook Formation (Middle)	zircon	U-Pb	353±3	Dunning et al. (2002)
Diamond Brook Formation (Middle-Lower)		palynology	359±2	Martel et al. (1993)
Pleasant Hills pluton main granite	zircon	U-Pb	358±2	Doig et al. (1996)
Pleasant Hills pluton porphyritic rhyolite	zircon	U-Pb	356±3	Dunning et al. (2002)
Pleasant Hills pluton fine-grained granite	zircon	U-Pb	360±2	Dunning et al. (2002)
Pleasant Hills pluton- granodiorite	hornblende	Ar-Ar	358±4	Pe-Piper et al. (2004)
Pleasant Hills pluton- diorite	hornblende	Ar-Ar	359±4	Pe-Piper et al. (2004)
Cape Chignecto pluton main granite	zircon	U-Pb	361 ±2	Doig et al. (1996)
Cape Chignecto pluton- rhyolite	zircon	U-Pb	355 ±2	Dunning et al. (2002)
Post-emplacement dated events				
Albitized granite, West Moose River pluton	hydrothermal riebeckite	Ar-Ar	353±4	Pe-Piper et al. (2004)
Deformed diorite, Cape Chignecto pluton, metamorphic biotite	biotized hornblende	Ar-Ar	347±3	Pe-Piper et al. (2004)
Altered diorite, southwestern Cape Chignecto pluton	low-Ti biotite	Ar-Ar	343±3	Pe-Piper et al. (2004)
Gneissose granodiorite south of the Rockland Brook fault	mixed hornblende-biotite separates	Ar-Ar	336-343 ±4	Pe-Piper et al. (2004)
Medium-grained diorite, Cape Chignecto pluton	hydrothermal biotite	Ar-Ar	342±3	Pe-Piper et al. (2004)
Lamprophyre dyke in the central Cobequid Highlands	whole-rock	Ar-Ar	334±3	Pe-Piper et al. (2004)
Lamprophyre dyke in the central Cobequid Highlands	green biotite	Ar-Ar	326±2	Pe-Piper et al. (2004)
Carbonate-suphide vein in Copper Lake deposit	pyrite	Re-Os	323±8	Kontak et al. (2008)
Altered siltstone adjacent to a carbonate-sulphide vein with intergrowths of hydrothermal muscovite and carbonate, Copper Lake deposit	hydrothermal muscovite	Ar-Ar	309.5 ±1.6	Kontak et al. (2008)

Notes: *: All Ar-Ar ages published prior 2008 have been corrected from the original data according to Kuiper et al. (2008), due to new intercalibrations in Ar-Ar dating.

1.4 OBJECTIVES AND THESIS ORGANIZATION

In order to understand the evolution of the late Paleozoic A-type granites in the Cobequid Highlands and their petrogenesis, this thesis is focused on specific mineralogical and geochemical differences, as discussed above. In this section the specific objectives of this thesis are described. This thesis is organized in a paper-based format and comprises three research manuscripts, presented in chapters 2-4.

1.4.1 CHAPTER 2

The origin of the variability in the Wentworth A-type granites is investigated in chapter 2. This chapter is entitled "*Geochemical variation of amphiboles in A-type granites as an indicator of complex magmatic systems: Wentworth pluton, Nova Scotia, Canada"* and a version of this chapter has been published as *Papoutsa, A., and Pe-Piper, G., 2014, Geochemical variation of amphiboles in A-type granites as an indicator of complex magmatic systems: Wentworth pluton, Nova Scotia, Canada: Chemical Geology, v. 384, p. 120-134*. This study investigates why the Wentworth granite has a bimodal abundance of Mg, and is, regionally, the only granite that contains both primary sodic and calcic amphiboles, and thus has more geochemical and mineralogical diversity than other plutons. Microprobe analyses of amphiboles were compared to the modal, whole-rock composition and Sm/Nd isotope data of the granites. Temperature (from zircon and amphibole), pressure (from amphibole), fluorine and water-in-melt contents have been calculated, to investigate the magmatic conditions. Correlation between whole-rock chemistry and modal composition revealed that the low-Mg granites are those containing sodic amphibole, whereas the high-Mg group includes granites with calcic amphiboles. Further systematic variations between the two groups are identified in terms of trace

element geochemistry, isotopes, and inferred magmatic conditions. The systematic differences between the granites indicate the presence of two magmatic systems in the Wentworth pluton. This study shows that a compositional variation in amphiboles of A-type granites can also result from the contribution of more than one magmatic source, not just extreme differentiation, and that the Wentworth magmatic system is more complex than previously proposed.

My contributions in this chapter include the development of the ideas presented, petrographic descriptions of the samples, mineral analyses, chemical modelling and interpretations. Geological maps and samples were provided by the co-author Georgia Pe-Piper. Furthermore as a co-author, she contributed in the writing of the manuscript by providing specific information and through constructive discussions that helped to develop the ideas presented.

1.4.2 CHAPTER 3

In chapter 3, the geochemical and mineralogical variations of the A-type granites from all studied plutons are examined in detail. This Chapter is entitled "*Systematic mineralogical diversity in A-type granitic intrusions: Control of magmatic source and geological processes"* and is currently in press in the Geological Society of America Bulletin. In this chapter, the ideas and hypotheses introduced for the Wentworth pluton are further tested in the A-type granites from all plutons, which are classified into mineralogical types according to the ferromagnesian mineral present. The whole-rock geochemistry, radiogenic and stable isotope chemistry, and estimates of magmatic parameters for these types are compared and evaluated. Systematic differences between these different types suggest that they do not have the same source. The origin of each

mineralogical type is approached by chemical modelling of partial melting and fractionation processes and potential magmatic sources are identified. As a result, a regional petrogenetic model is proposed that includes the variable modes of origins required for the late Paleozoic A-type granites of the Cobequid Highlands, by correlating specific geological processes with the observed variations in mineralogy and geochemistry.

My contributions in this chapter include the original development of the ideas presented regarding origins of the different granites, geochemical modelling and synthesizing a petrogenetic model. The co-authors Georgia Pe-Piper and David Piper provided all the geological maps, samples, and most whole-rock analyses. Furthermore, several discussions with the co-authors and their constructive comments helped to refine the proposed models and improve the presentation of the new ideas in this chapter.

1.4.3 CHAPTER 4

The REE-enrichment of the A-type granites is one of the most important diagnostic features that is often used as a petrogenetic indicator of these rocks but the correlation with the mineralogy of the granites, particularly in the Cobequid Highlands is not well established. In order to evaluate the nature and conditions of this enrichment, an understanding of the formation of the REE-hosting minerals present is necessary. In chapter 4 the petrographic study of REE-enriched samples from the Wentworth, Pleasant Hills, North River and Cape Chignecto plutons revealed that although the Wentworth pluton contains the highest amounts of primary REE-minerals (Papoutsa and Pe-Piper, 2013), the rest of the plutons record a predominantly hydrothermal enrichment. As described in the previous section, the A-type granites of the Cobequid Highlands show

strong deformation and fracturing close to the main faults. Therefore it is important to evaluate the conditions of REE-mobility in post-magmatic stages and investigate the effect of repeated hydrothermal activity on the mineralogy and geochemistry of the A-type granites. The chapter is entitled "*Variation of the REE-hydrothermal Circulation in Complex Shear Zones: The Cobequid Highlands, Nova Scotia"* and a version of this chapter has been published as *Papoutsa, A., and Pe-Piper, G., 2015, Variation of the REE-hydrothermal Circulation in Complex Shear Zones: The Cobequid Highlands, Nova Scotia: Canadian Mineralogist, v. 52, p. 943-968*. This study correlates the presence of specific hydrothermal REE-minerals with types of fractures, providing insight into the hydrothermal behavior of these elements. Furthermore, observations on textural relationships and the distribution of different fractures in the studied plutons provide information about the evolution of the regional hydrothermal system during the Carboniferous. A paragenetic sequence of hydrothermal REE-minerals is proposed and correlated with different dated hydrothermal events and the tectonic evolution of the Cobequid Shear Zone.

My contributions as a first author in this chapter, besides the writing of the manuscript, include the analytical work, mineral identification and interpretation, and the development of the ideas regarding the proposed paragenetic sequence of the minerals as well as the correlations with dated hydrothermal events. As a co-author, Georgia Pe-Piper provided the geological maps, samples, additional whole-rock analyses, as well as important information and comments about the geology of the study area that greatly helped the development of a model for the regional hydrothermal system.

An extension of this project includes a detailed petrographic study of fractured granites in the West Moose River pluton in the central Cobequid Highlands. In this pluton the hydrothermal precipitation of REE was studied in specifically selected fractured granites, and was correlated with the formation of associated late hydrothermal Fe-oxyhydroxides. This study has been published as "*Pe-Piper, G., Wisen, J., Papoutsa, A., Piper, D.J.W., 2015. Mineralisation of fractured granites along the Cobequid Fault Zone: West Moose River Pluton, Cumberland Co., Nova Scotia; Geological Survey of Canada, Open File 7759, 252 p.*" but is not included in this thesis.

1.4.5 CHAPTER 5

Besides the geochemical and mineralogical assessment of the A-type granites in an attempt to determine their genesis, it is equally important to understand the evolution of the lower crust since it played an important role in the petrogenesis of these rocks in terms of magmatic sources and crustal structure (faults and formation of deep crustal hot zones). Therefore the geological evolution of the lower crust must be evaluated as well. This chapter is entitled "*An evolutionary history of Avalonia: new insights from the Cobequid Highlands*". The data and the concepts of the petrogenesis of the A-type granites developed in this thesis can be used to constrain the geodynamic evolution of the deep crust in the Cobequid Highlands. The contrasting character of the Neoproterozoic basement in the two crustal blocks of the area is inherited by the late Paleozoic granites. In this chapter, the known geochemistry and stratigraphy of the Neoproterozoic basement in the Cobequid Highlands is reviewed and compared with other parts of the Avalon terrane. The correlations made between different areas are then used for paleogeographic and geodynamic reconstructions of Avalonia over the last billion years. Although the

modelling presented here may be a subject for future study and will be refined, it has implications for the early evolution stages of this terrane, and the current concept of "proto-Avalonia".

CHAPTER 2 GEOCHEMICAL VARIATION OF AMPHIBOLES IN A-TYPE GRANITES AS AN INDICATOR OF COMPLEX MAGMATIC SYSTEMS: WENTWORTH PLUTON, NOVA SCOTIA, CANADA

PREFACE

A version of this chapter has been published as: "Papoutsa, A., and Pe-Piper, G., 2014, Geochemical variation of amphiboles in A-type granites as an indicator of complex magmatic systems: Wentworth pluton, Nova Scotia, Canada: Chemical Geology, v. 384, p. 120-134".

2.1 ABSTRACT

The Wentworth pluton is the most complex intrusion among a series of A-type granitic plutons emplaced along an active shear zone in the Cobequid Highlands of Nova Scotia during the latest Devonian-earliest Carboniferous. This pluton consists of A-type granites of different generations and a large gabbroic body. Among all late Paleozoic plutons in the Cobequid Highlands, only the Wentworth granites contain both primary calcic (edenite, hornblende) and sodic (arfvedsonite) amphiboles. Whole-rock and mineral chemical data were examined along with estimated magmatic parameters, such as temperature, emplacement pressure, oxygen fugacity and volatile contents, in order to understand the geological factors responsible for this mineralogical variation. The granites with calcic amphiboles show systematically lower ε_{Nd} values, magmatic temperatures, and F-in-melt contents. All granites, however, appear geochemically homogeneous with limited evidence of fractionation. Specific chemical differences between these two types of granites indicate the presence of two coeval but distinct granitic systems in the Wentworth pluton. The granites with the calcic amphiboles formed from a geochemically less evolved, hydrous, relatively calcic melt, whereas the

granites with sodic amphiboles were derived from a relatively drier sodic melt, which had a larger mantle component and was enriched in F. Coexistence of these two magmas is indicated by the presence of interstitial sodic-calcic amphiboles in a late granitic dyke. This study provides evidence that in A-type granites extreme variation in the type of amphibole can be the result of a very complex magmatic history.

2.2 INTRODUCTION

Amphiboles are the major ferromagnesian phase in many igneous rocks. In A-type granites, the presence of amphiboles not only indicates derivation from hydrous melts but also is considered to play an important role in the geochemical evolution of the parent magma (Martin, 2007). Compositional variation of amphiboles in felsic rocks has been interpreted as the result of either magmatic crystallization or oxidative re-equilibration (Strong and Taylor, 1984). In peralkaline rocks, in particular, the magmatic trend of amphiboles is represented by a continuous change from katophorite through richterite to arfvedsonite, whereas the post-solidus oxidative trend is from actinolite towards riebeckite (Table 2.1).

Even though sodic amphiboles appear to be the dominant ferromagnesian minerals in many A-type granites (Wang et al., 2001; Schmitt et al., 2002; Ogunleye et al., 2005; Kinicky et al., 2011), calcic amphiboles are also present in several A-type granites (Han et al., 1996; Dall'Agnol et al., 1999; Wu et al., 2002). The presence of both sodic and calcic amphiboles in A-type granites in the same area has been reported in the literature (Han et al., 1997; Wu et al., 2002). In most cases the sodic amphiboles are found either in different plutons than the calcic amphiboles and belong to different ages

and tectonic regimes or they are found in the same intrusion as the result of fractionation of calcic-amphibole-bearing syenites (Han et al., 1996; Vlach and Gualda, 2007).

Table 2.1 Ideal chemical formulae of the types of amphibole mentioned in this work.

Amphibole mineral name	Type	Chemical formula
Ferro-edenite	Calcic	$NaCa_2Fe^{2+}_5Si_7AlO_{22}(OH)_2$
Ferrohornblende	Calcic	$\square Ca_2(Fe^{2+}_4(Al,Fe^{3+}))Si_7AlO_{22}(OH)_2$
Magnesiohornblende	Calcic	$\square Ca_2(Mg_4(Al,Fe^{3+}))Si_7AlO_{22}(OH)_2$
Ferro-actinolite	Calcic	$\square Ca_2Fe^{2+}_5Si_8AlO_{22}(OH)_2$
Actinolite	Calcic	$\square Ca_2(Mg,Fe^{2+}_{5)}Si_8AlO_{22}(OH)_2$
Richterite	Sodic-calcic	$Na(Ca,Na)Mg_5Si_8O_{22}(OH)_2$
Ferro-richterite	Sodic-calcic	$Na(Ca,Na)Fe^{2+}_5Si_8O_{22}(OH)_2$
Ferro-winchite	Sodic-calcic	$\square(Ca,Na)Fe^{2+}_4(Al,Fe^{3+})Si_8O_{22}(OH)_2$
Katophorite	Sodic-calcic	$Na(Ca,Na)Fe^{2+}_4(Al,Fe^{3+})Si_7AlO_{22}(OH)_2$
Barroisite	Sodic-calcic	$\square(Ca,Na)Mg_3AlFe^{3+}Si_7AlO_{22}(OH)_2$
Arfvedsonite	Sodic	$NaNa_2(Fe^{2+}_4Fe^{3+})Si_8O_{22}(OH)_2$
Ferro-eckermannite	Sodic	$NaNa_2(Fe^{2+}_4Al)Si_8O_{22}(OH)_2$
Riebeckite	Sodic	$\square Na_2(Fe^{2+}_3Fe^{3+})Si_8O_{22}(OH)_2$

Notes: □= vacancy in crystallographic site.

The Wentworth pluton in the Cobequid Highlands, in mainland Nova Scotia, belongs to a series of plutonic bodies which were emplaced along an active shear zone in the late Paleozoic (Pe-Piper and Piper, 2003). All late Paleozoic granites of the Cobequid Highlands have A-type affinities and similar major oxides compositions. The Wentworth pluton, however, is the only composite intrusion hosting both primary sodic and calcic amphiboles in different granitic bodies within the pluton (Pe-Piper, 2007). Previous mapping (Koukouvelas et al., 2002) showed that coeval sodic amphibole-bearing and calcic amphibole-bearing granites do not show a systematic distribution within the pluton.

Contrasting types of granites have been described in the literature from alkaline provinces. Gualda and Vlach (2007) reported the two mineralogically different, alkaline and aluminous associations of the felsic rocks in the Graciosa Province in Brazil. In the alkaline association, calcic amphibole occurs only in the alkali-feldspar and alkali-feldspar-quartz syenites, whereas peralkaline alkali-feldspar granites present a wide range of amphibole compositions, from sodic-calcic to sodic, and are related to the syenites through magmatic differentiation. The aluminous petrographic association contains metaluminous biotite granites with only calcic amphiboles in the less evolved varieties and with a narrow compositional range, suggesting contrasting sources between the two associations.

The amphiboles of the Wentworth pluton were studied by Pe-Piper (2007). The magmatic amphiboles include arfvedsonite (sodic) and edenite (calcic), whereas secondary amphiboles are represented by riebeckite (sodic) and actinolite (calcic). Even though there is a compositional variation in the amphiboles of this pluton, these minerals are not zoned. The lack of zoning was considered evidence of limited fractionation of the parental magma (Pe-Piper, 2007).

It is not clear why the Wentworth granites present such an extreme chemical variation of magmatic amphiboles, in a pluton with limited evidence of magmatic differentiation. Several factors can control the type of amphibole that will form, such as the composition of the magma, oxygen fugacity, temperature, pressure, and the presence or type of volatiles (Martin, 2007). The purpose of this study is to examine and evaluate the role of each of these factors on the composition of the amphiboles present, and

thereby provide insight into the geological history of this distinct and complex magmatic system.

2.2.1 REGIONAL GEOLOGY

The late Paleozoic Cobequid Highlands provide a record of a large scale alkaline magmatic event, which is spatially associated with strike-slip motion on the main faults of the coeval Cobequid Shear Zone (Pe-Piper and Piper, 2003). Underplating of mafic melts beneath the centre of the Magdalen Basin during the late Paleozoic has been inferred from seismic refraction and gravity data (Marillier and Reid, 1990) and is believed to be associated with the magmatism in the Cobequid Highlands (Piper et al., 1993). The underplating is spatially related to distributed regional extension and crustal thinning in the late Devonian and early Carboniferous between bounding master faults in southern New Brunswick in the west and in the Cobequid Shear Zone, western Cape Breton Island, and Newfoundland in the east (Fig. 2.1A) (Hibbert and Waldron, 2009).

A number of plutonic bodies and chemically equivalent extrusive rocks were emplaced along active faults of the Cobequid Shear zone within the Cobequid Highlands. These plutons, which vary in size and complexity, consist of granitic rocks with various amounts of coeval gabbro (Pe-Piper and Piper, 2003). The granites are mostly alkali-calcic to alkalic (using the classification of Frost et al., 2001), with geochemistry resembling A-type granites, whereas the mafic rocks are ferro-gabbros. The coeval volcanic rocks are rhyolites with chemistry similar to A-type granites and basalts with continental tholeiite chemistry (Pe-Piper and Piper, 2003). The Wentworth pluton is the largest and most complex of the plutons in the Cobequid Shear Zone, and is located in the eastern part of the Cobequid Highlands along with the nearby Pleasant Hills pluton (Fig.

2.1B). The Wentworth pluton is bounded by the Rockland Brook fault to the south, and consists of a major gabbroic body to the southwest, passing through a complex zone with gabbro and granite bodies to a granitic zone to the northeast. The gabbro is younger (357±4 Ma Ar-Ar on hornblende, Pe-Piper et al., 2004; Murphy et al., 2011) than the other mafic intrusions in the Cobequid Highlands and based on cross-cutting relationships, post-dates the emplacement of the main Wentworth granite (362±2 Ma U-Pb on zircon, Doig et al., 1996).

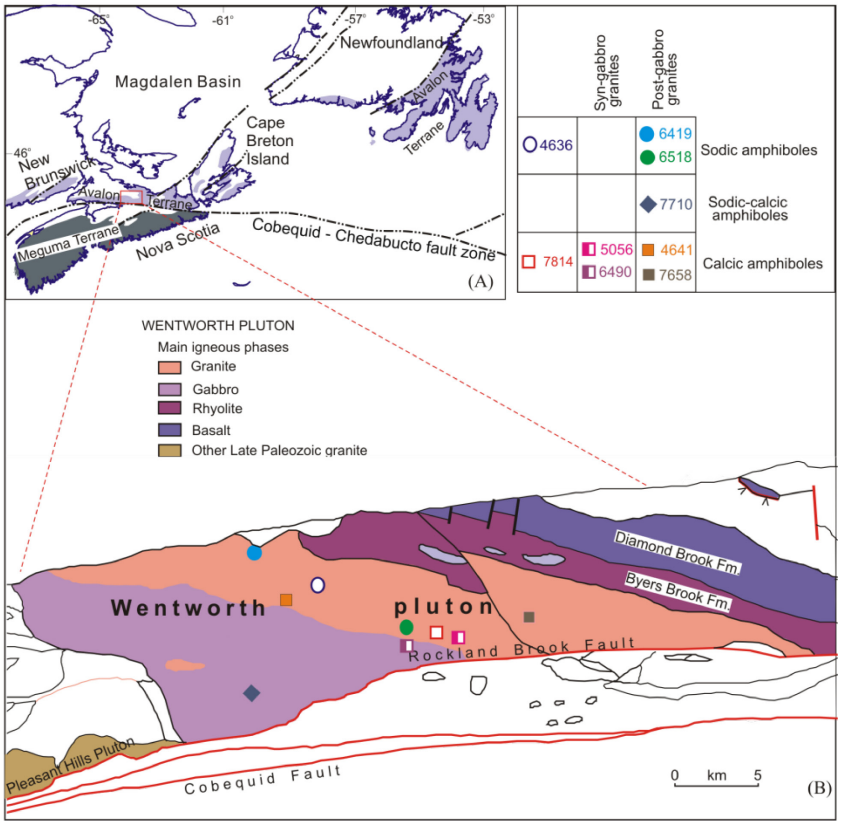

Figure 2. 1 Simplified maps (A) of eastern Canada showing the location of the Avalon and Meguma terranes and the Cobequid-Chedabucto fault zone and (B) the distribution of igneous phases and sample locations in the Wentworth Pluton (modified from Koukouvelas et al. 2002). Open symbols represent early granites, half-filled symbols are used for syn-gabbro granites, and post-gabbro granites are shown in filled symbols.

The late Paleozoic granites of the western part of the Cobequid Highlands are of similar age to the main Wentworth granite (Doig et al., 1996; Dunning et al,. 2002).

These granites contain biotite as their ferromagnesian phase, whereas the Pleasant Hills and Wentworth granites contain additional amphibole.

2.2.2 PREVIOUS WORK ON THE WENTWORTH GRANITES

The A-type granites of the Wentworth pluton, based on their field relationship with the gabbro, are classified either as early (predating the gabbro) or late granites (synchronous with or post-dating the gabbro). Syn-gabbro granites show lobate, mutually chilled contacts with gabbro, but previous studies have shown little evidence for geochemical exchange between the gabbro and the granite (Pe-Piper, 1998). Hybrid rocks formed by mixing and mingling of the mafic and felsic magmas are relatively uncommon. Mafic enclaves are common in the late granites, which commonly have sharp linear contacts with gabbro.

The early granite of the Wentworth pluton is mainly a K-feldspar-rich, medium-grained granite that contains sodic and calcic amphibole, has an average of 76% SiO_2, and relatively high F (up to 1600 ppm) (Koukouvelas et al., 2002; Pe-Piper, 2007). A few granites, interpreted as synchronous with the gabbro, occur as pods within the gabbro and are geochemically distinct, with a wide range of SiO_2 contents and have somewhat higher TiO_2 contents than the alkali granites of the early phase (Koukouvelas et al., 2002). The syn-gabbro and post-gabbro granites have lower concentrations of F than the early granites, a geochemical feature that is also reflected in the composition of the amphiboles. These subtle differences in the geochemistry of the late granites were interpreted by Koukouvelas et al. (2002) to have resulted from partial melting and remobilization of the early granite by heat from the gabbro.

2.3 SAMPLES AND METHODS

2.3.1 SAMPLE SELECTION AND CLASSIFICATION

The samples described in this study were selected on the basis of relative age, as deduced from field relationships, the type of amphibole present, and the availability of chemical and mineralogical data. The nine selected samples include two early granites (7814 and 4636), two syn-gabbro granites (6490 and 5056), and five post-gabbro granites (4641, 7658, 7710, 6419 and 6518). These samples are located on the 1:50000 scale geological maps of Pe-Piper and Piper (2005). Except for sample 5056, which appears to be of hybrid origin, all granite samples were collected away from gabbro contacts and their geochemistry shows no evidence of mixing with gabbro.

2.3.2 RADIOGENIC ISOTOPE ANALYSES

With the exception of sample 7814 for which Sm-Nd isotope data are reported in Pe-Piper and Piper 1998, all other samples have been analyzed for Sm-Nd isotopes for this study by Activation Laboratories Ltd. Rock powders for Sm-Nd isotope analyses were dissolved in a mixture of HF, HNO_3 and $HClO_4$. Before the decomposition sample was totally spiked with ^{149}Sm-^{146}Nd mixed solution. Rare earth elements were separated using conventional cation-exchange techniques. Samarium and Nd were separated by extraction chromatography on HDEHP covered Teflon powder. Accuracy of the measurements of Sm and Nd contents is ±0.5%. The $^{143}Nd/^{144}Nd$ ratios are relative to the value of 0.511860 for the La Jolla standard. Analyses were performed on Triton-MC mass-spectrometer.

2.3.3 OPTICAL MINERALOGY

The samples presented in this study were examined under the petrographic microscope, scanning electron microscope (SEM) and electron microprobe (EMP) for the determination of their mineralogy. The microscope used is a Nikon Eclipse E400 POL. Micro-pointcounting of the samples was performed using an automated stepping stage of Conwy Valley Systems and the acquired data were processed with the use of PETROG software for Windows. The density of the pointcounting grid and the distance between incremental movements of the stepping stage are automatically calculated by the operating program, based on the total surface of the thin section and the number of points to be counted. Selection of the number of points is based on the coarseness of the rock and the desired level of precision. Based on the grain size of these rocks (medium- to coarse-grained granites) a minimum of 300 points should be counted. The point counting runs in this study were, done with 300 and 1000 points. The difference in the occurrence of common minerals from the two runs was less than 2%, however, only the results of the 1000-point run are reported (Table 2.3), since the precision of the method increases with the number of points counted. No reference rocks were examined for comparison, however the results herein are comparable to those from other samples from the same pluton reported in Pe-Piper (1998), for which macro-pointcounting on stained slabs was employed.

2.3.4 EDS AND WDS CHEMICAL ANALYSES

All polished thin sections were carbon-coated and analyzed by energy dispersive spectroscopy (EDS). For these analyses, a LEO 1450 VP SEM scanning electron microscope was used, with a maximum resolution of 3.5 nm at 30 kV. The EDS, semi-

quantitative analyses were performed using an Oxford X-mac 80 mm^2 silicon-drift detector (SDD) with the X-ray production radius being less than 10 microns. Wavelength dispersive spectroscopy (WDS) geochemical analyses of the ferromagnesian minerals present, such as amphibole and biotite, were made using a JEOL-8200 electron microprobe with five wavelength spectrometers and a Noran 133 eV energy dispersion detector. The operating conditions were 15kV of accelerating voltage with a 20nA beam current, and a beam diameter of 1 micron. The crystals used for the analyses were the LIFH for Mn and Fe, PETJ for K, Cl, Ca and Ti, TAP for Al and Si, and the TAPH for F, Na and Mg. The standards used for the calibration of the instrument were sanidine (Al, K, and Si), pyrolusite (Mn), fluorapatite (F), kaersutite (Ca, Mg and Ti), tugtupite (Cl), jadeite (Na), and garnet (Fe). The raw data were corrected with the ZAF method for matrix effects (Armstrong, 1988). Calculation of amphibole formulas from electron microprobe data is challenging because of uncertainty in the oxidation state of Fe and Mn, as recently reviewed by Giesting and Filiberto (2014) and Locock (2014). Various normalization procedures are imprecise compared to the measured values of Fe3+ and Fe2+, but better than the default assumption of all Fe being either Fe2+ or $Fe3^+$ (Hawthorn and Oberti, 2007). The calculations follow Leake et al. (1997). All cations were initially normalized on the basis of 23 oxygens producing a formula where all iron is assumed to be ferrous. According to Leake et al. (1997), ferric iron may be estimated if the following conditions are met: a) Si $\leq$ 8 a.p.f.u., b) Σcat $\leq$ 16, and c) Σcat (excluding Na and K) $\leq$ 15 a.p.f.u. All these conditions are met for the amphibole analyses included in this study. The most widely used cation normalization procedure for estimating Fe3+ (Hawthorn and Oberti, 2007) is the 13eCNK method, in which 13 cations excluding Ca,

Na and K are assumed to fill the tetrahedral and octahedral sites. The 13eCNK method is specifically applicable to calcic and sodic amphiboles of the type found in this study (Giesting and Filiberto, 2014). This procedure was carried out using MINPET software for Windows (Richard, 1995). Amphibole nomenclature follows Leake et al. (1997); all names used in this study are retained in the newer nomenclature of Hawthorne et al. (2012).

2.3.5 ESTIMATE OF INTENSIVE CRYSTALLIZATION PARAMETERS

The temperature and pressure for the Wentworth granites have been estimated by the use of the zircon-saturation thermometer (Boehnke et al., 2013, Table 2.2), Al-in-hornblende thermobarometer (Anderson and Smith 1995, Table 2.2), and the amphibole thermometer of Ridolfi and Rinzulli (2012) (Table 2.2). This new zircon-saturation thermometer is a revised version of the Watson and Harrison (1983) calibration. This thermometer works under the principle that zircon solubility in crustal magmas is a simple function of temperature, and composition of the melt (both in terms of Zr, and alkalinity represented as the M-value). The use of this method requires the presence of magmatic zircon in the rocks, a composition of the melt that is within the calibration range (M-value from 1 to 2.2), and an accurate measurement of Zr in the melt (Boehnke et al., 2013). In the absence of in situ analyses on volcanic glass or melt inclusions, an approximation of the melt composition is through whole-rock analysis (Hanchar and Watson, 2003). Saturation of zircon in the Wentworth granites is indicated by the presence of magmatic zircon. Zircon grains in the Wentworth granites are found both as inclusions on major minerals and in between grains. Watson (1979) demonstrated that most magmatic accessory minerals tend to form along grain boundaries. The occurrence

of zircon, on the other hand, as inclusion in major minerals may be related to growth occlusion. The presence of magmatic zircon in the Wentworth granites is not only texturally inferred, but also suggested by geochronological data that demonstrate a zircon crystallization age similar to those for dated amphiboles (Dunning et al., 2002). Furthermore, based on their whole-rock composition, the Wentworth granites are mostly alkalic-calcic to alkalic rocks and well within the calibration range of this method, and thus the application of the zircon-thermometer was considered appropriate.

The hornblende thermometer of Rifolfi and Renzulli (2012) is used to determine the temperature at which the calcic amphiboles of the Wentworth granites crystallized. This internally consistent method relies solely on amphibole chemistry for which a series of thermobarometric equations are applied to retrieve not only temperature, but also pressure and water contents of the melt. The parameters of this method require the recalculation of the amphibole formula using the 13 cation (excluding Ca, Na and K) normalization. Temperature and pressure estimates may be considered reliable if they plot within the defined fields in the T-P diagrams proposed by Ridolfi and Renzulli (2012) (Appendix A.1). These equations are only applicable to euhedral, homogeneous crystals from either volcanic or plutonic rocks and are not recommended for hydrothermal amphiboles or disequilibrium compositions. As it is described in the next section, the calcic amphiboles of the Wentworth pluton satisfy both textural and chemical criteria of this method.

For the Al-in-hornblende thermobarometer to be applied, the mineral assemblage alkali feldspar + plagioclase + hornblende + biotite + iron oxide + titanite must be present and that requirement is satisfied in the granites of the Wentworth pluton. The hornblende

grains chosen had Al_2O_3 > 6 wt. %, more than 1.0 $Al_{(total)}$ a.p.f.u., and are in contact with quartz or K-feldspar. Anderson and Smith (1995) argued that Fe# is indicative of oxygen fugacity. Amphiboles with high Fe# ($Fe_T/(Fe_T+Mg)>0.65$) are indicative of low oxygen fugacity, and should be avoided for geobarometric calculations because they tend to yield anomalously high pressures by a factor of ≥ 2 kbar. Several analyses of calcic amphiboles from the Wentworth pluton, however, show Fe# > 0.65 and were still used for geobarometric calculations. The reasons for this are discussed later in this work. Even though this geobarometer is based on the principle that the Al-content in amphiboles is indicative of pressure through the tschermakite substitution, increasing Al-content can be also a result of temperature due to edenite substitution. To eliminate the influence of temperature in the estimate of pressure, the recalibration of Anderson and Smith (1995) has been used which enables pressure calculations for igneous amphiboles that have been affected by the edenite substitution.

The initial contents of H_2O in the granitic melt were estimated by the plagioclase-melt hygrometer of Al'meev and Ariskin (1996) (Table 2.2). The hygrometer estimates the initial H_2O contents of a melt as a function of pressure, temperature and chemical composition. The authors developed this model primarily for mafic rocks, however the experimental database that was used as an input included not only basaltic and andesitic compositions but also 49 analyses of granitic rocks for a total range of pressure between 1 and 3.5 kbar and temperatures from 800 to 1300 °C. The equation includes a correction for the dependence of water solubility on temperature, which is different between basaltic and granitic systems. Therefore, the produced equations may be applied to both mafic and felsic systems (Al'meev and Ariskin, 1996). The error of the estimated H_2O contents

is up to 0.3 wt. %. The estimated H_2O contents were also compared with those derived from the plagioclase-melt equilibrium hygrometer of Putirka (2005), where applicable, for a better evaluation of the estimates. The plagioclase-melt hygrometer is based on the anorthitic-albitic exchange of the melt and estimates the magmatic H_2O content, with an error of 1.4 wt. % (Putirka, 2005). For the estimate of the initial magmatic contents of F, the equation of Eby and Charnley (2010) was used (Table 2.2). According to this equation, the concentration ratio D of F between the melt and crystallizing amphiboles is proportional to the Mg number of the latter (Table 2.2). The concentration ratio is the amount of the element measured in the mineral divided by the concentration of that element in the melt. From the estimated concentration ratios and the chemical analyses of the amphiboles, the initial concentrations of fluorine in the melt were thus calculated. The viscosities of the granitic melts were estimated by the empirical model of Giordano et al. (2008) for granitic melts (Table 2.2). The estimates for calcic granites are within an error of ± 0.35 log units whereas viscosities for sodic granites have an associated error of ± 0.25 log units.

2.4 RESULTS

The majority of the studied samples plot within the alkali-feldspar granite field of the modal composition diagram of Streckeisen (1974) with a few exceptions (Fig. 2.2). The textures vary from granular to granophyric and the grain sizes range from fine to coarse grained (Table 2.3). The granites with sodic amphiboles are coarser grained and contain only perthitic K-feldspar, with the composition of orthoclase, indicative of hypersolvus granites. The perthitic albite is almost pure sodic feldspar with a composition of

Table 2. 2 Equations used in this work for estimates of various intensive parameters.

Estimate	Equation	Reference	Notes
Zircon-saturation thermometer	$T=(10108 \pm 32)/ \{\ln D_{Zr} + (1.16 \pm 0.15) * (M-1) + (1.48 \pm 0.09)$	Boehnke et al. (2013)	T is temperature in °K, M is the cationic ratio of the melt: (Na+K+2Ca)/(Al*Si). D_{Zr} is the concentration ratio of zirconium in zircon over that of the melt, in ppm.
Al-in-hornblende barometer	P= 4.76Al -3.01 -{[T-675]/85} *{0.530 Al+ 0.005294 *(T-675)}	Anderson and Smith (1995)	T is temperature in °C, Al is the total Al (a.p.f.u.) in hornblende.
Hbl thermometer	T= 17098 +1322.3Si+1035.1Ti +1208.2Al+1230.4Fe + 1152.9 Mg+ 130.4 Ca+200.54 Na + 29.408K + 12.410 lnP	Ridolfi and Renzulli (2012)	T is temperature in °C, Pressure is given by the equation lnP = 125.93 + 9.5876Si + 10.116Ti + 8.1735Al + 9.2261Fe + 8.7934Mg + 1.6659Ca + 2.4835Na + 2.5192K. Elements are in a.p.f.u. on the basis of 13 cations excluding Ca,Na and K.
Water-in-melt	$H_2O(wt.\%)= 24.757- 2.26 * 10^{-3} * T* \ln[An^{plag}/ (Ca^{melt}*(Al^{melt})^2 * (Si^{melt})^2)]- 3.847* Ab^{plag}+ 1.927* [An^{plag}/(Ca^{melt}/(Ca^{melt}+Na^{melt}))]$	Putirka (2005)	Temperature is in °K, superscripts indicate the cationic fractions of the melt and the plagioclase.
	$\ln H_2O=(4.39 \pm 1.5) + [(38438.3 \pm 5402.4) * Si/O- (14710.2 \pm 2142.9)] /T + (0.59 \pm 0.01) * \ln P- (21.45 \pm 3.8) * Si/O + (3.89 \pm 0.69) * Al/Si$	Al'meev and Ariskin (1996)	H_2O in wt%, T in °K, P in bars and elements in atom fractions.
F-in-melt	$D^{Famph/Fmelt} = 1.03 + 0.06*Mg\#$	Eby and Charnley (2010)	D is the concentration ratio of fluorine in amphibole over the amount of fluorine in the melt. Mg#: (Mg/(Mg+Fe)*100, elements in a.p.f.u.
Viscosity	$\log\eta= -4.55 + B/(T-C)$	Giordano et al. (2008)	η in Pascal seconds (Pa*s), T in °K, B and C parameters are calculated from whole-rock composition with oxides normalized as mol%.

Ab_{96} to Ab_{100} (Appendix A.2). The granites with calcic amphiboles are finer grained and contain discrete grains of both plagioclase and K-feldspar, characteristic of subsolvus granites. The plagioclase has a composition that ranges from Ab_{70} (andesine) to Ab_{96} (albite) (Appendix A.1). Biotite is present in various amounts in many samples with calcic amphiboles, but is completely absent from granites with sodic amphiboles. Most of the studied samples contain magnetite as the dominant iron oxide phase, but a few have ilmenite (Table 2.3).

2.4.1 AMPHIBOLE COMPOSITION

The amphibole-group minerals have a double silicate chain structure and a generic chemical formula of $AB_2C_5^{VI}T_8^{IV}O_{22}(OH)_2$ (Leake et al., 1997). The A-site contains primarily alkalies, whereas the B-site is occupied by Ca and any excess K and Na. Divalent cations such as Mg, Fe^{2+}, Mn^{2+} and Li are distributed between the B- and C-sites (Table 2.1). The trivalent cations such as Al, Fe^{3+}, Mn^{3+} and Cr^{3+} are accommodated in the C-site. The high valency cations such as Al^{4+} and Si^{4+} are hosted in the T-site with any excess Ti, whereas the F and Cl anions substitute for OH in the amphibole structure. According to the Leake et al. (1997) nomenclature scheme, all calcic amphiboles must have Ca+Na >1 a.p.f.u. in the B-site with Na being less than 0.5 a.p.f.u. The sodic-calcic amphiboles have, in general, Ca+Na>1 a.p.f.u. in the B-site with Na ranging between 0.5 and 1.5 a.p.f.u. High amounts of Na in the B-site (>1.5 a.p.f.u.) and alkalies in the A-site (>0.5 a.p.f.u.) are indicative of sodic amphiboles (Table 2.1). A complete set of EMP analyses of amphiboles from the studied samples is included in Appendix A.3.

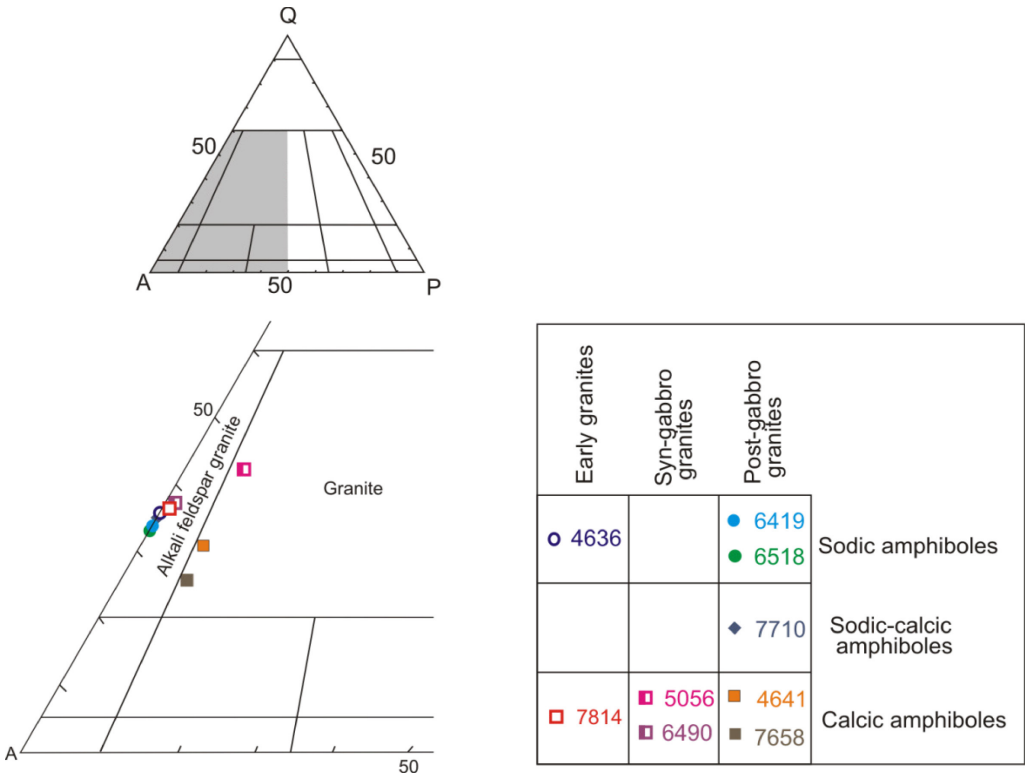

Figure 2. 2 Modal classification of the studied granitic samples (after Streckeisen, 1974). Squares indicate samples with calcic amphiboles and circles indicate the presence of sodic amphiboles. A: alkali feldspar, Q: quartz, P: plagioclase.

2.4.1.1 Early granites

The early granites contain magmatic arfvedsonite (sample 4636, Fig. 2.3A), and ferro-edenite and ferro-hornblende (sample 7814, Fig. 2.3B) (Tables 2.3, 2.4). The ferro-edenite occurs as subhedral grains and contains inclusions of magnetite. Ferro-hornblende forms either discrete subhedral grains or patches in ferro-edenite. Calcic amphiboles are commonly altered along cleavage planes to epidote, titanite, chlorite, actinolite, calcite and in some samples, secondary biotite (7814, Fig. 2.3B). Arfvedsonite, on the other hand, occurs as distinct grains that can reach 400 microns in diameter (Fig. 2.3A). The sodic amphibole contains inclusions of magnetite and is associated with secondary fluorite. The analyses from core-to-rim traverses suggest that the grains are

relatively homogenous with no zoning, except for alteration products along the rims that include ferro-eckermannite, riebeckite and chlorite (4636).

2.4.1.2 Syn-gabbro granites

Two studied syn-gabbro granites contain calcic amphiboles represented by Mg-rich ferro-hornblende (5056, Fig. 2.3C), and ferro-edenite (6490, Fig. 2.3D). Sample 5056, which has been interpreted as hybrid, chemically resembles granodiorite and is one of the samples that plot within the granite field instead of the alkali feldspar granite field (Fig. 2.2) of Streckeisen (1974). This sample is the only one containing Mg-rich amphiboles and no ferro-edenite (Table 2.4). The dominant amphibole is Mg-rich ferro-hornblende with patches of magnesiohornblende along surfaces of weakness such as microfractures and cleavage (Fig. 2.3C). The Mg-rich ferro-hornblende forms large, discrete, subhedral to euhedral grains in contact with Fe-oxides and biotite. The primary amphibole in sample 5056 has altered to chlorite, biotite, titanite, epidote, calcite and actinolite (Fig. 2.3C). Ferro-edenite in sample 6490 occurs as medium to small, subhedral to anhedral grains.

2.4.1.3 Post-gabbro granites

The post-gabbro granites contain ferro-edenite, ferro-hornblende (samples 4641, 7658, 7710), ferro-richterite, ferro-winchite (sample 7710, Fig. 2.3E), and arfvedsonite (sample 6419) (Table 2.3). Like the early and syn-gabbro granites, the calcic amphiboles alter to titanite, epidote and actinolite. Sample 7710 comes from a late equigranular, fine-grained granitic dyke that intruded the Wentworth gabbro, and it is somewhat different from most samples. It contains a wide variety of amphiboles calcic ferro-edenite to sodic-calcic ferro-richterite and ferro-winchite (Table 2.4).

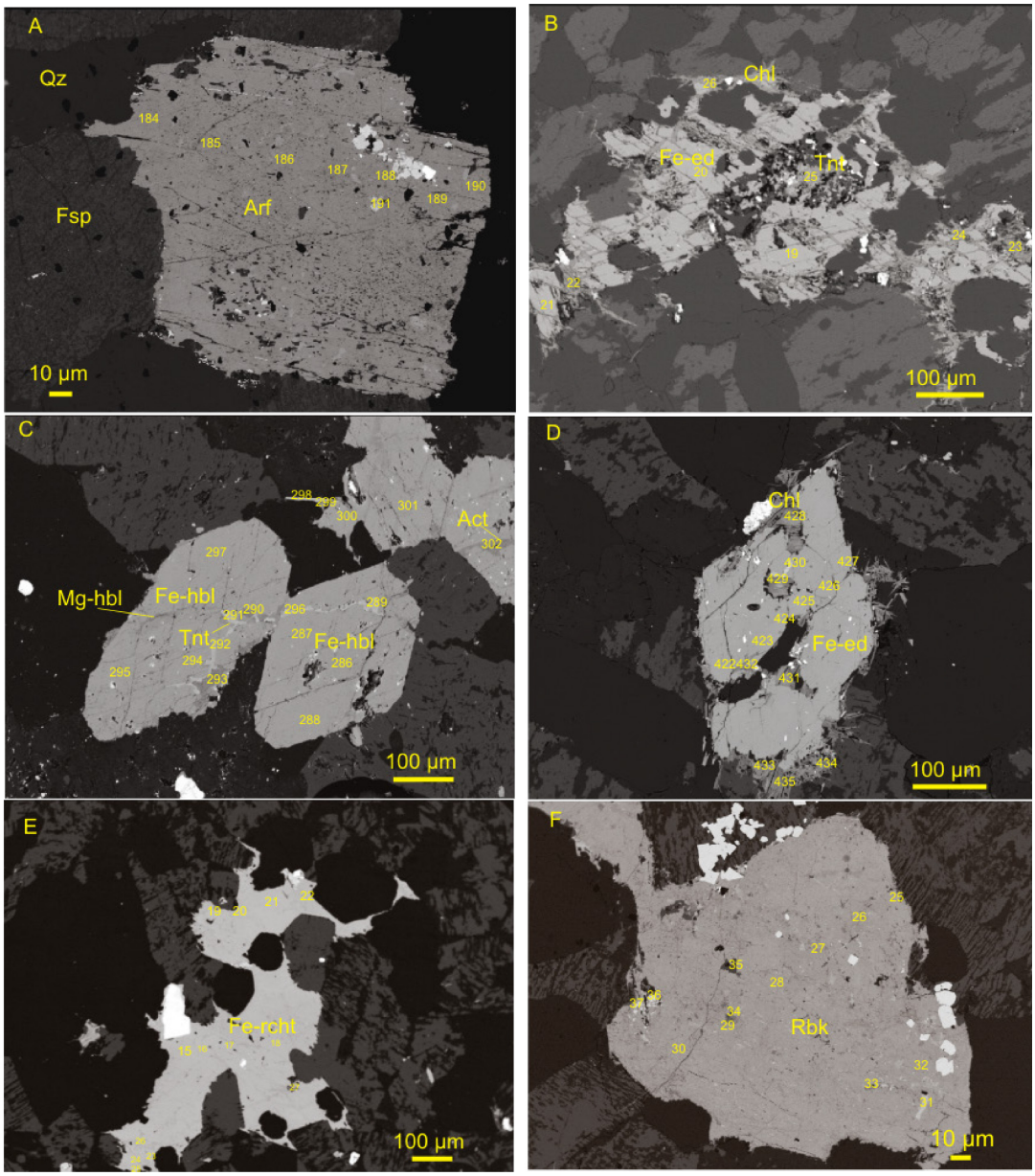

Figure 2. 3 Selected backscattered electron (BSE) images of amphiboles from the Wentworth granites. Figures (a) and (b) are from early granites with arfvedsonite (Arf), and ferro-edenite (Fe-ed) which is altered to titanite (Tnt) and chlorite (Chl). Figure (c) is an Mg-rich ferro-hornblende (Fe-hbl) from a hybrid rock altered to magnesiohornblende (Mg-hbl) and actinolite (Act), and (d) is a euhedral ferro-edenite from a syn-gabbro granite. Figure (e) is an interstitial, sodic-calcic amphibole (Fe-richt) and (f) a megacrystic riebeckite (Rbk) from post gabbro granites. Abbreviations after Whitney and Evans (2010). Numbers indicate positions of analyses.

Furthermore, it is the only sample in which ferro-richterite has patches of hedenbergitic augite, mainly along cleavage planes. Primary ferro-edenite and ferro-richterite occur as interstitial, subhedral grains, and contain inclusions of Fe-oxides. Secondary riebeckite,

katophorite and ferro-winchite have formed by the alteration of ferro-richterite. The primary sodic amphibole in sample 6419 is arfvedsonite, occurring as megacrysts with the same alteration products as the sodic amphiboles in other samples. In this sample, arfvedsonite appears more altered compared to other samples and secondary ferro-eckermannite is more abundant. Sample 6518, however contains principally riebeckite with smaller amounts of ferro-winchite and minor actinolite. In this sample, riebeckite occurs in two forms: a) megacrystic riebeckite with inclusions of ilmenite (Fig. 2.3F) and b) slender, independent prisms. The chemical composition of the riebeckitic megacrysts and the prisms is identical.

In all samples, calcic amphiboles like ferro-edenite or ferro-hornblende have not been observed to coexist with primary sodic amphiboles such as arfvedsonite. Furthermore, the analyses from the Wentworth amphiboles show that arfvedsonite has almost double the amount of F compared to ferro-edenite and ferro-hornblende (Table 2.4).

2.4.2 INTENSIVE CRYSTALLIZATION PARAMETERS

With the exception of one sample (7814), all the calculated zircon-saturation temperatures for the studied samples from the Wentworth Pluton appear higher than 850±50 °C (Table 2.3), within the expected range for A-type granites (Clemens et al., 1986). The samples with sodic amphiboles have higher zircon-saturation temperatures than those with calcic amphiboles (Table 2.3). The magmatic temperatures of calcic amphiboles do not vary significantly from those estimated from zircon saturation for the parental rock and all are greater than 760 °C ± 50 °C (Table 2.3).

The Wentworth calcic amphiboles show evidence for both edenite and tschermakite substitutions (Fig. 2.4), and therefore, a temperature correction has been applied when

using the hornblende Al content to estimate pressures, as mentioned above. The pressure estimated by the Al-in hornblende barometer for the Wentworth granites ranges between 2.1 and 3.2 ±0.6 kbar (Table 2.2).

2.4.3 OTHER MAGMATIC PARAMETERS

The dominance of magmatic magnetite indicates that these granites belong to the magnetite series granites, which formed under oxidizing conditions (Table 2.3). The hygrometric calculations for the Wentworth granites suggest that the calcic amphibole-bearing samples formed in a magma richer in H_2O (4–11.6 wt. % H_2O), whereas the samples with sodic amphiboles were derived from a drier magma (3.6–1.3 wt. % H_2O, Table 2.3).There is no correlation between the estimated pressures and the calculated H_2O for these granites to suggest a large influence of PH_2O on the pressure estimates.

The amount of F in the granitic melt of the Wentworth pluton ranged from 0% to 0.8 wt.%. The samples with calcic amphiboles had smaller amounts of F in the melt than the samples with sodic amphiboles (Table 2.3). The estimated viscosities show that there are systematic variations between the two types of granites. The granites with calcic amphiboles were derived from a melt with a higher average viscosity of $10^{9.79\pm0.35}$ Pa*s, whereas the granites with sodic amphiboles show relatively lower viscosities between $10^{7.08}$ and $10^{9.42\pm0.25}$ Pa*s (Table 2.3).

2.5 DISCUSSION

The main factors that control the type of amphibole present in the rocks are: a) chemical composition of the melt, b) temperature, c) pressure, d) oxygen fugacity, and e)

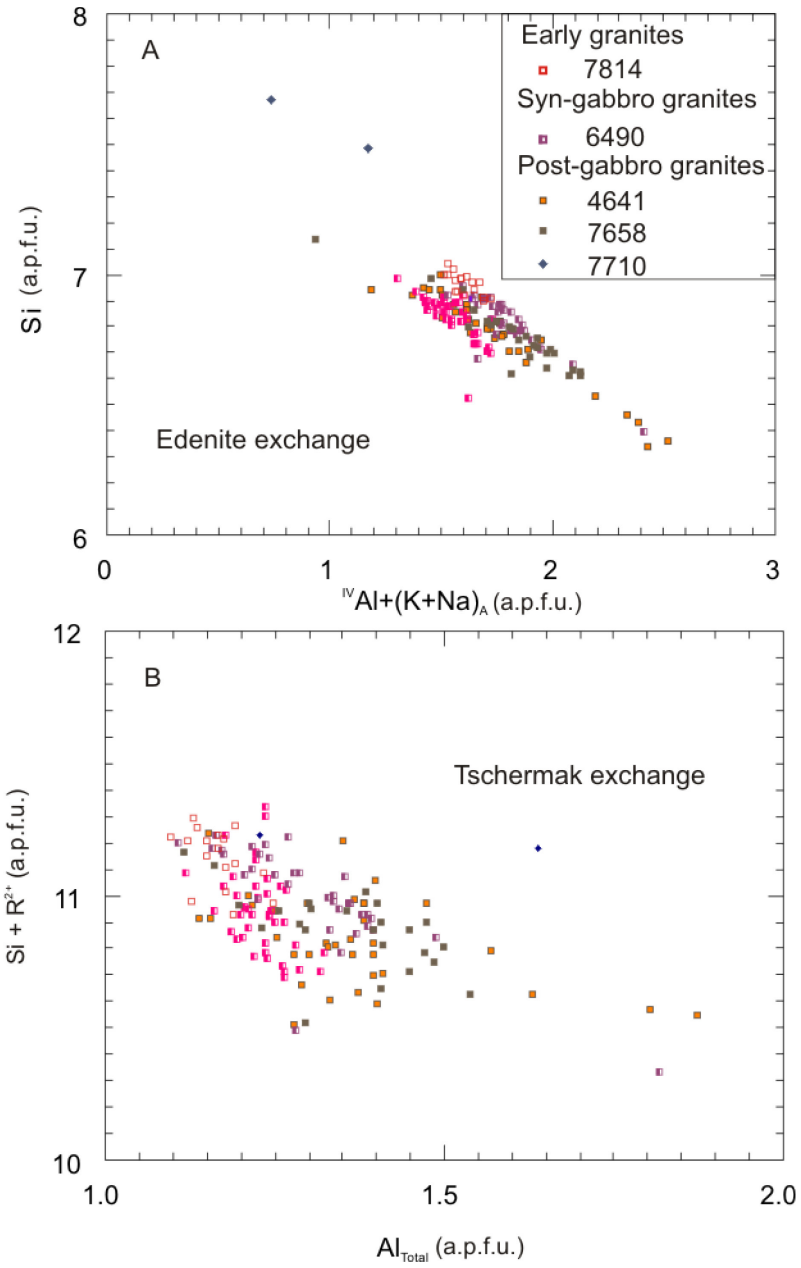

Figure 2. 4 Edenitic and tschermakitic substitutions for the Wentworth hornblendes. The tschermak exchange shows a better defined linear trend for all calcic amphiboles, demonstrating a larger influence of pressure over temperature on the chemistry of these minerals. The parameter R in tschermak exchange refers to divalent cations (such as Mg and Fe) in octahedral sites.

presence and type of volatiles (Martin, 2007). In this section, the influence of each of these factors is evaluated in an attempt to understand the geological processes responsible for the wide chemical variation observed in the amphiboles of the Wentworth granites.

2.5.1 CORRELATION BETWEEN THE TYPE OF AMPHIBOLE AND WHOLE-ROCK COMPOSITION

Comparison of the types and amounts of amphiboles present with the whole-rock geochemistry of the samples suggests that there is a correlation with MgO. Most of the samples with relatively high MgO have relatively high modal abundances of calcic amphiboles, whereas the samples with low MgO concentrations contain either sodic amphiboles or very small amounts of calcic amphiboles. Barium is used as an indicator of fractionation of the melt. Barium is incompatible in mafic to intermediate melts, however it is highly compatible in evolved magmas (Rollinson, 1993). The hornblende-bearing rocks have significantly higher amounts of Ba than the samples with sodic amphiboles (Table 2.5). Assuming that Ba content reflects the content of the magma and was not affected by subsolidus alteration, these differences suggest a geochemically less evolved parental magma for the rocks with calcic amphiboles.

In silica-oversaturated rocks, the spectrum of amphibole compositions found in extension-related suites could result from either fractional crystallization of a mafic melt or anatexis of suitably metasomatized crust (Martin, 2007). There is no good evidence for fractional crystallization from a mafic melt in the Wentworth granites. The lack of homogeneous intermediate rock-types in the area or chemical zoning (Appendix A.4) in the rock-forming minerals that could suggest a fractionating melt leads to the conclusion that melting of a suitable source in the deep crust was responsible for the Wentworth granites. In that case, Sm-Nd isotopes are considered an effective method to determine the nature of that source.

The Sm-Nd isotopic composition of the Wentworth granites (Pe-Piper and Piper, 1998b, and new data reported here, Table 2.3) shows a range of ε_{Nd} values from +1.1 to

Table 2. 3 Petrographic description of the studied samples.

	Sample	4636	7814	5056	6490	4641	6419	6518	7658	7710
	Relative age	**Early**	**Early**	**Syn-gabbro**	**Syn-gabbro**	**Post-gabbro**	**Post-gabbro**	**Post-gabbro**	**Post-gabbro**	**Post-gabbro**
UTM	**Easting**	455400	463361	463975	461724	452932	451203	460683	468260	450747
	Northing	5048118	5044863	5044528	5043853	5046282	5049916	5044932	5045537	5040441
Modal Composition	**qz**	35.0	37.6	32.4	36.6	32.4	31.0	31.3	25.4	33.6
	plg (An)	0.0	0.4 (An_4)	8.8(An_{27-4})	1.7 (An_{7-4})	6.6 (An_{7-3})	0.0	0.0	7.7 (An_{9-5})	0.0
	K-fsp	61.0	61.6	43.2	59.8	57.8	62.0	59.7	61.6	62.5
	amp	4.0	0.4	7.9	0.7	2.4	6.0	6.7	0.8	3.9
	bt	0.0	<1	7.8	1.2	3.7	0.0	0.0	4.4	0.0
	Fe-oxide[1]	mgt 100%	mgt 91%	mgt 88%	mgt 99%	mgt 99%	mgt 99%	mgt 59%	ilm 65%	mgt 92%
	Streckeisen classification	alkali feldspar granite	alkali feldspar granite	granite	alkali feldspar granite	granite	alkali feldspar granite	alkali feldspar granite	granite	alkali feldspar granite
Type of amphibole	**Primary**	Arf (80%)	Ferro-edenite (96%), Ferro-hbl (4%)	Ferro-hbl (65%)	Ferro-edenite (80%), Ferro-hbl (15%)	Ferro-edenite (29%), Ferro-hbl (63%)	Arf (30%)	Rbk** (63%)	Ferro-edenite (88%), ferro-hbl (12%)	Ferro-edenite (41%), Ferro-richt (28%)
	Secondary	Ferro-eck (16%), rbk (4%)		Mg-hbl (18%), actin (17%)	Ferro-actin (5%)	Ferro-actin (8%)	Ferro-eck (66%), rbk (4%)	Ferro-winch (32%), Ferro-actin (5%)		Ferro-actin (3%), Ferro-winch (6%), rbk (22%)
		sodic	calcic	calcic	calcic	calcic	sodic	sodic	calcic	calcic, sodic-calcic
	Texture	granular	granophyric	granular	granophyric	granular	granular	granular	granular	equigranular
	Grain Size	coarse	coarse	medium-fine	medium	medium	medium-coarse	medium-coarse	medium	medium-fine
	ASI	0.92	1.03	1.15	1.06	1.43	0.98	0.92	1.08	1.00
	MALI	8.89	7.91	6.29	8.49	6.51	8.36	8.51	8.06	8.28

	Sample	4636	7814	5056	6490	4641	6419	6518	7658	7710
	Relative age	Early	Early	Syn-gabbro	Syn-gabbro	Post-gabbro	Post-gabbro	Post-gabbro	Post-gabbro	Post-gabbro
	Ba (ppm)	39		669	89	599	32	12	276	125.3
	$\varepsilon_{Nd(360)}$ ± 0.5 units	3.60	1.36*	2.46	1.15	2.52	3.15	3.13	2.24	3.19
Intensive parameters	**T_{Zr} (°C) ± 35**	891	830	884	836	874	919	1045	863	940
	M-value	1.56	1.4	1.7	1.37	1.13	1.42	1.63	1.44	1.45
	T_{hbl} (°C) ± 50°C		857	764	821	795			826	887
	$P_{Al\text{-}in\text{-}hbl}$ ± 0.6 kbar		2.1	2.5	2.8	3.2			3	1.3
	$F_{in\text{-}melt}$ (wt%) ± 0.24	0.8	0.2	0.0	0.2	0.0	0.6	1.0	0.1	0.5
	$H_2O_{in\ melt}$ (wt%) ± 0.3 wt. %[a]	3.6	11.6	5.0	10.6	4.0	3.5	1.3	6.6	5.6
	$H_2O_{in\ melt}$ (wt%) ± 1.2 wt. %[b]		5.5	6.3	5.7	4.0			5.6	4.3
	Melt viscosity (log (Pa*s))	9.42	10.35	9.25	10.32	9.30	9.03	7.08	9.73	8.51

Notes: The UTMs reported are based on the GCS 1983 datum for North America, UTM zone 20N, [1]: Indicates the dominant iron oxide on the sample, percentages were calculated out of the total number of EDS analyses on opaque minerals, *: Isotope data from Pe-Piper and Piper (1998). ** Riebeckite in this sample is considered as possibly primary mineral on the basis of its occurence as well formed megacrystic crystals in the body of the rock and interlocking textures with magmatic feldspars. Mineral abbreviations: qz: quartz, plg: plagioclase, K-fsp: alkali feldspar, amp: amphibole, bt: biotite, mgt: magnetite, ilm: ilmenite, arf: arfvedsonite, ferro-eck: ferro-eckermannite, rbk: riebeckite, ferro-hbl: ferrohornblende, Mg-hbl: magnesiohornblende, ferro-actin: ferro-actinolite, ferro-winch: ferro-winchite, ferro-richt: ferro-richterite (after Whitney and Evans, 2010), ASI: Aluminum Saturation Index (Al/(Na+K+Ca-1.67*P) elements in cationic proportions, MALI: Modified Alkali Lime Index (Na_2O+K_2O-CaO) oxides in wt% (Frost et al., 2001). [a] represents magmatic water contents estimated by the Al'meev and Ariskin (1996) model and [b] are the magmatic water estimates by the use of the plagioclase-melt hygrometer of Putirka (2005). Pointcounting based on 1000 points.

Table 2. 4 Representative electron microprobe analyses of amphiboles from the Wentworth granites.

Sample	**7814**	**4641**	**5056**	**5056**	**5056**	**7710**	**7710**	**4636**	**6419**	**6419**	**6518**
Analysis	**19**	**190**	**202**	**204**	**233**	**296**	**297**	**174**	**461**	**462**	**25**
Mineral	**fe-ed**	**fe-ed**	**mg-hb**	**mg-hbl**	**act**	**fe-rcht**	**fe-rcht**	**arf**	**arf**	**fe-eck**	**rbk**
Oxides (wt.%)											
SiO_2	44.68	43.58	45.48	45.26	50.48	47.09	46.84	50.53	50.25	48.78	51.65
TiO_2	0.77	0.69	1.59	1.32	0.28	1.24	1.18	1.30	0.60	1.32	0.43
Al_2O_3	6.01	7.27	6.91	7.48	2.13	3.43	3.56	1.42	1.30	2.36	0.96
FeOt	28.33	26.00	20.80	21.22	17.05	29.85	27.84	32.50	30.66	30.45	35.33
MnO	1.38	0.86	0.49	0.48	0.41	0.71	0.69	0.73	0.72	0.73	0.92
MgO	4.27	4.70	8.96	8.74	12.81	2.69	4.10	1.28	2.66	2.19	0.45
CaO	10.50	10.79	10.69	10.58	11.85	7.80	8.73	2.17	2.67	3.20	1.61
Na_2O	2.18	1.76	1.76	1.51	0.63	3.86	3.75	7.60	7.56	7.30	6.23
K_2O	1.18	1.13	0.86	0.92	0.24	1.07	1.09	1.35	1.28	1.31	0.32
F	0.71	0.35	0.23	0.17	0.23	0.58	1.01	1.06	1.38	1.15	0.00
Cl	0.30	0.79	0.15	0.18	0.07	0.07	0.07	0.04	0.04	0.03	0.00
Total	100.3	97.9	97.90	97.86	96.17	98.39	98.84	99.98	99.10	98.82	0.00
Si	6.951	6.897	6.877	6.822	7.551	7.499	7.436	7.925	7.924	7.744	7.984
Al	1.049	1.103	1.123	1.178	0.376	0.501	0.564	0.075	0.076	0.256	0.016
T-site	**8.000**	**8.000**	**8.000**	**8.000**	**8.000**	**8.000**	**8.000**	**8.000**	**8.000**	**8.000**	**8.000**
Al	0.053	0.253	0.106	0.150	0.000	0.142	0.101	0.187	0.165	0.185	0.159
Fe^{3+}	0.425	0.259	0.511	0.694	0.358	0.000	0.000	0.269	0.298	0.157	1.296
Ti	0.090	0.082	0.181	0.149	0.032	0.149	0.141	0.153	0.071	0.158	0.049
Mg	0.990	1.109	2.020	1.965	2.856	0.638	0.970	0.299	0.625	0.518	0.104
Fe^{2+}	3.261	3.183	2.119	1.981	1.702	3.975	3.695	3.995	3.744	3.885	3.271
Mn	0.181	0.116	0.063	0.061	0.052	0.096	0.093	0.097	0.096	0.097	0.120
C-site	**5.000**	**5.000**	**5.000**	**5.000**	**5.000**	**5.000**	**5.000**	**5.000**	**5.000**	**5.000**	**5.000**
Ca	1.750	1.830	1.732	1.709	1.899	1.331	1.485	0.365	0.451	0.544	0.266
Na	0.250	0.170	0.268	0.291	0.101	0.669	0.515	1.635	1.549	1.456	1.734
B-site	**2.000**	**2.000**	**2.000**	**2.000**	**2.000**	**2.000**	**2.000**	**2.000**	**2.000**	**2.000**	**2.000**
Na	0.408	0.371	0.247	0.149	0.083	0.523	0.638	0.677	0.764	0.790	0.133
K	0.233	0.227	0.166	0.176	0.046	0.217	0.220	0.271	0.257	0.265	0.063
A-site	**0.642**	**0.598**	**0.413**	**0.326**	**0.128**	**0.741**	**0.858**	**0.947**	**1.021**	**1.055**	**0.196**
Σ cations	**15.64**	**15.60**	**15.41**	**15.33**	**15.13**	**15.74**	**15.86**	**15.95**	**16.02**	**16.06**	**15.20**
Al (total)	1.10	1.36	1.23	1.33	0.38	0.64	0.67	0.26	0.24	0.44	0.18
Fe#	0.79	0.76	0.57	0.58	0.42	0.86	0.79	0.93	0.87	0.89	0.98
R	0.11	0.07	0.19	0.25	0.17			0.06	0.07	0.04	0.28

Notes: fe-ed: ferro-edenite, mg-hbl: magnesiohornblende, act: actinolite, fe-rcht: ferro-richterite, arf: arfvedsonite, fe-eck: ferro-eckermannite, rbk: riebeckite. Fe#: $Fe_T/(Fe_T+Mg)$. Mg#: $Mg/(Mg+Fe_T)$. R: $Fe^{3+}/(Fe^{3+}+Fe^{2+})$. Structural formulae calculated on the basis of 23 oxygens and normalized using the 13eCNK method as in Leake et al. (1997).

+3.6. Rocks with low ε_{Nd} (+1.1 to +2.5) have only calcic amphiboles, whereas samples with sodic-calcic and sodic amphiboles have higher values of ε_{Nd} (Fig. 2.5). This suggests the presence of two different sources for the granitic magma. A calcic magma was derived from a source with a more crustal isotopic signature that crystallized only calcic amphiboles, whereas a relatively more alkaline magma was derived from a source with a larger mantle component, from which sodic amphiboles crystallized.

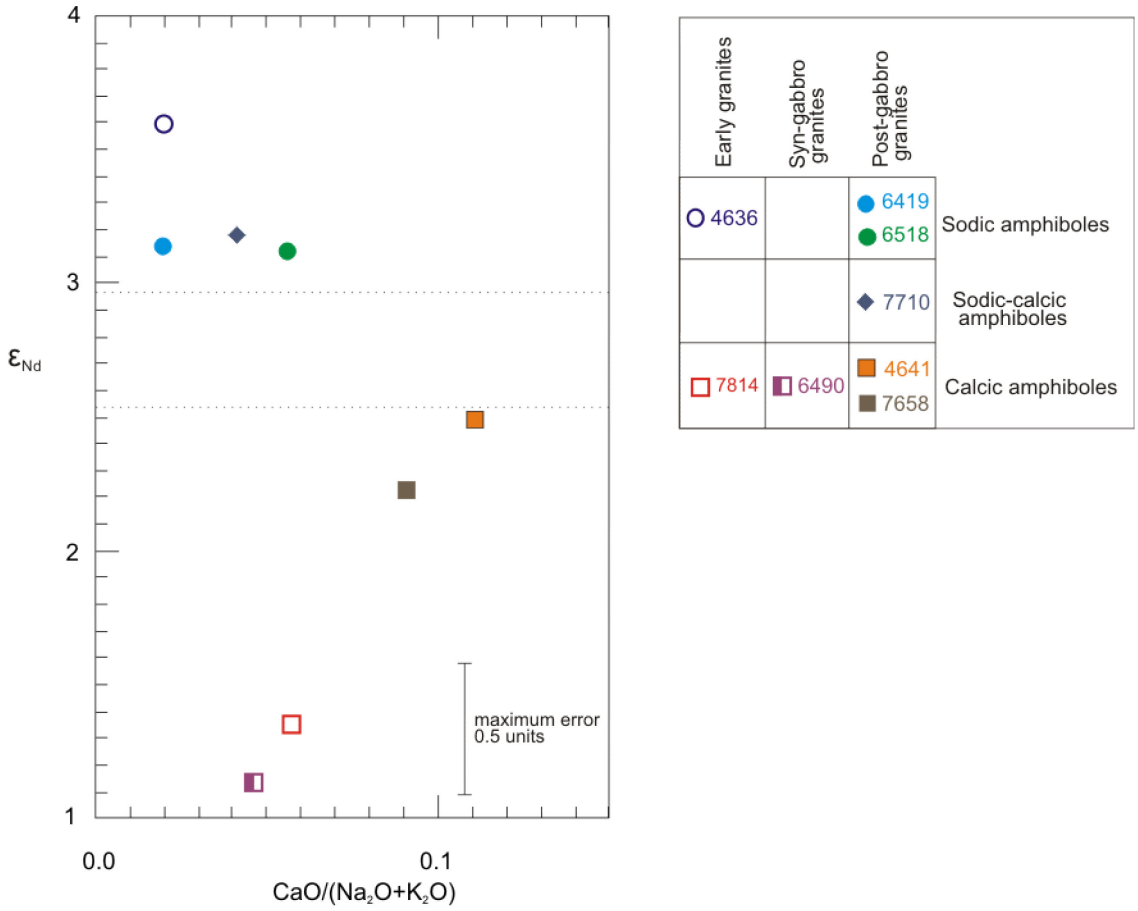

Figure 2. 5 ε_{Nd} versus $CaO/(Na_2O+K_2O)$ from whole-rock composition, showing two distinct groups of granites (separated by dotted lines). Samples with sodic amphiboles show ε_{Nd} values higher than +3, whereas all samples with calcic amphiboles have less than +2.5. Isotopic data from Pe-Piper and Piper (1998) and new data from the same laboratory presented in this work.

There is a difference in alkalinity (Agpaitic index, Table 2.5) that distinguishes the samples with sodic amphiboles from the granites with calcic amphiboles. The calculated values for the granites with sodic and calcic amphiboles of the Wentworth pluton

Table 2. 5 Whole-rock analyses of the studied samples from the Wentworth pluton.

Sample	**4636**	**7814**	**6490**	**5056**	**4641**	**6419**	**6518**	**7658**	**7710**
Type of amp.	**sodic**	**calcic**	**calcic**	**calcic**	**calcic**	**sodic**	**sodic**	**calcic**	**calcic, sodic-calcic**
Relative age	**Early**	**Early**	**Syn-gabbro**	**Syn-gabbro**	**Post-gabbro**	**Post-gabbro**	**Post-gabbro**	**Post-gabbro**	**Post-gabbro**
Major Oxides (wt. %) (Recalculated on a volatile-free basis)									
SiO_2	75.69	76.99	76.22	64.88	71.62	77.16	73.41	72.98	76.03
TiO_2	0.17	0.19	0.17	0.87	0.46	0.18	0.43	0.32	0.23
Al_2O_3	11.51	11.85	12.59	15.91	14.57	11.18	11.79	13.67	11.94
Fe_2O_3t	2.51	1.88	1.67	5.41	3.56	2.83	4.56	2.73	2.55
MgO	0.82	0.03	0.04	1.06	1.07	0.02	0.02	0.24	0.09
MnO	0.04	0.03	0.03	0.07	0.07	0.05	0.1	0.08	0.04
CaO	0.21	0.53	0.45	2.64	0.94	0.18	0.56	0.9	0.4
Na_2O	4.42	3.38	3.5	3.46	2.12	3.77	4.27	3.74	3.92
K_2O	4.62	5.09	5.31	5.51	5.48	4.61	4.84	5.27	4.78
P_2O_5	0.01	0.02	0.02	0.2	0.1	0.01	0.02	0.07	0.02
Total	100.00	99.99	100.0	100.01	99.99	99.99	100.00	100.00	100.00
Trace elements (ppm)									
Ba	39	b.d	89	669	599	32	12	276	125.3
Rb	224	174	163	176	212	243	170	241	212.6
Sr	10	33	18	148	91	11	12	63	17.7
Y	90	88	65	93	53	84	102	76	93.3
Zr	552	262	232	579	324	635	2136	344	786.5
Nb	69	60	62	50	20	101	77	45	55.7
Pb	3	16	18	30	41	33	14	32	10.3
Ga	30	27	28	23	19	37	34	24	29.2
Zn	131	40	44	68	72	163	138	58	138
Cu	n.d	6	12	10	n.d	13	22	13	18
Ni	4	4	b.d	6	3	b.d	b.d	b.d	b.d
V	2	b.d	6	49	15	b.d	b.d	7	10
Cr	32	12	b.d	12	34	b.d	7	b.d	b.d
La	71.2	n.d	n.d	n.d	n.d	n.d	232	n.d	n.d
Ce	152	122	n.d	n.d	n.d	n.d	437	n.d	n.d
Nd	68	n.d	n.d	n.d	n.d	n.d	176	n.d	n.d
Sm	15.3	n.d	n.d	n.d	n.d	n.d	30.1	n.d	n.d
Eu	0.59	n.d	n.d	n.d	n.d	n.d	1.44	n.d	n.d
Tb	2.3	n.d	n.d	n.d	n.d	n.d	3.3	n.d	n.d
Yb	10.7	n.d	n.d	n.d	n.d	n.d	13.4	n.d	n.d
Lu	1.67	n.d	n.d	n.d	n.d	n.d	2.1	n.d	n.d
Th	16	17	18	19	17	24	21	36	9.9
U	5.9	7	n.d	n.d	n.d	n.d	3.5	n.d	1.3
Agpaitic Index	1.07	0.93	0.91	0.73	0.65	1.00	1.04	0.87	0.97
Fe#	0.73	0.98	0.97	0.82	0.75	0.99	1.00	0.91	0.96

Notes: Agpaitic Index= molar $(Na_2O+K_2O)/Al_2O_3$, Fe# number= $FeO_T/ (FeO_T+MgO)$ in wt% oxides (Frost et al., 2001), n.d.= not determined, b.d.= below detection limit. Whole-rock chemical data previously reported by Pe-Piper (1998).

correspond to those for the alkaline and aluminous petrographic associations, respectively, described by Gualda and Vlach (2007) for the Graciosa granites. Mineralogically, however, there are important differences. The hypersolvus granites are restricted to the granites with sodic amphibole, which in the case of the Wentworth pluton is predominantly primary arfvedsonite, in contrast to dominant riebeckite and minor arfvedsonite found in the Graciosa alkaline association. Furthermore, the wide compositional range in amphiboles found in the alkaline association of the Graciosa syenites and granites implies a link between the syenites and the granites by fractionation. Such evidence is lacking in the granites of the Wentworth pluton, as well as chemical zoning in the studied amphiboles (Appendix A.4). There is no evidence, therefore for a genetic link between the granites with sodic and the granites with calcic amphiboles.

2.5.2 INFLUENCE OF TEMPERATURE AND PRESSURE

There is a positive correlation between estimated zircon-saturation temperature and ε_{Nd} values of the studied samples (Fig. 2.6). Samples with calcic amphiboles have low ε_{Nd} values and low temperatures. As temperature and ε_{Nd} increases the samples pass from calcic amphibole-bearing to more sodic-calcic compositions and finally to sodic compositions in higher temperatures (Fig. 2.6). The calcic amphiboles crystallized at similar temperatures with the zircons, as indicated by the hornblende thermometer, and therefore the two minerals probably crystallized broadly at the same time. The higher T_{Zr} values of the granites with sodic amphiboles do not necessarily mean that the sodic amphiboles formed at higher temperatures. Rather, the sodic amphiboles crystallized from a magma with a higher liquidus temperature than the one that formed the calcic amphiboles.

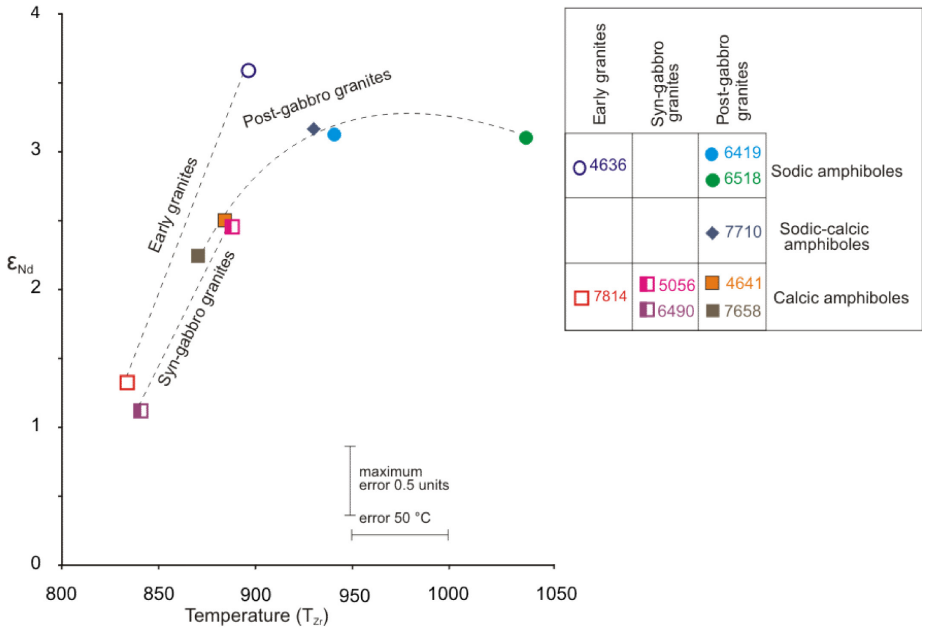

Figure 2. 6 ε_{Nd} versus temperature diagram, demonstrating the positive correlation of temperature and isotopic signature to the type of amphibole present in the granites of the Wentworth pluton. Temperatures estimated from zircon-saturation thermometer.

2.5.3 THE IMPACT OF OXYGEN FUGACITY ON THE CALCIC AMPHIBOLES OF THE WENTWORTH PLUTON

Oxygen fugacity is believed to have an impact on the chemistry of calcic amphiboles. With increasing oxygen fugacity the amphiboles crystallizing from a magma become progressively enriched in Mg (Wones, 1981) as the result of precipitation of magnetite. Amphiboles thus with high Fe# ($Fe_T/(Fe_T+Mg)$ in a.p.f.u.) are believed to have formed under low oxygen fugacity (Anderson and Smith, 1995). The majority of the analyzed amphiboles in the Wentworth granites have moderate to high Fe# (0.5-0.8) (Fig. 2.7).

However, this inference conflicts with the presence in these samples of magnetite as the dominant Fe-oxide, which suggests oxidizing conditions (Table 2.3), like those for the magnetite series of granites. Anderson and Smith (1995) interpreted an oxygen fugacity below QFM for the Enchanted Rock batholith, on the basis of high Fe# in the

magmatic amphiboles, even though the Enchanted Rock batholith belongs to the magnetite series. The granites of the Wentworth pluton, however, contain Fe-rich amphiboles and yet the oxygen fugacity indicated by the assemblage of magnetite, titanite and quartz is probably above the QFM, suggesting that for some reason, oxygen fugacity had a limited effect on the Fe# of the amphiboles.

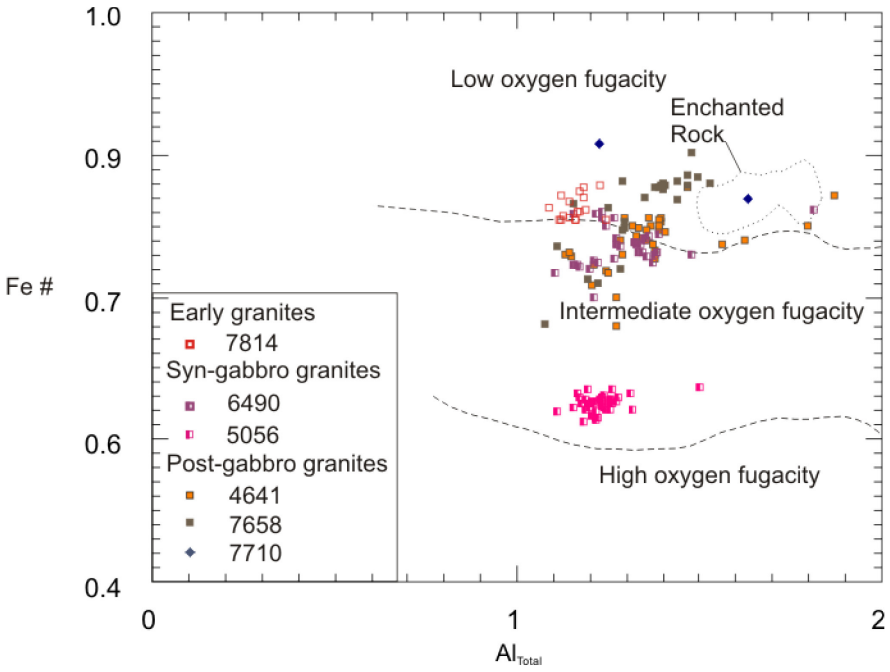

Figure 2. 7 Fe-number (Fe#: $(Fe^{2+} + Fe^{3+})/ (Fe^{2+} + Fe^{3+}+Mg)$) versus Al of the hornblendes from the Wentworth granites (fields after Anderson and Smith 1995), suggesting their formation under moderate to low oxygen fugacity. The range of the amphiboles from the Enchanted Rock batholith formed under low oxygen fugacity (as described in Anderson and Smith, 1995) is plotted for comparison.

The molar ratio R $(Fe^{3+}/ (Fe^{3+}+Fe^{2+})$ of the calcic amphiboles from the Wentworth pluton ranges from 0.07 to 0.25 (Table 2.4). This ratio can be affected by the oxygen fugacity of the parent magma and such values indicate oxygen fugacity above the QFM buffer (Clowe et al., 1988), suggesting crystallization under moderately oxidizing conditions.

With the exception of Mg-rich ferro-hornblende, present in the hybrid sample, all primary calcic amphiboles in the Wentworth pluton show almost constant values of molar Mg (0.9–1.1 a.p.f.u., Table 2.4) suggesting that these minerals did not become as enriched in Mg as amphiboles that form under moderate to high oxygen fugacity do. The data from the calcic amphiboles of the Wentworth pluton, therefore, are ambiguous. The R ratio indicates oxidizing conditions above the QFM buffer, whereas their relatively low Mg amounts suggest crystallization under low oxygen fugacity and consequently affected the calculation of the Fe# values.

The second ferromagnesian mineral in the granites is biotite (Table 2.6, Appendix A.5) and is almost exclusively found in the granites with calcic amphiboles. The biotites present in these granites, even though close to the annite end-member, still contain significant amounts of Mg and therefore the timing of their crystallization needs to be evaluated. Interlocking textures of biotite with hornblende in the granitic samples (Fig. 2.8) indicate that the crystallization of these minerals took place almost simultaneously. As such, the crystallizing biotites could also incorporate significant amounts of Mg from the crystallizing melt, as indicated by their mineral chemistry (Table 2.6). Kretz (1959) demonstrated that the distribution of Mg between coexisting biotite and calcic amphibole can be approached graphically by plotting the XMg ratio (Mg/(Mg+Fe+Mn+Ti) in a.p.f.u.) of both minerals in a Roozeboom diagram (Fig 2.9). A regular distribution of Mg should produce a linear trend with positive slope if the two minerals represent ideal binary mixtures (i.e. under constant temperature or pressure) (Saxena, 1968). The plotted ratios for biotite and coexisting calcic amphiboles from three studied samples do form broadly a linear trend as a whole (Fig 2.9). However, in each sample the plotted data

form negative linear trends that deviate from a regular distribution. These trends show that an increase of Mg in biotite was accompanied by a decrease of Mg in amphibole. Such deviations may be the result of a change in the pressure and temperature, or other chemical changes in the coexisting minerals (Kretz, 1959). Thus a possible explanation for this deviation could be a rapid ascent and emplacement of the granitic magma that could significantly change the pressure, however this cannot be evaluated at this point. Nonetheless, the textural and chemical evidence from the amphiboles and the biotites suggests that during the crystallization of the calcic amphiboles of the Wentworth pluton

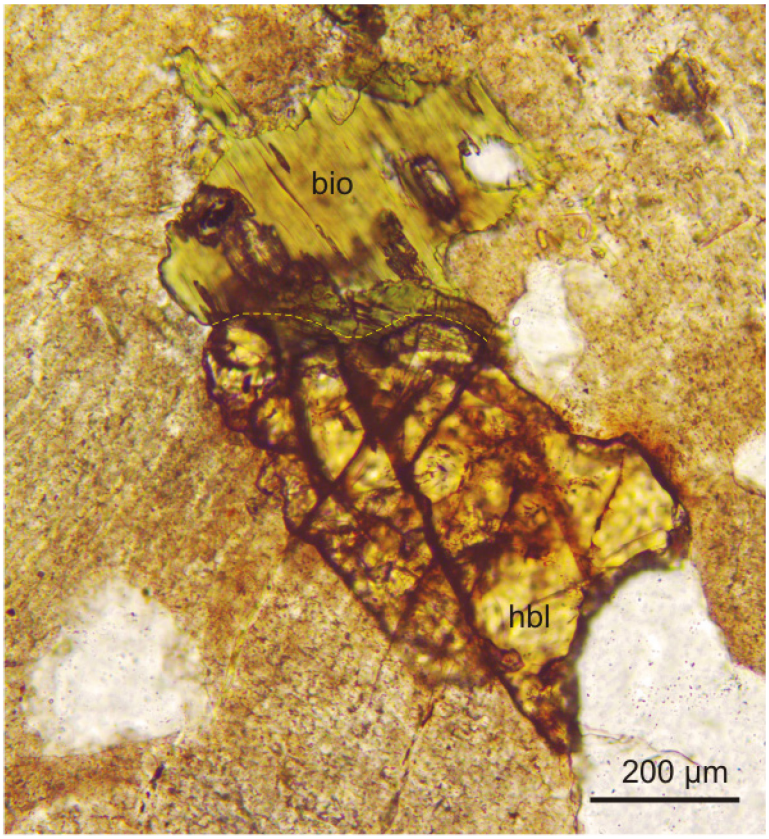

Figure 2. 8 Coexisting anhedral calcic amphibole with biotite in the granites of the Wentworth pluton. The two grains are in contact and present an interlocking texture.

there was also simultaneous crystallization of biotite, in which Mg was incorporated as well. The partitioning of magnesium into the biotite, under high oxygen fugacity,

prevented the Mg-enrichment of the amphiboles, leading to the formation of Fe-rich calcic amphiboles, even under oxidizing conditions.

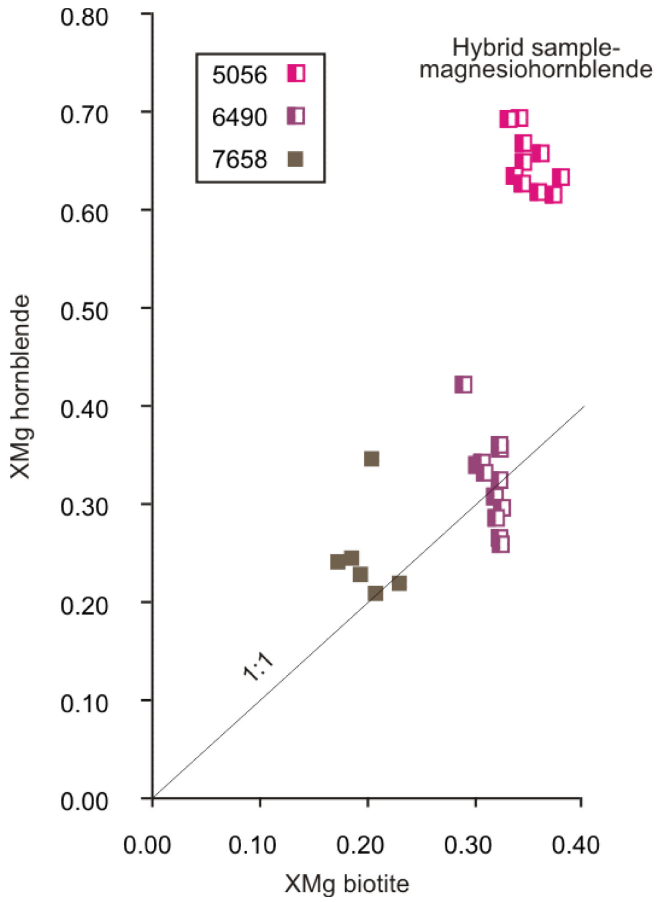

Figure 2. 9 Roozeboom diagram showing the XMg ratio (octahedral Mg/Mg+Mn+Fe_T+Ti in a.p.f.u) of coexisting biotite and calcic amphibole in the granites of the Wentworth pluton. With the exception of the hybrid sample which contains magnesiohornblende, the samples plot close to the 1:1 curve of the diagram that indicates a regular distribution of Mg between the two minerals. Within each mineral there is a negative correlation between the two ratios.

2.5.4 PRESENCE OF VOLATILES

The fact that the calcic amphiboles are related to a magma with mean 6 wt. % H_2O (Table 2.3) can explain why these samples contain biotite and also why they have lower zircon-saturation temperatures than those with sodic amphiboles. According to experimental data of Baker et al. (2002), zircon solubility is significantly lower in melts with 2 wt. %

H_2O at high temperatures, compared to more hydrous melts. Therefore, precipitation of zircon was early in the samples with sodic amphiboles, at temperatures higher than 850 °C, whereas it came later in the melt with calcic amphiboles due to the presence of high amounts of H_2O. The presence of volatiles can affect the stability and composition of amphiboles (Martin, 2007). The H_2O content of the melt can control the mineral chemistry of crystallizing amphiboles; a decrease in H_2O concentrations in the melt can lead to more sodic compositions (Scaillet and Macdonald, 2003; Ridolfi et al., 2010).

Scaillet and Macdonald (2003) demonstrated that a decrease in H_2O of the melt is associated with an increase of F in the amphiboles. The granites with sodic amphiboles show systematically higher initial amounts of F in the melt than the granites with calcic amphiboles, suggesting a negative correlation between these two volatile phases (Fig. 2.10).

The variations in initial H_2O contents between the two granitic magmas may have affected the F enrichment of the amphiboles, besides the availability of F itself. The more hydrous calcic magma produced additional biotite, thus leading F to participate in that mineral as well (Table 2.6) and resulting in smaller F contents in the crystallizing amphiboles. The variations in F contents between sodic and calcic amphiboles reflect the control of different initial magmatic contents of both H_2O and F on the mineral chemistry of the produced amphibole.

2.5.5 IMPLICATIONS FOR THE MAGMATIC EVOLUTION OF THE WENTWORTH GRANITES

The systematic differences in H_2O and F contents of the melt, temperature, ε_{Nd} values, Ba and alkalinity, suggest that the samples with calcic amphiboles and sodic

amphiboles represent two different, coeval, granitic magmas: a relatively sodic and a relatively calcic melt.

Table 2. 6 Representative microprobe analyses of biotite from the granites of the Wentworth pluton.

Sample	**5056**	**5056**	**6490**	**6490**	**6490**	**7658**	**7658**
Oxides (wt. %)							
SiO_2	37.34	37.04	38.45	38.27	38.53	36.15	35.22
TiO_2	4.12	3.78	2.51	2.66	2.41	3.72	4.02
Al_2O_3	13.27	13.37	14.68	13.60	14.26	12.79	12.49
FeOt	23.81	23.95	24.76	24.83	24.73	30.09	30.74
MnO	0.19	0.18	0.52	0.40	0.51	0.26	0.35
MgO	8.93	8.79	6.28	7.41	6.69	4.19	4.08
CaO	0.01	0.03	0.03	0.02	0.05	0.02	0.02
Na_2O	0.14	0.14	0.09	0.06	0.04	0.04	0.06
K_2O	9.58	9.54	9.38	9.35	9.53	9.01	9.15
CuO	0.00	0.00	0.00	0.02	0.02	0.04	0.02
F	0.43	0.41	0.42	0.63	0.41	0.19	0.22
Cl	0.35	0.40	0.14	0.10	0.18	0.27	0.33
H_2O	1.59	1.57	1.64	1.54	1.63	1.64	1.59
O≡F,Cl	0.26	0.26	0.21	0.29	0.21	0.14	0.16
Total	99.75	99.19	98.89	98.89	98.98	98.39	98.28
Structural formulae based on 22 oxygens							
Si	5.964	5.959	6.173	6.165	6.189	6.027	5.930
Al^{IV}	2.036	2.041	1.827	1.835	1.811	1.973	2.070
Al^{VI}	0.461	0.493	0.949	0.744	0.887	0.537	0.407
Ti	0.495	0.458	0.304	0.322	0.291	0.466	0.509
Fe^{2+}	3.180	3.222	3.325	3.345	3.322	4.194	4.329
Mn	0.026	0.025	0.071	0.055	0.069	0.036	0.050
Mg	2.126	2.109	1.503	1.779	1.602	1.042	1.025
Ca	0.002	0.005	0.005	0.004	0.008	0.003	0.003
Na	0.042	0.044	0.026	0.017	0.013	0.011	0.019
K	1.953	1.958	1.921	1.920	1.953	1.916	1.965
ΣCations	16.3	16.3	16.1	16.2	16.1	16.2	16.3
F	0.43	0.42	0.42	0.64	0.41	0.2	0.23
Cl	0.19	0.22	0.07	0.06	0.1	0.15	0.19
OH	1.69	1.68	1.75	1.65	1.74	1.83	1.79
$DF_{bt/melt}$	2.95	2.95	2.04	2.45	2.25	0.94	0.84
Fe#	0.60	0.60	0.69	0.65	0.67	0.80	0.81
F^1	0.19	0.18	0.19	0.27	0.18	0.09	0.10

Notes: Fe#: $Fe_T/(Fe_T+Mg)$ elements in a.p.f.u., [1] indicates mole fractions.

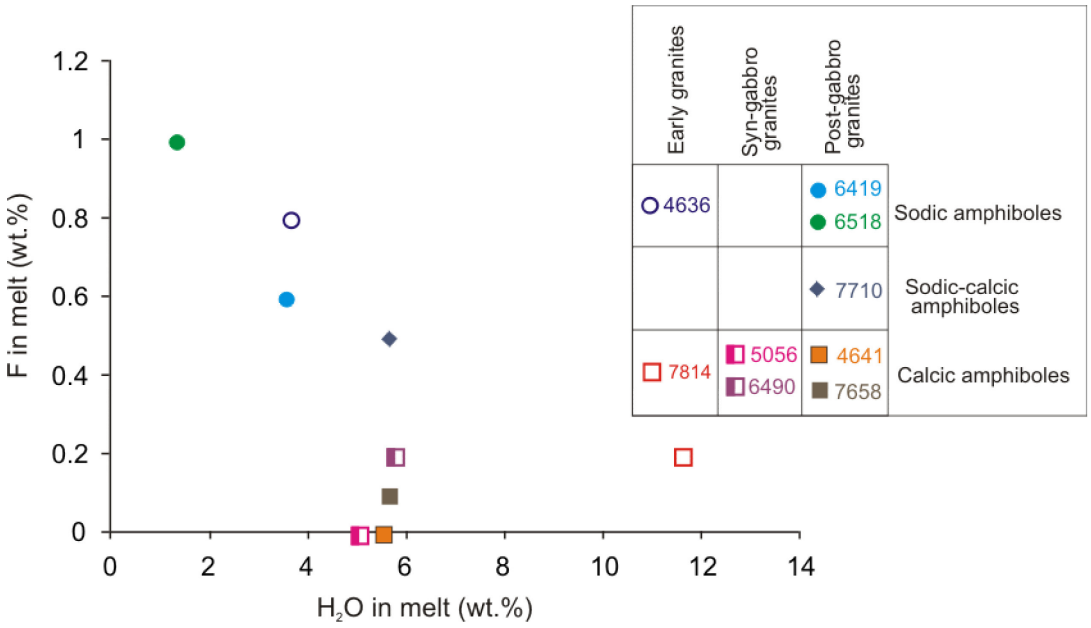

Figure 2. 10 Initial fluorine-in-melt contents versus magmatic water contents for the granites of the Wentworth pluton.

The sodic magma shows lower values of estimated viscosity compared to the calcic magma. The presence of H_2O can reduce the viscosity of the melt (Goto et al., 2005) and enhance the magma ascent. However in mid- to upper crustal levels the influence of water may be limited due to the release of volatiles at low pressures and decrease in temperature. The high magmatic temperatures and F can also reduce the viscosity of the melts and drive the emplacement of the melt in the upper crust (Dingwell et al., 1985). Therefore, while the mobility of the calcic melt may have been influenced by the presence of water, in the sodic melts the shallow emplacement was the result of reduced viscosity due to higher temperatures and probably F.

The granites of the Wentworth pluton show a systematic increase of emplacement pressures with decreasing age (Fig. 2.11). The differences in the pressure estimates for granites of different ages could be either the result of differences in the level of emplacement or due to changes in overlying lithostatic load with time. During the

emplacement of the Wentworth early granites (from 368±4 to 362±2 Ma, Table 2.7) the volcanic pile included a part of the Byers Brook rhyolites, less than 3 km thick, (<1 kbar assuming a density of a felsic continental crust) (Fig. 2.11). The syn-gabbro granites (356±3 Ma, Table 2.7) are probably synchronous with either the uppermost Byers Brook Formation, or the lower Diamond Brook basalts, and also with the intrusion of the gabbro (Fig. 2.12). Therefore, at the time of the emplacement of the syn-gabbro granites, the volcanic pile included 3 km of the Byers Brook Formation and at least some of the Diamond Brook basalts, thus equivalent to 1.0–1.5 kbar lithostatic load. The post-gabbro granites post-date most or all the denser gabbro (Koukouvelas et al., 2002), and most or all of the present volcanic pile (~4.5 km, ~ 1.5 kbar), suggesting that the lithostatic load was the highest during the emplacement of these rocks.

Taking into account the age uncertainties and the mean pressure estimates for the studied samples, it seems that the observed increase of pressure over time broadly correlates with the likely increase of thickness of the volcanic pile (including the thick succession of basalts) and the emplacement of the voluminous and denser gabbro. Thus the absolute structural level of the syn-gabbro and post-gabbro granites probably did not vary significantly. The systematically higher magmatic temperatures (T_{Zr}) in the post-gabbro granites compared to the early and the syn-gabbro granites (Table 2.3) reflects the relatively greater depth of emplacement created by the overlying volcanic pile. The very low pressure of emplacement of the late dyke that intruded the gabbro (sample 7710) may be related to a decreased lithostatic load due to erosion, after the volcanic succession was completed. Rapid erosion and unroofing of the plutons are recorded throughout the

Cobequid Highlands, where A-type granitic clasts are found in the sediments of the Horton Group which is in turn intruded by younger granitic phases (Pe-Piper et al.,

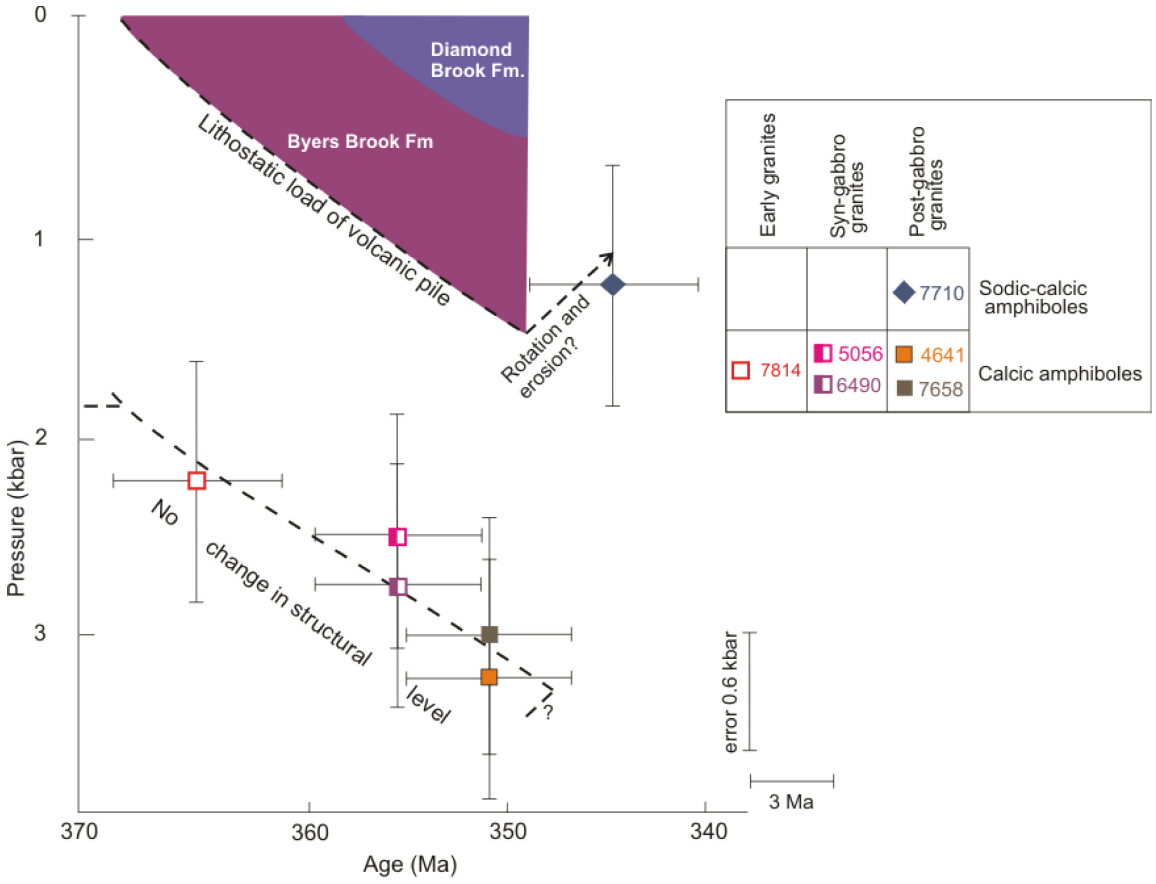

Figure 2. 11 Distribution of estimated pressures of emplacement for the Wentworth granites plotted against age (error bar for pressure estimates equal to 0.6 kbar, Anderson and Smith 1995, average error of age estimates 3 Ma). The approximate lithostatic load of the volcanic pile over time is also plotted for comparison.

1998). The fine grained granitic dyke contains sodic-calcic amphiboles interstitial between larger grains of quartz and feldspar (Table 2.3). Even though it was emplaced at very low pressures, the magmatic temperatures were high, as indicated by the zircon-saturation thermometer (Table 2.3). There is no correlation between the estimated viscosities and the observed increase of pressure with time, which could indicate a dominant influence of the ascent process on the latter.

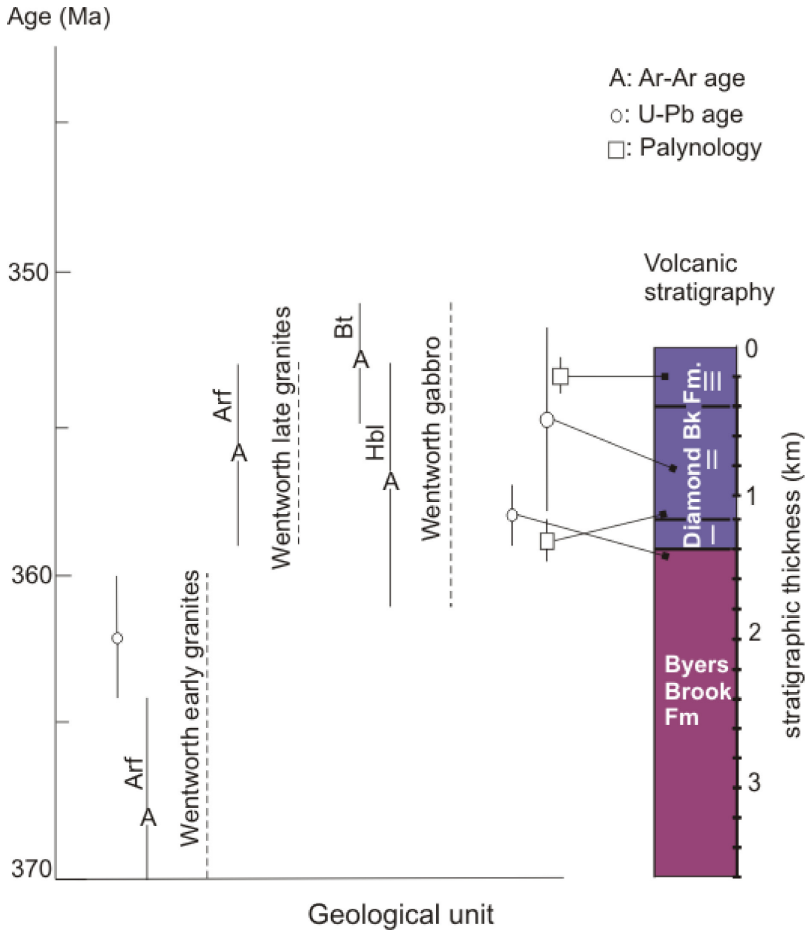

Figure 2. 12 Geochronological data for the various geological units in the area of the Wentworth pluton, along with the stratigraphic column of the volcanic rocks, indicating the positions of dated samples. Data compiled from Utting et al. (1989), Martel et al. (1993), Doig et al. (1996), Dunning et al. (2002) and Pe-Piper et al. (2004). All Ar-Ar ages have been corrected from the original papers according to Kuiper et al. (2008).

Furthermore, the presence of the interstitial amphiboles in the fine-grained granite dyke, indicates that these minerals were the last to crystallize from a residual melt, in the space between the larger pre-existing quartz and feldspar. The sodic-calcic composition of the interstitial amphiboles in this sample suggests that the residual melt had an intermediate composition between the identified calcic and sodic granitic magmas. This originally calcic magmatic pulse, as indicated by the presence of primary ferro-edenite, may have been partially hybridized during ascent by the sodic melts that had been

Table 2. 7 Chronological data for the geological units in the area of the Wentworth pluton.

Geological Unit	Age (Ma)	Method	Reference
Early granites of the Wentworth pluton	362±2	U-Pb (zrn)	Doig et al. (1996)
	368±4	Ar-Ar (arf)	Pe-Piper et al. (2004)
Late granites (probable syn-gabbro granites)	356±3	Ar-Ar (arf)	Pe-Piper et al. (2004)
Wentworth gabbro	357±4	Ar-Ar (hbl)	Pe-Piper et al. (2004)
	353±2	Ar-Ar (bt)	Pe-Piper et al. (2004)
Byers Brook Formation (Upper)	358±1	U-Pb (zrn)	Dunning et al. (2002)
Diamond Brook Formation (Upper)	348±3	palynology	Utting et al. (1989), Menning et al. (2006)
Diamond Brook Formation (Middle)	353±3	U-Pb (zrn)	Dunning et al. (2002)
Diamond Brook Formation (Middle-Lower)	359±2	palynology	Martel et al. (1993)

Notes: All Ar-Ar ages have been corrected from the original ages reported in the cited papers, according to Kuiper et al. (2008). Biostratigraphic ages are corrected according to ICS 2013. Reported age uncertainties are given in 2σ.

previously emplaced at lower crustal levels, so that the residual melt that finally reached the upper crust has chemical affinities of both granitic melts and thus produced amphiboles of sodic-calcic composition. Granites with sodic-calcic amphiboles are only known from one dyke and as enclaves in outcrops of granites that contain sodic amphiboles. Such a mode of occurrence implies that these granites do not represent a major magmatic phase in Wentworth pluton; rather they are the result of mingling of coexisting sodic and calcic granitic melts.

2.6 CONCLUSIONS

The types of primary amphiboles in the Wentworth pluton are represented principally by calcic and sodic compositions with rare sodic-calcic varieties. The pressure estimates suggest that the pluton was emplaced between 1 to 3 kbar, which corresponds to upper crust. Differences in temperature, ε_{Nd}, Ba, H_2O and F in-melt contents suggest the presence of two coeval granitic magmatic systems: one that formed the calcic amphibole-bearing granites and another that formed the sodic amphibole-bearing granites. The calcic

magma was H_2O -rich producing granites in a range of pressure and temperature and with textures that vary from medium to fine grained granular and granophyric. The sodic magma derived from a source with larger mantle component, was drier, and less viscous due to elevated magmatic temperatures. Coexistence of both magmas is indicated by a late fine-grained granite dyke, with interstitial amphiboles of calcic and sodic-calcic composition that show the lowest estimated pressure. These observations suggest that a younger batch of the calcic melt was mixed with the sodic granitic magma and reached the upper crust before complete crystallization, producing sodic-calcic amphiboles upon emplacement.

The Wentworth pluton is composite, constructed by two distinct granitic magmas and a gabbroic magma. The present work shows that extreme variations in the type of magmatic amphiboles present in an A-type granitic pluton may reflect the complexity of the parental magmatic system. Other A-type granites with such a mineralogical diversity and limited evidence of fractionation may have similarly complex origins.

CHAPTER 3 SYSTEMATIC MINERALOGICAL DIVERSITY IN A-TYPE GRANITIC INTRUSIONS: CONTROL OF MAGMATIC SOURCE AND GEOLOGICAL PROCESSES

PREFACE

This chapter has been submitted as: "Papoutsa, A., Pe-Piper, G., and Piper, D.J.W., Systematic mineralogical diversity in A-type granitic intrusions: control of magmatic source and geological processes", and is currently in press in Geological Society of America Bulletin.

3.1 ABSTRACT

The origin and causes of mineralogical diversity of A-type granites are debated. A series of A-type granite plutons, with distinct mineralogical differences, emplaced along an late Paleozoic crustal-scale shear zone in the Cobequid Highlands, Nova Scotia, provide an opportunity to examine the origin of different A-type plutons in a similar tectonic setting. Based on the ferromagnesian minerals present, the plutons are classified into sodic granites with sodic amphibole, calcic granites with calcic amphibole, and biotite granites. Sodic and calcic granites occur exclusively in complex intrusions with subequal amounts of gabbro in the eastern part of the Cobequid Highlands, whereas plutons in the western part, with lesser gabbro, comprise only biotite granites. Trace elements and radiogenic isotopes show that the three granite types have different sources. Intensive parameters including temperature, pressure, and water-in-melt contents were estimated from mineralogical and geochemical data. Modeling of these geochemical data suggests that the biotite and calcic granites were derived by 20-40% partial melting of intracrustal feldspathic rocks, whereas the sodic granites are extreme fractionates (90%) of coeval mafic magma. We propose that

supply of late Paleozoic mafic magma, probably related to regional extension and underplating beneath the Magdalen Basin, reached the Cobequid Highlands and created a deep crustal hot zone. Extreme fractionation of these underplated mafic melts produced the sodic granites. Heat transfer from crystallizing mafic magma induced partial melting of the surrounding crust, creating batches of biotite and calcic granitic melts in different depths. Fractionated and crustally-derived melts segregated along crustal-scale faults, as indicated from field evidence, constructing the complex plutons in the east. Melting of the crust was further facilitated by the release of water from the crustal rocks upon heating. In the eastern part of the Cobequid Highlands, water was released predominantly by magmatic rocks and in lesser amounts compared to the west where Neoproterozoic sedimentary and volcaniclastic rocks are more abundant. The volatile-rich granitic melts in the western part of the study area crystallized rapidly, stabilizing only biotite. This study demonstrates that the mineralogical variations in A-type granites arise from rather similar magma compositions, but are important petrogenetic indicators of varying sources, specific magmatic processes and emplacement conditions.

3.2 INTRODUCTION

A-type granites comprise a distinct group of granitoid rocks, the origin of which is well-debated. This group of rocks was recognized by Chappell and White (1974) in their proposed genetic "alphabet" classification scheme, in which these granites were separated from the I-, S- and M-types on the basis of their distinct alkaline trace element geochemistry and anorogenic tectonic setting. The authors proposed that these granites originated from a crustal residue that remained after a previous event of partial melting. Loiselle and Wones (1979) introduced the term "A-type" and proposed that differentiation

of alkali basalt may also produce a suitable parent magma. However A-type granites, identified solely from their trace elements, also have been reported from post-orogenic tectonic settings, and include rocks of variable alkalinity ranging from peralkaline to even peraluminous compositions (Bonin, 2007).

The term "A-type granite" (Loiselle and Wones, 1979) initially referred to granites with mildly alkaline geochemistry emplaced along continental rift zones and crystallized under low water fugacities. Such granites are richer in Fe, K, rare metals and rare earth elements (REE) compared to other granitoids (Whalen et al., 1987), implying a distinctive petrogenesis. As such, the importance of A-type granites is also economic since they may be associated with polymetallic deposits of Sn, Nb, Ta, U, Th, F, and REE (Bettencourt et al., 2005; Costi et al., 2009; Dall'Agnol et al., 2012). Current concepts of A-type granite petrogenesis include partial melting of tonalitic to granodioritic crust (Creaser et al., 1991; Frost and Frost, 2010), high-temperature dehydration melting of calc-alkaline granitoids in the shallow crust (Patiño Douce, 1997), or differentiation of mafic magma (Loiselle and Wones, 1979; Frost and Frost, 2010).Variation in primary ferromagnesian minerals in A-type granites suggests contrasting sources and magmatic conditions, even within a single alkaline province (Gualda and Vlach, 2007; Shellnutt and Zhou, 2007; Shellnutt and Iizuka, 2011). In this paper we show that systematic mineralogical differences in coeval A-type granites within the same magmatic province are the result of varying sources, specific magmatic processes, and styles of magma emplacement.

The Cobequid Highlands in Nova Scotia provide a suitable opportunity for such a study. Several coeval A-type granite plutons were emplaced along the active faults of a shear zone active in the late Devonian. These granitic plutons were emplaced under the

same regional tectonic regime and have similar overall geochemistry, but they present important mineralogical differences. The plutons include biotite-bearing and both sodic- and calcic-amphibole-bearing A-type granites, with only minor chemical zoning in the ferromagnesian minerals. The mineralogical diversity may thus reflect deeper magmatic processes and variations in magmatic sources.

3.3 GEOLOGICAL SETTING

The Cobequid Highlands are located in the Avalon terrane of the Canadian Appalachians, just north of the Cobequid-Chedabucto fault zone, which separates this

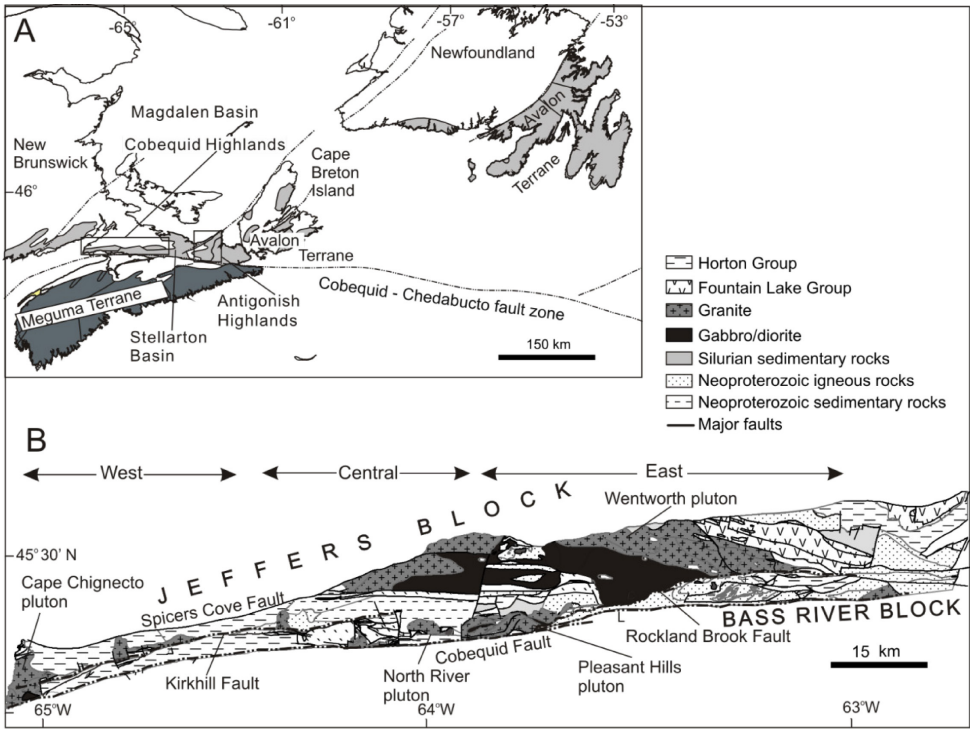

Figure 3. 1 Simplified geological map of Nova Scotia (A) showing the position of the study area and (B) geological map of the Cobequid Highlands (modified from Pe-Piper and Piper, 2003).

terrane from the Meguma terrane (Fig. 3.1A). The Cobequid Highlands are underlain by Neoproterozoic subduction-related igneous and metasedimentary rocks, minor Ordovician igneous rocks, Silurian to lower Devonian sedimentary rocks and late Paleozoic plutons and their extrusive equivalents (Pe-Piper and Piper, 2003). Within the Cobequid

Highlands, the Cobequid Shear Zone consists of a series of strike-slip faults that were initially active in the Neoproterozoic and reactived during latest Devonian to earliest Carboniferous. Plutons were emplaced along the active faults of the deforming Cobequid Shear Zone and consist of granite and gabbro bodies. The Rockland Brook fault, the major fault of the Cobequid Shear Zone in the eastern part of the Highlands, separates the Neoproterozoic Jeffers Block to the north from the Bass River Block to the south (Fig. 3.1B). The Cobequid fault marks the southern margin of the Cobequid Highlands (Pe-Piper and Piper, 2003).

Lower crust of the Avalon terrane has a distinctive seismic signature compared to both inboard and outboard Appalachian terranes (Marillier et al., 1989; Keen et al., 1991), and its seismic velocity of 6.8 km/s (Marillier et al., 1994) may indicate a significant mafic component, related to its long history of subduction in the Neoproterozoic.

In the late Devonian, subduction of the Rheic Ocean beneath Nova Scotia was associated with the emplacement of the voluminous South Mountain Batholith and satellite plutons in the Meguma terrane (Clarke et al., 1997). Towards the end of the Devonian, incipient closure of the Rheic Ocean at the Virginia and Hermitage promontories led to dextral strike-slip faulting parallel to the strike of the orogen (Hibbard and Waldron, 2009). This resulted in distributed extension of the basement beneath the Gulf of St. Laurence and the opening of the Magdalen Basin (Fig. 3.1A) as a step-over zone. Crustal thinning continued through at least the early Carboniferous, accompanied by underplating of a thick gabbroic layer beneath the Magdalen Basin (Marillier and Verhoef, 1989; Marillier and Reid, 1990). The Cobequid Shear Zone and its continuation along the west coast of Cape Breton Island marked the southwestern edge of the Magdalen Basin and

acted as a pathway for magma, which formed flood basalts >1 km thick in the Fisset Brook Formation of western Cape Breton Island and 1.5 km thick in the Fountain Lake Group of the eastern Cobequid Highlands (Pe-Piper and Piper, 2003).

All late Paleozoic granites in the Cobequid Highlands have A-type affinities, whereas the gabbros are ferro-gabbros. Synchronous with the plutons were the basalts and rhyolites of the Fountain Lake Group that show similar chemical affinities to their intrusive equivalents (Dessureau et al., 2000; Pe-Piper and Piper, 2003). The plutons selected for this study are the Wentworth (WP) and Pleasant Hills (PHP) plutons (complex intrusions with significant amounts of gabbro) in the eastern part, the North River pluton (NRP) in the central part (small intrusion with minor gabbro), and the Cape Chignecto pluton (CCP) in the western part of the Cobequid Highlands (homogeneous granite intrusion with moderate amounts of gabbro). All are coeval (365±4 Ma to 358±4 Ma), with the latest plutonic body being the large gabbro in the Wentworth pluton (357±4 Ma) (Dunning et al, 2002; Pe-Piper et al., 2004; Murphy et al., 2011).

3.4 METHODS

A total of 127 thin and polished thin sections from the four representative plutons were examined by petrographic microscope. Some samples used in this study were previously analyzed geochemically by X-ray fluorescence (XRF) for major elements and certain trace elements (Ba, Rb, Sr, Y, Zr, Nb, Pb, Ga, Zn, Cu, Ni, V, Cr and Co) and by instrumental neutron activation analysis (INAA) for the REEs and specific trace elements (Cr, Cs, Hf, Sb, Sc, Ta, Th, and U). The analytical precision is better than 2%, except for MgO, Na_2O and Nb for which is better than 5%, and Th which is better than 10% (Pe-Piper and Piper, 1989). Some of these samples, together with some new samples, were re-

analyzed for this study at Activation Laboratories. Major elements were analyzed by fusion ICP-MS with a detection limit of 0.01 wt.% for most oxides except MnO (0.001 wt.%). Trace elements including REE were also analyzed by fusion ICP-MS, except for Ni, Cu, Zn, and Pb for which total digestion ICP-MS was employed. Trace elements have detection limits below 5 ppm, except for Cr (20 ppm). Geochemical data were processed using MINPET 2.2 (Richard, 1995) software for Windows and the plotted data were recalculated to 100% on volatile-free basis.

Oxygen isotope analyses of selected samples were determined at the Laboratory of Stable Isotope Science of the University of Western Ontario, using the ClF_3 extraction method for silicates and oxides with a precision of 0.3 ‰. Oxygen isotope data are presented in the normal delta notation relative to the Vienna Standard Mean Ocean Water (V-SMOW). Neodymium-Sm and Pb isotope analyses were mostly reported by Pe-Piper and Piper (1998), where details of methods and precision are given, and some analyses were made by the same laboratory reported in Papoutsa and Pe-Piper (2014).

3.5 PETROGRAPHY OF THE LATE PALEOZOIC A-TYPE GRANITES

3.5.1 MINERALOGICAL VARIATIONS

The granites are fine- to coarse-grained alkali-feldspar granites with a variety of textures including granular, granophyric, and porphyritic. Most granites are subsolvus with two types of subhedral magmatic feldspar. Plagioclase ranges from oligoclase to calcic albite whereas the K-feldspar is orthoclase. Hypersolvus granites have been identified where the only feldspar present is a perthitic K-feldspar. The granites host variable amounts and types of magmatic ferromagnesian minerals such as biotite and amphibole. Biotite has an annitic composition whereas the amphibole can be calcic, sodic-calcic or

sodic. The primary calcic amphiboles include ferro-edenite and ferro-hornblende, sodic-calcic amphiboles are represented by ferro-richterite and the sodic amphiboles by arfvedsonite (as described in Pe-Piper, 2007; Papoutsa and Pe-Piper, 2014). Secondary minerals include epidote, chlorite, titanite, actinolite, ferro-winchite, ferro-eckermannite, riebeckite, and green biotite, derived mostly from the breakdown of the primary ferromagnesian phases. Magnetite is the dominant opaque mineral, but ilmenite and pyrite are also present in small amounts. Accessory primary minerals include apatite, zircon, titanite, allanite-(Ce), and chevkinite-(Ce).

Based on the type of magmatic ferromagnesian mineral present, five granitic types are recognized: a) sodic granite with arfvedsonite, b) calcic granite with ferro-edenite or ferro-hornblende, with or without biotite, c) sodic-calcic granite with sodic-calcic amphibole coexisting with either sodic or calcic amphibole, d) biotite granite with biotite but no amphibole, and e) leucogranite with ferromagnesian silicate minerals absent.

With the exception of sodic granites, which are exclusively hypersolvus and some leucogranites, all other granite types are subsolvus. The sodic-calcic granites are found as late microgranitic dykes and enclaves in either gabbro or sodic granite. The leucogranites occur exclusively as late dykes cutting all lithologies in the plutons. These two minor lithologies are not considered further in this study. The Cape Chignecto and North River plutons contain only biotite granite, the Pleasant Hills pluton contains calcic and biotite granite, whereas the Wentworth pluton is the largest and most complex intrusion and contains all three major granite types. The three main granite types show no systematic geographic distribution within the composite Pleasant Hills and Wentworth plutons.

3.5.2 WHOLE-ROCK CHEMISTRY

All granite types plot within the A-type field in the geochemical diagrams of Whalen et al. (1987) (Fig. 3.2A), and range from mildly peralkaline to metaluminous and peraluminous compositions (Fig. 3.2B).

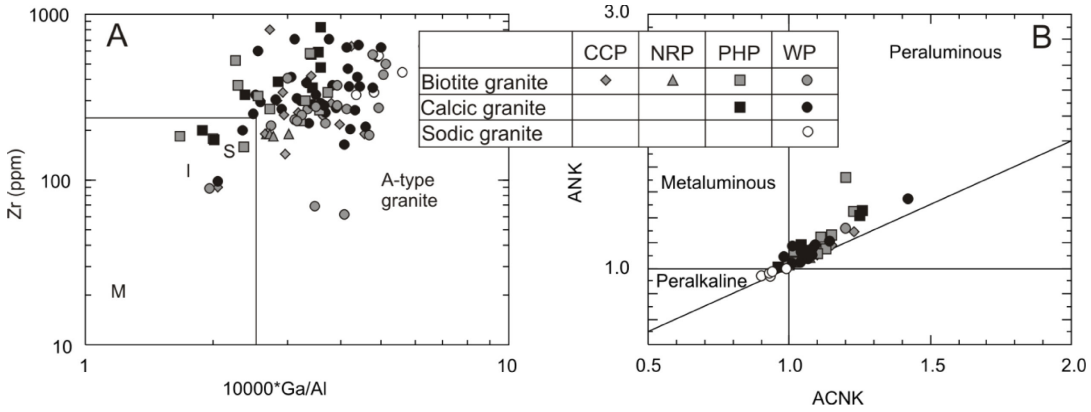

Figure 3. 2 Geochemical classification diagrams for the Late Paleozoic granites from the Cobeqiod Highlands. (A) shows the classification of the studied granites as A-type (after Whalen et al., 1987). (B) shows the alkaline character of the sodic, calcic and biotite granites (as in Maniar and Piccoli, 1989).

The sodic granites are the most peralkaline, the calcic granites range from metaluminous to peraluminous, whereas the biotite granites are mainly peraluminous. The sodic granites are the only ones to plot in the A1 field (Fig. 3.3A) in the discrimination diagrams of Eby (1992), whereas the calcic and biotite granites are classified as A2 granites (Fig. 3.3B and C), although all three types plot close to the boundary between the two fields. The chondrite-normalized REE patterns of all granitic types show the typical characteristics of A-type granites such as a strong negative Eu anomaly, strong light (L) REE enrichment and a relatively flat heavy (H) REE pattern (Fig. 3.4A to C). Although there are no significant variations in whole-rock geochemistry of major oxides between the main granitic types (Table 3.1), some trace elements do show systematic variations (Fig. 3.5).

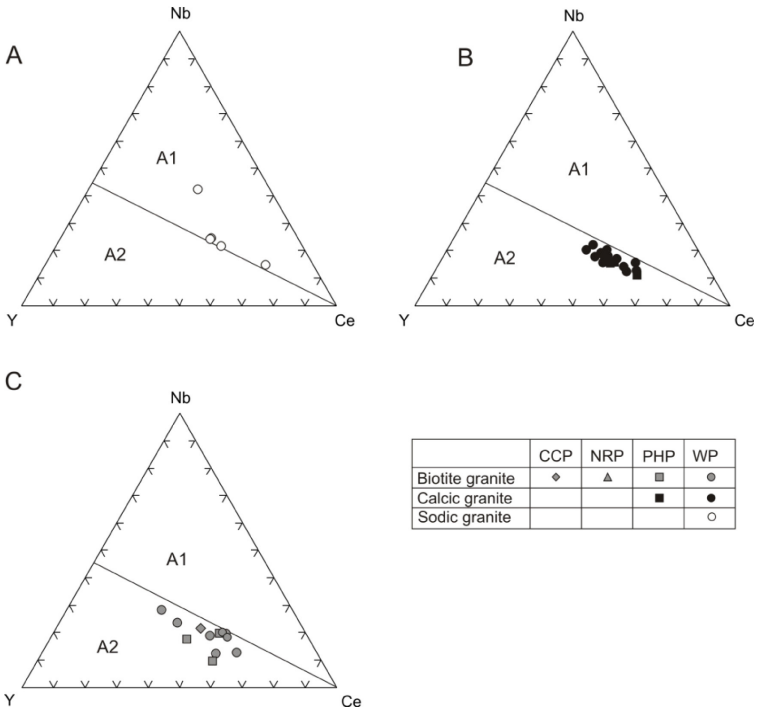

Figure 3. 3 A-type discrimination diagrams (after Eby, 1992) for (A) sodic, (B) calcic and (C) biotite granites. A1 field includes granites derived by fractionation of mafic melts whereas A2 field is for granites derived by partial melting of crustal rocks.

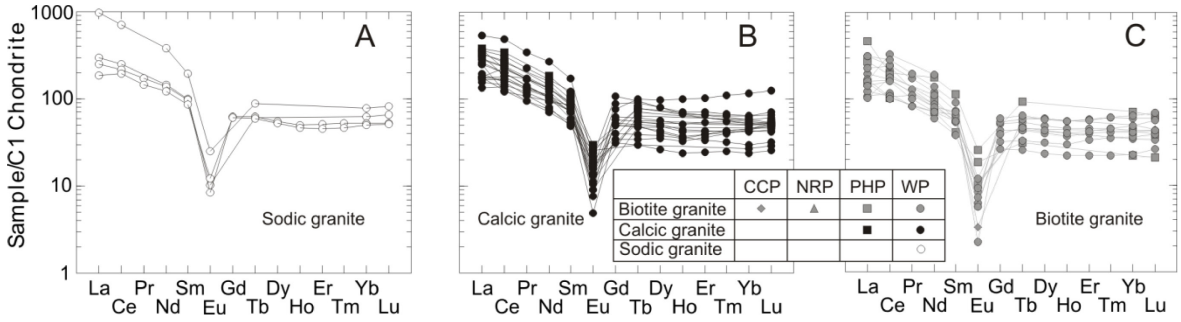

Figure 3. 4 Chondrite-normalized REE patterns for (A) sodic, (B) calcic and (C) biotite granites from the Upper Paleozoic plutons of the Cobequid Highlands. Normalizing values after Sun and MacDonough (1989).

At high SiO_2 values, Ba is generally more concentrated in the biotite and calcic granites, whereas the sodic granites are noticeably poorer (Fig. 3.5A).The calcic granites show higher amounts of Cr compared to the sodic and most biotite granites (Fig. 3.5B). Nb is in higher concentrations in the sodic granites, whereas it is lower in the biotite granites

(Fig. 3.5C). The sodic granites are also the most enriched in Zn (>90 ppm, Table 3.1) and Ga (>30 ppm) (Figs. 3.5D and E), whereas both the biotite and calcic granites show similar amounts of these elements (10–100 ppm and 10–35 ppm, respectively). Strontium shows significant scatter, but is generally in higher concentrations in the calcic granites, whereas the sodic granites show the lowest concentrations (Fig. 3.5F). Whole-rock oxygen isotopes from the North River and Cape Chignecto biotite granites have higher $\delta^{18}O$ (6.1–7.6 ‰, Table 3.2) than the granites of the eastern Cobequid Highlands (mean 5.7 ‰).

3.6 DISCUSSION

The presence of mineralogically different A-type granites with systematic trace element variations provides the opportunity to better understand the variable petrogenetic conditions that formed these rocks. Since multiple granite types can coexist in the same pluton, it needs to be established whether these different granite types have the same source. Are the observed chemical variations controlled by the nature of the magmatic source, or do they result from geological processes such as varying degrees of partial melting and fractionation? In this section, the mineralogy and geochemistry of the sodic, calcic and biotite A-type granites are discussed further, in order to define the petrogenetic evolution of these rocks.

3.6.1 ESTIMATES OF INTENSIVE PARAMETERS

The magmatic temperatures for the late Paleozoic granites have been estimated by the use of the zircon-saturation thermometer (Boehnke et al., 2013) within an uncertainty of ± 30-50°C to account for errors in elemental abundances and ratio precision. Saturation of Zr in all these granites is indicated by the presence of magmatic zircon, the calculated M-ratios (molar (Na+K+2Ca)/(Al*Si)) are within the calibration range (from 0.7 to 1.7,

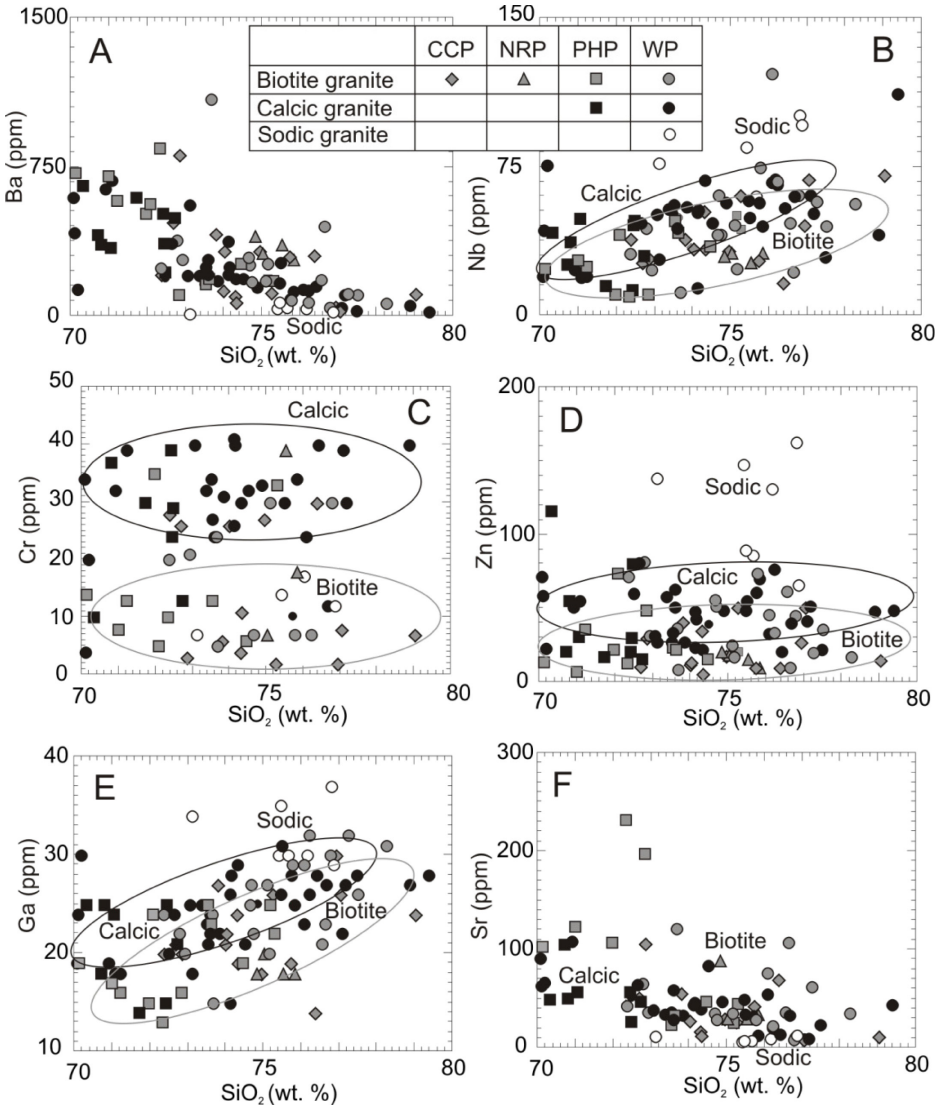

Figure 3. 5 Harker-type geochemical plots of selected trace elements (A) Ba, (B) Nb, (C) Cr, (D) Zn, (E) Ga and (F) Sr for the different granitic types present in the Upper Paleozoic plutons of the Cobequid Highlands. Sodic granites appear quite distinct from the other types in terms of Ba, Nb and Zn, whereas the calcic and biotite granites show significant overlaps except for Cr.

Table 3.3), and therefore the application of this zircon thermometer was considered appropriate. Textural evidence from the subsolvus granites suggests that plagioclase was one of the first phases to crystallize from the melt. Experimental work shows that plagioclase crystallizes as a near-liquidus phase in A-type granitic partial melts (Dall'Agnol et al., 1999). The plagioclase-melt barometer of Putirka (2005) was, therefore, employed to determine the pressure that best approaches the pressure of magma generation

(pressure of partial crystallization) in all subsolvus granites. This barometer is based on albite-anorthite exchange and provides pressure estimates within an error of ± 1.8 kbar.

The initial contents of water in the granitic melt were estimated by the plagioclase-melt hygrometer of Putirka (2005). The error of the estimated water contents with this method may be up to ±1.2 wt. %. Estimates in the viscosity of the granitic melts were done using the model of Giordano et al. (2008). The associated error of this method for anhydrous (sodic granites) and hydrous melts (calcic and biotite granites) is ± 0.25 and 0.35 log units, respectively.

Most of the studied granites are related to melts with zircon saturation temperatures between 800 and 950 °C (Table 3.3). However, the alkalinity of the melt is a major factor that controls zircon solubility, and consequently affects the temperature estimates. Solubility of zircon is lower in metaluminous and peraluminous melts, and therefore any inherited zircon may be preserved. Miller et al. (2003) argued that zircon-saturation temperature estimates from highly fractionated felsic melts and melts with limited evidence of zircon inheritance represent minimum estimates, whereas the opposite stands for granitoids with abundant zircon inheritance. Dunning et al. (2002) demonstrated that there is only minor zircon inheritance in the granites of the studied plutons, except for their sample J of a late leucogranite from the Pleasant Hills pluton. Therefore, the estimated magmatic temperatures in this work are taken as minimum estimates.

The estimated pressures of partial crystallization from the plagioclase geobarometer range from 3 to 14 kbar for most granites (Table 3.3). There is a systematic variation, however, in the estimated pressures between the calcic and the biotite granites.

Table 3. 1 Representative whole-rock analyses of A-type granites from the Cobequid Highlands.

Pluton	CCP	NRP	PHP	WP	WP	PHP	PHP	WP	WP	WP	WP	Detection limit (%)	
Type	bio	bio	bio	bio	bio	cal	cal	cal	cal	sod	sod		
Sample	6284	1779	4672	9827b	36-2-1	4681	4689	6468	6489	4636	6490	A	B
Method	B	B	B	A	B	B	B	B	B	B	B		
Major oxides (wt.%)													
SiO_2	77.10	74.92	75.16	78.23	72.90	70.77	72.45	76.40	77.16	76.15	75.44	0.01	0.03
TiO_2	0.16	0.19	0.25	0.13	0.22	0.48	0.38	5.30	5.03	0.17	4.88	0.001	0.005
Al_2O_3	12.20	12.81	12.64	11.92	13.76	13.18	13.17	11.88	12.09	11.58	11.81	0.01	0.03
Fe_2O_3	1.13	1.97	2.42	1.51	1.85	4.09	3.23	2.17	1.90	2.53	2.67	0.01	0.03
MnO	0.10	0.01	0.02	0.02	0.03	0.07	0.07	0.01	0.03	0.04	0.04	0.001	0.005
MgO	0.22	0.19	0.83	0.13	0.89	1.13	0.99	0.15	0.09	0.82	0.13	0.01	0.03
CaO	0.68	0.16	0.26	0.44	0.44	0.91	0.65	0.17	0.16	0.21	0.18	0.01	0.03
Na_2O	5.10	3.59	3.74	3.40	4.00	3.45	3.89	3.39	3.33	4.45	3.68	0.01	0.03
K_2O	2.92	5.45	4.79	4.80	5.55	5.49	5.11	0.17	0.35	4.65	0.33	0.01	0.03
P_2O_5	0.04	0.02	0.04	0.02	0.03	0.09	0.07	0.02	0.03	0.01	0.03	0.01	0.005
LOI	0.30	0.31	0.40	0.13	0.40	0.20	0.30	0.49	0.39	0.30	0.56		C
Trace elements (ppm)													
Method	A	A	C	A	C	C	C	A	A	C	A		
Ba	504	529	186	64	285	360	223	152	108	39	73	3	25
Rb	180	32	211	226	240	206	262	174	180	224	203	1	2
Sr	54	66	26	36	37	51	27	14	10	10	8	2	5
Y	39.8	63.4	111	55.9	60	78	88	50.5	57.0	90	60.1	0.5	3
Zr	273	162	337	273	212	831	361	365	202	552	446	1	4
Nb	19	20	50	56	23	37	48	55	52	69	43	0.2	1
Pb	59	13	20	6	17	3	45	8	9	3	18	5	3
Ga	21	18	25	31	20	25	24	28	27	30	35	1	5
Zn	b.d.	60	22	17	32	55	80	21	52	131	90	1	5
Cu	b.d.	b.d.	b.d.	10	b.d	b.d	2	7	10	0	7	1	4
Ni	b.d.	b.d.	10	5	5	12	9	5	5	4	6	1	3
V	8	8	6	7	21	10	9	b.d.	b.d.	2	b.d.	5	4
Cr	b.d.	b.d.	44	b.d.	21	37	29	40	30	32	40	20	4
La	68.40	28.90	109.0	33.20	46.0	91.2	77.8	41.50	40.30	71.2	43.90	0.05	0.5
Ce	122.0	97.10	124	97.20	102	213	169	112.0	102.0	152	118.0	0.05	3
Pr	15.80	7.26	n.d.	9.44	n.d.	n.d.	n.d	12.60	12.20	n.d.	13.60	0.01	
Nd	56.50	25.30	82	33.30	n.d.	87	68	51.00	49.60	68	56.40	0.05	5
Sm	10.90	6.10	17.2	8.41	8.7	17.2	13.7	10.90	11.20	15.3	13.10	0.01	0.1
Eu	0.90	0.34	1.49	0.33	0.62	1.72	1.1	0.79	0.61	0.6	0.71	0.005	0.2
Gd	8.45	6.65	n.d.	7.99	n.d.	n.d.	n.d	10.30	10.90	n.d.	12.60	0.01	
Tb	1.52	1.56	3.51	1.74	1.64	2.95	2.6	1.78	1.93	2.3	2.21	0.01	0.5
Dy	8.19	9.95	n.d.	10.90	n.d.	n.d.	n.d	11.00	12.30	n.d.	13.50	0.01	
Ho	1.56	2.09	n.d.	2.29	n.d.	n.d.	n.d	2.13	2.40	n.d.	2.61	0.01	
Er	4.07	6.18	n.d.	6.93	n.d.	n.d.	n.d	6.40	7.00	n.d.	7.59	0.01	
Tm	0.59	0.98	n.d.	1.16	n.d.	n.d.	n.d	1.04	1.11	n.d.	1.18	0.005	
Yb	3.87	6.56	12.0	8.33	5.8	8.9	9.3	7.33	7.80	10.7	8.41	0.01	0.2
Lu	0.63	1.00	1.62	1.45	0.85	1.27	1.32	1.06	1.28	1.67	1.29	0.002	0.05
Co	1.00	84.0	0.63	b.d.	b.d.	b.d	b.d.	b.d.	1	n.d.	1	1	5
Cs	4.5	0.9	2.4	2.4	n.d.	3.2	3.1	2.1	3.3	n.d.	2.1	0.1	0.2
Hf	7.4	5.5	12.7	8.5	7.9	22.4	12.6	12.2	8.2	n.d.	12.6	0.1	0.2
Sc	n.d.	n.d.	2.13	1.00	3.23	4.15	3.68	1.0	1.0	n.d.	b.d.	0.1	0.01
Ta	n.d.	n.d.	5.5	5.80	2.6	3.9	5.1	4.15	3.97	n.d.	3.06	0.01	0.3
Th	20.4	24.5	23.0	19.7	22.0	17.0	21.0	15.7	17.4	16.0	11.8	0.05	0.2
U	n.d.	n.d.	4.3	4.43	n.d.	3.6	4.2	3.28	3.06	5.9	2.88	0.01	0.5

Note: All major oxides were measured with XRF, trace elements were determined with INAA and ICP-MS. A: Major and trace elements analyzed by ICP-MS, B: Major elements analyzed by XRF, C: trace elements from Ba to Cr and Co analyzed by XRF, REE and elements from Cs to U by INAA. Abbreviations: b.d.=below detection limit, n.d.= not determined, bio= biotite granite, cal= calcic granite, sod= sodic granite, CCP= Cape Chignecto pluton, NRP= North River pluton, PHP= Pleasant Hills pluton, WP= Wentworth pluton.

Table 3. 2 Summary of intensive parameters, for the late Paleozoic A-type granites, and available isotope data for the late Paleozoic and Neoproterozoic rocks of the Cobequid Highlands.

	Late Paleozoic granites					Late Paleozoic rocks			Neoproterozoic rocks							
Unit	CCP	NRP	WP	WP	WP	WP	Fountain Lake Group		Jeffers Block			Bass River Block				
Sample	3927	1779	4641	4636	6419	9826	4601	6061	1347	3709	2106	3500	449	3135	3171	4156
Type	bio	bio	cal	sod	sod	gabbro	bas	bas	gabbro	quartz diorite	grd	grd	rhy	gabbro	grd	granite
Intensive parameters																
T_{Zr} (± 30-50 °C)	814	805	874	891	919	–	–	–	–	–	–	–	–	–	–	–
P (± 0.18 GPa)	12	2	5.4	–	–	–	–	–	–	–	–	–	–	–	–	–
$H_2O_{in\ melt}$ (± 1.2 wt. %)	5.28	3.86	3.97	–	–	–	–	–	–	–	–	–	–	–	–	–
[1]Melt fr. (%)	27.5	28.2	37.8	–	–	–	–	–	–	–	–	–	–	–	–	–
Isotopic composition																
$\varepsilon_{Nd\ (360)}$	+2	+0.2	+2.5	+3.6	+3.1	+3.8	+3.4	+3.9	+3.6	+2.5	-0.6	-4.7	-0.4	+0.6	-1.75	-2.05
$\delta\ ^{18}O$ (‰)	7.6	6.1	5.7	5.5	6.0	4.5	–	–	–	–	–	–	–	–	–	–

Note: Data for ε_{Nd} from Pe-Piper and Piper (1998) and Papoutsa and Pe-Piper (2014).

[1]Degree of partial melting in this table is the average value estimated for three highly incompatible elements (Th, Nb, Rb). All elements in selected analyses showed minor variations in both late Paleozoic and Neoproterozoic rocks, and are therefore taken to represent primary magmatic contents. Abbreviations: bio= biotite granite, cal= calcic granite, sod= sodic granite, bas= basalt, grd= granodiorite.

The latter appear to yield higher pressures (9 to 13 kbar) than the calcic granites, for which pressures as low as 3 kbar were estimated (Fig. 3.6). The biotite granites also show higher amounts of initial H_2O content in the melt than the calcic granites (Tables 3.2, Appendix B.1). The estimated pressures from plagioclase are significantly higher than those from Al-in-hbl barometer (2–3 kbar: Chapter 2). Textural evidence suggests that plagioclase in the calcic granites crystallized before amphibole. Therefore the large differences in pressure estimates between the two barometers may reflect a rapid ascent from deep crustal levels, with Al-in-hbl estimates reflecting the level of emplacement of these plutons.

3.6.2 DID THE MAIN GRANITE TYPES HAVE A SIMILAR SOURCE?

The available geochronological data from the Wentworth, Pleasant Hills and Cape Chignecto plutons (U-Pb on zircon, Doig et al., 1996; Dunning et al., 2002) suggest that the A-type granites and their extrusive equivalents are contemporaneous and emplaced at ca 360 Ma. Furthermore, the ages yielded by both zircons and amphiboles in these rocks are quite comparable and do not show an age progression that could be related to closure temperatures, suggesting a rapid unroofing and cooling of the plutons (Pe-Piper et al., 2004). The sodic, calcic and biotite granites differ in their Nd-isotope composition (Table 3.2). The sodic granites show the highest values of $\varepsilon_{Nd(360\ Ma)}$ (> +3), the calcic granites range from +1.1 to +2.7, whereas the biotite granites show the lowest ε_{Nd} values, from +0.2 to +2.0 (Pe-Piper and Piper, 1998; Papoutsa and Pe-Piper, 2014). Although there is a great overlap in ε_{Nd} between the calcic and biotite granites, the hypersolvus sodic granites have systematically higher ε_{Nd} and a distinct trace element signature (Fig. 3.5), which suggest that the sodic granites are products of a different magmatic source.

With the exception of the mafic minerals and specific trace elements, the biotite and calcic granites present a rather similar mineralogy and whole-rock geochemistry, which could imply a comagmatic origin modified by fractionation or assimilation. If the biotite granites were fractionates of the calcic granites, they should be more enriched in incompatible elements and silica as more evolved melts. In Harker-type diagrams, however, the biotite and the calcic granites do not show a continuum, rather they present two parallel trends (Fig. 3.5), with no significant variation in highly incompatible elements, including Ga which can be used as a fractionation index in granitic systems (Breiter et al., 2013).

Alternatively, the variations between the calcic and biotite granites could be attributed to varying degrees of crustal assimilation of an originally similar melt. The granites show no evidence for substantial upper crustal assimilation. This conclusion is based on the following: a) lack of xenoliths and xenocrysts in the granites; b) absence of reaction textures such as corona rims; c) the complete absence of calcic and sodic granites in the homogeneous biotite granite plutons in the western Cobequid Highlands; d) the rapid emplacement and cooling of the plutons as indicated by geochronology and by the presence of petrologically similar granitic clasts in the sediments of the coeval Horton Group, and e) the chemical similarities with the coeval rhyolites, which represent the melts with the most limited interaction with the crust.

Assimilation at deeper crustal levels is more difficult to evaluate. If the Avalonian lower crust evolved in the late Neoproterozoic during complex subduction, then felsic differentiates of underplated mafic magma would be susceptible to assimilation in the late Paleozoic. Such a process is difficult to distinguish from partial melting of the same rocks and is evaluated further below.

Table 3. 3 Estimated magmatic parameters for the A-type granites of the Cobequid Highlands.

Pluton	Type	sample	Tzr (°C)	M value	P (GPa)	Water wt%	Viscosity (Pa*s)
CCP	biotite	2039	851	1.3	0.94	5.2	9.78
CCP	biotite	3920	856	1.2	1.08	5.0	9.91
NRP	biotite	1675	801	1.4	1.5	6.5	10.77
NRP	biotite	7071	797	1.5	1.3	6.0	10.79
NRP	biotite	7082	794	1.5	1.3	6.6	10.76
PHP	biotite	4672	861	1.3	1.36	5.2	9.59
PHP	biotite	4690	833	1.4	0.94	5.5	9.83
PHP	biotite	4704	772	1.6	0.31	7.4	11.82
PHP	biotite	7385	842	1.5	0.73	5.7	9.91
PHP	calcic	4670	889	1.4	1.11	4.8	8.9
PHP	calcic	4681	941	1.4	1.30	4.1	8.32
PHP	calcic	4689	856	1.1	0.83	5.0	9.76
PHP	calcic	7393	859	1.5	1.21	5.7	9.61
WP	biotite	6970	866	1.1	1.21	4.6	10.03
WP	biotite	7372	884	1.4	1.52	4.2	9.41
WP	calcic	6969	921	0.7	1.34	3.9	9.7
WP	calcic	7658	864	1.1	1.28	5.6	9.73
WP	sodic	6518	1045	1.6	–	–	7.08
WP	sodic	6419	920	1.4	–	–	9.03
WP	sodic	4636	891	1.5	–	–	9.42

Notes: Abbreviations for pluton names as in Table 1. Magmatic temperatures are given within an error of ± 30-50 °C and pressures in an error of ± 0.18 GPa. Water estimates may be within an error of ± 1.2 wt%. Pressures and water contents were not estimated for the sodic granites due to the lack of magmatic plagioclase. Viscosity estimated using the model of Giordano et al. (2008). Biotite and calcic granites are within an error of ± 0.35 log units and viscosities for sodic granites have an associated error of ± 0.25 log units.

Evidence of magma mixing between contemporaneous mafic and felsic melts is widespread in the Wentworth pluton, as seen from local development of mingling textures, and enclaves of gabbro with lobate contacts in the granite. Rocks of granodioritic composition, one end result of such mixing, are very rare. Samples from outcrops with any field evidence of mixing were not included in this study. However, evidence of interaction between felsic and mafic melts are potentially recorded in the geochemistry of the calcic granites. This is the only granite type that shows a positive trend between ε_{Nd} and

CaO/Na_2O+K_2O, which could result from either mixing with gabbro or mantle-derived fluids (Fig. 3.7). The ε_{Nd} in the calcic granites correlates positively with the estimated

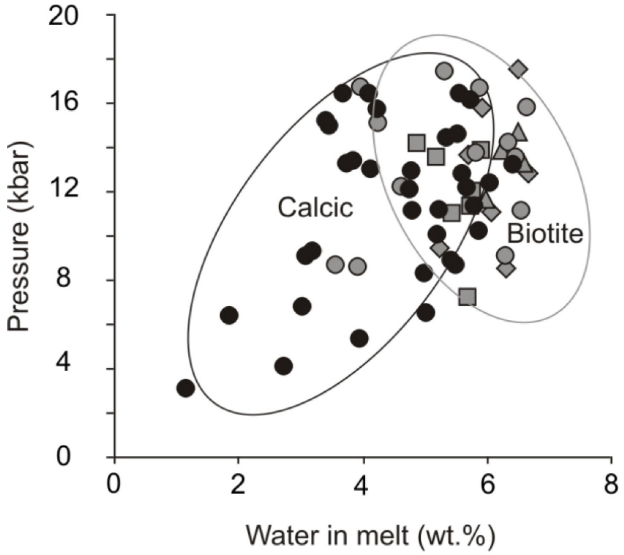

	CCP	NRP	PHP	WP
Biotite granite	◇	△	□	○
Calcic granite			■	●

Figure 3. 6 Pressure (estimated from plagioclase-melt barometer) vs. H_2O-in-melt concentrations, demonstrating the systematic differences of those parameters between the calcic and biotite A-type granites.

magmatic temperatures and negatively with pressure and viscosity (Fig. 3.8). The variations in the H_2O contents in the melt are too small to account for a systematic decrease in viscosity and do not correlate with ε_{Nd}, precluding substantial mixing with mantle-derived fluids. Ruprecht and Bachmann (2010) interpreted such correlations between viscosity and temperature as the result of heating by mafic melts. The negative trend that is observed for pressure suggests that such heating was more prominent at upper crustal levels. Textural evidence of substantial mixing (such as reverse chemical zoning of minerals and presence of mafic clots) in the studied granites is lacking; furthermore, the

only covariation with ε_{Nd} is that of CaO and the alkalies. Therefore substantial assimilation of mafic melts by the granitic melts is unlikely. It is possible that the observed isotopic and chemical variations reflect magma mixing at the source (such as a hybrid granodiorite), coupled with later heating by a coeval mafic melt after the calcic granitic melt was produced.

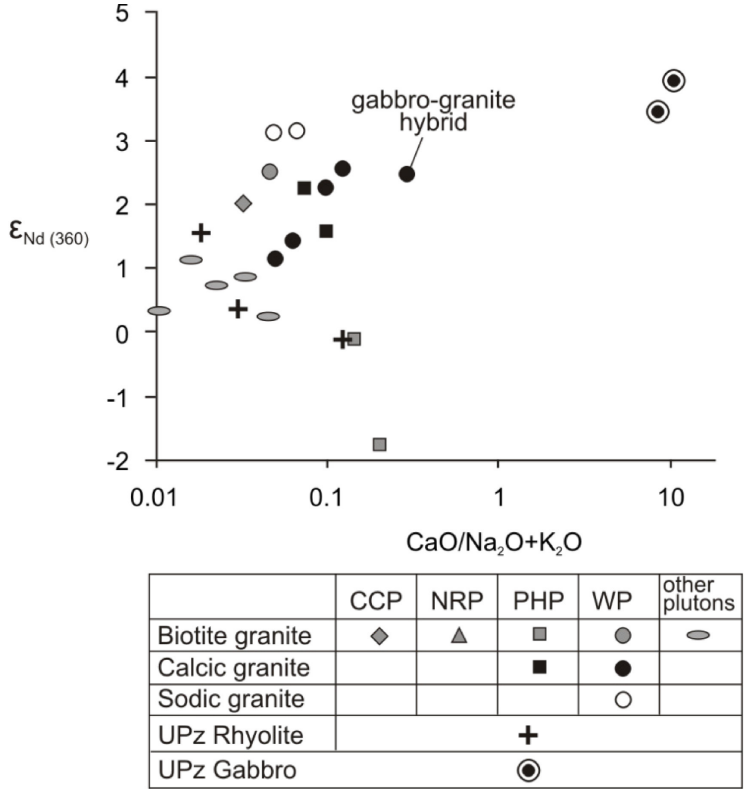

Figure 3. 7 ε_{Nd} vs. CaO/Na_2O+K_2O plot showing the possible mixing trend of the calcic granites. Upper Paleozoic gabbro and rhyolite are also plotted for comparison.

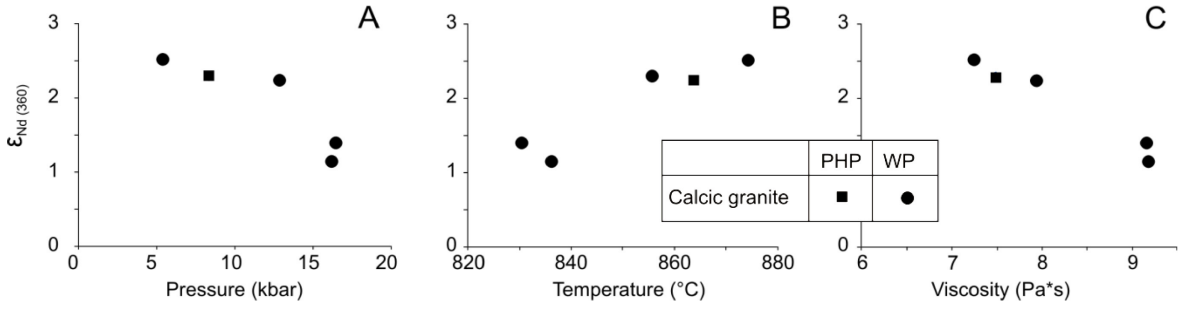

Figure 3. 8 ε_{Nd} vs. pressure (A), temperature (B), and estimated viscosity (C) for the calcic granites.

Taken together, the differences in Cr, Nb (Fig. 3.5), trends of ε_{Nd} (Fig, 3.7), magmatic temperature (Table 3.3), and trends between pressure and magmatic H_2O contents (Fig. 3.6, Table 3.3) point to an origin from different magmatic sources. In addition, the distinct spatial clustering of the granitic types between the western plutons (only biotite granites in North River and Cape Chignecto) and the eastern plutons (dominant calcic granite, Wentworth and Pleasant Hills), suggest that the calcic and the biotite granites, even though are coeval, probably do not have the same source.

3.6.3 POTENTIAL MAGMATIC SOURCES

A-type granites are interpreted to be derived from magmas that have an exclusively igneous source (Whalen et al., 1987), whether by partial melting of granodiorite or tonalite, or extreme fractionation of mafic magma (Loiselle and Wones, 1979; Frost and Frost, 2010). In the Cobequid Highlands and nearby Avalonian Antigonish Highlands, the only older igneous rocks are the Neoproterozoic arc-related rocks and minor Ordovician A-type granites in the Jeffers Block and Antigonish Highlands, and the Neoproterozoic arc-related and minor ocean-crust rocks of the Bass River block, all with well documented geochemistry and radiogenic isotopes (Pe-Piper and Piper, 1998; Escarraga et al., 2011; MacHattie and White, 2012). The Ordovician A-type granites of the Antigonish Highlands are less REE-enriched than the late Paleozoic granites of the Cobequid Highlands, and contain calcic, sodic-calcic amphibole and hedenbergite, with only minor biotite and no sodic amphibole (Escarraga et al., 2011).

Both biotite and calcic granites are classified as A2-type granites in Eby's (1992) diagrams, suggesting that they are probably not the fractionates of mafic melts. Furthermore, a crustal source for the biotite and calcic granites may be indicated by their

metaluminous to peraluminous composition (Fig. 3.2B), and by the range of ε_{Nd} for these rocks which is similar to that of Neoproterozoic intermediate rocks (Table 3.2). Using the whole-rock composition of Neoproterozoic intermediate rocks, and applying batch partial melting (Shaw, 1970) geochemical models for specific highly incompatible trace elements (such as Nb, Rb, Th, and U), it is suggested that both biotite and calcic granites could have been formed by similar degrees of partial melting, ranging between 20% and 40% of extracted melt (Appendix B.1). Therefore, the observed systematic geochemical differences between the two granitic types are likely the result of source rocks of different composition, or differences in deep-crustal processes such as assimilation, since a significant role for upper crustal mixing or assimilation has been ruled out.

The sodic granite type is only present in the Wentworth pluton and is geochemically quite distinct from the other main granite types. Not only it is closer to the late Paleozoic and Neoproterozoic mafic rocks of the Jeffers Block in Nd isotopes compared to the other granite types (Table 3.2), but also shows strong depletion in Ba and Sr, and enrichment in Ga, which are indicative of strong fractionation. The sodic granites, however, show the highest amounts of Zn compared to the other granitic types (> 90 ppm, Table 3.1). Zinc is generally more concentrated in mafic melts, and many A-type granites interpreted as partial melts of intermediate feldspathic rocks have lower amounts of Zn (Jung et al., 1998; Wenner and Lloyd, 2006) similar to the biotite and calcic granites. In contrast A-type granites generated by fractionation of mafic melts appear more Zn-enriched (Vander Auwera et al., 2003; Shellnutt and Iizuka, 2011). Thus the trace element geochemistry along with the high ε_{Nd} values of Neoproterozoic and late Paleozoic mafic rocks in the Cobequid Highlands suggests that the sodic granite is a high-degree

fractionate of a mafic parent magma. Fractionation models for the sodic granites were performed for major and trace elements. Fractionation sequences for selected magmatic sources were thermodynamically simulated with the use of PELE (Boudreau, 1999) which is a minimization of the MELTS algorithm developed by Ghiorso and Sack (1995). The output data from PELE were used to model trace elements through Rayleigh fractionation as applied by Neuman et al. (1954). Detailed description of the models and data used are provided as supplementary material (Appendices B.2, B.3). Fractionation models for several trace elements (Fig. 3.9), suggest that the sodic granites could have been derived by extreme fractionation (90%) either of a source resembling the low-Ti mafic rocks of the Jeffers Block or a source chemically similar to the Fountain Lake basalt (Fig 3.9). Only an origin through fractionation of Late Paleozoic mafic magma is geologically feasible.

In the Cobequid Highlands, basalt in three main extrusion cycles (Dessureau et al., 2000) is dated by zircon in interbedded rhyolite between 358±1 Ma and 355±2 Ma (Dunning et al., 2002), but associated mafic plutonic rocks are older, with five amphibole ages between 367 and 358 ±<4 Ma (Pe-Piper et al., 2004) and one zircon age of 370±2 Ma (Gibbons et al., 1996). The top of the 1 km of basalt in western Cape Breton Island is dated at 371±1 Ma (Dunning et al., 2002). There was thus mafic magma available several million years before emplacement of the sodic granite (362±2 Ma, Dunning et al. 2002; 368±4 Ma, Pe-Piper et al., 2004). Evolved rhyolitic melts can be produced from fractionation of mafic magma in the deep crust, with minor crustal assimilation, in less than 2 Ma (Turner et al., 1992; Annen and Sparks, 2002, Lowenstern et al., 2006). Stratigraphically, the rhyolites of the Fountain Lake Group are older than the main phase of the basalts, and chronologically, the granites of the eastern plutons are older or coeval

with some of the gabbros. These suggest that some late Paleozoic mafic magma may have been trapped deep in the crust or upper mantle and the timing of basaltic volcanism was related to faulting producing pathways through the crust rather than the availability of mafic magma from the upper mantle.

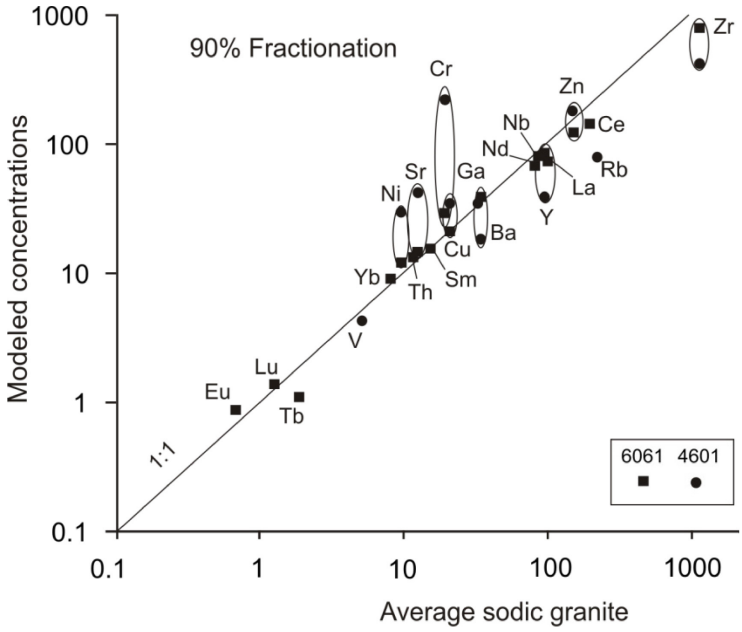

Figure 3. 9 Fractionation trace element modeling of selected isotopically suitable mafic sources for the sodic granites.

3.6.4 CONSTRAINTS ON PARTIAL MELTING FOR THE BIOTITE AND CALCIC A-TYPE GRANITES

The alkalinity (Fig. 3.2) and trace element classification (Fig. 3.3) of the late Paleozoic biotite and calcic A-type granites from the Cobequid Highlands suggests an origin through partial melting of crustal rocks as the dominant process. Therefore, in order to understand the origin of the observed trace element variations between these two granite types, four main factors need to be evaluated: a) the composition of the magmatic source, b) the control of various degrees of partial melting, c) the role of mixing with mafic magma in the deep crust and d) the role of crustal assimilation particularly in the deep crust. As previously mentioned, the biotite and calcic granites appear to have been derived

by similar degrees of partial melting (Fig. 3.10; Appendix B.1).

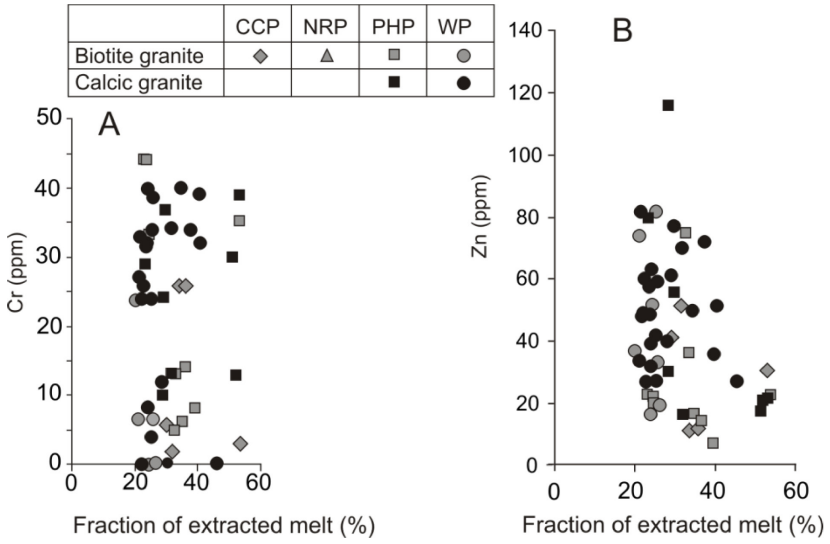

Figure 3. 10 Plots of the modeled fraction of extracted melt for the biotite and calcic granites vs (A) Cr, and (B) Zn, demonstrating the limited control of partial melting on the systematic variations of these elements.

Calcic granites are found only in the two larger complex plutons along the Rockland Brook Fault. The higher geothermal gradient implied by the higher magmatic temperatures (Table 3.3) may be related to the abundance of gabbros in this area, reflecting greater supply of mafic magma to the base of the crust and producing a large gravity anomaly and thick Fountain Lake Group volcanic successions (Pe-Piper and Piper, 2003). The higher Cr content of the calcic compared with biotite granite is unlikely to be due to mixing with gabbroic magma, since the Zn content of the two granite types is similar (Fig. 3.10).

Models of partial melting (Appendix B.2) of Neoproterozoic quartz diorites, granodiorites and tonalites from both the Jeffers and Bass River blocks (Appendix B.4) produce the best fit for chondrite-normalized REE patterns at 30-40% fraction of extracted melt (Fig. 3.11). The Bass River block tonalites, however, show systematically higher Cr, and depletion in Sr, in their whole-rock chemistry (Appendix B.5) and consequently

produce Cr-enriched, Sr-depleted partial melts, compared to their equivalents from the Jeffers Block (Fig. 3.12A and 3.12B). The partial melts from the Bass River Block are more enriched in HFSE and depleted in LILE, matching broadly the characteristics of the calcic granites (Fig. 3.12C).

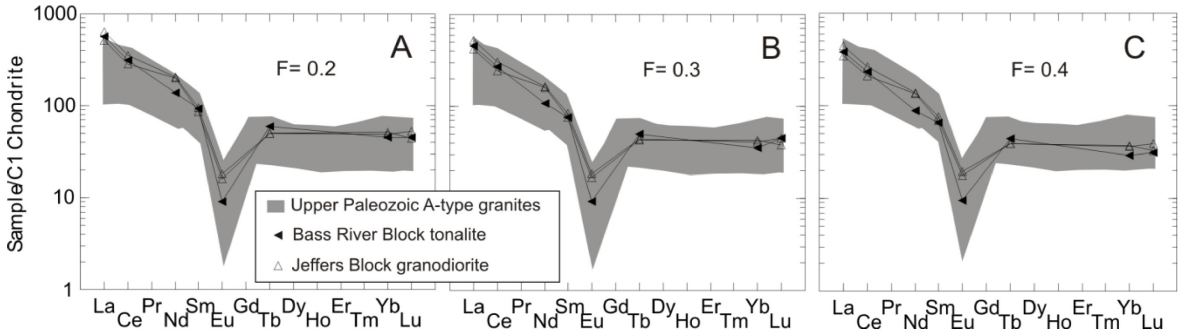

Figure 3. 11 Chondrite-normalized patterns of modeled REE, under (A) 20%, (B) 30%) and (C) 40% of partial melting of Neoproterozoic intermediate rocks. Shaded areas correspond to the REE-patterns of the granites.

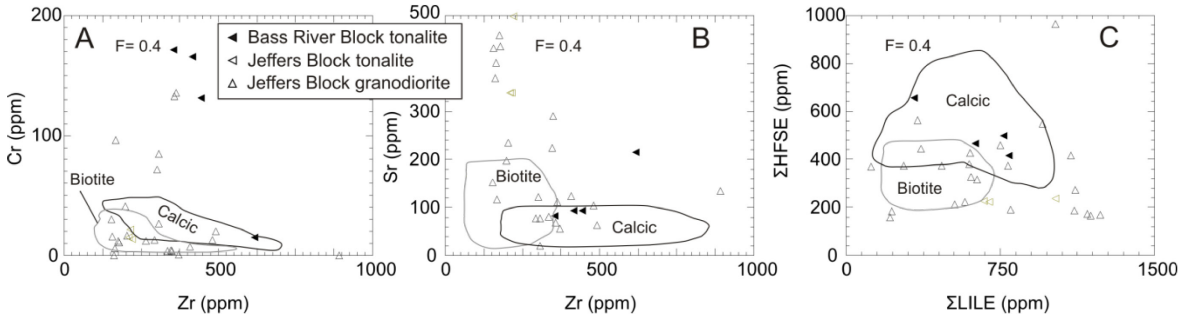

Figure 3. 12 Plots of modeled (A) Cr, and (B) Sr vs. modeled Zr during 40% of partial melting of Neoproterozoic intermediate rocks. Panel (C) shows the modeled concentrations of total high field strength elements (HFSE) vs. total large ion lithophile elements (LILE). The ranges of these elements measured in the biotite (dashed lines) and calcic granite (solid lines) are plotted for comparison.

The intermediate plutonic rocks of the Jeffers and Bass River blocks differ in major oxides only in that the granodiorites and tonalites of the former appear to be more Al-rich (Appendix B.5). The peraluminous biotite granites show lower estimated magmatic temperature and higher water contents than the calcic granites. The estimated magmatic H_2O contents of the melt for the biotite granites correlate positively with increasing fraction of extracted melt (Fig. 3.13A), whereas magmatic temperatures show a negative

correlation (Fig. 3.13B). The exact opposite trends are observed for the calcic granites. These data suggest that partial melting that produced the biotite granites was enhanced by the presence of H_2O (fluid-present melting), whereas the production of the calcic granitic melts was predominately controlled by high temperatures (dehydration melting). Holtz and Johannes (1994) argued that at moderate crustal depths, melts at ~750 °C require 6 wt.% H_2O, and for melt fractions of ~40% an additional 1–2 wt.% of H_2O is required. Although the temperature estimates for the biotite granites are higher than those for the "cold

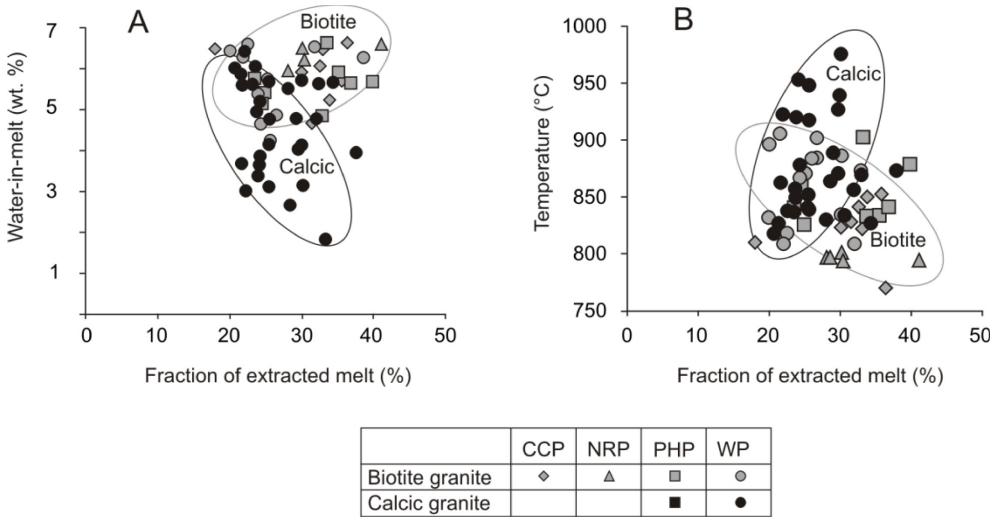

Figure 3. 13 Plots of (A) estimated water-in-melt amounts and (B) zircon-saturation temperatures vs. the degree of partial melting for the calcic and the biotite granites, demonstrating the control of water availability and temperature on the fraction of produced melt.

granites" of Miller et al. (2003), the observed variations of temperature and H_2O with increasing fraction of extracted melt may favor a scenario similar to that of Miller et al. (2003), in which influx of H_2O is generated during dehydration of crustal lithologies. In hydrous alkaline melts, the stability of biotite is restricted to temperatures below 700°C (Scaillet and Macdonald, 2001). Calcic amphibole, on the other hand, is stable under higher magmatic temperatures, above 800 °C, and below this temperature reacts with the melt to form biotite and titanite (Dall'Agnol et al., 1999). The low magmatic temperatures

and the availability of Al and H_2O in the crustal rocks during partial melting might have favored a preferential crystallization of biotite over amphibole in the A-type granites of the central and western Cobequid Highlands.

The hypothesis that mafic magma contributed significantly to the calcic or biotite granite melts through magma mixing can be excluded, as there is no consistent pattern of trace elements associated with mafic melts (Fig. 3.10) and no mixing is apparent from variations in Nd isotopes with particular elements for the biotite granites (Fig. 3.7). It is likely that crustal assimilation played a role in the deep crust in modifying the partial melts of Neoproterozoic tonalite and granodiorite as they rose through the crust, but such a process would have enhanced the element and isotopic signatures already derived by partial melting from the different Neoproterozoic crustal blocks and is thus difficult to quantify.

Experimental work of Gardien et al. (2000) demonstrated that hornblende-bearing granitic rocks can be the partial melting products of plagioclase-biotite-quartz mineral assemblages. Mogk (1992) argued that formation of hornblende-bearing migmatites in tonalitic gneisses can be the result of incongruent melting of biotite-plagioclase assemblages according to the reaction

Bt+Pl+Qz+Ep+fluid = Hbl+Pl+Kfs-rich granitic melt. (1)

Mineral assemblages similar to the reactants of the above equation have been observed in the tonalites of the Bass River Block (Pe-Piper et al., 2010) although they are not migmatitic. Outcrop of the Bass River Block is limited to the area south of the Rockland Brook fault (Fig. 3.1B) and thus south of the Pleasant Hills and Wentworth plutons where the calcic granite is found.

3.6.5 GEOLOGICAL SYNTHESIS

The large volumes of gabbro in the Wentworth and Pleasant Hills plutons and the 1.5 km thick basalt in the Fountain Lake Group (Pe-Piper and Piper, 2003) suggest the presence of a major heat source in the eastern part of the Cobequid Highlands. The elemental and isotopic characteristics of the most primitive Fountain Lake basalts were interpreted by Dessureau et al. (2000) as indicative of an origin from asthenospheric and subcontinental mantle with elevated potential temperature suggesting mantle upwelling. It is therefore likely that in the late Paleozoic there was substantial interaction between the lower Avalonian crust and shallow upper mantle at the fault-bounded margin of the extending Magdalen Basin.

Magnetic data from the Cobequid Highlands (Piper et al., 1993) show that the eastern part of the Cobequid Highlands has high amplitude and long-wavelength magnetic anomalies, which was taken to suggest that the plutons in the area are underlain by gabbro. This interpretation is supported by a high gravity anomaly beneath the Rockland Brook fault in the southern Wentworth pluton (Koukouvelas et al., 2002). This gabbro may be related to the underplated mafic layer of high velocity identified from seismic refraction in the centre of the extensional Magdalen Basin (Marillier and Reid, 1990). Its surface expression may be the voluminous gabbroic body in the Wentworth pluton. The western part of the Cobequid Highlands, however, shows significantly lower magnetic and gravity anomalies, suggesting that this area was beyond the limits of significant mafic underplating (Piper et al., 1993). Published Pb isotopes for the late Paleozoic Avalonian rocks of the Cobequid Highlands (Pe-Piper and Piper, 1998b) show that the granites in the eastern part of the area (Pleasant Hills and Wentworth plutons) are generally more

enriched in ^{206}Pb compared to the other plutons suggesting the presence of newly-formed crust (Rollinson, 1993).

It has been proposed that the mafic underplating of Magdalen Basin and the extrusion of the late Paleozoic continental tholeiites were related to a NW-migrating mantle plume (Dessureau et al., 2000). An origin for the continental tholeiites within a mantle plume was suggested on the basis of geochemistry (high FeO_T suggesting high potential temperature) although the isotopes and trace elements suggest significant contamination from the lithospheric mantle (Dessureau et al., 2000). Based on the timing of the similar tholeiitic igneous activity that followed from Visean to Permian in western Europe it was hypothesized that the plume was originally active in the Maritimes in the mid-Devonian (Keppie and Krogh, 1999) that later moved beneath Scotland and southern Norway (Dessureau et al., 2000; Wilson et al., 2004).The timing of these events was also synchronous with, and followed, the ongoing closure of the Rheic ocean by NW-directed intra-oceanic subduction beneath the Canadian Appalachians (Nance et al., 2012). The latter could result in mantle upwelling and mafic underplating by a number of processes, including slab detachment (Fig. 3.14A and B), perhaps aided by a pre-existing plume and the crustal extension in the Magdalen Basin. Whatever the mechanism, a deep crustal hot zone (DCHZ), such as that proposed by Annen et al. (2006) and Hyndman and Currie (2011), would have formed. In such zones, the felsic melts may be derived by two possible mechanisms: 1) partial melting of pre-existing crustal rocks, and 2) fractional crystallization of mafic sills emplaced in the lower crust.

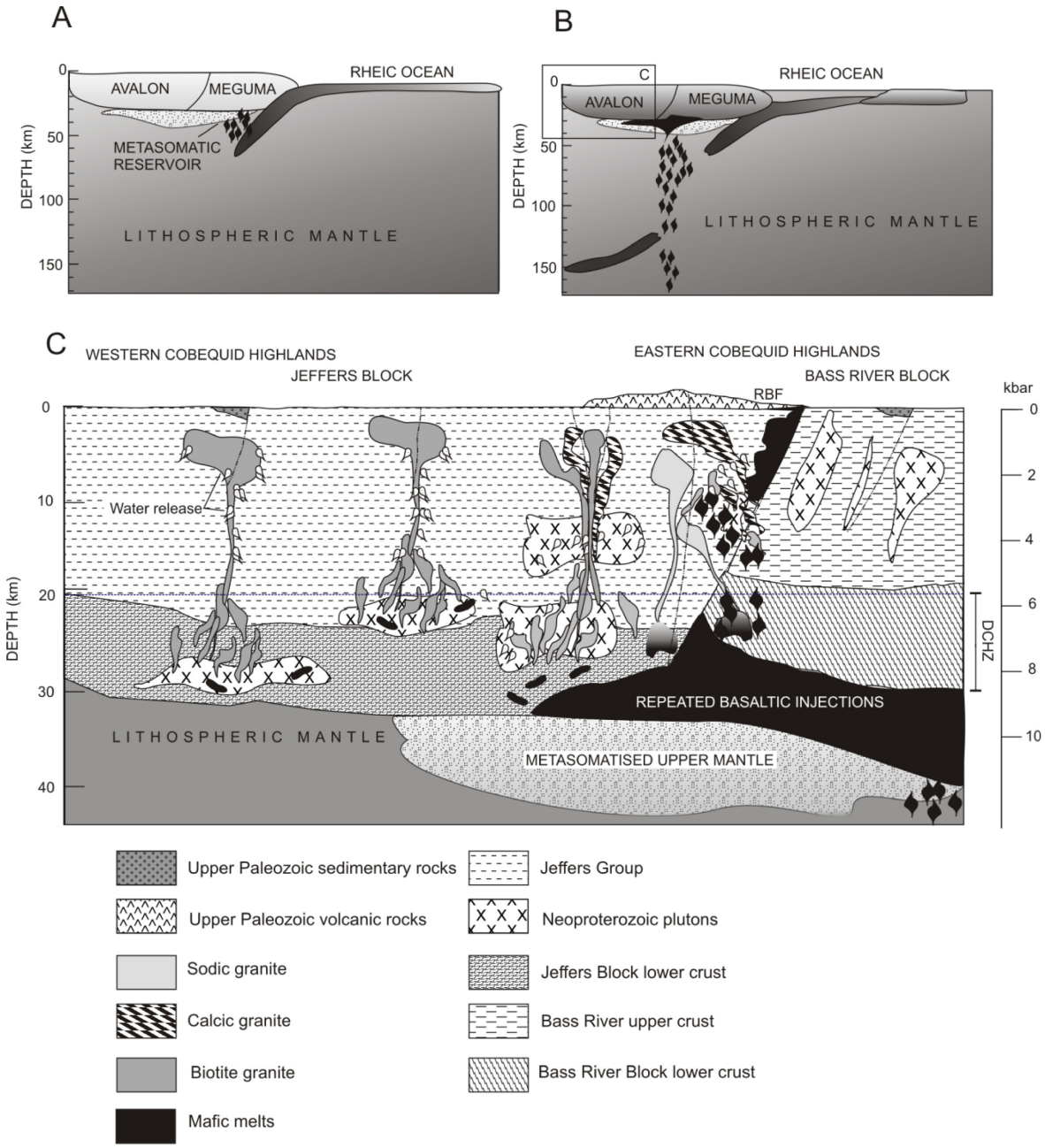

Figure 3. 14 Suggested evolution of the late Paleozoic A-type granites of the Cobequid Highlands. Images (A) and (B) show the presence of a metasomatic reservoir in the upper mantle, and the mafic underplating following slab detachment during the closure of the Rheic Ocean. Image (C) shows the production and emplacement of the various A-type granite types from a deep crustal hot zone and the adjacent area (see text for details).

According to Annen et al. (2006), the repeated injection of hydrous basaltic melts into the crust leads to continuous fractionation of emplaced mafic sills (Fig. 3.14C), associated with release of H_2O and heat, promoting partial melting of the surrounding crust. The

felsic melts ascend from the hot zone to reservoirs in the upper crust, leaving behind the dense restites and cumulates. Crustal-scale strike-slip faults in the Cobequid Shear Zone may have provided effective pathways for magma ascent. This is indicated a) by the spatial relationship between the plutons with syn-magmatic deformation, and the major faults regionally (Koukouvelas et al., 1996), b) the earliest magmatic phases are segregated along distinct faults as reported from the Pleasant Hills pluton (Pe-Piper et al. 1998) and, c) pre-full crystallization structures, such as lineation of amphiboles in the Wentworth pluton, show a systematic parallelism to the Rockland Brook fault suggesting an along-fault flow of magma (Koukouvelas et al., 2002). In the Cobequid Highlands, however, the mineralogy of the extruded late Paleozoic tholeiites suggests they were rather anhydrous melts. The coeval mid-crustal gabbros of the Wentworth pluton (3-5 kbar), on the other hand, appear substantially more hydrated (5–6 wt.% H_2O, Zhang personal communication, 2015). The DCHZ in the Cobequid Highlands thus deviates from the proposed model of Annen et al. (2006) in that the underplated mafic magma was originally anhydrous. However the repeated injection of mafic melts could increase the volatile contents through remelting of previously emplaced sills and continuous fractionation, and thus trigger partial melting of the crust. We suggest that such mechanisms are involved in the Cobequid Highlands. Furthermore, we propose that H_2O present in the hydrous phases of crustal rocks such as micas and amphiboles, was released upon heating and further induced partial melting.

In the eastern part of the Cobequid Highlands, the large variety in the granitic types present in the plutons of the area indicates derivation from such a hot zone, where the larger amounts of underplated mafic melts led to larger volumes of produced granitic

magmas. Crustal-derived biotite and calcic granites of the eastern Cobequids were produced at mean pressures between 9.6 and 13 kbar (Table 3.3, plagioclase-melt barometer), which corresponds to a 32–40 km depth in the continental crust. For comparison, the estimated crustal thickness, based on seismic refraction data (excluding sediment cover and underplated mafic rocks) in the central Magdalen Basin is 36 km (Marillier and Reid, 1990), probably rather thicker at the margins. The depth at which the granitic melts were produced, was therefore, at the base of the crust, and matches the depth proposed for deep crustal hot zones (Annen et al., 2006). The high temperatures in the area induced partial melting of the Avalonian crustal rocks, producing granitic melts that could then be emplaced at shallow crustal levels to form subsolvus granites. The moderate to low amounts of H_2O in the crustally-derived melts of the area could either be coming from lower crustal rocks, or released upon heating of mid-crustal lithologies as the melts migrated. Experimental work of Singh and Johannes (1996) demonstrated that at mid-crustal pressures (~5 kbar) dehydration melting of tonalitic rocks starts at approximately 740 °C. The extreme fractionation of the underplated mafic sills, however, produced exclusively hypersolvus granites, due to their originally anhydrous nature. Even though all the studied subsolvus granites of the eastern Cobequid Highlands have a crustal trace element signature, they show a range of $\delta\ ^{18}O$ from 5.5 to 5.8‰ (Table 3.2), which is lower than the majority of Avalonian granitoids (Whalen et al., 1996). This suggests that the rocks comprising the Avalonian lower crust and supplying oxygen to the melt were principally magmatic as suggested by seismic velocities (Marillier et al., 1994). The lower $\delta\ ^{18}O$ values of these granites could also be the result of hydrothermal alteration (Simon,

1990). However the analyzed samples show very limited evidence of hydrothermal alteration and therefore the $\delta^{18}O$ values are taken to be representative of the parent melts.

Experimental work of Castro et al. (1999) on partial melting of crustal rocks has demonstrated the potential role of volatiles in the generation of peraluminous granitic melts and associated phase relations. At pressures of 15 kbar, the volume of extracted melt from anhydrous melting of a granodiorite gneiss and a biotite gneiss was generally less than 5 and 8%, respectively. Addition of 2 wt.% H_2O in the runs for the biotite gneiss increased the volume of extracted melt and stabilized plagioclase, absent in the anhydrous runs. Furthermore, plagioclase and K-feldspar in all runs were the earliest phases to be consumed in the starting materials. Their work may suggest that the higher amounts of Ba in the biotite and calcic granites could reflect the early melting of plagioclase and K-feldspar in the source, and thus enrichment of the melt, in contrast to the fractionation process of a K-feldspar-poor source, such as the one proposed for the sodic granite. Furthermore, in order to attain the observed fractions of partial melts and crystallize early plagioclase, small amounts of H_2O must be added to the system.

The relative abundances of the produced crustal and residual fractionated granitic melts in deep crustal hot zones depend greatly on the emplacement rate of the intruded mafic magma (Annen and Sparks, 2002; Solano et al., 2012). In their models, Solano et al. (2012) demonstrated that at high emplacement rates of mafic magma, evolved melt segregation occurred in the overlying crust, and the produced granitic melts were predominantly derived from partial melting of the crustal rocks. The opposite was observed for low emplacement rates, where melt segregation occurred within the underplated layer and the granitic melts were produced predominantly through

fractionation. In the eastern Cobequid Highlands, the larger volumes of crustally-derived calcic and biotite granites, compared to the less abundant sodic granites, are consistent with high emplacement rates of mafic magma, and may, therefore, be related to the late Paleozoic mafic underplating. In these cases, the elevated temperature would affect a rather large volume of the crust, with the felsic melts forming initially as batches at various depths (Solano et al., 2012) (Fig. 3.14C).

If felsic melts are segregated through fractures, which can effectively drain the crustal hot zone, then the produced plutons would have resulted from the mixing of various individual batches of partial and residual melts, and would, therefore, have a polybaric geochemical signature (Solano et al., 2012). In the complex plutons of the eastern Cobequid Highlands the presence of different coeval granitic types of different sources indicates multiple batches of granitic melt. The systematically different pressures for the various granitic types (Fig. 3.6) within these plutons (Appendix B.1) suggest that these granitic batches probably originated from different depths, and segregated along the crustal-scale Rockland Brook Fault (Fig. 3.14C). The presence of multiple granite types in these plutons, particularly in the Wentworth pluton, is consistent with the concept of of crustally-derived and residual felsic melt batches that result from generation in deep crustal hot zones (Annen and Sparks, 2002).

In the central and western Cobequid Highlands, however, the H_2O in the granitic melt is in relatively higher amounts (Fig. 3.6) and has a different affinity, as indicated by the difference in oxygen isotopes (Table 3.2). Although some H_2O may have been derived from fractionating mafic melts, the systematically higher values of $\delta\ ^{18}O$ (Table 3.2), if primary, suggest a difference supply from the crust of the western part of the Cobequid

Highlands, dominated by the sedimentary and volcaniclastic rocks of the Jeffers Group. Water released from these rocks would have a different isotopic signature from H_2O released from magmatic rocks (Rollinson, 1993). These relatively higher values of $\delta\ ^{18}O$ are not consistent with hydrothermal alteration that would involve meteoric H_2O, since such post-magmatic processes result in the reduction of $\delta\ ^{18}O$ (Simon, 1990).

The chemical affinities of A-type granites worldwide have been the subject of several detailed studies, and it is well established that these rocks may form by different geological processes. This study shows that it is possible for different geological processes to create mineralogically distinct A-type granites. The variations in the ferromagnesian minerals present in the A-type granites of the Cobequid Highlands result from source heterogeneity, mode of emplacement, and processes of melt generation. The granites with sodic amphibole are associated with fractionation of mafic melts, the granites with calcic amphibole were derived through dehydration melting of the crust at high temperatures, whereas the biotite granites were produced from H_2O-present melting of crustal rocks at lower temperatures. The mineralogical character of the A-type granites is thus a useful indicator of the magmatic conditions under which these rocks were formed.

3.7 CONCLUSIONS

The coeval A-type granites of the Cobequid Highlands, although emplaced under the same regional tectonic regime but not resulting from different sources, present the mineralogical variations that have been observed in the majority of A-type granites elsewhere. Both the biotite and calcic granites were derived by 20-40% partial melting of Neoproterozoic intermediate crustal rocks, whereas the sodic granites show characteristics

of extreme (90 %) fractionation from a mafic parent melt that resembles the coeval Fountain Lake basalts.

Asthenospheric mantle upwelling and large-scale tholeiitic magmatism in the late Devonian underplated the lower crust beneath the Magdalen Basin and presumably the eastern Cobequid Highlands. Repeated injections of mafic melts into the lower crust created, thus, a deep crustal hot zone. In this zone, the emplacement of mafic sills triggered partial melting of the surrounding hydrated crustal rocks which would, in turn, released water upon heating (dehydration melting), further inducing partial melting. Differences in crustal lithology between the eastern and western part of the Cobequid Highlands resulted in the production of variably hydrous granitic melts with systematic differences in oxygen isotopic signatures. Such melts ascended and were emplaced at shallow crustal levels, producing the subsolvus biotite and calcic granites. The extreme fractionates of anhydrous mafic sills would eventually produce the hypersolvus sodic granites. The late Paleozoic plutons of the area were thus constructed by several distinct A-type granitic magmatic batches, derived by specific geological processes such as extreme fractionation and partial melting of crustal rocks and magmatic conditions, such as temperature, pressure and water-in-melt, that resulted in systematic differences in mineralogy.

CHAPTER 4 VARIATION OF THE REE-HYDROTHERMAL CIRCULATION IN COMPLEX SHEAR ZONES: THE COBEQUID HIGHLANDS, NOVA SCOTIA

PREFACE

A version of this chapter is published as: "Papoutsa, A., and Pe-Piper, G., 2015, Variation of the REE-hydrothermal circulation in complex shear zones: The Cobequid Highlands, Nova Scotia: Canadian Mineralogist, v.52, p. 943-968".

4.1 ABSTRACT

The Cobequid Highlands in Nova Scotia comprise a series of 365–360 Ma, REE–enriched A–type granite plutons, emplaced along an active shear zone. The purpose of the paper is to identify the sequence of REE–minerals produced during long–lived, regional, hydrothermal circulation and its evolution through time. The fractures hosted in these granites were investigated under the petrographic and scanning electron microscopes and microprobe. Epidote–rich, biotite–rich, chlorite–rich and Fe–oxide–rich fracture fillings have been observed. Mineral analyses revealed a variety of REE–minerals in the fractures, including hydroxylbastnäsite–(Ce), parisite–(Ce), synchysite–(Ce), cerianite, thorite, Nb–minerals, hingganite–(Y) and chernovite–(Y). Cross–cutting relationships and mineral associations indicate that the REE–minerals have precipitated at different times and are associated with specific styles of hydrothermal alteration. Epidote was one of the earliest minerals to precipitate in the fractures, associated only with minor precipitation of thorite and hydroxylbastnäsite–(Ce) and removal of As from sedimentary rocks, under low temperatures and reducing conditions. Biotite and chlorite precipitated shortly after epidote under more oxidizing conditions during which comparatively larger amounts of hydroxylbastnäsite–(Ce), thorite, hingganite–(Y) and cerianite formed. The

Fe–oxide–filled fractures formed in the latest stages of hydrothermal circulation and are associated with the largest variety and highest amounts of hydrothermal REE–minerals, such as parisite–(Ce), synchysite–(Y), thorite, Nb–minerals and chernovite–(Y). The oxidizing conditions led to the precipitation of As and the formation of chernovite–(Y) after the alteration of hingganite–(Y). Thus the greatest remobilization and concentration of REE–minerals took place during a late, high–temperature, oxidizing hydrothermal circulation, apparently driven by minor late mafic intrusions.

4.2 INTRODUCTION

In igneous systems, the rare earth elements (REE) are concentrated as incompatible elements in the late stages of magmatic evolution. The majority of economically valuable REE–deposits are associated with either carbonatites or alkaline silicic intrusions (Chakhmouradian and Wall, 2012). The high amounts of REE hosted in such rocks cannot always be explained only by fractionation processes, suggesting their late–stage remobilization by fluids (Williams–Jones et al., 2012). The hydrothermal REE–minerals tend to be more variable and complex than those of magmatic origin due to variable conditions during hydrothermal circulation (Jiang, 2006). Chemistry of the fluid, pressure, temperature, the REE source, and the nature of the country rock are some of the factors that control the hydrothermal transportation and precipitation of REE (Smith et al., 2000).

Many hydrothermal REE deposits are spatially related to alkaline rocks, particularly A–type granites that are interpreted as the primary source of REE (Förster et al., 2011). Such rocks are usually enriched in REE and host magmatic REE–minerals (Whalen et al., 1989; Uher et al., 2009), whose fluid–induced breakdown can result in a

number of hydrothermal REE–phases (Meintzer and Mitchell, 1988; Jiang, 2006). The presence of F, Cl, S and CO_3 ions in the fluids promote the hydrothermal mobility of REE (Rolland et al., 2003; Uher et al., 2009). Based on their charge/radius ratio, the REE tend to form stable complexes principally with F at ambient temperatures, whose stability increases systematically from La to Lu (Williams–Jones et al., 2012). Hydrothermal mobilization of REE is common in areas with iron oxide–copper–gold (IOCG) mineralization (Kontak et al., 2008).

Latest Devonian post–collisional granite plutons, with varying amounts of gabbro, were emplaced along the active Cobequid Shear Zone in the Cobequid Highlands of the Canadian Appalachians (Pe–Piper and Piper, 2003). On the basis of their high alkalies, high concentrations of large ion lithophile elements (LILE) and Ga/Al ratio, these granites show A–type affinities, with within–plate chemical characteristics (Pe–Piper et al., 1991). These plutons, and particularly the mafic rocks, are thought to have provided the heat and possibly fluids for regional–scale hydrothermal activity that produced widespread IOCG mineralization (Pe–Piper et al., 2004; MacHattie and O'Reilly, 2008). The granitic rocks of these plutons are REE–enriched, as is commonly observed in A–type granites, and significant amounts of magmatic allanite–(Ce) and chevkinite–(Ce) are found in the largest pluton, the Wentworth plutonic complex, in the eastern part of the area (Papoutsa and Pe–Piper, 2013). Remobilization of REE has been inferred from the presence of hydrothermal minerals replacing primary REE–minerals in these rocks. There has been no previous attempt, however, to define the nature and the extent of the REE–enrichment, either primary or hydrothermal, in the rest of the late Paleozoic plutons in the Cobequid Highlands. Whole–rock geochemical data reported in Pe–Piper (1991, 1995a,

1995b, 1998), and Pe–Piper and Piper (1998a) show that all A–type granites have REE concentrations comparable to those in the Wentworth pluton, with an average range between 100 and 400 ppm total REE. Preliminary petrographic examination of these rocks revealed that the Pleasant Hills, North River, and Cape Chignecto plutons have considerably lower amounts of magmatic REE–minerals than the Wentworth pluton. Only minor allanite–(Ce) is found in these plutons, and yet they contain similar bulk REE concentrations to the Wentworth granites. The motivation for this study came from the petrographic investigation of mm–scale, fractured granitic samples from the North River pluton, which contain more than 300 ppm of total REE but completely lack magmatic REE–minerals, suggesting possible hydrothermal enrichment. As the style of hydrothermal alteration varies along the Cobequid Highlands (Pe–Piper et al., 2004), this area provides a unique opportunity to assess the nature and controls on REE–hydrothermal enrichment, where present, along more than 100 km of the shear zone.

The purpose of this study, therefore, is to document the extent, mineral composition and relative age of post–magmatic REE–circulation in the late Paleozoic plutons in the Cobequid Highlands, and to correlate the changes in the abundance and type of REE–mineral assemblages with specific styles of hydrothermal alteration. Such a study will identify the regional sequence of hydrothermal processes associated with REE–mobility, and also provide information on the behavior of REE under different hydrothermal conditions.

4.3 GEOLOGICAL SETTING

The Cobequid Highlands in mainland Nova Scotia (Fig. 4.1A) consist of a basement of Neoproterozoic juvenile Avalonian crust (Pe–Piper and Piper, 2003). In the

late Devonian, the closure of the Rheic Ocean at promontories led to dextral strike slip faulting (Hibbard and Waldron, 2009). This resulted in a distributed extension of the Magdalen Basin as a stepover zone. Crustal thinning continued from latest Devonian until at least the early Carboniferous, accompanied by underplating of a thick gabbroic layer beneath the Gulf of St Lawrence (Marillier and Verhoef, 1989; Marillier and Reid, 1990). At the same time in the Cobequid Highlands, granite plutons with lesser amounts of gabbro were intruded along the faults of the Cobequid Shear Zone, which formed the southeastern margin of the extensional basin (Pe–Piper et al., 1998). Thick rhyolite pyroclastic rocks and voluminous flood basalts of the Fountain Lake Group were the volcanic equivalents of the plutons (Dunning et al., 2002).

The Cobequid Shear Zone consists of a series of subparallel dextral strike–slip faults, comprising the upper crustal expression of the Minas Geofracture between the Avalon and the Meguma terranes (Keppie, 1982; Koukouvelas et al., 2002; Pe–Piper and Piper, 2003). Major fault strands of the shear zone include the Kirkhill fault in the west, the Rockland Brook fault in the east, and the younger Cobequid fault that encompasses the entire area of the Cobequid Highlands (Fig. 4.1B). The Kirkhill and Rockland Brook faults were probably reactivated Neoproterozoic faults that acted as the pathways for magma during pluton emplacement between 365±4 Ma and 358±4 Ma (Murphy et al., 2011).

The faults of the Cobequid Shear Zone experienced ductile dextral strike–slip motion until at least 340 Ma (Visean) (Gibbons et al., 1996; Pe–Piper et al., 2004) with the intrusion of mafic dykes in the Cape Chignecto, West Moose River, and North River plutons during transtension (Piper et al., 1993). Later magmatism consists of <334 Ma

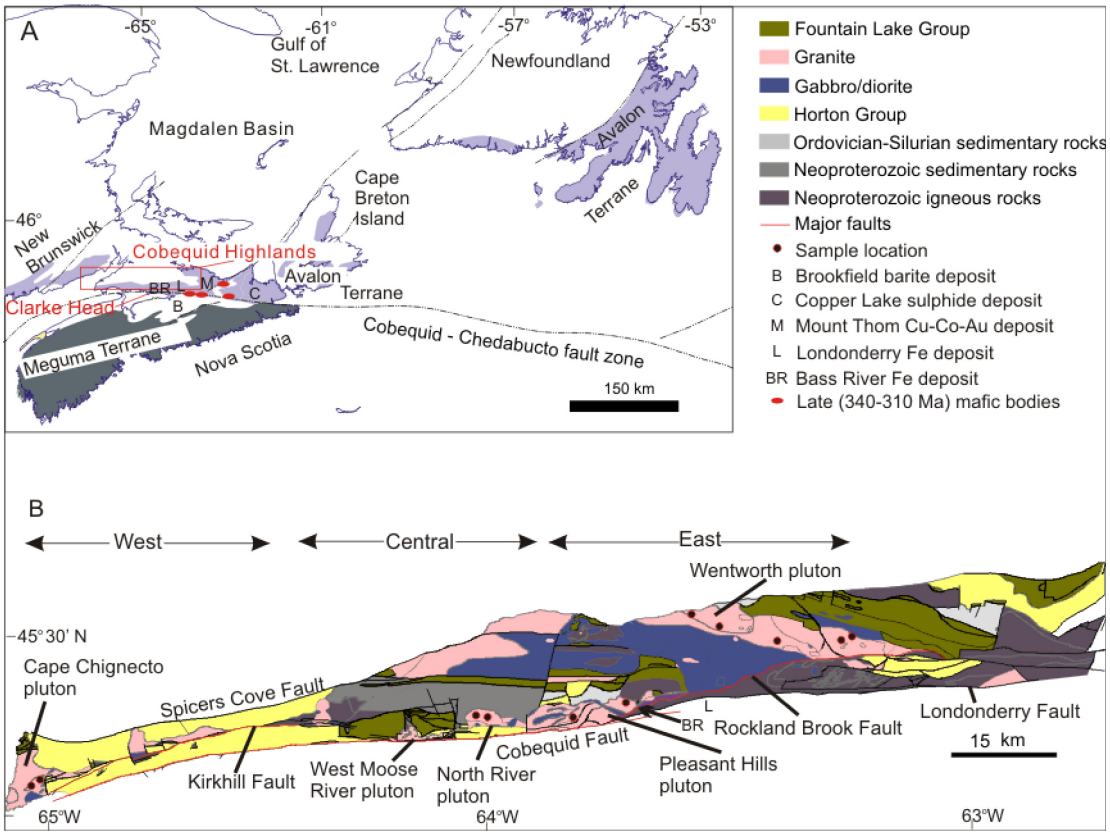

Figure 4. 1 (A) Map showing Appalachian terranes and Carboniferous faults in Atlantic Canada; (B) simplified geological map of the Cobequid Highlands in mainland Nova Scotia.

lamprophyre dykes in the central Cobequid Highlands and a series of alkaline mafic stocks near the Cobequid fault southeast of the Cobequid Highlands, which are dated stratigraphically between 340 and 310 Ma (MacHattie and O'Reilly, 2008). The evolution of the regional fault system was accompanied by the development of the composite Maritimes basin (Piper et al., 1993; Murphy et al., 2011). In the Cobequid Highlands the major stratified units are represented by the latest Devonian–early Carboniferous clastic rocks of the Horton Group and the volcanic rocks of the Fountain Lake Group (Pe-Piper and Piper, 2003).

Several episodes of post–magmatic deformation are recorded in the Cobequid Highlands as indicated by the solid-state deformation recorded in the late Paleozoic

plutons (Waldron et al., 1989; Piper et al., 1993; Miller et al., 1995; Pe-Piper and Piper, 2003). The first phase of post-magmatic deformation that followed pluton emplacement is characterized by NW-vergent thrusting of late Tournaisian age, as indicated along the northern margin of the Wentworth pluton (Koukouvelas et al., 1996; Piper et al., 1996). North of the Cobequid fault, the sedimentary rocks of the Horton Group appear strongly deformed and cut by late granitic dykes which are no older than 355 Ma, (Pe-Piper et al., 1989; Pe–Piper and Piper, 2003) and therefore the deformation of the Horton Group predates Visean (Murphy et al., 2011). In the Cape Chignecto pluton, similar late granitic dykes were interpreted to occupy thrust planes (Waldron et al., 1989) and may thus indicate NW-vergent thrusting of similar age to that observed in the area of the Wentworth pluton (Piper et al., 1993). Close to the Serpukhovian–Bashkirian boundary, another phase of deformation is recorded along the northern and southern margins of the Cobequid Highlands. To the south, the Clarke Head megabreccia lies 4 km north of the Cobequid fault and contains mafic granulites whose metamorphism is dated at 370 ±2 Ma (Gibbons et al., 1996). The Clarke Head area reflects the episodic nature of deformation along the faults of the Cobequid Shear Zone. The early stage of deformation that post-dates metamorphism occurred at 338−346 ±3 Ma (corrected Ar–Ar age on hydrothermal amphibole in veins that cut the mylonitic fabric) (Gibbons et al., 1996). By the mid–Carboniferous (~320 Ma– Serpukhovian) a new E–W fault system developed as a result of continued Alleghanian convergence of Gondwana with Laurentia (Murphy et al., 2011). This fault system comprises the Cobequid–Chedabucto Fault Zone, which in the western part of the Cobequid Highlands reactivated the older Cobequid fault as a cataclastic dextral strike–slip fault, but in the east the newer part of the fault cuts lower

Carboniferous sedimentary rocks (Pe–Piper and Piper, 2003). Megabrecciation in Clarke Head is interpreted to have occurred in the late Carboniferous (ca. 315-310 Ma), since the megabrecciated rocks contain dispersed clasts of evaporites interpreted as Windsor Group (Gibbons et al., 1996) and may therefore be related to the Alleghanian deformation.

The Wentworth pluton (Fig. 4.1B), north of the Rockland Brook fault, has the most complex distribution of igneous rock types, mineralogy, and geochemistry of all the latest Devonian intrusions in the Cobequid Highlands. In the southwestern part of the pluton lies the largest gabbroic body in the area, whereas the northeastern part consists principally of biotite–amphibole granite (Koukouvelas et al., 2002). The Pleasant Hills pluton (Fig. 4.1B) lies north of the Cobequid and Rockland Brook faults in the eastern Cobequid Highlands. This composite pluton consists of gabbro, granodiorite, and hornblende–bearing granite of several generations (Pe–Piper et al., 1998). The North River pluton (Fig. 4.1B), in the central Cobequid Highlands, is a simple intrusion located in the stepover zone between the Rockland Brook and Kirkhill faults. It consists mainly of a homogeneous coarse–grained biotite–granite with minor gabbroic bodies near the margins and mafic dykes that cut the granite (Pe–Piper, 1991). The large Cape Chignecto pluton (Fig. 4.1B) is located immediately north of the Cobequid Fault in the western Cobequid Highlands, and consists of biotite–bearing A–type granite, diorite, and hybrid rocks that are interpreted to be products of mixing between granitic and mafic magmas (Pe–Piper, 1995b). In the Wentworth pluton Koukouvelas and Pe-Piper (1996) concluded that magma emplacement took place under shearing and E-W extension, as indicated by the shapes of deformed mafic enclaves in some of the granites. Magma emplacement during dextral shearing and NW-thrusting is inferred for the Pleasant Hills, North River

and Cape Chignecto plutons from field observations (Koukouvelas et al., 1996). The plutons have rim zones along their northern margin for which a sinistral sense of movement is interpreted, while dextral shearing more prominent of the southern margins of the plutons and closer to the main faults (Pe-Piper et al., 1998).

The latest Devonian granites of the Cobequid Highlands are metaluminous to peralkaline alkali–feldspar A–type granites (Koukouvelas et al., 2002). They are fine- to medium-grained rocks with granular texture that can be granophyric in places. The Wentworth pluton is the most alkaline, and is the only pluton that contains primary sodic amphibole (Pe–Piper, 2007). Calcic amphibole of ferro–edenitic composition is present in both the Wentworth and Pleasant Hills plutons (Pe–Piper et al., 1998; Pe–Piper, 2007), whereas the other granite plutons are biotite–bearing (Pe–Piper, 1991; 1995b). The Wentworth pluton granites contain many REE–minerals, including magmatic minerals like allanite–(Ce) and chevkinite–(Ce) as parts of the granite assemblage, late magmatic hingganite–(Y), and post–magmatic samarskite–(Y), fersmite, aeschynite–(Y) and hydroxylbastnäsite–(Ce) (Papoutsa and Pe–Piper, 2013). Even though the Wentworth granites host a variety of hydrothermal REE–minerals, most are dispersed within the body of the rock, rather than in fractures.

The granites of the late Paleozoic plutons in the Cobequid Highlands are commonly fractured, and the density of these fractures increases towards the major faults of the Cobequid Shear Zone (Nearing, 1991). The Cape Chignecto pluton is mylonitic, however mylonitic fabrics are absent in the North River pluton (Waldron et al., 1989; Pe–Piper, 1991). Hydrothermal alteration occured in places throughout most of the Carboniferous in the Cobequid Highlands. Sodic alteration is expressed by the formation of

hydrothermal albite and riebeckite, and was focused in the western part of the Cobequid Highlands along the Cobequid and Kirkhill faults (Pe–Piper et al., 2004), dated at 353±4 Ma in the West Moose River pluton (corrected Ar–Ar age on hydrothermal riebeckite, Table 4.1).

Table 4. 1 Geochronological data from various styles of hydrothermal alteration.

Description	Mineral	Method	Age (Ma)*	Reference
Albitized granite, West Moose River pluton	hydrothermal riebeckite	Ar-Ar	353±4	Pe-Piper et al. (2004)
Deformed diorite, Cape Chignecto pluton, metamorphic biotite	biotized hornblende	Ar-Ar	347±3	Pe-Piper et al. (2004)
Altered diorite, southwestern Cape Chignecto pluton	low-Ti biotite	Ar-Ar	343±3	Pe-Piper et al. (2004)
Gneissose granodiorite south of the Rockland Brook fault	mixed hornblende-biotite separates	Ar-Ar	336-343 ±4	Pe-Piper et al. (2004)
Medium-grained diorite, Cape Chignecto pluton	hydrothermal biotite	Ar-Ar	342±3	Pe-Piper et al. (2004)
Lamprophyre dyke in the central Cobequid Highlands	whole-rock	Ar-Ar	334±3	Pe-Piper et al. (2004)
Lamprophyre dyke in the central Cobequid Highlands	green biotite	Ar-Ar	326±2	Pe-Piper et al. (2004)
Carbonate-suphide vein in Copper Lake deposit	pyrite	Re-Os	323±8	Kontak et al. (2008)
Altered siltstone adjacent to a carbonate-sulphide vein with intergrowths of hydrothermal muscovite and carbonate, Copper Lake deposit	hydrothermal muscovite	Ar-Ar	309.5 ±1.6	Kontak et al. (2008)

Notes: *: All Ar-Ar ages published prior 2008 have been corrected from the original data according to Kuiper et al. (2008), due to new intercalibrations in Ar-Ar dating.

Among the plutons involved in this study, albitization of the granites is reported from only a few localities in the Cape Chignecto pluton (Nearing, 1991). In those cases, the association of albitization with ductile deformation fabrics is interpreted as evidence for an early, high–temperature hydrothermal event that was localized and took place in

deep structural levels. Epidotization is observed along spaced fracture sets in the volcanic rocks of the Fountain Lake Group in the central and western parts of the Cobequid Highlands (Waldron et al., 1989; Nearing, 1991). In the Wentworth pluton, plastically folded epidote–rich dykes have been reported to cut ductile deformed granites (Koukouvelas et al., 2002).

Widespread biotization has been observed in the mafic rocks of the Cape Chignecto pluton and is dated at 343 ±3 Ma (corrected Ar–Ar age on hydrothermal biotite), while hydrothermal green biotite in the central Cobequid Highlands yielded an age of 334 ±2 Ma (corrected Ar–Ar age, Pe–Piper et al., 2004, Table 4.1), suggesting that potassic alteration in the Cobequid Highlands was long-lived. Biotization in the granites is macroscopically expressed as mafic stringers and clots up to 3 mm in width mostly containing secondary biotite, magnetite, and hematite (Nearing, 1991). In the most deformed rocks of the Cape Chignecto pluton, secondary biotite and magnetite are concentrated along brittle fractures at high angles to the foliation which generally has a NNE trend (Waldron et al., 1989). Brittle deformation in the North River pluton is more pronounced in the southern part of the intrusion closer to the Cobequid fault (Pe–Piper, 1995a). In the central part of the pluton, north–trending dykes, representing the last major structures, are dextrally offset by late fracture sets with a W–E shear trend, parallel to the Cobequid fault (Piper et al., 1993). There is limited information on the fracture systems in the eastern part of the Cobequid Shear Zone. Miller et al. (1995), however, reported that the majority of the fractures in the deformed granites of the Pleasant Hills and Wentworth plutons are parallel to the trace of the Rockland Brook fault and only secondary fractures occur as conjugate sets.

Widespread mineralization along the late Carboniferous Cobequid–Chedabucto Fault Zone occurs as veins or areas of intense alteration and includes barite, siderite, pyrite, ankerite and manganese deposits in brecciated rocks (Murphy et al., 2011). The most significant deposits are the Londonderry and Mt. Thom iron carbonate deposits, Copper Lake Cu–Au deposit, and the Brookfield barite deposit, all interpreted as IOCG mineralization (MacHattie and O'Reilly, 2008). The mineralization in many areas is demonstrably post–Visean (< 330 Ma). Mineralization has been dated directly at 323 Ma (Re–Os age on hydrothermal pyrite, Table 4.1) in the sulfide deposits of Copper Lake (Kontak et al., 2008), 100 km east of the Cobequid Highlands. The presence of monazite, thorite and xenotime in the fractures of Copper Lake indicates that REE–circulation accompanied this late hydrothermal event (Kontak et al., 2008). The presence of albitite dykes within the young 340–310 Ma gabbro stocks east of the Cobequid Highlands implies that a late stage, volatile–rich phase differentiated from the gabbro and may have played a role in generating the iron–rich hydrothermal fluids of the ~323 Ma IOCG mineralizing event in the Cobequid–Chedabucto fault zone (MacHattie and O'Reilly, 2008).

4.4 METHODS

The samples of this study were collected from the Wentworth, Pleasant Hills, North River and Cape Chignecto plutons using the maps of Pe–Piper and Piper (2005). Thin and polished thin sections were already available for these granites, and whole–rock analyses were previously done for most samples. For the purpose of this work, additional analyses of trace elements were done at the Activation Laboratories, using their code 4B1 for Lithoresearch. The concentrations of trace elements were determined by

metaborate/tetraborate fusion ICP–MS. For the investigation of the hydrothermal REE–minerals, the samples were selected on the basis of high fracture density (>5% measured surface of fractures on thin section) and with microscopic evidence of alteration. Out of a total of 150 thin and polished thin sections from all plutons, 11 strongly fractured samples were eventually selected. These include 5 samples from the Wentworth pluton, 2 samples from the Pleasant Hills pluton, 2 samples from the North River and 2 samples from the Cape Chignecto pluton. The fracture fillings were first observed under a Nikon Eclipse E400 POL petrographic microscope, with a PixelINK PL–A686C camera, and then analyzed by electron dispersion spectroscopy for a qualitative mineral identification (EDS). A LEO 1450 VP scanning electron microscope (SEM) was used with a maximum resolution up to 3.5 nm at 30 kV and a detection limit > 0.1%, at the Regional Electron Microscopy Centre at Saint Mary's University. The operating conditions were at 15kV of accelerating voltage with a 25nA beam current and a beam diameter of 1 micron. Selected grains of all minerals identified with EDS were further analyzed for a more quantitative chemical description. All wavelength dispersive spectroscopy (WDS) mineral analyses were made at the Robert MacKay Electron Microprobe Laboratory at Dalhousie University, using a JEOL–8200 electron microprobe with five wavelength spectrometers and a Noran 133 eV energy dispersion detector. The operating conditions were at 15kV of accelerating voltage with a 20nA beam current, and a beam diameter of 1 micron. The standards, peaks and crystals used for the analyses of REE-minerals are: monazite (P, Kα, PETJ), columbite (Nb, Lα, PETJ), tantalite (Ta, Lα, LIFH), ThO_2_MAX (Th, Mα, PETJ), UO_2 (U, Mβ, PETJ), zirconia (Zr and Hf, Lα, PETJ and LIFH respectively), Y-Al-garnet (Y, Lα, TAP), $LaPO_4$_MAX (La, Lα, LIF),

$CePO_4$_MAX (Ce, Lα, LIF). Drake and Weill (1972) REE glasses were used for: Pr (Lβ, LIFH), Nd (Lβ, LIFH), Sm (Lβ, LIFH), Eu (Lα, LIFH), Gd (Lβ, LIFH), Dy (Lα, LIF), Ho (Lα, LIFH), Er (Lα, LIF), and Yb (Lα, LIF). Fluorine was calibrated using F-apatite (Kα, TAPH). Certain pairs of elements (Ti-Hf, Zr-P, Hf-Ho, Er-Nb, and F-Ce), created peak overlaps. For those elements the standards were carefully selected as to not contain the overlapping element, and correction factors were calculated from the measured intensities of the peaks, in order to determine the real concentrations of the elements present.

In order to correlate the presence of specific hydrothermal REE–minerals with different styles of hydrothermal alteration, the modal and bulk compositions of the fracture fillings and the total amount of fractures present in selected samples were estimated by point–counting on thin sections. This was carried out on an automated stepping stage of Conwy Valley Systems and PETROG software for Windows. The polished thin sections were then scanned for a better relocation of the fractures of interest under the SEM. The EDS analyses and the backscattered electron (BSE) images were also used to estimate the modal composition of the fracture fillings. The area of each phase with a different brightness in BSE images was measured using ImageJ software for Windows. Each phase was identified from the EDS analyses and the final modal compositions were calculated in Excel. Bulk chemical compositions of the fracture fillings were estimated from the calculated modal compositions and the mineral analyses.

The temperature of the hydrothermal fluids was estimated by the chlorite thermometer of Kranidiotis and Maclean (1987), where applicable. The chemistry of chlorite can be affected by temperature and leads to an increase of Al^{iv} (Cathelineau and Nieva, 1985). The chlorite thermometer used in this work includes a correction for Fe–

Mg substitution in chlorites, which can also affect the amount of Al^{iv} present (Kranidiotis and Maclean, 1987). Using the correction of Zang and Fyfe (1995) for Al^{iv} in the equation of Kranidiotis and Maclean (1987), the estimated error is 25°C (Lana et al., 2003). This work follows the nomenclature schemes of Wiéwiora and Weiss (1990), Rieder et al. (1998), and Armbruster et al. (2006) for chlorite, biotite and epidote, respectively.

4.5 RESULTS

4.5.1 MAJOR MODAL COMPOSITION OF THE FRACTURE FILLINGS, DISTRIBUTION AND PARAGENETIC SEQUENCE

Epidote–rich fractures. The majority of these fractures are mm–scale and contain up to 94 % epidote, with titanite also being a major component in the fracture filling, up to 44 % (Table 4.2). The epidote approaches the composition of clinozoisite (Fig. 4.2A) with no more than 33% of the "pistacite" component, and locally coexists with andradite (Table 4.2 and Appendix C.1). In fractures where dominant epidote coexists with magnetite, the latter comprises less than 20% of the modal composition of the fracture filling. In some fractures chlorite appears in varying amounts (up to 41%) as mixture with fine–grained epidote or calcite. Pyrite (Figs. 4.3a and b) has been found in a few epidote–titanite fractures.

Biotite–rich fractures. Secondary biotite of annite composition (Fig. 4.2B) is abundant in these fractures (up to 96%, Table 4.2, Appendix C.2). The biotite is commonly mixed with varying amounts of epidote (Figs. 4.3C). Magnetite (less than 40%) is also present.

Chlorite–rich fractures. The main component of these fractures is chlorite with a composition ranging from ripidolite to chamosite (Figs. 4.2C and D) and magnetite (Fig.

4.3D, Table 4.2, Appendix C.3). Titanite, ilmenite, TiO_2 mineral, epidote and zircon are also present in these fractures (< 2 mm width). From chemical analyses alone it was not possible to accurately determine which TiO_2 polymorph (rutile, anatase or brookite) is present in the fracture fillings, and therefore, in this work this composition will be

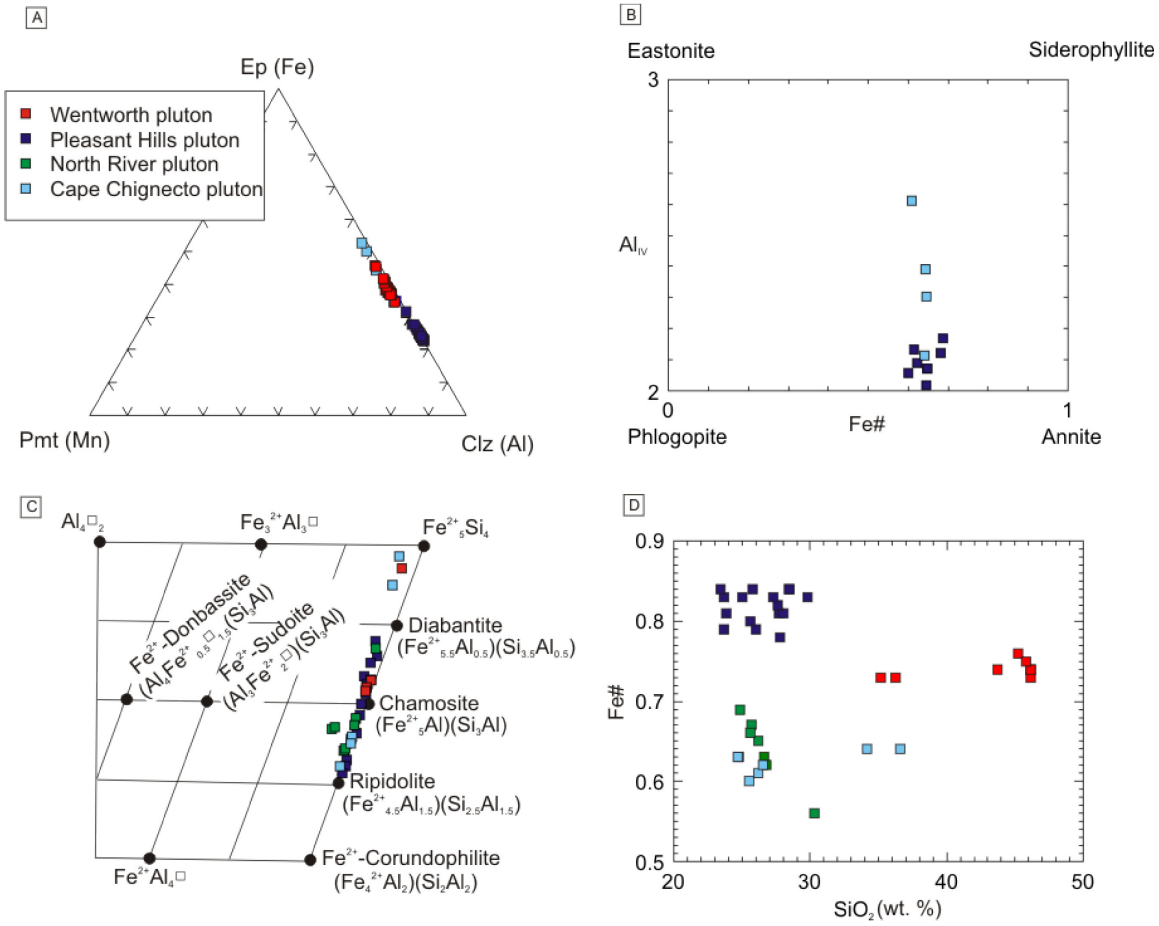

Figure 4. 2 Chemical discrimination diagrams for the major hydrothermal minerals found in the granites of the Cobequid Highlands. Variations in the chemistry of hydrothermal epidote are shown in plot (A), biotites are classified in plot (B), and plot (C) is a discrimination diagram of Fe-rich chlorites (after Wiewióra and Weiss, 1990). Plot (D) shows variations in Fe-number (Fe#) for the hydrothermal chlorites from all plutons.

referred to as TiO_2 mineral. Epidote and titanite occur as fine–grained patches in rare fractures, whereas hydrothermal zircon occurs as subhedral to anhedral grains associated with chlorite.

Fe–rich fractures. These fractures are characterized by dominant magnetite (up to 88 %) coexisting with lesser amounts of epidote, biotite and chlorite. Pyrite and barite inclusions rarely occur in magnetite–rich fractures (Fig. 4.3E).

Calcite–rich fractures. This is the least common type of fracture–filling in the studied samples. This type comprises high amounts of calcite coexisting with lesser chlorite and titanite, while epidote is absent (Table 4.2). In the Wentworth granites, the main type of fracture, in terms of abundance and size, observed in the samples is epidote–rich. In a total of 102 studied fractures from the Wentworth granites, 60% are epidote–rich, 28% are calcite–rich, 10% are magnetite–rich and 2% are titanite–rich.

In rare cases, magnetite–rich fractures cross–cut epidote–filled fractures at a high angle, forming conjugate sets (Fig. 4.3B), and the former appear more continuous, suggesting a probable younger age. Irregular patches of titanite, andradite and chlorite in the epidote suggest that these minerals precipitated at the same time from the fluids in the epidote–filled fractures. Pyrite inclusions in magnetite indicate pyrite probably formed first.

In the Pleasant Hills pluton, the fractures show a larger variation in the distribution of hydrothermal minerals than in the Wentworth pluton and epidote occurs in lower amounts (Table 4.2). The texturally older fractures comprise biotite mixed with epidote, cut by younger magnetite–bearing biotite fractures that contain no epidote, at high angles as conjugate sets (Fig. 4.3C). These younger fractures offset the old ones, and have the highest concentration of biotite close to the intersection with the older biotite fractures. Conversely, the amount of magnetite increases away from the intersection point, until the fractures are filled by almost monomineralic magnetite. There is no clear relationship

Table 4. 2 Petrographic description of the studied samples.

Pluton	Sample (No of studied fractures)	% fractures	Type of fracture	Modal composition (%)													REE minerals
				andradite	barite	biotite	calcite	chlorite	epidote	ilmenite	magnetite	pyrite	REE	TiO_2 mineral	titanite	zircon	
Wentworth	30-9-1 (18)	11	ep-tnt (77%)					10-20	30-50		5-8		0-4		20-30	0-4	thorite
			tnt-rich (15%)					20	30						44	2	
			mag-rich (8%)					12	20		43				23		
	6484 (13)	12	ep-tnt (43%)						47-60		16-36	0-12			10-20		
			ep-rich (50%)						60-94		2-20	<1			8-14		
			mag-rich (7%)		1				20		55	11			10		
	6497 (24)	17	cal-rich (95%)	0-5.5			30-85	14-30			1-23		0-5		7-26	<1	hydroxylbastnäsite-(Ce), thorite
			chl-rich (5%)				15	41			7		<1		37		hydroxylbastnäsite-(Ce), hingganite-(Y)
	6591 (23)	16	ep-tnt (40%)						36-50		16-35				15-20	0-6	
			ep-rich (30%)						52-82		7-16		<0.5		8-10	<1	hydroxylbastnäsite-(Ce)
			mag-rich (26%)						20-22		50-58		<0.5		12-26	<1	hydroxylbastnäsite-(Ce), thorite
			tnt-rich (4%)						26		15				40	0-4	
	6686 (24)	12	ep-tnt (38%)	0-46					30-60		14-27		<0.5		15-35	0-4	hydroxylbastnäsite-(Ce)
			ep-rich (38%)	17					60		0-9				0-15		
			mag-rich (24%)	0-17							43-88				8-33	<1	
Pleasant Hills	4106 (32)	40	ep-bt (48%)			30-50			37-60		0-40		<0.5				hydroxylbastnäsite-(Ce)
			bt-rich (26%)			55-85							0-2	<1	8-20		hydroxylbastnäsite-(Ce), cerianite
			ep-rich (26%)			18-27			60-75				<1				thorite, hydroxylbastnäsite-(Ce)
	4672 (31)	8	bt-chl (41%)			40-50		18-30			0-32		0-2				hydroxylbastnäsite-(Ce), Nb-minerals
			bt-rich (59%)			60-96		3-30									

Pluton	Sample (No of studied fractures)	% fractures	Type of fracture	Modal composition (%) andradite	barite	biotite	calcite	chlorite	epidote	ilmenite	magnetite	pyrite	REE	TiO_2 mineral	titanite	zircon	REE minerals
North River	1779 (34)	9	chl-rich (38%)					70-92			6-24		1-3				synchysite-(Ce), hydroxylbastnäsite-(Ce)
			mag-rich (52%)					5-11		7-12	60-88		0-5			<1	synchysite-(Ce), parisite-(Ce), hydroxylbastnäsite-(Ce), thorite
			ep-rich (10%)						60-85		6-30		0-2			<1	hydroxylbastnäsite-(Ce)
	4824 (39)	7	chl-rich (18%)					68-90			6-30		2-12				hingganite-(Y), chernovite-(Y)
			chl-mag-rich (38%)					20-50		0-39	31-50		1-25			0-5	hingganite-(Y), chernovite-(Y), parisite-(Ce), Nb-minerals
			mag-rich (44%)					6-13		0-21	58-84		0-18			0-5	thorite, synchysite-(Ce), parisite-(Ce), hydroxylbastnäsite-(Ce), chernovite-(Y)
Cape Chignecto	2039 (27)	28	bt-rich (79%)			60-91				2-11	2-30		0-6			<1	hydroxylbastnäsite-(Ce), parisite-(Ce), thorite
			chl-ilm (16%)					37-48		4-40	5-20		4			0-2	hydroxylbastnäsite-(ce)
			mag-rich (5%)			30					45		<0.5	20		4	hydroxylbastnäsite-(ce)
	6284 (25)	40	bt-rich (18%)			62-90			0-20				0-2		0-4	0.5	chernovite-(Y), thorite
			ep-rich (11%)					0-6	60-92	0-6						<1	
			chl-rich (71%)			0-24		60-92					0-18	0-5		0-4	cerianite, chernovite-(Y)

between hydrothermal biotite and chlorite, but only the biotite fractures contain epidote. In the chlorite fractures of the Pleasant Hills pluton, magnetite appears to either rim corroded chlorite, or fill empty spaces in fractured and deformed chlorite veins, and therefore appears to post–date them (Fig. 4.3F). In rare cases, magnetite grains show interlocking textures with chlorite, suggesting that the formation of those two minerals was at one time contemporaneous.

In the North River pluton, the main variation in the modal composition of the fracture fillings is in the distribution of chlorite and magnetite. From the 73 studied fractures of this pluton, 61% are magnetite–rich, 33% are chlorite–rich, 4% are epidote–rich and only 1% are biotite–rich (Table 4.2).

Magnetite may occur as grains intergrown with chlorite suggesting co–precipitation from the fluids. However, some magnetite fills pores or penetrates corroded chlorite, indicating a later formation. Rare chlorite–rich fractures appear to have been deformed and fractured. As in the other plutons, some secondary magnetite–rich fractures that contain chernovite–(Y) appear to form conjugate sets with pre–existing chlorite–rich fractures.

The major hydrothermal minerals common in the mm–scale fractures of Cape Chignecto pluton include chlorite, biotite, magnetite and smaller amounts of epidote, ilmenite, TiO_2 mineral, zircon, and titanite (Table 4.2 and 4.3). The fractures of the Cape Chignecto granites do not show clear textural relationships between biotite and chlorite. Both minerals appear corroded and are replaced by magnetite associated with TiO_2 mineral, rare pyrochroite (Table 4.3) and REE–carbonate minerals. Some chlorite is associated with chernovite–(Y), which appears to be a late mineral. Locally TiO_2

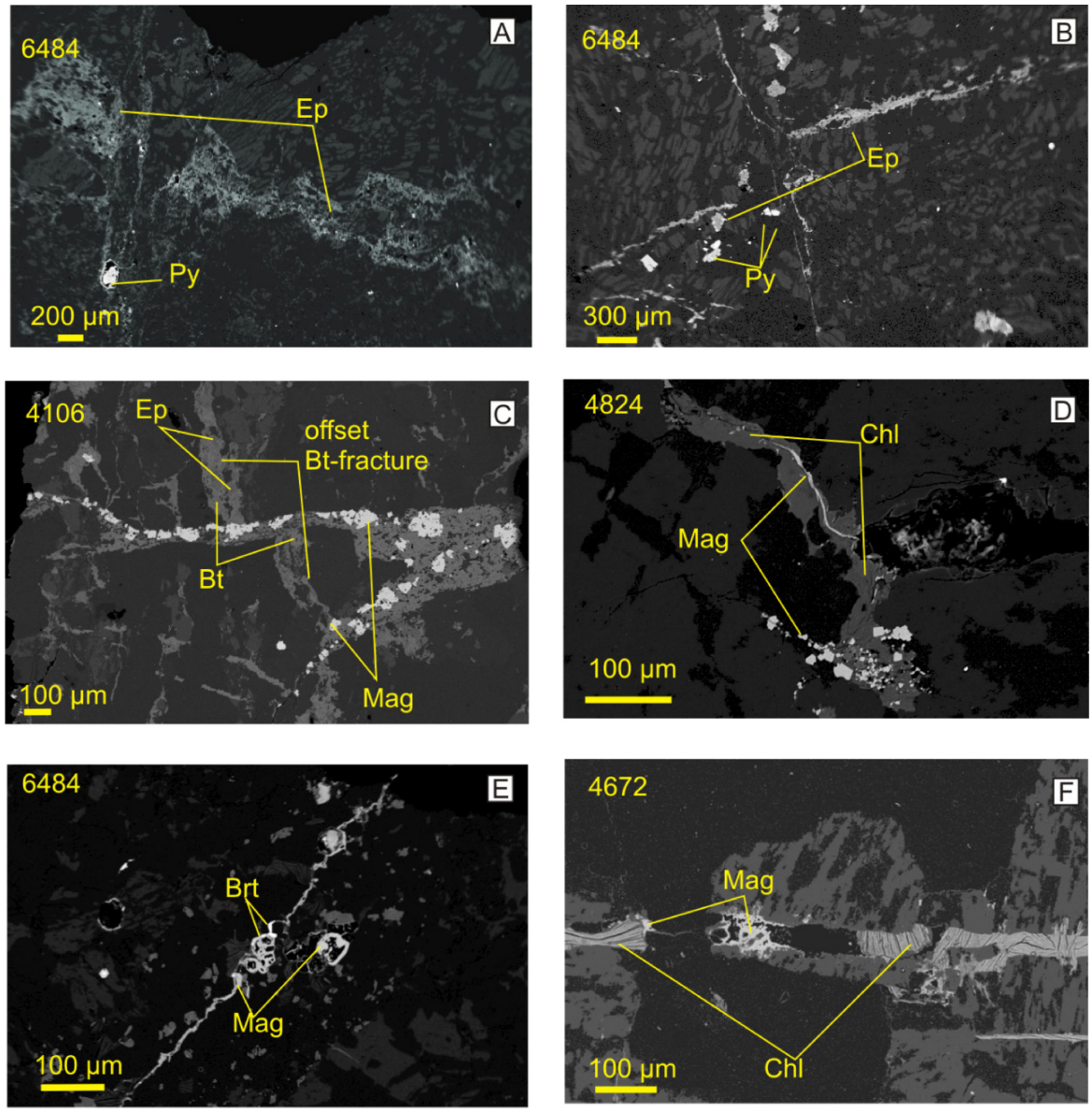

Figure 4. 3 Back–scattered electron (BSE) images of selected fractures from the granites of the Cobequid Highlands. Images (A) and (B) show offset epidote–rich fractures with presence of pyrite from the Wentworth pluton. Image (C) shows a pre–existing biotite–epidote fracture that is offset by a younger biotite–magnetite fracture in Pleasant Hills pluton. Image (D) shows a chlorite–filled fracture that is irregularly cut by a later magnetite veinlet in North River pluton. Image (E) shows grains of barite found in a rare magnetite vein in the Wentworth granites. Image (F) shows late magnetite filling a dismembered chlorite fracture in the Pleasant Hills pluton. Mineral abbreviations: Ep: epidote, Py: Pyrite, Brt: Barite, Bt: Biotite, Mag: Magnetite, Chl: Chlorite.

mineral–bearing chlorite fractures are cut by younger, almost barren veinlets that only in places are filled with magnetite. Some chlorite shows ilmenite forming along the

Table 4. 3 Representative microprobe analyses of all the mineral phases present in the fracture fillings of the A-type granites of the Cobequid Highlands.

Pluton	WP	WP	WP	PHP	PHP	NRP	WP	CCP	CCP	CCP	PHP	NRP	NRP	WP	PHP	CCP	NRP	NRP	CCP
Sample	**6497**	**6497**	**6498**	**4106**	**4672**	**1779**	**6497**	**6284**	**6284**	**6284**	**4106**	**4829**	**1779**	**6497**	**4106**	**6284**	**4824**	**1779**	**6284**
Mineral	**ep**	**and**	**tnt**	**bt**	**ilm**	**chl**	**cal**	**Ti-min**	**pyr**	**aln**	**H-bas**	**par**	**syn**	**thr**	**cer**	**cher**	**hing-Y**	**zrn**	**cher-thr**
P_2O_5	b.d.	b.d.	b.d.	b.d.	b.d.	b.d.	b.d.	b.d.	b.d.	b.d.	0.37	n.d	0.07	0.08	2.04	2.64	0.06	0.12	3.03
Nb_2O_5	b.d.	b.d.	b.d.	b.d.	b.d.	b.d.	b.d.	b.d.	b.d.	0.07	b.d.	0.05	0.03	b.d.	0.04	b.d.	n.d	b.d.	b.d.
Ta_2O_5	b.d.	b.d.	b.d.	b.d.	b.d.	b.d.	b.d.	b.d.	b.d.	0.01	b.d.	n.d	n.d	b.d.	n.d	b.d.	n.d	b.d.	b.d.
As_2O_5	b.d.	b.d.	b.d.	b.d.	b.d.	b.d.	b.d.	b.d.	b.d.	b.d.	0.06	n.d	n.d	0.01	3.36	33.73	n.d	0.02	25.83
SiO_2	38.86	34.39	31.50	37.98	0.11	26.63	1.77	2.49	0.56	30.26	3.13	1.23	0.61	22.26	13.24	3.02	29.43	32.11	3.02
TiO_2	0.10	1.20	34.78	2.05	49.25	b.d.	0.03	88.97	0.13	1.39	b.d.	n.d	n.d	0.56	0.03	b.d.	0.06	b.d.	0.14
ZrO_2	b.d.	b.d.	b.d.	b.d.	b.d.	b.d.	b.d.	b.d.	b.d.	b.d.	0.07	n.d	n.d	1.25	n.d	0.07	0.01	59.67	0.21
HfO_2	b.d.	b.d.	b.d.	b.d.	b.d.	b.d.	b.d.	b.d.	b.d.	b.d.	0.07	n.d	n.d	b.d.	n.d	b.d.	n.d	2.50	b.d.
ThO_2	b.d.	b.d.	b.d.	b.d.	b.d.	b.d.	b.d.	b.d.	b.d.	0.04	3.11	0.33	0.16	42.14	0.69	2.00	0.25	0.38	23.52
UO_2	b.d.	b.d.	b.d.	b.d.	b.d.	b.d.	b.d.	b.d.	b.d.	b.d.	0.23	0.04	n.d	1.46	0.03	0.30	0.01	0.65	0.76
Al_2O_3	24.61	3.26	3.47	19.28	0.02	16.65	0.15	0.45	0.97	11.46	0.65	0.47	0.23	4.82	2.00	b.d.	0.18	0.03	0.04
Y_2O_3	b.d.	b.d.	b.d.	b.d.	b.d.	b.d.	b.d.	b.d.	b.d.	0.30	1.31	2.06	4.92	0.93	8.74	30.91	27.84	1.64	19.02
La_2O_3	b.d.	b.d.	b.d.	b.d.	b.d.	b.d.	b.d.	b.d.	b.d.	6.51	15.40	10.55	8.63	1.29	0.10	0.06	n.d	b.d.	0.07
Ce_2O_3	b.d.	b.d.	b.d.	b.d.	b.d.	b.d.	b.d.	b.d.	b.d.	12.78	25.11	18.15	19.99	3.57	47.90	4.55	0.34	0.01	5.67
Pr_2O_3	b.d.	b.d.	b.d.	b.d.	b.d.	b.d.	b.d.	b.d.	b.d.	1.16	2.17	2.26	2.01	0.41	0.13	0.18	0.17	b.d.	0.16
Nd_2O_3	b.d.	b.d.	b.d.	b.d.	b.d.	b.d.	b.d.	b.d.	b.d.	4.31	9.77	10.05	9.15	1.71	0.68	1.26	0.84	b.d.	1.11
Eu_2O_3	b.d.	b.d.	b.d.	b.d.	b.d.	b.d.	b.d.	b.d.	b.d.	0.31	0.76	1.88	1.88	0.13	0.30	0.06	1.08	0.02	0.09
Sm_2O_3	b.d.	b.d.	b.d.	b.d.	b.d.	b.d.	b.d.	b.d.	b.d.	0.56	1.15	0.82	0.58	0.52	n.d	1.57	0.12	b.d.	1.35
Dy_2O_3	b.d.	b.d.	b.d.	b.d.	b.d.	b.d.	b.d.	b.d.	b.d.	0.31	0.36	1.27	1.79	0.29	0.92	5.49	4.69	0.24	3.31
Gd_2O_3	b.d.	b.d.	b.d.	b.d.	b.d.	b.d.	b.d.	b.d.	b.d.	0.42	0.68	0.58	0.84	0.28	1.85	5.17	5.11	0.03	3.43
Er_2O_3	b.d.	b.d.	b.d.	b.d.	b.d.	b.d.	b.d.	b.d.	b.d.	0.10	0.05	n.d	0.12	0.12	0.44	2.75	2.28	0.41	1.39
Ho_2O_3	b.d.	b.d.	b.d.	b.d.	b.d.	b.d.	b.d.	b.d.	b.d.	b.d.	b.d.	0.02	0.20	b.d.	0.71	2.44	3.01	0.13	1.56
Yb_2O_3	b.d.	b.d.	b.d.	b.d.	b.d.	b.d.	b.d.	b.d.	b.d.	b.d.	b.d.	n.d	n.d	0.01	0.42	1.67	1.78	0.48	0.95
FeO	11.55	25.11	0.88	19.66	40.93	31.72	0.89	2.18	0.29	17.94	2.24	9.10	0.91	7.05	4.73	0.96	7.73	0.70	0.38
MgO	0.15	0.69	0.05	7.36	6.76	10.43	0.03	0.00	0.09	0.37	0.01	n.d	0.25	0.20	n.d	b.d.	0.00	0.01	b.d.
MnO	b.d.	0.06	0.02	0.06	0.03	0.54	0.20	0.02	74.11	0.41	b.d.	n.d	n.d	b.d.	1.75	b.d.	0.08	0.07	0.16
CaO	23.77	32.90	29.31	0.03	0.07	b.d.	52.25	2.46	0.13	9.43	4.41	12.20	17.85	6.63	0.24	0.39	5.34	0.22	0.53
Na_2O	b.d.	b.d.	0.02	0.10	0.06	0.02	0.03	0.01	0.03	0.00	b.d.	n.d	n.d	0.08	n.d	b.d.	n.d	0.06	b.d.
K_2O	b.d.	b.d.	0.14	9.83	0.06	0.05	0.07	0.03	0.08	0.02	0.22	0.11	0.07	0.06	0.03	0.02	0.03	0.07	0.03
F	b.d.	b.d.	b.d.	b.d.	b.d.	b.d.	b.d.	b.d.	b.d.	0.04	3.81	3.14	2.68	0.08	n.d	b.d.	0.14	0.08	b.d.
CO_2 calc	-	-	-	-	-	-	22.95	-	-	-	23.08	27.26	29.67	-	-	-	-	-	-
O-F	-	-	-	-	-	-	-	-	-	-0.02	-1.60	-1.32	-1.13	-	-	-	-	-	-
Total	99.04	97.61	100.16	96.35	97.29	86.03	78.36	96.59	76.39	98.12	96.58	100.23	101.52	95.92	90.39	99.22	90.58	99.66	95.76

Pluton	WP	WP	WP	PHP	PHP	NRP	WP	CCP	CCP	CCP	PHP	NRP	NRP	WP	PHP	CCP	NRP	NRP	CCP
Sample	6497	6497	6498	4106	4672	1779	6497	6284	6284	6284	4106	4829	1779	6497	4106	6284	4824	1779	6284
Mineral	ep	and	tnt	bt	ilm	chl	cal	Ti-min	pyr	aln	H-bas	par	syn	thr	cer	cher	hing-Y	zrn	cher-thr
Norm.	O=12.5	O=12	O=5	O=10, OH=2	O=3	O=10, OH=8	C=1	C=1	C=1	C=8	C=1	C=3	C=2	O=4	C=1	O=4	O=10	O=4	O=4
P	0.000	0.000	0.000	0.000	0.000	0.000	0.000	0.000	0.000	0.000	0.009	0.000	0.003	0.002	0.035	0.082	0.003	0.003	0.061
Nb	0.000	0.000	0.000	0.000	0.000	0.000	0.000	0.000	0.000	0.003	0.000	0.002	0.001	0.000	0.000	0.000	0.000	0.000	0.000
Ta	0.000	0.000	0.000	0.000	0.000	0.000	0.000	0.000	0.000	0.000	0.000	0.000	0.000	0.000	0.000	0.000	0.000	0.000	0.000
As	0.000	0.000	0.000	0.000	0.000	0.000	0.000	0.000	0.000	0.000	0.001	0.000	0.000	0.000	0.036	0.649	0.000	0.000	0.323
Si	3.041	2.929	1.024	2.842	0.003	2.860	0.030	0.034	0.008	3.003	0.095	0.092	0.030	0.795	0.270	0.222	1.862	0.993	0.144
Ti	0.000	0.077	0.850	0.115	0.935	0.000	0.000	0.929	0.001	0.104	0.000	0.000	0.000	0.015	0.001	0.000	0.003	0.000	0.005
Zr	0.000	0.000	0.000	0.000	0.000	0.000	0.000	0.000	0.000	0.000	0.001	0.000	0.000	0.022	0.000	0.003	0.000	0.900	0.005
Hf	0.000	0.000	0.000	0.000	0.000	0.000	0.000	0.000	0.000	0.000	0.001	0.000	0.000	0.000	0.000	0.000	0.000	0.022	0.000
Th	0.000	0.000	0.000	0.000	0.000	0.000	0.000	0.000	0.000	0.001	0.022	0.006	0.002	0.343	0.003	0.034	0.004	0.003	0.256
U	0.000	0.000	0.000	0.000	0.000	0.000	0.000	0.000	0.000	0.000	0.002	0.001	0.000	0.012	0.000	0.005	0.000	0.004	0.008
Al	2.268	0.327	0.066	1.699	0.000	2.107	0.003	0.004	0.009	1.341	0.023	0.041	0.013	0.203	0.048	0.000	0.013	0.001	0.001
Y	0.000	0.000	0.000	0.000	0.000	0.000	0.000	0.000	0.000	0.016	0.021	0.082	0.130	0.018	0.095	0.606	0.937	0.027	0.242
La	0.000	0.000	0.000	0.000	0.000	0.000	0.000	0.000	0.000	0.238	0.173	0.290	0.158	0.017	0.001	0.001	0.000	0.000	0.001
Ce	0.000	0.000	0.000	0.000	0.000	0.000	0.000	0.000	0.000	0.462	0.280	0.495	0.364	0.047	0.358	0.061	0.008	0.000	0.050
Pr	0.000	0.000	0.000	0.000	0.000	0.000	0.000	0.000	0.000	0.042	0.024	0.061	0.036	0.005	0.001	0.002	0.004	0.000	0.001
Nd	0.000	0.000	0.000	0.000	0.000	0.000	0.000	0.000	0.000	0.153	0.106	0.267	0.162	0.022	0.005	0.017	0.019	0.000	0.010
Sm	0.000	0.000	0.000	0.000	0.000	0.000	0.000	0.000	0.000	0.010	0.012	0.048	0.032	0.006	0.002	0.020	0.024	0.000	0.001
Eu	0.000	0.000	0.000	0.000	0.000	0.000	0.000	0.000	0.000	0.019	0.008	0.021	0.010	0.002	0.000	0.001	0.003	0.000	0.011
Gd	0.000	0.000	0.000	0.000	0.000	0.000	0.000	0.000	0.000	0.010	0.007	0.031	0.029	0.003	0.006	0.063	0.098	0.002	0.026
Dy	0.000	0.000	0.000	0.000	0.000	0.000	0.000	0.000	0.000	0.013	0.004	0.014	0.013	0.003	0.012	0.065	0.104	0.000	0.026
Er	0.000	0.000	0.000	0.000	0.000	0.000	0.000	0.000	0.000	0.003	0.000	0.000	0.002	0.000	0.003	0.029	0.046	0.004	0.011
Ho	0.000	0.000	0.000	0.000	0.000	0.000	0.000	0.000	0.000	0.000	0.000	0.001	0.003	0.001	0.005	0.032	0.060	0.001	0.012
Yb	0.000	0.000	0.000	0.000	0.000	0.000	0.000	0.000	0.000	0.000	0.000	0.000	0.000	0.000	0.003	0.019	0.034	0.004	0.007
Fe	0.680	1.608	0.024	1.230	0.864	3.309	0.013	0.025	0.004	1.489	0.057	0.566	0.038	0.211	0.081	0.059	0.409	0.018	0.015
Mg	0.000	0.008	0.002	0.821	0.254	1.670	0.001	0.000	0.002	0.054	0.000	0.000	0.018	0.010	0.000	0.000	0.000	0.000	0.000
Mn	0.000	0.050	0.001	0.004	0.001	0.049	0.003	0.000	0.946	0.034	0.000	0.000	0.000	0.000	0.030	0.000	0.004	0.002	0.007
Ca	1.993	3.002	1.021	0.002	0.002	0.005	0.948	0.037	0.002	1.002	0.144	0.973	0.950	0.254	0.005	0.031	0.362	0.007	0.027
Na	0.000	0.000	0.001	0.015	0.001	0.000	0.001	0.000	0.000	0.000	0.000	0.000	0.000	0.006	0.000	0.000	0.000	0.004	0.000
K	0.000	0.000	0.003	0.938	0.001	0.000	0.002	0.000	0.001	0.003	0.008	0.011	0.004	0.003	0.001	0.001	0.002	0.003	0.001
F	0.000	0.000	0.000	0.000	0.000	0.000	0.000	0.000	0.000	0.006	0.090	0.123	0.105	0.005	0.000	0.000	0.028	0.004	0.000
Total	7.982	8.001	2.992	7.666	2.061	10.000	1.000	1.029	0.973	8.006	1.090	3.123	2.11	2.005	1.000	2.000	4.000	2.000	1.250

Notes: ep: epidote, and: andradite, tnt: titanite, bt: biotite, ilm: ilmenite, chl: chlorite, cal: calcite, Ti-min: TiO_2-mineral, pyr: pyrochroite, aln: allanite-(Ce), H-bas: hydroxylbastnäsite-(Ce), par: parisite-(Ce), syn: synchysite-(Ce), thr: thorite, cer: cerianite, cher: chernovite-(Y), hing-Y: hingganite-(Y), zrn: zircon, cher-thr: mixture of thorite and chernovite-(Y). CO_2 was calculated based on charge-balance calculations, Norm. indicates the number of oxygens used for the normalization of the structural formula, b,d= below detection limit.

cleavage that also fills pores in the corroded parts of the same grain, suggesting a later origin.

4.5.2 WHOLE-ROCK REE CONTENTS

In terms of whole–rock composition, the REE concentrations of unaltered granites of the area range from 120 to 409 ppm, with an average concentration of 280 ppm (Pe–Piper 1991, 1995a, 1995b, 1998, and Pe–Piper and Piper 1998a). The bulk REE concentrations of the studied fractured samples range from 216 to 413 ppm in the Wentworth granites, 403 ppm in the Pleasant Hills pluton, 313−356 ppm in the North River granites, and from 199 to 303 ppm in the Cape Chignecto pluton (Table 4.4).

The only magmatic REE–phases found in the studied samples were grains of allanite–(Ce) and chevkinite–(Ce) in the Wentworth granites, and extremely rare relics of dissolved allanite–(Ce) in the granites of the Cape Chignecto. Therefore, a magmatic REE contribution may be recorded in the bulk REE concentrations of these samples. The rest of the REE–minerals reported in this work (Table 4.4), however, are found only in fracture–fillings, showing a clearly hydrothermal origin. Although the size of most of the studied samples is rather small (< 1mm width), fractured granites of the North River and Pleasant Hills plutons with ~8% fractures and no magmatic REE–minerals, contain up to 350 ppm of total REE in their whole–rock composition (Table 4.5).

4.5.3 HYDROTHERMAL REE-MINERALS

Hydroxylbastnäsite–(Ce). This mineral is found principally in epidote–rich fractures of the Wentworth pluton, and in lesser amounts in the biotite fractures of the Pleasant Hills pluton (Table 4.3, Appendix C.4). This carbonate replaces epidote and/or TiO_2 minerals,

Table 4. 4 Ideal chemical formulae of the studied REE-minerals.

Mineral name	Ideal chemical formula
Silicates	
Allanite-(Ce)	$\{CaCe\}\{Al2Fe^{2+}\}(Si_2O_7)(SiO_4)O(OH)$
Hingganite-(Y)	$(Y,REE,Ca)_2(\square,Fe^{2+})Be_2[SiO_4]_2(OH)_2$
Zircon	$ZrSiO_4$
Thorite	$(Th,U)SiO_4$
Oxides	
Cerianite	$(Ce^{4+},Th)O_2$
Samarskite-(Y)	$(Y,Fe^{3+},Fe^{2+},U,Th,Ca)_2(Nb,Ta)_2O_8$
Chernovite-(Y)	$YAsO_4$
Carbonates	
Hydroxylbastnäsite-(Ce)	$(Ce,La)(CO_3)(OH,F)$
Parisite-(Ce)	$Ca(Ce,La)_2(CO_3)_3F_2$
Synchysite-(Ce)	$Ca(Ce,La)(CO_3)_2F$

either as anhedral crystallites < 10 μm in diameter or as 10–30 μm slender prisms (Fig. 4.4A), and is highly enriched in LREE, with a positive Eu anomaly (Fig. 4.5A).

Allanite–(Ce). Allanite–(Ce) is rarely found in fracture fillings but is always associated with epidote–rich fractures in Wentworth and Cape Chignecto plutons (Table 4.3). It occurs as irregular patches replacing hydrothermal epidote in 300 μm sized vugs (Fig. 4.4B). Allanite–(Ce) presents a REE pattern very similar to that of the REE–carbonate and also has a positive Eu anomaly (Fig. 4.5B).

Thorite. Hydrothermal thorite is found in small amounts but is widespread throughout the plutons and associated with all fracture types (Table 4.3, Appendix C.5). The most common mode of occurrence is as inclusions in allanite–(Ce), biotite, REE–carbonates and zircon. These inclusions range in diameter from 30–60 μm (Fig. 4.4C) although some discrete thorite grains less than 10 μm have also been found. This mineral shows variable REE–patterns showing a HREE enrichment in North River and Cape

Table 4. 5 Whole-rock analyses of the studied granites.

Pluton	**CCP**	**CCP**	**NRP**	**NRP**	**PHP**	**WP**	**WP**	**WP**
Sample	**2039**	**6284**	**1779**	**4824**	**4672**	**6686**	**6591**	**6484**
Major oxides (wt. %)								
SiO_2	72.64	77.10	74.92	75.85	75.16	73.59	74.02	77.24
TiO_2	0.33	0.16	0.19	0.15	0.25	0.29	0.22	0.19
Al_2O_3	14.02	12.20	12.81	12.51	12.64	13.49	13.27	11.95
Fe_2O_{3T}	2.73	1.13	1.97	1.47	2.42	2.88	1.94	1.21
MnO	0.02	0.10	0.01	0.03	0.02	0.07	0.03	0.02
MgO	0.39	0.22	0.19	0.45	0.83	0.02	0.09	0.07
CaO	0.34	0.68	0.16	0.20	0.26	0.63	0.56	0.79
Na_2O	3.68	5.10	3.59	3.59	3.74	5.24	3.90	3.32
K_2O	5.38	2.92	5.45	5.43	4.79	3.75	5.37	4.85
P_2O_5	0.11	0.04	0.02	0.01	0.04	0.02	0.03	0.03
LOI	0.46	0.30	0.31	0.40	0.40	0.29	0.30	0.40
Total	100.10	99.95	99.62	100.09	100.55	100.27	99.73	100.07
Trace elements (ppm)								
Ba	504	529	403	436	226	535	224	96
Rb	180	32	195	137	195	133	182	180
Sr	54	66	33	54	27	27	32	44
Y	39.8	63.4	71.5	54.2	102	95.5	67.9	56.4
Zr	273	162	162	162	342	469	274	227
Nb	18.7	19.7	20.9	20.1	37.9	37.7	36.3	46.4
Pb	59	13	15	10	16	13	19	71
Ga	21	18	21	16	28	27	22	18
As	b.d.	b.d.	b.d.	7	b.d.	b.d	b.d	21
Zn	b.d.	60	b.d.	b.d	b.d.	60	60	b.d.
Cu	b.d.	b.d.	b.d.	30	b.d.	10	b.d	10
V	8	8	b.d.	b.d	5	5	b.d	8
Cr	b.d.	b.d.	20	b.d	30	b.d	b.d	b.d.
La	68.4	28.9	72.3	63.5	108	83.5	65.9	39
Ce	122	97.1	142	122	111	150	128	82.1
Pr	15.8	7.26	17.4	16.4	22.9	20.3	15.7	10.2
Nd	56.5	25.3	62.7	60.1	80.1	77.9	56.2	39.5
Sm	10.9	6.1	13.5	12.2	16.5	17.4	11.8	9.1
Eu	0.9	0.34	0.75	0.73	1.27	1.51	0.5	0.45
Gd	8.45	6.65	11.2	9.77	15	14.8	9.8	9.1
Tb	1.52	1.56	2.13	1.75	2.84	2.73	1.85	1.61
Dy	8.19	9.95	13	10.9	17.2	17.2	11.6	9.85
Ho	1.56	2.09	2.59	2.12	3.61	3.57	2.46	2.04
Er	4.07	6.18	8.06	5.76	11.2	10.8	7.75	5.84
Tm	0.59	0.98	1.27	0.9	1.76	1.73	1.23	0.88
Yb	3.87	6.56	7.97	6.07	11	10.8	7.96	5.82
Lu	0.63	1	1.17	0.93	1.55	1.64	1.12	0.86
Co	1	84	b.d.	49	b.d.	84	73	75
Cs	4.5	0.9	1.2	0.4	2.5	1.3	1.6	1.9
Hf	7.4	5.5	5.6	5.6	10	12.8	8.8	8
Sb	b.d.	b.d.	b.d.	0.5	0.2	b.d	b.d	b.d.
Ta	1.82	3.2	2.61	2.72	4.42	5.32	4.62	4.18
Th	20.4	24.5	23.2	21.1	28.7	22.8	25.9	18.2
U	3.15	4.23	5.41	4.27	4.73	6.36	6.6	4.45
ΣREE	303.38	199.97	356.04	313.13	403.93	413.88	321.87	216.35

Chignecto plutons whereas appears LREE–enriched in Wentworth pluton (Fig. 4.5C). Low analytical totals of this phase also indicate that the thorite is hydrated.

Parisite–(Ce) and synchysite–(Ce). Parisite–(Ce) and synchysite–(Y) are both members of the bastnäsite group and they are mostly found in chlorite–rich and Fe–rich fractures in North River and Cape Chignecto plutons (Table 4.3, Appendix C.4). Parisite and synchysite appear as small (10 μm) inclusions in chlorite or as well–formed 60−100 μm crystals with a fibrous appearance with thorite inclusions and associated with magnetite (Fig. 4.4D). Parisite–(Ce) (Fig. 4.5D) shows weaker positive Eu anomalies than hydroxylbastnäsite–(Ce), and synchysite–(Ce) (Fig. 4.5E) shows no Eu anomalies with reference to Sm and Gd. Both parisite–(Ce) and synchysite–(Ce) show deviations from the ideal chemical formula by having smaller amounts of F (less than 0.5 a.p.f.u.) suggesting, presumably, the presence of OH^-.

Cerianite. Cerianite was found in Pleasant Hills and Cape Chignecto plutons (Table 4.3, Appendix C.5). Cerianite is found as anhedral crystallites of few μm in diameter, filling some micro–fractures adjacent to larger biotite–filled fractures (Fig. 4.4E). Cerianite although systematically LREE–enriched shows a large scatter in its REE patterns for HREE and no Eu anomalies are observed (Fig. 4.5F).

Hingganite–(Y). This mineral occurs predominantly in North River pluton associated mostly with Fe–rich fractures, and to a lesser degree with chlorite–rich fracture fillings. Rare hingganite is also found in rare Fe–rich fractures in Wentworth pluton (Table 4.3, Appendix C.6). Texturally it appears as irregular patches on magnetite clots (Fig. 4.4F) or as 20 μm inclusions in corroded hydrothermal chlorite. This mineral is HREE–enriched and shows a well–defined negative Eu anomaly in the REE patterns (Fig. 4.5G).

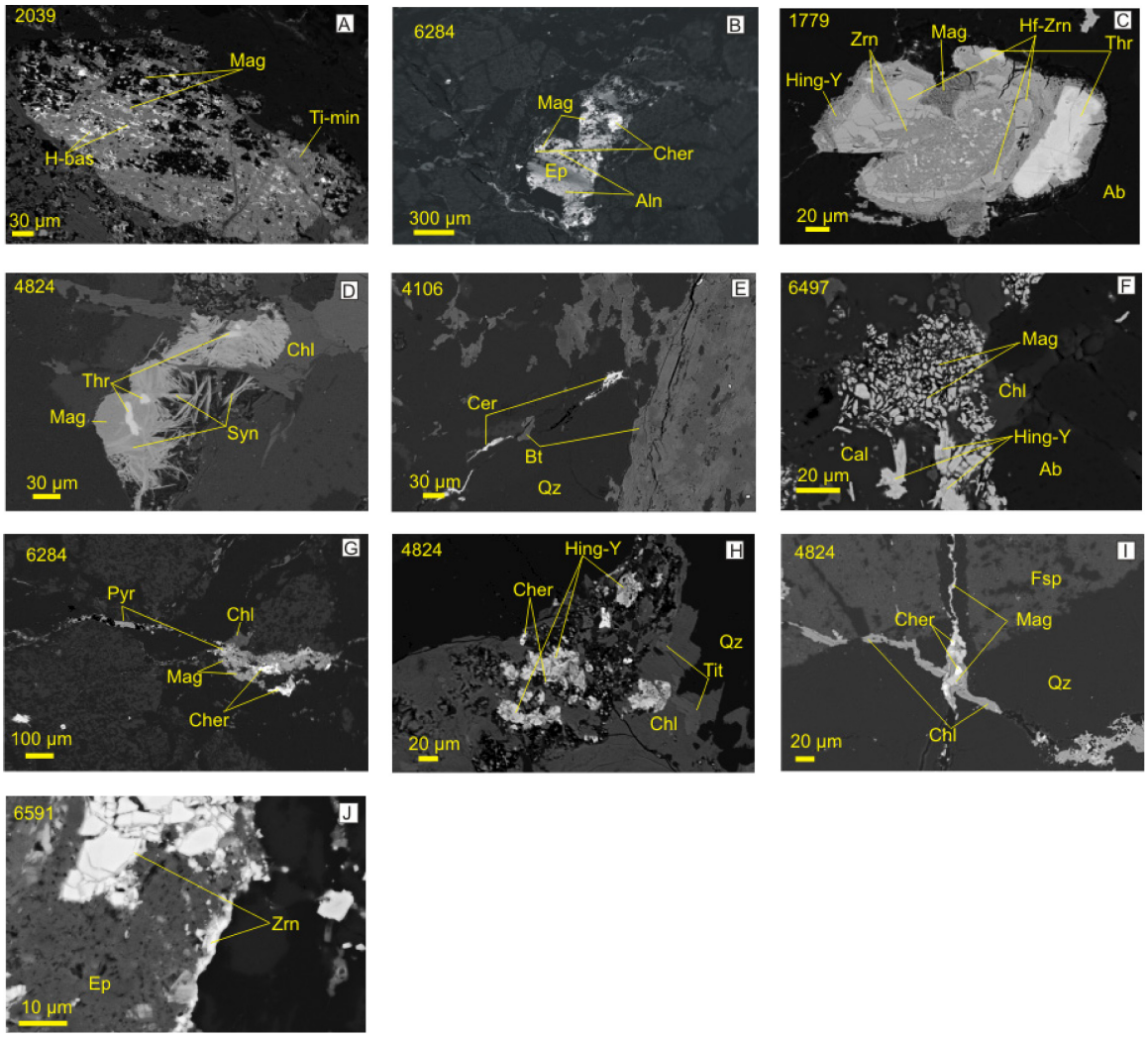

Figure 4. 4 BSE images of selected REE–bearing fractures from the granites of the Cobequid Highlands. Image (A) shows needles of hydroxylbastnäsite–(Ce) forming on a mixture of TiO_2 mineral and magnetite. Image (B) shows repeated alteration of an epidote–filled vug. Epidote has been replaced initially by allanite–(Ce) while chernovite–(Y) was the last mineral to precipitate. Image (C) shows a thorite as an inclusion in a zoned zircon that fills a void in quartz. Image (D) shows needle–like synchysite–(Ce) growing on magnetite. Image (E) shows a veinlet partially filled by cerianite, adjacent to a biotite vein. Image (F) shows the association of hingganite–(Y) with Fe–rich minerals such as magnetite and chlorite, in the rare calcite–bearing fractures from the Wentworth pluton. Image (G) shows a chernovite–(Y)–bearing chlorite–magnetite fracture associated with pyrochroite. Image (H) shows grains of hingganite–(Y) in corroded chlorite, being replaced by chernovite–(Y). Image (I) shows an older chlorite–rich fracture cut by a younger chernovite–(Y)–bearing magnetite fracture. Image (J) shows crystals of zircon both as inclusions and as overgrowths on hydrothermal epidote in the Wentworth granites. Mineral abbreviations: Ab: Albite, Aln: Allanite–(Ce), Ca: Calcite, Cer: Cerianite, Cher: Chernovite–(Y), Hing–(Y): Hingganite–(Y), Qz: Quartz, Syn: Synchysite−(Ce), Ti−min: TiO2 mineral, Tit: Titanite, Fsp: Feldspar, Thr: Thorite, Hf–Zrn: hafnium–bearing zircon, H-bas: Hydroxylbastnäsite–(Ce), Pyr: Pyrochroite.

Chernovite–(Y). Chernovite–(Y) is found only in the North River and Cape Chignecto plutons in late Fe–rich and chlorite–rich fractures (Table 4.3, Appendix C.5). It occurs as discrete 10 μm grains or filling veinlets in altered titanite, and in places associated with pyrochroite (Fig. 4.4G). In North River pluton, this mineral is found replacing a Y–rich silicate that resembles hingganite–(Y) or appears in late magnetite–filled fractures that cut older fractures filled with chlorite (Figs. 4.4H and I). This is the only REE–mineral with a systematic association with other REE–phases; it is associated with cerianite and thorite, most commonly with the latter. Chernovite–(Y) is a HREE–enriched mineral with a strong negative Eu and a positive Ce anomaly in its REE pattern (Fig. 4.5H) and contains high amounts of As (Table 4.3).

Nb–rich phases. Rare crystals of Nb–minerals are found in Pleasant Hills pluton associated with chlorite–rich fractures. They occur as inclusions in corroded chlorite, filling surfaces of crystallographic weakness such as cleavage planes and altered parts of the host grain. These grains have subequal amounts of Nb and Y and thus resemble samarskite–(Y), but due to the small size of the grains and the low analytical totals in WDS analyses, these minerals remain unidentified.

Hydrothermal zircon is present in small amounts in Wentworth pluton and occurs both as subhedral to anhedral discrete grains and as overgrowths on epidote (Fig. 4.4J). The REE–carbonates in the Pleasant Hills pluton appear more F–rich than the ones found in Wentworth pluton. The North River pluton hosts several types of hydrothermal REE–minerals found in varying amounts in the fracture fillings (0–25%). Most fractures with >3 % REE– minerals are either magnetite–rich or chlorite–magnetite fractures. The rare hydrothermal allanite–(Ce) from the Cape Chignecto pluton is chemically similar to

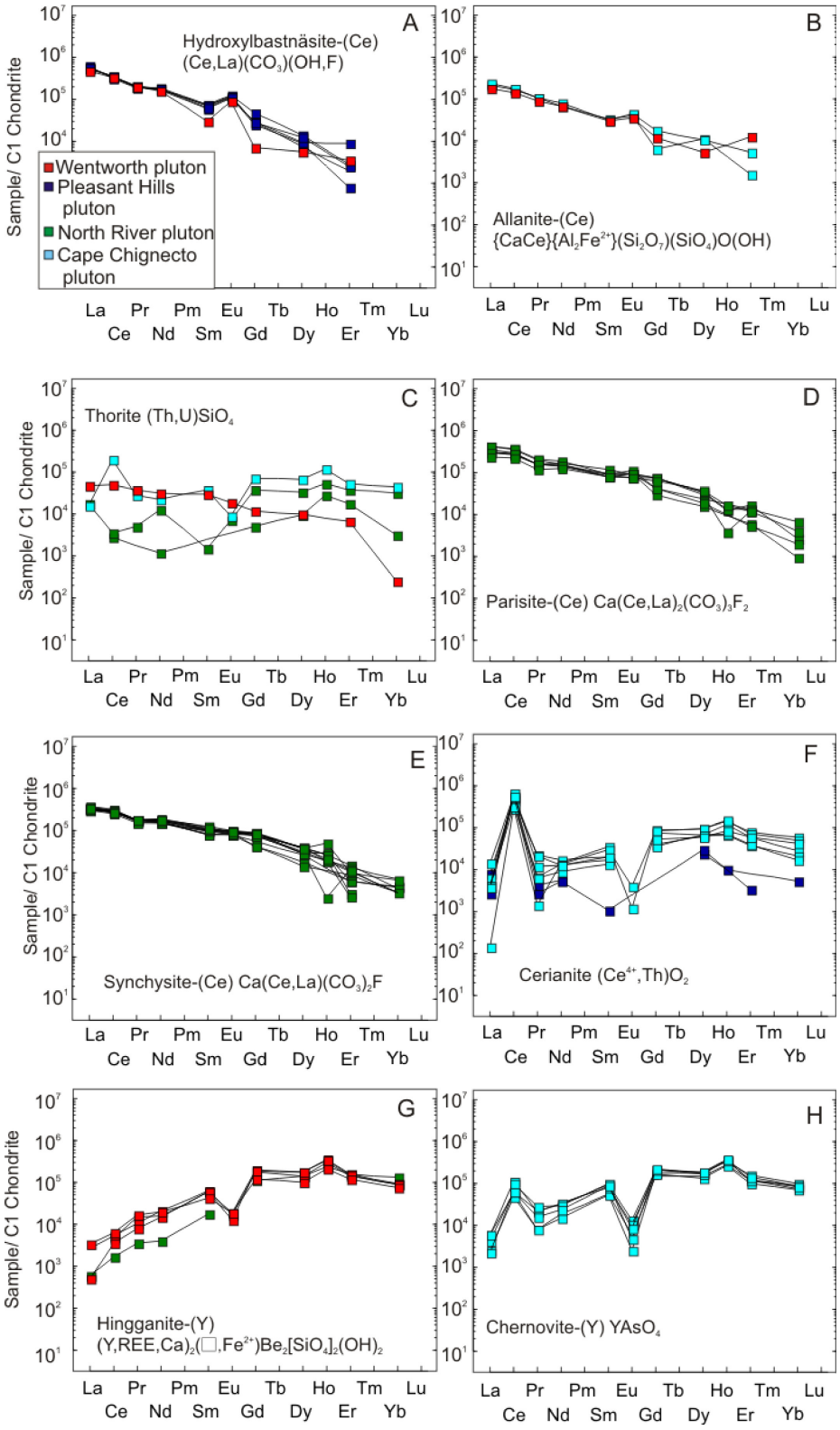

Figure 4. 5 Chondrite-normalized REE patterns for the hydrothermal hydroxylbastnäsite-(Ce) (A), allanite-(Ce) (B), hingganite-(Y) (C), thorite (D), cerianite (E), synchysite-(Ce) (F), parisite-(Ce) (G), and chernovite-(Y) (H), found in the granites of the Cobequid Highlands. Chondrite values after Sun and McDonough (1989).

that in Wentworth pluton, however there is a larger scatter of HREE in its REE patterns (Fig. 4.5B). In the same pluton, many of the thorite and cerianite analyses show a negative Eu anomaly (Fig. 4.5C and F). The total amount of REE minerals in the fractures of the Cape Chignecto granites is in rare cases as high as 18%. In most fractures the REE minerals vary from 0 to 6% of the modal composition of the fracture filling. There is no clear relationship between the type of the fracture filling (e.g. biotite–rich, chlorite–rich) and the type of hydrothermal REE–minerals present. It is noteworthy that the REE–carbonates not only show geographic variations in relative abundance but also in the distribution of the type of carbonate. The Wentworth and Pleasant Hills plutons host principally hydroxylbastnäsite–(Ce) in their fractures. The second most abundant REE–carbonate after hydroxylbastnäsite–(Ce) regionally is synchysite–(Ce), which together with parisite–(Ce), is mostly found in the North River pluton (Fig. 4.6).

4.5.4 TEMPERATURE ESTIMATES

The chlorite thermometer estimates show a range of temperature between 134°C and 278°C for the hydrothermal fluids circulated through the A–type granites of the Cobequid Highlands. The epidote–rich fractures of the Wentworth pluton, where patches of chlorite coexist with epidote, yield low temperatures of 157°C. The biotite–rich fractures of the Pleasant Hills pluton show temperatures from 132°C to 171°C. The chlorite–magnetite rich fractures of the North River pluton show the highest temperature estimates that range from 117°C to 236°C. The chlorites in the Cape Chignecto pluton yield hydrothermal temperatures between 152°C and 168°C, close to the range for the chlorites of the Pleasant Hills pluton.

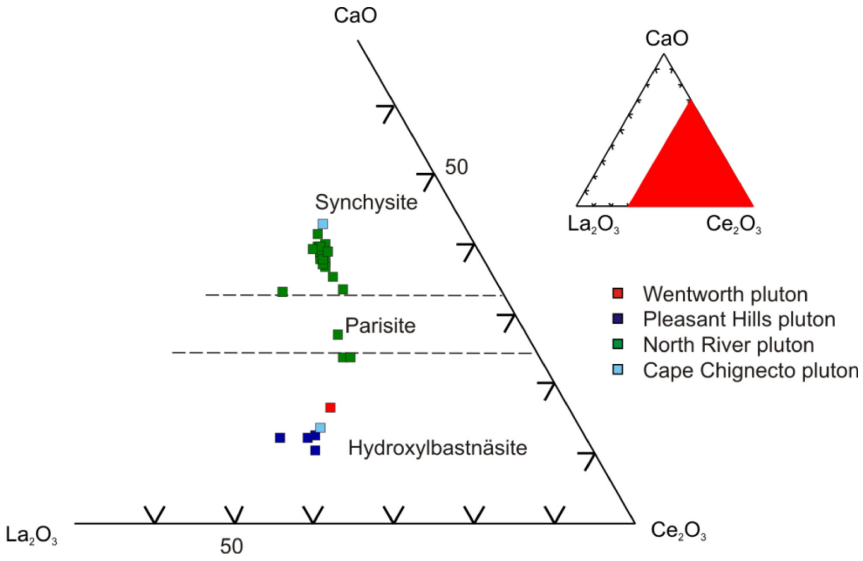

Figure 4. 6 Ternary diagram demonstrating the distribution of the different types of REE–carbonates found in the granite plutons of the Cobequid Highlands.

4.6 DISCUSSION

A large variety of hydrothermal REE–minerals are found in mm–scale fractures hosted in the A–type granites of the Cobequid Highlands. The majority of the granitic samples reported in this work do not contain magmatic REE–minerals but have moderate amount of REE in whole–rock analyses, suggesting hydrothermal enrichment. The mode of occurrence of the post–magmatic REE minerals in the Pleasant Hills, North River and Cape Chignecto plutons is significantly different than that of the hydrothermal REE–Nb–rich minerals reported from the Wentworth pluton (Papoutsa and Pe–Piper, 2013). In the Wentworth pluton, most of the post–magmatic REE–minerals are dispersed in the body of the rock, whereas in the rest of the plutons they are found mostly in fractures, suggesting a more efficient circulation and transport of these elements through hydrothermal fluids.

The data show that the style of hydrothermal alteration recorded in fractures in granite plutons in the Cobequid Highlands varies not only in time but also

geographically. The fundamental question this study aims to answer is how these variations in hydrothermal alteration are related to the variations of the post–magmatic REE–circulation in the Cobequid Shear Zone, as recorded by the A–type granites in the area.

4.6.1 STYLES OF HYDROTHERMAL ALTERATION IN THE COBEQUID HIGHLANDS

Based on field observations reported in the literature from all plutons, it is evident the earliest stages of hydrothermal alteration involved Na–rich (albitization) and Ca–rich (epidotization) styles (Waldron et al., 1989; Nearing, 1991, Koukouvelas et al., 2002; Pe–Piper et al., 2004). The localized character of albitization and epidotization regionally, and also the fact that evidence of albitization was not found in the studied samples, prevents establishing their relative ages in this study. The geochemical affinity of later hydrothermal alteration is progressively more Fe–rich and is associated at first with potassic alteration (precipitation of hydrothermal biotite), and then precipitation of hydrothermal magnetite with or without coeval chlorite (Fe–rich alteration).

In the Cobequid Highlands, the early circulating fluids associated with albitization were of magmatic origin, as suggested by oxygen isotope data on mineral separates of hydrothermal albite (Pe–Piper, unpublished data). Epidotization in A–type granites can be closely associated with albitization, and may occur when the country rock is hydrated by the circulating fluids (Kaur et al., 2012). It has been observed that such metasomatic events can be associated with leaching of REE from the country rock and with the development of micro–porosity during dissolution–reprecipitation processes (Kaur et al., 2012; Putnis, 2002). The A–type granites of the Cobequid Highlands contain primary plagioclase (An_6) (Pe–Piper, 1991; 1995a, 1995b; 1998; Pe–Piper and Piper, 1998). Dissolution of feldspars has been observed in the albitized granites of the central

Cobequid Highlands and that process could be associated with the formation of sodic hydrothermal fluids. Iron–rich epidote tends to be more stable under oxidizing conditions, close to the hematite–magnetite buffer (Bird and Helgeson, 1981). The Al–Ca–rich composition of epidote (clinozoisite) that is present in the fractures of the granites indicates that epidotization in the Cobequid Highlands most likely took place under relatively reducing conditions.

Biotization in the Cobequid Highlands is observed in plutons that contain hornblende–bearing granites, whereas chloritization is observed only in biotite–bearing granites. The Cape Chignecto pluton shows evidence for both biotization and chloritization, even though it contains biotite–bearing granites, probably because hornblende occurs in the abundant mafic rocks (Waldron et al., 1989). Biotization most commonly occurs during the hydrothermal alteration of magmatic hornblende to hydrothermal biotite (Brimhal et al., 1985). Chloritization, on the other hand, usually occurs after the breakdown of magmatic biotite (Parry and Downey, 1982; Parneix et al., 1985) at low temperatures (Morad et al., 2011). The distribution of hydrothermal chlorite and biotite in the fractures of the granites in the Cobequid Highlands appears to depend on the availability of magmatic biotite versus calcic amphibole, whether in the granites or gabbro.

In the Cobequid Highlands, both hydrothermal biotite and chlorite approach iron–rich end–members (Fig. 4.2B and C), suggesting either that fluids or bulk rock, or both, were iron–rich. The A–type granites of the Cobequid Highlands are in general ferroan rocks and therefore may have provided some iron for the formation of hydrothermal biotite and chlorite. Other possible sources of iron for the fluids are the mafic rocks in these plutons

which are ferro–gabbros (Pe–Piper and Piper, 2003) or the late lamprophyre dykes and gabbro stocks (MacHattie and O'Reilly, 2008).

The ~323 Ma iron–rich hydrothermal event along the Cobequid Shear Zone is associated with carbon–rich fluids, as indicated by the presence of iron–carbonates such as ankerite and siderite in fractures, for example in the large Londonderry iron deposit (Kontak et al., 2008). Iron is the most abundant element in high–temperature hydrothermal fluids that evolve from high–level magmas (Simon et al., 2004). Precipitation of Fe–oxides such as magnetite, hematite and martite has been interpreted to result from evolving, progressively more oxidizing, hydrothermal fluids (Figueiredo e Silva et al., 2011). Fluids related to this type of mineralization are usually characterized by very high temperatures, high salinity, and coexist with carbon–rich fluids (Borrok et al., 1998). Iron–enrichment of hydrothermal fluids has been observed to be associated with circulation of REE and as a result, hydrothermal REE–minerals have been found in magnetite deposits (Pršek et al., 2010; Figueiredo e Silva et al., 2011).

Although there is no direct evidence (i.e. measurements from fluid inclusions) for increased salinity in the hydrothermal fluids in the Cobequid Highlands, observations have been made that may support that hypothesis. The early Na-rich alteration in the central Cobequid Highlands was associated with fluids of increased halogen component, on the basis of high Rb, Cs, Hf, Nb and Zn concentrations in areas of pervasive alteration (Pe-Piper et al., 1991). In the same area, biotite from late minette dykes (>80% modal biotite) shows elevated concentrations of Cl (up to 1.6 wt.%) and F (up to 1.3 wt.%) (Pe-Piper, unpublished data), and high concentrations of synchysite-(Ce) in fractures (Wisen, 2015). Finally, Owen and Greenough (1999) reported the presence of scapolite-bearing pegmatite in the western Cobequid Highlands, whose marialitic composition was

interpreted to reflect the presence of fluids with at least 30-40 mol% NaCl. Smith and Henderson (2000) demonstrated, from their fluid inclusion study in the Bayan Obo REE deposit, that REE can be efficiently mobilized in hydrothermal fluids with 6-10 wt% NaCl equivalent at temperatures from 240 to 340 °C. The hydrothermal temperatures necessary for the mobility of REE decreased with increasing salinity. The West Moose River granites, adjacent to the North River pluton, are strongly fractured and albitized (Pe-Piper et al., 1991). These granites also have an impressive variety of hydrothermal REE-minerals, but no primary REE-minerals were recognized except for zircon, and a strongly altered grain that resembles a relict chevkinite-(Ce) (Pe-Piper et al., 2015). Therefore it is possible that hydrothermal fluids of significant salinity were circulating through the faults and associated fracture systems of the Cobequid Zhear Zone from early stages (Na-alteration). Such fluids could therefore sufficiently mobilize the REE from the fractured host granites, which could explain the small amounts of magmatic REE minerals that were preserved in the plutons of the central Cobequid Highlands.

4.6.2 SPATIAL VARIATION IN HYDROTHERMAL ALTERATION

In the eastern part of the Cobequid Highlands, the dominant style of hydrothermal alteration is epidotization, as indicated by the widespread epidote–rich fractures in the Wentworth pluton. The decreased amounts of epidote in the biotite–rich fractures of the nearby Pleasant Hills pluton shows a westward transition in the style of hydrothermal alteration, from epidotization to biotization, which is dominant mostly in the western Cobequid Highlands.

A gradual increase of magnetite in the fractures is observed mainly from the Pleasant Hills pluton towards the central part of the Cobequid Shear Zone, with the highest concentration in the fractures of the North River pluton. However, the largest Fe deposits

of the Cobequid-Chedabucto Fault Zone – the Bass River magnetite deposit and the giant Londonderry deposits – developed along faults south of the Pleasant Hills and Wentworth plutons (Fig. 4.7). This suggests that in the Cobequid Highlands during the late Carboniferous, Fe–rich hydrothermal alteration was focused mainly along the Cobequid fault.

4.6.3 CORRELATION OF THE OBSERVED HYDROTHERMAL STYLES WITH DATED HYDROTHERMAL EVENTS

The sequence of changes in the hydrothermal circulation through the faults and fracture systems across the Cobequid Shear Zone can be extrapolated from geochronological data and textural evidence of minerals. Epidotization probably took place shortly after the emplacement of the plutons, while these faults were still active. The epidotization of the Wentworth granites represents, therefore, one of the earliest stages of hydrothermal circulation. Epidotization occurred until the first stages of biotization, in order for epidote to precipitate in the oldest biotite–filled fractures of the Pleasant Hills pluton (Fig. 4.7). The formation of biotite–filled fractures, during potassic alteration, probably postdated the 353±4 Ma riebeckite in the West Moose River pluton and continued for ~20 Ma after pluton emplacement (Fig. 4.7).

The age of the magnetite–rich fractures found in the granites cannot be precisely determined by textural data alone. Formation of hydrothermal magnetite in the fractures of the A–type granites in the Cobequid Highlands seems to have been active for a long time, as indicated by textural data (Fig. 4.3C to F). This suggests precipitation of hydrothermal magnetite from, at least the later stages of biotization (Fig. 4.7) until the latest hydrothermal stages, when almost monomineralic magnetite fractures formed.

Magnetite is absent from the largest S– and Fe–rich deposits in mainland Nova Scotia related to the ~323 Ma IOCG mineralization, such as the Copper Lake and the Londonderry deposits (Murphy et al. 2011). However, the Bass River Co–bearing

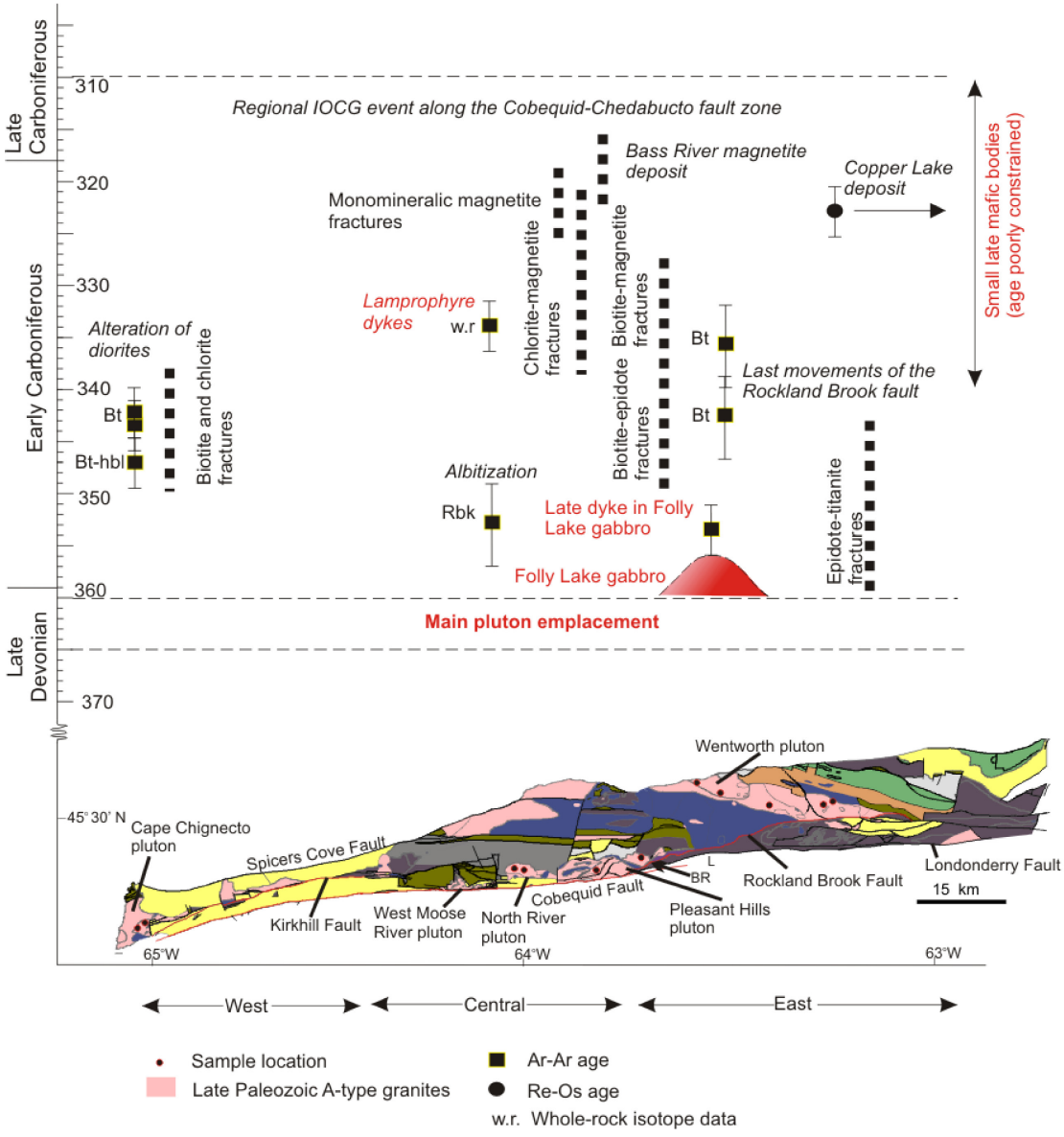

Figure 4. 7 Simplified geological map of the late Paleozoic intrusions (modified from Pe–Piper and Piper, 2003) of the studied area demonstrating the variations in the styles of hydrothermal alterations spatially and over time, as defined by textural relationships.

magnetite deposit (Belperio, 2010), close to the Londonderry fault at the southern edge of the Pleasant Hills pluton, has abundant magnetite in breccias of the 321–324 Ma

Londonderry Formation (ages from Murphy et al., 2011) that include clasts of the Pleasant Hills granite. The high gravity anomaly that characterizes the Bass River magnetite deposit coincides with an area of high gravity anomaly between the North River and Pleasant Hills plutons and is represented by hematite–rich fractures (Belperio, 2010). Furthermore, the high linear magnetic anomaly that follows the nearby Londonderry fault is interpreted as the result of discontinuous fault–controlled emplacement of hydrothermal magnetite (Belperio, 2010). This suggest that during the ~323 Ma IOCG mineralizing event magnetite precipitated in the area and that these iron–rich fluids which circulated along the Cobequid and Londonderry faults reached the A–type granites in the central part of the Cobequid Highlands. The late magnetite–rich fractures in the Pleasant Hills and North River pluton are probably of the same age.

4.6.4 CHANGES IN THE HYDROTHERMAL FLUIDS

In the eastern part of the Cobequid Highlands, the epidote–rich fractures indicate Ca–rich fluids. The presence of minor chlorite, in places mixed with the epidote, suggests that at some stage during epidotization, the fluids became relatively more enriched in Fe. This led to co–precipitation of chlorite with epidote in the Wentworth pluton. The hydrothermal fluids appear to be even more enriched in Fe in the Pleasant Hills pluton, where Fe–rich minerals like biotite dominate over epidote in the fracture fillings.

The sequence of the hydrothermal types of fluids, as recorded by fractures in the late Devonian granites in the Cobequid Highlands, suggest that the chemistry of the fluids, in general, became progressively more Fe–rich. Pyrite is stable under extremely reducing conditions (Hutcheon, 1998) and its presence in the fracture fillings of the Wentworth pluton further suggests that epidotization took place under reducing conditions. Grains of pyrite surrounded by colloidal hematite have been found dispersed in the Wentworth

granites (Papoutsa and Pe–Piper, 2013), which is interpreted as a product of pyrite oxidation at very low pressure (Bhargava et al., 2010). Pyrite is also present in small inclusions in the magnetite–rich fractures of the Wentworth pluton. These observations suggest that the oxidation state of the fluids changed from reducing during epidotization to more oxidizing during biotization.

The bulk Fe content of fracture fillings, estimated from abundances of different minerals, shows a positive correlation with temperature estimated from chlorite composition, suggesting the influence of temperature on the solubility and circulation of Fe in aqueous solutions (Fig. 4.8). In some cases, the chlorite appears in patches, coexisting with other minerals, and it could have formed later as a product of alteration. Therefore the chlorite–derived temperature estimates for those fractures should be used with caution.

The mineral assemblages in the fracture fillings of each style of hydrothermal alteration suggest that there were changes in the chemistry of the fluids not only on a regional scale, but also locally and over a short time scale. The patches of andradite in the epidote–rich fractures of the Wentworth pluton (Table 4.2) suggest that the water fugacity was probably variable, so as to form a less hydrated, but otherwise Ca-Al-rich, mineral phase such as andradite during epidotization. The limited presence of calcite, fluorite, and pyrite in the studied epidote–rich fractures suggest that although Ca, C, F, and S were present in the fluids, their concentrations were probably moderate to low, at the time.

4.6.5 CORRELATION OF REE-RICH SECONDARY MINERALS WITH STYLES OF HYDROTHERMAL ALTERATION

The epidote fractures of the Wentworth pluton have the smallest amounts of hydrothermal REE–minerals (hydroxylbastnäsite–(Ce) and thorite), compared to biotization and Fe–rich hydrothermal alteration (Table 4.2). These fractures are hosted in the intrusions with the highest amounts of magmatic REE–minerals, regionally.

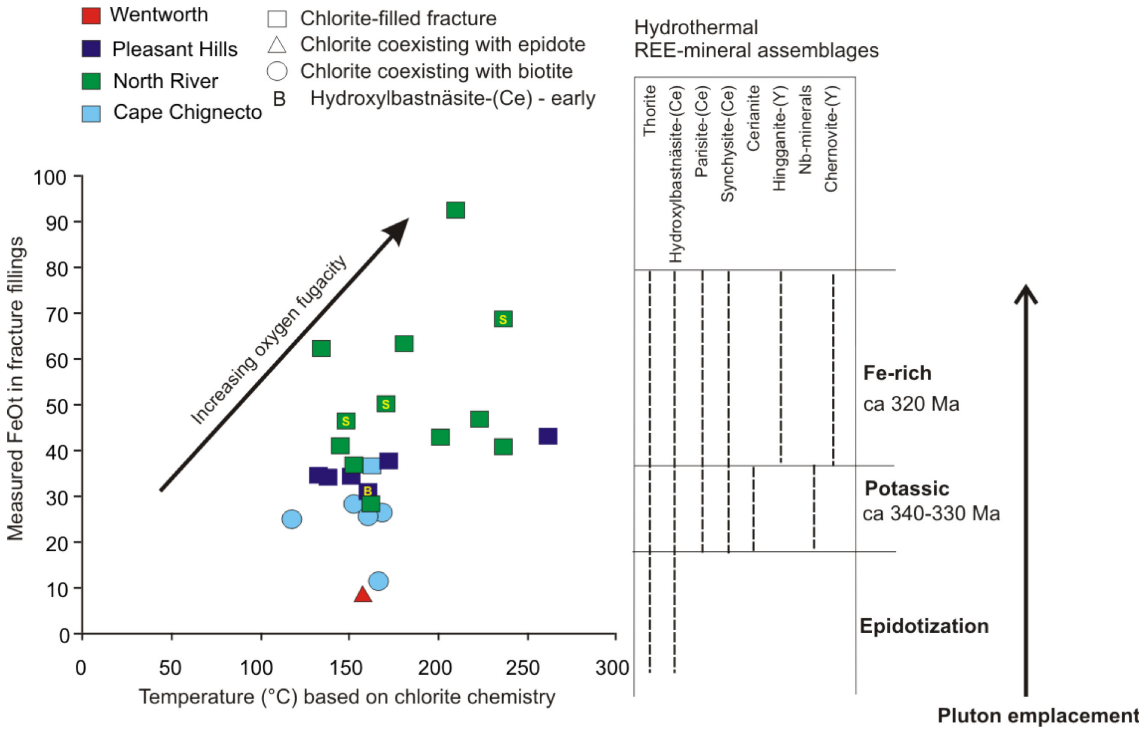

Figure 4. 8 Variation of the FeOt bulk composition from the fracture fillings of the A–type granites of the Cobequid Highlands, in relation to the observed styles of hydrothermal alteration and the observed REE–mineral assemblages. Increase in oxygen fugacity is qualitatively implied based on the relative abundance of magnetite.

Replacement of primary allanite–(Ce) by hydrothermal REE–carbonates in the Wentworth (Papoutsa and Pe–Piper, 2013) and Cape Chignecto granites suggest that the magmatic REE–minerals were the primary source of REE in hydrothermal stages. The low concentrations of hydrothermal REE–minerals in the fractures of the Wentworth

granites can therefore be attributed to limited mobility and transport of REE in the hydrothermal fluids during epidotization.

Secondary fluorite is scarce in these fractures, although it is generally present as rare dispersed grains in the Wentworth granites, most commonly associated with amphiboles. The release of F into the hydrothermal system is taken to be the result of the alteration of amphibole in the early granites of the Wentworth (Pe–Piper, 2007), and resulted in the mobilization of REE (Papoutsa and Pe–Piper, 2013). The epidote fractures, however, lack hydrothermal biotite, which is abundant in the nearby Pleasant Hills pluton and is associated with the amphibole breakdown. Therefore, the epidotization in the Wentworth pluton was probably an early event that predated the breakdown of the primary amphiboles and the major introduction of REE in the hydrothermal system.

The amount of hydrothermal REE–minerals in the plutons of the Cobequid Highlands appears to increase from epidotization to biotization (Fig. 4.8), with a dominance of LREE minerals and particularly REE–carbonates. The solubility of carbonate minerals decreases from reducing to oxidizing conditions (Tabelin and Igarashi, 2009). Therefore the increase of the oxidation state of the fluids from epidotization to biotization was an important factor that enhanced the precipitation of REE–carbonate minerals.

The Fe–rich style of hydrothermal alteration presents the largest variety and highest amounts of hydrothermal REE–minerals, such as hingganite–(Y), hydroxylbastnäsite–(Ce), parisite–(Ce), synchysite–(Ce), cerianite and chernovite–(Y). The precipitation of chernovite–(Y) is also enhanced by strongly oxidizing fluids

(Tabelin and Igarashi, 2009) and therefore, the increasing oxidation state of the fluids during the Fe–rich hydrothermal alteration resulted in the formation of that mineral.

4.6.6 CONTRIBUTION OF OTHER SOURCES TO THE FORMATION OF THE HYDROTHERMAL REE-MINERALS

Unaltered A–type granitic rocks of the Cobequid Highlands (on the basis of low LOI values and absence of fractures) show lower amounts of bulk REE (average of 280 ppm, Pe–Piper, 1991; 1993a; 1995b; 1998; Pe–Piper and Piper, 1998a), and particularly the LREE, compared to the fractured granites in this study (Fig. 4.9A), which correlates with the presence of the strongly LREE–rich hydrothermal minerals. Furthermore, the positive correlation between the bulk Y−Nb−Th−U−REE and Fe_2O_3 corresponds with an increase in magnetite–rich fractures (Fig. 4.9B) in the studied samples for each pluton, confirming a hydrothermal REE overprint on the whole–rock composition of these rocks.

The presence of minerals like parisite–(Ce) and synchysite–(Ce) (Table 4.3) suggest elevated amounts of Ca and C in the hydrothermal fluids. The late Paleozoic granites of the Cobequid Highlands, however, are alkali feldspar granites with small amounts of primary calcic minerals like plagioclase, less than 1 wt. % CaO and no primary carbonate minerals. Therefore, even though the REE were released from the granite during hydrothermal alteration, the amount of Ca and C released from the granites alone was probably not sufficient as to form Ca–rich REE–carbonates.

A potential source of Ca would be the mafic rocks associated with the granites, however, the North River pluton consists predominantly of granite with only minor marginal gabbro (Pe–Piper, 1991). A larger potential source of Ca and especially C for the formation of the REE–carbonates is the succession of carbonate rocks and

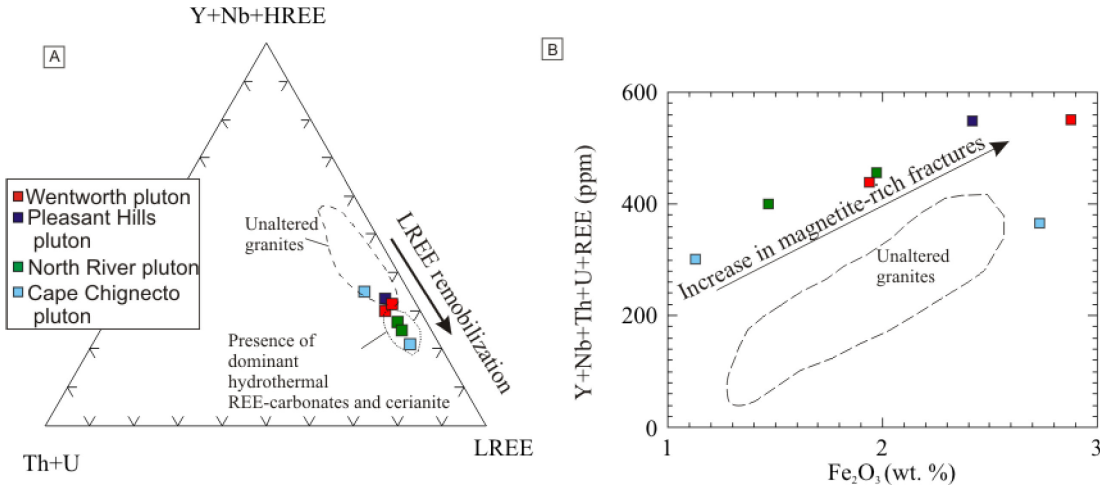

Figure 4. 9 Comparison between the whole–rock composition of the studied fractured granites and unaltered granites of the area (data for unaltered granites compiled from Pe–Piper, 1991; 1995a; 1995b; 1998; and Pe–Piper and Piper 1998a). Figure (A) shows the distinct increase in LREE in the fractured granites as a result of hydrothermal LREE–carbonates and cerianite precipitation. Image (B) shows the positive correlation of rare metals, the abundance of magnetite–rich fractures and the whole–rock Fe_2O_3 of the studied granites.

evaporites of the Visean Windsor Group (south of the central and eastern Cobequid Highlands), or carbonate rocks of the Horton Group south of the North River pluton (Pe–Piper, 1995a; Piper, 1996). Mineralization related to fluids derived from the Windsor Group is characterized by the presence of Pb, Zn and Cu (Kontak et al., 2006), but no minerals with these elements has been found in the REE–carbonate-bearing fractures. It is therefore more likely that the host granites together with the carbonates of the Horton Group were responsible for locally elevated amounts of Ca and C in the hydrothermal fluids, leading to preferential precipitation of parisite–(Ce) and synchysite–(Ce) in the fractures of the central Cobequid Shear Zone.

The presence of the As–rich mineral chernovite–(Y) in the fractures of the North River and Cape Chignecto plutons suggests the circulation of As in the late REE–bearing hydrothermal fluids. The only granitic samples that show As above detection limit are those with chernovite–(Y)–bearing fractures (Table 4.4). Therefore, the host granites

were unlikely to have been the source of As in the hydrothermal system. The most probable sources of As in the area are the shales of the Horton Group which contain moderate amounts of As (13 ppm, Pe–Piper, unpublished data). The release of As into hydrothermal fluids is believed to be associated with the breakdown of Fe–Mn oxides (Tabelin and Igarashi, 2009). The presence of pyrochroite in the chlorite fractures of Cape Chignecto could be related to the formation of chernovite–(Y).

4.6.7 GEOLOGICAL CONTROLS ON THE HYDROTHERMAL REE-ENRICHMENT IN THE COBEQUID HIGHLANDS

It is evident from the spatial variations in the style of hydrothermal alteration and abundance of hydrothermal REE–rich minerals (Fig. 4.7) that specific geological factors have favored the concentration of these elements in certain areas of the Cobequid Highlands. The behavior of REE is greatly influenced not only by chemical parameters, such as the composition of the hydrothermal fluid and the country rock, but also by physical parameters like pressure and temperature that will be evaluated in this section.

The importance of large scale crustal structures in focusing hydrothermal fluids and controlling mineralization has been underlined in several studies (McCaig et al., 1990; Abraham and Spooner, 1995; Kreiner and Barton, 2009; Murphy et al., 2011). During movement along the faults of the Cobequid Shear Zone, the plutons in the central part of the Cobequid Highlands were located in the stepover zone between the Rockland Brook fault to the east and the Kirkhill fault to the west and became strongly fractured (Pe–Piper and Piper, 2003). Therefore that area provided more pathways for an effective circulation of the hydrothermal fluids, compared to the rest of the shear zone. The Cobequid–Chedabucto Fault Zone saw its main activity at the Serpukhovian–Bashkirian boundary at ~318 Ma, but as shown by the Copper Lake ~323 Ma date the fault zone was

active before that time and motion continued at least until the Moscovian (~307 Ma) (Murphy et al., 2011). Plutons such as the North River and Cape Chignecto plutons, closer to the late cataclastic motion on the Cobequid fault, were able to interact with hydrothermal fluids for longer periods of time, compared to the Wentworth pluton which is bounded by the Rockland Brook fault. Furthermore, this suggests that the later REE–Fe–rich, oxidizing fluids, which were concentrated along the Cobequid and Londonderry faults in late Carboniferous, did not significantly affect the Wentworth pluton.

Besides the creation of pathways for the hydrothermal fluids by faulting, the tectonic setting plays an equally important role in influencing hydrothermal pressure that in turn affects the stability and solubility of hydrothermal minerals. High pressures increase the solubility of Fe and Mg in hydrothermal stages, permitting the fluids to reach oversaturation (Kalczynski et al., 2012). A decrease of pressure, therefore, can control the precipitation of Fe–rich minerals, such as magnetite and siderite. Such a decrease may occur in shear zones when the pressure changes from lithostatic to hydrostatic in the extensional segments of the faults (Kalczynski et al., 2012). Fluctuation of the pressure of fluids during hydrothermal circulation is a phenomenon that has been correlated with vein systems associated with shear zones. In such settings, the pressure of fluid circulation may reach suprahydrostatic values when fluids migrate into shallow, heterogeneous, and stressed crust during shear (Sibson, 1996). The faults through which the fluids circulate may control the hydrostatic pressures through what is known as fault-valve behavior (Sibson, 1992). Even though fault-valve behavior is influenced mainly from the prevailing stress, and the existing faults of the area, the pressurized fluids that result from such behavior may, in turn, have an impact on the permeability of the area by creating fracture meshes. These structures are best developed in areas of transfer faults,

dilational jogs, and may precede the formation of large fault zones (Sibson, 1996). Sibson et al. (1988) associated the creation of these vein sets with shear zones where pre-existing high angle faults were reactivated during horizontal compression from crustal shortening and strike-slip faulting with a sense of thrusting. Fractures in these vein systems through which pressurized fluids have passed tend to form conjugate sets (Sibson, 1996).

In the central part of the Cobequid Highlands (North River and West Moose River plutons) Piper et al. (1993) described similar deformation to that associated with pressurized fluids as mentioned above. This area is characterized by high angle faults at the margins of the intrusions, while the brittle deformation in the plutons is manifested by joint sets of fractures, some of which with dilational features. Furthermore, the late Carboniferous deformation in the Cobequid Shear Zone which is associated with the IOCG mineralization, involved dextral strike-slip motion and with a sense of thrusting (Murphy et al., 2011), resembling thus the tectonic setting required for high hydrostatic pressures and high Fe solubility in the fluids. Therefore intense fracturing of the plutons in the central part of the Cobequid Highlands could be taken as evidence of the presence of Fe-rich pressurized fluids and local release of stress that enhanced the precipitation of Fe oxides, particularly in the fractures of that area.

Temperature is another important factor that controls the stability of minerals from magmatic to hydrothermal stages. Hydroxylbastnäsite–(Ce) is stable at low hydrothermal temperatures (Fig. 4.8), whereas parisite–(Ce) and synchysite–(Ce) form under relatively higher temperatures (Williams–Jones and Wood, 1992). Positive Eu anomalies in hydrothermal minerals are indicative of low (below 250 °C) hydrothermal temperatures (Sverjensky, 1984). The association of calcite with synchysite–(Ce), which is abundant only in the fractures of the central Cobequid Shear Zone, requires higher

temperature (Fig. 4.8) and pressure in hydrothermal stages, compared to the other REE–carbonates. In the east, lower temperatures led to the formation of hydroxylbastnäsite–(Ce) with positive Eu anomaly (Fig. 4.5A). High–temperature metasomatism (>400 °C) in the central Cobequid Highlands has been inferred by Pe–Piper (1995a) from the chemistry of garnets found in meta–carbonates south of the North River pluton. It is, therefore, evident that there is a correlation between temperature and the type of the dominant REE–carbonate in the fractures, which suggests a significant control as well of temperature on the REE–mineral species that precipitated from the fluids.

The present work shows that the hydrothermal REE–enrichment of the A–type granites of the Cobequid Highlands shows a systematic variation that is highly dependent on the timing and style of regional hydrothermal alteration. The abundance of hydrothermal REE–minerals as well as REE mineral speciation increased with time as the regional hydrothermal system became more Fe–rich, progressively oxidizing and of higher temperature. High temperatures may have been driven by the minor late mafic intrusions: lamprophyre dykes in the west and small alkaline gabbro stocks in the east. Other sources besides the granitic rocks have contributed to the chemistry of some hydrothermal REE–minerals, such as chernovite–(Y).

The observed correlation between the abundance of hydrothermal REE–minerals, timing and specific types of hydrothermal alteration may have implications for REE mineral exploration. Hydrothermal systems elsewhere, with high amounts of REE and fluids with similar chemical evolution, may form significant mineral deposits at the final stages of circulation.

4.7 CONCLUSIONS

The late Devonian A–type granites of the Cobequid Highlands in Nova Scotia are located in an area where different styles of hydrothermal alteration persisted over a period of several tens of million years after magmatic emplacement. The nature of the hydrothermal fluids varies both geographically and in time and has affected the behavior and distribution of hydrothermal REE–minerals that precipitated in fractures.

Epidotization in the Cobequid Highlands was accompanied by the circulation of minor S, resulting in the formation of hydrothermal pyrite under reducing conditions and low temperatures. These conditions enhanced the release of As from the sedimentary rocks of the area and along with the presence of C and F, probably initiated the mobilization of the REE hosted in primary minerals in the granites, preventing, however, the precipitation of hydrothermal REE–carbonates in these fractures.

As the hydrothermal fluids became progressively more Fe–rich and relatively more oxidizing, REE–fluorocarbonates precipitated, principally in the biotite–filled fractures of the Pleasant Hills pluton and the chlorite–rich fractures of the North River pluton. Early hydrothermal biotite co–precipitated with epidote, whereas in the later stages of biotization the formation of epidote ceased and magnetite started to precipitate with biotite. There is no clear textural relationship between hydrothermal biotite and chlorite that would indicate a paragenetic sequence between these two minerals, however the latter is mixed with higher amounts of magnetite and is concentrated mostly in the North River pluton. These fractures contain the highest amounts and the largest variety of hydrothermal REE–minerals including hingganite–(Y) and minerals of the bastnäsite group. Localized increase of Ca and C in the fluids, as well as higher hydrothermal temperature, resulted in preferential concentration of synchysite–(Ce) and parisite–(Ce)

in the fractures of the central part of the Cobequid Shear Zone over hydroxylbastnäsite–(Ce) which dominates in the east.

By Bashkirian time, most of the hydrothermal circulation was focused along the Cobequid–Chedabucto Fault Zone, resulting in the widespread iron alteration of the adjacent plutonic bodies in the central and western Cobequid Highlands. The younger almost monomineralic magnetite fractures that contain chernovite–(Y) and cut the chlorite–rich fractures in the North River pluton are probably related to that Fe–alteration event. Chernovite–(Y) formed in these fractures from the alteration of hingganite–(Y), which was enhanced by the change of the oxidation state of the hydrothermal fluids and precipitation of As.

CHAPTER 5 AN EVOLUTIONARY HISTORY OF AVALONIA: NEW INSIGHTS FROM THE COBEQUID HIGHLANDS

5.1 INTRODUCTION

In chapter 3 it was shown that the mantle and lower crust have played an important role in the petrogenesis of the A-type granites in the Cobequid Highlands. It is therefore important to understand the geological evolution of the Avalonian crust in order to evaluate the changes in the Avalonian lithosphere since it provided a) the necessary lithologies as magmatic sources, and b) the geodynamic conditions for the late Paleozoic A-type granites to form throughout west Avalonia. This chapter shows how geochemical evidence from dated igneous rocks can provide essential data pertinent to paleogeographic reconstructions since they provide a snapshot of mantle and crustal conditions at different times.

The scope of this chapter is not only to review the geological evolution of Avalonia from Neoproterozoic to late Paleozoic, as presented in the literature, but most importantly to correlate specific evolutionary stages of the paleocontinent with relevant geological evidence from the Cobequid Highlands and elsewhere in west Avalonia. The geodynamic evolution of the Neoproterozoic Cobequid Highlands is approached through stratigraphic, structural, geochemical, and isotopic comparisons with Avalonian basement elsewhere in order to evaluate the crustal conditions that gave rise to A-type granitic magmas. As demonstrated in chapter 3, the isotopic character of the late Paleozoic A-type granites may be variable and thus reflect a significant lower crustal heterogeneity. This heterogeneity is further explored in this chapter, and the above correlations are combined with available paleomagnetic data in order to evaluate the ultimate origin of

the Neoproterozoic crustal blocks in the Cobequid Highlands and other parts of the now-dismembered Avalonia. Geochemical data, predominantly from mafic rocks from different parts of west Avalonia, are compared since they can provide evidence for the lithospheric mantle from different crustal blocks. These findings are then compared with previous and new paleoreconstructions in an attempt to explain the evolution of Avalonia from the Neoproterozoic to late Paleozoic.

In this chapter, the nature and timing of Ordovician magmatism in west Avalonia is reviewed and discussed in order to evaluate the paleogeography of several parts of the microcontinent during the closure of Iapetus and the opening of the Rheic oceans. The last part of the chapter deals with the late Paleozoic evolution of west Avalonia during the closure of the Rheic Ocean. A brief comparison of known coeval A-type granites in west Avalonia is presented with evidence from the literature and from the findings of this thesis, in order to evaluate any petrogenetic similarities between these rocks, on a broader scale. Finally, the late Carboniferous fluid circulation and mineralization observed in the Cobequid Highlands is discussed with an emphasis on the structural controls along the Cobequid-Chedabucto Fault Zone during the amalgamation of Pangea.

Avalonia is a terrane with a rather complex history (Keppie and Dallmeyer, 1989), which is subdivided into west Avalonia (Atlantic Canada and US), and east Avalonia (British Isles and Belgium). West Avalonia, as part of the Appalachian Orogen, is considered to be a peri-Gondwanan fragment that was accreted to the Laurentian margin after Ganderia and before the docking of Meguma in late Devonian (van Staal et al., 2009). Although the peri-Gondwanan origin of Avalonia is now well established, the original position and orientation of this terrane in the Neoproterozoic are still

controversial. To make things more complicated, different parts of the Avalonian basement show contrasting isotopic and chemical characteristics that have led researchers to interpret Avalonia as a collage of different crustal fragments, and therefore a composite terrane (Nance and Murphy, 1996). Willner et al. (2013), however, argued that Avalonian fragments originated from an originally coherent microcontinent along the continental margin of Gondwana. Isotopic evidence (Sm-Nd) from crustally derived rocks in west Avalonia indicates the presence of a basement formed at ca 1 Ga as juvenile crust, whereas east Avalonia shows isotopic signatures of an older (1.3-1.8 Ga) basement (Nance and Murphy, 1996). It is argued thus that west Avalonia was adjacent to the Amazonian craton in the Neoproterozoic, whereas east Avalonia occupied positions adjacent to the West African craton (Nance and Murphy, 1996).

5.2 PRECAMBRIAN AVALONIA - AN EARLY AVALONIAN ASSEMBLY

The Neoproterozoic eon is an important interval in Earth's history that was manifested by widespread rifting and orogenic activity accompanying the breakup of Rodinia and the assembly of Gondwana (Trompette, 1997). During mid-Neoproterozoic (800-700 Ma), extensive rifting within Rodinia initiated its breakup (Evans, 2009). The final stages of the evolution of Rodinia are critical to most studies concerning the subsequent assembly of Gondwana, since that period is the starting point for many paleoreconstruction models for the latter (Faleiros et al., 2011; Saraiva dos Santos et al., 2014).

Although understanding the arrangement of the numerous cratons within Rodinia (i.e. the paleolatitudes for Laurentia and Baltica) has suffered from the lack of reliable paleomagnetic data, reconstruction models were used in the past decades, based on

isotopic data and assumptions, about the location of paleopoles (Nance and Murphy, 1996, Thompson et al., 2012). Nonetheless there is always a degree of uncertainty when modelling plate reconstructions, and particularly in the Proterozoic. The fact that the ancient oceans have been consumed by subduction and that, by definition, all paleomagnetic poles can only provide constraints for latitude and not longitude cause major uncertainties. Rodinia itself has several different paleogeographical versions as summarized in Evans (2009). The applied model of Rodinia used in this work is the one, which in the author's opinion, reconciles best the published data reported in this chapter. Such uncertainties may influence not only the modelled paleogeography of Gondwana, but have further implications on the early evolution of Neoproterozoic proto-Avalonia as a peri-Gondwanan terrane. As Murphy et al. (2004) argued, there is a need for more paleomagnetic data to document the movement histories and connections of West Gondwana and peri-Gondwanan terranes.

In the past decade, more paleomagnetic data became available for Laurentia (Weil et al., 2004), Baltica (Brown and McEnroe, 2004; Pisarevsky and Bylund, 2006), Amazonia (D'Agrella-Filho et al. 2008) and the African cratons (D'Agrella-Filho et al., 2004). For the evolution of Avalonia, the histories of these cratons are critical, since it is argued that they all have been proximal to parts of Avalonia at different times (Nance and Murphy, 1996; Murphy et al., 2004). The updated paleomagnetic database (such as the PALEOMAGIA archive), as well as more precise geochronological controls, resulted in the most up-to-date reconstruction models for Rodinia (Evans, 2009; Johansson, 2014) and Gondwana (Torsvik and Cocks, 2013). For the purpose of this thesis, this section will

focus mostly on the evolution of West Gondwana, along the periphery of which Avalonia is suggested to have evolved (Murphy et al., 2001).

In order to understand the Neoproterozoic history of Avalonia, it is necessary to evaluate the configuration of Rodinia during its breakup at ca 750 Ma. For that purpose, paleoreconstructions have been made using G-Plates software for Windows (www.gplates.org). The model for Rodinia adopted here includes the refined version of the SAMBA (South AMerica-BAltica) configuration (Gower et al., 1990; Hoffman, 1991; Moores, 1991; Dalziel, 1997; Li et al., 2008) in which Amazonia, West Africa and Baltica formed a single coherent landmass until at least 800 Ma (Johansson, 2014). In this configuration, the Rodinia supercontinent is all-inclusive, as proposed by Evans (2009), and surrounded by a Panthalassan-type ocean, the Brasiliano Ocean (Fig. 5.1A). Johansson (2014), however, did not present any paleolatitudes for the various cratons. Therefore the Neoproterozoic paleolatitudes, in the models herein, were constrained with reference to the position of Laurentia, which itself has been determined by published paleopoles (Table 5.1).

At the onset of Rodinia breakup at ca 750 Ma, Baltica, according to the SAMBA configuration, is considered to have occupied the southern margin of Rodinia. Pisarevsky et al. (2003) and Li et al. (2008) showed Amazonia south of Laurentia on the western flank of Baltica and that position is adopted here as well. Amazonia at 750 Ma, in the models here, is separated from the Congo craton and eastern South America (Parana, Rio de la Plata cratons) by the Brasiliano Ocean. Amazonia is separated from the Laurentian margin by the Grenville-Sunsas orogenic belts (Johansson, 2014).

The position of Avalonia in the Neoproterozoic is still controversial. Based on isotopic data from crustally derived rocks, it is interpreted that the Avalonian juvenile basement developed in the peri-Rodinian ocean (Murphy et al., 2001). There are no

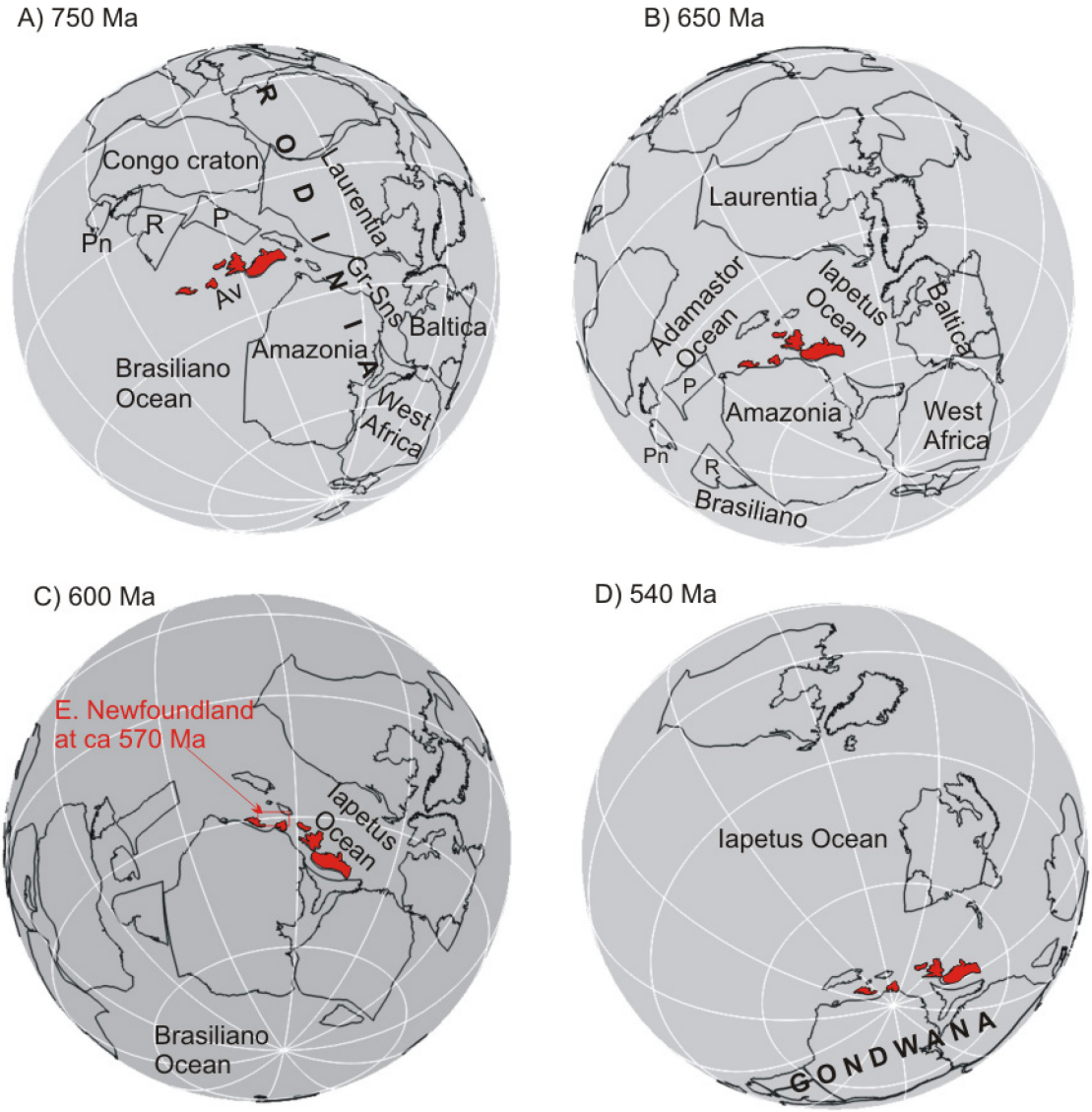

Figure 5. 1 Reconstruction models produced by G-plates illustrating (A) the break-up of Rodinia at ca 750 Ma, (B) and (C) the transition to a Gondwanan configuration from 650 to 600 Ma based on the SAMBA model (Johansson, 2014), and (D) the separation of Gondwana, Laurentia and Baltica during the opening of Iapetus Ocean at 540 Ma (as in Torsvik et al., 2014). Paleolatitudes for west Avalonia at ca 570 Ma (Pisarevsky et al., 2012) are indicated for comparison. Lines of latitude and longitude are at 30 ° intervals. Abbreviations: Av= Avalonia, Gr-Sns= Grenville-Sunsas orogenic belts, P= Pampean craton, R= Rio de la Plata, Pn= Parana.

paleomagnetic data from Avalonian rocks of this age, however Murphy et al. (2004) placed the 1 Ga proto-Avalonian crust at high southern latitudes (~90°S). Even though that is not paleomagnetically constrained, it was the preferred position in order that Avalonia would occupy a position along the western flank of Amazonia at the time. The configuration of Rodinia used in Murphy et al. (2004), however, was different from the one adopted here. Therefore, although the position of Avalonia relative to Amazonia remains the same, the paleolatitudes in the configuration presented here are significantly different.

The published paleomagnetic studies for the Neoproterozoic Avalonia (McNamara et al. 2001, Vizan et al. 2003, Thompson et al. 2007, Murphy et al. 2012) are all on Ediacaran rocks (ca 620 Ma), and they place west and east Avalonia at a paleolatitude between 12 to 34°S, with the exception of New England Avalon that shows a higher paleolatitude of 37-55°S (Pisarevsky et al., 2012). Prior to Ediacaran, the Amazonian affinity of Neoproterozoic detrital zircons (Barr et al., 2012) favors a position within the Brasiliano Ocean along the margin of the Amazonian craton (Fig. 5.1a). This, however, precludes an association of West Africa with east Avalonia at that time, a view that is further supported by the presence of early Neoproterozoic zircons in east Avalonian rocks that are absent in West African sources (Pollock et al., 2012; Willner et al., 2013). Given the configuration of Rodinia at the time, proto-Avalonia is placed in the reconstructions herein at southerly paleolatitudes of ~20° (Fig. 5.1A).

5.2.1 BREAKUP OF RODINIA

The Rodinia breakup began at ca 750 Ma, with rifting west of Laurentia (Fig. 5.1A) (Johansson, 2014). Counterclockwise rotation of eastern South American and the

African cratons initiated the change from a Rodinian to Gondwanan configuration (Li et al., 2008). These rotations resulted in the closure of the Brasiliano Ocean, while the separation of the South American cratons (Parana, Rio de la Plata) from Congo led to the opening of the intervening Adamastor Ocean (Fig. 5.1B). The closing of Brasiliano and subsequently of Adamastor oceans would have created long-lived subduction systems adjacent to the Amazonian margin until the final collision of Amazonia with the eastern South American cratons and Africa in the Ediacaran (Fig. 5.1C) (Johansson, 2014). This is indicated by the Brasiliano Orogenic Belts which lie between the Amazonian and South American cratons and record 670-550 Ma arc-related magmatism (Bento dos Santos et al., 2015). This is when the Avalonian terranes also record a major phase of arc-related magmatism (Murphy et al., 2001). Avalonia is thought to have accreted to Amazonia before ca 600 Ma (Fig. 5.1C), since it records intracontinental extension by 590 Ma (Balintoni and Balica, 2013). During that period, the Brasiliano fold belts within Amazonia record substantial reworking of the crust, in a branched system of mobile belts, with dextral shear zones extending to the African cratons (Fuck et al., 2008). There was, therefore, a large amount of strike-slip motion accommodating the assembly of West Gondwana (Evans, 2009).

5.2.2 AVALONIA DURING THE ASSEMBLY OF GONDWANA

By 550 Ma West Gondwana was assembled, or nearly so (Johansson, 2014). By that time, Avalonia in the models herein is predicted to have dextrally transferred along the margin of Gondwana during counterclockwise rotation of Amazonia (Fig. 5.1C). Laurentia, on the other hand, maintained an equatorial paleolatitude at ca 550 Ma (Hodych et al., 2004), while Gondwana drifted at high southern paleolatitudes during the

opening of Iapetus Ocean (Fig. 5.1D). Faunal and stratigraphic data from Avalonia also favor a position at high southern paleolatitudes during the late Neoproterozoic (Pollock et al., 2012). This lateral transport of Avalonia along the margin of Gondwana is documented by syn-igneous shearing of the Neoproterozoic Frog Lake and Debert River plutons in the Cobequid Highlands (Pe-Piper et al., 2010; Pe-Piper et al., 1996). Syn-magmatic deformation is indicated by pre-full-crystallization orientation of feldspar in granodioritic rocks, plastically deformed veins, and presence of C-S structures. Dextral strike-slip displacement has also been interpreted in late Neoproterozoic- early Cambrian sedimentary rocks of New Brunswick, where the detrital zircons reflect a change from purely Amazonian sources in the Neoproterozoic to Amazonian-West African sources by early Cambrian (Satkoski et al., 2010).

There is, however, evidence suggesting that Avalonia in the early Neoproterozoic might not have included all the present-day Avalonian terranes, and that some crustal blocks may have originated elsewhere. In west Avalonia, in particular, there are areas that remain problematic and present important differences in their Neoproterozoic geological histories. Such an area is the Avalon Zone of SE New England. Revised geochronology of the granitoid rocks of SE New England revealed that the main Avalonian arc phase in the area was rather short-lived and spanned between 610 and 590 Ma (high precision U-Pb dating on zircons, Thompson et al., 2010). This episode of arc-related magmatism broadly resembles the timing of intermediate and felsic magmatism in the Bass River Block of the Cobequid Highlands (609 ±4 Ma Debert River, and 603 Ma McCallum Settlement plutons, MacHattie and White, 2012). The absence of older felsic rocks in SE New England, such the ca 630 Ma rhyolites of the Jeffers Group and the ca 620 Ma

Table 5. 1 Laurentian paleopoles used for the Neoproterozoic reconstructions presented in this work.

Age (Ma)	Slat	Slon	D	I	α_{95} (°)	Plat	Plon	dp (°)	dm (°)	Rock unit	Reference
552	50.2	293.5	105.4	82.1	5.1	-44	134.5	9.7	9.9	Sept-Iles dykes and baked contacts	Tanczyc et al., 1987
565	50.2	293.5	333	-29	8	20	141	5	9	Sept-Iles layered intrusion	Tanczyc et al., 1987
571	54	300.5	110.8	50.1	11.7	-13.7	176.2	10.5	15.7	Double Mer formation	Murthy et al., 1992
575	46.2	280.6	82.2	82.7	3.1	-46.3	121.4	5.9	6.1	Callander alkaline complex	Symons and Chiasson, 1991
581	46	282	316	75	9	60	240	14	14	Grenville diabases	Murthy, 1971
600	54.5	301.5	331	-49	9	2	146	8	11	Pre-Grenvillian mafic intrusions	Park and Gower, 1996
615	45.6	283.4	135	30	8.4	16	148	5.2	9.3	Cheneaux metagabbro	Seguin and Brun, 1984
615	53.7	303.4	279.1	28.1	7.3	17.4	215.2	4.4	8	Long Range dykes	Murthy et al., 1992
670	45.6	284.6	288.7	-49.3	7.3	-9.5	160.8	6.5	9.7	Buckingham volcanics	Dankers and Lapointe, 1981
725	44.3	283.6	315	-15	5	24	154	2.6	5.2	Kingston dyke 4	Irving, 1972
750	46.1	285.6	114	38	10	0	164	9	12	Morin anorthosite complex	Irving et al., 1974

Notes: Slat and Slon are present-day geographic coordinates of sample location, Plat and Plon are present-day coordinates of the paleopoles, D= mean magnetic declination, I= mean magnetic inclination, α_{95}= radius of 95% confidence ellipse, dp and dm are lengths of minor and major semi-axes of confidence ellipse, respectively.

Georgeville Group (Murphy et al., 1997) was taken by Thompson et al. (2010) to imply either different histories between these areas or different crustal levels. Thus, the chronological similarities in arc-sequences between SE New England, and parts of the Cobequid Highlands, set them apart as distinct domains within the Avalonian collage (Thompson et al., 2010).

5.2.3 COMPARISON BETWEEN OLDEST NEOPROTEROZOIC UNITS IN WEST AVALONIA

Knowledge of the Avalonian basement is rather limited due to its sparse exposure (Murphy and Nance, 1991). Indirect evidence for the nature of this basement has been obtained through isotopic characteristics of igneous rocks derived either from crustal anatexis or the lithospheric mantle. In the following sections, published stratigraphic, isotopic, and whole-rock geochemical data for Neoproterozoic west Avalonia will be further evaluated and compared in order to understand the early stages of crustal accretion.

In the Cobequid Highlands, the Neoproterozoic Bass River and Jeffers blocks are separated by a crustal-scale fault. The Rockland Brook fault (RBF) is interpreted to be a reactivated Neoproterozoic fault (Miller, 1991; Pe-Piper and Piper, 2003) and consists of two parts: a W-E trending section and a NE-trending segment. The NE-trending western part is younger and records mostly late Paleozoic motion, whereas the eastern part of the fault is older (ancestral Rockland Brook fault of Miller, 1991), and considered to represent a steep, parallel-walled ductile shear zone (Miller, 1991).

Stratigraphically, the Bass River and Jeffers blocks show important differences in their Precambrian basements (Fig. 5.2). The oldest unit in the Bass River Block is the metasedimentary ca 1 Ga Gamble Brook Formation (Barr et al., 2012). Although the

depositional age of the Gamble Brook Formation is placed around 1 Ga, Archean zircons (ca. 2.8 Ga) have also been reported (Barr et al., 2003). In the absence of volcanic beds, however, the age of the Gamble Brook Formation is based on youngest detrital zircon

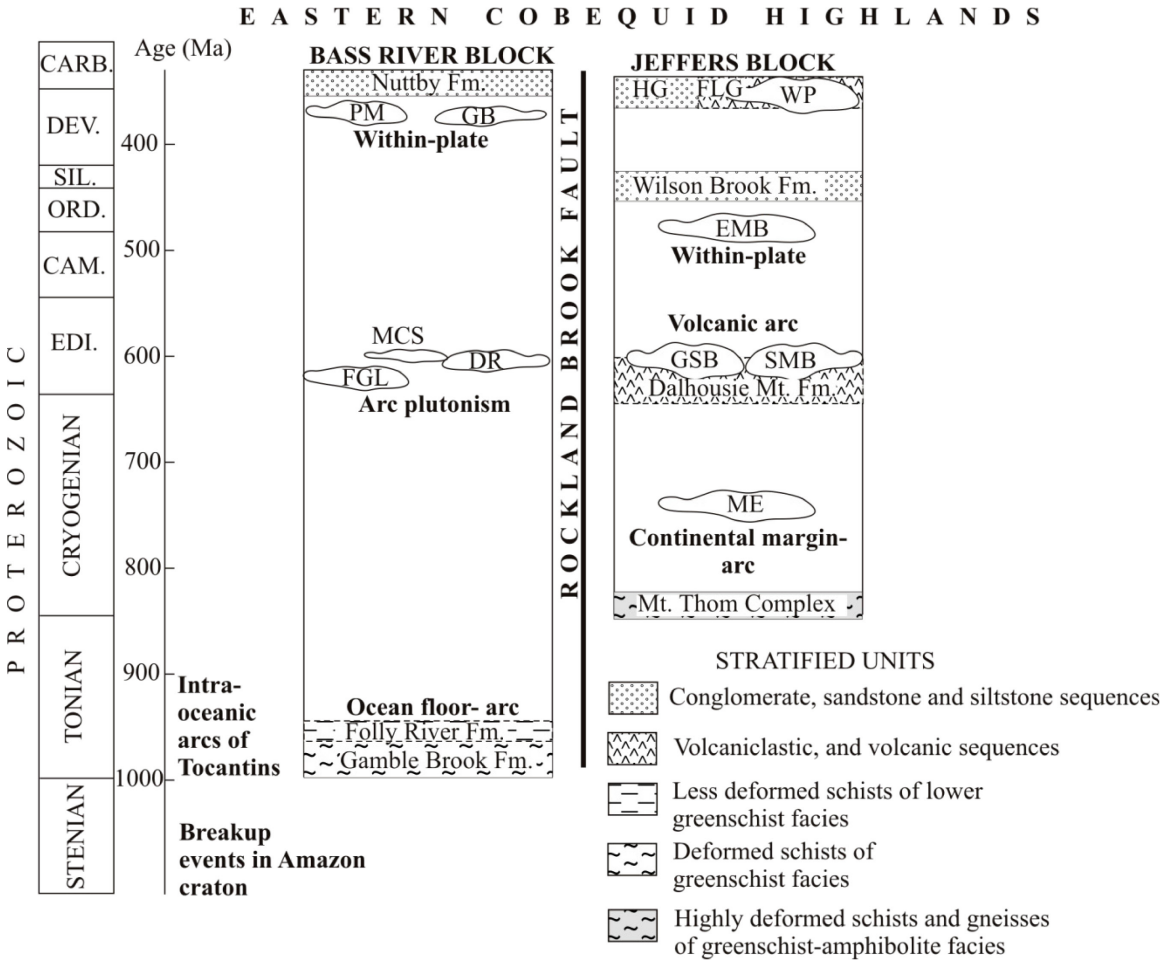

Figure 5. 2 Distribution of mapped geological units with time between the Bass River and the Jeffers blocks of the eastern Cobequid Highlands (data compiled from MacHattie and White, 2012). Abbreviations: CARB.= Carboniferous, DEV.= Devonian, SIL.= Silurian, ORD.= Ordovician, CAM.= Cambrian, EDI.= Ediacaran, PM= Polson Mountain pluton, GB= Gain Brook pluton, MCS= McCallum Settlement pluton, DR= Debert River pluton, FGL= Frog Lake pluton, WP= Wentworth pluton, HG= Horton Group, FLG= Fountain Lake Group, EMB= Eight Mile Brook pluton, GSB= Gunshot Brook pluton, SMB= Six Mile Brook pluton, ME= Mount Ephraim pluton.

dated, and therefore must be treated with caution. The Gamble Brook Formation, which has been metamorphosed under greenschist conditions, is interpreted to have been

originally deposited within a rifted island-arc setting based on the geochemistry of the sediments and the presence of contrasting sources (Murphy, 2002). The upper Gamble Brook Formation contains pelitic layers which based on their Sm-Nd isotope composition were assumed to have derived from a juvenile mafic source, whereas the structurally lower quartzites were derived from an older cratonic basement. Murphy (2002) associated the juvenile source of the upper pelites with the proto-Avalonian crust.
The Economy River Gneiss (734 ±2 Ma, Doig et al., 1993) is a granodioritic orthogneiss that was interpreted by Murphy et al. (2001) to represent an earlier phase of arc-related magmatism. Even though the Economy River Gneiss was assigned by Murphy et al. (2001) and Pe-Piper and Piper (2005) to the Bass River Block, the unit is located just south of the Pleasant Hills pluton, north of the Cobequid Fault, and in the stepover zone between the Rockland Brook and Kirkhill faults. Therefore its affinity based on its location is unclear (Pe-Piper and Piper, 2003), since there is no obvious spatial relationship with the faults that separate the two crustal blocks, and it is not considered further in this chapter. The Folly River Formation comprises metasedimentary rocks interlayered with volcanogenic sediments and pillow lavas. According to their geochemistry, the lavas were deposited on an ocean floor as within-plate continental tholeiites related to rifting (Pe-Piper and Murphy, 1989; Murphy et al., 2001).

The sedimentary rocks of the Gamble Brook Formation show the development and subsequent folding of a mylonitic fabric, which was interpreted by Nance and Murphy (1990) as the result of a single deformational event related to shearing. The age of this shearing was estimated at ca 640-625 Ma based on synmagmatic deformation in dated granites of the area. This deformational event was not identified in the Folly River

Formation, which in contrast shows polyphase deformation, and thus the rocks were interpreted to be much younger than that of the Gamble Brook Formation. This was based on the observed truncation of the mylonitic fabric in the Gamble Brook Formation by a mafic dyke assigned to the Folly River Formation (Nance and Murphy, 1990). The changes in the mylonitic fabric between the Folly River and the underlying Gamble Brook formations were taken by Murphy et al. (2001) to result from contrasting structural styles, and the contact between the two formations was suggested to be an unconformity. Therefore, the Folly River Formation was thought to be much younger than the Gamble Brook Formation. MacHattie and White (2012), however, argued that the observed change in deformation between the two units is because the Folly River Formation resides at the core of the Bass River Block, away from mylonitic bounding faults. They state that the two formations are not in contact and based on petrographic similarities between the two (metamorphic grade and presence of quartzite beds) these units are lateral stratigraphic facies equivalents.

The oldest unit in the Jeffers Block (Fig. 5.2) is the polymetamorphic 810 ±12 Ma Mount Thom Complex (Donohoe and Wallace, 1982; zircon U-Pb age from MacHattie et al., 2013). The Mount Thom Complex consists of paragneiss, granite gneiss and amphibolite (MacHattie and White, 2012). Even though the tectonic environment of Mount Thom Complex remains controversial, Meagher (1995) concluded that the amphibolites have subalkaline and tholeiitic protoliths, whereas the granite gneisses resemble volcanic arc granites (Pe-Piper et al., 1998). The Dalhousie Mountain Formation of volcanic and volcaniclastic rocks has no geochronological data available. However it is suggested to be of Neoproterozoic age, based on the similarities with

Neoproterozoic formations in the Antigonish Highlands and the fact that is intruded by the ca 605 Ma Gunshot Brook pluton (Donohoe and Wallace, 1982; Murphy et al., 1991; Pe-Piper and Piper, 2003; MacHattie and White, 2012). A Neoproterozoic age for the Dalhousie Mountain Formation is consistent with the presence of the lithologically similar Neoproterozoic Jeffers Group throughout the northern and western Cobequid Highlands (Pe-Piper and Piper, 2003).

Lithostratigraphic correlations have been suggested between the Neoproterozoic fault-bounded blocks in the Antigonish and the Cobequid Highlands. The Jeffers Block of the Cobequid Highlands was correlated with the Keppoch Block, whereas the Bass River Block was correlated with Clydesdale block (Murphy et al., 1991). Therefore, the correlations made between the Neoproterozoic units of Antigonish and the Cobequid Highlands may indicate the presence of two Avalonian fault-bound blocks, the Jeffers-Keppoch and the Bass River-Clydesdale that can be traced throughout mainland Nova Scotia (Fig. 5.3).

Murphy and Dostal (2007) argued, on the basis of consistent isotopic characteristics in Avalonian igneous rocks through time, that Avalonian crustal fragments remained attached to their lithospheric mantle from Neoproterozoic to Devonian. In this case, the isotopic signature of the Neoproterozoic basalts should record systematic differences in mantle sources if they originated in entirely different microplates. Published Nd-Sm and Pb isotope data (Pe-Piper and Piper, 1998b) indicate that there are significant and systematic differences between the Jeffers and Bass River blocks. The $\varepsilon_{Nd(t)}$ values of late Neoproterozoic (ca 650 Ma) mafic rocks from these blocks show strongly positive values for the Jeffers Block (+ 4.5 to + 5.7), whereas their equivalents in

the Bass River Block, range from +2.5 to -0.1 (Pe-Piper and Piper, 1998b). These values, when plotted on the ε_{Nd} evolution diagrams for Avalonia (Nance and Murphy, 1996), show that the Neoproterozoic gabbroic rocks of the Jeffers Block have a definite west Avalonian signature, whereas those from the Bass River Block plot in the overlapping area between west Avalonia and the envelope defined for the Tocantins Province of the Amazonian craton (Fig. 5.4), a part of Gondwana that has been interpreted to be proximal to Avalonia in the Neoproterozoic, and source of detritus (Murphy et al., 2001; Barr et al., 2012). This isotopic diversity could be interpreted either as a) reflecting the presence of Tocantins basement rocks, or b) derivation from a source similar to that of Tocantins Province. The Neoproterozoic gabbros of the Bass River Block have a Pb isotopic signature chemically resembling the Kerguelen oceanic basalts, for which an enriched mantle component is interpreted (Zindler and Hart, 1986) (Fig. 5.5). Hawkesworth et al. (1986) correlated the EM II reservoir with the continental lithosphere of South America and Africa cratons in Gondwana.

Pb isotope data are not available for the Neoproterozoic gabbros from the Jeffers Block. Systematic differences in whole-rock geochemistry between the mafic rocks of the two crustal blocks, however, may indicate contrasting mantle sources. The Bass River Block Neoproterozoic gabbros show systematically higher concentrations of REE (Fig. 5.6A) and Nb (Fig. 5.6B) than the gabbros of the Jeffers Block, suggesting a larger EM II component (Zindler and Hart, 1986). The Bass River Block gabbros have lower Sr (Fig. 5.6C) and higher Zn (Fig. 5.6D) and TiO_2 (Fig. 5.6E) concentrations than those from Jeffers Block. In the Mn-Ti-P ternary diagram, the basalts of the Folly River Formation plot clearly within the MORB field (Fig. 5.7A), and in the Ti-Zr-Sr diagram have a

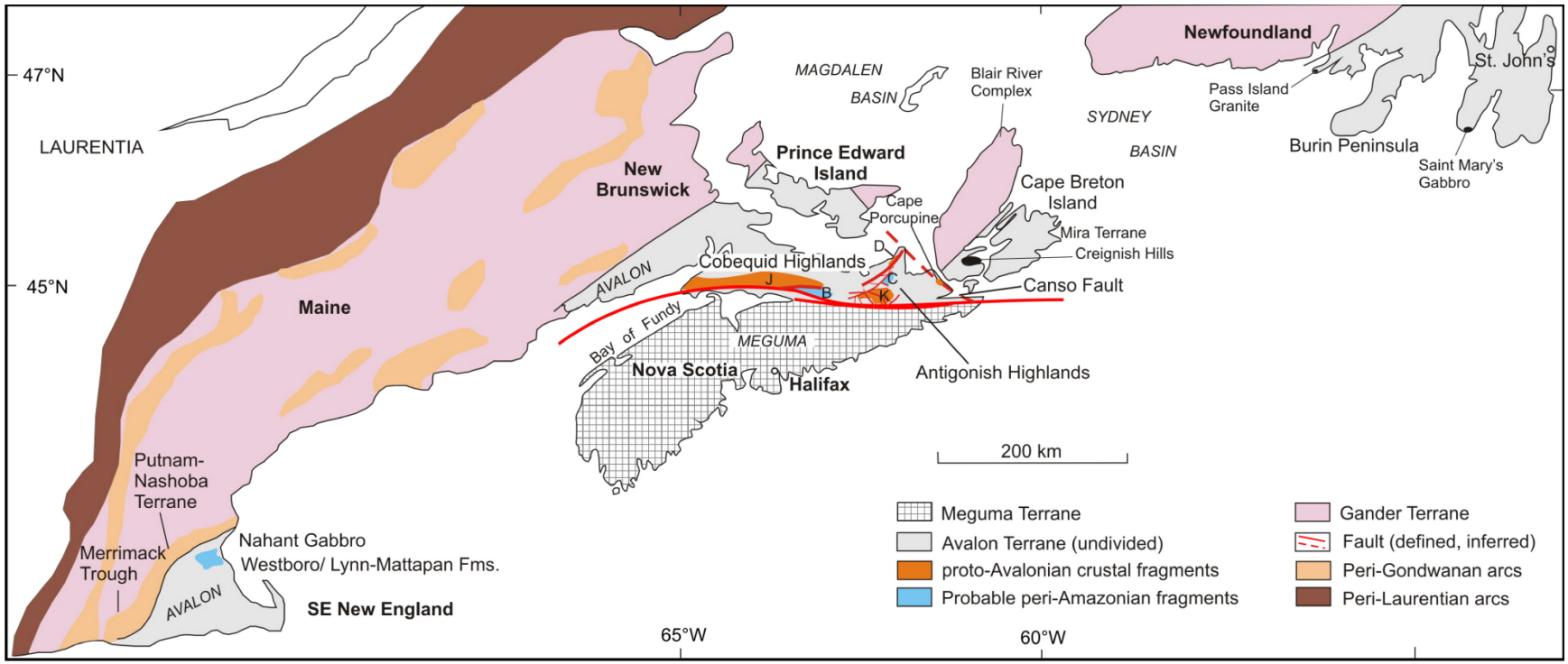

Figure 5.3 Simplified geological map of the Northern Appalachians (modified after Pe-Piper and Piper, 2003 and Barr et al., 2012). Positions of Iapetan arcs are after Hibbard et al. (2006). Abbreviations: J= Jeffers Block, B= Bass River Block, K= Keppoch Block, C= Clydesdale Block, D= Dunn Point Formation.

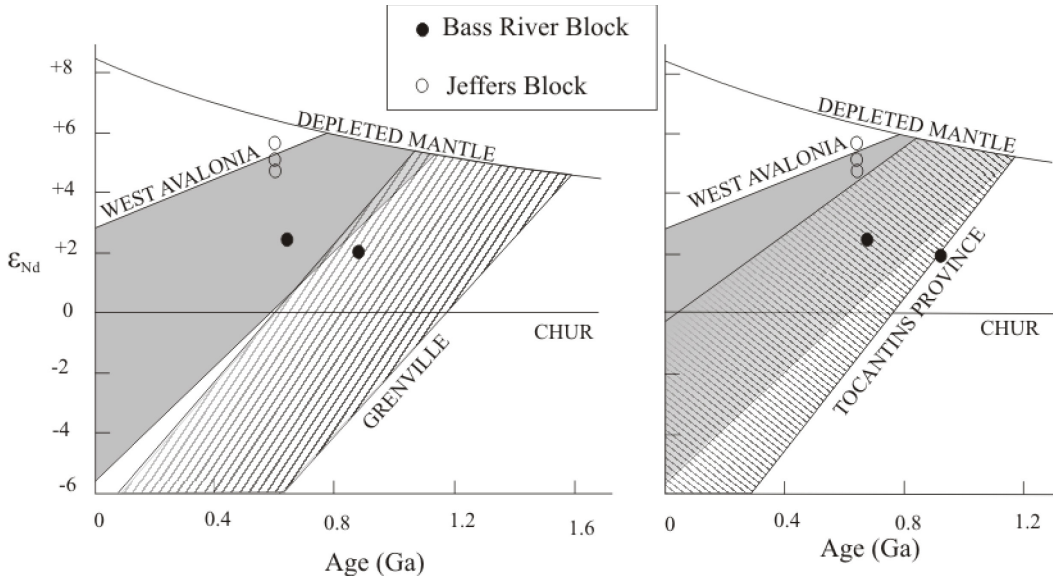

Figure 5. 4 Neoproterozoic mafic rocks from the Bass River and Jeffers blocks (data from Pe-Piper and Piper, 1998b, ages modified after MacHattie and White, 2012) plotted on ε_{Nd} evolution curve diagrams for west Avalonia, Grenvillem and Tocantins Province (fields after Nance and Murphy, 1996).

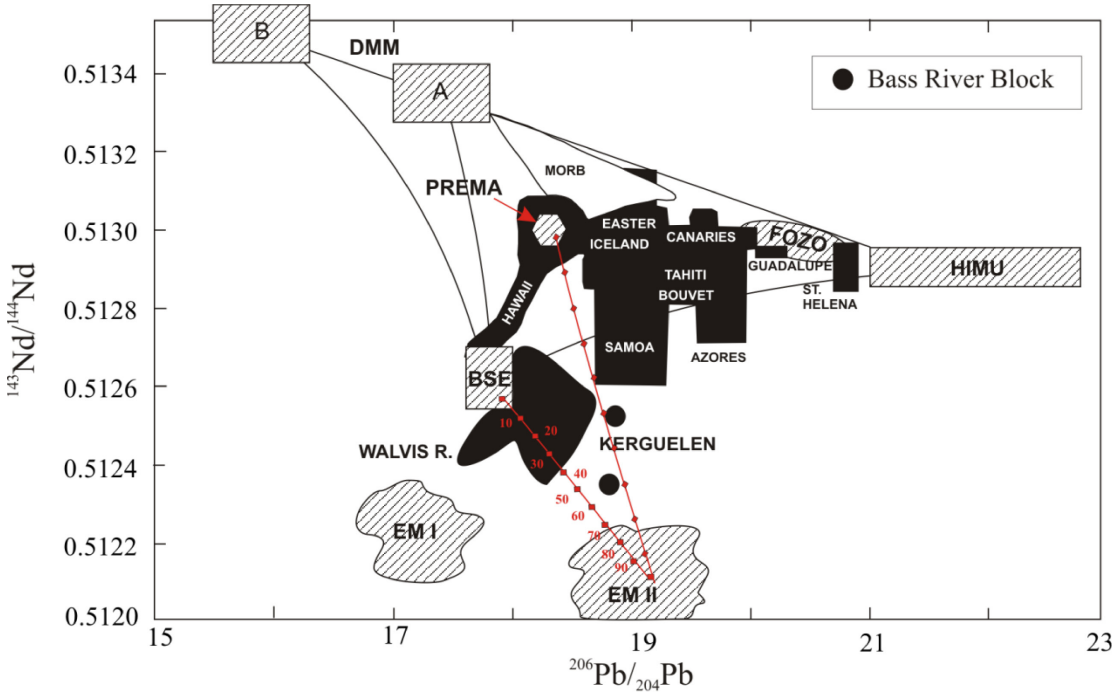

Figure 5. 5 $^{143}Nd/^{144}Nd$ vs $^{206}Pb/^{204}Pb$ variation diagram for oceanic basalt suites (modified from Zindler and Hart, 1986) with positions for the Neoproterozoic gabbros from the Bass River Block. DMM= depleted mantle, PREMA= prevalent mantle, HIMU= high-μ mantle, FOZO= undegassed (volatile-rich) mantle. Red lines represent the modelled trends for isotopic mixing between selected end-members. Numbers along lines refer to the relative proportions of one end-member.

definite ocean floor affinity (Fig. 5.7B) which is different from the ca 620 Ma Neoproterozoic arc-related basalts from the same crustal block, suggesting probably an origin in a different tectonic environment.

The systematic differences in trace elements between the ca 620 Ma arc-related gabbros from the Bass River and Jeffers blocks may reflect substantial differences in their lithospheric mantle sources that could indicate derivation from different lithospheric fragments. Furthermore, the rift affinity of the Folly River basalts correlates more with the tectonic setting of the Gamble Brook Formation, rather than the arc-related ca 620 Ma gabbros from the same block.

Compared to west Avalonian rock units elsewhere, the basement of the Bass River Block (Gamble Brook and Folly River formations) correlates in lithologic character and metamorphic grade only with the oldest Avalonian rocks of SE New England, namely the ca 1 Ga Westboro Formation and the 1170 Ma Blackstone Group (Barr et al., 2012; Thompson et al., 2012). The Blackstone Group contains metapelites, quartzites and metavolcanic rocks of greenschist facies, notably pillow basalts, resembling the lithological character of the Folly River Formation. The Westboro Formation is overlain by the Middlesex Fells complex which contains basaltic flows and tuffs with transitional to alkalic compositions (Cardoza et al., 1990). Comparison between the basalts of the Folly River Formation and the Middlesex Fells complex reveal that they are chemically similar and quite distinct from the Jeffers basalts (Fig. 5.8A to E). The Mesoproterozoic Westboro and Blackstone formations of SE New England have been interpreted as crustal fragments of a pre-Avalonian continental margin (Bailey et al., 1989). The stratigraphic, chronological and chemical similarities between the Avalonian Folly River and the

Westboro and Middlesex formations could imply not only that a) the Neoproterozoic basements of SE New England and Bass River Block are probably related, but also that b) the Folly River Formation, the age of which is still controversial, resembles known early Neoproterozoic Avalonian basement elsewhere, rather than late Neoproterozoic. Comparison of U-Pb ages from detrital zircons from the Westboro and Gamble Brook formations reveals that the two formations share similar distributions in zircon age populations (Table 5.2), resembling ages from Amazonian source belts (Thompson et al., 2012).

5.2.4 LITHOSTRATIGRAPHIC CORRELATIONS BETWEEN THE BASEMENT UNITS OF BASS RIVER AND SE NEW ENGLAND WITH AMAZONIA

The Bass River Block has a distinct isotopic signature that resembles the Tocantins structural province (Fig. 5.4), and contains detrital zircons interpreted to come from Amazonian sources. The understanding of the Precambrian evolution of South America is, therefore, important if any correlation with the Avalonian blocks of the Cobequid Highlands is to be attempted.

Structurally, the present-day South American platform has been divided into cratons that represent older crustal fragments of pre-existing microplates and structural provinces that surround the cratons (de Brito Neves and Fuck, 2013). The structural provinces closest to the Amazonian craton are the Borborema, Tocantins, and Mantiqueira provinces, which are orogenic belts. The cratonic fragments were initially brought together during the assembly of Rodinia by subduction systems known as Tonian orogenic belts which are restricted to the cratonic basements (850-1000 Ma) (de Brito Neves and Fuck, 2013). In the late Neoproterozoic, the Brasiliano orogenies, which developed along a branching system of subduction zones, are characterized by 650-600

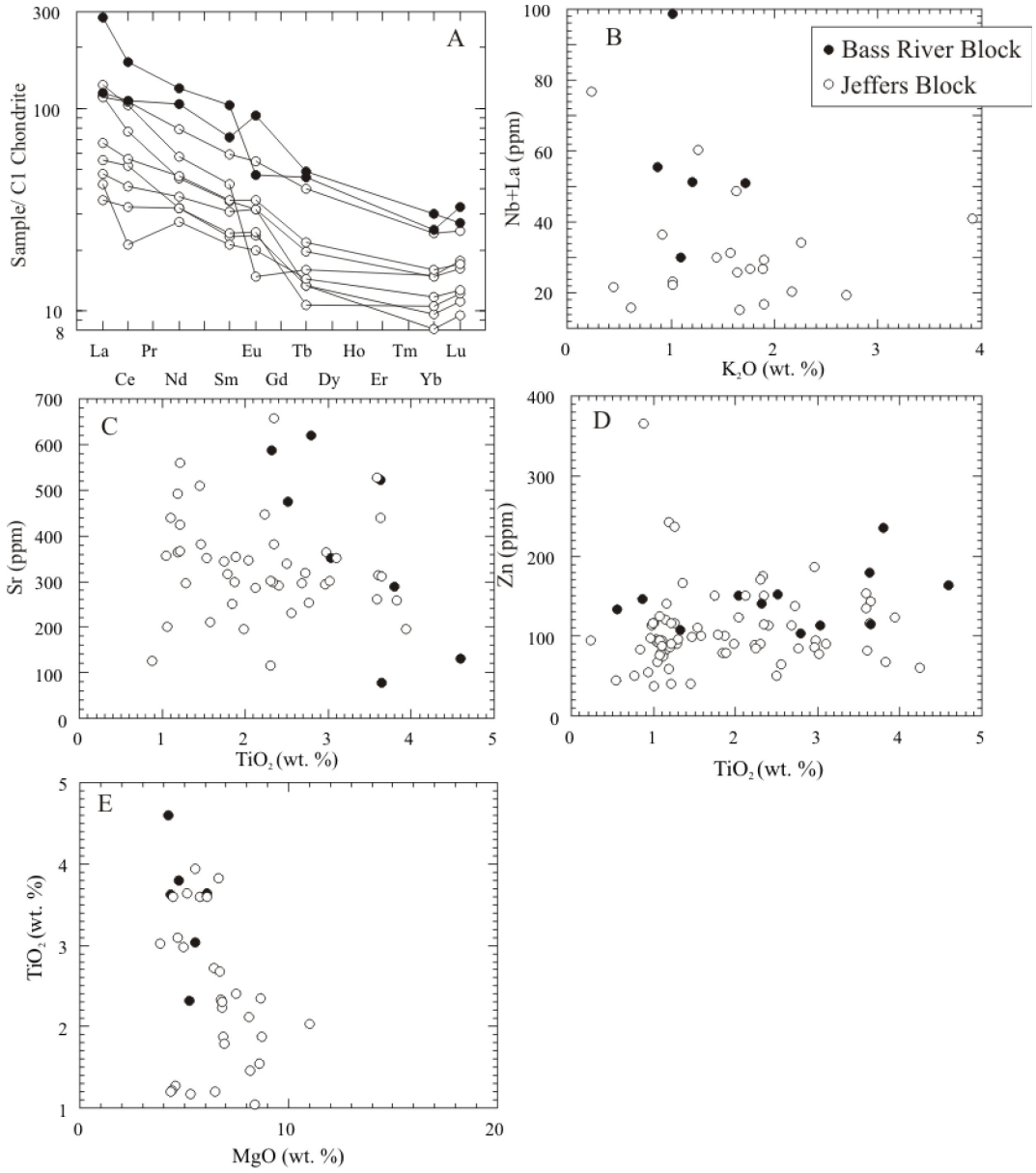

Figure 5. 6 Chondrite-normalized REE patterns (normalizing values after Sun and McDonough, 1989) (A) and selected geochemical diagrams (B to E) that demonstrate best the chemical differences between the Neoproterozoic mafic rocks of the Bass River and Jeffers blocks.

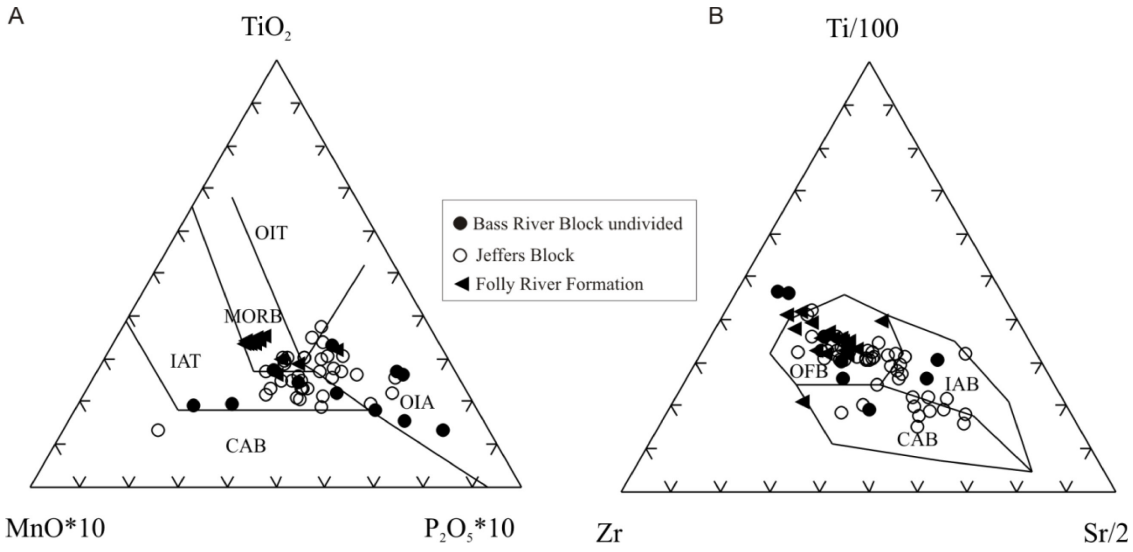

Figure 5. 7 Trace element classification diagrams after (a) Mullen (1983) and (b) Pearce and Cann (1973) for the Neoproterozoic mafic rocks of the Cobequid Highlands.

Ma arc sequences in all provinces and record substantial crustal reworking (de Brito Neves and Fuck, 2013). The distal parts of the provinces are compositionally diverse, and present evolved volcano-sedimentary arc sequences, whereas the marginal belts that surround the cratons are dominantly quartzite-pelite-carbonate assemblages (de Brito Neves and Fuck, 2013). The basement of the Bass River Block (Gamble Brook Formation) is broadly similar in age and stratigraphy to the Tocantins Group (lower quartzite unit and upper chlorite schist) of the Araguaia belt present only in the Tocantins province (de Brito Neves and Fuck, 2013; Goodwin, 2013).

The stratigraphic and chemical similarities discussed above between the Neoproterozoic basements of the Bass River Block and the Avalon Zone of SE New England (Table 5.2) suggest that these parts of the Avalon composite terrane either a) reflect different crustal levels of the Avalonian crust; or b) comprise a distinct unit of Avalonia that did not originate within the same microcontinent of proto-Avalonia, but

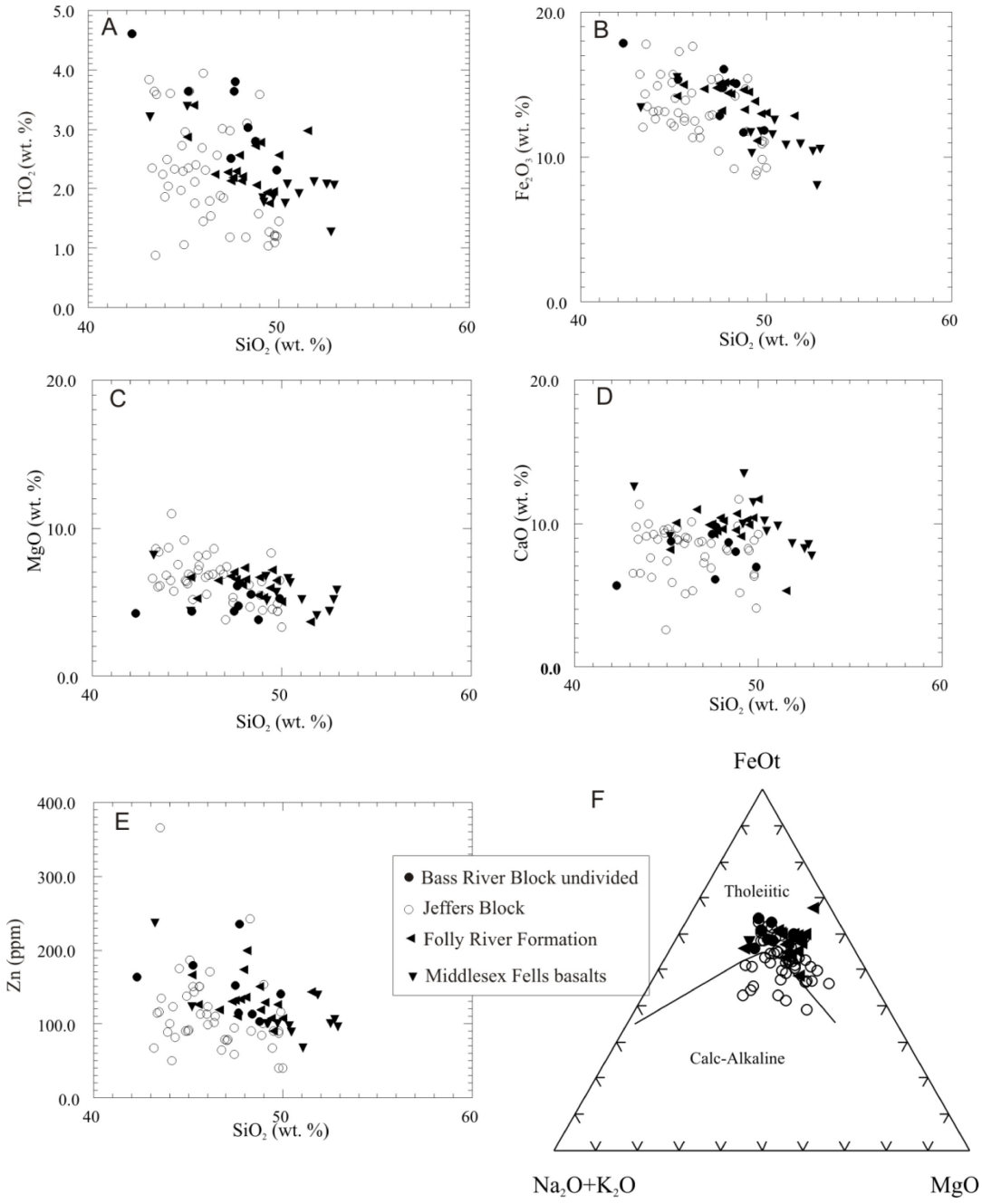

Figure 5. 8 Harker-type geochemical plots for the Neoproterozoic mafic rocks of the Cobequid Highlands and SE New England (A to E). AFM classification diagram (F) after Irving and Baragar (1971). Chemical data for SE New England compiled from Cardoza et al. (1990).

have an Amazonian affinity. Given the substantial variations in isotopic signatures and paleomagnetic data between these areas and the rest of Avalonia, the preferred interpretation followed in this chapter is that of a different origin. For that reason, these

two areas are plotted as separate fragments along the Amazonian margin in the Neoproterozoic reconstructions presented here. The Jeffers Block, on the other hand, shows isotopic and stratigraphic similarities with the Antigonish Highlands, which are taken as representative of typical west Avalonian crust (Fig. 5.3) (Murphy et al., 1989). The Jeffers Block, along with the Antigonish Highlands, records substantial arc activity in the late Neoproterozoic, which could have been related to the closure of the Brasiliano Ocean. These areas may have been, therefore, parts of a proto-Avalonia drifting in the Brasiliano Ocean towards the Amazonian margin of Gondwana in the Neoproterozoic.

Proto-Avalonia and other peri-Amazonian fragments were probably brought together in the late Neoproterozoic. Paleomagnetic data from the ca 590 Ma Lynn-Mattapan Formation in SE New England indicate that this part of Avalonia occupied a paleolatitude of ~ 30°S (Thompson et al., 2007), which according to the reconstructions presented here, corresponds to the Amazonian margin (Fig. 5.1C) and not to the West African craton as previously proposed. Similar paleolatitudes have been reported from Newfoundland, at ca 580 Ma (McNamara et al., 2001), suggesting that proto-Avalonia approached the Amazonian craton at the time. The significantly shorter phase of arc-related magmatism in SE New England may record the final collision of the Amazonian margin with proto-Avalonia at 610-590 Ma. The early convergence between proto-Avalonia and these peri-Amazonian fragments is indicated by differences between these Avalonian fragments, which are restricted only to their earliest Neoproterozoic units. Whether the fragments of SE New England and Bass River Block joined proto-Avalonia as one coherent piece and separated later, however, cannot be determined.

5.3 EARLY PALEOZOIC AVALONIA: DRIFTING BETWEEN TWO OCEANS

Paleozoic reconstructions that involve the assembly of Gondwana and later Pangaea follow the most up-to-date models of Torsvik et al. (2014), which relate the movements of the plates to deep mantle structure. The lowermost mantle is dominated by two large low shear-wave velocity provinces beneath present-day Africa and the Pacific Ocean. It is argued that in the last 300 Ma, large igneous provinces and kimberlites have been emplaced directly above the margins of these mantle provinces, in plume generation zones (Torsvik et al., 2014). Correlation between the large igneous provinces and kimberlites with the plume generation zones, at the time of their formation, was used by the authors as a reference frame for their reconstruction models. Their published Euler rotation parameters are followed, with the exception of Avalonia and Ganderia, whose movements have been modified based on published paleomagnetic data and other geological constraints (Appendix D.1).

By early Cambrian (ca 540 Ma) West Gondwana had been assembled and separated from Laurentia, Greenland and Baltica by the Iapetus Ocean (Cawood et al., 2001). Although a high southern paleolatitude is accepted for the Amazonian margin of Gondwana (Murphy et al., 2010), the position of the peri-Gondwanan terranes proposed here, is different from that proposed by these authors. Following the late Neoproterozoic reconstructions, the early Paleozoic position of Avalonia is predicted here along the NW margin of the Amazonian craton, with west Avalonia being the most proximal while east Avalonia is relatively closer to the West African craton, both facing the Iapetus Ocean (Fig. 5.1D). Ganderia is placed outboard of west Avalonia along the Amazonian margin.

Table 5. 2 Summary of the main characteristics for the discussed Neoproterozoic geological units in west Avalonia.

Affinity	**Amazonia**	**Avalon SE New England**		**Bass River Block- Cobequid Highlands**		**Jeffers Block- Cobequid Highlands**
Unit Name	**Tocantins Group**	**Westboro**	**Blackstone**	**Gamble Brook Fm.**	**Folly River Fm.**	**Mount Thom Complex**
Age	ca 1.3-0.9 Ga	ca 1 Ga (inferred age)	ca 1.1 Ga (inferred age)	ca 1 Ga (inferred age)	not determined	ca 810 Ma (U-Pb)
Petrographic description	upper meta-pelite, lower quartzite, pillow basalts	pelite, quartzite, overlain by basaltic flows (Middlesex Fells Fm.)	pelite, quartzite, pillow lavas	Upper pelite-lower quartzite	pelite, quartzite, pillow lavas	paragneiss, granite gneiss, amphibolite
Metamorphic grade	Greenschist facies	Greenschist facies	Greenschist facies	Greenschist facies	Greenschist facies	Amphibolite facies
Tectonic environment	Passive margin	continental rifting	continental rifting	rifted island arc	Ocean floor-rifting	volcanic arc
Description of igneous rocks	not determined	Transitional-alkali basalt	transitional-alkali basalt		MORB basalt	calc-alkaline, tholeitic
Detrital zircon populations (peaks)	not determined	1200, 1500, 2100 Ma	not determined	1200, 1500, 2100, 2800 Ma	not determined	not determined

Murphy et al. (2010) favored placing Avalonia along the SE margin of Amazonia, which rotated clockwise by 460 Ma, bringing Avalonia opposite the Laurentian margin. The reconstructions presented here place Avalonia facing the Laurentian margin since Cambrian times, although that is not paleomagnetically constrained. This position is used, however, since a clockwise rotation of Amazonia was not predicted in the Neoproterozoic-Early Paleozoic models. This position nonetheless favors a later drift of Avalonia that can accommodate an oblique collision with Laurentia before the formation of Pangaea.

Current paleotectonic models suggest that after the formation of Avalonia along the margin of West Gondwana, the terrane was separated from the latter during the opening of the Rheic Ocean (Fig. 5.9A and B) (Murphy et al., 2001). Although there is considerable debate with regards to the time of rifting, it is generally accepted that it took place between the late Neoproterozoic and Silurian. Landing (2005) supported a late Neoproterozoic separation of Avalonia, based on the differences in Cambrian fauna and stratigraphic sequences between Newfoundland and Morocco. Isotopic and paleomagnetic constraints, however, suggest that Avalonia occupied a high southerly latitude close to Gondwana from late Neoproterozoic to early Ordovician (van Staal et al., 1998; Pisarevsky et al., 2012).

Early Ordovician rifting of Avalonia is indicated by a major change in the tectonic regime, reflected in the detrital zircons of early Paleozoic Avalonian platformal sequences and the presence of Ordovician rift-related volcanic rocks in England (van Staal et al., 1998), and in southern Mexico, along the southern margin of the Rheic Ocean (Keppie et al., 2008). Pollock et al. (2009) reported that the sedimentary sequences of the

main Avalonian arc phase (650-600 Ma) in Newfoundland contain large populations of coeval zircons suggesting their deposition as first-cycle sediments, locally derived from

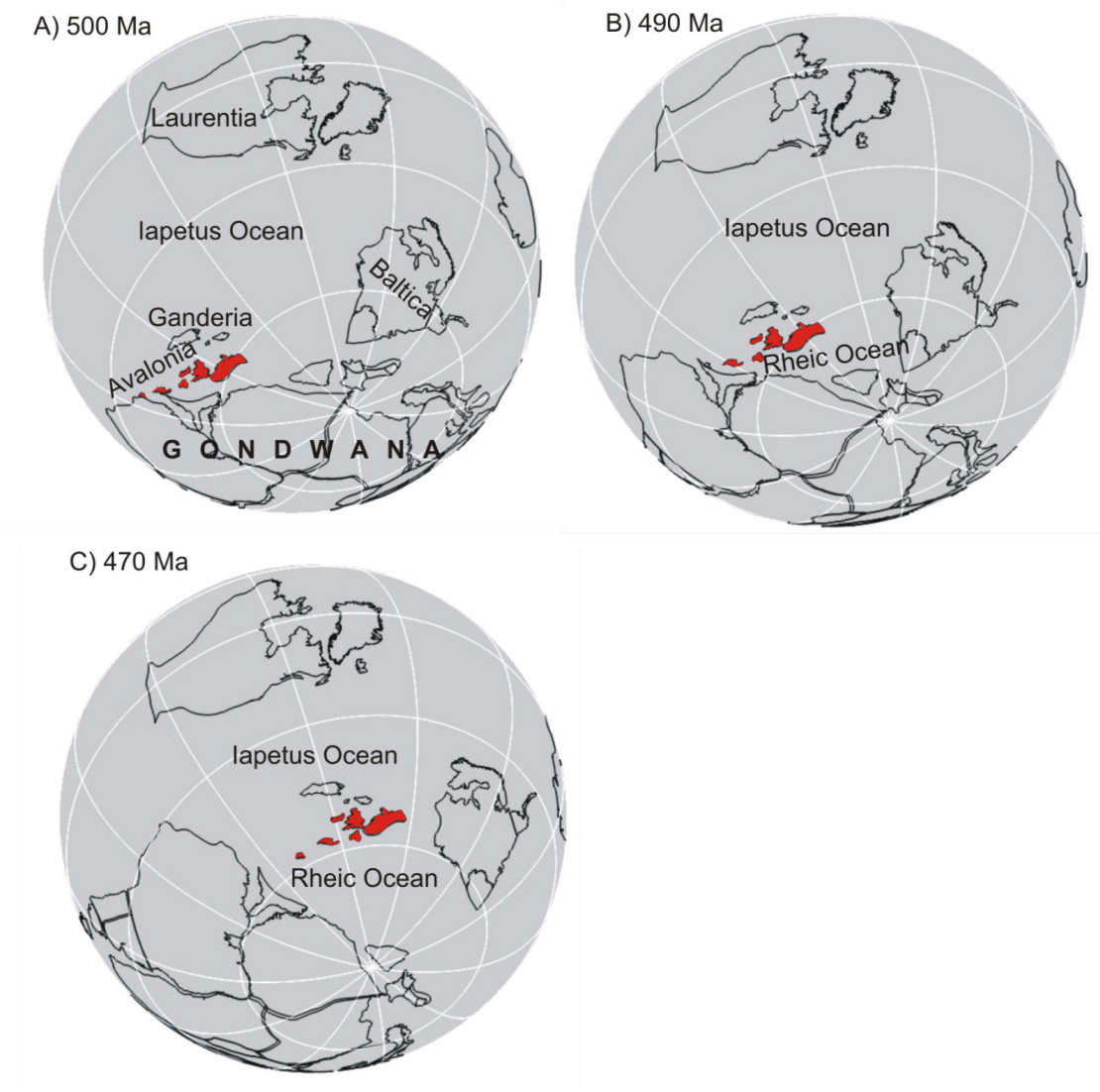

Figure 5. 9 Early Paleozoic reconstructions showing (A) rifting of Ganderia in early Cambrian followed by the separation of Avalonia from west Gondwana in early Ordovician (B). Figure (C) shows the possible arrangement of Avalonia and Ganderia as they drifted together during the closure of Iapetus Ocean.

igneous rocks in the surrounding arc. The younger platform sedimentary sequences, on the other hand, contain large populations of Mesoproterozoic and Paleoproterozoic zircons (1.6-2.3 Ga). The presence of Mesoproterozoic zircon was considered consistent

with the presence of a Mesoproterozoic Avalonian basement, although no rocks of such age are exposed but the age is inferred from isotope data of crustal rocks. Based on the absence of a Paleoproterozoic Avalonian crust, Pollock et al. (2009) argued that the source of such zircons was from an older crustal source external to Avalonia. An alternative hypothesis for the origin of these zircons would be the derivation from Avalonian basement rocks with xenocrystic zircons such as those reported from Mira terrane (Bevier and Barr, 1990).

Avalonia is suggested to have amalgamated to a composite Laurentian margin as a distinct microcontinent, separated from Ganderia, in the Silurian (Murphy et al., 2008). The two terranes separated from West Gondwana as distinct domains in early Paleozoic (Pollock et al., 2012). The identical estimated drift rates between Avalonia and Ganderia between 490 and 460 Ma suggest that the two were on the same microplate after they separated from Gondwana (Thompson et al., 2010; van Staal et al., 2012). The contrasting geological histories between the two terranes are attributed to a narrow intervening oceanic seaway in the Ordovician (Fig. 5.9C) (van Staal et al., 2012).

MacNiocaill et al. (1997), on the basis of paleomagnetic and faunal data from the Appalachian Orogen, identified several early to middle Ordovician arcs within Iapetus Ocean: a) a peri-Laurentian arc at 10-20°S, b) an intra-oceanic arc at 30°S, and c) a peri-Avalonian arc at ~50-60°S. Hibbard et al. (2006), however, placed the peri-Gondwanan arc systems outboard of the northern Gander margin. Ordovician magmatism in west Avalonia is almost exclusively alkaline and extension-related, with no reports of arc-related activity. Back-arc sequences, however, are well preserved in the eastern part of Avalonia (van Staal et al., 1998), while of limited extent in its western portion (Hamilton

and Murphy, 2004). An extensional tectonic environment for Ordovician magmatism could be equally related to either back-arc extension, since Iapetus is thought to have been subducted beneath the Laurentian margin (Torsvik and Rehnström, 2003), or rifting associated with the opening of Rheic Ocean, south of Avalonia (Fig. 5.10).

5.3.1 CORRELATION BETWEEN ORDOVICIAN MAGMATISM AND PLATE TECTONICS

In order to evaluate the relative positions of the Avalonian blocks in the early Paleozoic it is important to compare the nature of magmatism throughout the microcontinent, since it may be related to geodynamics. While Avalonia occupied a position between the closing Iapetus and the spreading Rheic oceans from Ordovician to Silurian, this time interval is characterized by limited magmatism in west Avalonia (Pollock et al., 2009). Ganderia, on the other hand, records substantial arc-related magmatism during middle Ordovician (Moench and Aleinikoff, 2003). The Ordovician marks an important change in the nature of Avalonian magmatism. It is during that period that the first alkaline magmatic events are recorded in west Avalonia, with A-type affinities, which set them apart from the Precambrian arc-related magmatism.

Ordovician alkaline magmatism, however, is not synchronous throughout west Avalonia. Early Paleozoic A-type magmatism is observed in the Jeffers Block of the Cobequid Highlands (481.6 ±4.1 Ma, U-Pb, Eight Mile pluton, MacHattie et al., 2013), in the Antigonish Highlands (469.4 ±0.5 Ma- Brora Lake Haggarts Lake, West Barneys River, McGraths Mountain, and Leadbetter Road plutons, 460 ± 3.4 Ma- Dunn Point Formation, 454.5 ± 0.7 Ma- McGillivray Formation), and in northeastern mainland Nova Scotia (478± 3 Ma, Cape Porcupine Complex) (White et al., 2002; Hamilton and Murphy, 2004; MacHattie and White, 2012; Escarraga et al., 2012; Barr et al., 2012).

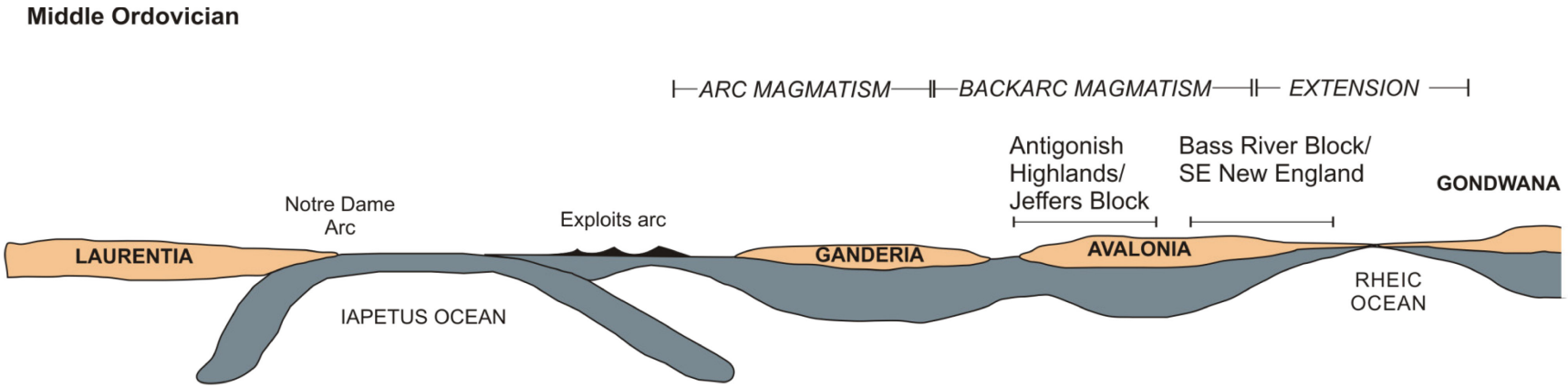

Figure 5. 10 Simplified cross-section of the Ordovician rifting of Avalonia during the closure of Iapetus Ocean and the opening of the Rheic Ocean (modified from van Staal et al., 1998).

Ordovician arc-related magmatism has been reported in the fault-bounded Putnam-Nashoba terrane of SE New England (Fig. 5.3), where it has been interpreted to reflect the closing of an ocean separating Avalonia and Laurentia (Acaster and Bickford, 1999). This block, however, has also been described as the trailing edge of Ganderia (Wintsch et al., 2014). The middle Ordovician (460 ± 3.4 Ma) volcanic rocks of the Dunn Point Formation in the Antigonish Highlands (Fig. 5.3), have a paleolatitude of ~40°S (Fig. 5.11A) (Johnson and van der Voo, 1990). Hamilton and Murphy (2004) interpreted these rocks, based on their geochemistry and bimodal character, to reflect a rifted arc tectonic setting and placed this rifted arc on the Avalonian microcontinent, outboard from Laurentia, within Iapetus.

In the Avalon zone of SE New England, Ordovician alkaline intrusions include the Cape Ann, Peabody, and Quincy granites, while the bimodal Nahant alkaline suite was intruded between ca 490 and 488 Ma (Buma et al, 1971; Thompson et al., 2010). The early Paleozoic alkaline magmatic events, where present in west Avalonia, were broadly synchronous with rifting of Avalonia from West Gondwana. A-type granites are related to extensional tectonic regimes (Loiselle and Wones, 1979), and therefore, could be related to the opening of the Rheic Ocean in the early Ordovician. The coeval mafic rocks show some distinct variations in their trace element characteristics. Mafic rocks from Cape Porcupine (Fig. 5.3) have negative Nb and Ti anomalies relative to MORB (Fig. 5.12A) (Barr et al., 2012), which could indicate derivation close to a volcanic arc (Xu et al., 2000). Mafic rocks from both the Antigonish Highlands and SE New England show positive Ti and Nb anomalies relative to MORB (Fig. 5.12B and C). The early

Ordovician Nahant Gabbro of SE New England, however, is geochemically distinct, showing an additional positive Th anomaly (Fig. 5.12C).

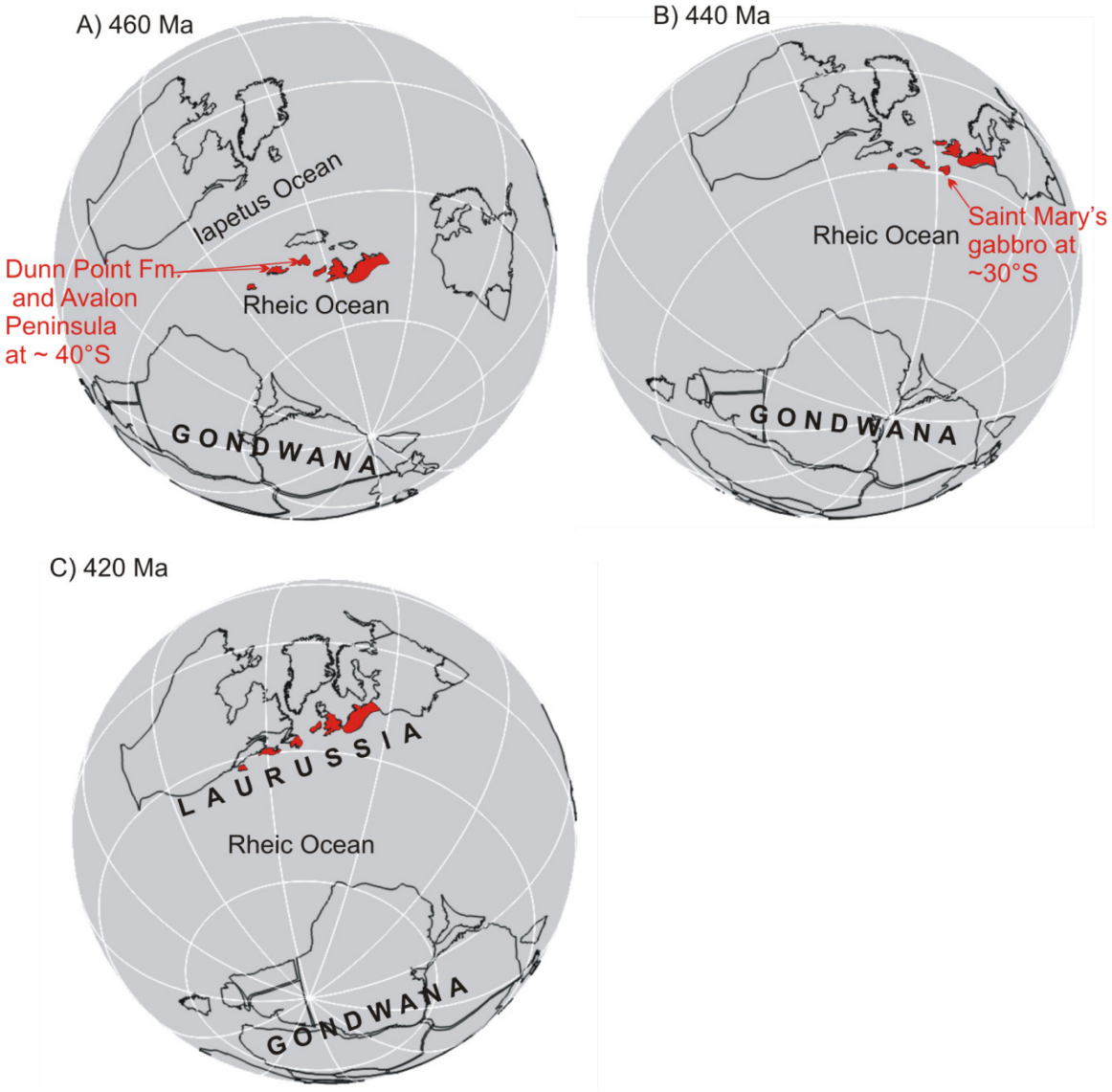

Figure 5. 11 Ordovician-Silurian reconstructions showing (A) the position of Avalonia in mid-Ordovician, and (B) the approach of the microcontinent with Laurentia and Baltica in late Ordovician as indicated by the paleomagnetism in Newfoundland (Hodych and Buchan, 1998). Figure (C) shows the amalgamation of Ganderia and Avalonia by Silurian and the formation of Laurussia following the closure of Iapetus Ocean.

Even though the Ordovician felsic rocks in Avalonia all present A-type alkaline affinities, the earlier initiation of alkaline magmatism in SE New England compared to the rest of

west Avalonia, together with a paleolatitude of 65°S ±7° (Thompson et al., 2010), could indicate a position in the southern part of Avalonia adjacent to the northern margin of the spreading Rheic Ocean.

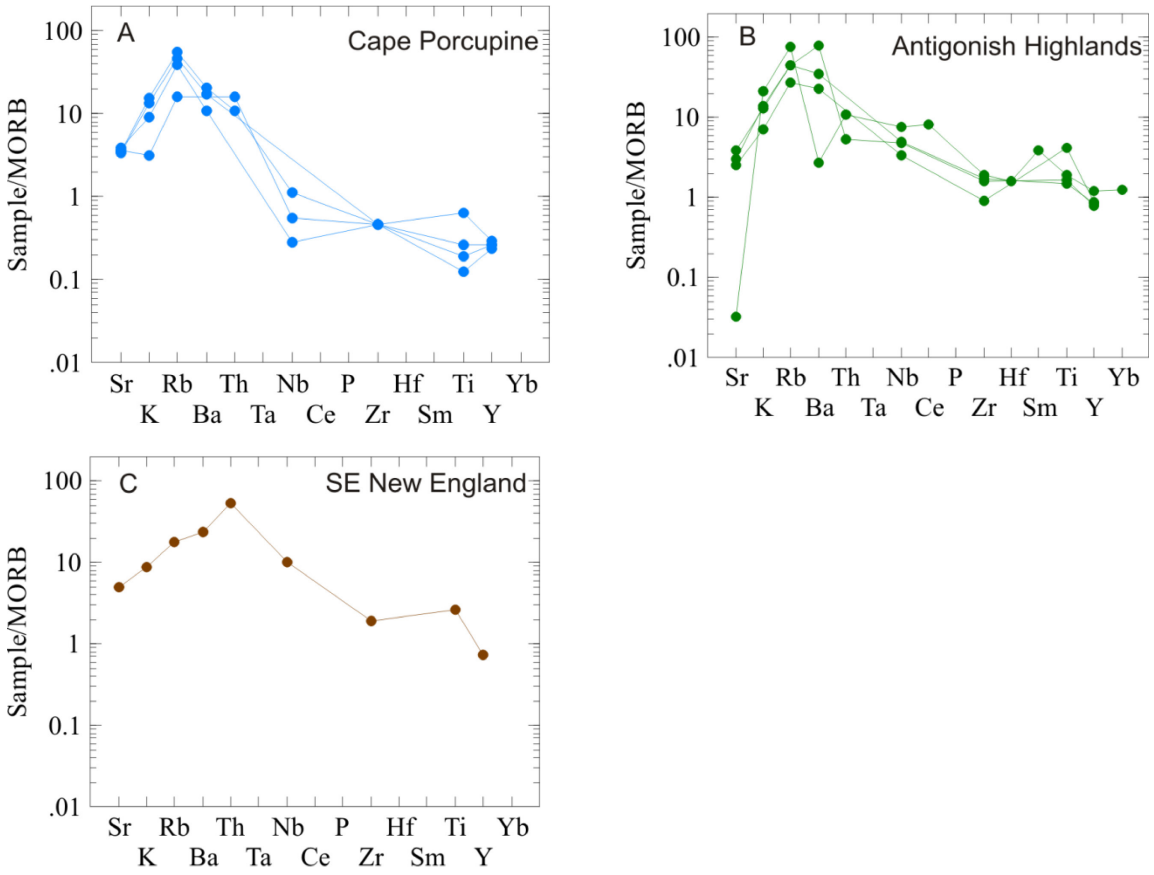

Figure 5. 12 MORB-normalized spider diagrams for the Ordovician mafic rocks of west Avalonia as recorded (a) in Cape Porcupine, (b) Antigonish Highlands and (c) SE New England (Nahant Gabbro). Geochemical data compiled from Murphy et al. (1991), Thompson et al. (2010), and Barr et al. (2012).

The above geochemical differences and paleomagnetic data in igneous rocks could imply that in the Ordovician the western part of the Avalonian microcontinent could be divided into three zones with respect to the southern Iapetan margin : a) a proximal zone, either as trailing edge of a Ganderia connected to Avalonia, or as the leading edge of Avalonia, as exposed in Putnam-Nashoba terrane with volcanic arc, calc-alkaline characteristics; b) a back-arc zone (~50-60°S), well within the main Avalonian

domain of the Ordovician Avalo-Ganderian connection, characterized by alkaline magmatism with A-type affinities in felsic rocks, as exposed in Jeffers Block, Antigonish Highlands, and Cape Porcupine; and c) the part of the microcontinent adjacent to the trailing edge facing the Rheic Ocean, which is characterized by southerly Ordovician paleolatitudes (>60°S) and alkaline rift-related rocks as exposed in SE New England.

The 490 Ma Avalonia is placed at the northern margin of Gondwana at a paleolatitude of ~60°S between the Amazonian and the African cratons, in these reconstructions (Fig. 5.9B). However, there are some issues to be addressed. A paleolatitude of 65°S for SE New England at the time, as reported for the Nahant Gabbro, should position Avalonia along the West African margin and adjacent to east Avalonia for which a paleolatitude of 62°S ± 9° has been reported (Trench et al., 1992). Thompson et al. (2010) argued on that basis that Avalonia was adjacent to the West African craton, and the Nahant paleopole could be used without rotation corrections. In the reconstructions presented here, west Avalonia, including SE New England, is positioned at ~60°S, still within error from the published paleolatitude. A 65°S paleolatitude for SE New England in this configuration could be explained only by oblique movements bringing that part of the terrane adjacent to east Avalonia. To the author's knowledge no such fault kinematics have been reported for Avalonia so far, however this hypothesis should be tested. The alternative would be that Avalonia at 490 Ma had drifted away from Gondwana and was closer to Baltica; however a change to a Baltic fauna is reported only after the Tremadoc (Pollock et al., 2012). Therefore, SE New England is positioned at the trailing edge of west Avalonia, on the basis of its distinct and longer-lived alkaline magmatism in the early Paleozoic.

5.3.2 VARIATIONS IN THE ORDOVICIAN GEOLOGICAL HISTORIES BETWEEN PARTS OF THE AVALONIAN CANADIAN MARITIMES

The lack of Ordovician igneous rocks in parts of west Avalonia such as the Bass River Block and in Newfoundland makes them difficult to be assigned into zones within the Avalonian microcontinent during that period. Early Silurian (441 ± 2 Ma, U-Pb on baddeleyite) mafic sills of the Avalon Peninsula in Newfoundland, however, show a paleolatitude of 32°S ± 8° (Fig. 5.11B) (Hodych and Buchan, 1998), suggesting that either: a) this part of Avalonia was closer to Ganderia and the Iapetan margin than SE New England and the Antigonish Highlands; or b) that Avalonia had drifted to that paleolatitude by early Silurian. Based on the differences in paleolatitudes of geological units of different ages within a paleocontinent, the drift rates may be estimated. Avalonia drifted from Gondwana towards Laurentia between Cambrian and middle Ordovician at a rate of 9.2 cm/a (Thompson et al., 2010), based on paleomagnetic data from Nahant. These rapid drift rates were interpreted as the effect of slab rollback beneath the leading edge of Ganderia during the closure of Iapetus Ocean (van Staal et al., 2012). Taking into consideration a Laurentian paleolatitude of ~20 °S between 460 and 420 Ma and the paleolatitude of the coeval Dunn Point Formation, Hamilton and Murphy (2004) argued that the approach to of Avalonia to Laurentia from middle Ordovician to early Silurian was characterized by slower drift rates of 5.5 cm/a. The decrease in drift rates close to the Silurian was considered, the result of the opening of the Tetagouche-Exploits back-arc basin and the docking of Ganderia to Laurentia (van Staal et al., 2012). Taking into account these drift rates and back-calculating the distance covered during the drift, a 441 Ma paleolatitude of 32° in the Avalon Peninsula would correspond to a paleolatitude of 41°S at 460 Ma, which is similar to that of the middle Ordovician Dunn Point Formation

of the Antigonish Highlands. Therefore, the Avalon Zone of Newfoundland should have been located further north than SE New England, within the Avalonian microcontinent, but possibly at the same latitude as the Antigonish Highlands (Fig. 5.11), as originally proposed by Hodych and Buchan (1998).

5.3.3 SILURIAN ACCRETION OF AVALONIA TO LAURENTIA, RELATED MAGMATISM AND MANTLE METASOMATISM

Silurian magmatism in west Avalonia reflects subduction during the final stages of the closure of Iapetus Ocean. The Pass Island granite in SW Newfoundland, just south of the Hermitage fault (Fig. 5.3), has yielded a Silurian age of 423 ± 4 Ma (SHRIMP U-Pb on zircon, Kellett et al., 2014), with trace-element characteristics of volcanic-arc and syn-collisional granites (Kerr et al., 1995), which could be linked to the collision of Avalonia with the Laurentian margin (Fig. 5.11C). In SE New England, the Silurian Franklin pluton (ca 417 Ma) presents alkaline post-orogenic characteristics (Hermes and Zartman, 1992), whereas in Cape Breton, Silurian arc magmatism in the Creignish Hills (Fig. 5.3) was interpreted to represent subduction along the northern margin of the Rheic Ocean (Keppie et al., 2000). In the Cobequid and Antigonish Highlands, however, no Silurian igneous rocks have been reported, although sedimentary clastic sequences of that period are present. In the Cobequid Highlands, the Silurian shales, siltstones and sandstones of the Wilson Brook and Portapique River formations are known only within the Jeffers Block, and are considered identical with the sequences of the Arisaig area in the Antigonish Highlands (Murphy et al., 1996; Pe-Piper and Piper, 2003). These sedimentary successions are quite different from the Devonian-Carboniferous Horton Group, which commonly contains conglomerate and lacustrine deposits, suggesting terrestrial basins (Pe-Piper and Piper, 2003). On the basis of whole-rock geochemistry,

isotopic data and paleocontinental reconstructions, Murphy et al. (1996) argued that the source of the Silurian strata in the Antigonish Highlands is probably eastern Laurentia or Baltica.

Murphy et al. (2004) argued that the late Ordovician-early Silurian sediments of the Arisaig Group in the Antigonish Highlands do not contain detrital zircons of Avalonian origin. All studied sedimentary rocks of that rock unit are characterized by strongly negative ε_{Nd} values (-4.8 to -9.3) and T_{DM} ages greater than 1.5 Ga. In the nearby Cobequid Highlands, the comparative study of Pe-Piper and Piper (1998b) demonstrated that this isotopic signature is not observed in the younger igneous rocks of the area, while Pb isotopes in the late Paleozoic felsic rocks show a strong Neoproterozoic component. This is consistent with subduction of terrigenous sediment in Neoproterozoic, but predominantly ocean crust in the early Paleozoic. Furthermore, Murphy et al. (2008) concluded on the basis of trace element geochemistry that the Ordovician mafic rocks in the Antigonish Highlands show only a minor influence from a crustal component. Thus, there is no evidence across mainland Nova Scotia of mantle metasomatism in the Ordovician, despite the subduction that was presumably required for the closure of Iapetus Ocean.

5.4 LATE PALEOZOIC WEST AVALONIA: SHEARING AND MAGMATISM

After the collision of Ganderia with the Laurentian margin during the Salinic orogeny in Silurian, the subsequent collision of Avalonia and Meguma terranes marked the onset of the closure of the Rheic Ocean during the late Silurian-early Devonian Acadian orogeny (van Staal et al., 2009). The 423-416 Ma arc sequences along the trailing edge of Ganderia and coeval HP-LT metamorphism east of that arc, as well as the

development of early Devonian NW-directed shear zones and fold belts in Ganderia all suggest that the collision of Avalonia was oblique and had a westward polarity (Keppie, 1993, Zagorevski et al., 2007; Dolmeier and Torsvik, 2014). Hibbard and Waldron (2009) hypothesized late Paleozoic strike-slip motion along the length of the Appalachian Orogen on the basis of misalignment of the Hermitage flexure in Newfoundland with the Laurentian margin and crustal thinning beneath the Gulf of St. Lawrence. The scale of this orogen-parallel displacement, from Devonian to early Mississippian, was estimated to be ~220-250 km, and was related to the accretion of the peri-Gondwanan Meguma terrane (Hibbard and Waldron, 2009). Intra-continental deformation can be interpreted as far-field response to plate tectonics and is associated with the reactivation of pre-existing crustal lineaments (Murphy et al., 1999). The oblique collision of Avalonia during the Acadian orogeny after the oblique convergence with Gondwana in the Neoproterozoic, could be related to the reactivation of pre-existing paths of weakness such as W-E trending faults like the Kirkhill and the Rockland Brook faults in the Cobequid Highlands.

The synchronous initiation of igneous activity in west Avalonia, and especially the voluminous mafic volcanism in mainland Nova Scotia (Dessureau et al., 2000) with the late Paleozoic strike-slip tectonics, could be evidence of edge-driven mantle convection (Anderson, 1998). Edge-driven convection theory states that in mature cooling planets the mantle-core boundary is a highly conductive cooling layer. According to Archimedes principle parts of the cooling layer will sink into the interior and displace older material underneath. As a result, mantle updrafts are created and are expressed as hotspots in the interior of plates (Anderson and Natland, 2014). A similar scenario is

proposed for the upper mantle underneath drifting plates. Colder mantle that has interacted with the lithosphere in subduction zones will sink into the deeper mantle. The hot mantle updrafts in this case will be expressed as voluminous mafic volcanism with asthenospheric chemical characteristics (Anderson and Natland, 2014). Such excess volcanism is focused at major lithospheric discontinuities, such as cratonic boundaries and continental margins, during rapid lithospheric extension. Regionally, the thickest late Paleozoic basalt succession, with primitive asthenospheric chemical signature (Dessureau et al., 2000), is found along the Rockland Brook in the Cobequid Highlands (Diamond Brook Formation). This volcanism may provide further evidence that this tectonic segment could reflect a deep crustal-scale discontinuity, probably an early Neoproterozoic suture, as discussed earlier in this chapter.

Pre-existing crustal heterogeneities can profoundly influence the lithosphere's response to subsequent deformation. This tectonic inheritance is well documented in cratons, where long-lived lineaments originated as Archean shear-zones (Butler et al., 1997). Repeated episodes of displacements along these faults generate highly heterogeneous kinematics in their sub-structure, the rheology of which will try to adapt to different conditions of temperature, strain and stress of each deformational phase (Butler et al., 1997). Experimental work of Henza et al. (2011) demonstrated that in a sequence of deformational events: a) reactivation of pre-existing faults will occur only if the first phase of deformation is well-developed; and b) the pre-existing faults act as obstacles for the propagation of younger faults. The longevity of the Rockland Brook fault (and possibly Kirkhill fault as its westward continuation) could therefore be indicative of the

presence of a significant crustal scale lineament in the Neoproterozoic that affected the Avalonian continental lithosphere until 300 Ma later.

5.4.1 COMPARISON BETWEEN THE LATE PALEOZOIC A-TYPE GRANITES IN WEST AVALONIA

Devonian peralkaline granites with either sodic or sodic-calcic amphibole, are also found in SE New England (Quincy Granite) and in the Antigonish Highlands (West Barneys River and Brora Lake plutons) (Sayer, 1974; Escarraga et al., 2012). The Antigonish peralkaline granites have the strongest negative Eu anomalies and show the highest REE-enrichment compared to the other A-type granites of the area. Furthermore, they present similar isotopic characteristics with the coeval mafic rocks, and a comagmatic relationship between the two has been proposed (Escarraga et al., 2012), consistent with the character of the Wentworth sodic granites. A similar pattern has been described for the early Devonian Quincy Granite in SE New England (Sayer, 1974). The peralkaline granites have been described to have more pronounced negative Eu anomalies and enrichment in Zr, Yb, Hf and Ta relative to other coeval granites of the area (Sayer, 1974). Therefore, throughout west Avalonia, the late Paleozoic peralkaline granitic melts point to a common petrogenetic origin associated with fractionation of coeval mafic melts.

5.4.2 LATE PALEOZOIC HYDROTHERMAL CIRCULATION AND MINERALIZATION

Closure of the Rheic Ocean continued through the Mississippian to Pennsylvanian and culminated in collision between Laurussia and Gondwana during the late Carboniferous Alleghanian orogeny, resulting in the formation of Pangaea (Domeier and Torsvik, 2014). In the Cobequid Highlands, the latest phase of ductile deformation recorded in the plutons occurred at ca 339 Ma (Murphy et al., 2011). During that time,

the master faults of the Cobequid Shear Zone record dextral shear associated with the precipitation of hydrothermal biotite (Pe-Piper et al., 2004). In the early Pennsylvanian (~320 Ma), an intense phase of deformation is evident along the southern and northern margins of the Cobequid Highlands. Structures in these areas indicate transpressional strain and shortening during dextral shear (MacInnes and White, 2004). From that period until late Pennsylvanian, the Cobequid-Chedabucto Fault Zone records mylonitization and focussed mineralization (Murphy et al., 2011).

Although the regional character of Pennsylvanian mineralization in the Cobequid Highlands is predominantly IOCG (MacHattie and O'Reilly, 2009), this thesis demonstrated that it was also associated with hydrothermal circulation of rare metals through fractures. The circulation of these metals was long-lived, and the association of minerals such as thorite and hydroxylbastnäsite-(Ce) with hydrothermal epidote and biotite indicates that the precipitation of these minerals started probably in the Visean, as demonstrated in chapter 4. The sources for REE in these fluids were the A-type granites of the area, with primary enrichment by the presence of various magmatic REE-minerals such as allanite-(Ce) and chevkinite-(Ce) (Papoutsa and Pe-Piper, 2013). The mobilization of REE was probably initiated by complexing with F during the breakdown of amphiboles (Pe-Piper, 2007; Papoutsa and Pe-Piper, 2013). Although mobilization of these metals can be facilitated by the presence of halogens and S, their precipitation can be controlled by the oxidation state of the fluids.

The hydrothermal behavior of the REE metals throughout the Cobequid Highlands revealed two major characteristics of the regional system: a) the chemistry of the fluids and consequently the hydrothermal REE-minerals was greatly influenced by

lithologies in both source and depositional areas such as carbonates and shales of the Horton Group that provided C and As and possibly lamprophyres that provided Cl, F and S, and b) as the chemistry of the fluids changed over time and so did the abundance and variety of the REE-minerals. The presence of carbonates and As-rich REE-minerals points to additional sources for C and As from the sedimentary rocks of the Horton Group. On the other hand, precipitation most REE-minerals, as reported in this thesis, was associated with Fe-rich hydrothermal assemblages that are probably related to the Pennsylvanian IOCG mineralization. Important variations in the distribution of the hydrothermal REE-minerals reveal structural changes related to the evolution of the major faults of the shear zone. The lack of substantial hydrothermal REE-minerals in fractures in the Wentworth pluton indicates that the Rockland Brook fault was probably not active during late Carboniferous REE circulation.

Murphy et al. (2011) argued that the Cobequid-Chedabucto Fault Zone was a metallotect, a large-scale crustal structure that controls mineralization. Micklethwaite and Cox (2004) demonstrated that in ancient fault systems, hydrothermal mineralization is focused is areas of rupture arrest. In this process, when an earthquake occurs on a fault the aftershocks are mainly distributed in areas of stress transfer around the seismogenic fault rupture. Such areas form where older faults are linked with younger segments. This process results in the formation of areas with transient permeability and localized fluid flow (Micklethwaite and Cox, 2004). Such relationships may be present in the Cobequid-Chedabucto Fault Zone. The Bass River magnetite deposit lies south of the Pleasant Hills pluton and adjacent to the area where the older Rockland Brook fault merges with the younger Cobequid fault (Pe-Piper and Piper, 2003; MacHattie and O'Reilly, 2008). The

Londonderry iron deposit is located between the Londonderry and Cobequid faults. The Mount Thom (Cu-Co-Au), Brookfield (Ba), and Bridgeville (Fe) deposits are located along the part of the fault zone where the Cobequid fault merges with the younger Chedabucto fault (MacHattie and O'Reilly, 2008). Thus the correlation between the distribution of known IOCG deposits and areas of potential rupture release, along the Minas Fault Zone, may reveal a genetic relationship between the two. Such a correlation, along with the hydrothermal distribution of REE reported in this thesis, could provide guidelines for REE mineral exploration.

CHAPTER 6 DISCUSSION AND CONCLUSIONS

6.1 POST-OROGENIC VERSUS ANOROGENIC A-TYPE GRANITE SUITES: VARIATIONS IN MAGMA SOURCES AND PETROGRAPHY OF GRANITES

A-type granites belong to a distinct group of granitoids which is characterized by alkaline geochemical character and elevated concentrations of incompatible elements (Loiselle and Wones, 1979). These granitoids are reported from both anorogenic and post-orogenic tectonic environments (Whalen et al., 1986). Examples of anorogenic granites include the Younger Granites in Nigeria (Ogunleye et al., 2005), south India (Ambalavayal granite, Rajesh, 2000), Canada (Sept Iles granites in Quebec, Namur et al., 2011), Brazil (Redenção granite, Oliveira et al., 2009), and Yemen Republic (El-Gharbawy, 2010). Post-orogenic A-type granites, besides from the areas described in this thesis, are reported from several parts of the world such as southern Brazil (Serra da Graciosa Province, Gualda and Vlach, 2006), several intrusions in SE China (Xie et al., 2006), NW China (Karamaili granites, Su et al., 2007), Australia (Lachlan fold belt and New England belt, as reviewed in Sylvester, 1989) and Newfoundland (Topsails suite, Whalen et al., 1996).

Anorogenic A-type magmatism follows a major orogenic event after more than 100 Ma and is not directly related to the after effects of orogeny (Condie, 1991). The emplacement of post-orogenic A-type granites, on the other hand, is mostly observed during the final orogenic stages during continent-continent collision dominated by transcurrent-fault tectonics during accretion of continental blocks or terranes (Bonin et al., 1998), as in the Appalachians and the Central Asian Orogenic Belt (Keppie and Dallmeyer, 1987; Windley et al., 2007). Anorogenic A-type granites are mostly found in

the interior of stable areas such as the Amazonian craton and the Arabian Shield (Oliveira et al., 2009; El-Gharbawy, 2010).

In anorogenic environments the dominant variety of A-type granite is the peralkaline type with sodic amphibole or pyroxene. Metaluminous A-type granites with calcic amphibole and biotite are much less common (Rajesh, 2000; Ogunleye et al., 2005; El-Gharbawy, 2010). The higher magmatic temperatures and primitive isotopic signatures of the peralkaline granites are evidence of fractionation from mafic melts, whereas the metaluminous varieties have been interpreted to reflect either less evolved melts or products of crustal contamination (Oliveira et al., 2009; Namur et al., 2011).

A-type granites emplaced in post-orogenic settings include peralkaline, metaluminous and peraluminous rocks (King et al., 1997; Gualda and Vlach, 2006). The metaluminous and peraluminous A-type granites generally dominate over the peralkaline varieties. The metaluminous and peraluminous A-type granites form by melting of crustal rocks (Creaser, 1991) and consequently tend to be more K and LILE-rich (Bonin et al., 1998; Li, 1998).

In the Cobequid Highlands, the emplacement of mainly metaluminous and peraluminous rather than peralkaline A-type granites in the latest Devonian-earliest Carboniferous constitutes a typical example of post-orogenic A-type magmatism that followed the early Devonian Acadian orogeny. These late Paleozoic granites present distinct geochemical and mineralogical differences which can be observed in A-type granites in similar settings elsewhere, such as the variations in ferromagnesian minerals and trace elements.

6.2 IMPACT OF THE CRUSTAL STRUCTURE ON THE POST-OROGENIC A-TYPE GRANITES

A common feature in several post-orogenic A-type granite suites appears to be the association with major strike-slip shear zones. The association of post-orogenic A-type granites with crustal-scale shear zones suggests that the strike-slip faults in the lower crust provide pathways for a) the mafic melts to substantially interact with the crust, and b) for the produced felsic melts to effectively migrate in upper crustal levels and produce the large variety of A-type granites. Such crustal-scale strike-slip systems have been reported from the Aegean area where the deformational fabric appears to extend to the lithospheric mantle (Endrun et al., 2011). Such crustal structures provide favourable conditions for interaction of the upper mantle with the lower crust and therefore can create a deep crustal hot zone (Annen and Sparks, 2002).

In the Cobequid Highlands, mafic rocks are most abundant in the eastern plutons, where sodic, calcic, and biotite granites are present. Elsewhere, variations in the abundance of mafic rocks also appear to be correlated with the mineralogical types of A-type granites present. The peraluminous Barabazar biotite A-type granites in India were emplaced along the faults of the reactivated South Purulia Shear Zone (Dwivedi et al., 2011). Mafic rocks are very limited (Dwivedi et al., 2011) and biotite granite is the only A-type granite present. Seltmann et al. (2000) reported metaluminous biotite and calcic granites along crustal-scale strike-slip shear zones in Kokshaal Range, Kyrgyzstan, with associated tholeiitic mafic rocks of asthenospheric origin. A large mineralogical variety of A-type granites were reported from southern Brazil, where several post-orogenic A-type granites were emplaced along the Southern Brazilian Shear Belt along with abundant

mafic rocks (Bitencourt and Nardi, 1993). Metaluminous biotite A-type granites are the dominant lithology with lesser calcic granites with edenitic amphibole (Nardi and Bitencourt, 2009). Sodic A-type granites are also present, and occur only as late phases coeval with mafic rocks of alkaline affinity, that are considered cogenetic (Nardi and Bitencourt, 2009). The variety in the mineralogy of A-type granites in post-collisional settings, therefore, may depend on whether there is abundant mafic magma to produce calcic amphibole and sodic amphibole granites.

Besides the necessary lithologies as magmatic sources for the late Paleozoic A-type granites of the Cobequid Highlands, the deep Avalonian crust also had the structure necessary to create the deep crustal hot zone. The crustal-scale faults were active in the late Paleozoic but their origin may be much older than that (Pe-Piper and Piper, 2003). Pe-Piper and Piper (1998b) demonstrated on the basis of radiogenic isotope data that the Neoproterozoic basement north and south of the Rockland Brook and Kirkhill faults has a different signature. Miller (1991) recognized structures along the Rockland Brook fault that suggest it is a Neoproterozoic reactivated fault, which is consistent with the syn-magmatic deformation of dated Neoproterozoic plutons of the area (Pe-Piper et al., 1996). As reviewed in chapter 5, this Neoproterozoic lineament separates blocks with differences in stratigraphy (MacHattie and White, 2012) as well as in chemistry.

Comparison between the two Neoproterozoic blocks in the Cobequid Highlands with other parts of west Avalonia, suggests that the Bass River block is similar to the basement of SE New England, whereas the Jeffers Block resembles typical proto-Avalonian crust as exposed in the Antigonish Highlands. The available paleomagnetic data and the nature of Neoproterozoic magmatism in these terranes suggests that SE New

England and the Bass River block may have an Avalonian affinity and did not originate within proto-Avalonia. If this is correct, then the Rockland Brook fault may not have originated as a Neoproterozoic intra-plate fault, but as a suture zone. In the case of the latter, the crustal scale of this lineament not only reflects the boundaries between different Neoproterozoic crustal fragments, but also influenced the deformation in the area millions of years later.

The creation of a deep crustal hot zone soon after the main phase of orogeny could explain the variability in A-type granites that is commonly observed in post-orogenic environments. The different processes, such as crustal melting and fractionation of mafic melts that result in the production of felsic melts (Annen and Sparks, 2006) may be responsible for the contrasting conditions and sources in the A-type granites in these environments (Bonin, 2004). The injected mafic melts will provide the heat necessary to create crustally-derived (Annen and Sparks, 2002) metaluminous and peraluminous A-type granites, whereas the peralkaline A-type granites (or sodic granites in this thesis) are produced through fractionation of these mafic melts. Part of the mantle-derived melts has to remain uncontaminated in order to fractionate and produce peralkaline granites. It is, therefore, not surprising that peralkaline A-type granites are the least common variety in post-orogenic settings (Bonin 2004).

The proposed petrogenetic model for the late Paleozoic A-type granites of the Cobequid Highlands includes, thus, both partial melting of feldspathic crustal rocks and extreme fractionation of a mafic source. The substantial mafic underplating and the voluminous coeval flood basalts and gabbros are associated with the genesis of the sodic granites as demonstrated in chapter 3.The reason for the observed variation in these post-

orogenic granite suites is principally because these geological processes were synchronous. These processes took place in a deep crustal hot zone that was created beneath the eastern Cobequid Highlands, during late Paleozoic mafic underplating, and associated with crustal extension in the Magdalen Basin (Fig. 3.14). While the calcic granites formed by relatively less hydrated melts compared to the biotite granites, and closer to the underplated area, the latter formed further to the west at lower magmatic temperatures. Partial melting for the biotite granites, however, was facilitated by the presence of additional water released from the volcaniclastic rocks of the Neoproterozoic Jeffers Group, which is abundant in the area (Fig. 3.14).

The A-type granites in the Cobequid Highlands comprise not only ferroan compositions, which are typical of A-type granites (Frost and Frost, 2010), but also magnesian compositions (Fig. 6.1). These magnesian compositions do not correspond to a specific mineralogical type but include biotite and calcic granites from all plutons. Frost and Frost (2010) noted that oxidized A-type granites from the literature tend to be magnesian, whereas the strongly reduced A-type granites are ferroan. As demonstrated in chapter 3, all the granites belong to the magnetite series and are therefore created under oxidizing conditions. Thus there is no convincing evidence that the ferroan and magnesian affinity of these rocks is the result of variations of the oxidation state of the parent melt. On the other hand, a significant difference of the source or magma mixing for the magnesian biotite and calcic granites is not supported by isotope data and trace element geochemistry as explained in chapter 3. Experimental work on partial melting of crustal rocks of Patiño-Douce (1997) demonstrated that with increasing pressure (>8 kbar) the produced melts will change from ferroan to magnesian compositions with a

peraluminous affinity. High pressures during partial melting may have been responsible for the magnesian A-type granites in the Cobequid Highlands. According to the estimated pressures (plag-melt) of these granites partial melting of the crust took place over a range of pressures (7-15 kbar), and based on the estimated thickness of the Avalonian crust (Marillier and Reid, 1990), it is suggested that the partial melting that produced the biotite and calcic granites took place in the mid- to lower crust.

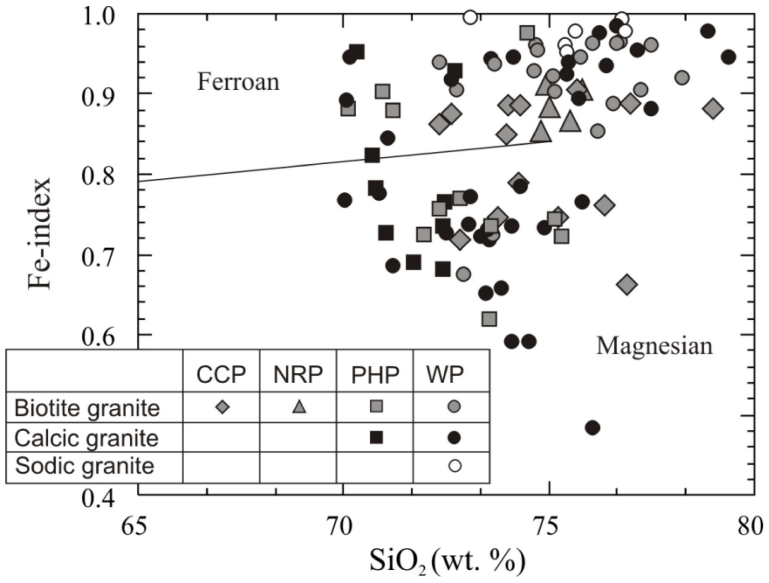

Figure 6. 1 Ferroan vs. magnesian affinity of the A-type granites in the Cobequid Highlands (as defined from Frost and Frost, 2010).

6.3 REE-ENRICHMENT AND MINERALIZATION IN A-TYPE GRANITES

A-type granites are characteristically enriched in REE and other incompatible elements (Loiselle and Wones, 1979; Whalen et al., 1989). This is an important geochemical feature of these rocks, since A-type intrusions are often associated with economic deposits of these metals. There are several studies that demonstrate a magmatic REE-enrichment of A-type granites on the basis of primary mineralogical assemblages

(Schmitt et al., 2001; Vlach and Gualda, 2007; Uher et al., 2009). Such an enrichment, however, is not as evident from whole-rock geochemistry alone. Among the studied plutons, the Wentworth pluton best records a primary enrichment, expressed by the presence of magmatic allanite-(Ce) and chevkinite-(Ce) (Papoutsa and Pe-Piper, 2013). In chapter 4 is demonstrated that although REE-enriched, the granites of the Pleasant Hills, North River and Cape Chignecto plutons host predominantly hydrothermal REE-mineral assemblages that are found in fractures.

The structure of the crust, dominated by crustal scale strike-slip faults, not only had an impact on the genesis of A-type granites as discussed above, but it also had a profound effect on the intrusions and surrounding rocks in post-magmatic stages, as demonstrated in chapter 4.Textural relationships and mineral associations provide evidence of repeated REE hydrothermal circulation that resulted to the formation of several types of minerals, such as hydroxylbastnäsite-(Ce), parisite-(Ce), synchysite-(Ce), cerite, thorite, hingannite-(Y), chernovite-(Y) and Nb-rich minerals, in several generations. Hydroxylbastnäsite-(Ce) and thorite were among the first REE-minerals to precipitate in epidote veins in the eastern part of the Cobequid Highlands, under rather reducing conditions, probably soon after the emplacement of the granites. The majority of the REE-minerals, such as cerite, parisite-(Ce), synchysite-(Ce) and hingganite-(Y), are hosted in chlorite-magnetite and biotite veins in the central and western parts of the Cobequid Highlands. These minerals were deposited in the Visean according to published ages from hydrothermal biotite in the area. The highest abundances of hydrothermal REE-minerals are observed in late magnetite-rich veins, formed under strongly oxidizing conditions, in the central part of the Cobequid Shear Zone close to the Cobequid fault. In

such veins, chernovite-(Y) formed after the alteration of hydrothermal hingganite-(Y). These iron-rich hydrothermal assemblages may be related to the regional iron oxide-copper-gold IOCG hydrothermal circulation and mineralization event that is observed along the Cobequid-Chedabucto fault zone.

The association of REE with IOCG mineralization and A-type granites has been observed not only in Nova Scotia (Copper Lake, Kontak et al., 2009) but has also been reported from other parts of the world, such as in NW China (Pirajno et al., 2008) and south Australia (Elburg et al., 2012). Massive IOCG deposits throughout the Bushveld Complex are associated with LREE circulation that is represented by the mineral association of fluorite, copper, barite, gold and U-LREE minerals in strongly chloritized granitic rocks (Hunt, 2005). As in the Cobequid Highlands, the IOCG mineralization in Bushveld shows multiple episodes of hydrothermal alteration including potassic alteration, sericitisation and silicification. Sodic-calcic alteration in IOCG systems is commonly observed as an early stage alteration and can be transitional to a more K-rich alteration and chloritization when conditions become more oxidizing (Dilles et al., 2000; Kreiner, 2011). The association of calcic phases with hydrothermal biotite (calc-potassic alteration), which is observed in the Pleasant Hills pluton, is interpreted to form from moderate temperature fluids, whereas the presence of scapolite with biotite is considered a relatively low-temperature assemblage (Barton, 2014 and references therein). Extensive sodic alteration followed by potassic alteration and then by pervasive Fe-rich circulation is also reported from Wernecke Breccia in Yukon Territory (Hunt et al., 2005).

It appears, thus, that in several IOCG systems (Mt.Mainter-Mt. Babbage Inliers and Olympic Dam-Australia, Carajás Mineral Province in Brazil, Yukon Territories,

Cobequid Highlands) the hydrothermal fluids changed progressively from Na-Ca rich to K-rich to Fe-rich (Hunt et al., 2005; Groves et al., 2010; Elburg et al., 2012). The circulation of REE during IOCG events depends principally on the presence of suitable sources for these elements, such as alkaline magmatic rocks (Corriveau, 2007). In the granites of the Cobequid Highlands the replacement textures of hydrothermal phases on primary REE-minerals (Papoutsa and Pe-Piper, 2013) suggest that these rocks were the main sources of REE in the regional hydrothermal system. Kontak et al. (2009) reported the hydrothermal circulation of REE in the IOCG-associated Copper Lake Deposit, from the presence of monazite in sulfide-rich veins. The deposit is near an Ordovician A-type pluton in the Antigonish Highlands (Escarraga et al., 2012), which could have been the source of REE. The conditions of the REE-circulation and especially precipitation, however, are controlled by the progressive changes in the hydrothermal fluids, as documented in this thesis (Fig. 4.7).

As Midgisov and Williams-Jones (2014) argued, it is important for the REE not to be removed from the fluids in early stages through precipitation of highly insoluble phases, in order to reach the latest stages of hydrothermal circulation and consequently IOCG mineralization. Phases such as REE-oxides and REE-chlorides are highly soluble from reducing to weakly oxidizing conditions, however REE-fluorides may be insoluble in a range of conditions (Midgisov et al., 2009). This is compatible with the distribution of hydrothermal REE-minerals in the fractures of the Cobequid Highlands. The first REE-oxides precipitated probably during biotization (Fig. 4.7), when the fluids became weakly oxidizing. Post-Visean the hydrothermal fluids were probably saline as indicated by the presence of scapolite in the western Cobequid Highlands (Owen and Greenough,

1999) and the halogen-rich biotites of fractured mafic sills just north of the Cobequid fault in the central part of the area (Wisen, 2015). The presence of hydrothermal fluorite in calcite-rich fractures (Wisen, 2015) suggests that during the late hydrothermal stages the solubility of fluorite was limited, and that may also have influenced the solubility of the REE leading to significant precipitation of REE-minerals (Fig. 4.7).

Another feature of the hydrothermal circulation in the Cobequid Highlands is that the increase in REE concentrations in the fractures was accompanied by an increase in temperature as well (Fig. 4.7). The stability of REE-complexes correlates positively with temperature, and therefore high-temperature saline solutions can efficiently transport REE (Gieré, 1996). Such a transport of REE is indicated in the Cobequid Highlands after the Visean, since REE-hydrothermal mineral assemblages are found throughout the shear zone and in various lithologies beyond the borders of the A-type granite plutons (Wisen, 2015). Such late-stage REE circulation in IOCG systems is associated with Fe-oxides (Williams et al., 2005). It is mainly governed by the changes in the hydrothermal fluids (composition, temperature, oxidation state) compared with early stages that consequently affect the solubility of REE-complexes.

6.4 CONCLUSIONS

The original definition of the term “A-type” as proposed by Loiselle and Wones (1979) appears to concur with anorogenic A-type granites, the peralkaline geochemistry of which indicates a significant mantle input. In post-orogenic settings, however, the produced “A-type” granites are principally metaluminous and peraluminous with higher amounts of LILE and involve mainly crustal sources. Peralkaline granites may occur in

post-orogenic settings as well, as in the Cobequid Highlands, where the sodic granites have predominantly a mantle-derived source.

The presence of crustal-scale strike-slip systems in post-orogenic settings, during extension and partial melting of the mantle that results in mantle upwelling, creates the conditions for the formation of deep crustal hot zones. The distribution of the various mineralogical types of A-type granites seems to be associated with the abundance of coeval mafic melts. The variability in the produced A-type granites in these environments may be, therefore, due to the more effective penetration of mafic magma into the fabric of the lower crust. Thus the dominant varieties of A-type granites in these settings have a crustal signature. Partial melting of the crust in these zones may occur in a range of depths from middle to lower crust and under variable pressure. The magnesian affinity of many A-type granites could, therefore be related to their derivation from a deep crustal hot zone.

Assessment and evaluation of REE-enrichment in the A-type granites must be done always in association with a mineralogical investigation since, as has been demonstrated in the Cobequid Highlands, such an enrichment is not necessarily a primary feature. The widespread hydrothermal REE remobilization and their concentration primarily in fractures across the Cobequid Shear Zone may lead to the local potential for ore bodies. It appears that the changes in the conditions of the hydrothermal fluids with time are similar to IOCG systems elsewhere. However, whether this similarity is due to local details of the geological history or a consequence of a general set of processes remains unclear.

REFERENCES

Abraham, A.P.G., and Spooner, E.T.C., 1995, Late Archean regional deformation and structural controls on gold-quartz vein mineralization in the northwestern Slave Province, N.W.T., Canada: Canadian Journal of Earth Sciences, v. 32, p. 1132-1154.

Acaster, M., and Bickford, M.E., 1999, Geochronology and geochemistry of Putnam-Nashoba terrane metavolcanic and plutonic rocks, eastern Massachusetts: Constraints on the early Paleozoic evolution of eastern North America: Geological Society of America Bulletin, v. 111, p. 240-253.

Aignertorres, M., Blundy, J., Ulmer, P., and Pettke, T., 2007, Laser Ablation ICPMS study of trace element partitioning between plagioclase and basaltic melts: an experimental approach: Contributions to Mineralogy and Petrology, v. 153, p. 647-667.

Al'meev, R.R., and Ariskin, A.A., 1996, Mineral-melt equilibria in a hydrous basaltic system: Computer modeling: Geochemistry International, v. 34, p. 563-573.

Anderson, D.L., 1998, The EDGES of the Mantle: Geodynamics, v. 28, p. 255-271.

Anderson, J.L., and Smith, D.R., 1995, The effects of temperature and fO_2 on the Al-in-hornblende barometer: American Mineralogist, v. 80, p. 549-559.

Anderson, D.L., and Natland, J.H., 2014, Mantle updrafts of oceanic volcanism: Proceedings of the National Academy of Sciences of the United States, v. 111, p. 4298-4304.

Annen, C., and Sparks, R.S.J., 2002, Effects of repetitive emplacement of basaltic intrusions on thermal evolution and melt generation in the crust: Earth and Planetary Science Letters, v. 203, p. 937-955.

Annen, C., Blundy, J.D., and Sparks, S.J., 2006, The genesis of intermediate and silicic magmas in deep crustal hot zones: Journal of Petrology, v. 47, p. 505-539.

Armbruster, T., Bonazzi, P., Akasaka, M., Bermanec, V., Chopin, C., Gieré, R., Heuss–Assbichler, A., Liebscher, A., Menchetti., S., Pan, Y., and Pasero., M., 2006, Recommended nomenclature of epidote–group minerals: European Journal of Mineralogy, v. 18, p. 551–567.

Armstrong, J.T., 1988, Quantitative analysis of silicates and oxide minerals: Comparison of Monte-Carlo, ZAF and Phi-Rho-Z procedures, in: Newbury, D.E. (Ed.), Microbeam Analysis. San Francisco Press Inc., San Francisco, pp. 239-246.

Bacon, C.R., and Druitt, T.H., 1988, Compositional Evolution of the Zoned Calcalkaline Magma Chamber of Mount Mazama, Crater Lake, Oregon: Contributions to Mineralogy and Petrology, v. 98, no. 2, p. 224-256.

Baker, D.R., Conte, A.M., Freda, C., and Ottolini, L., 2002, The effect of halogens on Zr diffusion and zircon dissolution in hydrous metaluminous granitic melts: Contributions to Mineralogy and Petrology, v. 142, p. 666-678.

Balintoni, I., and Balica, C., 2013, Avalonian, Ganderian, and East Cadomian terranes in South Carpathians, Romania, and Pan-African events recorded in their basement: Mineralogy and Petrology, v. 107, p. 709-925.

Bailey, R.H., Skehan, J.W., Dreier, R.B., and Webster, M., 1989, Olistostromes of the Avalonian terrane of southeastern New England, in Horton, J.W., Jr., and Rast, N. (eds) Melanges and olistostromes of the U.S. Appalachians: Geological Society of America Special Paper 228, p. 93-112.

Barr, S.M., and Raeside, R.P., 1989, Tectono-stratigraphic terranes in Cape Breton Island, Nova Scotia: Implications for the configuration of the northern Appalachian orogen: Geology, v. 17, p. 822-825.

Barr, S.M., Brisebois, D., and MacDonald, A.S., 1985, Carboniferous volcanic rocks of the Magdalen Islands, Gulf of St. Lawrence: Canadian Journal of Earth Sciences, v. 22, p. 1679-1688.

Barr, S.M., Raeside, R.P., and White, C.E., 1998, Geological correlations between Cape Breton Island and Newfoundland, northern Appalachian Orogen: Canadian Journal of Earth Sciences, v. 35, p. 1252-1270.

Barr, S.M., White, C.E., and Miller, B.V., 2003, Age and geochemistry of the late Neoproterozoic and early Cambrian igneous rocks in southern New Brunswick: similarities and contrasts: Atlantic Geology, v. 39, p. 55-73.

Barr, S.M., Hamilton, M.A., Samson, S.D., Satkoski, A.M. and White, C.E., 2012, Provenance variations in northern Appalachian Avalonia based on detrital zircon age patterns in Ediacaran and Cambrian sedimentary rocks, New Brunswick and Nova Scotia, Canada: Canadian Journal of Earth Sciences, v. 49, p. 533-546.

Barr, S.M., White, C.E., and Ketchum, J.W.F., 2012, The Cape Porcupine Complex, northern mainland Nova Scotia- no longer a geological orphan: Atlantic Geology, v. 48, p. 70-85.

Barton, M.D., 2014, Iron oxide(-Cu-Au-REE-P-Ag-U-Co) systems: Treatise on Geochemistry, 2nd edition, Volume 11, Chapter 23, Elsevier, p. 515-541.

Beattie, P., 1993, The effect of partial melting of spinel peridotite on uranium series disequilibria: constraints from partitioning studies: Earth and Planetary Science Letters, v. 177, p. 379-391.

Beattie, P., 1994, Systematics and energetics of trace-element partitioning between olivine and silicate melts: Implications for the nature of mineral/melt partitioning: Chemical Geology, v. 117, p. 57-71.

Bettencourt, J.S., Leite Jr., W.B., Goraieb, C.L., Sparrenberger, I., Bello, R.M.S., and Payolla, B.L., 2005, Sn-polymetallic greisen type deposits associated with late stage rapakivi granites, Brazil: fluid inclusion and stable isotope characteristics: Lithos, v. 80, p. 363-386.

Belperio, A.P., 2010, Nova Scotia IOCG project: Minotaur Exploration Ltd, Open file report 2010–004, NS Dept. of Natural Resources.

Bento dos Santos, T.M., Tassinari, C.C.G., and Fonseca, P.E., 2015, Diachronic collision, slab break-off and long-term high thermal flux in the Brasiliano–Pan-African orogeny: Implications for the geodynamic evolution of the Mantiqueira Province: Precambrian Research, v. 260, p. 1-22.

Bevier, M.L., and Barr, S.M., 1990, U–Pb constraints on the stratigraphy and tectonic history of the Avalon terrane, New Brunswick, Canada: The Journal of Geology, v. 98, p. 53-63

Bindeman, I., and Davis, A., 2000, Trace element partitioning between plagioclase and melt: Investigation of dopant influence on partition behavior: Geochimica et Cosmochimica Acta, v. 64, p. 2863-2878.

Bindeman, I.N., Davis, A.M., and Drake, M.J., 1998, Ion microprobe study of plagioclase-basalt partition experiments at natural concentration levels of trace elements: Geochimica et Cosmochimica Acta, v. 62, p. 1175-1193.

Bird, D.K., and Helgenson, H.C., 1981, Chemical interaction of aqueous solutions with epidote–feldspar mineral assemblages in geologic systems. 1. Thermodynamic analysis of phase relations in the system $CaO–FeO–Fe_2O_3–Al_2O_3–SiO_2–H_2O–CO_2$: American Journal of Science, v. 280, p. 907–941.

Bitencourt, M.F., and Nardi , L.V.S., 1993, Late to post-collisional Brasiliano granitic magmatism in southernmost Brazil: Anais de Academia Brasileira de Ciências, v. 65, p. 3-16.

Bhargava, S.K., Garg, A., and Subansinghe, N.D., 2010, In situ high–temperature transformation phase transformation studies on pyrite. Fuel, v. 88, p. 988–993.

Boehnke, P., Watson, E.B., Trail, D., Harrison, T.M., and Schmitt, A.K., 2013, Zircon saturation re-revisited: Chemical Geology, v. 352, 324-334.

Bonin, B., 2004, Do coeval mafic and felsic magmas in postcollisional to within-plate regimes necessarily imply two contrasting, mantle and crustal, sources? A review: Lithos, v. 78, p. 1–24.

Bonin, B., 2007, A-type granites and related rocks: Evolution of a concept, problems and prospects: Lithos, v. 97, p. 1-29.

Bonin, B., Azzouni -Sekkal, A ., Bussy, F., and Ferrag, S., 1998, Alkali-calcic and alkaline post-orogenic (PO) granite magmatism: petrologic constraints and geodynamic settings: Lithos, v. 45, p. 45-70.

Borrok, D.M., Boer, R.H., and Essene, E.J., 1998, The Vergenoeg magnetite–fluorite deposit, South Africa: support for a hydrothermal model for massive iron oxide deposits: Economic Geology, v. 93, p. 564–586.

Boudreau, A.E., 1999, PELE− a version of the MELTS software program for the PC platform: Computers and Geosciences, v. 25, p. 201-203.

Bougault, H., and Hekinian, R., 1974, Rift valley in the Atlantic Ocean near 36 degrees 50'N; petrology and geochemistry of basalt rocks: Earth and Planetary Science Letters, v. 24, p. 249-261.

Bradshaw, T.K., 1992, The adaptation of Pearce element ratio diagrams to complex high silica systems: Contributions to Mineralogy and Petrology, v. 109, p. 450-458.

Breiter, K., Gardenová, N., Kanický, V., and Vaculovič, T., 2013, Gallium and germanium geochemistry during magmatic fractionation and post-magmatic alteration in different types of granitoids: a case study from the Bohemian Massif (Czech Republic): Geologica Carpathica, v. 64, p. 171-180.

Brimhal, G.H., Agee, C., and Stroffregen, R., 1985, The hydrothermal conversion of hornblende to biotite: The Canadian Mineralogist, v. 23, p. 369–379.

Brown, L.L., and McEnroe, S.A., 2004, Paleomagnetism of the Egersund-Ogna anorthosite, Rogaland, Norway, and the position of Fennoscandia in the late Proterozoic: Geophysical Journal International, v. 158, p. 479-488.

Bunge, H., and Grand, S., 2000, Mesozoic plate-motion history below the northeast Pacific Ocean from seismic images of the subducted Farallon slab: Nature, v. 405, p. 337-340.

Buma, G., Frey, F.A., and Wones D.R., 1971, New England granites: trace element evidence regarding their origin and differentiation: Contributions to Mineralogy and Petrology, v. 31, p. 300-320.

Butler, R.W.H., Holdsworth, R.E., and Lloyd, R.E., 1997, The role of basement reactivation in continental deformation: Journal of the Geological Society, London, v. 154, p. 69-71.

Cardoza, K.D., Hepburn, J.C., and Hon, R., 1990, Geochemical constraints on the paleotectonic settings of two late Proterozoic mafic volcanic suites, Boston Avalon zone, eastern Massachisetts *in*: Socci, A.D., Skehan, J.W., and Smith, G.W. (eds) Geology of the composite Avalon Terrane of southeastern New England: Geological Society of America Special Paper 245, p. 113-131.

Castro, A., Patiño Douce, A.E., Corretgé, L.G., de la Rosa, J.D., El-Biad, M., and El-Hmidi, H., 1999, Origin of peraluminous granites and granodiorites, Iberian massif, Spain: an experimental test of granite petrogenesis: Contributions to Mineralogy and Petrology, v. 135, p. 255-276.

Cathelineau, M., and Nieva, D., 1985, A chlorite solid solution geothermometer: The Los Azufres (Mexico) geothermal system: Contributions to Mineralogy and Petrology, v. 91, p. 235–244.

Cawood, P.A., McCausland, P.J.A., and Dunning, G.R., 2001, Opening Iapetus: Constraints from the Laurentian margin in Newfoundland: Geological Society of America Bulletin, v. 113, p. 443-453.

Chakhmouradian, A.M., and Wall, F., 2012, Rare Earth Elements: minerals, mines, magnets (and more): Elements, v. 8, p. 333–346.

Chappell, B.W., and White, A.J.R., 1974, Two contrasting granite types: Pacific Geology, v. 8, p. 173-174.

Chevychelov, V.Yu., Botcharnikov, R.E., and Holtz, F., 2008, Experimental study of fluorine and chlorine contents in mica (biotite) and their partitioning between mica, phonolite melt, and fluid: Geochemistry International, v. 46, p.1081-1089.

Clarke, D.B., MacDonald, M.A., and Tate, M.C., 1997, Late Devonian mafic-felsic magmatism in the Meguma Zone, Nova Scotia, in the nature of magmatism in the Appalachian orogeny: Geological Society of America Memoir, v. 191, p. 107-127.

Clemens, J.D., Holloway, J.R., and White, A.J.R., 1986, Origin of an A-type granite: Experimental constraints: American Mineralogist, v. 71, p. 317-324.

Clowe, C.A., Popp, R.K., and Fritz, S.J., 1988, Experimental investigation of oxygen fugacity on ferric-ferrous ratios and unit-cell parameters of four natural clinoamphiboles: American Mineralogist, v. 73, p. 487-499.

Cocks, L.R.M., and Fortey, R.A., 1982, Faunal evidence for oceanic separations in the Paleozoic of Britain: Journal of the Geological Society, v. 139, p. 465-480.

Collins, W.J., Beams S.D., White, A.J.R., and Chappell, B.W., 1982, Nature and origin of A-type granites with particular reference to southeastern Australia: Contributions to Mineralogy and Petrology, v. 80, p. 189-200.

Condie, K.C., 1991, Precambrian granulites and anorogenic granites: are they related?: Precambrian Research, v. 51, p.161–72.

Corriveau, L., 2007, Mineral deposits of Canada: iron oxide copper-gold deposits: A Canadian Perspective *in:* Mineral deposits of Canada: a synthesis of major deposit-types, district metallogeny, the evolution of geological provinces, and exploration methods, Goodfellow, W.D. Special Publication no. 5. Geological Association of Canada, Mineral Deposits Division. p. 307–328.

Cosca, M. A., Sutter, J. F., and Essene, E. J., 1991, Cooling and inferred uplift/erosion history of the Grenville Orogen, Ontario: Constraints from $^{40}Ar/^{39}Ar$ thermochronology: Tectonics, v. 10, p. 959–977.

Costi, H.T., Dall'Agnol, R., Pichavant, M., and Rämö, O.T., 2009, The peralkaline tin-mineralized Madeira cryolite albite-rich granite of Pitinga, Amazonian Craton, Brazil: petrography, mineralogy, and crystallization processes: The Canadian Mineralogist, v. 47, p. 1301–1327.

Creaser, R.A., Prince, R.C., and Wormald, R.J., 1991, A-type granites revisited: assessment of a residual source model: Geology, v. 19, p. 163-166.

D'Agrella-Filho, M.S., Pacca, I.I.G., Trindade, R.I.F., Texeira, W., Raposo, M.I.B., and Onstott, T.C., 2004, Paleomagnetism and $^{40}Ar/^{39}Ar$ ages of mafic dykes from Salvador (Brazil): new constraints on the São Fransisco craton APW path between 1080 and 1010 Ma: Precambrian Research, v. 132, p. 55-77.

D'Agrella-Filho, M.S., Tohver, E., Santos, J.O.S., Elming, S.-Å., Trindade, R.I.F., Pacca, I.I.G., and Geraldes, M.C., 2008, Direct dating of paleomagnetic results from Precambrian sediments in the Amazon craton: evidence for Grenvillian emplacement of exotic crust in SE Appalachians of North America: Earth and Planetary Science Letters, v. 267, p. 188-199.

Dall'Agnol, R., Frost, C.D., and Rämö, O.T., 2012, IGCP Project 510 "A-type Granites and Related Rocks through Time": Project vita, results, and contribution to granite research: Lithos, v. 151, p. 1-16.

Dall'Agnol, R., Scaillet, B., and Pichavant, M., 1999, An experimental study of a lower Proterozoic A-type granite from the eastern Amazonian Craton, Brazil: Journal of Petrology, v. 40, p. 1673-1698.

Dalziel, I.W.D., 1997, Overview: Neoproterozoic-Paleozoic geography and tectonics: review, hypotheses and environmental speculations: Geological Society of America Bulletin, v. 109, p. 16-42.

Dankers, P., and Lapointe, P., 1981, Paleomagnetism of Lower Cambrian volcanics and a cross-cutting Cambro-Ordovician diabase dyke from Buckingham (Quebec): Canadian Journal of Earth Sciences, v. 18, p. 1174-1186.

De Brito Neves, B.B., and Fuck, R.A., 2013, Neoproterozoic evolution of the basement of the South American platform: Journal of South American Earth Sciences, v. 47, p. 72-89.

Dessureau, G., Piper, D.J.W., and Pe-Piper, G., 2000, Geochemical evolution of earliest Carboniferous continental tholeitic basalts along a crystal-scale shear zone: southwestern Maritimes Basin, eastern Canada: Lithos, v. 50, p. 27-50.

Dilles, J.H., Einaudi, M.T., Proffett, J.M., and Barton, M.D., 2000, Overview of the Yerington porphyry copper district: Magmatic to non-magmatic sources of hydrothermal fluids, their flow paths, alteration affects on rocks, and Cu–Mo–Fe–Au ores: Society of Economic Geologists Guide Book Series, v. 32, p. 55–66.

Dingwell, D.B., Scarfe, C.M., and Cronin, D.J., 1985, The effect of fluorine on viscosities in the system Na_2O-Al_2O_3-SiO_2: implications for phonolites, trachytes and rhyolites: American Mineralogist, v. 70, p. 80-87.

Drake, M.J., and Weill, D.F., 1975, Partition of Sr, Ba, Ca, Y, Eu2+, Eu3+, and Other REE between Plagioclase Feldspar and Magmatic Liquid - Experimental Study: Geochimica et Cosmochimica Acta, v. 39, p. 689-712.

Doig, R., Murphy, J.B., and Nance, R. D., 1993, Tectonic significance of the Late Proterozoic Economy River gneiss, Cobequid Highlands, Avalon Composite Terrane, Nova Scotia: Canadian Journal of Earth Sciences, v. 30, p. 474-479.

Doig, R., Murphy, J.B., Pe-Piper, G., Piper D.J.W., 1996, U-Pb geochronology of the late Paleozoic plutons, Cobequid Highlands, Nova Scotia, Canada: Evidence for late Devonian emplacement adjacent to the Meguma-Avalon terrane boundary in the Canadian Appalachians: Geological Journal, v. 31, p. 179-188.

Domeier, M., and Torsvik, T.H., 2014, Plate tectonics in the late Paleozoic: Geoscience Frontiers, v. 5, p. 303-350.

Donohoe, H.V., and Wallace, P.I., 1982, Geological map of the Cobequid Highlands, Colchester, Cumberland, and Pictou counties, Nova Scotia, Sheet 4 of 4, Nova Scotia Department of Mines and Energy, Map 82-9, scale 1:50000.

Dostal, J., Dupuy, C., Carron, J.P., Dekerneizon, M.L., and Maury, R.C., 1983, Partition-Coefficients of Trace-Elements - Application to Volcanic Rocks of St Vincent, West Indies: Geochimica et Cosmochimica Acta, v. 47, p. 525-533.

Dudas, M.J., Schmitt, R.A, and Harward, M.E., 1971, Trace element partitioning between volcanic plagioclase and dacitic pyroclastic matrix: Earth and Planetary Science Letters, v. 11, p. 440-446.

Duke, J.M., 1976, Distribution of the period four transition elements among olivine, calcic clinopyroxene and mafic silicate liquid; experimental results: Journal of Petrology, v. 17, p. 499-521.

Dunn, T., and Sen, C., 1994, Mineral/Matrix Partition-Coefficients for Ortho-Pyroxene, Plagioclase, and Olivine in Basaltic to Andesitic Systems - a Combined Analytical and Experimental Study: Geochimica et Cosmochimica Acta, v. 58, p. 717-733.

Dunning G. R., Barr S. M., Giles P. S., McGregor D. C., Pe-Piper G., and Piper D. J.W., 2002. Chronology of Devonian to early Carboniferous rifting and igneous activity in southern Magdalen Basin based on U-Pb (zircon) dating: Canadian Journal of Earth Sciences, v. 39, p. 1219-1237.

Dwivedi, A.K., Pandey, U.K., Murugan, C., Bhatt, A.K., Babu, P.V.R., and Mallikarjun, J., 2011, Geochemistry and geochronology of A-type Barabazar Granite: implications on the geodynamics of South Purulia Shear Zone, Singhbhum Craton, Eastern India: Journal Geological Society of India, v. 77, p. 527-538.

Eby, G.N., 1992, Chemical subdivision of the A-type granitoids: petrogenetic and tectonic implications: Geology, v. 20, p. 641-644.

Eby, G. N., and Charnley, N., 2010, Fluorine and chlorine in alkaline rocks and A-type granites, in: Ramo, O. T., Lukkari, S. R., Heinonen, A.P. (Eds.), International Conference on A-type Granites and Related Rocks through Time (IGCP-510). Helsinki, Finland, August 18-20, 2010. Abstract Volume pp. 26-28.

El-Gharbawy, R.I., 2011, Contribution to the Geochemistry and Tectonic Setting of the Oligo-Miocene A-Type Granites, South West of the Arabian Shield, Yemen Republic: JAKU Earth Science, v. 22, p. 37-68.

Elburg, M.A., Andersen, T., Bons, P.D., Weisheit, A., Simonsen, S.L., Smet, I., 2012, Metasomatism and metallogeny of A-type granites of the Mt Painter–Mt Babbage Inliers, South Australia: Lithos, v. 151, p. 83-104.

Endrun, B., Lebedev, S., Meier, T., Tirel, C., and Friederich, W., 2011, Complex layered deformation within the Aegean crust and mantle revealed by seismic anisotropy: Nature Geoscience, v. 4, p. 203–207.

Escarraga, E.A., Barr, S.M., Murphy, J.B., and Hamilton, M.A., 2012, Ordovician A-type plutons in the Antigonish Highlands, Nova Scotia: Canadian Journal of Earth Science, v. 49, p. 329-345.

Esperança, S., Carlson, R.W., Shirey, S.B., and Smith, D., 1997, Dating crust-mantle separation: Re-Os isotopic study of mafic xenoliths from central Arizona: Geology, v. 25, p. 651-654.

Evans, A.D., 2009, The paleomagnetically viable, long-lived and all-inclusive Rodinia supercontinent reconstruction: Geological Society, London, Special Publications, v. 327, p. 371-404.

Ewart, A., and Griffin, W.L., 1994, Application of Proton-Microprobe Data to Trace-Element Partitioning in Volcanic-Rocks: Chemical Geology, v. 117, p. 251-284.

Ewart, A., Bryan, W.B., and Gill, J.B., 1973, Mineralogy and Geochemistry of the Younger Volcanic Islands of Tonga, S. W. Pacific: Journal of Petrology, v. 14, p. 429-465.

Faleiros, F.M., Ademar da Cruz Campanha, G., Martins, L., Vlach, S.R.F., and Vanconcelos, P.M., 2011, Ediacaran high-pressure collision metamorphism and tectonics of the southern Ribeira Belt (SE Brazil): Evidence for terrane accretion and dispersion during Gondwana assembly: Precambrian Research, v. 189, p. 263-291.

Figueiredo e Silva, R.C., Lobato, L.M., Rosière, C.A., and Hagemann, S., 2011, Petrographic and geochemical studies at giant Sierra Norte iron ore deposits in the Carajás mineral province, Pará State, Brazil: Geonomos, v. 19, p. 198–223.

Frey, F.A., 1969, Rare earth abundances in a high-temperature peridotite intrusion: Geochimica et Cosmochimica Acta, v. 33, p. 1429-1447.

Förster, H.J., Ondrejka, M., and Uher, P., 2011, Mineralogical responses to subsolidus alteration of granitic rocks by oxidizing As-bearing fluids: REE-arsenates and As–rich silicates from the Zinnwald granite, eastern Erzgebirge, Germany: The Canadian Mineralogist, v. 49, p. 913-930.

Fortey, R.A., and Cocks, L.R.M., 2003, Paleontological evidence bearing on global Ordovician-Silurian continental reconstructions: Earth-Science Reviews, v. 61, p. 245-307.

Frost, C.D., and Frost, B.R., 2010, On ferroan (A-type) granitoids: their compositional variability and modes of origin: Journal of Petrology, v. 52, p. 39-53.

Fu, B., Cliff, J., and Zartman, R.E., 2014, Zircon oxygen isotopic constraints from plutonic rocks on the magmatic and crustal evolution of the northern Appalachians in southern New England, USA: Canadian Journal of Earth Sciences, v. 51, p. 485-499.

Fuck, R.A., Brito Neves, B.B., and Schobbenhaus, C., 2008, Rodinia descendants in South America: Precambrian Research, v. 160, p. 108-126.

Fyffe, L.R., and Barr, S.M., 1986, Petrochemistry and tectonic significance of Carboniferous volcanic rocks in New Brunswick: Canadian Journal of Earth Sciences, v. 23, p. 1243-1256.

Fujimaki, H., Tatsumoto, M., and Aoki, K.-I., 1984, Partition coefficients of Hf, Zr, and REE between phenocrysts and groundmasses: Journal of Geophysical Research, v. 89, p. 662-672.

Gaetani, G.A., and Grove, T.L., 1997, Partitioning of moderately siderophile elements among olivine, silicate melt, and sulfide melt: Constraints on core formation in the Earth and Mars: Geochimica et Cosmochimica Acta, v. 61, p. 1829-1846.

Gallahan, W.E., and Nielsen, R.L., 1992, The Partitioning of Sc, Y, and the Rare-Earth Elements between High-Ca Pyroxene and Natural Mafic to Intermediate Lavas at 1-Atmosphere: Geochimica et Cosmochimica Acta, v. 56, p. 2387-2404.

Gardien, V., Thompson, A.B., and Ulmer, P., 2000, Melting of biotite + plagioclase + quartz gneisses: the role of H_2O in the stability of amphibole: Journal of Petrology, v. 41, p. 651-666.

Ghiorso, M.S., and Sack, R.O., 1995, Chemical mass transfer in magmatic processes IV. A revised and internally consistent thermodynamic model for the interpretation and extrapolation of liquid±solid equilibria in magmatic systems at elevated temperatures and pressures: Contributions to Mineralogy and Petrology, v. 119, p. 197-212.

Gibbons,W., Doig, R., Gordon, T., Murphy, B., Reynolds, P., and White, J.C., 1996, Mylonite to megabreccia: Tracking fault events within a transcurrent terrane boundary in Nova Scotia, Canada: Geology, v. 24, p. 411–414.

Gieré, R., 1996, Formation of rare earth minerals in hydrothermal systems, *in:* Jones, A.P., Wall, F., and Williams, C.T. (eds), Rare earth minerals: Chemistry, origin and ore deposits: London, Chapman and Hall, p. 105–150.

Giesting, P.A., and Filiberto, J., 2014, Quantitative models linking igneous amphibole composition with magma Cl and OH content: American Mineralogist, v. 99, p. 852-865.

Giordano, D., Russell, J. K., and Dingwell, D. B., 2008, Viscosity of magmatic liquids: A model: Earth and Planetary Science Letters, v. 271, p. 123-134.

Goodwin, A.M., 2013 Precambrian Geology: The Dynamic Evolution of the Continental Crust: United States Edition published by Academic Press, Inc. San Diego, CA, 666 p.

Goto, A., Taniguchi, H., and Kitakaze, A., 2005, Viscosity measurements of hydrous rhyolitic melts using the fiber elongation method: Bulletin of Volcanology, v. 67, p. 590-596.

Gower, C.F., Ryan, A.B., and Rivers, T., 1990, Mid-Proterozoic Laurentia-Baltica: an overview of its geological evolution and a summary of the contributions made by this volume *in:* Gower, C.F., Ryan, A.B., and Rivers, T. (eds) Mid-Proterozoic Laurentia-Baltica, Geological Association of Canada, Special Papers, v. 38, p. 1-20.

Groves, D.I., Bierlein, F.P., Meinert, L.D., and Hitzman, M.W., 2010, Iron oxide copper-gold (IOCG) deposits through Earth history: Implications for origin, lithospheric setting, and distinction from other epigenetic iron oxide deposits: Economic Geology, v. 105, p. 641–654.

Gualda, G.A.R., and Vlach, S.R.F., 2007, The Serra de Graciosa A-type granites and syenites, southern Brazil, Part I: Regional and geological characterization: Anais Academia Brasileira Ciências, v. 79, p. 405-430.

Gualda, G.A.R., and Vlach. S.R.F., 2007, The Serra De Graciosa A-type granites and syenites, southern Brazil Part 2: Petrographic and mineralogical evolution of the alkaline and aluminous associations: Lithos, v. 93, p. 310-327.

Hamilton, M.A., and Murphy, J.B., 2004, Tectonic significance of a Llanvirn age for the Dunn Point volcanic rocks, Avalon terrane, Nova Scotia, Canada: implications for the evolution of the Iapetus and Rheic Oceans: Tectonophysics, v. 379, p. 199-209.

Han, B., Wang, S., Jahn, B., Hong, D., Kagami, H., and Sun, Y., 1996, Depleted-mantle source for the Ulungur River A-type granites from north Xinjiang, China: geochemistry and Nd-Sr isotopic evidence, and implications for Phanerozoic crustal growth: Chemical Geology, v. 138, p. 135-159.

Hanchar, J.M., and Watson, E.B., 2003, Zircon saturation-thermometry: Reviews in Mineralogy and Geochemistry, v. 53, p. 89-112.

Harrison, T.M.,Watson, E.B., 1983, Kinetics of zircon dissolution and zirconium diffusion in granitic melts of variable water content: Contributions to Mineralogy and Petrology, v. 84, p. 66–72.

Hart, S.R., and Brooks, C., 1974, Clinopyroxene-matrix partitioning of K, Rb, Cs, Sr and Ba: Geochimica et Cosmochimica Acta, v. 38, p. 1799-1806.

Hart, S.R., and Dunn, T.,1993, Experimental cpx/melt partitioning of 24 trace elements: Contributions to Mineralogy and Petrology, v. 113, p. 1-8.

Hauri, E.H., Wagner, T.P., and Grove, T.L., 1994, Experimental and natural partitioning of Th, U, Pb and other trace elements between garnet, clinopyroxene and basaltic melts: Chemical Geology, v. 117, p. 149-166.

Hawkesworth, C.J., Mantovani, M.S.M., Taylor, P.N., and Palacz, A., 1986, Evidence from the Parana of south Brazil for a continental contribution to Dupal basalts: Nature, v. 322, p. 356-359.

Hawthorne, F.C., and Oberti, r., 2007, Amphiboles: crystal chemistry *in:* Hawthorne, F. C., Oberti, R., Della Ventura, G, Mottana, A. (eds), Amphiboles: Crystal Chemistry, Occurrence and Health Issues, v. 67, p. 1–54. Reviews in Mineralogy and Geochemistry, Mineralogical Society of America, Chantilly, Virginia.

Henza, A.A., Withjack, M.O., and Schlische, R.W., 2011, How do the properties of a pre-existing normal-fault population influence fault development during a subsequent phase of extension?: Journal of Structural Geology, v. 33, p. 1312-1324.

Hermes, O.D., and Zartman, R.E., 1992, Late Proterozoic and Silurian alkaline plutons within the southeastern New England Avalon zone: Journal of Geology, v. 100, p. 477-486.

Hess, K-U., and Dingwell, B.B., 1996, Viscosities of hydrous leucogranitic melts: A non-Arrhenian model: American Mineralogist, v. 81, p. 1297-1300.

Hibbard, J., and Waldron, J.W.F., 2009, Truncation and translation of Appalachian promontories: mid–Paleozoic strike–slip tectonics and basin initiation: Geology, v. 37, p. 487–490.

Hibbard, J.P., van Staal, C.R., and Miller, B.V., 2006, Links between Carolinia, Avalonia, and Ganderia in the Appalachian peri-Gondwanan Realm *in:* Sears, J.W., Harms, T.A., and Evenchick, C.A. (eds), Whence the Mountains? Inquiries into the evolution of orogenic systems: A volume in honor of Raymond A. Price, Geological Society of America, Special Papers, v. 433, p. 291-311.

Hodych, J.P., and Buchan, K.L., 1998, Paleomagnetism of the ca. 440 Ma Cape St Mary's sills of the Avalon Peninsula of Newfoundland: implications for Iapetus Ocean closure: Geophysical Journal International, v. 135, p. 155-164.

Hodych, J.P., Cox, R.A., and Kosler, J., 2004, An equatorial Laurentia at 550 Ma confirmed by Grenvillian inherited zircons dated by LAM ICP-MS in the Skinner Cove volcanics of Western Newfoundland: implications for inertial interchange true polar wander: Precambrian Research, v. 129, p. 93-113.

Hoffman, P.F., 1991, Did the breakout of Laurentia turn Gondwanaland inside out?: Science, v. 252, p. 1409-1412.

Holdsworth, R.E., 1994, Structural evolution of the Gander-Avalon terrane boundary: a reactivated transpression zone in the NE Newfoundland Appalachians, Journal of the Geological Society, London: v. 151, p. 629–646.

Holtz, F., and Johannes, W., 1994, Maximum and minimum water contents of granitic melts: Implications for chemical and physical properties of ascending magmas: Lithos, v. 32, p. 149-159.

Housh, T.B., and Luhr, J.F., 1991, Plagioclase-melt equilibria in hydrous systems: American Mineralogist, v. 76, p. 477-492.

Hunt, J.P., 2005, Geological characteristics of iron oxide-copper-gold (IOCG) type mineralisation in the Western Bushveld Complex: unpublished M.Sc thesis, p. 267, University of Witwatersrand.

Hunt, J., Baker, T., and Thorkelson, D., 2005, Regional-scale Proterozoic IOCG-mineralized breccia systems: examples from the Wernecke Mountains, Yukon, Canada: Mineralium Deposita, v. 40, p. 492-514.

Hutcheon, I., 1998, The potential role of pyrite oxidation in corrosion and reservoir souring: The Journal of Canadian Petroleum Technology, v. 37, p. 27–31.

Huang, F., Lundstrom, C., and Mcdonough, W., 2006, Effect of melt structure on trace-element partitioning between clinopyroxene and silicic, alkaline, aluminous melts: American Mineralogist, v. 91, p. 1385-1400.

Hyndman, R.D., and Currie, C.A., 2011, Why is the North America Cordillera high? Hot backarcs, thermal isostasy, and mountain belts: Geology, v. 39, p. 783-786.

Icenhower, J., and London, D., 1997, Partitioning of fluorine and chlorine between biotite and granitic melt: experimental calibration at 200 MPa H_2O: Contributions to Mineralogy and Petrology, v. 127, p. 17-29.

Irving, E., 1972, Paleomagnetism of the Et-Then Group and Mackenzie Diabase in the Great Slave Lake Area: Canadian Journal of Earth Sciences, v. 9, p. 763-765.

Irving, E., Park, J.K., and Emslie, R.F., 1974, Paleomagnetism of the Morin Complex: Journal of Geophysical Research, v. 79, p. 5482-5490.

Irvine, T.N., and Baragar, W.R.A., 1971. A guide to the geochemical classification of the common volcanic rocks of orogenic areas, Geological Society of America Bulletin, v. 83, p. 29-40.

Jenner, G.A., Foley, S.F., Jackson, S.E., Green, T.H., Fryer, B.J., and Longerich, H.P., 1994, Determination of partition coefficients for trace elements in high pressure-temperature experimental run products by laser ablation microprobe-inductively coupled plasma-mass spectrometry (LAM-ICP-MS): Geochimica et Cosmochimica Acta, v. 57, p. 5099-5103.

Jiang, N., 2006, Hydrothermal alteration of chevkinite–(Ce) in the Shuiquangou syenitic intrusion, northern China: Chemical Geology, v. 227, p. 100-112.

Johansson, Å., 2014, From Rodinia to Gondwana with the 'SAMBA' model− A distant view from Baltica towards Amazonia and beyond: Precambrian Research, v. 244, p. 226-235.

Johnson, K.T.M., 1994, Experimental cpx/ and garnet/melt partitioning of REE and other trace elements at high pressures; petrogenetic implications: Mineralogical Magazine, v. 58, p. 454-455.

Johnson, K.T.M., 1998, Experimental determination of partition coefficients for rare earth and high-field-strength elements between clinopyroxene, garnet, and basaltic melt at high pressures: Contributions to Mineralogy and Petrology, v. 133, p. 60-68.

Johnson, R.J.E., and van der Voo, R., 1990, Pre-folding magnetization reconfirmed for the late Ordovician- early Silurian Dunn Point volcanics, Nova Scotia: Tectonophysics, v. 178, p. 193-205.

Jung, S., Mezger, K., and Hoernes, S., 1998, Petrology and geochemistry of syn- to post-collisional metaluminous A-type granites—a major and trace element and Nd–Sr–Pb–O-isotope study from the Proterozoic Damara Belt, Namibia: Lithos, v. 45, p. 147-175.

Kalczynski, M.J., Gates, A.E., Gorring, M.L., and Lupulescu, M.V., 2012, Hydrothermal alteration, mass transfer and magnetite mineralization in dextral shear zones, western Hudson Highlands, NY. Northeastern Section 47th Annual meeting: Geological Society of America, Abstracts, v. 44, p. 105.

Kaur, P., Chaudhri, N., Hofmann, A.W., Raczec, I., Okrusch, M., Skora, S., and Baumgartner, L.P., 2012, Two–stage extreme albitization of A–type granites from Rajasthan, NW India: Journal of Petrology, v. 53, p. 919–948.

Keen, C.E., Kay, W.A., Keppie, D., Marillier, F., Pe-Piper, G., and Waldron, J.W.F., 1991, Deep seismic reflection data from the Bay of Fundy and the Gulf of Maine: tectonic implications for the northern Appalachians: Canadian Journal of Earth Sciences, v. 28, p. 1096-1111.

Kellett, D.A., Rogers, N., McNicoll, V., Kerr, A., and van Staal, C., 2014, New age data refine extent and duration of Paleozoic and Neoproterozoic plutonism at Ganderia–Avalonia boundary, Newfoundland: Canadian Journal of Earth Sciences, v. 51, p. 943-972.

Keppie, J.D., 1982, The Minas geofracture *in:* St Julien, P., and J. Beland, J. (eds), Major structural zones and faults of the Northern Appalachians: Geological Association of Canada, Special Paper 24, p. 263–280.

Keppie, J.D., 1993, Synthesis of Paleozoic deformational events and terrane accretion in the Canadian Appalachians: Geologische Rundschau, v. 82, p. 381-431.

Kepple, J.D., and Dallmeyer, R.D., 1987, Dating transcurrent terrane accretion: an example from the Meguma and Avalon composite terranes in the northern Appalachians: Tectonics, v. 6, p. 831-47.

Keppie, D.J., and Dallmeyer, R.D., 1989, Map of pre-Mesozoic terranes in circum-Atlantic Phanerozoic Orogens: Nova Scotia Department of Mines and Energy, Halifax Nova Scotia, Canada.

Keppie, D., and Krogh, T.E., 1999, U-Pb geochronology of Devonian granites in the Meguma Terrane of Nova Scotia, Canada: Evidence for hotspot melting of a Neoproterozoic source: The Journal of Geology, v. 107, p. 555-568.

Keppie, J.D., Dostal, J., Dallmeyer, R.D., and Doig, R., 2000, Superposed Neoproterozoic and Silurian magmatic arcs in central Cape Breton Island, Canada: geochemical and geochronological constraints: Geological Magazine, v. 137, p. 137-153.

Keppie, J.D., Nance, R.D., Murphy, J.B., and Dostal, J., 2003, Tethyan, Mediterranean, and Pacific analogues for the Neoproterozoic-Paleozoic birth and development of peri-Gondwanan terranes and their transfer to Laurentia and Laurussia: Tectonophysics, v. 365, p. 195-219.

Keppie, J.D., Dostal, J., Miller, B.V., Ramos-Arias, M.A., Morales-Gámez, M., Nance, R.D., Murphy, J.B., Ortega-Rivera, A., Lee, J.W.K., Housh, T., and Cooper, P., 2008, Ordovician-earliest Silurian rift tholeiites in the Acatlán Complex, southern Mexico: Evidence of rifting on the southern margin of the Rheic Ocean: Tectonophysics, v. 461, p. 130-156.

Kerr, A., Jenner, G.A., and Fryer, B.J., 1995, Sm-Nd isotopic geochemistry of Precambrian to Paleozoic granitoid suites and the deep-crustal structure of the southern margin of the Newfoundland Appalachians: Canadian Journal of Earth Sciences, v. 32, p. 224-245.

King, P.L., White, A.J.R., Chappell, B.W., and Allen, C.M., 1997, Characterization and origin of aluminous Atype granites from the Lachlan fold belt, southeastern Australia: Journal of Petrology, v. 38, p. 371–91.

Klemme, S., 2004, Evidence for fluoride melts in Earth's mantle formed by liquid immiscibility: Geology, v. 32, p. 441-444.

Kloeck, W., and Palme, H., 1988, Partitioning of siderophile and chalcophile elements between sulfide, olivine, and glass in a naturally reduced basalt from Disko Island, Greenland, *in* Proceedings of the Lunar and Planetary Science Conference, Ryder, G. (Editors), Pergamon, New York, v. 18, p. 471-483.

Kogarko, L.N., 2006, Alkaline Magmatism and enriched mantle reservoirs: mechanisms, time and depth of formation: Geochemistry International, v. 44, p. 3-10.

Kontak, D.J., Archibald, D.A., Creaser, R.A., and Heaman, L.M., 2008, Dating hydrothermal alteration and IOCG mineralization along a terrane–bounding fault–zone: the Copper Lake deposit, Nova Scotia: Atlantic Geology, v. 44, p. 146–166.

Kontak, D.J., Kyser, K., Gize, A., and Marshall, D., 2006, Structurally controlled vein barite mineralization in the Maritimes Basin of eastern Canada: Geologic setting, stable isotopes, and fluid inclusions: Society of Economic Geologists, v. 101, p. 407–430.

Koukouvelas I., Pe-Piper G., and Piper, D. J.W., 2002, The role of dextral transpressional faulting in the evolution of an early Carboniferous mafic-felsic plutonic and volcanic complex: Cobequid Highlands, Nova Scotia, Canada: Tectonophysics, v. 348, p. 219-246.

Koukouvelas, I., Pe-Piper, G., and Piper, D. J. W., 2006, The relationship between length and width of plutons, within the crystal-scale Cobequid Shear Zone, northern Appalachians, Canada: International Journal of Earth Sciences, v. 95, p. 963-976.

Kranidiotis, P., and MacLean, W.H., 1987, Systematics of chlorite alteration at the Phelps Dodge massive sulphide deposit, Matagami, Quebec: Economic Geology, v. 82, p. 1898–1911.

Kreiner, D.C., 2011, Epithermal style Iron Oxide (-Cu-Au) (-IOCG) vein systems and related alteration, 659 p., Unpublished PhD Dissertation: University of Arizona.

Kreiner, D.C., and Barton, M.D., 2009, Hydrothermal alteration and mineralization zoning in iron oxide (Cu–Au) vein deposits near Copiapo, Chile, *in:* Williams, P.J. (ed), Smart Science for Exploration and Mining, p. 635–637. Townsville: James Cook University.

Kretz, R., 1959, Chemical study of garnet, biotite and hornblende from gneisses of southwestern Quebec, with emphasis on distribution of elements in coexisting minerals: Journal of Geology, v. 67, p. 371-402.

Kuiper, K.F., Deino, A., Hilgen, F.J., Krijgsman, W., Renne, P.R., and Wijbrans, J.R., 2008, Synchronizing rock clocks of earth history: Science, v. 320, p. 500-504.

Kynicky, J., Chakhmouradian, A., Xu, C., Krmicec, L., and Galiova, M., 2011, Distribution and evolution of zirconium mineralization in peralkaline granites and associated pegmatites of the Khan Bogd complex, southern Mongolia: Canadian Mineralogist, v. 49, p. 947-965.

La Fléche, M.R., Camiré, G., and Jenner, G.A., 1998, Geochemistry of post-Acadian, Carboniferous continental intraplate basalts from the Maritimes Basin, Magdalen Islands, Québec, Canada, Chemical Geology, v. 148, p. 115-136.

Larsen, L.M., 1979, Distribution of REE and Other Trace-Elements between Phenocrysts and Peralkaline Undersaturated Magmas, Exemplified by Rocks from the Gardar Igneous Province, South Greenland: Lithos, v. 12, p. 303-315.

Lana, C., Gibson, R.L., Reimond, W.U., and Minnitt, R.C.A., 2003, Geology and geochemistry of granite–greenstone association in the southeastern Vredefort dome, South Africa: South African Journal of Geology, v. 106, p. 291–314.

Landing, E., 2005, Early Paleozoic Avalon-Gondwana unity: an obituary- response to 'Paleontological evidence on global Ordovician-Silurian continental reconstructions' by R.A. Fortey and L.R.M. Cocks: Earth-Science Reviews, v. 69, p. 169-175.

Latourrette, T.Z., and Burnett, D.S., 1992, Experimental-Determination of U-Partitioning and Th-Partitioning between Clinopyroxene and Natural and Synthetic Basaltic Liquid: Earth and Planetary Science Letters, v. 110, p. 227-244.

Latourrette, T.Z., Burnett, D.S., and Bacon, C.R., 1991, Uranium and Minor-Element Partitioning in Fe-Ti Oxides and Zircon from Partially Melted Granodiorite, Crater Lake, Oregon: Geochimica et Cosmochimica Acta, v. 55, p. 457-469.

Leake, B.E., Wooley, A.R., Birch, W.D., Gilbert, M.C., Grice, J.D., Hawthorne, F.C., Kato, A., Kisch, H.J., Krivonichev, V.G., Linthout, K., Laird, J., Mandarino, J., Maresch, W.V., Nickel, E.H., Schumacher, J.C., Stephenson, N.C.N., Whittaker, E.J.W., and Youzhi, G., 1997, Nomenclature of amphiboles: report of the subcommittee on amphiboles of the International Mineralogical Association Commission on New Minerals and Mineral Names: Mineralogical Magazine, v. 61, p. 295-321.

Leeman, W.P., 1979, Partitioning of Pb between volcanic glass and coexisting sanidine and plagioclase feldspars: Geochimica et Cosmochimica Acta, v. 43, p. 171-175.

Lemarchand, F., Benoit, V., and Calais, G., 1987, Trace element distribution coefficients in alkaline series: Geochimica et Cosmochimica Acta, v. 51, p. 1071-1081.

Li, Z.X., Bogdanova, S.V., Collins, A.S., Davidson, A., De Waele, B., Ernst, R.E., Fitzsimons, I.C.W., Fuck, R.A., Gladkochub, D.P., Jacobs, J., Karlstrom, K.E., Lu, S., Natapov, L.M., Pease, V., Pisarevsky, S.A., Thrane, K., and Vernikovsky, V., 2008, Assembly, configuration, and break-up history of Rodinia: a synthesis: Precambrian Research, v. 160, p. 171-210.

Locock, A.J., 2014, An Excel spreadsheet to classify chemical analyses of amphiboles following the IMA 2012 recommendations: Computers & Geosciences, v. 62, p. 1-11.

Loiselle, M. C., and Wones, D., 1979, Characteristics and origin of anorogenic granites: Geological Society of America, Abstracts with Programs, v. 11, p. 468.

London, D., 1997, Estimating abundances of volatile and other mobile components in evolved silicic melts through mineral–melt equilibria: Journal of Petrology, v. 38, p. 1691-1706.

Long, P.E., 1978, Experimental determination of partition coefficients for Rb, Sr and Ba between alkali feldspar and silicate liquid: Geochimica et Cosmochimica Acta, v. 42, p. 833-846.

Lowerstern, J.B., Charlier, B.L.A., Clynne, M.A., and Wodden, J.L., 2005, Extreme U-Th disequilibrium in rift-related basalts, rhyolites and granophyric granite and the timescale of rhyolite generation, intrusion, and crystallization at Alid Volcanic Centre, Eritrea: Journal of Petrology, v. 47, p. 2105-2122.

Luhr, J.F., and Carmichael, I.S.E., 1980, The Colima volcanic complex, Mexico. I: post-caldera andesites from Volcan Colima: Contributions to Mineralogy and Petrology, v. 71, p. 343-372.

Luhr, J.F., Carmichael, I.S.E., and Varekamp, J.C., 1984, The 1982 eruptions of El Chichon volcano, Chiapas, Mexico: mineralogy and petrology of the anhydrite-bearing pumices: Journal of Volcanology and Geothermal Research, v. 23, p. 69-108.

Lukkari, S., and Holtz, F., 2007, Phase relations of a F-enriched peraluminous granite: An experimental study of the Kymi topaz granite stock, southern Finland: Contributions to Mineralogy and Petrology, v. 153, p. 273-288.

MacHattie, T.G., and O'Reilly, G.A., 2008, Field and geochemical evidence for contemporaneous mafic magmatism and iron oxide–copper–gold (IOCG) mineralization and alteration along the Cobequid–Chedabucto Fault Zone: in Nova Scotia Department of Natural Resources, Mineral Resources Branch, Report ME–2009–1, p. 71–83.

MacHattie, T.G., and White, C.E., 2012, Preliminary geology of the eastern Cobequid Highlands, Northern mainland Nova Scotia: in Nova Scotia Department of Natural Resourses, Mineral Resourses Branch Report of Activities, Report ME 2013-001, p. 27-47.

MacHattie, T., White, C. E., Beresford, V. and Reid, M. 2013, The eastern Cobequid Highlands: redefined geology and economic potential: Nova Scotia Department of Natural Resources, Minerals Resource Branch, Open File Illustration ME 2013-016.

MacInnes, E.A., and White, J.C., 2004, Geometric and kinematic analysis of a transpression terrane boundary: Minas fault system, Nova Scotia, Canada *in:* Alsop, G.I., Holdsworth, R.E. (eds.) Flow Processes in Faults and Shear Zones: Geological Society of London Special Publication, v. 224, p. 201-214.

Mac Niocaill, C., van der Pluijm, B.A., and van der Voo, R., 1997, Ordovician paleogeography and the evolution of the Iapetus Ocean: Geology, v. 25, p. 159-162.

Mahood, G.A., and Hildreth, E.W., 1983, Large partition coefficients for trace elements in high-silica rhyolites: Geochimica et Cosmochimica Acta, v. 47, p. 11-30.

Mahood, G.A., and Stimac, J.A., 1990, Trace-element partitioning in pantellerites and trachytes: Geochimica et Cosmochimica Acta, v. 54, p. 2257-2276.

Maniar, P.D., and Piccoli, P.M., 1989, Tectonic discrimination of granitoids: Geological Society of America Bulletin, v. 101, p. 635-643.

Manning, C.E., 2004, The chemistry of subduction-zone fluids: Earth and Planetary Science Letters, v. 223, p. 1-16.

Marillier, F., Keen, C.E., Stockmal, G.S., Quinlan, G., Williams, H., Colman-Sadd, S.P., and O'Brien, S.J., 1989, Crustal structure and surface zonation of the Canadian Appalachians: implications of deep seismic reflection data: Canadian Journal of Earth Sciences, v. 26, p. 305-321.

Marillier, F., and Verhoef, J., 1989, Crustal thickness under the Gulf of St. Lawrence, northern Appalachians, from gravity and deep seismic data: Canadian Journal of Earth Sciences, v. 26, p. 1517–1532.

Marillier, F., and Reid, I., 1990, Crustal underplating beneath the Carboniferous Magdalen Basin (Eastern Canada): evidence from seismic reflection and refraction *in:* Pinet, B., Bois, C., (eds) The Potential of Deep Seismic Profiling for Hydrocarbon Exploration: Éditions Technip, Paris, 209–218.

Marks, M., Halama, R., Wenzel, T., and Markl, G., 2004, Trace element variations in clinopyroxene and amphibole from alkaline to peralkaline syenites and granites: implications for mineral-melt trace-element partitioning: Chemical Geology, v. 211, p. 185-215.

Martel, A.T., McGregor, D.C., and Utting, J., 1993, Stratigraphic significance of Upper Devonian and Lower Carboniferous miospores from the type area of the Horton Group, Nova Scotia: Canadian Journal of Earth Sciences, v. 30, p. 1091–1098.

Martin, R.F., 2007, Amphiboles in the igneous environment: Reviews in Mineralogy and Geochemistry, v. 67, p. 323-358.

Mason, R.A., 1992, Models of order and iron-fluorine avoidance in biotite: Canadian Mineralogist, v. 30, p. 343-354.

McCaig, A.M., Wickham, S.M., and Taylor H.P.Jr., 1990, Deep fluid circulation in alpine shear zones, Pyrenees, France: field and oxygen isotope studies: Contributions to Mineralogy and Petrology, v. 106, p. 41-60.

McKay, G.A., and Weill, D.F., 1977, KREEP petrogenesis revisited *in* Proceedings, Lunar Science Conference, 8th, Houston, Volume 2: Pergamon Press Inc., p. 2339-2355.

McKenzie, D., and O'Nions, R.K., 1991, Partial melt distributions from inversion of rare Earth element concentrations: Journal of Petrology, v. 32, p. 1021-1091.

McNamara, A.K., Mac Niocaill, C., van der Pluijm, B.A., and van der Voo, R., 2001, West African proximity of Avalon in the latest Precambrian: Geological Society of America Bulletin, v. 113, p. 1161-1170.

Meagher, C., 1995, Petrology of the Mount Thom Complex (unpublished B.Sc Honours thesis), Saint Francis Xavier University, 89 p.

Meintzer, R.E., and Mitchell, R.S., 1988, The epigene alteration of allanite: Canadian Mineralogist, v. 26, p. 945–955.

Menning, M, Alekseev, A.S., Chuvashov, B.I., Davydov, V.I., Devuyst, F.-X., Forke, H.C., Grunt, T.A., Hance, L., Heckel, P.H., Izokh, N.G., Jin, Y.-G., Jones, P.J., Kotlyar, G.V., Kozur, H.W., Nemyrovska, T.I., Schneider, J.W., Wang, X.-D., Weddige, K., Weyer. D., and Work, D.M., 2006, Global time scale and regional reference scales of Central and Western Europe, Tethys, South China, and North America as used in the Devonian-Carboniferous-Permian Correlation Chart 2003 (DCP 2003): Palaeogeography, Palaeoclimatology, Palaeoecology, v. 240, p. 318-372.

Michael, P.J., 1988, Partition coefficients for rare earth elements in mafic minerals of high silica rhyolites: The importance of accessory mineral inclusions: Geochimica et Cosmochimica Acta, v. 52, p. 275-282.

Micklethwaite, S., and Cox, S.F., 2002, Fault-segment rupture, aftershock-zone fluid flow, and mineralization: Geology, v. 32, p. 813-816.

Migdisov, A.A., and Williams-Jones, A.E., 2014, Hydrothermal transport and deposition of the rare earth elements by fluorine-bearing aqueous liquids: Mineralium Deposita, v. 49, p. 987-997.

Migdisov, A.A., Williams-Jones, A.E., and Wagner, T., 2009, An experimental study of the solubility and speciation of the Rare Earth Elements (III) in fluoride- and chloride-bearing aqueous solutions at temperatures up to 300°C: Geochimica et Cosmochimica Acta, v. 73, p. 7087–7109.

Miller, B.V., 1991, Kinematic, structural and tectonic analysis of the Rockland Brook Fault, Cobequid Highlands, Nova Scotia [M.Sc. thesis]: Athens, Ohio University, 163 p.

Miller, B.V., Nance, R.D., and Murphy, J.B., 1995, Kinematics of the Rockland Brook fault, Nova Scotia: implications for the interaction of the Meguma and Avalon terranes: Journal of Geodynamics, v. 19, p. 253–270.

Moench, R.H., and Aleinikoff, J.N. 2003, Stratigraphy, geochronology,and accretionary terrane settings of two Bronson Hill arc sequences, northern New England: Physics and Chemistry of the Earth, v. 28, p. 113–160.

Mogk, D.W., 1992, Ductile shearing and migmatization at mid crustal levels in an Archean high grade gneiss belt, northern Gallatin Range, Montana, USA: Journal of Metamorphic Petrology, v. 10, p. 427-438.

Moores, E.M., 1991, Southwest U.S.-East Antarctic (SWEAT) connection: a hypothesis: Geology, v. 19, p. 425-428.

Morad, S., Sirat, M., El–Ghali, M.A.K., and Mansurbeg, H., 2011, Chloritization in Proterozoic granite from the Äspö Laboratory, southeastern Sweden: record of hydrothermal alterations and implications for nuclear waste storage: Clay Minerals, v. 46, p. 495–513.

Mullen, E. D., 1983, $MnO/TiO_2/P_2O_5$: A minor element discriminant for basaltic rocks of oceanic environments and its implications for petrogenesis: Earth and Planetary Science Letters, v. 62, p. 53–62.

Murphy, J.B., 2002, Geochemistry of the Neoproterozoic metasedimentary Gamble Brook Formation, Avalon Terrane, Nova Scotia: evidence for a rifted-arc environment along the west Gondwanan margin of Rodinia: Journal of Geology, v. 110, p. 407–419.

Murphy, J.B., and Nance, R.D., 1991, Supercontinent model for the contrasting character of Late Proterozoic orogenic belts: Geology, v. 10, p. 469-472.

Murphy, J.B., and Nance, R.D., 2002, Nd-Sm isotopic systematics as tectonic tracers: an example from West Avalonia, Canadian Appalachians: Earth Science Reviews, v. 59, p. 77–100.

Murphy, J.B., and Dostal, J., 2007, Continental mafic magmatism of different ages in the same terrane: Constraints on the evolution of an enriched mantle source: Geology, v. 35, p. 335-338.

Murphy, J.B., Pe-Piper, G., Keppie, J.D., and Piper, D.J.W., 1991, Correlation of Neoproterozoic III sequences in the Avalon Composite Terrane of mainland Nova Scotia: tectonic implications: Atlantic Geology, v. 28, p. 143-151.

Murphy, J.B., Keppie, J.D., Dostal, J., Waldron, J.W.F., and Cude, M.P., 1996, Geochemical and isotopic characteristics of Early Silurian clastic sediments in Antigonish Highlanda, Nova Scotia, Canada: constraints on the accretion of Avalonia in the Appalachian-Caledonide Orogen: Canadian Journal of Earth Sciences, v. 33, p. 379-388.

Murphy, J.B., Keppie, J.D., Davis, D., and Krogh, T.E., 1997, Regional significance of new U-Pb age data for Neoproterozoic igneous units in Avalonian rocks of northern mainland Nova Scotia, Canada: Geological Magazine, v. 134, p. 113-120.

Murphy, J.B., Pisarevsky, S.A., Nance, R.D., and Keppie, J.D., 2001, Animated history of Avalonia in Neoproterozoic-Early Palaeozoic *in:* Jessel, M.J. (ed) General Contributions: 2001, Journal of the Virtual Explorer, v. 3, p. 45-58.

Murphy, J.B., Pisarevsky, S.A., Nance, R.D., and Keppie, J.D., 2004, Neoproterozoic-Early Paleozoic evolution of peri-Gondwanan terranes: implicationa for Laurentia-Gondwana connections: International Journal of Earth Sciences, v. 93, p. 659-682.

Murphy, J.B., Dostal, J., and Keppie, J.D., 2008, Neoproterozoic-Early Devonian magmatism in the Antigonish Highlands, Avalon terrane, Nova Scotia: tracking the evolution of the mantle and crustal sources during the evolution of the Rheic Ocean: Tectonophysics, v. 461, p. 181-201.

Murphy, J.B., Keppie, J.D., Nance, R.D., and Dostal, J., 2010, Comparative evolution of the Iapetus and Rheic Oceans: A North America perspective: Gondwana Research, v. 17, p. 482-499.

Murphy, J.B., Waldron, J.W.F., Kontak, D.J., Pe-Piper, G., and Piper, D.J.W., 2011, Minas Fault Zone: Late Paleozoic history of an intra-continental orogenic transform fault in the Canadian Appalachians: Journal of Structural Geology, v. 33, p. 312-328.

Murphy, J.B., Hamilton, M.A., and LeBlanc, B., 2012, Tectonic significance of Late Ordovician silicic magmatism, Avalon terrane, northern Antigonish Highlands, Nova Scotia: Canadian Journal of Earth Sciences, v. 49, p. 346-358.

Murthy, G.S., 1971, The paleomagnetism of diabase dikes from the Grenville Province: Canadian Journal of Earth Sciences, v. 8, p. 802-812.

Murthy, G., Gower, C., Tubrett, M., and Pätzold, R., 1992, Paleomagnetism of Eocambrian Long Range dykes and Double Mer Formation from Labrador, Canada: Canadian Journal of Earth Sciences, v. 29, p. 1224-1234.

Mysen, B., 1976, Partitioning of samarium and nickel between olivine, orthopyroxene, and liquid: preliminary data at 20 kbar and 1025 °C: Earth and Planetary Science Letters, v. 31, p. 1-7.

Mysen, B., 1978, Experimental determination of nickel partition coefficients between liquid, pargasite and garnet peridotite minerals and concentration limits of behavior according to Henry's Law at high pressure and temperature: American Journal of Science, v. 278, p. 217-243.

Mysen, B.O., and Virgo, D., 1980, Trace element partitioning and melt structure: an experimental study at 1 atm pressure: Geochimica et Cosmochimica Acta, v. 44, p. 1917-1930.

Nabelek, P.I., 1980, Nickel partitioning between olivine and liquid in natural basalts: Henry's Law behavior: Earth and Planetary Science Letters, v. 48, p. 293-302.

Nagasawa, H., 1973, Rare-Earth distribution in alkali rocks from Oki-Dogo Island, Japan: Contributions to Mineralogy and Petrology, v. 39, p. 301-308.

Nagasawa, H., and Schnetzler, C.C., 1971, Partitioning of rare Earth, alkali, and alkaline Earth elements between phenocrysts and acidic igneous magmas: Geochimica et Cosmochimica Acta, v. 35, p. 953-968.

Nagasawa, H., Wakita, H., Higuchi, H., and Onuma, N., 1969, Rare Earths in peridotite nodules: an explanation of the genetic relationship between basalt and peridotite nodules: Earth and Planetary Science Letters, v. 5, p. 377-381.

Namur, O., Charlier, B., Toplis, M.J., Higgins, M.D., Hounsell, V., Liégeois, J.P., and Vander Auwera, J., 2011, Differentiation of tholeiitic basalt to A-Type granite in the Sept Iles Layered Intrusion, Canada: Journal of Petrology, v. 52, p. 487-539.

Nance, R.D., and Murphy, J.B., 1990, Kinematic history of the Bass River Complex, Nova Scotia: Cadomian tectonostratigraphic relations in the Avalon terrane of the Canadian Appalachians, Geological Society Special Paper 51, p. 395–406.

Nance, R.D., and Murphy, J.B., 1996, Basement isotopic signatures and Neoproterozoic paleogeography of Avalonian-Cadomian and related terranes in the circum-North Atlantic in: Nance, R.D., and Thompson, M.D. (eds) Avalonian and related peri-Gondwanan terranes of the circum-North Atlantic, Geological Society of America Special Paper 304, p. 333-346.

Nance, R.D., Gutiérrez-Alonso, G., Keppie, J.K., Linnemann, U., Murphy, J.B., Quesada, C., Strachan, R.A., and Woodcock, N.H., 2012, A brief history of the Rheic Ocean: Geoscience Frontiers, v. 3, p. 125-135.

Nash, W.P., and Crecraft, H.R., 1985, Partition coefficients for trace elements in silicic magmas. Geochimica et Cosmochimica Acta, v. 49, p. 2309-2322.

Nardi, L.V.S., and Bitencourt, M.F., 2009, A-type granitic rocks in post-collisional settings in southernmost Brazil: their classification and relationship with tectonics and magmatic series: Canadian Mineralogist, v. 47, p. 1493-1503.

Nearing, J.D., 1991, Early Carboniferous hydrothermal events of the western Cobequid Highlands, Nova Scotia. Unpublished B.Sc. Honours Thesis: Halifax, Nova Scotia, Department of Geology, Saint Mary's University.

Neuman, H., Mead, J., and Vitaliano, C.J., 1954, Trace element variations during fractional crystallization as calculated from the distribution law: Geochimica et Cosmochimica Acta, v. 6, p. 90-101.

Nicholls, I.A., and Harris, K.L., 1980, Experimental rare Earth element partition coefficients for garnet, clinopyroxene and amphibole coexisting with andesitic and basaltic liquids: Geochimica et Cosmochimica Acta, v. 44, p. 287-308.

Nielsen, R.L., 1988, A model for the simulation of combined major and trace element liquid lines of descent: Geochimica et Cosmochimica Acta, v. 52, p. 27-38.

Nielsen, R.L., 1992, BIGD: a FORTRAN program to calculate trace-element partition coefficients for natural mafic and intermediate composition magmas: Computers and Geosciences, v. 18, p. 773-788.

Nielsen, R.L., Gallahan, W.E., and Newberger, F., 1992, Experimentally determined mineral-melt partition coefficients for Sc, Y and REE for olivine, orthopyroxene, pigeonite, magnetite and ilmenite: Contributions to Mineralogy and Petrology, v. 110, p. 488-499.

Ogunleye, P.O., Ike, E.C., and Garba, I., 2005, Geochemical characteristics of the niobium-rich arfvedsonite granites, Younger Granites province of Nigeria: Chemie der Erde, v. 65, p. 279-296.

Okamoto, K., 1979, Geochemical study on magmatic differentiation of Asama Volcano, central Japan: Journal of the Geological Society of Japan, v. 85, p. 525-535.

Oliveira, D.C., Dall'Agnol, R., Barros, C.E., and Oliveira, M.A., 2009, geology, geochemistry and magmatic evolution of the Paleoproterozoic, anorogenic oxidized A-type Redenção granite of the Jamon suite, eastern Amazonian craton, Brazil: Canadian Mineralogist, v. 47, p. 1441-1468.

Owen, J.V., and Greenough, J.D. 1999, Scapolite pegmatite from the Minas fault, Nova Scotia: tangible manifestation of Carboniferous, evaporite-derived hydrothermal fluids in the western Cobequid Highlands?: Mineralogical Magazine, v. 63, p. 387-397.

Papoutsa, A.,2012, The petrological evolution of the A-type granites of the Wentworth plutonic complex of the Cobequid Shear Zone (unpublished M.Sc thesis), Halifax, Saint Mary's University, 134 p.

Papoutsa, A., and Pe–Piper, G., 2013, The relationship between REE–Y–Nb–Th minerals and the evolution of an A–type granite, Wentworth pluton, Nova Scotia: American Mineralogist, v. 98, 444-462.

Park, J.K., and Gower, C.F., 1996, Paleomagnetism of pre-Grenvillian mafic rocks from the northeast Grenville Province, Labrador: implications for the Grenville Track: Canadian Journal of Earth Sciences, v. 33, p. 746-756.

Parneix, J.C., Beaufort, D., and Meunier, A., 1985, Biotite chloritization processes in hydrothermally altered granites: Chemical Geology, v. 51, p. 89–101.

Parry, W. T. and Downey, L. M., 1982, Geochemistry of hydrothermal chlorite replacing igneous biotite: Clays and Clay Minerals, v. 30, p. 81–90.

Patiño-Douce, A.E., 1997, Generation of metaluminous A-type granites by low-pressure melting of calc-alkaline granitoids: Geology, v. 25, p. 743-746.

Pearce, T.H., 1968, A contribution to the theory of variation diagrams: Contributions to Mineralogy and Petrology, v. 19, p. 142-157.

Pearce, J. A., and Cann, J. R., 1973, Tectonic setting of basic volcanic rocks determined using trace element analyses: Earth and Planetary Science Letters, v. 19, p. 290–300.

Pe–Piper, G., 1991, Granite and associated mafic phases, North River pluton, Cobequid Highlands, Nova Scotia: Atlantic Geology, v. 27, p. 15–28.

Pe–Piper, G., 1995a, The Devonian–Carboniferous North River and Gilbert Mountain plutons, Cobequid Highlands Nova Scotia: Geological Survey of Canada, Open file report No. 3874.

Pe–Piper, G., 1995b, The Carboniferous plutons and associated igneous rocks of the western Cobequid Highlands, Nova Scotia: Geological Survey of Canada, Open file report No. 3252.

Pe-Piper, G., 1998, The Devonian- Carboniferous Wentworth plutonic complex (Folly Lake and Hart Lake-Byers Lake plutons) of the central Cobequid Highlands, Nova Scotia: Geological Survey of Canada, Open file report 3373.

Pe-Piper, G., 2007, Relationship of amphibole composition to host-rock geochemistry: the A-type gabbro-granite Wentworth pluton, Cobequid Shear Zone, eastern Canada: European Journal of Mineralogy, v. 19, p. 29-38.

Pe-Piper, G., and Turner, D., 1988, The Jeffers Group, western Cobequid Hills, Nova Scotia: Geological Survey of Canada, Open File Report No. 1782.

Pe-Piper, G., and Murphy, J.B. 1989, Petrology of the Late Proterozoic Folly River Formation, Cobequid Highlands, Nova Scotia: a continental rift within a volcanic arc environment: Atlantic Geology, v. 25, p. 143–151.

Pe-Piper, G., and Piper, D.J.W., 1989, The upper Hadrynian Jeffers Group, Cobequid Highlands, Avalon zone of Nova Scotia: A back-arc volcanic complex: Geological Society of America Bulletin, v. 101, p. 364-376.

Pe-Piper, G., and Piper, D.J.W., 1998a, Geochemical and structural evolution of the Pleasant Hills pluton, Cobequid Highlands, Nova Scotia, Canada: Geological Survey of Canada, Open file report No. 3372.

Pe–Piper, G., and Piper, D.J.W., 1998b, Geochemical evolution of Devonian-Carboniferous igneous rocks of the Magdalen basin, Eastern Canada: Pb and Nd isotope evidence for mantle and lower crustal sources: Canadian Journal of Earth Sciences, v. 35, p. 201-221.

Pe-Piper, G., and Piper, D.J.W., 2003, A synopsis of the geology of the Cobequid Highlands, Nova Scotia: Atlantic Geology, v. 38, p. 145-160.

Pe-Piper, G., and Piper, D.J.W., 2005, Bedrock Geological Map of the Wentworth Area (parts of NTS sheets 11E/05, 11E/06, 11E/11 and 11E/12), Cobequid Highlands, Nova Scotia, scale 1:50 000: Nova Scotia Department of Natural Resources, Mineral Resources Branch, open file map, OFM ME 2005-116.

Pe-Piper, G., Cormier, R.F., and Piper, D.J.W., 1989, The age and significance of Carboniferous plutons of the western Cobequid Highlands, Nova Scotia: Canadian Journal of Earth Sciences, v. 26, p. 1297-1307.

Pe–Piper, G., Piper, D.J.W., and Clerk, S.B., 1991, Persistent mafic igneous activity in an A–type granite pluton, Cobequid Highlands, Nova Scotia: Canadian Journal of Earth Sciences, v. 28, p. 1058–1072.

Pe-Piper, G., Piper, D.J.W., and Koukouvelas, I., 1996, Precambrian plutons of the Cobequid Highlands, Nova Scotia, Canada in Nance R.D., and Thompson, M.D., eds, Avalonian and related Peri-Gondwanan terranes of the Circum-North Atlantic: Geological Society of America, Special Papers, v. 304, p. 121-132.

Pe–Piper, G., Koukouvelas, I., and Piper, D.J.W., 1998, Synkinematic granite emplacement in a shear zone: the Pleasant Hills pluton, Canadian Appalachians: Geological Society of America Bulletin, v. 110, p. 523–536.

Pe-Piper, G., Piper, D.J.W., and Hilton, E., 2002, Neoproterozoic plutonic rocks of the eastern Cobequid Highlands, N.S., Canada: Geological Survey of Canada, Open file report 4189.

Pe-Piper, G., Reynolds, P. H, Nearing, J., and Piper, D.J.W., 2004, Early Carboniferous deformation and mineralization in the Cobequid Shear Zone, Nova Scotia: an $^{40}Ar/^{39}Ar$ geochronology study: Canadian Journal of Earth Sciences, v. 41, p. 1425-1436.

Pe-Piper, G., Piper, D.J.W, and Tsikouras, B., 2010, The late Neoproterozoic Frog Lake hornblende gabbro pluton, Avalon terrane of Nova Scotia: evidence for the origins of appinites: Canadian Journal of Earth Sciences, v. 47, p. 103-120.

Pe-Piper, G., Wisen, J., Papoutsa, A., and Piper, D.J.W., 2015, Mineralisation of fractured granites along the Cobequid Fault Zone: West Moose River Pluton, Cumberland Co., Nova Scotia, Geological Survey of Canada, Open File 7759, 252 p.

Pedersen, A.K., 1979, Basaltic Glass with High-Temperature Equilibrated Immiscible Sulfide Bodies with Native Iron from Disko, Central West Greenland: Contributions to Mineralogy and Petrology, v. 69, p. 397-407.

Philpotts, J.A., and Schnetzler, C.C., 1970, Phenocryst-matrix partition coefficients for K, Rb, Sr and Ba, with applications to anorthosite and basalt genesis: Geochimica et Cosmochimica Acta, v. 34, p. 307-322.

Philippot, P., and Selverstone, L., 1991, Trace-element-rich brines in eclogitic veins: implications for fluid composition and transport during subduction: Contributions to Mineralogy and Petrology, v. 106, p. 417-430.

Piper, D.J.W., 1996, Horton Group sedimentary rocks adjacent to the Cobequid Highlands, Nova Scotia: in Current Research, Geological Survey of Canada: Ottawa, p. 55-60.

Piper, D.J.W., Pe-Piper, G., and Loncarevic, B.D., 1993, Devonian– Carboniferous deformation and igneous intrusion in the Cobequid Highlands: Atlantic Geology, v. 29, p. 219–232.

Pirajno, F., Jingwen, M., Zhang, Z., Zhang, Z., and Chai, F., 2008, The association of mafic-ultramafic intrusions and A-type magmatism in the Tian Shan and Altay orogens, NW China: Implications for geodynamic evolution and potential for the discovery of new ore deposits: Journal of Asian Earth Sciences, v. 32, p. 165-183.

Pisarevsky, S.A., and Bylund, G., 2006, Palaeomagnetism of 935 Ma mafic dykes in southern Sweden and implications for the Sveconorwegian Loop: Geophysical Journal International, v. 166, p. 1095-1104.

Pisarevsky, S.A., Wingate, M.T.D., Powell, C.M., Johnson, S., and Evans, D.A.D., 2003, Models of Rodinia assembly and fragmentation in: Yoshida, M., Windley, B., and Dasgupta, S. (eds) Proterozoic East Gondwana: supercontinent assembly and breakup, Geological Society, London, Special Publication 206, p. 35-55.

Pisarevsky, S.A., McCausland, P.J.A., Hodych, J.P., O'Brien, S.J., Tait, J.A., and Murphy, J.B., 2012, Paleomagnetic study of the late Neoproterozoic Bull Arm and Crown Hill formations (Musgravetown Group) of eastern Newfoundland: implications for Avalonia and West Gondwana paleogeography: Canadian Journal of Earth Sciences, v. 49, p. 308-327.

Pollock, J.C., Hibbard, J.P., and Sylvester, P.J., 2009, Early Ordovician rifting of Avalonia and birth of the Rheic Ocean: U-Pb detrital zircon constraints from Newfoundland: Journal of the Geological Society of London, v. 166, p. 501-515.

Pollock, J.C., Hibbard, J.P., and van Staal, C.R., 2012, A paleogeographical review of the peri-Gondwanan realm of the Appalachian Orogen: Canadian Journal of Earth Sciences, v. 49, p. 259-288.

Popov, V., Iosifidi, A., Khramov, A., Tait, A., and Bachtadse, V., 2002, Paleomagnetism of upper Vendian sediments from the Winter Coast, White Sea region, Russia: implications for the paleogeography of Baltica during Neoproterozoic times: Journal of Geophysical Research, v. 107, EPM 10, p. 1-8.

Pršek, J., Ondrejka, M., Bačíc, P., Budzyń, B., and Uher, P., 2010, Metamorphic-hydrothermal REE minerals in the Bacúch magnetite deposit, western Carpathians, Slovakia: (Sr,S)–rich monazite–(Ce) and Nd–dominant hingganite: Canadian Mineralogist, v. 48, p. 81-94.

Putirka, K., 2005, Igneous thermometers and barometers on plagioclase + liquid equilibria: Tests of some existing models and new calibrations: American Mineralogist, v. 90, p. 336-346.

Putnis, A., 2002, Mineral replacement reactions: from macroscopic observations to microscopic mechanisms: Mineralogical Magazine, v. 66, p. 689–708.

Rajesh, H.M., 2000, Characterization and origin of a compositionally zoned aluminous A-type granite from South India: Geological Magazine, v. 137, p. 291-318.

Ramberg, H., 1952, Chemical bonds and the distribution of cations in silicates: Journal of Geology, v. 60, p. 331-355.

Reid, F., 1983, Origin of the Rhyolitic Rocks of the Taupo Volcanic Zone, New-Zealand: Journal of Volcanology and Geothermal Research, v. 15, p. 315-338.

Richard, L., 1995, The ultimate mineralogical and petrological data processing system for Windows, Minpet Geological Software, Logiciel Geologique Minpet, Quebec.

Ridolfi, F., and Rinzulli, A., 2012, Calcic amphiboles in calc-alkaline and alkaline magmas: thermobarometric and chemometric empirical equations valid up to 1,130 °C and 2.2 GPa: Contributions to Mineralogy and Petrology, v. 163, p. 877-895.

Ridolfi, F., Renzulli, A., and Puerini, M., 2010, Stability and chemical equilibrium of amphibole in calc-alkaline magmas: an overview, new thermobarometric formulations and application to subduction-related volcanoes: Contributions to Mineralogy and Petrology, v. 160, p. 45-66.

Rieder, M., Cavazzini, G., D'Yakonov, Y., Frank–Kamenetskii, V.A., Gottardi, G., Guggenheim, S., Koval, P.V., Müller, G., Neiva, A.M.R., Radoslovich, E.W., Rober, J.L., Sassi, F.P., Takeda, H., Weiss, Z., and Wones, D.R., 1998, Nomenclature of the micas: Clays and Clay Minerals, v. 46, p. 586–595.

Rolland, Y., Cox, S., Boullier, A., Pennacchioni, G., and Mancktelow, N., 2003, Rare earth and trace element mobility in mid–crustal shear zones: insights from the Mont Blanc Massif (Western Alps): Earth and Planetary Science Letters, v. 214, p. 203–219.

Rollinson, H.R., 1993, Using geochemical data: evaluation, presentation, interpretation. Longman, UK [Co-published by J. Wiley & Sons. Inc. in the USA].

Ronov, A.B., and Yaroshevskiy, A.A., 1976, A new model for the chemical structure of the Earth's crust: Geochemistry International, v. 13, p. 89-121.

Ruprecht, P., and Bachmann, O., 2010, Pre-eruptive reheating during magma mixing at Quizapu volcano and the implications for the explosiveness of silicic arc volcanoes: Geological Society of America, v. 38, p. 919-922.

Russell, J.K., and Nicholls, J., 1988, Analysis of petrogenetic hypotheses with Pearce element ratios: Contributions to Mineralogy and Petrology, v. 99, p. 25-35.

Rutherford, M.J., and Devine, J.D., 2003, Magmatic conditions and magma ascent as indicated by hornblende phase equilibria and reactions in the 1995-2002 Soufrière Hills magma: Journal of Petrology, v. 44, p. 1433-1454.

Saraiva dos Santos, T.J., da Silva Amaral, W., Ancelmi, M.F., Pitarello, M.Z., Fuck, R.A., and Dantas, E.L., 2014, U–Pb age of the coesite-bearing eclogite from NW Borborema Province, NE Brazil: Implications for western Gondwana assembly: Gondwana Research, article in press, doi:10.1016/j.gr.2014.09.013.

Satkoski, A.M., Barr, S.M., and Sampson, S.D., 2010, Provenance of late Neoproterozoic and Cambrian sediments in Avalonia: Constraints from detrital zircon ages and Sm-Nd isotopic compositions in southern New Brunswick, Canada: The Journal of Geology, v. 118, p. 187-200.

Saxena, S.K., 1968, Distribution of elements between coexisting minerals and the nature of solid solution in garnet: American Mineralogist, v. 53, p. 994-1014.

Sayer, S., 1974, An integrated study of the Blue Hills Porphyry and related units Quincy and Milton, Massachusetts (unpublished M.Sc thesis), Massachusetts, Massachusetts Institute of Technology, 146 p.

Scaillet, B., and Macdonald, R., 2003, Fluorite stability in silicic magmas: Contributions to Mineralogy and Petrology, v. 147, p. 1867-1894.

Scaillet, B., Holtz, F., and Pichavant, M., 1998, Phase equilibrium constraints on the viscosity of silicic magmas: Journal of Geophysical Research, v. 103, p. 257-266.

Scaillet, B., and Macdonald, R., 2001, Phase relations of peralkaline silicic magmas and petrogenetic implications: Journal of Petrology, v. 42, p. 825-845.

Schmitt, A.K., Trumbull, R.B., Dulski P., and Emmermann, R., 2002, Zr-Nb-REE mineralization in peralkaline granites from the Amis Complex, Brandberg (Namibia): Evidence for magmatic pre-enrichment from melt inclusions: Economic Geology, v. 97, p. 399-413.

Schnetzler, C.C., and Philpotts, J.A., 1970, Partition coefficients of rare-earth elements between igneous matrix material and rock-forming mineral phenocrysts: II: Geochimica et Cosmochimica Acta, v. 34, p. 331-340.

Seguin, M.K., and Brun, J., 1984, Geology, geochemistry and paleomagnetism of the Cheneaux Metagabbro (Helikian) of southern Quebec and eastern Ontario: Precambrian Research, v. 26, p. 307-331.

Shaw, D.M., 1970, Trace element fractionation during anatexis: Geochimica et Cosmochimica Acta, v. 34, p. 237-243.

Shellnutt, J.G., and Iizuka, Y., 2011, Mineralogy from three peralkaline granitic plutons of the Late Permian Emeishan large igneous province (SW China): evidence for contrasting magmatic conditions for A-type granitoids: European Journal of Mineralogy, v. 23, p. 45-61.

Sibson, R.H., 1992, Implications of fault-valve behaviour for rupture nucleation and recurrence: Tectonophysics, v. 211, p. 283-293.

Sibson, R.H., 1996, Structural permeability of fluid-driven fault-fracture meshes: Journal of Structural Geology, v. 18, p. 1031-1042.

Sibson. R.H., Robert, F., and Paulsen. K.H., 1988, High-angle reverse faults, fluid-pressure cycling, and mesothermal gold-quartz deposits: Geology, v. 16, p. 551-555.

Simon, A.C., Pettke, T., Candela, P.A., Piccoli, P.M., and Heinrich, C.A., 2004, Magnetite solubility and iron transport in magmatic–hydrothermal environments: Geochimica et Cosmochimica Acta, v. 68, p. 4905–4914.

Sisson, T.W., 1991, Pyroxene-High Silica Rhyolite Trace-Element Partition-Coefficients Measured by Ion Microprobe: Geochimica et Cosmochimica Acta, v. 55, p. 1575-1585.

Sisson, T.W., 1994, Hornblende-Melt Trace-Element Partitioning Measured by Ion Microprobe: Chemical Geology, v. 117, p. 331-344.

Smith, M.P., and Henderson, P., 2000, Preliminary Fluid Inclusion Constraints on Fluid Evolution in the Bayan Obo Fe-REE-Nb Deposit, Inner Mongolia, China: Ecomonic Geology, v. 95, p. 1371-1388.

Smith, M.P., Henderson, P., and Campbell, S.L., 2000, Fractionation of the REE during hydrothermal processes: Constraints from the Bayan Obo Fe–REE–Nb deposit, Inner Mongolia, China: Geochimica et Cosmochimica Acta, v. 64, p. 3141–3160.

Skulski, T., Minarik, W., and Watson, E.B., 1994, High-pressure experimental trace-element partitioning between clinopyroxene and basaltic melts: Chemical Geology, v. 117, p. 127-147

Streckeisen, A. L., 1974, Classification and Nomenclature of Plutonic Rocks. Recommendations of the IUGS Subcommission on the Systematics of Igneous Rocks: Geologische Rundschau, v. 63, p. 773-785.

Stix, J., and Gorton, M.P., 1990, Variations in Trace-Element Partition-Coefficients in Sanidine in the Cerro Toledo Rhyolite, Jemez Mountains, New-Mexico - Effects of Composition, Temperature, and Volatiles: Geochimica et Cosmochimica Acta, v. 54, p. 2697-2708.

Streck, M.J., and Grunder, A.L., 1997, Compositional gradients and gaps in high-silica rhyolites of the Rattlesnake Tuff, Oregon: Journal of Petrology, v. 38, p. 133-163.

Solano, J.M.S., Jackson, M.D., Sparks, R.S.J., Blundy, J.D., and Annen, C., 2012, Melt segregation in deep crustal hot zones: a mechanism for chemical differentiation, crustal assimilation, and the formation of evolved magmas: Journal of Petrology, v. 53, p. 1999-2026.

Soper, N.J., Strachan, R.A., Holdsworth, R.E., Gayer, R.A., and Greiling, R.O., 1992, Sinistral transpression and the Silurian closure of Iapetus, Journal of the Geological Society, London,v. 149, p. 871-880.

Strong, D.F., and Taylor, R.P., 1984, Magmatic-subsolidus and oxidation trends in composition of amphiboles from silica-saturated peralkaline igneous rocks: Tschermarks Mineralogische und Petrographische Mitteilungen, v. 32, p. 211-222.

Su, Y., Tang, H., Sylvester, P.J., Liu, C., Qu, W., Hou, G., and Cong, F., 2007, Petrogenesis of Karamaili alkaline A-type granites from East Junggar, Xinjiang (NW China) and their relationship with tin mineralization: Geochemical Journal, v. 41, p. 341-357.

Sun, S.S., and McDonough, W.F., 1989, Chemical and isotopic systematics of oceanic basalts: implications for mantle composition and processes: Geological Society of London, Special Publications, v. 42, p. 313–345.

Sverjensky, D.A., 1984, Europium redox equilibria in aqueous solution. Earth and Planetary Science Letters, v. 67, p. 70–78.

Sylvester, P .J., 1989, Post-collisional alkaline granites: Journal of Geology, v. 97, p. 261-280.

Symons, D.T.A., and Chiasson, D., 1991, Paleomagnetism of the Callander Complex and the Cambrian apparent polar wander path for North America: Canadian Journal of Earth Sciences, v. 28, p. 355-363.

Tabelin, C.B., and Igarashi, T., 2009, Mechanisms of arsenic and lead release from hydrothermally altered rock: Journal of Hazardous Materials, v. 169, p. 980–990.

Takeuchi, M., and Arai, S., 2014, Lower crustal metasomatism inferred from mafic xenoliths from Ichinomegata crater, northeastern Japan arc: Journal of Mineralogical and Petrological Sciences, v. 109, p. 85-90.

Tanczyc, E.I., Lapointe, P., Morris, W.A., and Schmidt, P.W., 1987, Paleomagnetic study of the layered mafic intrusion at Sept- Îles, Quebec: Canadian Journal of Earth Sciences, v. 24, p. 1431-1438.

Thompson, M.D., Grunow, A.M., and Ramezani, J., 2007, Late Neoproterozoic paleogeography of the Southeastern New England Avalon Zone: Insights from U-Pb geochronology and paleomagnetism: Geological Society of America Bulletin, v. 119, p. 681-696.

Thompson, M.D., Ramezani, J., Barr, S.M., and Hermes, O.D., 2010, High precision U-Pb dates for Ediacaran granitoid rocks in SE New England: Revised magmatic chronology and correlation with other Avalonian terranes *in:* Tollo, R.P., Bartholomew, M.J., Hibbard, J.P., and Karabinos, P.M. (eds) From Rodinia to Pangea: The lithotectonic record of the Appalachian Region, Geological Society of America Memoir 206, p. 231-250.

Thompson, M.D., Barr, S.M., and Grunow, A.M., 2012, Avalonian perspectives on Neoproterozoic paleogeography: Evidence from Sm-Nd isotope geochemistry and detrital zircon geochronology in SE New England, USA: Geological Society of America Bulletin, v. 124, p. 517-531.

Torsvik, T.H., and Rehnström, E.F., 2003, The Tornquist Sea and Baltica–Avalonia docking: Tectonophysics, v. 362, p. 67-82.

Torsvik, T.H., and Cocks, L.R.M., 2013, Gondwana from top to base in space and time, Gondwana Research, v. 24, p. 999-1030.

Torsvik, T.H., Smethurst, M.A., and Meert, J.G., 1996, Continental break-up and collision in the Neoproterozoic- a tale of Baltica and Laurentia: Earth-Science Reviews, v. 40, p. 229-258.

Torsvik, T.H., van der Voo, R., Doubrovine, P.V., Burke, K., Steinberger, B., Ashwal, L.D., Trønnes, R.G., Webb, S.J., and Bull, A.L., 2014, Deep mantle structure as a reference frame for movements in and on Earth: Proceedings of the National Academy of Sciences, v. 111, p. 8735-8740.

Trench, A., Torsvik, T.H., and McKerrow, W., 1992, The paleogeographic evolution of southern Britain during early Paleozoic times: a reconciliation of paleomagnetic and biogeographic evidence: Tectonophysics, v. 201, p. 75-82.

Trompette, R., 1997, Neoproterozoic (c. 600 Ma) aggregation of Western Gondwana: a tentative scenario: Precambrian Research, v. 82, p. 101-102.

Turner, S.P., Foden, J.D., and Morrison, R.S., 1992, Derivation of some A-type magmas by fractionation of basaltic magma: An example from Padthaway Ridge, South Australia: Lithos, v. 28, p. 151-179.

Uher, P., Ondrejka, M., and Konečný, P., 2009, Magmatic and post–magmatic YREE–Th phosphate, silicate and Nb–Ta–Y–REE oxide minerals in A–type metagranite: an example from the Turčok massif, western Carpathians, Slovakia: Mineralogical Magazine, v. 73, p. 1009–1025.

Utting, J., Keppie, J.D., and Giles, P.S., 1989, Palynology and stratigraphy of the Lower Carboniferous Horton Group, Nova Scotia: Geological Survey of Canada Bulletin, v. 396, p. 117–143.

van Staal, C.R., Dewey, J.F., MacNiocaill, C., and McKerrow, W.S., 1998, The Cambrian-Silurian tectonic evolution of the northern Appalachians and British Caledonides: history of a complex west and southwest Pacific-type segment of Iapetus *in*: Blundell, D.J., and Scott, A.C. (eds), Lyell: The past is the key to the present, Geological Society of London, Special Publications, v. 143, p. 199-242.

van Staal, C.R., Whalen, J.B., Valverde-Vaquero, P., Zagorevski, A., and Rogers, N., 2009, Pre-Carboniferous episodic accretion-related, orogenesis along the Laurentian margin of the northern Appalachians in: Murphy, J.B., Keppie, J.D., and Hynes, A.J. (eds) Ancient orogens and Modern Analogues, Geological Society of London, Special Publication 327, p. 271-316.

van Staal, C.R., Barr, S.M., and Murphy, J.B., 2012, Provenance and tectonic evolution of Ganderia: Constraints on the evolution of the Iapetus and Rheic Oceans: Geology, v. 40, p. 987-990.

Vander Auwera, J., Bogaerts, M., Liégeois, J-P., Demaiffe, D., Bolle, O., and Duchesne, J.C., 2003, Derivation of the 1.0-0.9 Ga ferro-potassic A-type granitoids of southern Norway by extreme differentiation from basic magmas: Precambrian Research, v. 124, p. 107-148.

Veikkolainen, T., Pesonen, L.J., and Evans, D.A.D., 2014, PALEOMAGIA, a PHP/MYSQL paleomagnetic database for the Precambrian: Studia Geophysica et Geodaetica, v. 58, p. 425-441.

Vizan, H., Carney, J.N., Turner, P., Ixer, R.A., Tomassi, M., Mullen, R.P., ad Clarke, P., 2003, Late Neoproterozoic to early Paleozoic paleogeography of Avalonia: some paleomagnetic constraints from Nuneaton, central England: Geological Magazine, v. 140, p. 685-705.

Waldron, J.W.F., Piper, D.J.W., and Pe–Piper, G., 1989, Deformation of the Cape Chignecto pluton, Cobequid Highlands, Nova Scotia: thrusting at the Meguma–Avalon boundary: Atlantic Geology, v. 25, p. 51–62.

Wang, R.C., Wang, D.Z., Zhao G.T., Lu J.J., Chen, X.M., and Xu S.J., 2001, Accessory mineral record of magma-fluid interaction in the Laoshan I- and A-type granitic complex, eastern China: Physics and Chemistry of the Earth, v. 26, p. 835-849.

Watson, E.B., 1979, Zircon saturation in felsic liquids: experimental results and applications to trace element geochemistry: Contributions to Mineralogy and Petrology, v. 70, p. 407–419.

Webster, J.D., Tappen, C.M., and Mandenville, C.W., 2009, Partitioning behavior of chlorine and fluorine in the system apatite-melt-fluid. II: Felsic silicate systems at 200 Mpa: Geochimica et Cosmochimica Acta, v. 73, p. 559-581.

Weil, A.B., Geissman, J.W., and van der Voo, R., 2004, Paleomagnetism of the Neoproterozoic Chuar Group, Grand Canyon Supergroup, Arizona: implications for Laurentia's Neoproterozoic APWP and Rodinia break-up: Precambrian Research, v. 129, p. 71-92.

Wenner, J.M., and Lloyd, M.A., 2006, Trace-element signatures and tectonic affinities of Proterozoic A-type granites and rhyolites in central Wisconsin: Geoscience Wisconsin v. 17, p. 35-51.

Whalen, J. B., Currie, K. L., and Chappell, B. W., 1987, A-type granites: geochemical characteristics, discrimination and petrogenesis: Contributions to Mineralogy and Petrology, v. 95, p. 407-419.

Whalen, J. B., Currie, K. L., and Chappell, B. W., 1989, A–type granites: geochemical characteristics, discrimination and petrogenesis: Contributions to Mineralogy and Petrology, v. 95, p. 407–419.

Whalen, J.B., Jenner, G.A., Currie, K.L., Barr, S.M., Longstaffe, F.J., and Hegner, E., 1994, Geochemical and isotopic characteristics of granitoids of the Avalon zone, southern New Brunswick: possible evidence for repeated delamination events: Journal of Geology, v. 102, p. 269-282.

White, C.E., Barr, S.M., and Ketchum, J.W.F., 2002, New Age Controls on Rock Units in pre-Carboniferous Basement Blocks in Southwestern Cape Breton Island and Adjacent Mainland Nova Scotia *in:* Mineral Resources Branch, Report of Activities, Nova Scotia Department of Natural Resources, Report 2003-1, p. 163-178.

Whitney, D.L. Evans, B.W., 2010, Abbreviations for names of rock-forming minerals: American Mineralogist, v. 95, p. 185-187.

Wiewióra, A., and Weiss, Z., 1990, Crystallochemical classifications of phyllosilicates based on the unified system of projection of chemical composition: II. The chlorite group: Clay Minerals, v. 25, p. 83–92.

Windley, B.F., Alexeiev, D., Xiao, W., Kroner, A., And Badarch, G., 2007, Tectonic models for accretion of the Central Asian Orogenic Belt: Journal of the Geological Society, London, v. 164, p. 31-47.

Williams, P.J., Barton, M.D., Johnson, D.A., Fontboté, L., Halter, A.D., Mark, G., Oliver, N.H.S., and Marschik, R., 2005, Iron-oxide copper-gold deposits: Geology, space-time distribution, and possible modes of origin, Economic Geology 100th anniversary volume, p. 371–405.

Williams–Jones, A.E., and Wood, S.A., 1992, A preliminary petrogenetic grid for REE fluorocarbonates and associated minerals: Geochimica et Cosmochimica Acta, v. 56, p. 725–738.

Williams–Jones, A.E., Migdisov, A.A., and Samson, I.M., 2012, Hydrothermal mobilization of the Rare Earth Elements– a tale of "Ceria" and "Yttria": Elements, v. 8, p. 355–360.

Willner, A.P., Barr, S.M., Gerdes, A., Massonne, H.-J., and White, C.E., 2013, Origin and evolution Avalonia: evidence from U-Pb and Lu-Hf isotopes in zircon from the Mira terrane, Canada and the Stavelot-Venn Massif, Belgium: Journal of the Geological Society, London, v. 170, p. 769-784.

Wilson, M., Neumann, E.-R., Davies, G.R., Timmerman, M.J., Heeremans, M., and Larsen, B.T., 2004, Permo-Carboniferous rifting in Europe: introduction: Geological Society of London, Special Publications, v. 223, p. 1-10.

Wintsch, R.P., Keewook, Y., and Dorais, M.J., 2014, Crustal thickening by tectonic wedging of the Ganderian rocks, southern New England, USA: Evidence from cataclastic zircon microstructures and U-Pb ages: Journal of Structural Geology, v. 69, p. 428-448.

Wisen, J., 2015, REE and other minerals in the West Moose River Pluton and associated rocks, Cobequid Highlands, Nova Scotia, and their association with fracturing : Unpublished B.Sc thesis, Saint Mary's University, 261 p.

Wones, D. R., 1981, Mafic minerals as indicators of intensive variables in granitic magmas: Mining Geology, v. 31, p. l9-22.

Wu, F., Sun, D., Li, H., Jahn, B., and Wilde, S., 2001, A-type granites in northeastern China: age and geochemical constraints on their petrogenesis: Chemical Geology, v. 187, p. 143-173.

Xie, L., Wang, R.C., Wang, D.Z., and Qiu, J.S., 2006, A survey of accessory mineral assemblages in peralkaline and more aluminous A-type granites of the southeast coastal area of China: Mineralogical Magazine, v. 70, p. 709-729.

Zagorevsky, A., van Staal, C.R., and McNicoll, V.J., 2007, Distinct Taconic, Salinic, and Acadian deformation along the Iapetus suture zone, Newfoundland Appalachians, Canadian Journal of Earth Sciences, v. 44, p. 1574-1585.

Zang, W., and Fyfe, W.S., 1995, Chloritization of hydrothermally altered bedrock at the Igarape Bahia gold deposit, Carajas, Brazil: Mineralium Deposita, v. 30, p. 30–38.

Zindler, A., and Hart, S., 1986, Chemical geodynamics: Annual Reviews in Earth and Planetary Sciences, v. 14, p. 493-571.

WEB REFERENCES

ICS 2013. http://www.stratigraphy.org/index.php/ics-chart-timescale. Last accessed 03-06-2013.

www.gplates.org. Last accessed 06-06-2015.

APPENDIX A

Supplementary material for Chapter 2.

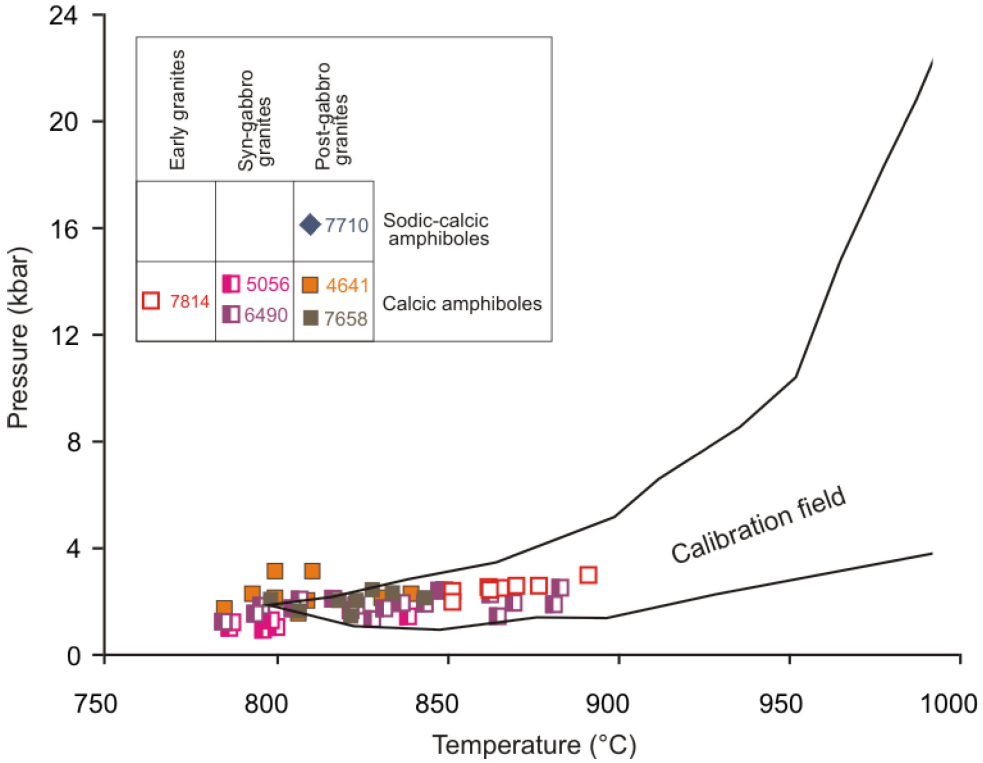

Appendix A.1 Graphic expression of the calibration range for the pressure and temperature estimates during crystallization of hornblende according to the method of Ridolfi and Renzulli (2012). In this diagram P and T estimates from the calcic amphiboles from the Wentworth pluton are plotted for comparison.

Appendix A.2 Representative EDS analyses of feldspars from the Wentworth granites.

Sample	**4636**	**4641**	**4641**	**4641**	**4641**	**4641**	**5056**	**5056**	**6419**	**6419**	**6419**	**6419**	**6419**	**6419**	**6419**
Mineral	Ab (p)	Ab	Ab	Ab	Ab	Ab	Ab	Ol	Ab (p)	Ab (p)	Ab (p)	Ab (p)	Ab (p)	Ab (p)	Ab (p)
SiO_2	69.48	66.57	67.26	67.19	68.33	67.00	64.63	61.82	69.48	69.10	67.23	69.35	68.63	68.52	68.78
Al_2O_3	17.93	19.90	20.20	20.18	19.35	19.71	22.75	24.30	18.95	18.67	18.74	18.37	19.42	18.57	19.14
FeO	0.62	0.77	0.33	1.33	0.00	0.00	0.55	0.00	0.35	0.00	0.00	0.00	0.50	0.69	0.00
CaO	0.00	1.57	1.51	0.85	0.57	0.78	0.92	4.98	0.00	0.00	0.00	0.00	0.00	0.00	0.00
Na_2O	11.47	10.65	10.22	9.94	11.76	11.11	9.56	8.52	11.22	12.24	12.67	12.28	11.06	10.97	11.28
K_2O	0.49	0.55	0.48	0.53	0.00	1.40	1.59	0.37	0.00	0.00	1.35	0.00	0.00	1.23	0.81
Total	99.99	100.01	100.00	100.02	100.01	100.00	100.00	99.99	100.00	100.01	99.99	100.00	99.61	99.98	100.01
Ab	**97**	**90**	**90**	**92**	**97**	**89**	**86**	**74**	**100**	**100**	**93**	**100**	**100**	**93**	**96**
An	**0**	**7**	**7**	**4**	**3**	**3**	**5**	**24**	**0**	**0**	**0**	**0**	**0**	**0**	**0**
Or	**3**	**3**	**3**	**3**	**0**	**7**	**9**	**2**	**0**	**0**	**7**	**0**	**0**	**7**	**5**
Sample	**6419**	**6419**	**6419**	**6419**	**6419**	**6490**	**6490**	**6490**	**6490**	**6490**	**6490**	**6490**	**6490**	**6490**	**6518**
Mineral	Ab (p)	Ab (p)	Ab (p)	Ab (p)	Ab (p)	Ab	Ab	Ab	Ab	Ab	Ab	Ab	Ab	Ab	Ab
SiO_2	68.65	69.82	68.60	69.61	69.46	67.66	67.19	67.45	66.72	67.45	67.64	68.18	66.98	67.77	69.65
Al_2O_3	18.44	18.78	18.67	18.88	18.52	19.35	20.16	19.24	20.43	20.56	19.48	19.93	20.22	20.27	17.93
FeO	0.00	0.00	0.00	0.00	0.00	0.00	0.00	0.00	0.00	0.00	0.00	0.00	0.00	0.00	0.45
CaO	0.00	0.00	0.00	0.00	0.00	1.09	0.92	1.32	1.44	1.47	1.01	0.80	0.87	1.23	0.00
Na_2O	12.93	11.39	10.91	10.61	12.01	11.92	11.72	12.00	10.79	10.53	11.88	11.10	11.93	10.73	11.73
K_2O	100.02	99.99	98.18	99.10	99.99	100.02	99.99	100.01	99.38	100.01	100.01	100.01	100.00	100.00	99.76
Total	0.00	0.00	1.83	0.89	0.00	0.00	0.00	0.00	0.61	0.00	0.00	0.00	0.00	0.00	0.25
Ab	**100**	**100**	**90**	**95**	**100**	**95**	**96**	**94**	**90**	**93**	**96**	**96**	**96**	**94**	**99**
An	**0**	**0**	**0**	**0**	**0**	**5**	**4**	**6**	**7**	**7**	**5**	**4**	**4**	**6**	**0**
Or	**0**	**0**	**10**	**5**	**0**	**0**	**0**	**0**	**3**	**0**	**0**	**0**	**0**	**0**	**1**

Appendix A.2 Representative EDS analyses of feldspars from the Wentworth granites (continued).

Sample	**6518**	**6518**	**6518**	**7658**	**7658**	**7658**	**7658**	**7658**	**7658**	**7658**	**7658**	**7658**	**7658**	**7658**	**7710**
Mineral	Ab	Ab	Ab	Ab	Ab	Ab	Ab	Ab	Ab	Ab	Ab	Ab	Ab	Ol	Ab
SiO_2	69.05	69.84	69.48	67.41	67.51	68.09	67.15	66.74	67.41	67.77	66.94	66.81	66.53	65.07	67.98
Al_2O_3	18.42	18.33	18.42	20.07	19.95	19.58	19.88	20.33	19.61	20.10	20.31	20.09	21.24	20.82	17.84
FeO	0.54	0.33	0.44	0.00	0.00	0.00	0.00	0.46	0.67	0.00	0.00	0.00	0.00	0.80	0.00
CaO	0.00	0.00	0.00	1.83	1.50	1.11	1.93	1.78	1.19	1.33	1.79	1.89	1.25	2.83	0.00
Na_2O	11.26	11.51	11.31	10.45	10.77	10.97	10.49	10.31	10.27	10.81	10.46	10.41	9.69	9.79	11.99
K_2O	0.73	0.00	0.36	0.24	0.28	0.25	0.55	0.39	0.86	0.00	0.49	0.81	1.29	0.70	2.19
Total	100.00	100.01	100.01	100.00	100.01	100.00	100.00	100.01	100.01	100.01	99.99	100.01	100.00	100.01	100.00
Ab	**96**	**100**	**98**	**90**	**91**	**93**	**88**	**89**	**89**	**94**	**89**	**87**	**86**	**83**	**89**
An	**0**	**0**	**0**	**9**	**7**	**5**	**9**	**9**	**6**	**6**	**8**	**9**	**6**	**13**	**0**
Or	**4**	**0**	**2**	**1**	**2**	**1**	**3**	**2**	**5**	**0**	**3**	**4**	**8**	**4**	**11**
Sample	**7710**	**7710**	**7710**	**7710**	**7814**	**7814**	**7814**	**7814**	**7814**	**4641**	**5056**	**5056**	**5056**	**5056**	**5056**
Mineral	Ab	Ab	Ab	Ab	Ab	Ab	Ab	Ab	Ab	Ab (p)	And	And	And	And	And
SiO_2	69.63	68.28	69.33	68.60	68.50	68.15	69.25	68.05	68.58	68.58	64.80	62.06	63.19	62.51	62.94
Al_2O_3	17.88	19.48	18.48	18.69	19.29	19.71	18.50	19.31	19.29	19.22	22.20	24.58	24.26	23.41	23.22
FeO	0.00	0.00	0.00	0.00	0.00	0.00	0.00	0.00	0.00	0.00	0.00	0.00	0.50	0.53	0.00
CaO	0.00	0.00	0.00	0.00	0.77	0.91	0.42	0.60	0.78	0.88	5.18	5.07	5.09	5.08	5.37
Na_2O	11.51	11.57	9.60	12.13	11.45	11.20	11.41	12.04	11.34	11.34	7.31	7.93	6.42	7.79	8.47
K_2O	0.99	0.67	2.61	0.58	0.00	0.00	0.42	0.00	0.00	0.00	0.53	0.36	0.54	0.69	0.00
Total	100.01	100.00	100.02	100.00	100.01	99.97	100.00	100.00	99.99	100.02	100.02	100.00	100.00	100.01	100.00
Ab	**95**	**96**	**85**	**97**	**96**	**96**	**96**	**97**	**96**	**96**	**70**	**72**	**67**	**71**	**74**
An	**0**	**0**	**0**	**0**	**4**	**4**	**2**	**3**	**4**	**4**	**27**	**26**	**29**	**25**	**26**
Or	**5**	**4**	**15**	**3**	**0**	**0**	**2**	**0**	**0**	**0**	**3**	**2**	**4**	**4**	**0**

Appendix A.2 Representative EDS analyses of feldspars from the Wentworth granites (continued).

Sample	**4636**	**4641**	**5056**	**6419**	**6490**	**6518**	**7658**	**7710**	**7814**
Mineral	Kfs	Kfs	Kfs	Kfs	Kfs	Kfs	Kfs	Kfs	Kfs
SiO_2	66.21	65.97	67.17	65.67	66.57	66.06	66.12	67.34	66.55
Al_2O_3	17.63	18.16	17.86	17.61	18.31	17.38	17.88	18.14	18.25
FeO	0.00	0.00	0.00	0.62	0.00	0.00	0.00	0.00	0.00
CaO	0.00	0.00	0.00	0.00	0.00	0.00	0.00	0.00	0.00
Na_2O	0.00	0.00	0.00	0.00	0.00	0.00	0.00	0.00	0.00
K_2O	16.18	15.86	14.96	16.10	15.12	16.54	16.01	14.50	15.20
Total	100.02	99.99	99.99	100.00	100.00	99.98	100.01	99.98	100.00
Ab	**0**	**0**	**0**	**0**	**0**	**0**	**0**	**0**	**0**
An	**0**	**0**	**0**	**0**	**0**	**0**	**0**	**0**	**0**
Or	**100**	**100**	**100**	**100**	**100**	**100**	**100**	**100**	**100**

Notes: Ab: albite, And: andesine, An: anorthite, Or: orthoclase, Ol: oligoclase, Kfs: K-feldspar, (p): perthite.

Appendix A.3 Electron microprobe analyses of amphiboles from the granites of the Wentworth pluton.

Sample	**4636**	**4636**	**4636**	**4636**	**4636**	**4636**	**4636**	**4636**	**4636**	**4636**	**4636**	**4636**	**4636**	**4636**	**4636**
Analysis	**169**	**171**	**172**	**173**	**174**	**175**	**176**	**177**	**178**	**179**	**184**	**187**	**188**	**190**	**193**
SiO_2	48.89	49.99	49.03	51.28	50.53	50.59	50.59	49.98	49.52	50.85	50.76	49.24	50.29	49.95	50.25
TiO_2	1.58	1.35	1.34	0.98	1.30	1.09	1.64	1.65	1.41	1.69	1.33	1.51	1.69	1.61	1.27
Al_2O_3	2.05	1.29	1.70	1.08	1.42	1.19	1.26	1.58	1.62	1.17	0.96	2.05	1.83	1.93	1.31
FeO	31.75	32.19	31.95	32.55	32.50	31.21	32.18	31.84	31.22	33.01	32.55	31.34	31.70	32.25	32.66
MnO	0.78	0.72	0.71	0.74	0.73	0.66	0.67	0.63	0.57	0.55	0.75	0.69	0.74	0.74	0.75
MgO	1.37	1.30	1.67	1.21	1.28	2.35	1.57	1.92	2.12	1.31	1.19	1.50	1.77	1.43	1.00
CaO	2.75	2.80	2.44	1.51	2.17	2.54	2.33	2.30	3.17	1.84	2.27	2.63	2.38	2.12	1.96
Na_2O	7.85	7.34	7.64	7.25	7.60	6.97	7.35	6.63	6.28	6.74	7.14	7.12	6.72	7.76	7.31
K_2O	1.35	1.16	1.35	1.14	1.35	1.09	1.25	1.29	1.02	1.08	1.16	1.27	1.28	1.39	1.19
F	1.54	1.37	1.14	0.52	1.06	0.70	1.02	0.60	1.63	0.56	1.03	1.30	0.74	1.13	1.06
Cl	0.04	0.03	0.04	0.03	0.04	0.03	0.05	0.03	0.03	0.05	0.04	0.05	0.05	0.05	0.08
Total	**99.95**	**99.52**	**98.99**	**98.29**	**99.98**	**98.40**	**99.91**	**98.44**	**98.59**	**98.83**	**99.16**	**98.69**	**99.19**	**100.35**	**98.83**
Structural formula calculated on the basis of 23 oxygens and Fe^{3+} estimated with the 13eCNK normalization															
Si	7.776	7.927	7.788	8.037	7.925	7.927	7.912	7.819	7.828	7.916	7.997	7.825	7.830	7.809	7.949
Al	0.224	0.073	0.212	0.000	0.075	0.073	0.088	0.181	0.172	0.084	0.003	0.175	0.170	0.191	0.051
T-site	**8.000**	**8.000**	**8.000**	**8.037**	**8.000**	**8.000**	**8.000**	**8.000**	**8.000**	**8.000**	**8.000**	**8.000**	**8.000**	**8.000**	**8.000**
Al	0.160	0.168	0.105	0.200	0.187	0.146	0.144	0.110	0.130	0.130	0.175	0.208	0.166	0.164	0.192
Fe^{3+}	0.057	0.140	0.332	0.559	0.269	0.482	0.297	0.644	0.503	0.695	0.332	0.259	0.530	0.311	0.410
Ti	0.189	0.161	0.160	0.115	0.153	0.128	0.193	0.194	0.168	0.198	0.157	0.181	0.198	0.189	0.152
Mg	0.324	0.306	0.396	0.283	0.299	0.549	0.366	0.448	0.498	0.303	0.279	0.354	0.411	0.332	0.236
Fe^{2+}	4.166	4.128	3.912	3.707	3.995	3.607	3.911	3.521	3.624	3.602	3.958	3.906	3.597	3.906	3.911
Mn	0.105	0.096	0.095	0.099	0.097	0.088	0.088	0.083	0.076	0.072	0.100	0.092	0.097	0.098	0.100
C-site	**5.000**	**5.000**	**5.000**	**5.000**	**5.000**	**5.000**	**5.000**	**5.000**	**5.000**	**5.000**	**5.000**	**5.000**	**5.000**	**5.000**	**5.000**
Ca	0.469	0.475	0.415	0.216	0.365	0.427	0.390	0.385	0.536	0.307	0.383	0.448	0.397	0.354	0.332
Na	1.531	1.525	1.585	1.784	1.635	1.573	1.610	1.615	1.464	1.693	1.617	1.552	1.603	1.646	1.668
B-site	**2.000**	**2.000**	**2.000**	**2.000**	**2.000**	**2.000**	**2.000**	**2.000**	**2.000**	**2.000**	**2.000**	**2.000**	**2.000**	**2.000**	**2.000**
Na	0.888	0.733	0.767	0.418	0.677	0.543	0.620	0.397	0.460	0.342	0.564	0.640	0.425	0.707	0.575
K	0.274	0.235	0.274	0.228	0.271	0.219	0.250	0.257	0.206	0.214	0.234	0.258	0.255	0.276	0.239
A-site	**1.162**	**0.968**	**1.041**	**0.646**	**0.947**	**0.761**	**0.870**	**0.653**	**0.666**	**0.556**	**0.798**	**0.899**	**0.680**	**0.983**	**0.814**
Cations	16.162	15.968	16.041	15.683	15.947	15.761	15.870	15.653	15.666	15.556	15.798	15.899	15.680	15.983	15.814
F	0.775	0.685	0.570	0.259	0.526	0.347	0.506	0.295	0.817	0.278	0.513	0.655	0.363	0.560	0.529
Cl	0.012	0.007	0.009	0.008	0.010	0.007	0.012	0.009	0.009	0.012	0.011	0.012	0.013	0.013	0.022
Oxygens	**23.000**	**23.000**	**23.000**	**23.000**	**23.000**	**23.000**	**23.000**	**23.000**	**23.000**	**23.000**	**23.000**	**23.000**	**23.000**	**23.000**	**23.000**

Appendix A.3 Electron microprobe analyses of amphiboles from the granites of the Wentworth pluton (continued).

Sample	**4636**	**4636**	**4636**	**4636**	**4636**	**4636**	**4636**	**4636**	**4636**	**4636**	**4636**	**4636**	**4636**	**4636**
Analysis	**220**	**221**	**224**	**225**	**226**	**227**	**228**	**229**	**230**	**231**	**238**	**239**	**240**	**242**
SiO_2	49.95	49.68	51.21	50.48	50.12	50.39	49.94	50.10	50.09	50.32	51.15	51.25	51.26	51.62
TiO_2	1.67	1.32	1.59	1.45	1.69	1.33	1.56	1.19	1.46	1.50	1.54	1.32	1.40	0.73
Al_2O_3	1.09	1.00	1.81	1.78	1.49	1.24	1.36	1.19	1.60	1.36	0.88	0.86	0.95	0.83
FeO	32.78	33.36	30.39	31.82	32.49	33.28	33.23	32.22	31.95	32.74	32.77	33.28	32.71	34.38
MnO	0.81	0.86	0.64	0.75	0.82	0.69	0.80	0.75	0.80	0.71	0.78	0.80	0.77	0.56
MgO	0.84	0.89	2.19	1.47	1.24	1.05	1.07	1.51	0.95	0.96	0.85	0.86	0.91	0.76
CaO	2.09	2.08	1.88	1.85	2.02	1.81	2.12	2.12	2.15	1.82	2.03	1.68	1.84	1.30
Na_2O	7.30	7.78	8.85	7.43	7.94	7.07	7.42	7.12	7.34	7.69	7.05	6.79	6.97	7.21
K_2O	1.30	1.33	1.16	1.24	1.37	1.21	1.35	1.17	1.44	1.37	1.26	1.12	1.21	0.82
F	0.81	1.36	0.76	0.85	1.13	0.64	1.11	0.95	1.07	1.10	0.70	0.63	0.58	0.30
Cl	0.04	0.05	0.05	0.04	0.05	0.04	0.05	0.05	0.04	0.05	0.03	0.03	0.04	0.06
Total	**98.69**	**99.71**	**100.54**	**99.15**	**100.35**	**98.76**	**100.01**	**98.36**	**98.90**	**99.62**	**99.03**	**98.62**	**98.64**	**98.57**
Structural formula calculated on the basis of 23 oxygens and Fe^{3+} estimated with the 13eCNK normalization														
Si	7.934	7.896	7.948	7.896	7.864	7.908	7.843	7.921	7.952	7.933	8.044	8.024	8.048	8.035
Al	0.066	0.104	0.052	0.104	0.136	0.092	0.157	0.079	0.048	0.067	0.000	0.000	0.000	0.000
T-site	**8.000**	**8.000**	**8.000**	**8.000**	**8.000**	**8.000**	**8.000**	**8.000**	**8.000**	**8.000**	**8.044**	**8.024**	**8.048**	**8.035**
Al	0.139	0.082	0.278	0.225	0.139	0.137	0.094	0.142	0.251	0.185	0.163	0.158	0.176	0.152
Fe^{3+}	0.304	0.330	0.000	0.418	0.233	0.639	0.449	0.518	0.165	0.286	0.300	0.635	0.412	0.836
Ti	0.200	0.158	0.186	0.171	0.199	0.157	0.185	0.141	0.175	0.177	0.182	0.155	0.166	0.085
Mg	0.199	0.211	0.508	0.343	0.290	0.246	0.250	0.357	0.225	0.226	0.198	0.200	0.212	0.177
Fe^{2+}	4.050	4.104	3.945	3.745	4.030	3.729	3.916	3.741	4.076	4.031	4.010	3.722	3.883	3.639
Mn	0.108	0.116	0.084	0.099	0.109	0.092	0.107	0.100	0.107	0.095	0.104	0.106	0.103	0.074
C-site	**5.000**	**5.000**	**5.000**	**5.000**	**5.000**	**5.000**	**5.000**	**5.000**	**5.000**	**5.000**	**5.000**	**5.000**	**5.000**	**5.000**
Ca	0.356	0.355	0.313	0.310	0.339	0.305	0.357	0.359	0.366	0.307	0.298	0.258	0.261	0.181
Na	1.644	1.645	1.687	1.690	1.661	1.695	1.643	1.641	1.634	1.693	1.702	1.742	1.739	1.819
B-site	**2.000**	**2.000**	**2.000**	**2.000**	**2.000**	**2.000**	**2.000**	**2.000**	**2.000**	**2.000**	**2.000**	**2.000**	**2.000**	**2.000**
Na	0.604	0.753	0.977	0.563	0.753	0.455	0.617	0.540	0.625	0.658	0.448	0.319	0.384	0.356
K	0.263	0.269	0.229	0.247	0.274	0.242	0.270	0.236	0.291	0.276	0.253	0.224	0.242	0.163
A-site	**0.867**	**1.021**	**1.206**	**0.810**	**1.027**	**0.698**	**0.888**	**0.776**	**0.916**	**0.935**	**0.701**	**0.543**	**0.627**	**0.519**
Cations	15.867	16.021	16.206	15.810	16.027	15.698	15.888	15.776	15.916	15.935	15.745	15.567	15.675	15.554
F	0.408	0.683	0.374	0.421	0.562	0.317	0.550	0.474	0.538	0.550	0.349	0.312	0.287	0.148
Cl	0.012	0.014	0.014	0.011	0.013	0.009	0.013	0.012	0.011	0.012	0.009	0.009	0.010	0.016
Oxygens	**23.000**	**23.000**	**23.058**	**23.000**	**23.000**	**23.000**	**23.000**	**23.000**	**23.000**	**23.000**	**23.000**	**23.000**	**23.000**	**23.000**

Appendix A.3 Electron microprobe analyses of amphiboles from the granites of the Wentworth pluton (continued).

Sample	**4641**	**4641**	**4641**	**4641**	**4641**	**4641**	**4641**	**4641**	**4641**	**4641**	**4641**	**4641**	**4641**	**4641**
Analysis	**102**	**108**	**112**	**128**	**129**	**131**	**135**	**139**	**140**	**146**	**148**	**157**	**161**	**164**
SiO_2	44.54	39.75	43.68	43.53	43.66	43.50	44.51	45.35	43.52	46.35	44.94	42.94	41.82	43.53
TiO_2	0.50	0.52	1.05	1.41	1.17	1.29	1.38	0.81	1.13	0.86	0.98	1.41	0.67	1.08
Al_2O_3	6.68	11.06	6.29	7.37	7.28	7.43	6.91	5.82	7.28	5.13	6.31	7.53	8.93	7.09
FeO	26.30	26.18	26.59	27.38	27.48	26.38	25.90	26.09	26.86	27.15	26.87	27.52	27.04	27.30
MnO	0.79	0.82	0.96	0.81	0.88	0.85	0.65	0.93	0.80	1.11	1.04	0.86	0.80	0.83
MgO	5.47	3.80	5.33	4.66	4.59	4.81	5.59	5.71	4.97	5.82	5.31	4.62	4.91	5.00
CaO	10.20	11.29	10.18	10.16	10.29	10.18	10.02	10.66	10.18	9.60	10.16	10.08	11.26	10.16
Na_2O	1.77	1.95	1.89	2.14	2.01	1.93	2.11	1.59	2.03	1.98	1.76	2.07	1.93	1.77
K_2O	1.04	1.73	0.99	1.06	0.95	0.94	0.81	0.75	1.04	0.72	0.96	1.03	1.33	0.94
F	0.60	0.48	0.52	0.38	0.48	0.39	0.52	0.39	0.48	0.40	0.47	0.39	0.58	0.46
Cl	0.41	1.13	0.59	0.53	0.41	0.50	0.25	0.40	0.59	0.52	0.66	0.56	0.33	0.81
Total	**98.28**	**98.69**	**98.08**	**99.44**	**99.19**	**98.21**	**98.65**	**98.49**	**98.87**	**99.62**	**99.44**	**99.00**	**99.58**	**98.97**
Structural formula calculated on the basis of 23 oxygens and Fe^{3+} estimated with the 13eCNK normalization														
Si	6.927	6.346	6.852	6.753	6.782	6.799	6.871	7.025	6.775	7.060	6.924	6.687	6.516	6.763
Al	1.073	1.654	1.148	1.247	1.218	1.201	1.129	0.975	1.225	0.920	1.076	1.313	1.484	1.237
T-site	**8.000**	**8.000**	**8.000**	**8.000**	**8.000**	**8.000**	**8.000**	**8.000**	**8.000**	**8.000**	**8.000**	**8.000**	**8.000**	**8.000**
Al	0.149	0.426	0.014	0.099	0.114	0.167	0.127	0.086	0.110	0.000	0.069	0.067	0.154	0.060
Fe^{3+}	0.668	0.284	0.692	0.588	0.612	0.547	0.574	0.537	0.635	0.886	0.711	0.725	0.566	0.822
Ti	0.058	0.063	0.124	0.165	0.137	0.152	0.160	0.094	0.132	0.099	0.114	0.165	0.078	0.126
Mg	1.268	0.904	1.247	1.078	1.063	1.120	1.285	1.318	1.154	1.320	1.220	1.072	1.139	1.157
Fe^{2+}	2.753	3.212	2.796	2.964	2.958	2.901	2.769	2.843	2.863	2.552	2.752	2.858	2.958	2.726
Mn	0.104	0.110	0.127	0.106	0.116	0.112	0.085	0.122	0.106	0.143	0.135	0.113	0.105	0.109
C-site	**5.000**	**5.000**	**5.000**	**5.000**	**5.000**	**5.000**	**5.000**	**5.000**	**5.000**	**5.000**	**5.000**	**5.000**	**5.000**	**5.000**
Ca	1.700	1.931	1.711	1.689	1.713	1.704	1.658	1.769	1.698	1.566	1.677	1.682	1.880	1.691
Na	0.300	0.069	0.289	0.311	0.287	0.296	0.342	0.231	0.302	0.434	0.323	0.318	0.120	0.309
B-site	**2.000**	**2.000**	**2.000**	**2.000**	**2.000**	**2.000**	**2.000**	**2.000**	**2.000**	**2.000**	**2.000**	**2.000**	**2.000**	**2.000**
Na	0.233	0.534	0.286	0.332	0.318	0.290	0.290	0.246	0.311	0.151	0.203	0.306	0.463	0.225
K	0.207	0.352	0.197	0.210	0.188	0.188	0.160	0.149	0.206	0.139	0.189	0.204	0.264	0.187
A-site	**0.440**	**0.886**	**0.484**	**0.542**	**0.506**	**0.478**	**0.451**	**0.395**	**0.517**	**0.290**	**0.392**	**0.510**	**0.728**	**0.412**
Cations	15.440	15.886	15.484	15.542	15.506	15.478	15.451	15.395	15.517	15.290	15.392	15.510	15.728	15.412
F	0.293	0.241	0.256	0.188	0.236	0.193	0.253	0.189	0.234	0.193	0.227	0.194	0.284	0.227
Cl	0.108	0.305	0.158	0.139	0.107	0.134	0.066	0.105	0.156	0.134	0.171	0.148	0.088	0.213
Oxygens	**23.000**	**23.000**	**23.000**	**23.000**	**23.000**	**23.000**	**23.000**	**23.000**	**23.000**	**23.000**	**23.000**	**23.000**	**23.000**	**23.000**

Appendix A.3 Electron microprobe analyses of amphiboles from the granites of the Wentworth pluton (continued).

Sample	**4641**	**4641**	**4641**	**4641**	**4641**	**4641**	**4641**	**4641**	**4641**	**4641**	**4641**	**4641**	**4641**	**4641**	**4641**
Analysis	**168**	**171**	**174**	**176**	**179**	**183**	**185**	**197**	**200**	**201**	**89**	**91**	**94**	**96**	**97**
SiO_2	44.43	45.45	45.49	43.77	43.96	43.00	43.48	39.80	40.32	40.49	43.39	44.01	43.37	44.64	42.29
TiO_2	1.42	1.28	1.46	1.27	0.92	0.79	1.11	0.42	0.62	0.57	1.48	1.37	1.22	1.07	0.59
Al_2O_3	6.98	7.18	6.81	7.51	7.33	8.59	7.54	11.17	10.04	9.66	7.66	7.15	7.44	6.29	7.89
FeO	26.32	25.02	25.78	27.26	27.11	26.03	25.90	27.79	27.27	26.37	27.14	27.47	27.13	26.21	28.00
MnO	0.65	0.62	0.61	0.76	0.87	0.91	0.94	0.83	0.84	0.86	0.93	0.90	0.84	0.78	0.86
MgO	5.73	6.19	6.01	4.68	4.81	4.87	5.02	3.07	3.75	4.42	4.40	4.36	4.31	5.14	3.66
CaO	10.21	9.68	10.15	10.02	9.81	10.89	10.57	11.07	11.25	11.18	10.18	9.81	10.41	10.29	10.69
Na_2O	2.04	1.94	2.11	2.13	1.75	1.88	1.92	1.78	1.84	1.82	2.13	2.01	1.97	1.90	1.94
K_2O	0.88	0.77	0.83	1.01	0.93	1.09	1.15	1.69	1.68	1.66	1.07	0.90	1.13	1.01	1.39
F	0.50	0.48	0.52	0.44	0.37	0.48	0.45	0.28	0.36	0.41	0.53	0.54	0.55	0.50	0.43
Cl	0.29	0.20	0.23	0.52	0.60	0.44	0.76	1.10	1.09	0.96	0.46	0.31	0.75	0.83	1.20
Total	**99.45**	**98.80**	**99.98**	**99.38**	**98.45**	**98.96**	**98.84**	**99.01**	**99.05**	**98.37**	**99.36**	**98.82**	**99.10**	**98.65**	**98.93**
Structural formula calculated on the basis of 23 oxygens and Fe^{3+} estimated with the 13eCNK normalization															
Si	6.808	6.907	6.906	6.775	6.815	6.693	6.798	6.326	6.415	6.446	6.750	6.836	6.804	6.984	6.735
Al	1.192	1.093	1.094	1.225	1.185	1.307	1.202	1.674	1.585	1.554	1.250	1.164	1.196	1.016	1.265
T-site	**8.000**	**8.000**	**8.000**	**8.000**	**8.000**	**8.000**	**8.000**	**8.000**	**8.000**	**8.000**	**8.000**	**8.000**	**8.000**	**8.000**	**8.000**
Al	0.068	0.192	0.124	0.145	0.153	0.268	0.187	0.416	0.296	0.257	0.153	0.143	0.178	0.143	0.216
Fe^{3+}	0.667	0.732	0.554	0.622	0.850	0.438	0.400	0.496	0.399	0.451	0.502	0.652	0.404	0.396	0.377
Ti	0.164	0.146	0.166	0.148	0.107	0.092	0.130	0.050	0.074	0.068	0.173	0.160	0.144	0.126	0.070
Mg	1.310	1.402	1.359	1.079	1.112	1.131	1.170	0.728	0.889	1.048	1.020	1.010	1.007	1.199	0.869
Fe^{2+}	2.707	2.448	2.719	2.907	2.664	2.950	2.987	3.197	3.229	3.060	3.030	2.916	3.155	3.033	3.352
Mn	0.085	0.080	0.078	0.100	0.114	0.120	0.125	0.112	0.113	0.115	0.122	0.119	0.111	0.104	0.115
C-site	**5.000**	**5.000**	**5.000**	**5.000**	**5.000**	**5.000**	**5.000**	**5.000**	**5.000**	**5.000**	**5.000**	**5.000**	**5.000**	**5.000**	**5.000**
Ca	1.676	1.576	1.651	1.661	1.629	1.816	1.771	1.884	1.918	1.906	1.697	1.632	1.750	1.724	1.825
Na	0.324	0.424	0.349	0.339	0.371	0.184	0.229	0.116	0.082	0.094	0.303	0.368	0.250	0.276	0.175
B-site	**2.000**	**2.000**	**2.000**	**2.000**	**2.000**	**2.000**	**2.000**	**2.000**	**2.000**	**2.000**	**2.000**	**2.000**	**2.000**	**2.000**	**2.000**
Na	0.281	0.149	0.271	0.301	0.154	0.384	0.353	0.434	0.484	0.467	0.340	0.238	0.349	0.301	0.424
K	0.171	0.150	0.161	0.200	0.185	0.216	0.229	0.343	0.340	0.336	0.212	0.179	0.227	0.201	0.283
A-site	**0.453**	**0.299**	**0.432**	**0.501**	**0.339**	**0.600**	**0.582**	**0.777**	**0.824**	**0.803**	**0.552**	**0.417**	**0.576**	**0.502**	**0.706**
Cations	15.453	15.299	15.432	15.501	15.339	15.600	15.582	15.777	15.824	15.803	15.552	15.417	15.576	15.502	15.706
F	0.244	0.229	0.247	0.216	0.179	0.234	0.225	0.142	0.180	0.206	0.263	0.263	0.273	0.249	0.216
Cl	0.075	0.053	0.059	0.137	0.157	0.116	0.200	0.295	0.295	0.258	0.120	0.082	0.198	0.219	0.324
Oxygens	**23.000**	**23.000**	**23.000**	**23.000**	**23.000**	**23.000**	**23.000**	**23.000**	**23.000**	**23.000**	**23.000**	**23.000**	**23.000**	**23.000**	**23.000**

Appendix A.3 Electron microprobe analyses of amphiboles from the granites of the Wentworth pluton (continued).

Sample	**4641**	**4641**	**5056**	**5056**	**5056**	**5056**	**5056**	**5056**	**5056**	**5056**	**5056**	**5056**	**5056**	**5056**	**5056**
Analysis	**98**	**99**	**203**	**205**	**223**	**253**	**254**	**256**	**258**	**266**	**267**	**280**	**282**	**285**	**286**
SiO_2	43.25	44.17	45.33	45.58	45.06	45.67	45.69	51.96	53.27	45.95	45.95	46.30	52.52	46.01	45.27
TiO_2	1.48	1.26	1.52	1.53	1.70	1.72	1.63	0.19	0.19	1.57	1.67	1.64	0.15	1.38	1.60
Al_2O_3	7.63	7.60	7.10	6.95	6.97	7.08	6.83	2.13	1.97	6.86	7.09	6.66	2.10	6.35	6.77
FeO	26.91	26.07	21.50	21.06	21.38	21.77	21.77	17.98	18.55	21.47	21.99	21.85	18.60	21.73	21.70
MnO	0.90	0.89	0.53	0.55	0.56	0.55	0.54	0.38	0.46	0.56	0.59	0.53	0.35	0.38	0.53
MgO	4.50	4.87	8.44	8.95	8.65	8.64	8.77	12.22	12.33	8.80	8.59	8.94	12.21	9.00	8.96
CaO	9.97	10.17	10.86	10.78	10.81	10.79	10.81	12.32	11.71	10.71	10.38	10.73	12.13	11.13	10.68
Na_2O	2.20	1.96	1.67	1.71	1.82	1.67	1.57	0.51	0.47	1.59	1.69	1.61	0.49	1.33	1.65
K_2O	1.04	1.02	0.89	0.89	0.90	0.87	0.84	0.23	0.23	0.84	0.85	0.83	0.20	0.75	0.81
F	0.68	0.43	0.18	0.22	0.14	0.20	0.19	0.21	0.17	0.19	0.23	0.22	0.17	0.17	0.20
Cl	0.45	0.37	0.14	0.17	0.16	0.15	0.15	0.05	0.04	0.16	0.16	0.15	0.08	0.15	0.15
Total	**98.99**	**98.81**	**98.16**	**98.38**	**98.15**	**99.10**	**98.77**	**98.18**	**99.36**	**98.70**	**99.19**	**99.46**	**98.97**	**98.38**	**98.30**
Structural formula calculated on the basis of 23 oxygens and Fe^{3+} estimated with the 13eCNK normalization															
Si	6.749	6.845	6.864	6.863	6.827	6.836	6.852	7.660	7.694	6.885	6.846	6.885	7.659	6.920	6.812
Al	1.251	1.155	1.136	1.137	1.173	1.164	1.148	0.340	0.306	1.115	1.154	1.115	0.341	1.080	1.188
T-site	**8.000**	**8.000**	**8.000**	**8.000**	**8.000**	**8.000**	**8.000**	**8.000**	**8.000**	**8.000**	**8.000**	**8.000**	**8.000**	**8.000**	**8.000**
Al	0.151	0.232	0.130	0.095	0.072	0.084	0.057	0.030	0.029	0.096	0.089	0.051	0.019	0.044	0.012
Fe^{3+}	0.547	0.463	0.474	0.547	0.496	0.581	0.632	0.189	0.440	0.603	0.725	0.656	0.325	0.605	0.737
Ti	0.173	0.146	0.173	0.173	0.194	0.193	0.183	0.021	0.020	0.177	0.188	0.183	0.016	0.156	0.181
Mg	1.046	1.126	1.905	2.009	1.953	1.927	1.960	2.686	2.655	1.965	1.909	1.982	2.654	2.019	2.009
Fe^{2+}	2.964	2.915	2.249	2.105	2.213	2.144	2.098	2.027	1.800	2.088	2.015	2.061	1.943	2.128	1.994
Mn	0.119	0.117	0.068	0.071	0.072	0.070	0.068	0.047	0.056	0.071	0.075	0.067	0.043	0.048	0.068
C-site	**5.000**	**5.000**	**5.000**	**5.000**	**5.000**	**5.000**	**5.000**	**5.000**	**5.000**	**5.000**	**5.000**	**5.000**	**5.000**	**5.000**	**5.000**
Ca	1.667	1.688	1.762	1.739	1.755	1.731	1.738	1.945	1.812	1.719	1.657	1.710	1.895	1.794	1.721
Na	0.333	0.312	0.238	0.261	0.245	0.269	0.262	0.055	0.131	0.281	0.343	0.290	0.105	0.206	0.279
B-site	**2.000**	**2.000**	**2.000**	**2.000**	**2.000**	**2.000**	**2.000**	**2.000**	**1.942**	**2.000**	**2.000**	**2.000**	**2.000**	**2.000**	**2.000**
Na	0.332	0.277	0.251	0.238	0.289	0.216	0.193	0.091	0.000	0.182	0.145	0.173	0.033	0.181	0.202
K	0.208	0.202	0.173	0.171	0.173	0.165	0.160	0.043	0.042	0.161	0.162	0.158	0.036	0.143	0.155
A-site	**0.539**	**0.479**	**0.424**	**0.408**	**0.462**	**0.381**	**0.354**	**0.134**	**0.042**	**0.343**	**0.307**	**0.331**	**0.070**	**0.324**	**0.356**
Cations	15.539	15.479	15.424	15.408	15.462	15.381	15.354	15.134	14.985	15.343	15.307	15.331	15.070	15.324	15.356
F	0.335	0.212	0.086	0.104	0.066	0.097	0.091	0.098	0.078	0.091	0.106	0.103	0.076	0.082	0.094
Cl	0.118	0.098	0.037	0.043	0.041	0.039	0.039	0.012	0.009	0.040	0.041	0.038	0.020	0.038	0.038
Oxygens	**23.000**	**23.000**	**23.000**	**23.000**	**23.000**	**23.000**	**23.000**	**23.000**	**23.000**	**23.000**	**23.000**	**23.000**	**23.000**	**23.000**	**23.000**

Appendix A.3 Electron microprobe analyses of amphiboles from the granites of the Wentworth pluton (continued).

Sample	**5056**	**5056**	**5056**	**5056**	**5056**	**5056**	**5056**	**5056**	**5056**	**5056**	**5056**	**5056**	**5056**	**5056**	**5056**
Analysis	**288**	**292**	**294**	**297**	**300**	**301**	**302**	**311**	**312**	**313**	**314**	**315**	**324**	**325**	**332**
SiO_2	44.17	44.26	44.70	44.72	44.92	45.45	52.00	51.46	50.15	45.53	45.56	44.94	44.35	45.64	45.17
TiO_2	1.74	3.52	1.81	1.74	1.65	1.47	0.14	0.24	0.41	1.50	1.32	1.55	1.67	1.97	1.80
Al_2O_3	7.41	6.85	7.13	6.99	7.13	6.74	2.16	2.53	3.64	6.64	6.64	6.77	6.98	7.07	7.04
FeO	22.03	20.40	21.62	22.00	22.01	21.82	18.59	18.86	20.19	22.15	21.95	22.38	22.03	21.22	21.95
MnO	0.53	0.49	0.55	0.57	0.49	0.55	0.41	0.39	0.43	0.45	0.42	0.52	0.55	0.45	0.55
MgO	8.46	8.08	8.67	8.68	8.29	8.59	12.23	11.98	10.90	8.52	8.57	8.44	8.77	8.67	8.51
CaO	10.63	11.92	10.96	10.77	11.19	10.89	11.92	11.96	11.51	11.05	11.63	10.68	10.81	10.65	10.90
Na_2O	1.83	1.47	1.74	1.77	1.55	1.58	0.58	0.60	0.82	1.45	1.36	1.64	1.73	1.55	1.68
K_2O	0.88	0.78	0.85	0.88	0.86	0.83	0.20	0.23	0.38	0.81	0.76	0.80	0.87	0.85	0.85
F	0.21	0.22	0.23	0.20	0.14	0.21	0.23	0.12	0.15	0.16	0.17	0.16	0.19	0.12	0.13
Cl	0.16	0.15	0.17	0.16	0.17	0.14	0.09	0.10	0.13	0.15	0.18	0.17	0.16	0.16	0.17
Total	**98.03**	**98.14**	**98.42**	**98.46**	**98.39**	**98.27**	**98.54**	**98.46**	**98.69**	**98.41**	**98.56**	**98.04**	**98.10**	**98.32**	**98.74**
Structural formula calculated on the basis of 23 oxygens and Fe^{3+} estimated with the 13eCNK normalization															
Si	6.702	6.809	6.762	6.754	6.811	6.868	7.615	7.553	7.389	6.875	6.898	6.807	6.721	6.859	6.803
Al	1.298	1.191	1.238	1.243	1.189	1.132	0.373	0.437	0.611	1.125	1.102	1.193	1.245	1.141	1.197
T-site	**8.000**	**8.000**	**8.000**	**8.000**	**8.000**	**8.000**	**8.000**	**8.000**	**8.000**	**8.000**	**8.000**	**8.000**	**8.000**	**8.000**	**8.000**
Al	0.025	0.051	0.032	0.000	0.084	0.068	0.000	0.000	0.020	0.056	0.082	0.015	0.000	0.109	0.052
Fe^{3+}	0.712	0.000	0.568	0.681	0.471	0.581	0.411	0.420	0.561	0.573	0.401	0.721	0.712	0.545	0.569
Ti	0.199	0.407	0.206	0.197	0.188	0.168	0.015	0.026	0.045	0.170	0.150	0.177	0.190	0.222	0.203
Mg	1.913	1.852	1.956	1.955	1.874	1.936	2.669	2.621	2.395	1.918	1.934	1.906	1.982	1.943	1.910
Fe^{2+}	2.083	2.625	2.167	2.095	2.319	2.177	1.853	1.885	1.926	2.224	2.379	2.114	2.046	2.122	2.196
Mn	0.068	0.064	0.071	0.072	0.063	0.070	0.051	0.048	0.053	0.058	0.054	0.067	0.070	0.058	0.070
C-site	**5.000**	**5.000**	**5.000**	**5.000**	**5.000**	**5.000**	**5.000**	**5.000**	**5.000**	**5.000**	**5.000**	**5.000**	**5.000**	**5.000**	**5.000**
Ca	1.728	1.964	1.776	1.742	1.817	1.763	1.871	1.881	1.817	1.787	1.887	1.733	1.756	1.714	1.759
Na	0.272	0.036	0.224	0.258	0.183	0.237	0.129	0.119	0.183	0.213	0.113	0.267	0.244	0.286	0.241
B-site	**2.000**	**2.000**	**2.000**	**2.000**	**2.000**	**2.000**	**2.000**	**2.000**	**2.000**	**2.000**	**2.000**	**2.000**	**2.000**	**2.000**	**2.000**
Na	0.265	0.404	0.285	0.259	0.274	0.225	0.035	0.052	0.052	0.212	0.286	0.216	0.264	0.166	0.248
K	0.170	0.153	0.164	0.169	0.167	0.160	0.037	0.042	0.072	0.156	0.146	0.154	0.167	0.162	0.163
A-site	**0.435**	**0.557**	**0.449**	**0.428**	**0.441**	**0.385**	**0.072**	**0.094**	**0.123**	**0.368**	**0.432**	**0.370**	**0.431**	**0.328**	**0.411**
Cations	15.435	15.557	15.449	15.428	15.441	15.385	15.072	15.094	15.123	15.368	15.432	15.370	15.431	15.328	15.411
F	0.101	0.106	0.109	0.096	0.065	0.099	0.106	0.058	0.070	0.074	0.082	0.076	0.092	0.055	0.063
Cl	0.041	0.039	0.044	0.041	0.043	0.035	0.023	0.024	0.032	0.037	0.046	0.042	0.042	0.039	0.042
Oxygens	**23.000**	**23.098**	**23.000**	**23.000**	**23.000**	**23.000**	**23.000**	**23.000**	**23.000**	**23.000**	**23.000**	**23.000**	**23.000**	**23.000**	**23.000**

Appendix A.3 Electron microprobe analyses of amphiboles from the granites of the Wentworth pluton (continued).

Sample	**6419**	**6419**	**6419**	**6419**	**6490**	**6490**	**6490**	**6490**	**6490**	**6490**	**6490**	**6490**	**6490**	**6490**	**6490**
Analysis	**484**	**485**	**492**	**493**	**308**	**312**	**326**	**328**	**332**	**338**	**339**	**340**	**341**	**342**	**354**
SiO_2	49.03	50.41	48.98	49.20	43.00	43.77	44.03	43.88	44.03	44.72	45.23	45.29	44.87	44.94	43.99
TiO_2	1.19	1.35	1.66	2.32	1.15	0.98	0.85	1.22	1.04	0.96	0.95	0.93	1.13	1.02	0.98
Al_2O_3	1.92	1.07	1.33	1.35	8.22	7.70	7.70	7.48	7.66	7.06	6.48	6.58	6.53	6.79	7.41
FeO	31.60	32.41	33.21	31.51	26.34	26.58	26.24	26.49	26.00	26.54	26.88	26.94	26.42	26.84	26.81
MnO	0.75	0.70	0.77	0.80	1.12	1.16	1.17	1.15	1.20	0.90	0.88	0.92	0.97	0.95	0.95
MgO	1.48	1.09	1.07	0.58	5.17	5.20	5.13	5.18	5.37	5.33	5.61	5.62	5.57	5.45	5.21
CaO	2.66	2.25	3.42	2.38	10.97	10.84	10.83	10.61	10.85	11.07	10.88	10.93	10.64	10.98	10.82
Na_2O	7.63	7.52	7.07	7.80	2.25	2.14	1.88	1.88	2.02	2.07	2.05	2.13	2.24	2.24	2.21
K_2O	1.33	1.06	1.18	1.35	1.32	1.19	1.19	1.07	1.19	1.11	0.96	0.96	0.94	0.97	1.14
F	1.05	0.86	0.99	0.94	0.33	0.26	0.26	0.22	0.28	0.34	0.42	0.75	0.78	0.36	0.49
Cl	0.06	0.05	0.07	0.05	0.22	0.14	0.17	0.22	0.17	0.13	0.13	0.16	0.17	0.18	0.24
Total	**98.70**	**98.77**	**99.74**	**98.27**	**100.08**	**99.96**	**99.44**	**99.41**	**99.80**	**100.24**	**100.46**	**101.20**	**100.26**	**100.72**	**100.24**
Structural formula calculated on the basis of 23 oxygens and Fe^{3+} estimated with the 13eCNK normalization															
Si	7.825	7.991	7.782	7.953	6.637	6.731	6.789	6.754	6.767	6.867	6.905	6.892	6.892	6.866	6.771
Al	0.175	0.009	0.218	0.047	1.363	1.269	1.211	1.246	1.233	1.133	1.095	1.108	1.108	1.134	1.229
T-site	**8.000**	**8.000**	**8.000**	**8.000**	**8.000**	**8.000**	**8.000**	**8.000**	**8.000**	**8.000**	**8.000**	**8.000**	**8.000**	**8.000**	**8.000**
Al	0.186	0.190	0.030	0.209	0.130	0.126	0.187	0.109	0.152	0.144	0.070	0.071	0.074	0.088	0.115
Fe^{3+}	0.160	0.205	0.208	0.000	0.405	0.473	0.453	0.583	0.430	0.288	0.453	0.443	0.421	0.367	0.435
Ti	0.143	0.161	0.199	0.281	0.133	0.113	0.098	0.142	0.120	0.111	0.110	0.106	0.130	0.117	0.114
Mg	0.352	0.258	0.254	0.140	1.190	1.193	1.179	1.189	1.229	1.220	1.276	1.275	1.276	1.242	1.196
Fe^{2+}	4.058	4.091	4.206	4.260	2.995	2.945	2.931	2.827	2.912	3.120	2.978	2.985	2.973	3.063	3.017
Mn	0.102	0.094	0.103	0.109	0.146	0.151	0.152	0.150	0.156	0.117	0.114	0.119	0.126	0.123	0.124
C-site	**5.000**	**5.000**	**5.000**	**5.000**	**5.000**	**5.000**	**5.000**	**5.000**	**5.000**	**5.000**	**5.000**	**5.000**	**5.000**	**5.000**	**5.000**
Ca	0.455	0.382	0.582	0.413	1.814	1.786	1.789	1.749	1.787	1.822	1.780	1.783	1.752	1.797	1.784
Na	1.545	1.618	1.418	1.587	0.186	0.214	0.211	0.251	0.213	0.178	0.220	0.217	0.248	0.203	0.216
B-site	**2.000**	**2.000**	**2.000**	**2.000**	**2.000**	**2.000**	**2.000**	**2.000**	**2.000**	**2.000**	**2.000**	**2.000**	**2.000**	**2.000**	**2.000**
Na	0.818	0.694	0.761	0.859	0.487	0.424	0.351	0.311	0.389	0.439	0.386	0.412	0.418	0.459	0.444
K	0.270	0.215	0.240	0.278	0.260	0.234	0.235	0.210	0.234	0.218	0.187	0.186	0.183	0.189	0.223
A-site	**1.088**	**0.908**	**1.000**	**1.137**	**0.747**	**0.658**	**0.586**	**0.521**	**0.623**	**0.657**	**0.573**	**0.598**	**0.601**	**0.648**	**0.667**
Cations	16.088	15.908	16.000	16.137	15.747	15.658	15.586	15.521	15.623	15.657	15.573	15.598	15.601	15.648	15.667
F	0.531	0.430	0.495	0.483	0.163	0.127	0.125	0.106	0.136	0.167	0.202	0.361	0.377	0.172	0.240
Cl	0.016	0.014	0.018	0.012	0.058	0.038	0.043	0.058	0.045	0.034	0.032	0.040	0.045	0.047	0.061
Oxygens	**23.000**	**23.000**	**23.000**	**23.137**	**23.000**	**23.000**	**23.000**	**23.000**	**23.000**	**23.000**	**23.000**	**23.000**	**23.000**	**23.000**	**23.000**

Appendix A.3 Electron microprobe analyses of amphiboles from the granites of the Wentworth pluton (continued).

Sample	**5056**	**5056**	**5056**	**5056**	**5056**	**6419**	**6419**	**6419**	**6419**	**6419**	**6419**	**6419**	**6419**	**6419**	**6419**
Analysis	**335**	**337**	**338**	**339**	**342**	**461**	**462**	**463**	**468**	**478**	**479**	**480**	**481**	**482**	**483**
SiO_2	51.80	46.07	52.98	45.83	46.01	50.25	48.78	48.31	49.59	49.83	49.16	49.70	49.03	48.43	48.83
TiO_2	0.18	1.62	0.15	1.66	1.59	0.60	1.32	1.24	1.61	1.73	1.31	1.51	1.79	1.34	1.32
Al_2O_3	2.64	6.93	2.06	7.16	6.90	1.30	2.36	2.37	1.18	1.15	1.72	1.26	1.51	2.37	1.98
FeO	18.92	21.25	18.50	21.50	21.66	30.66	30.45	31.13	32.73	32.83	31.11	31.71	31.70	30.37	31.13
MnO	0.41	0.53	0.45	0.49	0.53	0.72	0.73	0.72	0.78	0.81	0.74	0.70	0.75	0.79	0.71
MgO	11.64	9.02	12.23	8.88	8.64	2.66	2.19	1.67	0.42	0.38	1.63	1.63	1.14	2.34	2.00
CaO	11.83	10.44	11.80	10.69	10.61	2.67	3.20	2.91	2.36	2.67	3.09	2.93	2.55	3.34	3.23
Na_2O	0.62	1.71	0.53	1.71	1.63	7.56	7.30	7.46	7.76	7.57	7.34	6.93	7.55	7.31	7.31
K_2O	0.28	0.84	0.19	0.87	0.81	1.28	1.31	1.33	1.26	1.29	1.39	1.10	1.36	1.33	1.26
F	0.09	0.19	0.08	0.22	0.17	1.38	1.15	1.12	0.96	1.00	1.10	0.76	0.97	1.14	1.24
Cl	0.08	0.14	0.05	0.17	0.17	0.04	0.03	0.04	0.04	0.06	0.06	0.05	0.05	0.06	0.06
Total	**98.50**	**98.73**	**99.02**	**99.17**	**98.71**	**99.10**	**98.82**	**98.30**	**98.68**	**99.31**	**98.63**	**98.27**	**98.39**	**98.82**	**99.06**
Structural formula calculated on the basis of 23 oxygens and Fe^{3+} estimated with the 13eCNK normalization															
Si	7.603	6.876	7.686	6.838	6.893	7.924	7.744	7.738	7.974	7.978	7.867	7.892	7.870	7.698	7.764
Al	0.397	1.124	0.314	1.162	1.107	0.076	0.256	0.262	0.026	0.022	0.133	0.108	0.130	0.302	0.236
T-site	**8.000**	**8.000**	**8.000**	**8.000**	**8.000**	**8.000**	**8.000**	**8.000**	**8.000**	**8.000**	**8.000**	**8.000**	**8.000**	**8.000**	**8.000**
Al	0.059	0.093	0.038	0.096	0.110	0.165	0.185	0.185	0.197	0.195	0.191	0.129	0.155	0.142	0.135
Fe^{3+}	0.348	0.674	0.393	0.614	0.605	0.298	0.157	0.193	0.000	0.000	0.007	0.267	0.039	0.179	0.178
Ti	0.020	0.182	0.017	0.186	0.179	0.071	0.158	0.150	0.195	0.208	0.157	0.180	0.216	0.160	0.158
Mg	2.548	2.006	2.645	1.974	1.929	0.625	0.518	0.398	0.101	0.092	0.388	0.386	0.273	0.555	0.473
Fe^{2+}	1.974	1.978	1.852	2.068	2.109	3.744	3.885	3.976	4.402	4.396	4.156	3.944	4.215	3.858	3.960
Mn	0.051	0.067	0.055	0.062	0.068	0.096	0.097	0.098	0.106	0.109	0.100	0.094	0.102	0.107	0.096
C-site	**5.000**	**5.000**	**5.000**	**5.000**	**5.000**	**5.000**	**5.000**	**5.000**	**5.000**	**5.000**	**5.000**	**5.000**	**5.000**	**5.000**	**5.000**
Ca	1.861	1.670	1.833	1.709	1.703	0.451	0.544	0.499	0.406	0.459	0.530	0.499	0.438	0.568	0.549
Na	0.139	0.330	0.148	0.291	0.297	1.549	1.456	1.501	1.594	1.541	1.470	1.501	1.562	1.432	1.451
B-site	**2.000**	**2.000**	**1.981**	**2.000**	**2.000**	**2.000**	**2.000**	**2.000**	**2.000**	**2.000**	**2.000**	**2.000**	**2.000**	**2.000**	**2.000**
Na	0.037	0.164	0.000	0.204	0.177	0.764	0.790	0.816	0.825	0.807	0.807	0.631	0.787	0.822	0.802
K	0.052	0.160	0.035	0.166	0.154	0.257	0.265	0.271	0.259	0.264	0.283	0.222	0.279	0.270	0.255
A-site	**0.089**	**0.324**	**0.035**	**0.370**	**0.331**	**1.021**	**1.055**	**1.087**	**1.084**	**1.071**	**1.090**	**0.853**	**1.065**	**1.093**	**1.057**
Cations	15.089	15.324	15.016	15.370	15.331	16.021	16.055	16.087	16.084	16.071	16.090	15.853	16.065	16.093	16.057
F	0.042	0.090	0.038	0.102	0.081	0.690	0.578	0.568	0.489	0.504	0.555	0.383	0.493	0.573	0.625
Cl	0.020	0.036	0.013	0.043	0.042	0.010	0.009	0.011	0.010	0.017	0.015	0.012	0.012	0.015	0.015
Oxygens	**23.000**	**23.000**	**23.000**	**23.000**	**23.000**	**23.000**	**23.000**	**23.000**	**23.025**	**23.060**	**23.000**	**23.000**	**23.000**	**23.000**	**23.000**

Appendix A.3 Electron microprobe analyses of amphiboles from the granites of the Wentworth pluton (continued).

Sample	**6490**	**6490**	**6490**	**6490**	**6490**	**6490**	**6490**	**6490**	**6490**	**6490**	**6490**	**6490**	**6490**	**6490**	**6490**
Analysis	**401**	**402**	**403**	**404**	**405**	**406**	**407**	**422**	**423**	**424**	**425**	**426**	**427**	**430**	**432**
SiO_2	44.47	44.11	43.63	44.87	44.18	44.34	43.53	43.42	45.01	45.69	44.28	44.49	44.70	44.30	44.97
TiO_2	0.93	0.98	1.02	0.87	1.00	1.09	1.34	1.12	0.89	1.04	1.27	0.91	1.50	0.88	1.00
Al_2O_3	7.52	7.55	7.61	7.14	7.43	7.47	7.74	7.12	6.75	6.23	7.41	7.58	7.19	7.74	6.84
FeO	27.08	27.08	27.55	27.08	27.06	27.45	27.24	28.42	26.53	26.60	27.19	26.43	26.72	26.67	26.40
MnO	1.10	1.08	1.11	1.10	1.08	1.13	1.11	1.00	1.03	1.05	1.02	0.97	1.00	0.99	1.01
MgO	5.03	4.92	4.90	5.06	5.03	5.05	4.77	5.01	5.68	5.78	5.02	5.30	5.05	5.27	5.45
CaO	10.92	11.08	10.96	10.90	11.03	10.82	10.76	10.66	10.96	10.77	10.89	10.99	10.65	10.98	10.75
Na_2O	1.93	1.83	2.05	1.97	1.88	2.12	2.27	1.54	1.81	2.15	2.22	1.74	2.25	1.88	2.16
K_2O	1.21	1.23	1.26	1.23	1.24	1.12	1.11	0.97	1.16	0.89	1.04	1.20	1.01	1.27	1.03
F	0.29	0.25	0.52	0.36	0.27	0.62	0.44	0.19	0.32	0.57	0.47	0.24	0.55	0.25	0.52
Cl	0.14	0.19	0.16	0.13	0.14	0.15	0.25	0.11	0.11	0.11	0.17	0.13	0.19	0.16	0.13
Total	**100.63**	**100.29**	**100.79**	**100.69**	**100.36**	**101.36**	**100.56**	**99.54**	**100.24**	**100.88**	**100.98**	**99.97**	**100.81**	**100.39**	**100.25**
Structural formula calculated on the basis of 23 oxygens and Fe^{3+} estimated with the 13eCNK normalization															
Si	6.793	6.776	6.700	6.860	6.778	6.750	6.699	6.662	6.871	6.942	6.768	6.810	6.836	6.769	6.890
Al	1.207	1.224	1.300	1.140	1.222	1.250	1.301	1.286	1.129	1.058	1.232	1.190	1.164	1.231	1.110
T-site	**8.000**	**8.000**	**8.000**	**8.000**	**8.000**	**8.000**	**8.000**	**8.000**	**8.000**	**8.000**	**8.000**	**8.000**	**8.000**	**8.000**	**8.000**
Al	0.145	0.141	0.076	0.144	0.121	0.089	0.101	0.000	0.084	0.057	0.102	0.178	0.130	0.162	0.124
Fe^{3+}	0.467	0.425	0.523	0.405	0.438	0.537	0.447	0.929	0.493	0.451	0.411	0.448	0.335	0.469	0.381
Ti	0.106	0.114	0.118	0.099	0.116	0.125	0.155	0.129	0.102	0.118	0.146	0.104	0.173	0.101	0.116
Mg	1.146	1.126	1.123	1.152	1.150	1.145	1.094	1.147	1.293	1.309	1.145	1.208	1.152	1.201	1.246
Fe^{2+}	2.993	3.054	3.015	3.057	3.034	2.958	3.058	2.665	2.895	2.930	3.065	2.935	3.082	2.939	3.002
Mn	0.143	0.140	0.145	0.142	0.141	0.146	0.145	0.130	0.133	0.135	0.131	0.126	0.129	0.128	0.131
C-site	**5.000**	**5.000**	**5.000**	**5.000**	**5.000**	**5.000**	**5.000**	**5.000**	**5.000**	**5.000**	**5.000**	**5.000**	**5.000**	**5.000**	**5.000**
Ca	1.787	1.823	1.803	1.785	1.814	1.765	1.774	1.752	1.793	1.753	1.783	1.802	1.745	1.797	1.765
Na	0.213	0.177	0.197	0.215	0.186	0.235	0.226	0.248	0.207	0.247	0.217	0.198	0.255	0.203	0.235
B-site	**2.000**	**2.000**	**2.000**	**2.000**	**2.000**	**2.000**	**2.000**	**2.000**	**2.000**	**2.000**	**2.000**	**2.000**	**2.000**	**2.000**	**2.000**
Na	0.358	0.368	0.415	0.367	0.374	0.391	0.451	0.209	0.329	0.387	0.441	0.319	0.412	0.354	0.406
K	0.236	0.240	0.246	0.240	0.243	0.218	0.218	0.190	0.226	0.173	0.202	0.234	0.198	0.247	0.201
A-site	**0.595**	**0.608**	**0.661**	**0.608**	**0.617**	**0.609**	**0.669**	**0.399**	**0.555**	**0.560**	**0.643**	**0.553**	**0.610**	**0.601**	**0.607**
Cations	15.595	15.608	15.661	15.608	15.617	15.609	15.669	15.399	15.555	15.560	15.643	15.553	15.610	15.601	15.607
F	0.141	0.122	0.253	0.172	0.131	0.297	0.213	0.091	0.154	0.275	0.229	0.114	0.266	0.121	0.252
Cl	0.037	0.049	0.041	0.033	0.036	0.037	0.064	0.029	0.028	0.029	0.044	0.034	0.050	0.041	0.033
Oxygens	**23.000**	**23.000**	**23.000**	**23.000**	**23.000**	**23.000**	**23.000**	**23.000**	**23.000**	**23.000**	**23.000**	**23.000**	**23.000**	**23.000**	**23.000**

Appendix A.3 Electron microprobe analyses of amphiboles from the granites of the Wentworth pluton (continued).

Sample	**6490**	**6490**	**6490**	**6490**	**6490**	**6490**	**6490**	**6490**	**6490**	**6490**	**6490**	**6490**	**6490**	**6490**	**6518**
Analysis	**436**	**437**	**438**	**439**	**440**	**441**	**442**	**447**	**451**	**452**	**453**	**454**	**455**	**456**	**107**
SiO_2	41.49	44.17	44.29	44.58	45.05	44.72	44.46	44.33	46.26	45.14	47.53	49.07	48.81	45.28	49.03
TiO_2	0.31	1.08	0.88	0.93	0.93	0.93	1.14	0.83	0.90	1.02	0.47	0.35	0.33	0.33	1.85
Al_2O_3	10.07	7.06	6.86	6.96	6.82	6.43	6.84	7.52	5.86	5.89	5.17	3.97	4.43	6.83	1.63
FeO	28.28	28.27	28.37	27.89	28.22	28.45	27.95	27.08	25.68	28.21	25.13	24.41	24.72	25.90	33.80
MnO	1.04	1.08	1.06	1.11	1.05	1.03	1.01	1.05	0.89	0.96	0.95	0.92	0.86	0.83	1.30
MgO	4.29	4.50	4.36	4.67	4.42	4.42	4.48	4.88	6.52	6.45	7.28	7.65	7.47	6.40	0.46
CaO	11.16	10.86	10.86	10.77	10.65	10.87	10.96	10.89	11.20	10.62	11.22	11.12	11.13	11.24	5.19
Na_2O	2.46	2.22	2.28	2.18	1.60	2.15	2.08	2.17	1.74	1.76	1.61	1.04	0.96	1.67	4.30
K_2O	1.21	1.14	1.01	1.14	1.15	1.02	1.12	1.22	0.98	0.95	0.93	0.75	0.74	1.15	0.98
F	0.74	0.64	0.61	0.60	0.10	0.55	0.22	0.42	0.54	0.46	0.45	0.22	0.20	0.33	0.05
Cl	0.03	0.39	0.36	0.26	0.33	0.33	0.28	0.02	0.11	0.11	0.07	0.05	0.05	0.11	0.04
Total	**101.09**	**101.39**	**100.94**	**101.08**	**100.32**	**100.91**	**100.52**	**100.41**	**100.67**	**101.55**	**100.81**	**99.54**	**99.69**	**100.07**	**98.62**
Structural formula calculated on the basis of 23 oxygens and Fe^{3+} estimated with the 13eCNK normalization															
Si	6.382	6.791	6.841	6.843	6.901	6.900	6.857	6.811	7.011	6.756	7.131	7.367	7.309	6.887	7.737
Al	1.618	1.209	1.159	1.157	1.099	1.100	1.143	1.189	0.989	1.038	0.869	0.633	0.691	1.113	0.263
T-site	**8.000**	**8.000**	**8.000**	**8.000**	**8.000**	**8.000**	**8.000**	**8.000**	**8.000**	**8.000**	**8.000**	**8.000**	**8.000**	**8.000**	**8.000**
Al	0.207	0.068	0.089	0.100	0.132	0.069	0.100	0.172	0.056	0.000	0.044	0.068	0.091	0.110	0.039
Fe^{3+}	0.688	0.430	0.388	0.429	0.556	0.373	0.315	0.354	0.390	0.918	0.463	0.462	0.535	0.548	0.517
Ti	0.036	0.124	0.102	0.107	0.108	0.108	0.133	0.095	0.103	0.115	0.053	0.039	0.038	0.038	0.219
Mg	0.984	1.032	1.004	1.068	1.009	1.018	1.031	1.117	1.472	1.439	1.629	1.711	1.667	1.450	0.107
Fe^{2+}	2.950	3.205	3.278	3.152	3.060	3.297	3.290	3.125	2.864	2.406	2.690	2.603	2.561	2.746	3.943
Mn	0.135	0.140	0.139	0.144	0.136	0.134	0.132	0.136	0.115	0.122	0.120	0.116	0.108	0.107	0.173
C-site	**5.000**	**5.000**	**5.000**	**5.000**	**5.000**	**5.000**	**5.000**	**5.000**	**5.000**	**5.000**	**5.000**	**5.000**	**5.000**	**5.000**	**5.000**
Ca	1.840	1.790	1.797	1.770	1.749	1.797	1.811	1.793	1.818	1.702	1.804	1.789	1.786	1.832	0.877
Na	0.160	0.210	0.203	0.230	0.251	0.203	0.189	0.207	0.182	0.298	0.196	0.211	0.214	0.168	1.123
B-site	**2.000**	**2.000**	**2.000**	**2.000**	**2.000**	**2.000**	**2.000**	**2.000**	**2.000**	**2.000**	**2.000**	**2.000**	**2.000**	**2.000**	**2.000**
Na	0.572	0.450	0.480	0.420	0.223	0.442	0.432	0.440	0.329	0.212	0.273	0.092	0.063	0.324	0.194
K	0.238	0.223	0.199	0.223	0.224	0.202	0.220	0.239	0.189	0.181	0.177	0.143	0.140	0.223	0.197
A-site	**0.810**	**0.673**	**0.679**	**0.643**	**0.447**	**0.643**	**0.652**	**0.679**	**0.518**	**0.394**	**0.450**	**0.236**	**0.204**	**0.547**	**0.391**
Cations	15.810	15.673	15.679	15.643	15.447	15.643	15.652	15.679	15.518	15.394	15.450	15.236	15.204	15.547	15.391
F	0.358	0.313	0.297	0.292	0.049	0.266	0.105	0.203	0.261	0.218	0.211	0.105	0.094	0.160	0.025
Cl	0.009	0.101	0.095	0.066	0.087	0.085	0.073	0.006	0.029	0.027	0.019	0.014	0.013	0.029	0.010
Oxygens	**23.000**	**23.000**	**23.000**	**23.000**	**23.000**	**23.000**	**23.000**	**23.000**	**23.000**	**23.000**	**23.000**	**23.000**	**23.000**	**23.000**	**23.000**

Appendix A.3 Electron microprobe analyses of amphiboles from the granites of the Wentworth pluton (continued).

Sample	**6518**	**6518**	**6518**	**6518**	**6518**	**6518**	**6518**	**7658**	**7658**	**7658**	**7658**	**7658**	**7658**	**7658**	**7658**
Analysis	**142**	**145**	**162**	**165**	**30**	**83**	**86**	**261**	**286**	**292**	**294**	**298**	**301**	**302**	**303**
SiO_2	48.29	49.67	48.16	48.59	49.50	48.72	50.75	41.33	41.96	43.37	43.25	43.62	41.51	42.78	42.57
TiO_2	1.85	1.04	1.86	1.89	2.04	1.82	0.88	1.28	1.19	1.75	1.20	1.51	1.24	1.43	1.61
Al_2O_3	1.82	1.65	1.88	1.90	1.23	1.84	1.16	7.52	7.75	7.10	7.10	6.82	8.04	7.34	7.55
FeO	33.43	33.33	33.28	33.52	32.88	33.97	34.12	28.45	28.26	27.10	27.27	27.58	28.46	27.81	28.13
MnO	0.73	0.69	0.80	0.84	1.31	0.85	0.79	0.85	0.84	0.95	0.90	0.93	0.91	1.01	0.98
MgO	0.81	1.53	0.64	0.56	0.77	0.66	1.03	3.69	3.55	4.46	4.63	4.13	3.49	3.89	3.67
CaO	6.11	4.84	6.17	5.94	4.97	5.84	3.35	10.41	10.40	10.22	10.36	9.88	10.56	10.28	10.31
Na_2O	3.81	4.52	4.38	4.19	4.23	3.85	5.38	2.24	2.09	2.32	2.30	2.15	2.23	2.33	2.30
K_2O	1.05	0.70	1.08	1.08	1.18	0.97	0.79	1.23	1.29	0.95	0.92	0.98	1.29	1.01	0.99
F	0.07	0.01	0.06	0.07	0.04	0.00	0.03	0.75	0.34	0.48	0.60	0.21	0.56	0.36	0.38
Cl	0.05	0.02	0.05	0.05	0.02	0.04	0.01	0.30	0.43	0.23	0.15	0.22	0.36	0.27	0.25
Total	**98.02**	**98.00**	**98.34**	**98.61**	**98.16**	**98.56**	**98.28**	**98.05**	**98.09**	**98.91**	**98.66**	**98.02**	**98.63**	**98.51**	**98.72**
Structural formula calculated on the basis of 23 oxygens and Fe^{3+} estimated with the 13eCNK normalization															
Si	7.691	7.768	7.708	7.720	7.825	7.689	7.900	6.620	6.683	6.780	6.776	6.849	6.607	6.749	6.708
Al	0.309	0.232	0.292	0.280	0.175	0.311	0.100	1.380	1.317	1.220	1.224	1.151	1.393	1.251	1.292
T-site	**8.000**	**8.000**	**8.000**	**8.000**	**8.000**	**8.000**	**8.000**	**8.000**	**8.000**	**8.000**	**8.000**	**8.000**	**8.000**	**8.000**	**8.000**
Al	0.033	0.072	0.062	0.076	0.054	0.031	0.113	0.037	0.137	0.087	0.085	0.110	0.113	0.112	0.109
Fe^{3+}	0.358	0.784	0.088	0.223	0.421	0.497	0.884	0.514	0.440	0.405	0.498	0.510	0.431	0.408	0.422
Ti	0.222	0.122	0.224	0.226	0.242	0.217	0.103	0.154	0.143	0.205	0.142	0.178	0.148	0.170	0.191
Mg	0.193	0.356	0.152	0.133	0.182	0.155	0.238	0.882	0.843	1.039	1.081	0.967	0.828	0.914	0.862
Fe^{2+}	4.096	3.574	4.366	4.229	3.926	3.987	3.558	3.297	3.324	3.138	3.075	3.112	3.357	3.262	3.286
Mn	0.099	0.091	0.108	0.113	0.175	0.114	0.104	0.115	0.113	0.125	0.120	0.123	0.122	0.134	0.131
C-site	**5.000**	**5.000**	**5.000**	**5.000**	**5.000**	**5.000**	**5.000**	**5.000**	**5.000**	**5.000**	**5.000**	**5.000**	**5.000**	**5.000**	**5.000**
Ca	1.042	0.811	1.058	1.010	0.842	0.988	0.558	1.786	1.774	1.712	1.738	1.662	1.801	1.738	1.740
Na	0.958	1.189	0.942	0.990	1.158	1.012	1.442	0.214	0.226	0.288	0.262	0.338	0.199	0.262	0.260
B-site	**2.000**	**2.000**	**2.000**	**2.000**	**2.000**	**2.000**	**2.000**	**2.000**	**2.000**	**2.000**	**2.000**	**2.000**	**2.000**	**2.000**	**2.000**
Na	0.219	0.181	0.416	0.302	0.137	0.166	0.181	0.482	0.419	0.416	0.436	0.316	0.490	0.451	0.442
K	0.213	0.139	0.220	0.218	0.237	0.196	0.158	0.252	0.261	0.189	0.184	0.197	0.261	0.203	0.198
A-site	**0.432**	**0.320**	**0.636**	**0.520**	**0.374**	**0.362**	**0.339**	**0.734**	**0.680**	**0.605**	**0.620**	**0.513**	**0.751**	**0.654**	**0.640**
Cations	15.432	15.320	15.636	15.520	15.374	15.362	15.339	15.734	15.680	15.605	15.620	15.513	15.751	15.654	15.640
F	0.034	0.006	0.030	0.033	0.018	0.000	0.014	0.377	0.169	0.238	0.296	0.105	0.282	0.181	0.188
Cl	0.013	0.006	0.013	0.012	0.005	0.010	0.003	0.080	0.116	0.060	0.039	0.058	0.096	0.072	0.066
Oxygens	**23.000**	**23.000**	**23.000**	**23.000**	**23.000**	**23.000**	**23.000**	**23.000**	**23.000**	**23.000**	**23.000**	**23.000**	**23.000**	**23.000**	**23.000**

Appendix A.3 Electron microprobe analyses of amphiboles from the granites of the Wentworth pluton (continued).

Sample	**7658**	**7658**	**7658**	**7658**	**7658**	**7658**	**7658**	**7658**	**7658**	**7710**	**7710**	**7710**	**7710**	**7710**	**7710**
Analysis	**305**	**306**	**311**	**335**	**337**	**338**	**340**	**342**	**344**	**102**	**103**	**104**	**111**	**112**	**113**
SiO_2	44.22	42.36	41.68	44.44	42.47	42.33	44.53	45.12	43.93	48.20	47.73	48.45	47.06	47.23	48.44
TiO_2	1.23	1.51	1.40	1.57	1.63	1.58	1.60	1.21	1.62	1.37	1.40	1.30	1.19	1.24	1.33
Al_2O_3	6.33	7.59	7.93	6.68	7.10	7.68	6.89	6.18	7.10	2.53	2.51	2.31	3.26	3.42	2.56
FeO	28.09	28.23	28.51	26.34	28.45	28.76	26.17	27.04	25.73	30.16	30.23	30.08	29.35	29.06	29.27
MnO	0.97	0.89	0.91	0.71	0.81	0.86	0.67	0.87	0.85	0.80	0.83	0.90	0.80	0.80	0.80
MgO	4.10	3.61	3.67	5.90	4.76	3.84	6.01	5.07	5.51	2.53	2.65	2.68	3.03	3.44	3.13
CaO	10.11	10.38	10.59	10.22	10.07	10.07	10.10	10.53	10.04	6.85	6.66	6.68	7.90	8.04	6.91
Na_2O	2.24	2.22	2.22	2.44	2.25	2.42	2.43	1.69	2.26	4.30	4.26	4.43	4.02	3.87	4.18
K_2O	0.81	1.07	1.30	0.87	0.90	0.99	0.86	0.99	0.92	1.09	1.12	1.11	1.06	1.04	1.07
F	0.56	0.52	0.61	0.99	0.60	0.78	0.81	0.32	0.48	0.82	0.73	0.79	0.94	0.81	0.73
Cl	0.20	0.23	0.29	0.22	0.26	0.31	0.23	0.24	0.26	0.05	0.05	0.05	0.06	0.07	0.06
Total	**98.86**	**98.61**	**99.10**	**100.38**	**99.30**	**99.62**	**100.29**	**99.26**	**98.68**	**98.70**	**98.17**	**98.78**	**98.65**	**99.01**	**98.48**
Structural formula calculated on the basis of 23 oxygens and Fe^{3+} estimated with the 13eCNK normalization															
Si	6.924	6.702	6.596	6.805	6.602	6.625	6.790	6.966	6.804	7.653	7.597	7.676	7.503	7.461	7.652
Al	1.076	1.298	1.404	1.195	1.300	1.375	1.210	1.034	1.196	0.347	0.403	0.324	0.497	0.539	0.348
T-site	**8.000**	**8.000**	**8.000**	**8.000**	**8.000**	**8.000**	**8.000**	**8.000**	**8.000**	**8.000**	**8.000**	**8.000**	**8.000**	**8.000**	**8.000**
Al	0.091	0.116	0.074	0.009	0.000	0.039	0.027	0.088	0.098	0.125	0.066	0.106	0.115	0.096	0.129
Fe^{3+}	0.463	0.407	0.464	0.576	0.806	0.655	0.632	0.481	0.530	0.018	0.188	0.053	0.000	0.031	0.067
Ti	0.145	0.179	0.166	0.181	0.190	0.186	0.184	0.140	0.188	0.163	0.168	0.155	0.143	0.147	0.159
Mg	0.957	0.850	0.865	1.346	1.104	0.897	1.366	1.168	1.271	0.598	0.630	0.632	0.720	0.811	0.737
Fe^{2+}	3.216	3.328	3.309	2.797	2.794	3.109	2.705	3.010	2.802	3.988	3.836	3.932	3.914	3.807	3.800
Mn	0.128	0.120	0.123	0.092	0.107	0.113	0.086	0.113	0.111	0.108	0.112	0.121	0.107	0.107	0.108
C-site	**5.000**	**5.000**	**5.000**	**5.000**	**5.000**	**5.000**	**5.000**	**5.000**	**5.000**	**5.000**	**5.000**	**5.000**	**5.000**	**5.000**	**5.000**
Ca	1.695	1.760	1.795	1.677	1.677	1.688	1.650	1.742	1.665	1.166	1.136	1.133	1.349	1.361	1.169
Na	0.305	0.240	0.205	0.323	0.323	0.312	0.350	0.258	0.335	0.834	0.864	0.867	0.651	0.639	0.831
B-site	**2.000**	**2.000**	**2.000**	**2.000**	**2.000**	**2.000**	**2.000**	**2.000**	**2.000**	**2.000**	**2.000**	**2.000**	**2.000**	**2.000**	**2.000**
Na	0.376	0.441	0.477	0.402	0.356	0.423	0.367	0.248	0.345	0.490	0.450	0.495	0.592	0.547	0.450
K	0.162	0.216	0.262	0.170	0.179	0.198	0.167	0.195	0.182	0.221	0.227	0.225	0.215	0.210	0.215
A-site	**0.538**	**0.657**	**0.739**	**0.572**	**0.535**	**0.621**	**0.534**	**0.443**	**0.527**	**0.712**	**0.677**	**0.721**	**0.807**	**0.756**	**0.665**
Cations	15.538	15.657	15.739	15.572	15.535	15.621	15.534	15.443	15.527	15.712	15.677	15.721	15.807	15.756	15.665
F	0.276	0.260	0.307	0.478	0.296	0.385	0.392	0.155	0.234	0.413	0.367	0.393	0.472	0.403	0.365
Cl	0.054	0.063	0.077	0.058	0.068	0.083	0.060	0.063	0.069	0.014	0.015	0.014	0.016	0.019	0.015
Oxygens	**23.000**	**23.000**	**23.000**	**23.000**	**23.000**	**23.000**	**23.000**	**23.000**	**23.000**	**23.000**	**23.000**	**23.000**	**23.030**	**23.000**	**23.000**

Appendix A.3 Electron microprobe analyses of amphiboles from the granites of the Wentworth pluton (continued).

Sample	**7710**	**7710**	**7710**	**7710**	**7710**	**7710**	**7710**	**7710**	**7710**	**7710**	**7710**	**7710**	**7710**	**7710**	**7710**
Analysis	**115**	**15**	**154**	**155**	**164**	**17**	**175**	**176**	**177**	**187**	**188**	**189**	**190**	**21**	**221**
SiO_2	47.74	47.54	52.30	49.45	50.52	46.96	47.17	47.47	47.32	47.11	47.00	47.48	48.83	48.20	46.79
TiO_2	1.25	1.11	0.31	0.78	0.44	1.23	1.05	1.04	1.07	1.02	1.09	1.07	1.55	1.29	1.18
Al_2O_3	2.96	3.39	0.50	2.03	1.85	3.66	3.65	3.42	3.59	3.71	3.54	3.41	2.01	2.37	3.64
FeO	29.19	28.36	28.49	28.69	24.75	28.37	27.74	27.70	28.03	28.37	28.17	28.81	30.76	30.14	29.30
MnO	0.84	0.76	0.82	0.85	0.70	0.73	0.78	0.79	0.74	0.76	0.78	0.78	0.88	0.79	0.76
MgO	3.28	3.82	4.51	4.02	6.92	3.61	4.46	4.39	3.99	3.83	3.97	3.73	1.90	2.56	3.26
CaO	7.58	7.95	8.08	6.54	8.87	8.33	8.30	8.31	8.38	8.35	8.32	8.30	5.89	6.75	8.28
Na_2O	4.08	3.70	2.76	4.37	3.04	3.71	3.95	3.97	3.90	3.91	4.00	3.89	4.61	4.40	3.93
K_2O	1.05	1.01	0.99	1.35	0.59	0.97	0.87	0.92	0.89	0.92	0.90	0.88	1.14	1.15	1.03
F	0.89	0.54	0.29	0.86	1.03	0.73	1.04	1.13	0.95	1.01	0.99	0.86	0.64	0.76	0.94
Cl	0.07	0.05	0.04	0.04	0.03	0.07	0.05	0.05	0.04	0.06	0.04	0.06	0.07	0.05	0.07
Total	**98.92**	**98.24**	**99.06**	**98.98**	**98.73**	**98.38**	**99.05**	**99.20**	**98.89**	**99.04**	**98.80**	**99.27**	**98.27**	**98.47**	**99.18**
Structural formula calculated on the basis of 23 oxygens and Fe^{3+} estimated with the 13eCNK normalization															
Si	7.554	7.498	8.059	7.732	7.760	7.452	7.409	7.464	7.469	7.440	7.440	7.471	7.774	7.674	7.420
Al	0.446	0.502	0.000	0.268	0.240	0.548	0.591	0.536	0.531	0.560	0.560	0.529	0.226	0.326	0.580
T-site	**8.000**	**8.000**	**8.059**	**8.000**	**8.000**	**8.000**	**8.000**	**8.000**	**8.000**	**8.000**	**8.000**	**8.000**	**8.000**	**8.000**	**8.000**
Al	0.105	0.127	0.091	0.107	0.094	0.136	0.084	0.098	0.136	0.129	0.101	0.103	0.150	0.119	0.100
Fe^{3+}	0.012	0.088	0.036	0.191	0.105	0.000	0.089	0.000	0.000	0.000	0.000	0.013	0.043	0.005	0.000
Ti	0.148	0.132	0.035	0.092	0.051	0.147	0.124	0.123	0.126	0.121	0.129	0.126	0.185	0.155	0.141
Mg	0.773	0.899	1.036	0.937	1.585	0.855	1.044	1.030	0.939	0.902	0.937	0.875	0.450	0.608	0.770
Fe^{2+}	3.850	3.652	3.636	3.561	3.074	3.764	3.555	3.643	3.700	3.747	3.729	3.779	4.052	4.007	3.887
Mn	0.112	0.101	0.107	0.112	0.090	0.098	0.104	0.106	0.099	0.101	0.104	0.104	0.119	0.107	0.102
C-site	**5.000**	**5.000**	**5.000**	**5.000**	**5.000**	**5.000**	**5.000**	**5.000**	**5.000**	**5.000**	**5.000**	**5.000**	**5.000**	**5.000**	**5.000**
Ca	1.284	1.344	1.274	1.096	1.460	1.417	1.396	1.400	1.418	1.413	1.412	1.399	1.005	1.151	1.407
Na	0.716	0.656	0.726	0.904	0.540	0.583	0.604	0.600	0.582	0.587	0.588	0.601	0.995	0.849	0.593
B-site	**2.000**	**2.000**	**2.000**	**2.000**	**2.000**	**2.000**	**2.000**	**2.000**	**2.000**	**2.000**	**2.000**	**2.000**	**2.000**	**2.000**	**2.000**
Na	0.537	0.476	0.098	0.420	0.364	0.559	0.599	0.609	0.611	0.611	0.639	0.586	0.427	0.508	0.615
K	0.212	0.204	0.194	0.269	0.115	0.197	0.175	0.185	0.179	0.185	0.182	0.177	0.231	0.233	0.209
A-site	**0.749**	**0.679**	**0.291**	**0.689**	**0.479**	**0.756**	**0.774**	**0.794**	**0.790**	**0.796**	**0.821**	**0.763**	**0.658**	**0.742**	**0.824**
Cations	15.749	15.679	15.351	15.689	15.479	15.756	15.774	15.794	15.790	15.796	15.821	15.763	15.658	15.742	15.824
F	0.447	0.269	0.139	0.427	0.502	0.368	0.517	0.562	0.472	0.504	0.496	0.429	0.320	0.384	0.471
Cl	0.018	0.014	0.009	0.011	0.007	0.018	0.013	0.012	0.011	0.015	0.012	0.017	0.019	0.014	0.019
Oxygens	**23.000**	**23.000**	**23.000**	**23.000**	**23.000**	**23.027**	**23.000**	**23.002**	**23.033**	**23.010**	**23.016**	**23.000**	**23.000**	**23.000**	**23.017**

Appendix A.3 Electron microprobe analyses of amphiboles from the granites of the Wentworth pluton (continued).

Sample	**7710**	**7710**	**7710**	**7710**	**7710**	**7710**	**7710**	**7710**	**7710**	**7710**	**7710**	**7710**	**7710**	**7710**	**7710**
Analysis	**222**	**223**	**224**	**225**	**226**	**227**	**228**	**229**	**230**	**231**	**235**	**239**	**242**	**244**	**245**
SiO_2	47.48	47.09	46.76	46.80	48.35	47.63	47.73	46.87	46.63	47.09	47.80	48.60	47.06	47.15	47.01
TiO_2	1.09	1.05	1.19	1.17	1.26	1.11	1.17	1.20	1.24	1.09	1.07	1.36	1.09	1.03	1.02
Al_2O_3	3.27	3.60	3.66	3.25	3.49	3.63	3.35	3.64	3.66	3.47	3.29	2.34	3.33	3.54	3.63
FeO	27.98	28.37	28.63	28.78	28.17	27.89	27.03	27.83	28.57	28.00	28.82	29.97	27.89	27.22	27.60
MnO	0.76	0.79	0.75	0.78	0.73	0.75	0.73	0.72	0.77	0.75	0.69	0.79	0.73	0.81	0.79
MgO	4.20	3.82	3.49	3.23	4.05	4.36	5.00	4.30	4.00	4.16	3.76	2.60	3.99	4.59	4.17
CaO	8.33	8.50	8.42	8.17	8.18	8.49	8.39	8.53	8.56	8.41	8.32	6.65	8.29	8.50	8.34
Na_2O	4.04	4.07	3.86	3.98	3.93	4.08	4.01	3.82	3.85	3.88	3.66	4.26	3.84	3.90	4.00
K_2O	0.95	0.90	1.00	1.08	1.11	0.99	0.95	1.03	1.10	0.99	0.96	1.08	1.00	0.90	0.89
F	1.16	1.06	0.84	0.95	0.71	1.11	1.06	1.03	1.09	1.01	0.67	0.48	0.80	0.92	0.85
Cl	0.06	0.06	0.06	0.07	0.06	0.07	0.07	0.07	0.08	0.06	0.07	0.06	0.05	0.05	0.05
Total	**99.32**	**99.31**	**98.67**	**98.27**	**100.05**	**100.10**	**99.48**	**99.04**	**99.54**	**98.92**	**99.12**	**98.17**	**98.06**	**98.62**	**98.35**
Structural formula calculated on the basis of 23 oxygens and Fe^{3+} estimated with the 13eCNK normalization															
Si	7.486	7.447	7.436	7.506	7.516	7.443	7.454	7.399	7.359	7.443	7.507	7.706	7.489	7.440	7.451
Al	0.514	0.553	0.564	0.494	0.484	0.557	0.546	0.601	0.641	0.557	0.493	0.294	0.511	0.560	0.549
T-site	**8.000**	**8.000**	**8.000**	**8.000**	**8.000**	**8.000**	**8.000**	**8.000**	**8.000**	**8.000**	**8.000**	**8.000**	**8.000**	**8.000**	**8.000**
Al	0.093	0.117	0.121	0.121	0.155	0.111	0.071	0.075	0.038	0.089	0.116	0.144	0.113	0.098	0.129
Fe^{3+}	0.000	0.000	0.000	0.000	0.000	0.000	0.000	0.000	0.012	0.000	0.018	0.037	0.000	0.000	0.000
Ti	0.129	0.125	0.142	0.141	0.147	0.130	0.137	0.143	0.148	0.130	0.127	0.163	0.130	0.122	0.121
Mg	0.988	0.900	0.828	0.772	0.939	1.015	1.164	1.011	0.941	0.979	0.881	0.613	0.947	1.080	0.984
Fe^{2+}	3.689	3.752	3.807	3.861	3.663	3.645	3.531	3.674	3.758	3.701	3.767	3.937	3.712	3.592	3.659
Mn	0.101	0.106	0.102	0.106	0.095	0.099	0.097	0.097	0.103	0.101	0.092	0.106	0.098	0.108	0.107
C-site	**5.000**	**5.000**	**5.000**	**5.000**	**5.000**	**5.000**	**5.000**	**5.000**	**5.000**	**5.000**	**5.000**	**5.000**	**5.000**	**5.000**	**5.000**
Ca	1.408	1.441	1.435	1.404	1.362	1.422	1.404	1.443	1.447	1.424	1.399	1.130	1.413	1.438	1.417
Na	0.592	0.559	0.565	0.596	0.638	0.578	0.596	0.557	0.553	0.576	0.601	0.870	0.587	0.562	0.583
B-site	**2.000**	**2.000**	**2.000**	**2.000**	**2.000**	**2.000**	**2.000**	**2.000**	**2.000**	**2.000**	**2.000**	**2.000**	**2.000**	**2.000**	**2.000**
Na	0.642	0.690	0.626	0.642	0.547	0.657	0.618	0.613	0.626	0.614	0.514	0.439	0.597	0.632	0.646
K	0.192	0.181	0.203	0.222	0.219	0.198	0.189	0.207	0.222	0.200	0.192	0.218	0.202	0.182	0.179
A-site	**0.834**	**0.870**	**0.830**	**0.864**	**0.767**	**0.854**	**0.807**	**0.820**	**0.848**	**0.815**	**0.706**	**0.657**	**0.799**	**0.814**	**0.825**
Cations	15.834	15.870	15.830	15.864	15.767	15.854	15.807	15.820	15.848	15.815	15.706	15.657	15.799	15.814	15.825
F	0.580	0.528	0.422	0.480	0.351	0.551	0.525	0.515	0.544	0.506	0.333	0.239	0.402	0.461	0.428
Cl	0.016	0.015	0.015	0.019	0.017	0.017	0.017	0.018	0.020	0.016	0.020	0.016	0.014	0.014	0.015
Oxygens	**23.040**	**23.063**	**23.053**	**23.088**	**23.047**	**23.045**	**23.005**	**23.012**	**23.000**	**23.015**	**23.000**	**23.000**	**23.037**	**23.017**	**23.032**

Appendix A.3 Electron microprobe analyses of amphiboles from the granites of the Wentworth pluton (continued).

Sample	**7710**	**7710**	**7710**	**7710**	**7710**	**7710**	**7710**	**7710**	**7710**	**7710**	**7710**	**7710**	**7710**	**7710**	**7710**
Analysis	**246**	**247**	**256**	**259**	**260**	**261**	**266**	**267**	**268**	**269**	**27**	**270**	**271**	**272**	**273**
SiO_2	46.60	46.69	49.05	49.60	48.78	49.18	47.69	46.94	46.91	47.52	47.88	46.90	47.76	47.41	47.17
TiO_2	1.12	1.21	0.51	0.44	0.73	0.96	1.22	1.10	1.18	1.05	0.99	1.10	1.10	1.26	1.00
Al_2O_3	3.69	3.51	2.70	2.34	5.28	9.18	2.77	3.65	3.40	3.60	3.23	3.64	2.99	3.39	3.38
FeO	28.25	28.88	26.19	25.65	26.52	23.15	29.37	27.75	27.93	27.57	28.63	27.86	29.18	28.24	26.62
MnO	0.81	0.79	0.86	0.78	0.71	0.64	0.80	0.71	0.74	0.71	0.72	0.73	0.80	0.75	0.73
MgO	3.85	3.25	5.62	5.14	3.58	3.23	2.82	4.33	4.26	4.61	3.64	3.94	2.93	3.90	5.02
CaO	8.57	8.11	7.95	9.40	5.95	7.21	7.45	8.53	8.49	8.40	7.61	8.39	7.76	8.63	8.40
Na_2O	3.90	3.86	4.10	3.48	5.25	3.49	4.23	3.82	3.51	3.76	4.01	3.68	3.91	3.83	4.00
K_2O	0.97	1.08	0.95	0.77	0.84	2.34	1.04	0.96	0.99	0.88	0.88	1.01	0.98	1.05	0.93
F	1.01	0.69	1.09	0.62	0.80	0.83	0.76	1.10	0.69	1.01	0.67	0.71	0.64	0.99	1.07
Cl	0.06	0.08	0.05	0.04	0.06	0.06	0.06	0.06	0.07	0.05	0.07	0.06	0.06	0.07	0.07
Total	**98.82**	**98.14**	**99.06**	**98.26**	**98.48**	**100.26**	**98.20**	**98.94**	**98.16**	**99.16**	**98.31**	**98.02**	**98.10**	**99.53**	**98.38**
Structural formula calculated on the basis of 23 oxygens and Fe^{3+} estimated with the 13eCNK normalization															
Si	7.403	7.458	7.625	7.820	7.581	7.484	7.625	7.412	7.425	7.436	7.555	7.453	7.612	7.479	7.455
Al	0.597	0.542	0.375	0.180	0.419	0.516	0.375	0.588	0.575	0.564	0.445	0.547	0.388	0.521	0.545
T-site	**8.000**	**8.000**	**8.000**	**8.000**	**8.000**	**8.000**	**8.000**	**8.000**	**8.000**	**8.000**	**8.000**	**8.000**	**8.000**	**8.000**	**8.000**
Al	0.093	0.118	0.119	0.253	0.546	1.129	0.146	0.092	0.059	0.099	0.154	0.134	0.174	0.109	0.084
Fe^{3+}	0.000	0.000	0.065	0.000	0.000	0.000	0.000	0.000	0.078	0.082	0.080	0.000	0.000	0.000	0.000
Ti	0.133	0.145	0.060	0.052	0.085	0.109	0.147	0.130	0.140	0.124	0.117	0.131	0.131	0.150	0.119
Mg	0.911	0.774	1.303	1.208	0.828	0.733	0.672	1.019	1.005	1.075	0.855	0.934	0.696	0.916	1.183
Fe^{2+}	3.754	3.857	3.340	3.382	3.447	2.946	3.927	3.664	3.619	3.527	3.697	3.703	3.890	3.726	3.517
Mn	0.109	0.107	0.113	0.104	0.093	0.082	0.108	0.095	0.099	0.094	0.096	0.098	0.108	0.100	0.098
C-site	**5.000**	**5.000**	**5.000**	**5.000**	**5.000**	**5.000**	**5.000**	**5.000**	**5.000**	**5.000**	**5.000**	**5.000**	**5.000**	**5.000**	**5.000**
Ca	1.459	1.388	1.324	1.587	0.990	1.175	1.276	1.443	1.440	1.409	1.286	1.429	1.326	1.458	1.423
Na	0.541	0.612	0.676	0.413	1.010	0.825	0.724	0.557	0.560	0.591	0.714	0.571	0.674	0.542	0.577
B-site	**2.000**	**2.000**	**2.000**	**2.000**	**2.000**	**2.000**	**2.000**	**2.000**	**2.000**	**2.000**	**2.000**	**2.000**	**2.000**	**2.000**	**2.000**
Na	0.660	0.583	0.560	0.653	0.571	0.205	0.587	0.613	0.518	0.551	0.512	0.563	0.533	0.629	0.648
K	0.196	0.220	0.188	0.155	0.167	0.455	0.211	0.193	0.200	0.176	0.177	0.206	0.198	0.212	0.187
A-site	**0.856**	**0.803**	**0.747**	**0.808**	**0.738**	**0.659**	**0.799**	**0.806**	**0.717**	**0.727**	**0.690**	**0.769**	**0.731**	**0.841**	**0.835**
Cations	15.856	15.803	15.747	15.808	15.738	15.659	15.799	15.806	15.717	15.727	15.690	15.769	15.731	15.841	15.835
F	0.508	0.347	0.533	0.307	0.393	0.400	0.386	0.548	0.345	0.500	0.335	0.358	0.324	0.496	0.533
Cl	0.017	0.021	0.013	0.011	0.015	0.015	0.015	0.016	0.019	0.014	0.018	0.016	0.017	0.018	0.018
Oxygens	**23.039**	**23.029**	**23.000**	**23.286**	**23.013**	**23.333**	**23.070**	**23.007**	**23.000**	**23.000**	**23.000**	**23.024**	**23.053**	**23.093**	**23.016**

Appendix A.3 Electron microprobe analyses of amphiboles from the granites of the Wentworth pluton (continued).

Sample	**7710**	**7710**	**7710**	**7710**	**7710**	**7710**	**7710**	**7710**	**7710**	**7710**	**7710**	**7710**	**7710**	**7710**	**7710**
Analysis	**274**	**275**	**28**	**296**	**297**	**298**	**299**	**300**	**301**	**31**	**40**	**41**	**49**	**53**	**60**
SiO_2	47.00	48.32	48.14	47.09	46.84	47.01	47.16	46.62	47.97	50.01	47.12	47.04	47.04	51.32	49.92
TiO_2	1.18	1.14	0.94	1.24	1.18	1.11	1.19	1.12	1.38	0.82	1.24	1.07	1.13	0.16	0.49
Al_2O_3	3.66	2.27	3.05	3.43	3.56	3.57	3.52	3.67	2.47	1.65	3.62	3.71	3.65	0.40	2.42
FeO	27.73	29.84	24.18	29.85	27.84	27.88	27.41	27.48	29.84	27.94	27.73	27.62	27.25	25.28	21.27
MnO	0.72	0.83	0.64	0.71	0.69	0.78	0.73	0.74	0.83	0.82	0.78	0.76	0.73	0.93	0.58
MgO	4.20	2.96	6.95	2.69	4.10	4.14	4.59	4.44	2.52	4.07	4.24	4.48	4.49	3.72	9.31
CaO	8.54	6.88	8.63	7.80	8.73	8.47	8.44	8.42	6.99	6.46	8.37	8.36	8.50	13.62	8.93
Na_2O	3.93	4.43	3.54	3.86	3.75	3.81	3.68	3.84	4.50	4.53	3.75	3.66	3.73	3.25	3.84
K_2O	0.97	1.06	0.96	1.07	1.09	0.88	1.03	0.99	1.11	1.02	0.98	0.97	1.04	0.28	0.62
F	1.04	0.85	1.27	0.58	1.01	1.07	0.98	1.04	0.85	0.94	1.06	1.00	0.87	0.27	1.37
Cl	0.07	0.05	0.05	0.07	0.07	0.05	0.04	0.06	0.05	0.03	0.05	0.05	0.07	0.01	0.02
Total	**99.04**	**98.62**	**98.34**	**98.39**	**98.84**	**98.78**	**98.77**	**98.42**	**98.51**	**98.29**	**98.93**	**98.72**	**98.51**	**99.24**	**98.76**
Structural formula calculated on the basis of 23 oxygens and Fe^{3+} estimated with the 13eCNK normalization															
Si	7.428	7.669	7.490	7.499	7.436	7.435	7.423	7.389	7.667	7.861	7.426	7.400	7.431	8.404	7.608
Al	0.572	0.331	0.510	0.501	0.564	0.565	0.577	0.611	0.333	0.139	0.574	0.600	0.569	0.000	0.392
T-site	**8.000**	**8.000**	**8.000**	**8.000**	**8.000**	**8.000**	**8.000**	**8.000**	**8.000**	**8.000**	**8.000**	**8.000**	**8.000**	**8.404**	**8.000**
Al	0.109	0.092	0.048	0.142	0.101	0.100	0.076	0.075	0.133	0.167	0.099	0.086	0.109	0.076	0.043
Fe^{3+}	0.000	0.051	0.106	0.000	0.000	0.000	0.044	0.028	0.000	0.015	0.014	0.132	0.000	0.000	0.067
Ti	0.141	0.136	0.110	0.149	0.141	0.132	0.140	0.133	0.166	0.097	0.147	0.127	0.135	0.020	0.056
Mg	0.990	0.700	1.611	0.638	0.970	0.976	1.078	1.050	0.601	0.954	0.995	1.052	1.058	0.909	2.116
Fe^{2+}	3.665	3.908	3.041	3.975	3.695	3.688	3.565	3.615	3.988	3.658	3.641	3.502	3.601	3.461	2.645
Mn	0.096	0.112	0.084	0.096	0.093	0.104	0.097	0.099	0.112	0.109	0.104	0.101	0.098	0.130	0.074
C-site	**5.000**	**5.000**	**5.000**	**5.000**	**5.000**	**5.000**	**5.000**	**5.000**	**5.000**	**5.000**	**5.000**	**5.000**	**5.000**	**5.000**	**5.000**
Ca	1.446	1.170	1.439	1.331	1.485	1.436	1.423	1.430	1.197	1.089	1.413	1.408	1.439	1.986	1.459
Na	0.554	0.830	0.561	0.669	0.515	0.564	0.577	0.570	0.803	0.911	0.587	0.592	0.561	0.014	0.541
B-site	**2.000**	**2.000**	**2.000**	**2.000**	**2.000**	**2.000**	**2.000**	**2.000**	**2.000**	**2.000**	**2.000**	**2.000**	**2.000**	**2.000**	**2.000**
Na	0.652	0.532	0.507	0.523	0.638	0.603	0.547	0.609	0.591	0.469	0.557	0.524	0.583	1.018	0.592
K	0.195	0.215	0.191	0.217	0.220	0.178	0.206	0.201	0.227	0.205	0.196	0.195	0.209	0.058	0.120
A-site	**0.847**	**0.747**	**0.698**	**0.741**	**0.858**	**0.782**	**0.753**	**0.810**	**0.818**	**0.674**	**0.753**	**0.720**	**0.792**	**1.075**	**0.712**
Cations	15.847	15.747	15.698	15.741	15.858	15.782	15.753	15.810	15.818	15.674	15.753	15.720	15.792	16.479	15.712
F	0.518	0.428	0.622	0.290	0.506	0.537	0.489	0.520	0.432	0.466	0.527	0.498	0.435	0.138	0.660
Cl	0.018	0.012	0.013	0.020	0.018	0.013	0.011	0.017	0.013	0.007	0.014	0.014	0.019	0.002	0.004
Oxygens	**23.055**	**23.000**	**23.000**	**23.005**	**23.080**	**23.008**	**23.000**	**23.000**	**23.073**	**23.000**	**23.000**	**23.000**	**23.020**	**24.397**	**23.000**

Appendix A.3 Electron microprobe analyses of amphiboles from the granites of the Wentworth pluton (continued).

Sample	**7710**	**7710**	**7710**	**7710**	**7710**	**7710**	**7710**	**7710**	**7710**	**7814**	**7814**	**7814**	**7814**	**7814**	**7814**
Analysis	**65**	**66**	**71**	**72**	**73**	**74**	**82**	**83**	**84**	**11**	**13**	**14**	**19**	**20**	**21**
SiO_2	49.08	47.68	46.64	47.12	47.30	47.08	46.70	46.79	46.85	43.90	45.70	44.62	44.68	43.95	44.71
TiO_2	0.59	1.18	1.17	1.07	1.08	1.20	1.19	1.15	1.24	0.97	0.94	0.85	0.77	0.87	0.83
Al_2O_3	2.93	2.60	3.70	3.61	3.50	3.50	3.67	3.68	3.60	6.72	5.97	6.38	6.01	5.69	5.78
FeO	25.30	29.90	28.37	27.34	27.53	27.86	27.70	27.56	28.20	28.39	28.09	27.19	28.33	28.97	28.01
MnO	0.74	0.85	0.75	0.74	0.75	0.73	0.79	0.74	0.74	1.32	1.38	1.31	1.38	1.40	1.42
MgO	6.27	2.89	3.60	4.57	4.57	3.96	3.87	4.18	3.83	3.67	4.41	4.42	4.27	3.80	4.04
CaO	8.47	7.11	8.41	8.21	8.25	8.09	8.52	8.32	8.46	10.32	10.29	10.23	10.50	10.12	10.40
Na_2O	3.71	4.22	3.86	3.91	3.96	3.90	3.85	3.91	3.77	2.17	2.28	2.18	2.18	2.14	2.02
K_2O	0.82	1.06	0.98	1.05	0.86	1.04	0.95	0.96	1.06	1.16	1.11	1.06	1.18	1.16	1.12
F	0.64	0.84	0.87	0.86	1.06	1.00	0.96	0.97	0.92	0.49	0.67	0.54	0.71	0.69	0.62
Cl	0.04	0.05	0.07	0.06	0.05	0.06	0.06	0.05	0.06	0.25	0.26	0.27	0.30	0.32	0.23
Total	**98.60**	**98.38**	**98.42**	**98.54**	**98.91**	**98.43**	**98.25**	**98.31**	**98.73**	**99.35**	**101.09**	**99.04**	**100.29**	**99.10**	**99.18**
Structural formula calculated on the basis of 23 oxygens and Fe^{3+} estimated with the 13eCNK normalization															
Si	7.586	7.590	7.431	7.427	7.436	7.470	7.448	7.427	7.432	6.886	7.017	6.971	6.951	6.935	7.020
Al	0.414	0.410	0.569	0.573	0.564	0.530	0.552	0.573	0.568	1.114	0.983	1.029	1.049	1.058	0.980
T-site	**8.000**	**8.000**	**8.000**	**8.000**	**8.000**	**8.000**	**8.000**	**8.000**	**8.000**	**8.000**	**8.000**	**8.000**	**8.000**	**8.000**	**8.000**
Al	0.119	0.078	0.125	0.097	0.083	0.125	0.136	0.115	0.105	0.127	0.096	0.145	0.053	0.000	0.088
Fe^{3+}	0.078	0.107	0.000	0.044	0.066	0.000	0.000	0.000	0.000	0.399	0.386	0.389	0.425	0.548	0.358
Ti	0.068	0.141	0.140	0.127	0.127	0.143	0.143	0.137	0.148	0.114	0.109	0.100	0.090	0.103	0.098
Mg	1.444	0.687	0.855	1.074	1.071	0.936	0.920	0.989	0.905	0.859	1.009	1.029	0.990	0.893	0.947
Fe^{2+}	3.193	3.873	3.780	3.560	3.553	3.697	3.695	3.659	3.741	3.326	3.221	3.164	3.261	3.269	3.320
Mn	0.097	0.114	0.101	0.099	0.100	0.098	0.107	0.100	0.100	0.175	0.179	0.173	0.181	0.188	0.189
C-site	**5.000**	**5.000**	**5.000**	**5.000**	**5.000**	**5.000**	**5.000**	**5.000**	**5.000**	**5.000**	**5.000**	**5.000**	**5.000**	**5.000**	**5.000**
Ca	1.403	1.212	1.436	1.386	1.390	1.375	1.456	1.415	1.437	1.735	1.694	1.713	1.750	1.711	1.749
Na	0.597	0.788	0.564	0.614	0.610	0.625	0.544	0.585	0.563	0.265	0.306	0.287	0.250	0.289	0.251
B-site	**2.000**	**2.000**	**2.000**	**2.000**	**2.000**	**2.000**	**2.000**	**2.000**	**2.000**	**2.000**	**2.000**	**2.000**	**2.000**	**2.000**	**2.000**
Na	0.516	0.514	0.628	0.581	0.598	0.576	0.647	0.618	0.598	0.393	0.371	0.372	0.408	0.367	0.364
K	0.162	0.216	0.198	0.211	0.173	0.210	0.194	0.195	0.215	0.232	0.218	0.210	0.233	0.233	0.225
A-site	**0.678**	**0.730**	**0.826**	**0.792**	**0.771**	**0.786**	**0.841**	**0.813**	**0.812**	**0.625**	**0.589**	**0.582**	**0.642**	**0.599**	**0.589**
Cations	15.678	15.730	15.826	15.792	15.771	15.786	15.841	15.813	15.812	15.625	15.589	15.582	15.642	15.599	15.589
F	0.311	0.420	0.440	0.428	0.529	0.503	0.483	0.486	0.459	0.243	0.326	0.266	0.351	0.344	0.309
Cl	0.010	0.013	0.020	0.015	0.013	0.016	0.016	0.014	0.017	0.066	0.067	0.072	0.078	0.084	0.061
Oxygens	**23.000**	**23.000**	**23.049**	**23.000**	**23.000**	**23.021**	**23.083**	**23.022**	**23.042**	**23.000**	**23.000**	**23.000**	**23.000**	**23.000**	**23.000**

Appendix A.3 Electron microprobe analyses of amphiboles from the granites of the Wentworth pluton (continued).

Sample	**7814**	**7814**	**7814**	**7814**	**7814**	**7814**	**7814**	**7814**	**7814**	**7814**	**7814**	**7814**	**7814**	**7814**	**7814**
Analysis	**27**	**28**	**29**	**30**	**31**	**32**	**34**	**36**	**44**	**48**	**62**	**63**	**73**	**74**	**78**
SiO_2	44.51	44.40	44.99	44.43	45.67	45.14	44.97	45.15	44.29	44.97	44.48	44.23	45.04	44.20	44.99
TiO_2	1.04	1.01	1.20	0.78	0.75	1.07	0.73	1.00	1.11	1.02	1.00	0.86	0.95	0.93	1.02
Al_2O_3	6.31	5.98	6.26	6.38	6.49	6.60	5.86	6.20	6.46	5.83	6.53	6.16	6.51	6.24	5.86
FeO	27.60	27.54	27.54	27.32	27.67	27.63	28.77	27.67	27.85	27.90	28.13	28.50	27.87	27.75	27.22
MnO	1.35	1.39	1.35	1.38	1.33	1.37	1.39	1.23	1.32	1.42	1.44	1.52	1.41	1.45	1.27
MgO	4.41	4.36	4.34	4.21	4.46	4.22	4.62	4.48	4.27	4.34	3.96	3.95	3.63	3.98	4.75
CaO	10.40	10.32	10.58	10.32	10.45	10.24	9.82	10.45	10.41	10.26	9.86	10.30	10.18	10.36	9.84
Na_2O	2.12	1.97	2.01	2.12	2.16	2.13	2.16	1.98	2.10	2.22	2.11	1.87	2.11	2.10	1.95
K_2O	1.13	1.14	1.13	1.15	1.12	1.09	1.05	1.05	1.18	1.07	1.11	1.07	1.17	1.14	1.12
F	0.58	0.44	0.59	0.45	0.58	0.49	0.65	0.43	0.49	0.70	0.58	0.36	0.38	0.58	0.56
Cl	0.25	0.28	0.28	0.27	0.24	0.22	0.24	0.22	0.25	0.31	0.25	0.25	0.27	0.24	0.28
Total	**99.70**	**98.83**	**100.28**	**98.81**	**100.91**	**100.19**	**100.24**	**99.85**	**99.71**	**100.03**	**99.45**	**99.05**	**99.52**	**98.96**	**98.87**
Structural formula calculated on the basis of 23 oxygens and Fe^{3+} estimated with the 13eCNK normalization															
Si	6.927	6.962	6.970	6.973	7.002	6.963	6.916	6.983	6.895	6.993	6.919	6.916	7.025	6.956	6.997
Al	1.073	1.038	1.030	1.027	0.998	1.037	1.061	1.017	1.105	1.007	1.081	1.084	0.975	1.044	1.003
T-site	**8.000**	**8.000**	**8.000**	**8.000**	**8.000**	**8.000**	**8.000**	**8.000**	**8.000**	**8.000**	**8.000**	**8.000**	**8.000**	**8.000**	**8.000**
Al	0.084	0.066	0.112	0.153	0.174	0.162	0.000	0.112	0.080	0.060	0.115	0.050	0.222	0.111	0.071
Fe^{3+}	0.414	0.439	0.303	0.346	0.356	0.390	0.829	0.407	0.425	0.409	0.590	0.602	0.256	0.350	0.600
Ti	0.122	0.119	0.139	0.092	0.086	0.124	0.084	0.116	0.130	0.120	0.117	0.101	0.112	0.109	0.120
Mg	1.024	1.019	1.003	0.986	1.019	0.970	1.059	1.032	0.992	1.005	0.919	0.921	0.843	0.933	1.102
Fe^{2+}	3.179	3.173	3.265	3.240	3.191	3.174	2.848	3.172	3.200	3.219	3.070	3.125	3.380	3.303	2.941
Mn	0.178	0.185	0.178	0.183	0.173	0.179	0.181	0.161	0.174	0.187	0.189	0.201	0.187	0.194	0.167
C-site	**5.000**	**5.000**	**5.000**	**5.000**	**5.000**	**5.000**	**5.000**	**5.000**	**5.000**	**5.000**	**5.000**	**5.000**	**5.000**	**5.000**	**5.000**
Ca	1.734	1.734	1.755	1.735	1.717	1.693	1.619	1.732	1.737	1.709	1.643	1.726	1.701	1.747	1.640
Na	0.266	0.266	0.245	0.265	0.283	0.307	0.381	0.268	0.263	0.291	0.357	0.274	0.299	0.253	0.360
B-site	**2.000**	**2.000**	**2.000**	**2.000**	**2.000**	**2.000**	**2.000**	**2.000**	**2.000**	**2.000**	**2.000**	**2.000**	**2.000**	**2.000**	**2.000**
Na	0.373	0.334	0.358	0.379	0.359	0.329	0.263	0.327	0.370	0.377	0.280	0.291	0.340	0.388	0.230
K	0.225	0.228	0.224	0.230	0.218	0.214	0.205	0.207	0.234	0.213	0.220	0.214	0.232	0.229	0.222
A-site	**0.598**	**0.562**	**0.582**	**0.608**	**0.577**	**0.543**	**0.468**	**0.534**	**0.604**	**0.590**	**0.500**	**0.505**	**0.572**	**0.617**	**0.452**
Cations	15.598	15.562	15.582	15.608	15.577	15.543	15.468	15.534	15.604	15.590	15.500	15.505	15.572	15.617	15.452
F	0.283	0.216	0.289	0.223	0.279	0.240	0.317	0.210	0.239	0.343	0.285	0.176	0.186	0.288	0.275
Cl	0.067	0.074	0.073	0.073	0.063	0.057	0.062	0.057	0.065	0.081	0.067	0.067	0.072	0.064	0.073
Oxygens	**23.000**	**23.000**	**23.000**	**23.000**	**23.000**	**23.000**	**23.000**	**23.000**	**23.000**	**23.000**	**23.000**	**23.000**	**23.000**	**23.000**	**23.000**

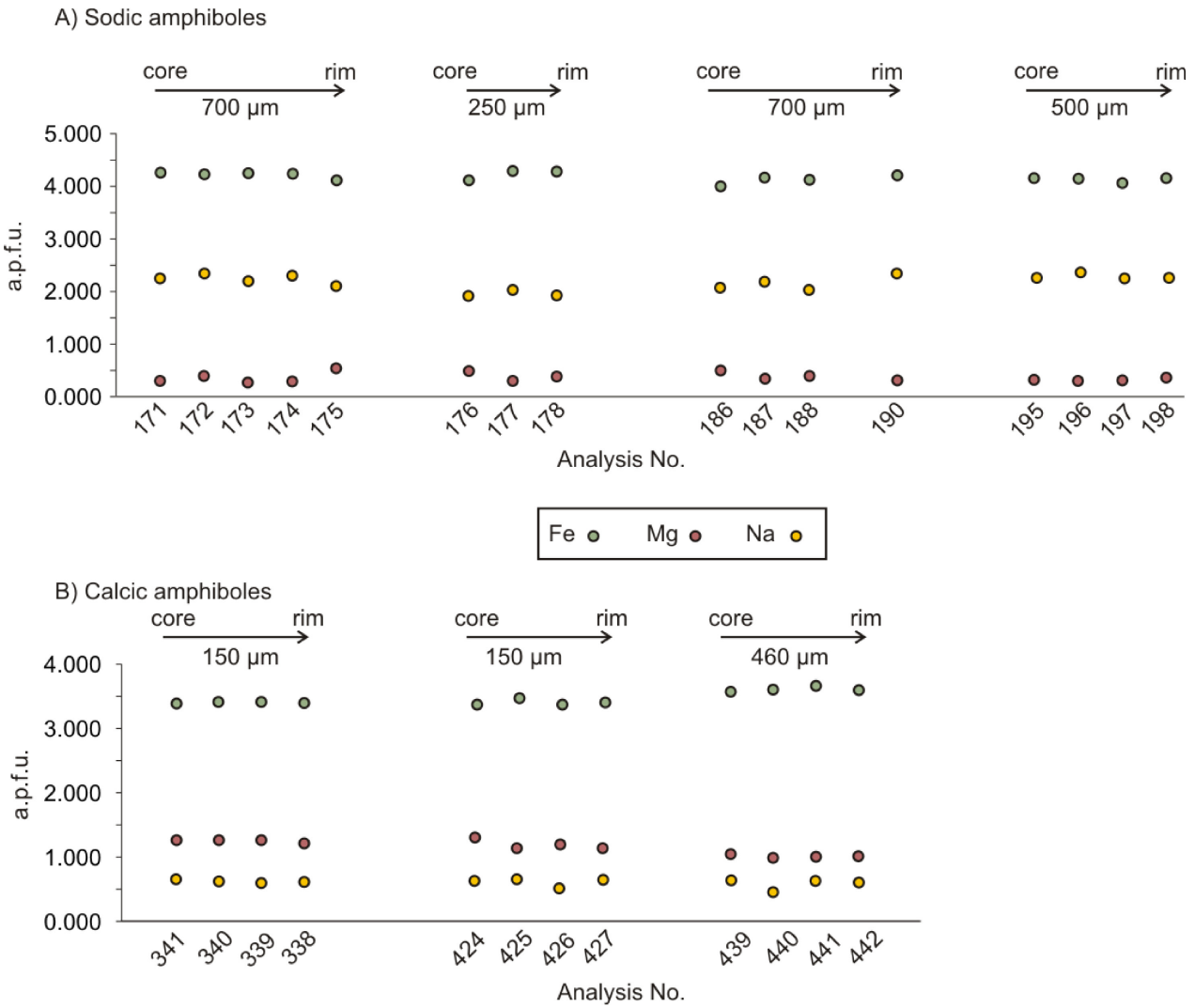

Appendix A.4 Zoning profiles for selected traverses on grains of (A) sodic and (B) calcic amphiboles in the granites of the Wentworth pluton.

Appendix A.5 Electron microprobe analyses of biotite from the granites of the Wentworth pluton.

Sample	**5056**	**5056**	**5056**	**5056**	**5056**	**5056**	**5056**	**5056**	**5056**	**5056**	**5056**	**5056**	**5056**	**5056**
Analysis	**238**	**239**	**240**	**246**	**247**	**250**	**251**	**252**	**271**	**272**	**273**	**274**	**275**	**316**
SiO_2	37.34	37.04	37.19	35.73	36.85	37.01	37.35	37.09	36.88	36.25	36.30	36.80	36.31	36.27
TiO_2	4.12	3.78	4.09	9.09	5.32	3.55	3.28	3.24	4.35	3.77	3.58	4.26	4.02	3.98
Al_2O_3	13.27	13.37	13.13	11.80	13.12	14.02	14.53	14.57	13.39	13.14	13.63	13.58	13.36	13.49
FeO	23.81	23.95	24.21	17.79	20.82	23.65	23.10	23.38	24.46	23.75	24.01	24.28	25.08	24.86
MnO	0.19	0.18	0.20	0.15	0.18	0.22	0.20	0.19	0.18	0.18	0.17	0.19	0.19	0.19
MgO	8.93	8.79	8.48	7.81	8.88	8.03	8.45	7.69	8.45	8.57	8.28	8.44	8.03	8.16
CaO	0.01	0.03	0.03	7.04	3.00	0.12	0.04	0.10	0.08	0.07	0.09	0.04	0.05	0.03
Na_2O	0.14	0.14	0.15	0.10	0.09	0.12	0.07	0.10	0.13	0.20	0.13	0.05	0.10	0.12
K_2O	9.58	9.54	9.51	5.89	8.34	9.36	9.63	9.43	9.74	8.93	9.03	9.77	9.09	9.42
F	0.43	0.41	0.40	0.42	0.52	0.32	0.33	0.29	0.38	0.42	0.42	0.38	0.40	0.39
Cl	0.35	0.40	0.42	0.20	0.24	0.29	0.28	0.27	0.34	0.35	0.31	0.34	0.34	0.33
O≡F,Cl	0.26	0.26	0.26	0.22	0.27	0.2	0.2	0.18	0.24	0.26	0.25	0.24	0.24	0.24
H_2O	1.59	1.57	1.57	1.63	1.57	1.63	1.65	1.65	1.60	1.54	1.56	1.60	1.57	1.58
Total	**100.01**	**99.45**	**99.63**	**97.87**	**99.19**	**98.48**	**99.12**	**98.17**	**100.23**	**97.42**	**97.74**	**99.97**	**98.79**	**99.06**
Structural formulae on the basis of 22 oxygens														
Si	5.964	5.959	5.98	5.703	5.873	5.981	5.977	5.997	5.905	5.948	5.937	5.902	5.908	5.887
Al^{IV}	2.036	2.041	2.02	2.218	2.127	2.019	2.023	2.003	2.095	2.052	2.063	2.098	2.092	2.113
Al^{VI}	0.461	0.493	0.466	0	0.335	0.649	0.716	0.771	0.43	0.487	0.563	0.467	0.468	0.465
Ti	0.495	0.458	0.495	1.092	0.638	0.431	0.395	0.394	0.524	0.466	0.44	0.514	0.492	0.486
Fe^{2+}	3.180	3.222	3.255	2.375	2.775	3.196	3.092	3.162	3.275	3.259	3.283	3.257	3.412	3.375
Mn	0.026	0.025	0.027	0.02	0.024	0.03	0.027	0.025	0.025	0.024	0.023	0.026	0.026	0.026
Mg	2.126	2.109	2.032	1.859	2.109	1.934	2.017	1.853	2.017	2.096	2.018	2.018	1.948	1.974
Ca	0.002	0.005	0.004	1.203	0.512	0.021	0.007	0.018	0.013	0.012	0.015	0.006	0.009	0.006
Na	0.042	0.044	0.046	0.032	0.028	0.037	0.023	0.032	0.04	0.063	0.04	0.015	0.033	0.037
K	1.953	1.958	1.952	1.2	1.696	1.929	1.966	1.945	1.99	1.87	1.885	1.999	1.888	1.951
Cations	**16.285**	**16.314**	**16.277**	**15.702**	**16.117**	**16.227**	**16.243**	**16.2**	**16.314**	**16.277**	**16.267**	**16.302**	**16.276**	**16.32**
F	0.429	0.416	0.404	0.421	0.52	0.322	0.33	0.301	0.389	0.438	0.43	0.384	0.407	0.397
Cl	0.187	0.216	0.23	0.109	0.131	0.156	0.154	0.146	0.186	0.195	0.173	0.187	0.189	0.182
OH	1.692	1.684	1.683	1.735	1.674	1.761	1.758	1.776	1.712	1.684	1.698	1.714	1.702	1.71

Appendix A.5 Electron microprobe analyses of biotite from the granites of the Wentworth pluton (continued).

Sample	**5056**	**5056**	**5056**	**5056**	**6490**	**6490**	**6490**	**6490**	**6490**	**6490**	**6490**	**7658**	**7658**	**7658**
Analysis	**318**	**328**	**330**	**340**	**314**	**318**	**361**	**362**	**386**	**394**	**431**	**276**	**278**	**346**
SiO_2	35.71	36.71	36.25	36.84	37.22	38.45	38.27	37.95	38.53	37.95	37.31	36.15	34.72	35.38
TiO_2	4.02	4.12	4.08	3.66	1.86	2.51	2.66	2.77	2.41	2.23	2.32	3.72	3.61	4.06
Al_2O_3	13.12	13.11	13.40	13.86	14.19	14.68	13.60	13.49	14.26	15.08	13.78	12.79	13.10	12.63
FeO	24.91	24.92	24.25	25.09	24.98	24.76	24.83	24.86	24.73	24.96	25.87	30.09	31.13	29.84
MnO	0.15	0.20	0.18	0.15	0.51	0.52	0.40	0.45	0.51	0.50	0.59	0.26	0.34	0.35
MgO	8.03	8.14	7.93	7.91	7.42	6.28	7.41	7.24	6.69	6.82	7.48	4.19	4.33	4.22
CaO	0.01	0.03	0.06	0.01	0.04	0.03	0.02	0.04	0.05	0.06	0.08	0.02	0.04	0.02
Na_2O	0.09	0.13	0.08	0.09	0.06	0.09	0.06	0.08	0.04	0.05	0.08	0.04	0.09	0.02
K_2O	9.28	9.57	9.35	9.44	8.32	9.38	9.35	8.91	9.53	8.29	7.92	9.01	8.06	9.19
F	0.36	0.35	0.31	0.35	0.46	0.42	0.63	0.63	0.41	0.28	0.41	0.19	0.14	0.19
Cl	0.35	0.36	0.33	0.35	0.14	0.14	0.10	0.12	0.18	0.12	0.12	0.27	0.33	0.34
O≡F,Cl	0.23	0.23	0.2	0.23	0.23	0.21	0.29	0.29	0.21	0.14	0.2	0.14	0.13	0.15
H_2O	1.56	1.60	1.61	1.60	1.57	1.64	1.54	1.52	1.63	1.70	1.61	1.64	1.63	1.61
Total	**97.82**	**99.47**	**98.03**	**99.58**	**97.01**	**99.10**	**99.16**	**98.34**	**99.17**	**98.16**	**97.77**	**98.49**	**97.66**	**97.98**
Structural formulae on the basis of 22 oxygens														
Si	5.882	5.934	5.925	5.935	6.11	6.173	6.165	6.16	6.189	6.113	6.087	6.027	5.868	5.955
Al^{IV}	2.118	2.066	2.075	2.065	1.89	1.827	1.835	1.84	1.811	1.887	1.913	1.973	2.132	2.045
Al^{VI}	0.428	0.431	0.504	0.565	0.853	0.949	0.744	0.74	0.887	0.973	0.734	0.537	0.475	0.459
Ti	0.498	0.501	0.501	0.443	0.229	0.304	0.322	0.338	0.291	0.27	0.285	0.466	0.459	0.514
Fe^{2+}	3.431	3.369	3.314	3.380	3.429	3.325	3.345	3.374	3.322	3.362	3.530	4.194	4.400	4.201
Mn	0.021	0.028	0.025	0.021	0.071	0.071	0.055	0.062	0.069	0.068	0.082	0.036	0.048	0.049
Mg	1.971	1.961	1.933	1.901	1.816	1.503	1.779	1.752	1.602	1.637	1.819	1.042	1.092	1.058
Ca	0.002	0.004	0.011	0.001	0.008	0.005	0.004	0.007	0.008	0.01	0.013	0.003	0.007	0.004
Na	0.029	0.041	0.024	0.027	0.018	0.026	0.017	0.025	0.013	0.015	0.026	0.011	0.03	0.007
K	1.949	1.975	1.95	1.941	1.743	1.921	1.92	1.846	1.953	1.703	1.648	1.916	1.738	1.973
Cations	**16.329**	**16.31**	**16.262**	**16.279**	**16.167**	**16.104**	**16.186**	**16.144**	**16.145**	**16.038**	**16.137**	**16.205**	**16.249**	**16.265**
F	0.374	0.358	0.317	0.36	0.48	0.421	0.642	0.642	0.414	0.281	0.426	0.195	0.145	0.198
Cl	0.197	0.197	0.181	0.191	0.08	0.074	0.055	0.066	0.098	0.064	0.069	0.153	0.191	0.194
OH	1.714	1.723	1.751	1.725	1.72	1.752	1.652	1.646	1.744	1.827	1.753	1.826	1.832	1.804

Appendix A.5 Electron microprobe analyses of biotite from the granites of the Wentworth pluton (continued).

Sample	**7658**	**7658**	**7658**	**7658**
Analysis	**347**	**348**	**351**	**354**
SiO_2	35.22	34.99	35.96	35.72
TiO_2	4.02	3.93	3.82	3.79
Al_2O_3	12.49	12.90	12.55	11.89
FeO	30.74	30.39	29.03	30.32
MnO	0.35	0.35	0.32	0.36
MgO	4.08	4.13	4.72	4.35
CaO	0.02	0.04	0.03	0.02
Na_2O	0.06	0.08	0.00	0.05
K_2O	9.15	9.14	9.00	9.02
F	0.22	0.10	0.15	0.18
Cl	0.33	0.29	0.31	0.31
O≡F,Cl	0.16	0.11	0.13	0.15
H_2O	1.59	1.66	1.64	1.61
Total	**98.42**	**98.10**	**97.66**	**97.78**
Structural formulae on the basis of 22 oxygens				
Si	5.930	5.895	6.027	6.035
Al^{IV}	2.070	2.105	1.973	1.965
Al^{VI}	0.407	0.455	0.505	0.401
Ti	0.509	0.498	0.482	0.481
Fe^{2+}	4.329	4.282	4.069	4.284
Mn	0.050	0.050	0.045	0.051
Mg	1.025	1.037	1.179	1.097
Ca	0.003	0.007	0.005	0.004
Na	0.019	0.025	0.001	0.017
K	1.965	1.965	1.923	1.945
Cations	**16.307**	**16.319**	**16.209**	**16.280**
F	0.230	0.102	0.154	0.196
Cl	0.187	0.165	0.178	0.179
OH	1.791	1.866	1.834	1.813

APPENDIX B

Whole-rock analytical data, estimated magmatic parameters, partial melt and fractionation modelling methodologies for the late Paleozoic A-type granites of the Cobequid Highlands are presented here as supplementary data for Chapter 3. Petrographic description and whole-rock analyses of the Neoproterozoic rocks used as sources in the geochemical models are included as well.

Appendix B. 1 Whole-rock geochemistry,estimated intensive parameters and fractions of extracted melt for the biotite and calcic granites from the Cobequid Highlands.

Granite type	biotite	biotite	biotite	biotite	biotite	biotite	biotite	biotite	biotite	biotite	biotite	biotite	biotite	biotite	biotite	biotite
Pluton	CCP	CCP	CCP	PHP	PHP	PHP	PHP	PHP	PHP	PHP	PHP	WP	WP	WP	WP	WP
Sample	2616	2039	1897	4686	7397	6262	4694	7385	4672	7391	7378	**4648**	**9827b**	6970	**7630**	**7372**
Major oxides (wt. %)																
SiO_2	75.2	72.64	73.97	75.29	74.45	71.2	73.59	70.11	75.16	70.96	72.05	73.62	78.23	74.67	72.76	76.2
TiO_2	0.11	0.33	0.15	0.19	0.25	0.41	0.24	0.39	0.25	0.54	0.28	0.21	0.126	0.27	0.3	0.22
Al_2O_3	13.5	14.02	13.57	12.86	13.15	13.2	13.16	14.09	12.64	14.16	13.39	13.58	11.92	12.93	13.87	11.99
Fe_2O_3	1.53	2.73	1.4	1.95	2.07	2.79	2.45	2.98	2.42	3.1	3.26	2.22	1.51	2.18	2.39	1.82
MnO	0.03	0.02	0.01	0.02	0.01	0.07	0.02	0.04	0.02	0.03	0.03	0.05	0.015	0.04	0.05	0.04
MgO	0.52	0.39	0.25	0.75	0.05	0.38	0.88	0.4	0.83	0.33	0	0.84	0.13	0.09	0.25	0.31
CaO	0.21	0.34	0.86	0.29	0.53	1.4	0.54	1.45	0.26	1.47	0.44	0.52	0.44	0.34	0.97	0.3
Na_2O	5.19	3.68	3.73	3.58	3.85	4.91	3.85	3.78	3.74	4.61	4.57	3.95	3.4	3.69	3.8	3.63
K_2O	3.35	5.38	5.2	4.87	5.03	4.6	5.04	4.77	4.79	4.6	4.84	5.21	4.8	5.39	5.17	4.81
P_2O_5	0.02	0.11	0.08	0.03	0.04	0.08	0.05	0.07	0.04	0.09	0.02	0.04	0.02	0.03	0.06	0.03
LOI	0.2	0.46	0.69	0.3	0.8	0.85	0.7	0.3	0.4	0.3	0.2	0.4	0.13	0.55	0.53	0.46
Trace elements (ppm)																
Ba	117	471	128	180	265	582	188	723	186	702	567	223	64	257	395	129
Rb	115	179	137	213	147	185	298	175	211	110	142	254	226	240	182	178
Sr	27	52	30	45	47	48	34	103	26	124	45	37	36	36	65	26
Y	79	42	51	60	44	50	84	46	111	54	92	69.9	55.9	70	60.2	79.3
Zr	241	298	334	228	269	372	301	318	337	521	582	328	273	372	394	492
Nb	61	27	34	43	35	25	42	24	50	28	41	68.9	56.4	61	51.4	68
Pb	17	17	16	14	16	b.d.	13	17	20	b.d.	19	18	6	5	94	14
Ga	26	21	21	22	19	16	23	19	25	17	24	23	31	27	20	24
Zn	51	11	12	20	16	36	22	14	22	7	74	30	17	52	50	34
Cu	b.d.	1	b.d.	b.d.	b.d.	b.d.	b.d.	b.d.	b.d.	5	15	b.d.	10	8	b.d.	30
Ni	37	16	15	6	6	b.d.	9	6	10	7	b.d.	b.d.	5	b.d.	b.d.	b.d.
V	b.d.	6	2	2	11	22	6	22	6	20	b.d.	b.d.	7	b.d.	7	9
Cr	2	26	26	33	6	13	44	14	44	8	5	b.d.	b.d.	b.d.	b.d.	7
La	n.d.	n.d.	n.d.	63.41	n.d.	n.d.	n.d.	n.d.	109	n.d.	n.d.	67.4	33.2	n.d.	72.9	51.4
Ce	n.d.	n.d.	n.d.	115	n.d.	n.d.	n.d.	n.d.	123.7	n.d.	n.d.	157	97.2	n.d.	137	121

Granite type	biotite	biotite	biotite	biotite	biotite	biotite	biotite	biotite	biotite	biotite	biotite	biotite	biotite	biotite	biotite	biotite
Pluton	CCP	CCP	CCP	PHP	PHP	PHP	PHP	PHP	PHP	PHP	PHP	WP	WP	WP	WP	WP
Sample	2616	2039	1897	4686	7397	6262	4694	7385	4672	7391	7378	**4648**	**9827b**	6970	**7630**	**7372**
Pr	n.d.	n.d.	n.d.	n.d.	n.d.	n.d.	n.d.	n.d.	n.d.	n.d.	n.d.	15.7	9.44	n.d.	15.7	14
Nd	n.d.	n.d.	n.d.	45.71	n.d.	n.d.	n.d.	n.d.	81.94	n.d.	n.d.	53.8	33.3	n.d.	53.2	52.1
Sm	n.d.	n.d.	n.d.	8.9	n.d.	n.d.	n.d.	n.d.	17.18	n.d.	n.d.	11.7	8.41	n.d.	10.9	12.6
Eu	n.d.	n.d.	n.d.	0.59	n.d.	n.d.	n.d.	n.d.	1.49	n.d.	n.d.	0.78	0.333	n.d.	1.03	0.57
Gd	n.d.	n.d.	n.d.	n.d.	n.d.	n.d.	n.d.	n.d.	n.d.	n.d.	n.d.	11.2	7.99	n.d.	10.4	13.1
Tb	n.d.	n.d.	n.d.	1.69	n.d.	n.d.	n.d.	n.d.	3.51	n.d.	n.d.	2.08	1.74	n.d.	1.84	2.41
Dy	n.d.	n.d.	n.d.	n.d.	n.d.	n.d.	n.d.	n.d.	n.d.	n.d.	n.d.	12.8	10.9	n.d.	11.1	15
Ho	n.d.	n.d.	n.d.	n.d.	n.d.	n.d.	n.d.	n.d.	n.d.	n.d.	n.d.	2.66	2.29	n.d.	2.3	3.21
Er	n.d.	n.d.	n.d.	n.d.	n.d.	n.d.	n.d.	n.d.	n.d.	n.d.	n.d.	7.67	6.93	n.d.	6.42	9.03
Tm	n.d.	n.d.	n.d.	n.d.	n.d.	n.d.	n.d.	n.d.	n.d.	n.d.	n.d.	1.28	1.16	n.d.	1.07	1.55
Yb	n.d.	n.d.	n.d.	7.09	n.d.	n.d.	n.d.	n.d.	12.02	n.d.	n.d.	8.14	8.33	n.d.	6.91	10.1
Lu	n.d.	n.d.	n.d.	0.99	n.d.	n.d.	n.d.	n.d.	1.62	n.d.	n.d.	1.15	1.45	n.d.	0.94	1.38
Co	n.d.	n.d.	n.d.	0.84	n.d.	n.d.	n.d.	n.d.	0.63	n.d.	n.d.	b.d.	b.d.	n.d.	67	107
Cs	n.d.	n.d.	n.d.	1.65	n.d.	n.d.	n.d.	n.d.	2.42	n.d.	n.d.	6	2.4	n.d.	1.8	1.3
Hf	n.d.	n.d.	n.d.	8.91	n.d.	n.d.	n.d.	n.d.	12.7	n.d.	n.d.	8.6	8.5	n.d.	9.1	11.7
Sb	n.d.	n.d.	n.d.	n.d.	n.d.	n.d.	n.d.	n.d.	n.d.	n.d.	n.d.	b.d.	n.d.	n.d.	b.d.	b.d.
Sc	n.d.	n.d.	n.d.	2.16	n.d.	n.d.	n.d.	n.d.	2.13	n.d.	n.d.	n.d.	1	n.d.	n.d.	n.d.
Ta	n.d.	n.d.	n.d.	4.4	n.d.	n.d.	n.d.	n.d.	5.53	n.d.	n.d.	4.58	5.8	n.d.	4.32	7.18
Th	22	19	17	25	16	21	22	17	23	20	18	30.5	19.7	18	30.2	19.5
U	n.d.	n.d.	n.d.	4.78	n.d.	n.d.	n.d.	n.d.	4.32	n.d.	n.d.	5.93	4.43	n.d.	5.6	4.27
Intensive parameters																
T_{Zr} (°C)	828.3	850.6	853.0	826.5	834.5	833.8	843.0	841.9	860.8	879.2	903.2	832.0	840.3	866.5	870.5	884.0
$P_{plg\text{-}melt}$ (kbar)	3.32	9.27	12.83	11.07	13.97	12.96	12.17	7.35	13.64	11.50	14.23	13.60	17.53	12.21	13.98	15.26
H_2O_{melt}	4.68	5.23	5.70	5.43	5.93	6.65	5.78	5.66	5.18	5.70	4.87	6.44	5.31	4.62	5.77	4.24
Fraction of extracted melt (%)																
Th	25.0	28.9	32.4	22.0	34.4	26.2	25.0	32.4	23.9	27.5	30.6	16.7	27.9	30.6	21.2	30.6
Rb	51.8	33.3	43.5	28.0	40.5	32.2	20.0	34.1	28.2	54.2	42.0	21.9	26.4	24.8	29.7	31.4
Nb	17.3	39.1	31.1	24.6	30.2	42.2	25.1	44.0	21.1	37.7	25.8	21.6	18.7	17.3	24.0	15.5
Average	31.4	33.8	35.6	24.8	35.0	33.5	23.4	36.8	24.4	39.8	32.8	20.0	24.3	24.2	24.9	25.8

Appendix B. 1 Whole-rock geochemistry,estimated intensive parameters and fractions of extracted melt for the biotite and calcic granites from the Cobequid Highlands (continued).

Granite type	biotite	biotite	calcic	calcic	calcic	calcic	calcic	calcic	calcic	calcic	calcic	calcic	calcic	calcic	calcic	calcic
Pluton	WP	WP	PHP	PHP	PHP	PHP	PHP	WP	WP	WP	WP	WP	WP	WP	WP	WP
Sample	8010	**9827a**	4689	7393	6260	4670	4681	4645	**4652**	4642	4640	35-5-1	**4663**	4651	4650	4626
Major oxides (wt. %)																
SiO_2	75.76	77.23	72.45	72.72	70.3	72.42	70.77	71.21	73.52	71.78	70.88	73.35	72.49	73.48	73.03	73.56
TiO_2	0.21	0.211	0.38	0.32	0.25	0.45	0.48	0.34	0.2	0.43	0.49	0.23	0.25	0.22	0.2	0.32
Al_2O_3	11.5	11.84	13.17	13.88	13.3	13.14	13.18	14.5	13.61	13.55	13.87	13.1	13.43	13.45	13.75	12.95
Fe_2O_3	2.47	2.37	3.23	2.63	3.06	3.2	4.09	2.18	2.1	3.27	3.49	2.14	2.4	1.94	2.33	2.51
MnO	0.03	0.016	0.07	0.03	0.09	0.05	0.07	0.06	0.06	0.06	0.07	0.04	0.05	0.03	0.06	0.04
MgO	0.14	0.25	0.99	0.2	0.15	1.15	1.13	1	0.77	1.1	1.01	0.82	0.9	1.04	0.83	0.98
CaO	0.41	0.57	0.65	0.7	0.81	0.84	0.91	1.04	0.64	0.74	1.29	0.46	0.74	0.34	0.57	0.61
Na_2O	3.7	3.86	3.89	4.62	4.84	3.39	3.45	4.06	4.05	3.59	4.65	4.29	4.09	4.28	3.84	3.68
K_2O	4.64	3.7	5.11	5.02	4.82	5.02	5.49	4.95	5.21	4.94	4.39	5.11	5.04	5.03	5.14	5.31
P_2O_5	0.02	0.02	0.07	0.05	0.04	0.09	0.09	0.08	0.04	0.1	0.11	0.03	0.06	0.04	0.05	0.05
LOI	0.5	0.26	0.3	0.1	0.35	0.3	0.2	0.1	0.2	0.8	0.4	0.1	0.6	0.5	0.2	0.3
Trace elements (ppm)																
Ba	83	113	223	496	655	368	360	570	316	555	642	206	254	158	204	287
Rb	228	152	262	174	177	176	206	143	232	210	166	254	230	211	240	223
Sr	29	63	27	47	50	57	51	152	38	88	109	35	54	30	39	59
Y	98	80.3	88	59	101	89	78	38	77	50	48	85	75.1	124	84	86
Zr	566	503	361	392	585	472	831	198	274	250	295	292	403	298	286	325
Nb	75	57.7	48	30	42	46	37	20	64.6	19	23	54	63.7	56	51	45
Pb	31	4	45	13	14	b.d.	3	21	18	23	8	25	22	b.d.	8	24
Ga	29	32	24	21	25	25	25	18	23	19	19	25	21	23	25	24
Zn	74	20	80	16	116	30	55	36	34	50	51	58	50	27	32	51
Cu	14	16	2	5	6	b.d.	b.d.	b.d.	b.d.	b.d.	b.d.	6	b.d.	b.d.	b.d.	b.d.
Ni	b.d.	6	9	b.d.	b.d.	7	12	8	8	9	6	7	8	9	9	8
V	b.d.	11	9	6	b.d.	17	10	16	1	6	15	4	8	4	1	10
Cr	7	b.d.	29	13	10	24	37	39	27	40	32	32	24	34	40	24
La	38	73.2	77.76	n.d.	n.d.	80.51	91.18	n.d.	81.7	37.8	41.4	n.d.	92.7	n.d.	87.8	61.8
Ce	200	175	168.98	n.d.	n.d.	160.04	213.09	n.d.	144	67	76	n.d.	176	n.d.	136	121

Granite type	biotite	biotite	calcic	calcic	calcic	calcic	calcic	calcic	calcic	calcic	calcic	calcic	calcic	calcic	calcic	calcic
Pluton	WP	WP	PHP	PHP	PHP	PHP	PHP	WP	WP	WP	WP	WP	WP	WP	WP	WP
Sample	8010	**9827a**	4689	7393	6260	4670	4681	4645	**4652**	4642	4640	35-5-1	**4663**	4651	4650	4626
Pr	n.d.	18.7	n.d.	n.d.	n.d.	n.d.	n.d.	n.d.	18.5	n.d.	n.d.	n.d.	19.2	n.d.	n.d.	n.d.
Nd	89	64.8	68.45	n.d.	n.d.	73.93	86.73	n.d.	64.7	31	33	n.d.	62.1	n.d.	62	48
Sm	n.d.	13.9	13.67	n.d.	n.d.	15.4	17.18	n.d.	13.8	7.16	7.92	n.d.	12.3	n.d.	14.2	10.8
Eu	n.d.	0.426	1.12	n.d.	n.d.	1.49	1.72	n.d.	0.78	1.24	1.47	n.d.	0.82	n.d.	0.96	0.99
Gd	n.d.	12.2	n.d.	n.d.	n.d.	n.d.	n.d.	n.d.	13.3	n.d.	n.d.	n.d.	12.3	n.d.	n.d.	n.d.
Tb	n.d.	2.4	2.62	n.d.	n.d.	2.94	2.95	n.d.	2.35	1	1.1	n.d.	2.19	n.d.	2	2.1
Dy	n.d.	14.8	n.d.	n.d.	n.d.	n.d.	n.d.	n.d.	14.2	n.d.	n.d.	n.d.	13.5	n.d.	n.d.	n.d.
Ho	n.d.	3.12	n.d.	n.d.	n.d.	n.d.	n.d.	n.d.	2.86	n.d.	n.d.	n.d.	2.84	n.d.	n.d.	n.d.
Er	n.d.	9.39	n.d.	n.d.	n.d.	n.d.	n.d.	n.d.	8.17	n.d.	n.d.	n.d.	8.04	n.d.	n.d.	n.d.
Tm	n.d.	1.54	n.d.	n.d.	n.d.	n.d.	n.d.	n.d.	1.33	n.d.	n.d.	n.d.	1.32	n.d.	n.d.	n.d.
Yb	n.d.	10.9	9.3	n.d.	n.d.	9.95	8.86	n.d.	8.44	4.3	4.6	n.d.	8.4	n.d.	8.51	8.81
Lu	n.d.	1.77	1.32	n.d.	n.d.	1.37	1.27	n.d.	1.18	0.67	0.73	n.d.	1.12	n.d.	1.31	1.34
Co	101	b.d.	3.3	n.d.	n.d.	2.38	3.21	n.d.	b.d.	4	4.4	n.d.	1	n.d.	2.1	n.d.
Cs	n.d.	2.3	3.08	n.d.	n.d.	2.42	3.15	n.d.	5.4	4.7	2.4	n.d.	4	n.d.	5.6	n.d.
Hf	n.d.	13	12.6	n.d.	n.d.	14.47	22.42	n.d.	7	8.3	9.7	n.d.	10.2	n.d.	10.5	n.d.
Sb	n.d.	n.d.	n.d.	n.d.	n.d.	n.d.	n.d.	n.d.	b.d.	n.d.	n.d.	n.d.	b.d.	n.d.	n.d.	n.d.
Sc	11	2	3.68	n.d.	n.d.	4.29	4.15	n.d.	n.d.	6.05	6.95	n.d.	n.d.	n.d.	3.06	n.d.
Ta	n.d.	6.58	5.05	n.d.	n.d.	4.07	3.87	n.d.	4.85	1.8	1.9	n.d.	4.31	n.d.	4.5	n.d.
Th	23	25.5	21	20	20	18	17	21	26.8	29	14	20	31	19	21	24
U	7	5.24	4.22	n.d.	n.d.	2.95	3.6	n.d.	6.25	4	4.6	n.d.	6.23	n.d.	5.4	4.4
Intensive parameters																
T_{Zr} (°C)	905.7	902.6	855.7	859.1	889.4	889.0	940.6	801.3	828.8	827.9	824.3	833.0	838.4	840.6	840.8	847.1
$P_{plg\text{-}melt}$ (kbar)	16.79	20.61	8.32	12.15	14.70	11.12	13.05	8.19	10.22	7.23	6.99	12.40	8.77	11.46	8.98	10.09
H_2O_{melt}	3.93	4.90	4.97	5.66	5.52	4.78	4.13	6.81	5.85	5.66	6.14	6.01	5.47	5.77	5.42	5.20
Fraction of extracted melt (%)																
Th	23.9	21.6	26.2	27.5	27.5	30.6	32.4	26.2	20.4	19.0	39.3	27.5	21.2	28.9	26.2	22.9
Rb	26.1	39.2	22.7	34.3	33.7	33.9	28.9	41.7	23.1	28.4	35.9	23.5	23.7	28.2	24.8	26.7
Nb	14.1	18.3	22.0	35.2	25.1	23.0	28.5	52.8	20.7	55.6	45.9	19.6	22.5	18.9	20.7	23.5
Average	21.4	26.4	23.6	32.3	28.8	29.1	29.9	40.2	21.4	34.3	40.4	23.5	22.4	25.4	23.9	24.4

Appendix B. 1 Whole-rock geochemistry,estimated intensive parameters and fractions of extracted melt for the biotite and calcic granites from the Cobequid Highlands (continued).

Granite type	calcic	calcic	calcic	calcic	calcic	calcic	calcic	calcic	calcic	calcic	calcic
Pluton	WP	WP	WP	WP	WP	WP	WP	WP	WP	WP	WP
Sample	4657	36-7-1	7658	**7373**	**4641**	6808	**9819**	**7374**	**8003**	4614	4615
Major oxides (wt. %)											
SiO_2	75.81	73.83	72.62	75.72	70.04	73.58	73.09	75.44	70.07	74.87	74.49
TiO_2	0.21	0.23	0.32	0.25	0.45	0.22	0.589	0.27	0.49	0.24	0.31
Al_2O_3	12.32	13.13	13.6	12.09	14.25	13.6	13.29	11.86	14.55	12.55	12.55
Fe_2O_3	2.3	2.04	2.72	2.35	3.48	2.57	2.41	3.08	3.18	2.25	1.46
MnO	0.04	0.03	0.08	0.05	0.07	0.02	0.085	0.03	0.05	0.04	0.04
MgO	0.7	1.06	0.24	0.28	1.05	0.15	0.71	0.25	0.38	0.82	1.01
CaO	0.31	0.43	0.9	0.71	0.92	0.45	1.98	0.73	0.83	0.77	1.37
Na_2O	3.57	4.1	3.72	3.78	2.07	4.07	4.2	2.89	4.5	3.66	3.21
K_2O	5.92	4.79	5.24	4.69	5.36	4.87	4.17	5.49	5.4	5.32	5.77
P_2O_5	0.02	0.05	0.07	0.03	0.1	0.02	0.13	0.03	0.06	0.03	0.05
LOI	0	0.3	0.57	0.29	0.9	0.74	0.34	0.32	0.3	0.2	0.3
Trace elements (ppm)											
Ba	125	179	365	126	684	209	561	310	419	147	187
Rb	169	220	253	171	185	221	108	189	219	242	214
Sr	13	33	65	36	90	29	124	53	64	47	84
Y	85	116	82	78.5	46.3	66	52.2	100	69	93	98
Zr	370	308	383	482	396	414	596	688	707	710	1009
Nb	45	55	47	64	24.3	44	28.8	68.7	43	57	47
Pb	8	15	29	10	27	43	6	19	27	b.d.	18
Ga	25	22	24	24	18	22	18	22	24	25	21
Zn	70	27	81	60	60	63	27	40	59	49	39
Cu	b.d.	2	6	b.d.	b.d.	31	17	15	27	b.d.	b.d.
Ni	6	7	b.d.	b.d.	b.d.	b.d.	10	b.d.	3	10	7
V	b.d.	4	11	11	11	b.d.	24	12	17	1	14
Cr	34	31	b.d.	10	34	b.d.	b.d.	8	4	33	32
La	n.d.	n.d.	n.d.	60.9	40.7	n.d.	67.5	43	43	69.2	n.d.
Ce	n.d.	n.d.	n.d.	136	87	n.d.	142	92.1	138	146	n.d.
Pr	n.d.	n.d.	n.d.	15.8	9.94	n.d.	15.8	14.7	n.d.	n.d.	n.d.
Nd	n.d.	n.d.	n.d.	58.2	36.8	n.d.	57.4	57.9	62	63	n.d.
Sm	n.d.	n.d.	n.d.	13	7.82	n.d.	11.7	15.7	n.d.	13	n.d.
Eu	n.d.	n.d.	n.d.	0.65	1.23	n.d.	1.39	0.89	n.d.	0.65	n.d.
Gd	n.d.	n.d.	n.d.	13.3	7.36	n.d.	10.4	17.5	n.d.	n.d.	n.d.
Tb	n.d.	n.d.	n.d.	2.37	1.31	n.d.	1.81	3.21	n.d.	2.4	n.d.
Dy	n.d.	n.d.	n.d.	14.4	7.75	n.d.	10.3	19.6	n.d.	n.d.	n.d.
Ho	n.d.	n.d.	n.d.	3.02	1.62	n.d.	2.03	4.1	n.d.	n.d.	n.d.
Er	n.d.	n.d.	n.d.	8.61	4.7	n.d.	5.54	11.2	n.d.	n.d.	n.d.
Tm	n.d.	n.d.	n.d.	1.44	0.75	n.d.	0.811	1.81	n.d.	n.d.	n.d.
Yb	n.d.	n.d.	n.d.	9.21	5.05	n.d.	5.1	11.3	n.d.	9.93	n.d.
Lu	n.d.	n.d.	n.d.	1.29	0.71	n.d.	0.824	1.53	n.d.	1.54	n.d.
Co	n.d.	n.d.	n.d.	83	2	n.d.	n.d.	81	72	n.d.	n.d.
Cs	n.d.	n.d.	n.d.	1.8	5.2	n.d.	0.7	3.4	n.d.	n.d.	n.d.
Hf	n.d.	n.d.	n.d.	11	8.8	n.d.	13.7	15	n.d.	n.d.	n.d.
Sb	n.d.	n.d.	n.d.	b.d.	b.d.	n.d.	n.d.	b.d.	n.d.	n.d.	n.d.
Sc	n.d.	n.d.	n.d.	n.d.	n.d.	n.d.	7	n.d.	12	n.d.	n.d.
Ta	n.d.	n.d.	n.d.	5.45	2.08	n.d.	1.8	6.18	n.d.	n.d.	n.d.

Granite type	calcic	calcic	calcic	calcic	calcic	calcic	calcic	calcic	calcic	calcic	calcic
Pluton	WP	WP	WP	WP	WP	WP	WP	WP	WP	WP	WP
Sample	4657	36-7-1	7658	**7373**	**4641**	6808	**9819**	**7374**	**8003**	4614	4615
Th	15	24	29	17.3	19.2	25	12.1	20.1	22	25	25
U	n.d.	n.d.	n.d.	4.43	4.64	n.d.	1.71	5.09	7	6.1	n.d.
Intensive parameters											
T_{Zr} (°C)	856.8	845.6	863.8	871.5	874.2	878.9	889.7	918.7	918.7	923.2	953.5
$P_{plg\text{-}melt}$ (kbar)	12.93	11.70	12.83	16.58	5.40	14.50	11.19	15.05	12.14	13.36	16.52
H_2O_{melt}	4.79	5.62	5.61	4.06	3.97	5.36	5.19	3.43	4.75	3.72	3.68
Fraction of extracted melt (%)											
Th	36.7	22.9	19.0	36.7	32.4	22.0	45.5	25.0	25.0	22.0	22.0
Rb	35.3	27.1	23.6	33.1	28.1	27.0	55.2	28.4	27.2	24.6	27.9
Nb	23.5	19.2	22.5	18.5	52.8	24.0	36.7	18.2	24.6	18.5	22.5
Average	31.8	23.1	21.7	29.4	37.8	24.3	45.8	23.9	25.6	21.7	24.1

Note: The fractions of extracted melt were estimated through the equation of batch partial melting and using as a source composition the average trace element concentration of Neoproterozoic intermediate rocks from both Jeffers and Bass River blocks. Samples in bold indicate new major and trace element analyses, underlined bold sample numbers indicate new trace element analyses. Abbreviations: b.d.= below detection limit, n.d.= not determined. When not specified, analytical data are from Pe-Piper (1991, 1995, 1998), and Pe-Piper and Piper (1998a).

APPENDIX B.2 METHODOLOGY FOR GEOCHEMICAL MODELS

Fractionation of mafic sources

The fractionation models used in this work include a two-step process. First the changes in major elements through fractionation were modeled by the use of PELE software for Windows (Boudreau, 1999). Whole-rock analyses of selected mafic sources were used as input. PELE uses a list of mineral phases that can crystallize during the fractionation sequence. From the given list certain minerals were excluded such as leucite, nepheline, mellilite, garnet, kalsilite, whitlockite, corundum, perovskite, muscovite, troilite, pyrrhotite, pyrite, sulphide liquid, graphite, calcite, dolomite, anhydrite and immiscible liquid. Although pyrite is reported as an accessory phase in the Wentworth gabbros, the exclusion of this mineral is not considered to significantly compromise the model, since there no S was determined in whole-rock for these rocks, and therefore there was no input for that element. Other parameters involve temperature, pressure, oxygen fugacity, entropy, enthalpy and volume. In the absence of constraints for entropy, enthalpy and volume, an isobaric fractionation was assumed and was tested for a range of pressures from 2 to 0.6 GPa. An initial 0.5 wt.% H_2O was assumed although not measured. An anhydrous composition for the Fountain Lake basalts is assumed from their mineralogy which includes olivine, plagioclase, pyroxene and Fe-oxides. Fractionation models were performed under different oxygen fugacities ranging from NNO to +3 QFM. For different oxygen fugacities the program will adjust the amounts of FeO and Fe_2O_3 in the whole-rock input. The range of temperature for all runs was from the liquidus, as determined by the program for a given pressure and oxygen

fugacity, to 800 °C, which is an average zircon-saturation temperature for the studied granites.

After the parameters were set, PELE performed a fractionation simulation until the lowest temperature was achieved. During the simulation, the program predicted mineralogical assemblages that would be in equilibrium with the remaining melt for a given temperature. For each equilibrium stage (or "step" as reported by the program) the following are predicted: mass of liquid, mass of solids, fractionating mineral phases (chemistry and mass for each phase), whole-rock chemistry of the remaining melt, viscosity, volume, enthalpy, entropy and oxygen fugacity. Any invalid parameters or unrealistic set of parameters would crash the program.

The most realistic output for the fractionation models was considered to be from the run at 0.6 GPa, under an oxygen fugacity of -2 QFM. The fractionated minerals predicted were olivine, plagioclase, pyroxene, apatite, and Fe-Ti oxides. The minerals predicted to remain in the melt at the latest stages were alkali feldspar, quartz, titanite, ilmenite, and aenigmatite. Since all the predicted fractionating minerals reflect the mineralogy of the mafic rocks, the output was considered reliable. The predicted viscosity was comparable with the viscosity estimates for the sodic granites, using the method of Giordano et al. (2008). The felsic melt under these conditions was produced in ten steps.

As a second procedure the trace elements were modeled using Rayleigh fractionation (Rayleigh, 1896) as applied by Neuman et al. (1954) which is described by the equation

$$C_L = C_O F^{(D-1)} \qquad (1)$$

Where C_L : concentration of element in remaining liquid, C_O : concentration of element in the parent melt, F: fraction of remaining melt defined as M_L/M_O (M_L: mass of original melt, M_O: mass of remaining melt), D: the bulk partition coefficient for element calculated as $\Sigma X_A D_i$ (X_A: weight fraction of mineral A in the rock, D_i: partition coefficient of element i in mineral A).

Trace elements were therefore modeled for each step produced by PELE, where D was estimated by the modal amounts of the predicted fractionating minerals and the chemistry of the remaining melt, and F was calculated by the estimated masses of the original and remaining melts. Since the produced melts varied from mafic to felsic, the partition coefficients used, varied accordingly. For produced melts with SiO_2 up to 52 wt.% the partition coefficients used were for basaltic melts. For melts from 52 to 54 wt.% the partition coefficients used were those for basaltic andesite. For melts with 54 to 62 wt.% SiO_2 partition coefficients for andesite were used. For melts with SiO_2 ranging from 62 to 69 wt.% partition coefficients for dacites were used. Melts more silicic than 69 wt.% were considered rhyolitic and the appropriate partition coefficients were used (Table DR2).

Partial melting models

Batch partial melting was modeled by the equation

$$C_L/C_O = 1/(D(1-F)+F) \qquad (2)$$

Where C_L: the concentration of element in extracted melt, C_O: concentration of element at the source, D: bulk partition coefficient as defined above, F: fraction of extracted melt. For highly incompatible elements such as Rb, Nb, and Th, the above equation may be simplified as:

$$C_L/C_O=1/F \quad (3)$$

which if rearranged will be:

$$F= C_O/C_L \quad (4)$$

Using the above simplified equation for selected highly incompatible elements, and their average concentrations in Neoproterozoic intermediate rocks, the degrees of partial melting were estimated. The rest of the trace elements were modeled with the original equation for the range of F values determined by the highly incompatible elements.

Appendix B. 3 Partition coefficients for selected trace elements used in geochemical models.

	Basalt				Basaltic andesite			
Mineral	pyroxene	plagioclase	olivine	magnetite	pyroxene	plagioclase	olivine	magnetite
Ba	0.03 [1]	0.151 [15]	0.005 [20]	0.028[28]	0.03 [1]	0.16 [32]	0.005 [20]	0.028 [28]
Rb	0.011 [2]	0.024 [16]	0.0133 [15]	0.11 [29]	0.00941 [33]	0.056 [38]	0.017 [38]	0.11 [29]
Sr	0.096 [3]	2.845 [17]	0.00025[21]		0.12 [35]	3.06 [32]	0.003 [20]	
Y	0.421 [4]	0.031 [17]	0.0125 [21]	0.0039 [26]	1 [35]	0.032 [32]		0.0039 [26]
Zr	0.128 [4]	0.0127 [17]	0.011 [22]	0.02 [30]	0.4 [35]	0.0009 [38]	0.12 [40]	0.02 [30]
Nb	0.004 [4]	0.0925 [17]	0.01 [2]	0.01 [30]	0.004 [4]	0.045 [38]	0.0065 [38]	0.01 [30]
Pb	0.0102 [5]	0.901 [17]	0.0001 [2]		0.0102 [5]	0.901 [17]		
Ga	0.74 [6]	0.71 [18]	0.04 [23]	2 [29]	0.74 [6]	0.71 [18]		2 [29]
Zn	0.5 [7]	0.11 [7]	0.86 [7]	2.6 [29]	0.5 [7]	0.11 [7]	1.2 [34]	2.6 [29]
Cu	0.36 [6]	0.38 [18]	0.5 [24]	0.42 [29]	0.12 [18]	0.38 [18]	0.19 [41]	0.42 [29]
Ni	2.6 [8]	1.16 [17]	12.8 [25]	29 [61]	4 [34]	0.06 [31]	12.8 [25]	9.6 [31]
Cr	3.8 [6]	0.191 [17]	1.85 [21]	40 [27]	30 [35]	0.075 [38]	1.08 [20]	40 [27]
La	0.05 [4]	0.258 [17]	0.000012 [21]	0.015 [29]	0.11 [35]	0.227 [32]		0.015 [29]
Ce	0.1 [3]	0.233 [17]	0.0001 [26]	0.016 [29]	0.13 [35]	0.085 [32]	0.012 [20]	0.016 [29]
Pr	0.112 [1]	0.282 [17]	0.000084 [21]		0.112 [1]	0.035 [38]	0.009 [38]	
Nd	0.382 [9]	0.276 [17]	0.0003 [26]	0.026 [29]	0.4 [35]	0.114 [32]		0.026 [29]
Sm	0.281 [4]	0.106 [17]	0.00063 [21]	0.024 [29]	0.6 [35]	0.083 [32]	0.028 [38]	0.024 [29]
Eu	0.32 [10]	0.061 [17]	0.001 [26]	0.025 [29]	0.72 [31]	0.078 [32]	0.023 [38]	0.025 [29]
Tb	0.28 [1]	0.102 [19]	0.0015 [26]	0.019 [29]	0.57 [34]	0.061 [38]	0.035 [38]	0.019 [29]
Dy	0.42 [4]	0.0318 [16]	0.002 [26]		0.8 [35]	0.052 [32]	0.034 [38]	
Er	0.36 [4]	0.0194 [17]	0.0025 [26]		0.8 [35]	0.056 [32]	0.045 [38]	
Yb	0.4 [12]	0.141 [19]	0.01 [26]	0.018 [29]	1.1 [35]	0.041 [28]	0.071 [38]	0.018 [29]
Lu	0.439 [4]	0.0093 [17]	0.051 [26]		0.55 [34]	0.043 [32]	0.11 [38]	
Co	1.7 [13]	1.03 [17]	3.56[21]	3.4 [29]	1.2 [34]	0.07 [39]	6.6 [34]	3.4 [29]
Th	0.014 [5]	0.382 [19]	0.00001 [27]	0.05 [31]	0.03 [34]	0.19 [38]	0.039 [38]	0.05 [31]
U	0.0146 [14]	0.073 [16]	0.00001 [27]	0.11 [29]	0.04 [34]	0.34 [38]		0.11 [29]

Appendix B. 3 Partition coefficients for selected trace elements used in geochemical models (continued).

	Andesite				Dacite			
Mineral	pyroxene	plagioclase	olivine	magnetite	pyroxene	plagioclase	olivine	magnetite
Ba	0.1 [39]	0.27 [39]	0.02 [40]	0.028 [28]	0.131 [15]	1.05 [42]	0.023 [51]	0.07 [54]
Rb	0.03 [39]	0.039 [15]	0.01 [40]	0.11 [29]	0.0366 [15]	0.041 [48]	0.01 [40]	0.01 [29]
Sr	0.5 [39]	3.4 [39]	0.018 [38]		0.39 [45]	2.9 [18]	0.31 [42]	0.077 [42]
Y	2.4 [42]	0.066 [42]		0.0039 [26]	7.6 [42]	0.51 [42]	0.12 [42]	0.95 [42]
Zr	0.33 [42]	0.15 [42]	0.12 [40]	0.02 [30]	0.23 [45]	0.55 [42]	0.01 [40]	3.98 [29]
Nb	2.1 [42]	1.3 [42]	0.11 [42]	0.01 [30]	0.03 [46]	2.5 [42]	0.049 [42]	
Pb	0.87 [42]	0.18 [38]	0.43 [42]		0.1 [46]	0.29 [49]	0.43 [42]	0.71 [42]
Ga	0.47 [42]	1.5 [42]	0.25 [42]	2 [29]	0.32 [42]	1.1 [18]	0.15 [42]	2.8 [42]
Zn	2 [39]	0.25 [31]	2.8 [42]	2.6 [29]	7.8 [42]	0.26 [50]		26.6 [42]
Cu	0.66 [42]	0.37 [42]	2.2 [42]	0.42 [29]	0.44 [18]	0.32 [18]	0.05 [34]	3.8 [42]
Ni	4.6 [31]	0.61 [31]	12.8 [25]	9.6 [31]	6 [40]	1.5 [42]	2.2 [52]	5.2 4[2]
Cr	30 [35]	0.25 [31]	5.5 [40]	40 [27]	2.3 [18]	0.67 [50]		5.23 [62]
La	0.28 [35]	0.18 [39]	0.01 [40]	0.015 [29]	0.67 [45]	0.49 [50]	0.4 [29]	0.29 [54]
Ce	0.47 [35]	0.12 [39]	0.01 [31]	0.016 [29]	0.96 [46]	0.241 [43]	0.1 [53]	0.35 [54]
Pr	0.112 [1]	0.13 [38]				0.13 [38]		
Nd	0.7 [31]	0.09 [39]	0.011 [38]	0.026 [29]	2.06 [45]	0.172 [43]		0.93 [39]
Sm	1.3 [31]	0.06 [39]	0.01 [31]	0.024 [29]	3.06 [45]	0.125 [43]	0.1 [53]	0.55 [54]
Eu	0.72 [31]	0.75 [39]	0.03 [31]	0.025 [29]	2.65 [45]	2.11 [43]	0.21 [29]	0.53 [54]
Tb	2.7 [39]	0.15 [39]	0.11 [31]	0.019 [29]	1.86 [45]	0.21 [50]	0.1 [53]	0.5 [54]
Dy	1.2 [31]	0.09 [31]	0.1 [31]		3.77 [47]	0.086 [43]	0.014 [38]	1.6 [56]
Er	1.33 [43]	0.041 [43]	0.045 [38]		3.21 [45]	0.084 [43]		
Yb	0.9 [12]	0.033 [43]	0.03 [31]	0.018 [29]	2.69 [45]	0.022 [43]	0.35 [53]	0.26 [54]
Lu	1.4 [31]	0.1 [39]	0.08 [31]			0.062 [43]	0.44 [53]	0.6 [54]
Co	5.5 [39]	0.07 [39]	1.96 [41]	3.4 [29]	3.2 [18]	0.51 [50]		72 [54]
Th	0.1 [39]	0.01 [39]	0.02 [31]	0.05 [31]	0.01 [46]	0.088 [50]	0.12 [29]	0.06 [54]
U	0.04 [34]	0.01 [34]	0.04 [38]	0.11 [29]	0.09 [46]		0.14 [29]	0.12 [54]

Appendix B. 3 Partition coefficients for selected trace elements used in geochemical models (continued).

			Rhyolite		
Mineral	pyroxene	plagioclase	K-feldspar	magnetite	hbl
Ba	0.3 [57]	4 [60]	4 [63]	0.1 [39]	0.28 [42]
Rb	0.013 [42]	0.011 [42]	0.74 [57]		0.37 [42]
Sr	6.4 [58]	4.04 [42]	2.1 [42]	0.01 [39]	4.7 [42]
Y	0.7 [42]	0.55 [42]	0.086 [42]	0.95 [42]	5.2 [42]
Zr	0.33 [58]	0.36 [56]	0.21 [42]	0.24 [42]	0.76 [42]
Nb	0.2 [42]	0.26 [42]	0.16 [42]		0.98 [42]
Pb	0.85 [42]	0.35 [42]	0.1 [42]	0.71 [42]	0.19 [42]
Ga	0.32 [42]	0.59 [42]	0.7 [42]	2.8 [42]	0.77 [42]
Zn	2 [39]	0.48 [39]	0.23 [42]	2 [65]	1.4 [42]
Cu	0.2 [42]	0.41 [42]	0.6 [42]	3.8 [42]	0.77 [42]
Ni	6 [40]	1.5 [42]	0.9 [42]	5.2 4[2]	1.5 [42]
Cr	2.6 [58]	0.01 [39]	0.15 [64]	5.23 [62]	3 [64]
La	0.3 [59]	0.3 [39]	0.15 [63]	0.8 [56]	0.36 [39]
Ce	0.646 [43]	0.22 [39]	0.06 [56]	1.02 [56]	0.68 [39]
Pr		0.13 [38]			
Nd	1.28 [43]	0.19 [39]	0.025 [43]	0.98 [39]	1.6 [39]
Sm	1.81 [43]	0.12 [39]	0.04 [56]	0.77 [65]	2.3 [39]
Eu	2.01 [43]	2 [39]	1.13 [43]	0.91 [39]	3.2 [39]
Tb	3.8 [39]	0.14 [39]	0.01 [56]	1.3 [39]	2.4 [39]
Dy	3.8 [58]	0.18 [56]	0.04 [56]	1.6 [56]	
Er	1.14 [43]		0.162 [43]		0.86 [64]
Yb	1.14 [43]	0.1 [39]	0.024 [57]	1 [56]	1.8 [39]
Lu	1.28 [43]	0.1 [39]	0.003 [63]	0.3 [39]	1.8 [39]
Co	17 [39]	0.15 [39]	0.39 [57]	80 [39]	7 [39]
Th	0.1 [39]	0.08 [56]	0.03 [56]	0.09 [56]	0.16 [39]
U	0.12 [56]	0.05 [56]	0.04 [56]	0.21 [56]	

Note: 1: Skulski et al. (1994), 2: McKenzie and O'Nions (1991), 3: Jenner et al. (1994), 4: Johnson (1994), 5: Hauri et al. (1994), 6: Hart and Dunn (1993), 7: Bougault and Hekinian (1974), 8: Mysen (1978), 9: Nagasawa et al. (1969), 10: Johnson (1998), 11: Frey (1969), 12: Nicholls and Harris (1980), 13: Duke (1976), 14: Latourette and Burnett (1982), 15: Philpotts and Schnetzler (1970), 16: Bindeman and Davis (2000), 17: Bindeman et al. (1998), 18: Ewart et al. (1973), 19: Aignertorres et al. (2007), 20: McKay and Weill (1977), 21: Beattie (1994), 22: Fujimaki et al. (1984), 23: Kloeck and Palme (1988), 24: Pedersen (1979), 25: Nabelek (1980), 26: Nielsen et al. (1992), 27: Beattie (1993), 28: Okamoto (1979), 29: Lemarchand et al. (1987), 30: Nielsen (1992), 31: Luhr and Carmichael (1980), 32: Drake and Weill (1975), 33: Hart and Brooks (1974), 34: Dostal et al. (1983), 35: Ronov and Yaroshevskiy (1976), 36: Reid (1983), 37: Gallahan and Nielsen (1992), 38: Dunn and Sen (1994), 39: Bacon and Druitt (1988), 40: Villemant (1988), 41: Gaetani and Grove (1997), 42: Ewart and Griffin (1994), 43: Schnetzler and Philpotts (1970), 44: Nielsen (1988), 45: Huang et al. (2006), 46: Marks et al. (2004), 47: Nasagawa (1973), 48: Nasagawa and Schnetzler (1971), 49: Leeman (1979), 50: Dudas et al. (1971), 51: Larsen (1979), 52: Mysen (1976), 53: Mahood and Stimac (1990), 54: Luhr et al. (1984), 55: Latourrette et al. (1991), 56: Nash and Crecraft (1985), 57: Mahood and Hildreth (1983), 58: Sisson (1991), 59: Michael (1988), 60: Long (1978), 61: Esperança et al. (1997), 62: Streck and Grunder (1997), 63: Stix and Gorton (1990), 64: Bea et al. (1994), 64: Sisson (1994), 65: Mysen and Virgo (1980).

Appendix B. 4 Mineralogical description of Neoproterozoic intermediate rocks from the Cobequid Highlands.

Block	Unit	Sample	Major minerals	SiO_2 (wt.%)	Rock-type*	Reference
Jeffers Block	Mount Thom	6980	Kfs, plg, qz, bt, hbl		Granodiorite	Pe-Piper et al. (1998)
	Gunshot Brook	7403	Kfs, plg, qz, ep, bt	67.82	Granodiorite	Pe-Piper et al. (1998)
	Gunshot Brook	7405	Kfs, plg, qz, bt, hbl	68.65	Granodiorite	Pe-Piper et al. (1998)
	Gunshot Brook	7408	Kfs, plg, qz, bt, hbl	68.7	Granodiorite	Pe-Piper et al. (1998)
	Gunshot Brook	7435	Kfs, plg, qz, bt	68.72	Granodiorite	Pe-Piper et al. (1998)
	Gunshot Brook	7440	Plg, qz, bt, ep	67.57	Tonalite	Pe-Piper et al. (1998)
	River John	7412	Kfs, plg, qz, ep, bt	63.91	Granodiorite	Pe-Piper et al. (1998)
	River John	7436	Plg, qz, bt, ep	64.69	Tonalite	Pe-Piper et al. (1998)
	River John	7437	Plg, qz, bt, ep, hbl	65.36	Tonalite	Pe-Piper et al. (1998)
	River John	7442	Plg, Kfs, qz, bt, ep	63.6	Granodiorite	Pe-Piper et al. (1998)
Bass River Block	Frog Lake	3134	Plg, qz, bt,	64.1	Tonalite	Pe-Piper et al. (2010)
	Debert River	7347	Kfs, plg, qz	69.88	Granodiorite	Pe-Piper et al. (1998)
	Debert River	6621	Kfs, plg, qz, hbl, bt	61.54	Granodiorite	Pe-Piper et al. (1998)
	Debert River	6633	plg, bt, qz, ep	61.44	Tonalite	Pe-Piper et al. (1998)
	Debert River	6636	qz, bt, plg	69.01	Tonalite	Pe-Piper et al. (1998)

* Names for rock types were assigned in the present work, based on the relative abudances of feldspars.

Appendix B. 5 Whole-rock compositions of intermediate and mafic rocks used for geochemical modelling.

	Jeffers Block													Bass River Block				
Sample	7403	7405	7408	7412	7435	7442	7440	7436	7437	1347	1950	4601	6061	6621	7347	3134	6633	6636
Rocktype	Gd	Gd	Gd	Gd	Gd	Gd	Ton	Ton	Ton	Gb	Gb	Bas	Bas	Gd	Gd	Ton	Ton	Ton
Major oxides (wt.%)																		
SiO_2	67.82	68.65	68.7	63.91	68.72	63.6	67.57	64.69	65.36	43.32	48.26	47.96	46.1	61.54	69.88	64.09	61.44	69.01
TiO_2	0.26	0.24	0.25	0.44	0.26	0.43	0.32	0.43	0.41	2.35	1.18	1.81	2.98	0.72	0.36	0.97	1.02	0.82
Al_2O_3	17.46	16.92	16.98	18.02	16.72	19.15	17.59	17.54	17.27	15.59	19.20	17.04	14.9	18.8	16.27	15.6	18.24	14.04
Fe_2O_3	1.81	1.83	1.88	3.33	2.39	2.93	2.27	4.16	4.01	12.03	9.16	11.85	15	4.31	2.83	5.38	7.8	5.13
MnO	0.07	0.04	0.06	0.08	0.08	0.08	0.07	0.11	0.12	0.20	0.20	0.26	0.21	0.14	0.1	0.09	0.1	0.06
MgO	0.65	0.57	0.63	1.32	0.75	1.07	0.8	1.44	1.44	8.63	6.19	5.81	5.24	1.32	0.95	2.77	2.72	1.5
CaO	2.12	2.53	3.12	3.97	3.36	4.53	3.62	5.16	5	9.78	8.25	5.42	9.8	3.66	1.87	5.95	1.03	1.18
Na_2O	5.15	4.68	5.05	4.77	4.26	5.27	4.9	4.41	4.18	2.49	2.57	4.75	2.65	5.02	4.21	3.04	2.11	1.97
K_2O	2.63	2.42	1.96	1.54	2.56	1.63	1.93	1.65	1.52	1.26	2.17	0.41	0.5	3.39	3.42	0.58	3.68	4.19
P_2O_5	0.09	0.09	0.09	0.17	0.12	0.15	0.11	0.17	0.17	0.43	0.19	0.23	0.43	0.25	0.14	0.25	0.08	0.1
LOI	1.2	1.3	0.8	1.8	0.75	1.22	1.03	0.56	0.72	2.85	2.23	3.8	2.3	0.6	0.89	0.8	2.6	1.5
Total	99.26	99.27	99.52	99.35	99.97	100.1	100.2	100.3	100.2	98.9	99.6	99.34	100	99.75	100.9	99.52	100.8	99.5
Trace elements (ppm)																		
Ba	1403	1398	1189	611	1598	1023	972	576	516	440	491	277	210	2712	1052	183	904	718
Rb	55	48	45	37	55	40	46	48	47	32	85	14	13	162	103	15	138	158
Sr	755	812	864	821	696	1041	865	588	590	656	363	316	289	756	300	375	143	162
Y	7	6	7	8	5	8	16	13	11	22	20	19	45	36	24	21	46	42
Zr	104	99	112	114	103	168	137	130	133	173	78	122	214	437	137	383	220	275
Nb	7	6	7	8	5	6	10	7	8	33	9	0	17	20	19	11	18	16
Th	n.d.	n.d.	n.d.	n.d.	n.d.	n.d.	n.d.	n.d.	n.d.	2.10	2.70	0.00	2.67	13	14	9	14	13
Pb	25	21	15	16	18	17	18	14	18	5	40	0	0	27	16	13	19	118
Ga	18	16	18	20	19	23	21	20	20	22	18	17	23	19	21	18	24	17
Zn	59	47	48	81	59	95	69	65	75	115	243	120	136	84	50	63	131	411
Cu	n.d.	n.d.	n.d.	n.d.	12	13	12	16	17	69	38	45	30	10	12	24	22	24
Ni	6	5	n.d.	n.d.	n.d.	n.d.	6	6	n.d.	228	23	127	69	8	19	10	39	32
V	27	24	28	61	35	46	28	69	62	236	266	273	365	47	49	120	172	105
Cr	5	13	10	9	n.d.	10	9	10	14	321	32	232	93	6	4	10	111	85
Co	n.d.	n.d.	n.d.	n.d.	n.d.	n.d.	n.d.	n.d.	n.d.	59.00	41.00	0.00	46.15	n.d.	5	n.d.	n.d.	n.d.
La	n.d.	n.d.	n.d.	n.d.	n.d.	n.d.	n.d.	n.d.	n.d.	27.20	11.50	0.00	18.73	n.d.	36	45.6	n.d.	n.d.
Ce	n.d.	n.d.	n.d.	n.d.	n.d.	n.d.	n.d.	n.d.	n.d.	47.00	27.00	0.00	40.66	n.d.	52	77	n.d.	n.d.
Pr	n.d.	n.d.	n.d.	n.d.	n.d.	n.d.	n.d.	n.d.	n.d.	0.00	0.00	0.00	0.00	n.d.	n.d.	n.d.	n.d.	n.d.

	Jeffers Block													Bass River Block				
Sample	7403	7405	7408	7412	7435	7442	7440	7436	7437	1347	1950	4601	6061	6621	7347	3134	6633	6636
Rocktype	Gd	Gd	Gd	Gd	Gd	Gd	Ton	Ton	Ton	Gb	Gb	Bas	Bas	Gd	Gd	Ton	Ton	Ton
Nd	n.d.	n.d.	n.d.	n.d.	n.d.	n.d.	n.d.	n.d.	n.d.	21.00	15.00	0.00	24.91	n.d.	22	20	n.d.	n.d.
Sm	n.d.	n.d.	n.d.	n.d.	n.d.	n.d.	n.d.	n.d.	n.d.	5.31	2.93	0.00	6.76	n.d.	n.d.	5.5	n.d.	n.d.
Eu	n.d.	n.d.	n.d.	n.d.	n.d.	n.d.	n.d.	n.d.	n.d.	1.85	0.97	0.00	2.56	n.d.	n.d.	0.62	n.d.	n.d.
Gd	n.d.	n.d.	n.d.	n.d.	n.d.	n.d.	n.d.	n.d.	n.d.	0.00	0.00	0.00	0.00	n.d.	n.d.	n.d.	n.d.	n.d.
Tb	n.d.	n.d.	n.d.	n.d.	n.d.	n.d.	n.d.	n.d.	n.d.	0.50	0.50	0.00	1.23	n.d.	n.d.	0.9	n.d.	n.d.
Dy	n.d.	n.d.	n.d.	n.d.	n.d.	n.d.	n.d.	n.d.	n.d.	0.00	0.00	0.00	0.00	n.d.	n.d.	n.d.	n.d.	n.d.
Ho	n.d.	n.d.	n.d.	n.d.	n.d.	n.d.	n.d.	n.d.	n.d.	0.00	0.00	0.00	0.00	n.d.	n.d.	n.d.	n.d.	n.d.
Er	n.d.	n.d.	n.d.	n.d.	n.d.	n.d.	n.d.	n.d.	n.d.	0.00	0.00	0.00	0.00	n.d.	n.d.	n.d.	n.d.	n.d.
Tm	n.d.	n.d.	n.d.	n.d.	n.d.	n.d.	n.d.	n.d.	n.d.	0.00	0.00	0.00	0.00	n.d.	n.d.	n.d.	n.d.	n.d.
Yb	n.d.	n.d.	n.d.	n.d.	n.d.	n.d.	n.d.	n.d.	n.d.	1.38	1.56	0.00	3.88	n.d.	n.d.	2.37	n.d.	n.d.
Lu	n.d.	n.d.	n.d.	n.d.	n.d.	n.d.	n.d.	n.d.	n.d.	0.24	0.27	0.00	0.49	n.d.	n.d.	0.41	n.d.	n.d.
Sc	n.d.	n.d.	n.d.	n.d.	n.d.	n.d.	n.d.	n.d.	n.d.	n.d.	n.d.	n.d.	n.d.	n.d.	12	n.d.	n.d.	n.d.
U	n.d.	n.d.	n.d.	n.d.	n.d.	n.d.	n.d.	n.d.	n.d.	0.70	0.60	0.00	0.01	n.d.	4	n.d.	n.d.	n.d.

Abbreviations: Gd= granodiorite, Ton= tonalite, Gb= gabbro, Bas= basalt n.d.= not determined. Data from Pe-Piper and Turner (1987) and Pe-Piper et al. (2002).

APPENDIX C

Electron Microprobe analyses and recalculated mineral formulae of important hydrothermal major and REE-bearing minerals hosted in the fractures of the late Paleozoic A-type granites of the Cobequid Highlands.

Appendix C. 1 Representative microprobe analyses of epidote and garnet.

Sample	**6497**	**4106**	**4106**	**4106**		**6497**	**6497**	**6497**
Mineral	**ep**	**ep**	**ep**	**ep**		**And**	**And**	**And**
SiO_2	36.01	38.86	39.01	39.01		34.39	35.48	35.31
TiO_2	b.d.	0.10	b.d.	0.01		1.20	1.04	1.12
Al_2O_3	21.40	24.61	24.86	24.55		3.26	4.33	3.92
FeO_T	12.88	11.55	11.17	11.50		25.11	23.04	23.79
MnO	0.11	0.15	0.11	0.22		0.69	0.70	0.61
MgO	b.d.	b.d.	b.d.	0.01		0.06	0.07	0.07
CaO	22.07	23.77	23.63	23.23		32.90	33.15	33.20
Total	92.48	99.04	98.78	98.52		97.61	97.81	98.02
Si	3.008	3.012	3.027	3.041	Si	2.929	2.991	2.978
Al^{IV}	0.000	0.000	0.000	0.000	Al^{IV}	0.071	0.009	0.022
T-site sum	**3.008**	**3.012**	**3.027**	**3.041**	**Sum_Z**	**3.000**	**3.000**	**3.000**
A1					Al^{VI}	0.256	0.421	0.367
Ca^{2+}	1.000	1.000	1.000	1.000	Fe^{3+}	1.608	1.460	1.508
Al^{VIII}	0.000	0.000	0.000	0.000	Ti	0.077	0.066	0.071
Fe^{3+}	0.000	0.000	0.000	0.000	**Sum_Y**	**1.940**	**1.947**	**1.948**
Mn^{2+}	0.015	0.026	0.013	0.008	Mg	0.008	0.009	0.009
Mg	0.000	0.000	0.000	0.000	Mn	0.050	0.050	0.044
sum	**1.015**	**1.026**	**1.013**	**1.008**	Ca	3.002	2.994	3.000
A2					**Sum_X**	**3.060**	**3.053**	**3.052**
Ca^{2+}	0.975	0.974	0.965	0.939	**Andradite**	**82.85**	**74.98**	**77.43**
Al^{VIII}	0.000	0.000	0.000	0.000	**Grossular**	**15.28**	**23.06**	**20.79**
Fe^{2+}	0.000	0.000	0.000	0.000	**Pyrope**	**0.25**	**0.28**	**0.29**
Fe^{3+}	0.000	0.000	0.000	0.000	**Spessartine**	**1.62**	**1.63**	**1.43**
Mn^{2+}	0.000	0.000	0.000	0.000	**Uvarovite**	**0.00**	**0.03**	**0.07**
Mg	0.000	0.000	0.000	0.000				
sum	**0.975**	**0.974**	**0.965**	**0.939**				
M1								
Al^{VIII}	1.000	1.000	1.000	1.000				
Ti	0.000	0.000	0.000	0.000				
Fe^{3+}	0.000	0.000	0.000	0.000				
Mn^{3+}	0.000	0.000	0.000	0.000				
Mg	0.000	0.000	0.000	0.000				
Fe^{2+}	0.000	0.000	0.000	0.000				
Mn^{2+}	0.007	0.005	0.000	0.000				
sum	**1.007**	**1.005**	**1.000**	**1.000**				
M2								
Al^{VIII}	1.000	1.000	1.000	1.000				
Fe^{3+}	0.000	0.000	0.000	0.000				
sum	**1.000**	**1.000**	**1.000**	**1.000**				
M3								
Al^{VIII}	0.107	0.248	0.274	0.225				
Ti	0.000	0.005	0.000	0.000				
Fe^{3+}	0.900	0.748	0.725	0.749				
Mn^{3+}	0.000	0.000	0.000	0.000				
Mg	0.000	0.000	0.000	0.000				
Fe^{2+}	0.000	0.000	0.000	0.000				
Mn^{2+}	0.000	0.000	0.001	0.026				
sum	**1.007**	**1.001**	**1.000**	**1.000**				

Notes: Chemical formula of epidote calculated on the basis of 8 cations (Armbruster et al. 2006), stoichiometric formula of garnet calculated on the basis of 12 oxygens, b.d.= below detection limit.

Appendix C. 2 Representative microprobe analyses of hydrothermal biotite.

Pluton	**PHP**	**PHP**	**PHP**	**PHP**	**CCP**	**CCP**
Sample	**4106**	**4106**	**4106**	**4106**	**6284**	**6284**
SiO_2	37.98	36.88	36.48	38.52	34.17	36.59
TiO_2	2.05	2.14	1.75	1.95	1.18	1.6
Al_2O_3	19.28	17.67	17.06	18.38	17.37	17.96
FeO_T	19.66	22.14	22.33	17.81	24.16	22.81
MnO	0.06	0.06	0.05	0.04	0.20	0.11
MgO	7.36	6.74	7.58	8.76	7.47	7.22
CaO	0.03	0.02	0.05	b.d.	b.d.	b.d.
Na_2O	0.10	0.05	0.09	0.07	0.04	0.03
K_2O	9.83	9.72	9.49	10.06	8.67	8.84
H_2O*	1.92	1.87	1.85	1.92	1.80	1.86
Total	98.27	97.29	96.73	97.51	95.06	97.02
Structural formula						
Si	2.842	2.835	2.827	2.883	2.725	2.816
Al	1.158	1.165	1.173	1.117	1.275	1.184
Ti	0.115	0.124	0.102	0.110	0.071	0.093
Al	0.541	0.434	0.384	0.503	0.357	0.444
Fe^{+2}	1.230	1.423	1.447	1.115	1.612	1.468
Mn	0.004	0.004	0.003	0.003	0.014	0.007
Mg	0.821	0.772	0.876	0.978	0.888	0.828
Ca	0.002	0.002	0.004	0.000	0.000	0.000
Na	0.015	0.007	0.014	0.010	0.006	0.004
K	0.938	0.953	0.938	0.961	0.882	0.868

Notes: Biotite formula calculated on the basis of 10 oxygens, and 2 OH atoms in the A-site as per Rieder et al. (1998).

Appendix C. 3 Representative microprobe analyses of chlorite.

Pluton	NRP	NRP	NRP	PHP	PHP	PHP	PHP	PHP	PHP	PHP	PHP	PHP	PHP	PHP
Sample	**1779**	**1779**	**1779**	**4672**	**4672**	**4672**	**4672**	**4672**	**4672**	**4672**	**4672**	**4672**	**4672**	**4672**
Analysis	**81**	**83**	**89**	**53**	**55**	**56**	**57**	**58**	**59**	**61**	**63**	**64**	**65**	**66**
SiO_2	26.63	26.78	30.30	29.83	23.86	23.66	27.68	26.06	28.44	23.68	23.44	24.99	28.47	25.75
TiO_2	b.d.	0.02	b.d.	0.02	0.06	b.d.	0.01	b.d.	b.d.	0.14	0.01	b.d.	b.d.	b.d.
Al_2O_3	16.65	17.32	14.93	19.28	20.16	20.94	19.50	19.39	19.21	20.06	20.81	20.86	19.29	19.67
FeO_T	31.72	29.64	25.76	30.05	37.65	36.46	31.86	31.69	31.48	37.57	38.88	35.78	30.47	34.45
MnO	0.54	0.42	0.29	0.17	0.16	0.16	0.15	0.12	0.15	0.20	0.18	0.16	0.14	0.18
MgO	10.43	10.37	11.17	3.45	5.00	5.57	4.13	4.76	3.35	4.30	4.20	3.98	3.25	3.75
CaO	0.05	0.16	0.43	0.27	b.d.	0.03	0.20	0.14	0.28	b.d.	b.d.	0.11	0.22	0.12
Na_2O	b.d.	0.02	0.08	0.45	b.d.	0.02	0.14	0.20	0.26	0.04	0.02	0.05	0.14	0.06
K_2O	0.02	0.02	0.26	0.59	0.03	0.04	0.41	0.94	0.47	0.05	0.02	0.23	0.53	0.22
Total	**86.03**	**84.75**	**83.22**	**84.10**	**86.92**	**86.87**	**84.07**	**83.30**	**83.63**	**86.03**	**87.57**	**86.15**	**82.51**	**84.19**
Structural formula														
Si	5.951	5.997	6.726	6.663	5.451	5.370	6.279	6.027	6.464	5.474	5.348	5.680	6.520	5.951
Al^{IV}	2.049	2.003	1.274	1.337	2.549	2.630	1.721	1.973	1.536	2.526	2.652	2.320	1.480	2.049
T-site	**8.000**	**8.000**	**8.000**	**8.000**	**8.000**	**8.000**	**8.000**	**8.000**	**8.000**	**8.000**	**8.000**	**8.000**	**8.000**	**8.000**
Al^{VI}	2.333	2.565	2.629	3.736	2.875	2.969	3.488	3.309	3.606	2.935	2.941	3.265	3.722	3.304
Ti	0.000	0.003	0.000	0.003	0.010	0.000	0.002	0.000	0.000	0.024	0.002	0.000	0.000	0.000
Fe^{3+}	0.000	0.000	0.000	0.000	0.000	0.000	0.000	0.000	0.000	0.000	0.000	0.000	0.000	0.000
Fe^{2+}	5.928	5.552	4.782	5.614	7.194	6.921	6.045	6.129	5.985	7.265	7.420	6.802	5.835	6.658
Cr	0.000	0.000	0.000	0.007	0.000	0.000	0.006	0.002	0.005	0.000	0.006	0.002	0.011	0.001
Mn	0.102	0.080	0.054	0.032	0.031	0.030	0.028	0.024	0.028	0.039	0.034	0.031	0.026	0.035
Mg	3.475	3.463	3.695	1.148	1.703	1.886	1.395	1.640	1.136	1.484	1.430	1.347	1.111	1.292
Ca	0.011	0.039	0.102	0.065	0.000	0.006	0.049	0.033	0.068	0.000	0.000	0.026	0.054	0.029
Na	0.000	0.007	0.034	0.193	0.002	0.008	0.060	0.090	0.114	0.018	0.009	0.024	0.061	0.027
K	0.007	0.006	0.074	0.169	0.009	0.011	0.119	0.278	0.136	0.014	0.007	0.067	0.155	0.063
Cations	19.856	19.715	19.370	18.967	19.824	19.831	19.192	19.505	19.078	19.779	19.849	19.564	18.975	19.409

Appendix C. 3 Representative microprobe analyses of chlorite (continued).

Pluton	PHP	PHP	PHP	PHP	PHP	NRP	NRP	NRP	NRP	CCP	CCP	CCP	CCP	CCP	CCP	CCP
Sample	**4672**	**4672**	**4672**	**4672**	**4672**	**4824**	**4824**	**4824**	**4824**	**6289**	**6289**	**6289**	**6289**	**6289**	**6289**	**6289**
Analysis	**67**	**68**	**69**	**70**	**71**	**74**	**75**	**77**	**80**	**102**	**107**	**111**	**115**	**90**	**93**	**96**
SiO_2	28.06	27.62	27.29	27.76	25.64	25.65	26.17	24.86	25.63	26.17	25.48	34.17	36.59	24.73	24.64	26.57
TiO_2	0.01	0.02	b.d.	b.d.	0.03	b.d.	0.02	0.01	0.09	0.08	0.16	1.18	1.60	0.17	b.d.	0.11
Al_2O_3	19.84	19.62	20.62	19.35	20.41	19.12	18.78	18.81	17.54	19.18	20.42	17.37	17.96	21.13	21.43	18.44
FeO_T	30.90	32.25	33.07	31.09	35.50	33.19	31.91	33.77	30.41	30.32	29.35	24.16	22.81	30.65	31.20	30.21
MnO	0.13	0.16	0.15	0.13	0.09	0.55	0.39	0.42	0.46	0.21	0.25	0.20	0.11	0.28	0.30	0.32
MgO	4.18	4.04	3.81	4.88	5.00	9.14	9.59	8.33	8.60	10.70	11.18	7.47	7.22	10.09	10.20	10.26
CaO	0.20	0.10	0.09	0.10	0.05	0.06	0.09	0.05	0.77	0.09	0.05	b.d.	b.d.	0.11	0.01	0.06
Na_2O	0.46	0.22	0.17	0.18	0.07	0.02	0.08	0.05	0.23	b.d.	b.d.	0.04	0.03	b.d.	b.d.	0.01
K_2O	0.35	0.29	0.55	0.88	0.18	0.07	0.10	0.04	0.12	0.15	b.d.	8.67	8.84	0.02	0.02	0.30
Total	**84.11**	**84.31**	**85.75**	**84.37**	**86.97**	**87.79**	**87.12**	**86.34**	**83.85**	**86.88**	**86.90**	**93.27**	**95.15**	**87.17**	**87.78**	**86.28**
Structural formula																
Si	6.319	6.255	6.106	6.269	5.750	5.651	5.765	5.606	5.873	5.722	5.539	6.937	7.168	5.404	5.360	5.857
Al^{IV}	1.681	1.745	1.894	1.731	2.250	2.349	2.235	2.394	2.127	2.278	2.461	1.063	0.832	2.596	2.640	2.143
T-site	**8.000**	**8.000**	**8.000**	**8.000**	**8.000**	**8.000**	**8.000**	**8.000**	**8.000**	**8.000**	**8.000**	**8.000**	**8.000**	**8.000**	**8.000**	**8.000**
Al^{VI}	3.581	3.487	3.539	3.415	3.141	2.612	2.637	2.603	2.607	2.661	2.768	3.089	3.312	2.843	2.848	2.644
Ti	0.002	0.003	0.000	0.000	0.005	0.000	0.003	0.001	0.015	0.012	0.026	0.181	0.235	0.027	0.000	0.018
Fe^{3+}	0.000	0.000	0.000	0.000	0.000	0.000	0.000	0.000	0.000	0.000	0.000	0.000	0.000	0.000	0.000	0.000
Fe^{2+}	5.820	6.110	6.187	5.871	6.657	6.116	5.878	6.370	5.828	5.545	5.337	4.103	3.737	5.602	5.675	5.570
Cr	0.010	0.006	0.005	0.005	0.000	0.000	0.000	0.000	0.000	0.000	0.000	0.000	0.000	0.000	0.000	0.000
Mn	0.024	0.031	0.029	0.024	0.017	0.103	0.072	0.080	0.089	0.039	0.046	0.034	0.018	0.053	0.055	0.061
Mg	1.402	1.365	1.269	1.644	1.670	3.002	3.147	2.801	2.939	3.489	3.624	2.262	2.108	3.287	3.306	3.372
Ca	0.048	0.023	0.022	0.024	0.011	0.014	0.022	0.013	0.190	0.020	0.011	0.000	0.000	0.025	0.003	0.015
Na	0.199	0.097	0.074	0.077	0.030	0.007	0.033	0.023	0.104	0.000	0.000	0.017	0.010	0.000	0.000	0.003
K	0.099	0.082	0.158	0.252	0.052	0.021	0.029	0.012	0.035	0.041	0.000	2.247	2.208	0.006	0.004	0.084
Cations	**19.185**	**19.204**	**19.283**	**19.312**	**19.583**	**19.875**	**19.821**	**19.903**	**19.807**	**19.807**	**19.812**	**19.933**	**19.628**	**19.843**	**19.891**	**19.767**

Notes: Structural formula calculate on the basis of 10 O and 8 OH atoms.

Appendix C. 4 Electron microprobe analyses of hydrothermal REE-fluorocarbonates.

Sample	6497	4106	1779	4829	4829	4829	4829	4829	4829	1779	1779
Mineral	bastnäsite	bastnäsite	bastnäsite	parisite	parisite	parisite	parisite	parisite	parisite	synchysite	synchysite
P_2O_5	b.d.	0.37	0.02	0.01	b.d.	0.07	0.01	0.10	b.d.	b.d.	0.07
Nb_2O_5	b.d.	b.d.	0.02	b.d.	0.05	0.03	0.08	b.d.	b.d.	b.d.	0.03
As_2O_5	b.d.	0.06	b.d.	b.d.	b.d.	b.d.	b.d.	b.d.	b.d.	b.d.	b.d.
SiO_2	6.99	3.13	2.06	1.17	1.23	0.71	1.53	0.76	1.96	1.02	0.61
ZrO_2	b.d.	0.07	0.02	b.d.	b.d.	0.01	0.05	0.01	0.02	0.03	b.d.
ThO_2	b.d.	3.11	0.26	0.23	0.33	1.77	0.26	0.33	0.36	0.12	0.16
UO_2	0.08	0.23	b.d.	0.02	0.04	0.07	b.d.	0.16	0.10	0.19	b.d.
Al_2O_3	0.67	0.65	0.51	0.40	0.47	0.34	0.64	0.11	1.26	0.39	0.23
Y_2O_3	b.d.	1.31	1.99	2.25	2.06	2.34	2.08	2.48	2.27	7.44	4.92
La_2O_3	12.90	15.40	12.76	8.53	10.55	11.32	8.81	11.47	9.67	8.19	8.63
Pr_2O_3	2.21	2.17	2.33	1.94	2.26	2.27	2.07	2.49	2.15	1.67	2.01
Ce_2O_3	24.20	25.11	26.53	15.65	18.15	17.08	16.23	17.14	17.29	18.07	19.99
Nd_2O_3	8.59	9.77	9.10	8.85	10.05	10.40	8.43	11.35	9.13	8.05	9.15
Sm_2O_3	0.53	1.15	1.33	1.74	1.88	1.84	1.57	2.18	1.65	1.78	1.88
Eu_2O_3	0.59	0.76	0.72	0.72	0.82	0.78	0.65	0.86	0.62	0.53	0.58
Gd_2O_3	0.17	0.68	0.78	1.38	1.27	1.23	1.21	1.68	1.18	2.12	1.79
Dy_2O_3	0.17	0.36	0.42	0.67	0.58	0.59	0.35	0.59	0.59	1.12	0.84
Ho_2O_3	b.d.	b.d.	b.d.	b.d.	b.d.	b.d.	b.d.	b.d.	b.d.	0.33	0.12
Er_2O_3	0.07	0.05	0.20	b.d.	0.02	0.12	0.20	0.11	0.10	0.19	0.20
Yb_2O_3	b.d.	b.d.	b.d.	b.d.	b.d.	b.d.	b.d.	b.d.	b.d.	0.13	b.d.
FeO_T	11.16	2.24	5.58	11.34	9.10	8.18	14.75	2.74	10.69	0.48	0.91
MgO	0.57	0.01	0.13	b.d.	b.d.	0.03	0.11	b.d.	0.01	b.d.	0.25
MnO	b.d.	b.d.	b.d.	b.d.	b.d.	b.d.	b.d.	b.d.	b.d.	b.d.	b.d.
CaO	6.95	4.41	7.86	15.02	12.20	11.21	12.41	13.73	10.79	17.95	17.85
K_2O	0.16	0.22	0.08	0.15	0.11	0.06	0.08	0.06	0.07	0.32	0.07
F	0.14	3.81	3.99	2.75	3.14	2.89	2.78	2.77	2.83	2.55	2.68
CO_2 calc	27.92	23.08	22.85	27.61	27.26	26.23	28.44	25.53	27.96	30.22	29.67
O-F	-0.06	-1.60	-1.68	-1.16	-1.32	-1.22	-1.17	-1.16	-1.19	-1.07	-1.13
Total	104.00	96.58	97.86	99.22	100.23	98.34	101.55	95.49	99.50	101.81	101.52

Sample	6497	4106	1779	4829	4829	4829	4829	4829	4829	1779	1779
Mineral	bastnäsite	bastnäsite	bastnäsite	parisite	parisite	parisite	parisite	parisite	parisite	synchysite	synchysite
C =	1	1	1	3	3	3	3	3	3	2	2
Structural formula											
P	0.000	0.009	0.000	0.000	0.000	0.004	0.000	0.007	0.000	0.000	0.003
Nb	0.000	0.000	0.000	0.000	0.002	0.001	0.002	0.000	0.000	0.000	0.001
As	0.000	0.001	0.000	0.000	0.000	0.000	0.000	0.000	0.000	0.000	0.000
Si	0.160	0.095	0.056	0.081	0.092	0.055	0.105	0.062	0.144	0.050	0.030
Zr	0.000	0.001	0.000	0.000	0.000	0.000	0.002	0.000	0.001	0.001	0.000
Th	0.000	0.022	0.002	0.004	0.006	0.032	0.004	0.006	0.006	0.001	0.002
U	0.000	0.002	0.000	0.000	0.001	0.001	0.000	0.003	0.002	0.002	0.000
Al	0.018	0.023	0.016	0.033	0.041	0.032	0.052	0.011	0.110	0.022	0.013
Y	0.000	0.021	0.029	0.084	0.082	0.098	0.076	0.108	0.089	0.194	0.130
La	0.109	0.173	0.128	0.220	0.290	0.327	0.223	0.345	0.263	0.148	0.158
Pr	0.018	0.024	0.023	0.049	0.061	0.065	0.052	0.074	0.058	0.030	0.036
Ce	0.203	0.280	0.263	0.401	0.495	0.489	0.408	0.512	0.466	0.325	0.364
Nd	0.070	0.106	0.088	0.221	0.267	0.291	0.207	0.331	0.240	0.141	0.162
Sm	0.004	0.012	0.012	0.042	0.048	0.050	0.037	0.061	0.042	0.030	0.032
Eu	0.005	0.008	0.007	0.017	0.021	0.021	0.015	0.024	0.016	0.009	0.010
Gd	0.001	0.007	0.007	0.032	0.031	0.032	0.028	0.046	0.029	0.034	0.029
Dy	0.001	0.004	0.004	0.015	0.014	0.015	0.008	0.016	0.014	0.018	0.013
Er	0.000	0.000	0.000	0.000	0.000	0.000	0.000	0.000	0.000	0.005	0.002
Ho	0.000	0.000	0.002	0.000	0.001	0.003	0.004	0.003	0.002	0.003	0.003
Yb	0.000	0.000	0.000	0.000	0.000	0.000	0.000	0.000	0.000	0.002	0.000
Fe	0.214	0.057	0.126	0.663	0.566	0.535	0.847	0.187	0.659	0.020	0.038
Mg	0.020	0.000	0.005	0.000	0.000	0.003	0.011	0.000	0.002	0.000	0.018
Mn	0.000	0.000	0.000	0.000	0.000	0.000	0.000	0.000	0.000	0.000	0.000
Ca	0.171	0.144	0.228	1.125	0.973	0.940	0.913	1.200	0.852	0.943	0.950
K	0.005	0.008	0.003	0.013	0.011	0.006	0.007	0.006	0.007	0.020	0.004

Notes: CO_2 calculated through charge-balance, the oxygen equivalent for fluorine is calculated on the basis of two F atoms for every O atom.

Appendix C. 5 Microprobe analyses of hydrothermal thorite, chernovite and cerianite.

Sample	**6497**	**4824**	**1779**	**6289**	**6289**	**6289**	**4106**	**4106**
Mineral	**Thorite**	**Thorite**	**Thorite**	**Thorite**	**Chernovite**	**Chernovite**	**Cerianite**	**Cerianite**
P_2O_5	0.08	0.65	0.47	3.04	1.62	2.64	2.04	1.28
As_2O_5	0.01	1.24	0.01	1.88	35.03	33.73	3.36	2.21
SiO_2	22.26	13.14	17.01	15.72	2.73	3.02	13.24	16.68
TiO_2	0.56	b.d.	b.d.	0.03	b.d.	b.d.	0.03	b.d.
ZrO_2	1.25	2.40	0.10	0.94	0.08	0.07	b.d.	b.d.
ThO_2	42.14	26.48	61.07	32.81	4.48	2.00	0.69	2.39
UO_2	1.46	1.77	8.43	1.68	0.48	0.30	0.03	0.69
Al_2O_3	4.82	0.39	0.13	1.17	b.d.	b.d.	2.00	1.68
Y_2O_3	0.93	9.18	0.63	9.75	27.42	30.91	8.74	8.29
La_2O_3	1.29	2.52	b.d.	0.44	b.d.	0.06	0.10	0.04
Ce_2O_3	3.57	6.34	0.20	14.07	7.00	4.55	47.90	43.80
Pr_2O_3	0.41	0.72	b.d.	0.31	0.32	0.18	0.13	0.08
Nd_2O_3	1.71	2.76	0.06	1.22	1.59	1.26	0.68	0.70
Sm_2O_3	0.52	0.74	b.d.	0.69	1.78	1.57	0.30	0.30
Eu_2O_3	0.13	0.30	b.d.	0.06	0.03	0.06	b.d.	b.d.
Gd_2O_3	0.28	1.64	0.12	1.71	5.04	5.17	0.92	1.30
Dy_2O_3	0.29	1.65	0.28	1.99	5.02	5.49	1.85	1.53
Ho_2O_3	b.d.	0.54	0.18	0.75	2.29	2.44	0.44	0.51
Er_2O_3	0.12	1.19	0.34	0.98	2.29	2.75	0.71	0.64
Yb_2O_3	0.01	0.64	0.06	0.88	1.74	1.67	0.42	0.64
FeO	7.05	5.02	2.34	0.89	1.43	0.96	4.73	3.57
MgO	0.20	b.d.	0.01	b.d.	b.d.	b.d.	b.d.	b.d.
MnO	b.d.	b.d.	0.09	0.06	0.17	b.d.	1.75	0.19
CaO	6.63	4.44	1.33	0.54	0.52	0.39	0.24	0.69
K_2O	0.06	0.05	b.d.	0.04	0.03	0.02	0.03	0.11
F	0.08	1.14	0.29	0.13	b.d.	b.d.	b.d.	b.d.
Total	95.83	83.06	92.68	91.73	101.09	99.22	90.39	87.40
Structural formula								
P	0.002	0.026	0.021	0.064	0.029	0.047	0.035	0.023
As	0.000	0.030	0.000	0.024	0.387	0.370	0.036	0.024
Si	0.795	0.611	0.904	0.782	0.116	0.127	0.270	0.348
Ti	0.015	0.000	0.000	0.001	0.000	0.000	0.001	0.000
Zr	0.022	0.054	0.003	0.023	0.002	0.002	0.000	0.000
Th	0.343	0.280	0.739	0.371	0.043	0.019	0.003	0.011
U	0.012	0.018	0.100	0.019	0.005	0.003	0.000	0.003
Al	0.203	0.021	0.008	0.034	0.000	0.000	0.048	0.041
Y	0.018	0.227	0.018	0.129	0.309	0.345	0.095	0.092
La	0.017	0.043	0.000	0.004	0.000	0.000	0.001	0.000
Ce	0.047	0.108	0.004	0.003	0.002	0.001	0.358	0.334
Pr	0.005	0.012	0.000	0.128	0.054	0.035	0.001	0.001
Nd	0.022	0.046	0.001	0.011	0.012	0.009	0.005	0.005
Sm	0.006	0.012	0.000	0.006	0.013	0.011	0.002	0.002
Eu	0.002	0.005	0.000	0.001	0.000	0.000	0.000	0.000
Gd	0.003	0.025	0.002	0.014	0.035	0.036	0.006	0.009
Dy	0.003	0.025	0.005	0.016	0.034	0.037	0.012	0.010
Er	0.000	0.008	0.003	0.006	0.015	0.016	0.003	0.003
Ho	0.001	0.017	0.006	0.008	0.015	0.018	0.005	0.004
Yb	0.000	0.009	0.001	0.007	0.011	0.011	0.003	0.004
Fe	0.211	0.195	0.104	0.037	0.051	0.034	0.081	0.062
Mg	0.010	0.000	0.000	0.000	0.000	0.000	0.000	0.000
Mn	0.000	0.000	0.004	0.002	0.006	0.000	0.030	0.003
Ca	0.254	0.221	0.076	0.029	0.023	0.018	0.005	0.015
K	0.003	0.003	0.000	0.001	0.001	0.000	0.001	0.003
F	0.005	0.084	0.025	0.000	0.000	0.000	0.000	0.000
Total	**2.005**	**2.084**	**2.025**	**1.719**	**1.165**	**1.140**	**1.001**	**1.007**

Notes: Thorite and chernovite formula calculated on the basis of 4 oxygens, cerianite formula normalized to 1 cation.

Appendix C. 6 Representative microprobe analyses of hydrothermal hingganite-(Y).

Sample	**6497**	**6497**	**6497**	**6497**
Mineral	**Hingganite**	**Hingganite**	**Hingganite**	**Hingganite**
P_2O_5	0.06	b.d.	0.05	0.05
SiO_2	29.43	28.77	29.07	34.88
ZrO_2	0.01	0.10	b.d.	0.03
ThO_2	0.25	0.18	0.12	0.29
UO_2	0.01	0.09	0.15	0.24
Al_2O_3	0.18	0.29	0.15	1.53
Y_2O_3	27.84	26.79	27.62	20.57
La_2O_3	b.d.	b.d.	0.01	0.09
Ce_2O_3	0.34	0.38	0.25	0.46
Pr_2O_3	0.17	0.12	0.09	0.18
Nd_2O_3	0.84	1.14	0.80	1.07
Sm_2O_3	1.08	1.12	1.06	0.74
Eu_2O_3	0.12	0.11	0.09	0.13
Gd_2O_3	4.69	4.15	4.47	2.78
Dy_2O_3	5.11	4.23	5.06	3.00
Ho_2O_3	2.28	1.99	2.18	1.39
Er_2O_3	3.01	2.64	2.83	2.27
Yb_2O_3	1.78	1.73	1.72	1.44
FeO	7.73	7.09	6.21	10.61
MgO	b.d.	0.13	b.d.	1.14
MnO	0.08	0.12	0.08	0.34
CaO	5.34	5.47	5.87	6.35
K_2O	0.03	0.07	0.03	0.29
F	0.14	0.09	0.13	0.29
Total	**90.54**	**86.82**	**87.98**	**90.14**
Structural formula on the basis of 10 oxygens				
P	0.003	0.000	0.003	0.002
Si	1.862	1.874	1.886	1.983
Zr	0.000	0.003	0.000	0.001
Th	0.004	0.003	0.002	0.004
U	0.000	0.001	0.002	0.003
Al	0.013	0.022	0.011	0.102
Y	0.937	0.929	0.953	0.622
La	0.000	0.000	0.000	0.002
Ce	0.008	0.009	0.006	0.010
Pr	0.004	0.003	0.002	0.004
Nd	0.019	0.026	0.018	0.022
Sm	0.024	0.025	0.024	0.014
Eu	0.003	0.003	0.002	0.002
Gd	0.098	0.090	0.096	0.052
Dy	0.104	0.089	0.106	0.055
Er	0.046	0.041	0.045	0.025
Ho	0.060	0.054	0.058	0.041
Yb	0.034	0.034	0.034	0.025
Fe	0.409	0.386	0.337	0.504
Mg	0.000	0.013	0.000	0.096
Mn	0.004	0.007	0.005	0.016
Ca	0.362	0.382	0.408	0.387
K	0.002	0.006	0.003	0.021
F	0.028	0.009	0.013	0.026
Total	4.028	4.009	4.013	4.026

APPENDIX D

Euler rotation parameters used as an input for G-Plates in order to produce the paleoreconstructions presented in Chapter 5.

Appendix D. 1 Euler rotation parameters used for the reconstructions presented in Chapter 5.

Moving plate	Age (Ma)	Latitude	Longitude	Angle	Fixed plate
Florida	250	63.19	-13.87	79.87	Congo
Florida	490	63.06	-11.94	80.86	Congo
Florida	540	63.19	-13.87	79.87	Congo
S. China	250	53.52	-99.21	37.90	Congo
S. China	260	41.85	-103.27	40.51	Congo
S. China	270	60.25	-175.17	39.00	Congo
S. China	280	60.92	164.36	30.78	Congo
S. China	290	56.92	168.31	31.11	Congo
S. China	300	53.62	164.62	29.94	Congo
S. China	310	49.96	161.26	28.91	Congo
S. China	320	45.23	141.21	25.42	Congo
S. China	330	42.25	140.57	25.53	Congo
S. China	340	39.29	140.00	25.70	Congo
S. China	350	38.76	128.78	23.61	Congo
S. China	360	37.38	120.92	22.89	Congo
S. China	370	35.40	113.01	22.45	Congo
S. China	380	24.03	126.78	22.48	Congo
S. China	390	11.30	132.00	22.90	Congo
S. China	400	13.94	140.65	25.56	Congo
S. China	410	19.95	152.09	29.24	Congo
S. China	420	1.97	-20.64	-19.18	Congo
S. China	430	14.35	-17.50	-18.47	Congo
S. China	440	29.81	-15.31	-17.97	Congo
S. China	450	44.95	-12.35	-18.80	Congo
S. China	460	57.92	-8.17	-20.79	Congo
S. China	470	53.67	62.99	-39.62	Congo
S. China	480	45.57	77.14	-64.30	Congo
S. China	540	45.57	77.17	-64.30	Congo
S. China	640	0.00	-117.80	90.20	Congo
S. China	650	-2.19	-92.99	108.88	Congo
S. China	750	-16.75	-94.25	144.23	Congo
Qiangtang	250	25.38	68.23	-30.37	Congo
Qiangtang	260	36.14	44.61	-35.20	Congo
Qiangtang	270	34.53	37.26	-43.97	Congo
Qiangtang	280	30.73	41.85	-54.31	Congo
Qiangtang	290	29.19	43.42	-59.60	Congo
Qiangtang	540	29.19	43.42	-59.60	Congo
Laurentia	250	63.19	-13.87	79.87	Congo
Laurentia	320	63.19	-13.87	79.87	Congo
Laurentia	330	52.34	-20.01	81.57	Congo
Laurentia	340	38.73	-15.87	86.18	Congo
Laurentia	350	29.94	-14.54	91.50	Congo
Laurentia	360	17.48	-18.96	111.39	Congo
Laurentia	370	8.90	-21.96	140.86	Congo
Laurentia	380	11.83	-25.00	141.71	Congo
Laurentia	390	9.60	-25.92	142.30	Congo
Laurentia	400	8.13	-24.99	134.63	Congo

Moving plate	Age (Ma)	Latitude	Longitude	Angle	Fixed plate
Laurentia	410	4.11	-23.77	122.42	Congo
Laurentia	420	4.12	-22.16	97.99	Congo
Laurentia	430	5.17	-27.94	81.20	Congo
Laurentia	440	7.75	-35.54	97.98	Congo
Laurentia	450	10.43	-38.78	108.64	Congo
Laurentia	460	14.83	-39.68	110.99	Congo
Laurentia	470	21.50	-44.25	93.69	Congo
Laurentia	480	28.05	-46.77	79.70	Congo
Laurentia	490	36.43	-59.04	63.74	Congo
Laurentia	500	39.32	-88.75	43.90	Congo
Laurentia	510	42.98	-66.44	25.65	Congo
Laurentia	520	11.65	-17.25	22.38	Congo
Laurentia	530	9.54	171.92	-43.53	Congo
Laurentia	540	17.95	166.47	-58.80	Congo
Laurentia	540.1	17.95	166.47	-58.80	Mantle
Laurentia	541	38.59	-159.21	-128.18	Mantle
Laurentia	550	49.80	-178.74	-158.23	Mantle
Laurentia	600	39.27	-158.20	-132.54	Mantle
Laurentia	620	33.62	-149.02	-123.65	Mantle
Laurentia	630	28.57	-142.05	-115.10	Mantle
Laurentia	650	18.00	-130.4 -	104.30	Mantle
Laurentia	750	-1.80	-108.72	-85.95	Mantle
Greenland	250	60.48	1.42	69.40	Congo
Greenland	320	60.48	1.42	69.40	Congo
Greenland	330	49.11	-7.55	72.39	Congo
Greenland	340	34.84	-5.18	79.73	Congo
Greenland	350	26.21	-4.67	86.48	Congo
Greenland	360	15.62	-10.41	108.92	Congo
Greenland	370	9.20	-14.45	139.77	Congo
Greenland	380	12.19	-17.49	139.67	Congo
Greenland	390	10.00	-18.45	140.48	Congo
Greenland	400	8.05	-17.33	133.48	Congo
Greenland	410	3.19	-15.82	122.40	Congo
Greenland	420	1.13	-13.39	98.39	Congo
Greenland	430	0.26	-18.34	81.80	Congo
Greenland	440	4.75	-26.71	96.33	Congo
Greenland	450	8.42	-30.38	105.95	Congo
Greenland	460	13.06	-31.35	107.23	Congo
Greenland	470	18.31	-35.23	88.29	Congo
Greenland	480	23.49	-36.87	72.31	Congo
Greenland	490	30.43	-48.19	54.68	Congo
Greenland	500	28.98	-78.43	32.94	Congo
Greenland	510	18.70	-45.13	16.64	Congo
Greenland	520	16.91	-178.45	-24.96	Congo
Greenland	530	21.03	-176.10	-49.28	Congo
Greenland	540	25.04	177.14	-64.58	Congo
Greenland	541	-6.83	164.33	-65.98	Congo
Greenland	550	29.88	-8.48	69.73	Congo
Greenland	560	34.10	-16.29	68.88	Congo

Moving plate	Age (Ma)	Latitude	Longitude	Angle	Fixed plate
Greenland	570	26.78	-22.87	79.29	Congo
Greenland	580	19.68	-28.83	91.21	Congo
Greenland	590	16.24	-31.96	102.93	Congo
Greenland	600	13.22	-33.93	115.19	Congo
Greenland	650	-0.83	-46.10	176.67	Congo
Greenland	750	-17.65	-56.37	194.67	Congo
W. Avalonia	250	63.19	-13.87	79.87	Congo
W. Avalonia	320	63.19	-13.87	79.87	Congo
W. Avalonia	330	52.34	-20.01	81.57	Congo
W. Avalonia	340	38.73	-15.87	86.18	Congo
W. Avalonia	350	29.94	-14.54	91.50	Congo
W. Avalonia	360	17.48	-18.96	111.39	Congo
W. Avalonia	370	8.90	-21.96	140.86	Congo
W. Avalonia	380	11.90	-24.83	141.42	Congo
W. Avalonia	390	9.60	-25.92	142.03	Congo
W. Avalonia	400	8.13	-24.99	134.63	Congo
W. Avalonia	410	4.11	-23.77	122.42	Congo
W. Avalonia	420	4.12	-22.16	97.99	Congo
W. Avalonia	430	5.17	-27.94	81.20	Congo
W. Avalonia	440	14.37	-34.41	81.19	Congo
W. Avalonia	450	23.05	-36.98	90.70	Congo
W. Avalonia	460	27.35	-39.43	116.94	Congo
W. Avalonia	470	41.05	-35.10	113.70	Congo
W. Avalonia	471	42.82	-28.83	92.21	Congo
W. Avalonia	480	43.67	-22.37	103.39	Congo
W. Avalonia	489	46.36	-15.33	93.16	Congo
W. Avalonia	490	46.24	-15.19	94.36	Congo
W. Avalonia	500	41.37	-9.58	86.86	Congo
W. Avalonia	510	36.22	-4.24	82.97	Congo
W. Avalonia	540	31.02	-6.35	89.86	Congo
W. Avalonia	550	28.56	-10.59	101.28	Congo
W. Avalonia	560	24.91	-16.57	111.74	Congo
W. Avalonia	570	21.93	-20.98	120.44	Congo
W. Avalonia	580	19.10	-24.72	129.10	Congo
W. Avalonia	590	16.68	-28.48	138.78	Congo
W. Avalonia	600	14.17	-33.19	151.61	Congo
W. Avalonia	610	11.39	-35.81	161.90	Congo
W. Avalonia	620	9.23	-37.74	171.68	Congo
W. Avalonia	640	5.15	-42.36	191.85	Congo
W. Avalonia	650	3.32	-44.93	201.75	Congo
W. Avalonia	660	0.58	-47.62	206.14	Congo
W. Avalonia	670	-0.57	-47.89	205.87	Congo
W. Avalonia	680	-4.79	-54.21	216.11	Congo
W. Avalonia	690	-4.03	-50.60	210.64	Congo
W. Avalonia	700	-8.90	-59.85	229.95	Congo
W. Avalonia	710	-10.54	-62.67	237.80	Congo
W. Avalonia	730	-8.70	-61.31	240.47	Congo
W. Avalonia	740	-9.14	-64.49	245.31	Congo
W. Avalonia	750	-8.90	-67.53	251.49	Congo

Moving plate	Age (Ma)	Latitude	Longitude	Angle	Fixed plate
Florida	250	63.19	-13.87	79.87	Congo
Florida	540	63.19	-13.87	79.87	Congo
Florida	550	54.01	-21.25	90.94	Congo
Florida	560	43.75	-35.11	103.27	Congo
Florida	570	38.53	-39.27	107.55	Congo
Florida	580	33.06	-42.35	110.89	Congo
Florida	590	28.60	-44.07	113.92	Congo
Florida	600	22.01	-50.76	131.64	Congo
Florida	650	4.12	-55.54	151.60	Congo
Florida	750	-17.27	-65.60	163.13	Congo
Amazonia	250	50.00	-32.50	55.08	Congo
Amazonia	540	50.00	-32.50	55.08	Congo
Amazonia	550	44.26	-29.27	59.51	Congo
Amazonia	650	-10.67	-44.66	158.15	Congo
Amazonia	750	-30.25	-49.22	170.16	Congo
Colorado	250	47.50	-33.30	57.30	Congo
Colorado	540	47.50	-33.30	57.30	Congo
Colorado	550	23.18	-26.69	61.42	Congo
Colorado	560	37.48	-28.94	52.71	Congo
Colorado	570	26.12	-32.14	59.22	Congo
Colorado	580	16.42	-33.46	66.28	Congo
Colorado	590	7.93	-32.25	72.23	Congo
Colorado	600	-9.30	-37.42	103.70	Congo
Colorado	610	-2.87	-41.80	97.21	Congo
Colorado	620	-5.29	-40.64	110.10	Congo
Colorado	630	-7.22	-40.06	122.60	Congo
Colorado	640	-10.48	-39.47	133.93	Congo
Colorado	650	-12.11	-38.72	144.85	Congo
Colorado	660	-14.53	-36.85	149.94	Congo
Colorado	670	-15.31	-37.22	159.85	Congo
Colorado	680	-18.02	-34.51	163.63	Congo
Colorado	690	-21.24	-31.00	166.98	Congo
Colorado	700	-22.40	-29.86	175.48	Congo
Colorado	710	-24.68	-27.55	180.12	Congo
Colorado	720	-15.83	-34.35	151.51	Congo
Colorado	730	-17.02	-32.82	150.56	Congo
Colorado	740	-16.04	-32.34	153.57	Congo
Colorado	750	-14.98	-32.65	155.82	Congo
Patagonia	250	47.50	-33.30	63.00	Congo
Patagonia	260	49.12	-30.35	62.28	Congo
Patagonia	270	50.68	-27.15	61.66	Congo
Patagonia	540	50.68	-27.15	61.66	Congo
Patagonia	550	0.43	-24.86	72.53	Congo
Patagonia	560	20.61	-28.71	58.90	Congo
Patagonia	570	9.19	-30.17	66.51	Congo
Patagonia	580	0.63	-28.83	75.31	Congo
Patagonia	590	-5.51	-27.66	79.73	Congo
Patagonia	600	-24.95	-31.65	112.61	Congo
Patagonia	610	-6.30	-40.82	106.62	Congo

Moving plate	Age (Ma)	Latitude	Longitude	Angle	Fixed plate
Patagonia	620	-13.26	-36.69	114.78	Congo
Patagonia	630	-18.43	-34.27	130.70	Congo
Patagonia	640	-21.43	-32.47	138.96	Congo
Patagonia	650	-25.04	-30.28	158.70	Congo
Patagonia	660	-28.50	-30.73	161.69	Congo
Patagonia	670	-28.59	-30.56	164.28	Congo
Patagonia	680	-29.42	-29.69	164.77	Congo
Patagonia	690	-30.99	-28.77	166.42	Congo
Patagonia	700	-29.81	-27.56	170.17	Congo
Patagonia	710	-31.72	-26.62	169.15	Congo
Patagonia	720	-31.70	-24.44	171.49	Congo
Patagonia	730	-33.29	-23.76	171.79	Congo
Patagonia	740	-32.83	-22.98	175.90	Congo
Patagonia	750	-32.06	-22.54	179.48	Congo
Baltica	250	46.04	3.89	58.20	Congo
Baltica	320	46.04	3.89	58.20	Congo
Baltica	330	34.10	-2.57	64.85	Congo
Baltica	340	20.86	0.32	76.70	Congo
Baltica	350	13.46	1.19	85.23	Congo
Baltica	360	6.41	-3.38	110.96	Congo
Baltica	370	3.38	-6.50	143.63	Congo
Baltica	380	6.45	-9.32	142.86	Congo
Baltica	390	4.42	-10.34	144.34	Congo
Baltica	400	1.82	-9.42	138.70	Congo
Baltica	410	4.01	171.62	-128.59	Congo
Baltica	420	8.73	173.11	-105.51	Congo
Baltica	430	11.72	167.67	-89.36	Congo
Baltica	440	14.27	168.23	-84.70	Congo
Baltica	450	19.32	167.39	-72.49	Congo
Baltica	460	28.57	168.91	-58.33	Congo
Baltica	470	46.54	174.95	-47.21	Congo
Baltica	480	75.11	-170.20	-47.40	Congo
Baltica	490	77.58	37.73	-69.40	Congo
Baltica	500	65.26	33.54	-105.39	Congo
Baltica	510	64.93	10.76	-113.77	Congo
Baltica	520	65.74	-22.11	-118.37	Congo
Baltica	530	63.24	-35.90	-135.10	Congo
Baltica	540	67.21	-74.31	-112.84	Congo
Baltica	550	16.46	-151.21	-59.70	Congo
Baltica	560	13.60	-163.59	-53.94	Congo
Baltica	570	12.48	-169.65	-66.90	Congo
Baltica	580	11.30	-175.83	-81.25	Congo
Baltica	590	8.50	-177.81	-93.28	Congo
Baltica	650	1.00	167.26	-169.16	Congo
Baltica	750	7.87	157.43	-202.74	Congo
Scotland	250	46.04	3.89	58.20	Congo
Scotland	320	46.04	3.89	58.20	Congo
Scotland	330	34.10	-2.57	64.85	Congo
Scotland	340	20.86	0.32	76.70	Congo

Moving plate	Age (Ma)	Latitude	Longitude	Angle	Fixed plate
Scotland	350	13.46	1.19	85.23	Congo
Scotland	360	6.41	-3.38	110.96	Congo
Scotland	370	3.38	-6.50	143.63	Congo
Scotland	380	6.45	-9.32	142.86	Congo
Scotland	390	4.42	-10.34	144.34	Congo
Scotland	400	1.82	-9.42	138.70	Congo
Scotland	410	4.01	171.62	-128.59	Congo
Scotland	420	8.73	173.11	-105.51	Congo
Scotland	430	11.72	167.67	-89.36	Congo
Scotland	440	4.92	160.65	-103.44	Congo
Scotland	450	0.07	157.66	-111.91	Congo
Scotland	460	4.54	-22.97	111.71	Congo
Scotland	470	7.08	-26.86	91.69	Congo
Scotland	480	8.92	-28.65	74.60	Congo
Scotland	490	10.71	-38.96	55.83	Congo
Scotland	500	1.50	115.95	-36.25	Congo
Scotland	510	28.48	139.21	-27.30	Congo
Scotland	520	43.27	175.34	-38.79	Congo
Scotland	530	37.42	-175.86	-62.13	Congo
Scotland	540	37.20	179.43	-78.39	Congo
Iberia	250	51.77	67.88	3.42	Congo
Iberia	320	51.77	67.88	3.42	Congo
Iberia	330	10.76	-166.02	-15.90	Congo
Iberia	340	14.04	-154.13	-33.63	Congo
Iberia	350	12.65	-153.64	-41.98	Congo
Iberia	360	9.43	-164.23	-64.97	Congo
Iberia	370	28.20	-144.20	-64.10	Congo
Iberia	380	-48.10	83.30	58.90	Congo
Iberia	390	47.30	-44.60	-88.90	Congo
Iberia	400	44.80	-26.3 -	101.80	Congo
Iberia	410	40.50	-11.6 -	113.90	Congo
Iberia	420	39.51	-6.66	-116.57	Congo
Iberia	520	38.41	-3.36	-163.12	Congo
Iberia	540	39.29	-5.98	-141.27	Congo
Iberia	550	40.25	15.98	-270.20	Congo
Iberia	650	10.14	-36.29	-215.73	Congo
Iberia	750	26.76	-76.07	-151.41	Congo
Armorica	250	46.04	3.89	58.20	Congo
Armorica	320	46.04	3.89	58.20	Congo
Armorica	330	34.10	-2.57	64.85	Congo
Armorica	340	20.86	0.32	76.70	Congo
Armorica	350	17.03	0.83	82.86	Congo
Armorica	360	11.58	-5.17	104.92	Congo
Armorica	370	-2.60	175.90	-99.80	Congo
Armorica	380	-7.20	174.10	-83.70	Congo
Armorica	390	10.60	-4.80	61.10	Congo
Armorica	400	16.90	2.50	39.50	Congo
Armorica	410	-39.40	-155.50	-23.30	Congo
Armorica	420	54.59	38.40	21.52	Congo

Moving plate	Age (Ma)	Latitude	Longitude	Angle	Fixed plate
Armorica	540	34.42	119.45	7.45	Congo
Armorica	550	0.00	-110.10	95.80	Congo
Armorica	650	50.53	-89.22	-100.24	Congo
Armorica	750	-38.95	56.23	128.47	Congo
E. Avalonia	250	46.04	3.89	58.20	Congo
E. Avalonia	320	46.04	3.89	58.20	Congo
E. Avalonia	330	34.10	-2.57	64.85	Congo
E. Avalonia	340	20.86	0.32	76.70	Congo
E. Avalonia	350	13.46	1.19	85.23	Congo
E. Avalonia	360	6.41	-3.38	110.96	Congo
E. Avalonia	370	3.38	-6.50	143.63	Congo
E. Avalonia	380	6.45	-9.32	142.86	Congo
E. Avalonia	390	4.42	-10.34	144.34	Congo
E. Avalonia	400	1.82	-9.42	138.70	Congo
E. Avalonia	410	4.01	171.62	-128.59	Congo
E. Avalonia	420	8.73	173.11	-105.51	Congo
E. Avalonia	430	11.72	167.67	-89.36	Congo
E. Avalonia	440	14.27	168.23	-84.70	Congo
E. Avalonia	450	-3.47	166.10	-93.75	Congo
E. Avalonia	460	-13.69	167.80	-90.77	Congo
E. Avalonia	470	20.79	-6.83	81.19	Congo
E. Avalonia	480	18.61	6.77	69.86	Congo
E. Avalonia	481	17.91	7.59	69.50	Congo
E. Avalonia	490	22.53	10.22	63.58	Congo
E. Avalonia	510	3.59	26.79	56.18	Congo
E. Avalonia	540	0.90	27.08	59.49	Congo
E. Avalonia	550	-0.34	28.94	67.57	Congo
E. Avalonia	560	5.16	16.38	83.17	Congo
E. Avalonia	570	5.18	11.58	91.37	Congo
E. Avalonia	580	6.77	3.97	105.24	Congo
E. Avalonia	590	2.30	5.80	105.97	Congo
E. Avalonia	600	4.09	0.80	116.72	Congo
E. Avalonia	650	6.02	-13.12	179.96	Congo
E. Avalonia	660	4.17	-11.81	178.15	Congo
E. Avalonia	670	2.65	-13.10	180.50	Congo
E. Avalonia	680	3.16	-20.16	198.91	Congo
E. Avalonia	700	3.51	-24.38	211.20	Congo
E. Avalonia	710	3.74	-29.99	224.32	Congo
E. Avalonia	720	4.07	-28.06	222.52	Congo
E. Avalonia	730	6.49	-32.20	233.30	Congo
E. Avalonia	740	6.44	-37.22	239.34	Congo
E. Avalonia	750	7.48	-43.04	248.10	Congo
Novaya	250	49.08	2.28	60.60	Congo
Novaya	320	49.08	2.28	60.60	Congo
Novaya	330	37.14	-4.34	66.50	Congo
Novaya	340	23.59	-1.42	76.85	Congo
Novaya	350	15.87	-0.56	85.51	Congo
Novaya	360	8.01	-5.21	110.69	Congo
Novaya	370	4.25	-8.41	143.10	Congo

Moving plate	Age (Ma)	Latitude	Longitude	Angle	Fixed plate
Novaya	380	7.31	-11.26	142.52	Congo
Novaya	390	5.25	-12.27	143.85	Congo
Novaya	400	2.77	-11.31	137.41	Congo
Novaya	410	2.88	169.79	-127.55	Congo
Novaya	420	7.08	171.38	-104.19	Congo
Novaya	430	9.66	165.98	-87.82	Congo
Novaya	440	12.06	166.58	-82.38	Congo
Novaya	450	16.76	165.82	-70.49	Congo
Novaya	460	25.55	167.54	-55.82	Congo
Novaya	470	43.70	174.15	-43.90	Congo
Novaya	480	74.27	-168.07	-43.47	Congo
Novaya	490	77.14	32.21	-65.66	Congo
Novaya	500	64.91	30.45	-102.00	Congo
Novaya	510	64.49	7.64	-110.52	Congo
Novaya	520	65.09	-25.16	-115.19	Congo
Novaya	530	62.67	-38.71	-131.95	Congo
Novaya	540	59.19	-40.36	-147.88	Congo
Novaya	550	-18.86	24.61	147.95	Mantle
Novaya	650	-9.92	64.93	145.54	Mantle
Novaya	750	-8.59	86.72	135.34	Mantle
Siberia	250	47.59	3.10	59.38	Congo
Siberia	260	48.22	2.61	60.90	Congo
Siberia	270	48.84	2.13	60.82	Congo
Siberia	280	49.44	1.64	61.55	Congo
Siberia	290	50.23	1.07	62.42	Congo
Siberia	300	50.99	0.49	63.30	Congo
Siberia	310	51.74	-0.09	64.20	Congo
Siberia	320	52.46	-0.67	65.10	Congo
Siberia	330	39.38	-3.08	62.59	Congo
Siberia	340	22.43	4.98	67.10	Congo
Siberia	350	21.45	3.04	68.86	Congo
Siberia	360	20.90	-4.62	76.42	Congo
Siberia	370	20.47	-9.82	98.57	Congo
Siberia	380	28.43	-13.96	96.64	Congo
Siberia	390	35.05	-11.14	91.83	Congo
Siberia	400	36.84	-6.25	92.28	Congo
Siberia	410	41.82	2.43	86.66	Congo
Siberia	420	57.21	22.75	75.91	Congo
Siberia	430	68.26	50.31	64.91	Congo
Siberia	440	76.32	16.57	52.80	Congo
Siberia	450	70.32	-42.78	43.22	Congo
Siberia	460	52.14	-37.70	46.13	Congo
Siberia	470	60.25	-20.27	48.70	Congo
Siberia	480	76.95	11.23	52.64	Congo
Siberia	490	71.96	149.46	47.95	Congo
Siberia	500	61.81	145.39	43.87	Congo
Siberia	510	56.69	100.51	46.80	Congo
Siberia	520	46.16	63.47	47.50	Congo
Siberia	530	27.04	50.10	47.50	Congo

Moving plate	Age (Ma)	Latitude	Longitude	Angle	Fixed plate
Siberia	540	3.59	45.81	55.49	Congo
Siberia	550	70.10	-75.49	161.90	Congo
Siberia	560	72.76	-81.25	159.62	Congo
Siberia	570	65.92	-85.41	156.72	Congo
Siberia	580	58.29	-90.50	151.97	Congo
Siberia	650	13.31	-94.77	155.76	Congo
Siberia	750	-7.97	-98.78	152.43	Congo
India	250	29.93	42.29	-60.47	Congo
India	540	29.93	42.29	-60.47	Congo
India	550	40.11	31.71	-50.76	Congo
India	650	-8.70	54.96	-84.75	Congo
India	750	19.29	45.50	-77.42	Congo
Arabia	250	37.11	17.11	-8.56	Congo
Arabia	540	37.11	17.11	-8.86	Congo
Arabia	550	27.12	47.50	136.16	Congo
Arabia	560	26.30	49.90	129.48	Congo
Arabia	570	24.03	50.55	133.97	Congo
Arabia	580	25.36	51.53	135.70	Congo
Arabia	590	27.06	52.45	122.21	Congo
Arabia	591	26.39	52.04	128.63	Congo
Arabia	600	5.62	54.00	134.20	Congo
Arabia	602	19.06	53.78	134.70	Congo
Arabia	610	12.36	56.24	134.25	Congo
Arabia	620	10.25	62.24	106.19	Congo
Arabia	630	9.43	64.66	100.28	Congo
Arabia	650	9.37	63.71	124.70	Congo
Arabia	750	35.38	-29.84	-99.90	Congo
Taurides	250	37.07	17.13	-8.83	Congo
Taurides	540	37.07	17.13	-8.83	Congo
Alborz	250	52.83	-11.13	7.73	Congo
Alborz	260	18.37	32.21	-3.18	Congo
Alborz	270	35.34	17.69	-7.89	Congo
Alborz	540	35.34	17.69	-7.89	Congo
Afghan	250	25.23	69.03	-55.70	Congo
Afghan	260	26.61	60.32	-61.61	Congo
Afghan	270	27.04	55.58	-66.30	Congo
Afghan	280	27.08	53.73	-67.75	Congo
Afghan	290	27.09	52.84	-68.62	Congo
Afghan	540	27.09	52.84	-68.62	Congo
Himalayas	250	27.91	45.28	-58.22	Congo
Himalayas	270	28.24	44.80	-58.56	Congo
Himalayas	280	-28.88	-136.11	59.25	Congo
Himalayas	290	-29.12	-136.58	59.59	Congo
Himalayas	540	-29.12	-136.58	59.59	Congo
Pontides	250	-37.06	-162.86	8.82	Congo
Pontides	540	-37.06	-162.86	8.82	Congo
Lut	250	31.56	-105.38	-105.38	Congo
Lut	260	-30.15	-121.24	112.63	Congo
Lut	270	-29.41	-123.44	116.35	Congo

Moving plate	Age (Ma)	Latitude	Longitude	Angle	Fixed plate
Lut	540	-29.41	-123.44	116.35	Congo
Sibumasu	250	14.56	110.76	48.20	Congo
Sibumasu	260	5.02	105.57	68.20	Congo
Sibumasu	270	-1.95	-76.03	-79.45	Congo
Sibumasu	540	-1.95	-76.03	-79.45	Congo
North China	250	23.87	130.20	-71.99	Congo
North China	260	31.33	124.88	-76.30	Congo
North China	270	37.09	120.13	-87.45	Congo
North China	280	44.71	117.46	-98.11	Congo
North China	290	43.96	112.10	-103.25	Congo
North China	300	43.20	109.46	-106.39	Congo
North China	310	47.21	108.32	-110.85	Congo
North China	320	50.76	111.26	-121.28	Congo
North China	330	52.88	111.21	-122.52	Congo
North China	340	-58.02	-61.02	123.54	Congo
North China	350	57.23	122.22	-121.37	Congo
North China	360	54.77	130.04	-122.23	Congo
North China	370	54.81	149.28	-130.31	Congo
North China	380	50.98	146.36	-130.91	Congo
North China	390	52.34	145.65	-128.95	Congo
North China	400	53.08	139.49	-121.55	Congo
North China	410	55.94	130.09	-118.91	Congo
North China	420	50.14	118.18	-118.36	Congo
North China	430	44.63	110.81	-127.58	Congo
North China	440	45.01	110.02	-144.79	Congo
North China	450	46.54	113.30	-158.29	Congo
North China	460	-49.64	-58.18	161.48	Congo
North China	470	50.05	125.75	-153.16	Congo
North China	480	46.76	120.48	-144.40	Congo
North China	490	36.08	109.76	-148.18	Congo
North China	500	32.54	105.78	-151.47	Congo
North China	510	40.37	104.68	-146.81	Congo
North China	520	50.59	100.50	-153.98	Congo
North China	530	54.17	88.76	-168.61	Congo
North China	540	58.81	81.38	-175.66	Congo
North China	650	-7.58	-81.79	118.20	Congo
North China	750	24.86	87.86	-125.15	Congo
Lhasa	250	25.38	68.23	-30.37	Congo
Lhasa	260	36.14	44.61	-35.20	Congo
Lhasa	270	34.53	37.26	-43.97	Congo
Lhasa	280	30.73	41.85	-54.31	Congo
Lhasa	290	29.19	43.42	-59.60	Congo
Lhasa	540	29.19	43.42	-59.60	Congo
Lhasa	750	-4.17	-85.61	-92.25	Congo
Madagascar	250	14.74	137.62	-15.64	Congo
Madagascar	540	14.74	137.62	-15.64	Congo
Madagascar	541	-34.16	41.83	86.51	Mantle
Madagascar	550	-43.76	44.79	201.29	Mantle
Madagascar	560	-38.72	41.56	188.97	Mantle

Moving plate	Age (Ma)	Latitude	Longitude	Angle	Fixed plate
Madagascar	570	-34.18	50.71	143.45	Mantle
Madagascar	580	-24.07	53.12	130.87	Mantle
Madagascar	590	-12.87	55.41	122.46	Mantle
Madagascar	591	-49.79	88.69	-68.37	Mantle
Madagascar	600	-0.34	57.81	120.14	Mantle
Madagascar	610	14.31	61.48	120.62	Mantle
Madagascar	620	27.25	61.89	127.78	Mantle
Madagascar	621	35.43	-65.68	117.76	Mantle
Madagascar	630	42.21	61.99	139.77	Mantle
Madagascar	631	26.41	-52.94	127.39	Mantle
Madagascar	640	50.30	70.62	163.53	Mantle
Madagascar	650	54.34	80.73	188.77	Mantle
Madagascar	660	-54.96	-96.88	-192.12	Mantle
Madagascar	670	58.24	74.81	195.96	Mantle
Madagascar	680	56.21	83.63	199.90	Mantle
Madagascar	681	15.96	-28.81	179.30	Mantle
Madagascar	690	-55.63	-91.42	154.57	Mantle
Madagascar	700	57.32	79.84	-151.39	Mantle
Madagascar	701	14.74	-24.09	-176.11	Mantle
Madagascar	710	55.91	86.13	-146.73	Mantle
Madagascar	720	-55.33	-89.82	142.98	Mantle
Madagascar	722	13.85	-18.53	-174.15	Mantle
Madagascar	730	-54.44	-86.03	-221.76	Mantle
Madagascar	740	-56.22	-92.28	-225.19	Mantle
Madagascar	750	53.74	95.13	230.58	Mantle
Somalia	250	9.89	143.00	-0.22	Congo
Somalia	540	9.89	142.99	0.22	Congo
Somalia	550	-9.33	60.90	23.30	Congo
Somalia	600	-80.98	-67.41	-19.76	Congo
Somalia	650	-63.56	29.46	-48.70	Congo
Somalia	740	-25.55	58.75	-33.79	Congo
Somalia	750	-21.29	60.78	-34.35	Congo
Lake Victoria Block	250	9.89	143.00	-0.22	Congo
Lake Victoria Block	540	9.89	142.99	0.22	Congo
NW Africa	250	33.65	26.02	2.34	Congo
NW Africa	540	33.65	26.02	2.34	Congo
NW Africa	550	28.48	0.95	-19.50	Congo
NW Africa	650	-36.59	-7.31	100.67	Congo
NW Africa	750	-35.33	-16.21	156.75	Congo
NE Africa	250	40.45	-61.40	-0.70	Congo
NE Africa	540	40.41	-61.40	-0.70	Congo
NE Africa	550	5.36	-139.78	9.10	Congo
NE Africa	650	-0.62	-156.52	65.66	Congo
NE Africa	750	-3.37	-155.50	55.27	Congo
Australia	250	19.57	117.90	-56.42	Congo
Australia	540	19.57	117.90	-56.42	Congo
Australia	550	16.33	121.83	-54.50	Congo
Australia	650	-29.67	106.96	-76.75	Congo
Australia	750	10.10	104.46	-62.70	Congo

Moving plate	Age (Ma)	Latitude	Longitude	Angle	Fixed plate
Antarctica	250	10.44	148.74	-58.41	Congo
Antarctica	540	10.44	148.74	-58.41	Congo
Antarctica	550	11.16	158.76	-58.76	Congo
Antarctica	650	-21.63	152.90	-42.17	Congo
Antarctica	750	12.13	142.01	-51.91	Congo
African craton	250	-2.78	150.08	45.34	Mantle
African craton	260	-3.81	148.98	45.87	Mantle
African craton	270	7.40	-35.85	-51.90	Mantle
African craton	280	-7.21	143.43	58.41	Mantle
African craton	290	-14.93	137.70	60.97	Mantle
African craton	300	20.57	-47.73	-64.52	Mantle
African craton	310	19.53	-53.66	-67.86	Mantle
African craton	320	11.50	-60.73	-74.46	Mantle
African craton	330	7.86	-66.19	-73.18	Mantle
African craton	340	13.52	-74.58	-76.26	Mantle
African craton	350	1.55	-69.58	-72.48	Mantle
African craton	360	8.81	115.68	77.64	Mantle
African craton	370	18.89	126.95	89.51	Mantle
African craton	380	15.33	120.65	88.91	Mantle
African craton	390	-15.29	-62.94	-81.53	Mantle
African craton	400	-14.06	-67.19	-72.25	Mantle
African craton	410	-9.35	-75.71	-64.60	Mantle
African craton	420	5.99	-92.66	-67.78	Mantle
African craton	430	14.65	-107.00	-82.48	Mantle
African craton	440	9.11	-108.91	-96.15	Mantle
African craton	450	6.94	-110.79	-111.15	Mantle
African craton	460	11.07	-118.20	-124.37	Mantle
African craton	470	12.77	-115.52	-129.29	Mantle
African craton	480	18.30	-120.15	-135.48	Mantle
African craton	490	23.06	-130.91	-148.84	Mantle
African craton	500	26.66	-140.67	-154.56	Mantle
African craton	510	31.24	-144.41	-146.64	Mantle
African craton	520	30.22	-139.72	-127.55	Mantle
African craton	530	25.12	-136.31	-109.38	Mantle
African craton	540	20.18	-135.59	-94.43	Mantle
African craton	550	40.26	-124.87	-160.88	Mantle
African craton	551	35.94	-4.16	-79.25	Laurentia
African craton	560	39.78	-17.47	-65.49	Laurentia
African craton	650	-5.21	-37.25	-164.97	Laurentia
African craton	750	-19.26	-55.95	-191.95	Laurentia
Ganderia	300	32.58	64.04	57.67	Mantle
Ganderia	320	23.26	58.54	74.37	Mantle
Ganderia	340	-4.04	30.42	73.36	Mantle
Ganderia	360	-8.83	23.43	81.51	Mantle
Ganderia	380	-12.63	11.21	88.92	Mantle
Ganderia	400	-15.02	3.41	94.22	Mantle
Ganderia	420	-32.17	6.68	92.70	Mantle
Ganderia	425	-36.57	9.86	94.74	Mantle
Ganderia	430	-40.58	12.07	97.12	Mantle

Moving plate	Age (Ma)	Latitude	Longitude	Angle	Fixed plate
Ganderia	440	-38.17	12.07	101.20	Mantle
Ganderia	460	-32.45	15.13	122.20	Mantle
Ganderia	470	-27.48	16.49	123.85	Mantle
Ganderia	480	-26.98	18.25	135.29	Mantle
Ganderia	490	-29.87	2.99	143.82	Mantle
Ganderia	510	-31.24	-2.71	168.78	Mantle
Ganderia	520	-27.34	-1.11	155.96	Mantle
Ganderia	530	-22.26	-0.09	146.82	Mantle
Ganderia	540	-16.36	-0.67	142.34	Mantle
Ganderia	550	-56.32	-22.33	167.93	Mantle
Ganderia	560	-50.07	-10.88	173.61	Mantle
Ganderia	570	-46.96	0.23	169.98	Mantle
Ganderia	580	-46.11	1.81	161.98	Mantle
Ganderia	590	-45.62	2.90	158.38	Mantle
Ganderia	600	-41.16	13.91	154.52	Mantle
Ganderia	610	-39.43	16.38	149.30	Mantle
Ganderia	620	-38.09	18.46	143.31	Mantle
Ganderia	650	-26.39	25.07	109.33	Mantle
Ganderia	690	-27.73	4.90	84.26	Mantle
Ganderia	700	-26.38	22.21	84.65	Mantle
Ganderia	710	-25.74	21.48	79.89	Mantle
Ganderia	720	-23.05	39.04	82.99	Mantle
Ganderia	730	-19.44	53.00	86.10	Mantle
Ganderia	740	-16.58	64.84	92.13	Mantle
Ganderia	750	-16.34	75.00	99.74	Mantle
Pampean	250	47.56	-31.66	57.74	Congo
Pampean	300	47.47	-31.29	55.94	Congo
Pampean	540	47.46	-32.29	56.60	Congo
Pampean	550	48.46	-28.45	58.46	Congo
Pampean	560	53.56	-30.34	52.93	Congo
Pampean	570	29.18	-33.23	57.11	Congo
Pampean	600	12.25	144.81	-102.90	Congo
Pampean	610	17.43	144.02	-121.76	Congo
Pampean	650	-18.43	-36.04	146.46	Congo
Pampean	660	-19.75	-35.40	143.86	Congo
Pampean	700	-18.25	-32.99	130.90	Congo
Pampean	710	-25.02	-32.27	148.50	Congo
Pampean	720	-26.75	-31.32	153.48	Congo
Pampean	750	-22.16	-30.39	136.69	Congo
Rio de la Plata	250	47.58	-33.30	56.20	Congo
Rio de la Plata	540	47.71	-31.93	56.46	Congo
Rio de la Plata	550	46.67	-29.38	58.63	Congo
Rio de la Plata	560	32.33	-32.38	63.29	Congo
Rio de la Plata	570	24.28	-35.32	69.35	Congo
Rio de la Plata	580	15.39	-36.14	78.58	Congo
Rio de la Plata	590	10.16	-37.21	86.66	Congo
Rio de la Plata	600	5.58	-38.14	95.00	Congo
Rio de la Plata	650	-12.87	-39.32	163.85	Congo
Rio de la Plata	660	-14.47	-38.84	154.84	Congo

Moving plate	Age (Ma)	Latitude	Longitude	Angle	Fixed plate
Rio de la Plata	740	-18.95	-29.46	154.64	Congo
Rio de la Plata	750	-18.84	-28.68	155.64	Congo
Tarim	300	48.36	-6.37	65.32	Mantle
Tarim	310	47.98	-6.40	70.96	Mantle
Tarim	320	44.52	-16.69	66.10	Mantle
Tarim	330	27.49	-24.03	54.31	Mantle
Tarim	340	33.92	-9.88	61.50	Mantle
Tarim	350	23.40	-8.43	59.56	Mantle
Tarim	360	15.19	-7.59	66.33	Mantle
Tarim	370	5.96	-7.58	94.36	Mantle
Tarim	380	10.83	-9.14	89.29	Mantle
Tarim	390	7.61	-8.15	77.45	Mantle
Tarim	400	1.23	-8.14	70.85	Mantle
Tarim	410	7.13	-10.27	56.68	Mantle
Tarim	420	20.70	-27.03	38.47	Mantle
Tarim	430	37.96	-53.98	30.65	Mantle
Tarim	440	3.96	-68.42	37.50	Mantle
Tarim	450	-5.76	-63.96	50.32	Mantle
Tarim	460	-73.26	-85.55	-87.46	Mantle
Tarim	470	72.25	88.63	97.11	Mantle
Tarim	480	-66.99	-82.82	-97.83	Mantle
Tarim	490	-53.02	-60.08	-84.57	Mantle
Tarim	500	-44.47	-61.47	-91.76	Mantle
Tarim	510	-47.98	-75.01	-90.30	Mantle
Tarim	520	52.62	74.47	73.39	Mantle
Tarim	530	45.24	60.66	75.17	Mantle
Tarim	540	39.57	46.52	72.56	Mantle
Tarim	650	-6.85	-13.20	80.50	Mantle
Tarim	750	21.02	-175.31	-70.70	Mantle
SE New England	490	-26.77	5.17	159.94	Mantle
SE New England	480	-27.60	5.51	143.80	Mantle
SE New England	460	-37.31	-4.44	128.47	Mantle
SE New England	440	-34.83	8.77	95.80	Mantle
SE New England	420	-31.92	2.92	92.38	Mantle
SE New England	400	-14.87	5.40	94.28	Mantle
SE New England	380	-12.63	11.32	88.97	Mantle
SE New England	360	-8.78	22.65	81.34	Mantle
SE New England	340	-3.87	28.95	73.60	Mantle
SE New England	320	23.23	58.64	74.39	Mantle
SE New England	300	32.48	64.07	57.63	Mantle
SE New England	430	-40.46	12.37	97.36	Mantle
SE New England	450	-31.88	12.11	108.90	Mantle
SE New England	470	-28.48	-5.14	128.30	Mantle
SE New England	490	52.69	-173.27	-214.34	Mantle
SE New England	491	27.43	-173.99	-161.88	Mantle
SE New England	500	-28.55	-1.12	174.60	Mantle
SE New England	510	29.87	173.35	-171.96	Mantle
SE New England	520	28.49	170.39	-156.32	Mantle
SE New England	530	-21.23	-3.24	148.41	Mantle

Moving plate	Age (Ma)	Latitude	Longitude	Angle	Fixed plate
SE New England	540	-17.36	-7.39	145.46	Mantle
SE New England	550	-54.01	-19.38	166.33	Mantle
SE New England	560	-51.07	-23.33	174.41	Mantle
SE New England	570	-51.42	-21.59	166.86	Mantle
SE New England	580	-49.96	-15.32	160.49	Mantle
SE New England	590	-47.22	-8.17	154.53	Mantle
SE New England	600	-44.84	-4.97	147.94	Mantle
SE New England	610	-43.46	-1.38	141.71	Mantle
SE New England	620	-39.37	8.16	140.41	Mantle
SE New England	630	-34.88	15.42	132.60	Mantle
SE New England	640	-29.29	25.00	128.69	Mantle
SE New England	650	-27.29	23.33	120.22	Mantle
SE New England	660	-25.75	28.75	117.47	Mantle
SE New England	670	-24.37	33.62	114.91	Mantle
SE New England	680	-22.17	38.89	111.18	Mantle
SE New England	690	-22.07	40.24	106.75	Mantle
SE New England	700	-20.38	43.77	102.93	Mantle
SE New England	710	-18.63	48.22	100.13	Mantle
SE New England	720	-16.47	54.01	99.50	Mantle
SE New England	730	-14.33	56.59	94.64	Mantle
SE New England	740	-11.95	60.88	92.41	Mantle
SE New England	750	-9.09	63.22	88.36	Mantle

APPENDIX E

Copyright permissions for published material reproduced in this Thesis.

Copyright Clearance Center

Confirmation Number: 11317101
Order Date: 03/13/2015

Customer Information

Customer: Angeliki Papoutsa
Account Number: 3000898488
Organization: Dalhousie University
Email: angeliki_papoutsa@hotmail.com
Phone: +1 (902) 449-4907
Payment Method: Invoice

This is not an invoice

Order Details

Chemical geology

Billing Status: **N/A**

Order detail ID: 66402127
ISSN: 0009-2541
Publication Type: Journal
Volume:
Issue:
Start page:
Publisher: ELSEVIER BV
Author/Editor: EUROPEAN ASSOCIATION OF GEOCHEMISTRY

Permission Status: Granted
Permission type: Republish or display content
Type of use: Thesis/Dissertation
Order License Id: 3587080742217

Requestor type	Academic institution
Format	Print, Electronic
Portion	chapter/article
Number of pages in chapter/article	15
Title or numeric reference of the portion (s)	Chapter 1, Chapter 2, Chapter 3, Chapter 4, Chapter 5, Table1, Table 2, Table 3, Table 4, Table 5, Table 6, Table S1, Figure1, Figure 2, Figure 3, Figure 4, Figure 5, Figure 6, Figure 7, Figure 8, Figure 9, Figure 10, Figure 11
Title of the article or chapter the portion is from	Geochemical variation of amphiboles in A-type granites as an indicator of complex magmatic systems: Wentworth pluton, Nova Scotia, Canada
Editor of portion(s)	Laurie Reisberg
Author of portion(s)	Angeliki Papoutsa, Georgia Pe-Piper
Volume of serial or monograph	384
Page range of portion	120-134
Publication date of portion	2014
Rights for	Main product
Duration of use	Life of current edition
Creation of copies for the disabled	no
With minor editing privileges	no

For distribution to	Canada
In the following language(s)	Original language of publication
With incidental promotional use	no
Lifetime unit quantity of new product	Up to 499
Made available in the following markets	education
The requesting person/organization	Dalhousie University, Library and Archives Canada
Order reference number	
Author/Editor	Angeliki Papoutsa
The standard identifier	n/a
Title	The petrological evolution of the late Paleozoic A-type granites of the Cobequid Highlands, Nova Scotia
Publisher	Dalhousie University, Library and Archives Canada
Expected publication date	May 2015
Estimated size (pages)	285

Note: This item was invoiced separately through our **RightsLink service.** More info **$ 0.00**

Total order items: 1 **Order Total: $0.00**

11 August 2015

Angeliki Papoutsa
Department of Earth Sciences
Dalhousie University
Halifax, Nova Scotia
Canada

Dear Angeliki,

Permission is granted for your use of the following paper, published in the December 2014 issue of *The Canadian Mineralogist*, in your thesis at Dalhousie University:

Papoutsa, A. and Pe-Piper, G. (2014) Variation of REE-hydrothermal circulation in complex shear zones: The Cobequid Highlands, Nova Scotia. *Canadian Mineralogist* **52(6)**, 943–968.

Proper citation of where the paper was originally published is all that is required.

Best regards,

Mackenzie Parker

Managing Editor
The Canadian Mineralogist